PAUL SCHERRER INSTITUT

rec'd Jan 96

PSI Proceedings 95-02
November 1995
ISSN 1019-6447

ICANS-XIII

Proceedings of the Meetings ICANS-XIII and ESS-PM4 – Volume I –

Villigen PSI, Switzerland, October 11 - 14, 1995 and
Weinfelden, Switzerland, October 16 - 19, 1995

PAUL SCHERRER INSTITUT

PSI-Proceedings 95-02
November 1995

ICANS-XIII

Joint Proceedings of the
13th meeting of the
International Collaboration on Advanced Neutron Sources
held at Paul Scherrer Institut
October 11 - 14, 1995
and the
4th Plenary Meeting of the
European Spallation Source Project, ESS,
held at Weinfelden
October 16 - 19, 1995

Volume I

Editors

G.S. Bauer
R. Bercher

Paul Scherrer Institut, CH-5232 Villigen PSI

PSI-Proceedings 95-02
ISSN 1019-6447
November 1995

Photographs:
A. Lehner (cover)
A. Müller
G. Bauer

This publication is available from:
Paul Scherrer Institut, PSI
Renate Bercher
Würenlingen and Villigen
CH-5232 Villigen PSI
Switzerland
Telephone: +41 56 310 3402
Telefax +41 56 310 3131
E-mail Renate.BERCHER@PSI.CH

PREFACE

It was a pleasure to host ICANS-XIII at the Paul Scherrer Institut from October 11 to 14, 1995. It was particularly rewarding to see that, besides the old friends we have shared our interest in new neutron sources with for many years, several young people have entered the scene and were able to make important contributions to the field.

The topic of new sources could be seen to be as acute as ever. Several important events since ICANS-XII made this meeting a particularly exciting one: The AUSTRON-study has been completed and both, ANL and LANL have produced impressive documents on upgrade options for their respective facilities. Crucial decisions were taken in Japan concerning the future of the KEK-accelerating complex which lead to a complete rethinking of the KENS-II-project. Also the European Spallation Source Study had finally received funding from the EU which gave the project work a significant boost. To acknowledge this and to make information exchange as intense as possible without requiring excessive duplication of presentations, ICANS-XIII and the 4th General Meeting of the ESS-project group were moved close together (in time and location). In this spirit it was decided to make these proceedings joint ones between ICANS-XIII and ESS-PM4 in order to give everyone the opportunity to have his paper included, irrespective of where it was presented.

The new interest in the long pulse option which has developed steadily since ICANS-XII reflected itself in a significant number of contributions to this topic, not all of which were received in written form, however.

Finally, the probably most decisive event, the negative decision on the ANS project in the US, which deprived the world neutron scattering community of its hope to have a next generation neutron source soon, had an immediate effect also on the ICANS-group of laboratories:
Oak Ridge National Laboratory as the preferred alternative site for the US spallation neutron source project study has applied and was warmly welcomed as a new member of the collaboration. We all wish them success in the duty they have taken on and will be happy to share our knowledge and experience in very possible way.

Last but not least, I would like to thank all the authors of the papers in these proceedings for complying with the deadlines we had to set in order to ensure speedy publication. The work presented at the ICANS-meetings traditionally represents latest results, often forwarded for discussions and critism. This is only possible, if the written documents become available soon after the meeting. We made every effort to accomplish this. The papers are published unreviewed and their form and contents are exclusively in the responsibility of the authors. Thanks again, for the co-operation!

Günter Bauer
Head
Spallation Neutron Source Division
Paul Scherrer Institut
November 2, 1995

ICANS XIII

Groups/Topics/Time zone/Papers/ Chairman

Session	Topics/Groups	Date	Start	End	Duration	Papers	min/p	Chairperson	Local assistan	Tel. Int.
N	News from existing ICANS facilities	11.Oct				5		Bauer Watanabe		
O1	Ongoing projects	12.Oct	08,00	10,30	02,30	5		Ikeda		
O2	Ongoing projects	12.Oct	11,00	12,30	01,30	5		Carpenter		
O3	Ongoing projects	12.Oct	15,30	16,30	01,00	2		Pynn	Y.Takeda	3568
R	Review talks					3		Furrer Taylor Aksenov		
G1A	Target-moderator system : Neutronics	13.Oct	10,30	12,30	02,00	6	20,00	Russell	E.Lehmann	2963
G1B	Target-moderator system : Target concepts	13.Oct	15,30	18,30	03,00	9	20,00	Filges	F. Atchison	3256
G1C	Target-moderator system : Moderators general	11.Oct	17,50	18,30	00,40	2	20,00	Broome	W.Wagner	2517
G1D	Target-moderator system : Cold moderators	13.Oct	08,00	10,00	02,00	6	20,00	Broome	W.Wagner	2517
G2A	Scattering methodology : Instrument components	13.Oct	08,00	10,00	02,00	6	20,00	Conrad	J. Schefer	3066
G2B	Scattering methodology : Elastic scattering	13.Oct	15,30	18,00	02,30	7	21,26	Cser	D.Clemens	2925
G2C	Scattering methodology : Inelastic scattering	13.Oct	10,30	12,30	02,00	5	24,00	Steigenberger	J. Mesot	4029
G3	Science in Q'w?	13.Oct	08,00	10,00	02,00	4	30,00	Arai	A. Dönni	4007
G4A	Source concepts : Instrumentations	13.Oct	10,30	12,30	02,00	5	24,00	Johnson	W. Marti	4044
G4B	Source concepts : Source	11.Oct	15,30	17,50	02,20	7	20,00	Hjelm	M. Gutmann	2092
T3	Fourier and correlation techniques	11.Oct	15,30	17,50	02,20	6	23,20	Aksenov	G. Boettger	2091
T4	Computational methods	11.Oct	15,30	17,50	02,20	6	23,20	Seeger	P. Allenspach	2527
S1	Summary : G1, G4, T4	13.Oct	08,00	10,00	02,00			Appleton		
S2	Summary : G2, G3, T3	13.Oct	10,30	12,00	01,30			Leadbetter		
S	Conference Summary : Carpenter	13.Oct	12,00	13,00	01,00			Fischer		
P	Poster	11.Oct	08,00			7				

Table of Contents

Volume I

Session Summaries 1

S-1 Science with Neutrons 3
J. Arai

S-2 Methods in Inelastic Scattering 5
L. Cser

S-3 Instrumentation for Inelastic Scattering Experiments 7
U. Steigenberger

S-4 Fourier RTOF Diffractometers 9
V. Aksenov

S-5 Target-Moderator-System: Target Concepts 11
D. Filges

S-6 Target-Moderator-Systems: Components 13
T. Broome

S-7 Computational Methods 15
P.A. Seeger

S-8 Source Concepts 17
R. Hjelm

S-9 Target Moderator System-Neutronics 19
G.J. Russell

S-10 Scattering Methodology: Instrument components 20
H. Conrad

General 22

G-1 ICANS on the World Wide Web 22
J.M. Carpenter, J.P. ~~Harnmonds~~ Hammonds

News from Existing ICANS-Facilities 29

N-1 ISIS: The First 10 Years 31
A. Taylor

N-2 News From IPNS 35
B.S. Brown

N-3 Progress On The PSR/LANSCE Upgrade 44
R.J. Macek

N-4 News From KENS 52
H. Ikeda

N-5 News From IBR-2 56
V.L. Aksenov

N-6 Spallation Neutron Sources at the INR RAS: Present Status and Prospects 63
Y.Y. Stavissky

N-7 SINQ A Continuous Spallation Neutron Source (An Approach to 1 Mwatt of Beam Power) 75
W.E. Fischer

Instruments, Methods and Components 85

I-1 Setup and Operation Mode of a Pulsed White Beam Angle-Dispersive ToF-Texture-Diffractometer 87
W. Schäfer, E. Jansen, W. Kockelmann, H. Tietze-Jaensch, K. Will

I-2 Neutron Time-of-Flight Diffractometer for Investigations of Microsamples under High External Pressure 93
V.L. Aksenov, A.M. Balagurov, S.L. Platonov, B.N. Savenko, D.V. Sheptyakov, V.P. Glazkov, V.P. Naumov, V.A. Somenkov, G.F. Syrykh

I-3 The New Small-Angle Diffractometer SAND at IPNS 99
R.K. Crawford, P. Thiyagarajan, J.E. Epperson, F. Trouw, R. Kleb, D. Wozniak, D. Leach

I-4 Novel Tendencies in Developing Small-Angle Neutron Scattering Methods for Studying the Structure of Biological Macromolecules 118
I. Serdyuk

I-5 SURF - A Second Generation Neutron Reflectometer 123
D.G. Bucknall, J. Penfold, J.R.P. Webster, A. Zarbakhsh, R.M. Richardson, A. Rennie, J.S. Higgins, R.A.L. Jones, P. Fletcher, R.K. Thomas, S. Roser, E. Dickinson

I-6 Evaluation of ROTAX 130
H. Tietze-Jaensch, W. Schmidt, R. Geick, G. Will

I-7 FOCUS: A New Time of Flight Spectrometer at the Neutron Spallation Source SINQ/CH 150
J. Mesot, S. Janssen, L. Holitzner, M. Prager, D. Richter, R. Hempelmann

I-8 Inelastic Neutron Scattering Spectrometer for the IN-06 Neutron Source at the Moscow Meson Factory 155
V.Y. Kazimirov, A.V. Belushkin

I-9 Future Opportunities and Present Possibilities for Coherent Inelastic Single Crystal Measurements on Pulsed Neutron Sources 164
M. Hagen, U. Steigenberger, C. Petrillo, F. Sacchetti

I-10 Pulsed Magnetic Fields and Pulsed Neutron Sources 164
U. Steigenberger, K. McEwen

I-11 Time Collimation for Elastic Neutron Scattering at a Pulsed Source 165
V.L. Aksenov, Yu.V. Nikitenko

I-12 Deconvoluting Source Pulse Broadening in Pulsed Source Time of Flight Measurements 175
J.M. Carpenter

I-13 Improvements in Resolution Calculation for Triple Axis and Time-of-Flight 184
W. Schmidt, H. Tietze-Jaensch, R. Geick, H. Grimm, G. Will

I-14	The MCLIB Library: Monte Carlo Simulation of Neutron Scattering Instruments *P.A. Seeger*	194
I-15	Development of the FLNP Measurement- and Computational Complex *Yu.A. Astakhov, A.A. Bogdzel, F.V. Levchanovsky, B. Michaelis, V.E. Novozhilov, A.I. Ostrovnoy, V.I. Prikhodko, V.E. Rezaev, V.E. Sirotin, G.A. Sukhomlinov, Yu.A. Volkov*	213
I-16	Principles of Reverse Time of Flight Method and Fourier Technique *P. Hiismäki*	228
I-17	Performance of the High Resolution Fourier Diffractometer at the IBR-2 Pulsed Reactor; Latest Results *V.L. Aksenov, A.M. Balagurov, V.A. Trounov, P. Hiismäki*	235
I-18	The Fourier RTOF Neutron Diffractometer FSS at the 5 MW Research Reactor FRG-I *H.G. Priesmeyer*	240
I-19	M.SFINKS Diffractometer at the Gatchina Reactor *V.A. Trounov*	247
I-20	Some Pecularities of RTOF Method and Calibration of Diffratometer "MINI-SFINKS" *D.Y. Chernyshov*	261
I-21	Wide Band Devices *L. Cser*	267
I-22	Morphology of Glass Surfaces: Influence On the Performance of Supermirrors *P. Böni, D. Clemens, H. Grimmer, H. Van Swygenhoven*	279
I-23	Neutron Composite Germanium Monochromators for Diffraction Instruments at SINQ *J. Schefer, S. Fischer, M. Medarde, R. Thut, M. Koch, P. Fischer, U. Staub, A. Dönni, G. Böttger, M. Horisberger*	288
I-24	Julios Detectors Combined to a PC-Based Data Acquisition System *E. Jansen, W. Schäfer, G. Will, R. Engels, R. Reinartz, K.D. Müller*	294
I-25	Proposal for a 30-T Pulsed Magnet Suitable for Neutron Scattering Experiments *R.A. Robinson, Y.M. Eyssa, H.J. Schneider-Muntau, H.J. Boenig*	300
I-26	A User-Friendly, Graphical Interface for the Monte Carlo Neutron Optics Code MCLIB *T. Thelliez, L. Daemen, P.A. Seeger, R.P.Hjelm*	307
I-27	Remanent Multilayers for Polarized Neutron Instrumentation *D. Clemens, W. Hahn, A. Vananti, P. Schubert-Bischoff, P. Böni, M. Horisberger*	312

The Long Pulse Option 321

L-1 Performance of Long-Pulse Source Reference Target-Moderator-Reflector Configurations 323
E. Pitcher, G. Russell, P.A. Seeger, P.D. Ferguson

L-2 The Performance of Neutron Spectrometers at a Long-Pulse Spallation Source 330
R. Pynn, L. Daemen

L-3 Instrument Options for Long Pulse Neutron Sources 339
G.S. Bauer

L-4 On Proton Pulse Lengths and Rep Rates with Emphasis on SANS 355
H. Conrad

L-5 Small-Angle Scattering Instruments on a 1 MW Long Pulse Spallation Source 370
G.A. Olah, R.P. Hjelm, P.A. Seeger

L-6 The Performance of Reflectometers at Continuous Wave and Pulsed-Neutron Sources 381
M.R. Fitzsimmons, R. Pynn

L-7 Monte Carlo Study of the Performance of a Time-of-Flight Multichopper Spectrometer 388
L.L. Daemen, J. Eckert, R. Pynn, P.A. Seeger

L-8 Complementarity of Long Pulse and Short Pulse Spallation Sources 400
F. Mezei

Volume II

Targets, Moderators and Handling Devices 429

T-1 Computation Methods for Neutron, Heat and Radiation Damage Properties of Pulsed Neutron Sources 431
A.V. Dementyev, S.G. Lebedev, O.N. Smirnova, N.M. Sobolevsky, Y.Y. Stavissky

T-2 Measurements of Spallation Neutrons from a Thick Lead Target Bombarded with 0.5 and 1.5 GeV Protons 442
S. Meigo, H. Takada, S. Chiba, T. Nakamoto, K. Ishibashi, N. Matsufuji, K. Maehata, N. Shigyo, Y. Wakuta, Y. Watanabe, M. Numajiri

T-3 Multiplying Target for a High-Intensity Spallation Neutron Source 454
V.G. Miroshnichenko, S.F. Sidorkin, Y.Y. Stavissky, V.F. Kolesov, E.P. Shabalin, Y.N. Likhachev

T-4 Tungsten and Uranium Targets for the Moscow Meson Factory 461
A.V. Dementyev, V.G. Miroshnichenko, S.F. Sidorkin, N.M. Sobolevsky, Y.Y. Stavissky, I.I. Konovalov, A.A. Maslov, I.T. Tretyakov, V.I. Trushkin, A.D. Rogov

T-5	The AUSTRON-Target: The Neutron Flux of Decoupled and Poisoned Moderators *G. Muhrer, W. Ninaus, E. Schachinger*	480
T-6	Radioactive Halogen Yields from the Tungsten Target Irradiated by High-Energy Protons *S.V. Ignatiev, D.V. Pankratov, E.I. Yefimov*	487
T-7	Coupled Moderator Neutronics *G.J. Russell, E. Pitcher, P. Ferguson*	495
T-8	Reference Moderator Calculated Performance for the LANSCE Upgrade Project *P. Ferguson, G.J. Russell, E. Pitcher*	510
T-9	Present State of the ESS Tantalum-Target *B. Guttek*	518
T-10	Neutronics Studies for the ESS Source *D.J. Picton, T.D. Beynon, T.A. Broome*	522
T-11	Nuclear Studies of Different Target Systems for the European Spallation Source (ESS) *D. Filges, R.D. Neef, H. Schaal*	537
T-12	Mercury as a Target Material for Pulsed (Fast) Spallation Neutron Sources *G.S. Bauer*	547
T-13	On the Pressure Wave Problem in Liquid Metal Targets for Pulsed Spallation Neutron Sources *K. Skala, G.S. Bauer*	559
T-14	Thermal Hydraulics of the ESS Liquid Metal Target *B.L. Smith*	577
T-15	Experience With ISOLDE Molten Metal Targets at the CERN-Booster *J. Lettry, R. Catherall, P. Drumm, A. Evensen, O. Jonsson, E. Kugler, J. Obert, J.C. Putaux, J. Sauvage, H. Ravn, M. Toulemonde*	595
T-16	Suitability of Steels as ESS Mercury Target Container Materials *Y. Dai*	604
T-17	Water/Monel Heat Pipes for Cooling of Liquid Metal Targets for SINQ and ESS *M.T.North, J.H. Rosenfeld, D.B. Sarraf, G.S. Bauer, Y. Takeda*	623
T-18	Prospects for Targets and Methane Moderators at ISIS *T.A. Broome*	632
T-19	A Pelletized Solid Methane Moderator for a Short Pulsed Neutron Source *A.T. Lucas, G.S. Bauer, C.D. Sulfredge*	644

T-20 Further Optimization of Coupled Liquid-Hydrogen Moderator for Intense Pulsed Neutron Source 654
Y. Kiyanagi, Y. Ogawa, N. Kosugi, H. Iwasa, M. Furusaka, N. Watanabe

T-21 Recent Progress in Developing High-Efficiency Cryogenic Moderators 659
N. Watanabe, Y. Kiyanagi, M. Furusaka

T-22 High-Efficiency Cryogenic Moderator System for Short Pulse Cold-Neutron Use 666
Y. Kiyanagi, N. Kosugi, Y. Ogawa, H. Iwasa, F. Hiraga, M. Furusaka, N. Watanabe

T-23 Supply System for Cold Neutron Sources for the ESS Proiect 672
K. Stendal

T-24 Handling Devices for the Beam Port- and Cold Moderator Inserts of SINQ 688
W. Wagner, J. Ehrat

T-25 Examination of Disks from the IPNS Depleted Uranium Target 697
R.V. Strain, J.M. Carpenter

T-26 Target and Structural Materials Under Dual Beam Irradiation 707
E. Camus, N. Wanderka, H. Wollenberger

Accelerator Systems and Components 715

A-1 The Los Alamos Long Pulse Spallation Source Driver 717
A.J. Jason

A-2 Moscow Meson Factory Linac for the Pulsed Neutron Source 724
L.V.Kravchuk

A-3 High Current Ion Source Development at Frankfurt 726
K. Volk, H. Klein, A. Lakatos, A. Maaser, M. Weber

A-4 LEBT Design Studies for ESS 732
J. Pozimski, P. Groß, R. Dölling, K. Reidelbach, H. Klein

A-5 Chopping- and Funneling-Studies for ESS at Frankfurt 736
J. Madlung, A. Firjahn-Andersch, A. Schempp

A-6 Recent Development of a Closed Orbit Monitor System in the KEK Booster Synchrotron 740
H. Someya, D. Arakawa, J. Kishiro, I. Yamane

A-7 FFAG Options for Spallation Neutron Sources 745
S. Martin, P.F. Meads, E. Zaplatine, K. Ziegler, R.L. Kustom

A-8 Pulsed Spallation Neutron Source with an Induction Linac and a Fixed-Field Alternating-Gradient Accelerator 750
A.G. Ruggiero, G.S. Bauer, A. Faltens, R.L. Kustom, S.A. Martin, P.F. Meads, E. Zaplatin, K. Ziegler

A-9 A 10-GeV, 5- MW Proton Source for a Pulsed Spallation Source 758
Y. Cho, Y.C.Chae, E. Crosbie, H. Friedsam, K. Harkay, D. Horan, R. Kustom, E. Lessner, W. McDowell, D. McGhee, H. Moe, R. Nielsen, G. Norek, K.J. Peterson, K. Primdahl, Y.L. Qian, K. Thompson, M. White

Project Studies 775

P-1 Feasibility Study for the IPNS Upgrade, A 1MW Pulsed Spallation Neutron Source - Target Stations 777
J.M.Carpenter

P-2 Feasibility Study of a 1- MW Pulsed Spallation Source 789
Y. Cho, Y.C. Chae, E. Crosbie, H. Friedsam, K. Harkay, D. Horan, S. Kim, R. Kustom, E. Lessner, W. McDowell, D. McGhee, F. Mills, H. Moe, R. Nielsen, G. Norek, K.J. Peterson, K. Primdahl, A. Rauchas, K. Symon, K. Thompson, M. White

P-3 A Proposal for a Long Pulse Spallation Source at Los Alamos National Laboratory 798
R. Pynn, D. Weinacht

P-4 BNL Feasibility studies of spallation neutron sources 802
Y.Y. Lee, A.G. Ruggiero, A. Van Steenbergen, W.T. Weng

P-5 Status of Pulsed Spallation Neutron Source Target Work at Brookhaven National Laboratory 808
H. Ludewig, M. Todosow, J. Powell

P-6 Status of the Oak Ridge Spallation Neutron Source (ORSNS) Project 814
B. Appleton

P-7 The European Spallation Source (ESS) Study 819
H. Lengeler

P-8 Status of the AUSTRON-Project 831
M. Schuster, P. Bryant

P-9 Current status of JHP N-arena 836
M. Furusaka, H. Ikeda

P-10 Use of Cold Source and Large Reflector Mirror Guide for Neutron-Antineutron Oscillation Search (Proposal) 843
Yu. Kamyshkov, W. Bugg, H. Cohn, G. Condo, Yu. Efremenko, S. Lamoreaux, R. Lillie, F. Plasil, S. Raman, M. Rennich, K. Shmakov, R. Wilson, G. Young

Our Sponsors 851

Q-1 Cilas 853

Q-2 Descote S.A. 854

Q-3 Helbling Technik AG 855

Q-4 KIWI Systemingenieure und Berater AG 856

Q-5 Linde Kryotechnik 857

Q-6	Loosli Formtech AG	858
Q-7	Noell GmbH	859
Q-8	Pier-Armaturen GmbH	860
Q-9	Prophysik AG	861
Q-10	Schär Engineering AG	862
Q-11	Sulzer Chemtech	863
Q-12	Tensol	864
Q-13	VAT Vakuumventile AG	865
Q-14	Von Roll	866
Q-15	Romabau AG	867
Q-16	Alcatel Kabel AG & Co	868
Q-17	Daimler Benz Aerospace, Dornier	869
Q-18	Alusuisse Road & Rail AG	870
Indices		871
	List of Authors	873
	List of Keywords	877
List of Participants		883
	ICANS-XIII	885
	ESS-PM4	893

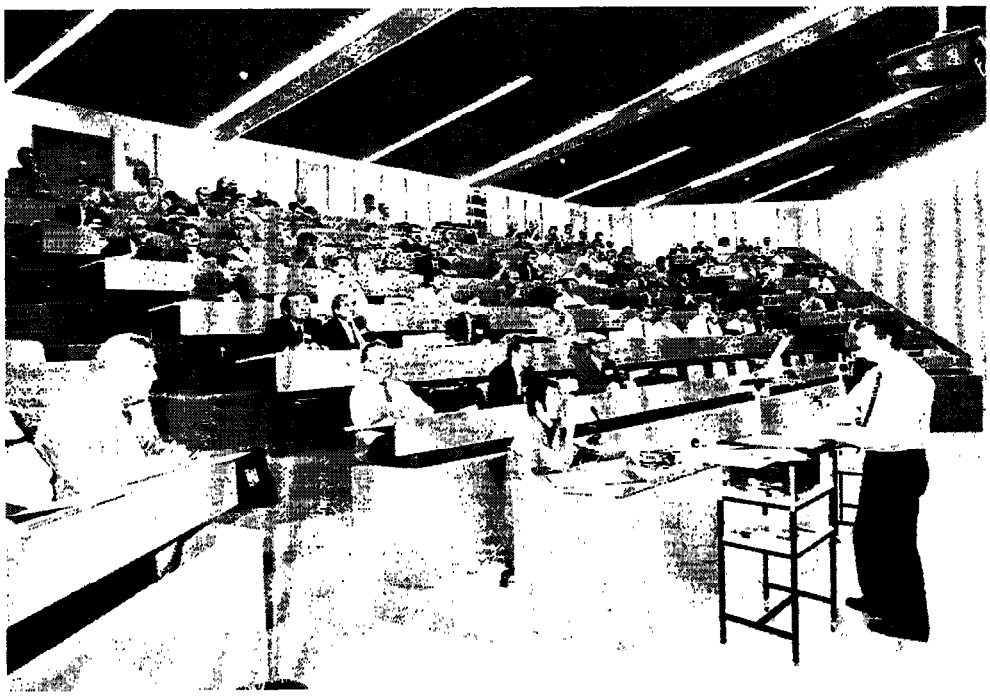

Session Summaries

ICANS-XIII
13th Meeting of the International Collaboration on
Advanced Neutron Sources
October 11-14, 1995
Paul Scherrer Institut, 5232 Villigen PSI, Switzerland

SCIENCE WITH NEUTRONS

Masatoshi Arai
Kobe University, Department of Physics, 1-1 Rokkodai, Nada, 657 Kobe, Japan

In this session we had five talks all together. The first two talks were on scientific results from SANS. The talk by R. Hjelm et al. (LANL) was on an industrial application of SANS. They studied the microscopic structure of carbon black in mobile tires. They found that the carbon black particles of several 10 nm, which have graphitic carbon shell with amorphous carbon in it, aggregate together by strong covalent bonds and form a one dimensional rod of several 100 nm. This kind of basic structural study on consuming goods is a promising demonstration of industrial use of neutron scattering and will give some guidance in improving them and to become more economical.

I. Serdyuk et al. (INR) developed clever ideas on the contrast variation method by introducing fractional hydrated and dehydrated substitution, so called triple level isotopic substitution. By this method it can be possible to extract single particle structure without the particle-particle interference term. They demonstrated a successful example of the observation of the structure of the core RNA only in 50S proteins.

The third talk was given by Y. Kamyshkov (ORNL) who talked about experiments to observe a possible neutron-antineutron transition. Because the characteristic transition time is so long, $\sim 3 \times 10^8$ s, the key issue on this kind of research is to make neutron flux as high as it can possibly be. They proposed a sort of focusing mirror guide so as to have the focal point at the detector surface 150 meters away from the reactor core, giving a 10'000 times enhancement in the neutron flux. He also emphasized to have colder neutron source in order to have more efficiency on the proposed mirror.

U. Steigenberger (RAL) summarized the kind of single crystalline excitation measurements that have been performed so far in pulsed neutron sources. In the early stage of history of pulsed neutrons, people did not admit any advantage on this kind of study. However, large arrays of detectors for TOF-type spectrometer together with rapid increase of computing power has made it possible to observe S(Q, E) in a wide range of the Q - E space simultaneously. Now it has become possible to obtain a constant-E and -Q scan in the computer memory if we wish. She raised future challenges for TOF spectrometer as follows: 1) high resolution capability for small energy transfer, 2) dispersion curve measurement of complex systems, 3) polarization analysis and 4) extremely high intensity spectroscopy.

The final talk was given by M. Johnson (RAL) on a new figure-of-merit (FOM) of instruments, which is INFORMATION. He gave a formalism of the INFORMATION by taking into account intensity, resolution, dynamic range etc. He showed how the INFORMATION of typical instruments develops with measuring time and he discussed its importance on designing and optimizing an instrument.

ICANS-XIII
13th Meeting of the International Collaboration on
Advanced Neutron Sources
October 11-14, 1995
Paul Scherrer Institut, 5232 Villigen PSI, Switzerland

METHODS IN ELASTIC SCATTERING

L.Cser
Research Institute for Solid State Physics, H-1525, Budapest, P.O.B. 49., Hungary

The session consisted of seven talks devoted to very different topics. The common essence of the talks I would distillate as follows:

Fundamental remarks

1. There is a continuous growth of interest in small-angle scattering and in reflectometry. (To my opinion this tendency remains valid at least for the next ten years).

2. The time-of-flight methods used at the pulsed source are incredibly efficient for carrying out elastic scattering measurements.

3. Proper instrument design even at modest flux allows to carry out unique investigations.

The most remarkable experimental results

- thanks to the methodical efforts the minimum size of the samples under investigation now varies between 20 and 100 mg, which makes it possible to investigate very expensive and tiny pieces of matters like high-T_c superconductor crystals, fullerenes, etc. (J. Jorgensen, ANL);
- real time experiments were done studying the intercalation kinetics of inert gases in C_{60} with characteristic measuring times from 5 minutes up to 24 hours (J. Jorgensen, ANL);
- a large variety of surface phenomena was studied on the new reflectometer SURF which has five times higher intensity at the sample position then the CRISP machine (D.Bucknall, RAL), e.g.:
  - Tris-chromophore oligomer LB films;
  - Thin PS film stabilized by a high molecular weight monofunctional telechelic PS;
  - Buried melt interfaces (amorphous PS and crystalline PE copolymers);
  - Time and pH dependence of the dichain cationic surfactant hydrolysis;
  - SURF will be potentially the most attractive facility for surface chemistry investigations;
- by the use of the upgraded QENS inverse geometry spectrometer the quasi elastic patterns can be investigated over almost unlimited Q-range, with resolution about 70 μeV. Amongst others the motion of the hydrogen in Cs-graphite intercalate was studied (F.Trouw, ANL);
- phase transitions in mercury High-T_c and in KNO_3 were observed. at relatively low pressure (6 kbar, J. Jorgensen, ANL) and at higher one (3 GPa, D.Sheptyakov, JINR);
- "in situ" investigations of the behaviour of High-T_c superconductors under high pressure, e.g., mercury-HTSC (J. Jorgensen, ANL).

Methodical improvements

The physical results enumerated above were obtained thanks to application of many methodical tricks such as:

- increase of the flux on the sample using focusing collimators or/and curved focusing supermirrors; supermirror neutron guides (ANL, RAL);
- increase of cold neutron flux installing cold moderators (solid methane, ANL);
- increased the efficiency of data collection by the use of large area detectors (all labs.);
- optimization of instrument performance (ANL, JINR);
- applying better data reduction methods (Rietveld refinement, ANL, RAL, JINR);
- the wide variety of the sample environment (SURF in RAL);
- decrease of the background (!)
  - MgO filter for fast neutrons (ANL);
  - curved guides (JINR);
  - focusing collimators (ANL);
  - improving the shielding of the sample environment (ANL);
- these improvements gave rise to the considerable widening of the scattering intensity range (up to 5 order) and the range of the momentum transfer down to $2*10^{-3}$ Å $^{-1}$ and up to tenths of Å^{-1}.
- Involving the high pressure into the arsenal of external parameters a wide area of new phenomena becomes accessible.

Conclusions

Although the talks did not deal with the far future projects, we can deduce from the experience of these works many important messages for the future instrumentation programmes:

- Think about the best performance of the instrument!
- Be careful with the background! (Remember: the largest amount of the background originates from the your own instrument, including the sample!).
- Do less, but better!

ICANS-XIII
13th Meeting of the International Collaboration on
Advanced Neutron Sources
October 11-14, 1995
Paul Scherrer Institut, 5232 Villigen PSI, Switzerland

INSTRUMENTATION FOR INELASTIC SCATTERING EXPERIMENTS

U. Steigenberger

ISIS Facility, Rutherford Appleton Laboratory, CCLRC, Chilton, Didcot, UK

This session was proof that the development of instrument and techniques at neutron sources is alive and well and the plans for the next generation instruments are showing an increased degree of sophistication. A Belushkin (Dubna) started this session with a brief guided tour of the IBR-2 spectrometer suite comprising the direct geometry spectrometer DIN and the two inverted geometry spectrometer KDSOG-P and NERA-P and the related scientific activities. He also described the planned update of the NERA-P instrument with supermirrors to enable full polarisation analysis.

H Tietze-Jaensch (ISIS, KFA Jülich) then presented the proof that longitudinal scans can be performed with the ambitious ROTAX spectrometer. ROTAX uses a non-uniformly rotating analyser crystal synchronised to ISIS and a linear position sensitive detector. The development of the sophisticated motor control hardware and software is now finished and demonstration experiments have been performed. A proposal was put forward for a ROTAX mark II version located at a 30 m guide on a 10 Hz source. This would allow to run the analyser motor and its control electronics under much less severe conditions and increase therefore the reliability and flexibility of the whole system and open up new opportunities.

J Mesot from the PSI/University of Saarbrücken Team presented the design for the time-of-flight spectrometer FOCUS which is being built at SINQ. The distance of its double focusing monochromator from the supermirror guide end is variable and thus will allow to operate the instrument either in time focused (TF) or monochromator focused (MF) mode. In MF mode FOCUS will give good resolution and good intensity over a wide wave length band and in TF mode it will have 70% of the intensity of IN6 at equal resolution. The use of a second chopper will make it possible to select higher order reflections from the monochromator (graphite or mica) and thus increase further the energy resolution.

V Kazimirov presented plans for a high intensity crystal analyser spectrometer for spectroscopic studies - MAINS - at the spallation neutron source at the Moscow Meson factory. The design is based on the proposed upgrade of the TFXA spectrometer at ISIS and involves two full circle analyser banks in transmission and reflection geometry together with two ring detector arrays. Careful resolution considerations suggest that employing 2 mm thick scintillator detectors rather than 8 mm diameter ^{3}He detector tubes will improve the spectrometer resolution.

F Mezei presented a comparison of crystal monochromators versus time-of-flight (tof) monochromators for use on reactor and long pulse spallation sources. For example, a tof monochromator on a triple-axis spectrometer , combined with a number of analyser crystals and a position sensitive detector can provide a whole set of constant-Q scans simultaneously, instead of only a single one (see also the RITA project in Risø). By installing a second fast chopper close to the sample with the frequency being a multiple integer of the monochromating chopper, a set of short pulses with different wavelengths can be obtained leading to a repetition rate multiplication.

ICANS-XIII
13th Meeting of the International Collaboration on
Advanced Neutron Sources
October 11-14, 1995
Paul Scherrer Institut, 5232 Villigen PSI, Switzerland

FOURIER RTOF DIFFRACTOMETERS

Victor L.Aksenov
Frank Laboratory of Neutron Physics, JINR, Dubna 141980 Russia

Structural investigations of matter can be performed effectively by thermal neutron scattering using a time-of-flight (TOF) diffractometer which for the first time was realized by B.Buras et al. at the steady state reactor in Warsaw in 1966 and at the IBR pulsed reactor in Dubna in 1964. A conventional TOF diffractometer at a pulsed neutron source with a narrow neutron pulse can provide high resolution at a reasonable neutron flux on the sample. In the case of a steady state neutron source or a pulsed neutron source with a large (> 100 μs) neutron pulse duration conventional TOF diffractometry is not an effective way of using the available neutron flux. In this case a Fourier chopper can be applied to provide a more economical use of available neutron fluxes without loss in resolution.

General ideas of neutron Fourier diffractometry were considered by J.F.Colwel, P.H.Miller and W.L.Whittemore in 1968. This technique involves neutron beam modulation by rotating a disk with a pattern of alternating neutron absorbing and neutron transparent slits which ensures little loss in neutron intensity. In this case, spectrum refinement requires exact knowledge of the phase of the chopper at the time the neutron wave passes through it. Solution of this problem in the form of the reverse TOF method (RTOF method) was proposed by P. Hiismäki in 1972.

The basic idea of the RTOF method is to check, for each detected neutron, whether certain postulated neutron histories have a high or low probability of occurrence on the basis of a knowledge of the actual state of the source or of the time-dependent selectors installed on the flight path. Because the detection of a neutron takes place at the very end of its flight, checking must extend from the instants of the immediate past all the way to the longest TOF expected. Therefore, the history of the state of the source and of the neutron selectors must be made available as contiuously updated arrays for real time classifications between the high or low probability histories. Such arrays are conventioanlly obtained from discrete electronic correlators which are essentially the time-shift registers provided with parallel outputs for every time channel.

The RTOF method was demonstrated at the low power steady state reactor of VTT in Espoo, Finland in 1975. In 1984, the first Fourier RTOF diffractometer, mini SFINKS, was constructed at the 16 MW reactor of PNPI in Gatchina, Russia, in collaboration with a group from Finland. The experience of the Gatchina group was utilized at the 5 MW reactor of GKSS in Geesthacht, Germany, where a specialized Fourier Strain Spectrometer (FSS) was constructed in 1988. A basic step forward was the construction of the HRFD high resolution Fourier diffractometer at the IBR-2 high flux pulsed reactor in Dubna, Russia. It was the first implementation of such a diffractometer at a pulsed source with a relatively long pulse. The

IBR-2 reactor is the most intense pulsed source in the world with a peak flux of 10^{16}n/cm^2/s and pulse width of 320 μs for thermal neutrons.

To illustrate the gist of the Fourier RTOF method, let us consider the spatial resolution of the TOF diffractometer

$$R = \Delta d/d = [(\Delta t/t)^2 + (\Delta\theta/tg\theta)^2]^{1/2},$$

where Δt is the neutron pulse width, and $t \sim L \cdot d \cdot \sin\theta$, θ is the scattering angle. We have several possibilities for improving the resolution: $R \to 0$ at $\Delta t \to 0$ or $L \to \infty$ and $\Delta\theta \to 0$ or $\theta \to \pi/2$.

A usual TOF diffractometer can give high resolution for a fixed narrow pulse at a large distance from the source, as in the case of HRPD at ISIS: $\theta \to \pi/2$, $\Delta t \approx 12$ μs, $L = 100$ m, $R = 5 \cdot 10^{-4}$.

The Fourier RTOF diffractometer produces a narrow pulse from an initially long pulse: $\Delta t \approx \Omega^{-1}_m$, the inverse maximum frequency of neutron beam modulation, and can give high resolution at a minimal distance, as in the case of HRFD at IBR-2:

$\Delta\theta \to 0$, Δt (reduced) ≈ 7 μs, $L = 20$ m, $R = 5 \cdot 10^{-4}$.

The session contained a review talk on the "Principles of the RTOF method and Fourier technique" by P.Hiismäki (VTT, Finland), reports on the operating Fourier RTOF diffractometers including "M.SFINKS diffractometer at the Gatchina reactor" by V.Trounov (PNPI, Russia), "The Fourier RTOF neutron diffractometer FSS at the 5 MW research reactor FRG-1" by H.-G.Priesmeyer (Kiel University, Germany), "Performance of the high resolution Fourier diffractometer at the IBR-2 pulsed reactor; latest results" by A.M. Balagurov (FLNP JINR, Russia) and a report on "Calibration of the RTOF mini SFINKS diffractometer for precision structure investigations" by D. Chernyshov (PNPI, Russia).

Table 1 summarizes the parameters of the reported diffractometers in comparison with the conventional TOF diffractometer HRPD at ISIS.

Table 1. Parameters of high resolution TOF diffractometers

Parameter	HRPD RAL UK	m-SFINKS PNPI Russia	FSS GKSS Germany	HRFD JINR Russia
λ	0.9-8	0.9-41.6-4	0.9-12	
Θ	$3 \cdot 10^6$	$1 \cdot 10^7$	$1 \cdot 10^7$	$1 \cdot 10^7$
S	2	4.5	5	2
Ω	0.2	0.09	0.1	0.16
$R \cdot 10^4$	5	20	20	5

λ(Å) is the interval of wavelength, Θ (n/cm^2/s) the neutron flux at the sample position, S(cm^2) the maximal "useful" cross-section of the sample, Ω(sr) the solid angle of the detector assembly, and $R = \Delta d/d$ - the resolution of the diffractometer.

Considering the experience of operating Fourier RTOF diffractometers and the results obtained by their users, we can conclude that today, we have a powerful and effective method for structural investigations with steady state and, especially, with large pulsed sources. This provides an additional argument in favour of the greater importance of higher flux rather than narrower pulse width for effective use of neutron sources.

ICANS-XIII
13th Meeting of the International Collaboration on
Advanced Neutron Sources
October 11-14, 1995
Paul Scherrer Institut, 5232 Villigen PSI, Switzerland

TARGET-MODERATOR-SYSTEM: TARGET CONCEPTS

D. Filges
Forschungszentrum Jülich GmbH, Institut für Kernphysik, D-52425 Jülich, Germany

There were nine presentations in this session under the broad heading of "Target-Moderator System: Target Concepts".

The first two papers were from G. Bauer (PSI) proposing Mercury (Hg) as a new challenge for liquid metal target material for pulsed spallation sources. The desirable properties for high power spallation target materials were summarized. Mercury looks good compared to Tantalum and Tungsten the discussed "standard" target materials. The nuclear physics-, material-, and chemical properties show clearly the advantage of Mercury. It was demonstrated that the material HT9 (low Ni content) is useful to maintain the strength for the target container up to 400 °C. A problem is the pressure and the resulting stress on the target container using liquid metal as target material for high power pulsed targets. A simple simulation model was used to calculate the time dependent stress level on the surface of the target container as a function of time. A solution to lower the stress levels by two orders of magnitude to tolerable levels by adding 3% He gas to the liquid Mercury was shown. The question was raised on potential cavitation and corrision problems, which should be studied immediately for the pressure and temperature in question.

The third paper was from J. Lettry (CERN) about development and operation experience on ISOLDE molten metal targets. The target materials were liquid Lanthanum, Tin and Lead in Tantalum target containers. The targets were driven with protons at 1 GeV energy with about 1.5 to 2.2 x 10^{13} protons per pulse at temperatures of 1250 °C, 750 °C and 830 °C respectively. After initial difficulties with the integrity of the containers at high pulse power the containers and the proton beam windows now are still operational after a dose of about 2 x 10^{18} protons.

The original pulse structure (2.4 μs pulse length) clearly caused pressure waves in the targets. However, after changing the extraction mode from the four rings of the CERN PS-Booster to a separation time of 500 μs (total effective pulse length 2ms) the target container of Tantalum showed no damage after this dose of 2.2 x 10^{18} protons.

The fourth paper given by J.H. Rosenfeld (Thermacore Inc.) reviewed the use of heat pipes for cooling Lead-Bismuth liquid metal targets for SINQ and ESS. The advantage of heat pipes is to transfer large amounts of heat with little temperature drop and the safety aspect. For SINQ 8 heat pipes and for ESS about 40 heat pipes are needed. A design for SINQ is about 80% complete and can be converted easily for ESS.

The fifth paper was from B. Guttek (KFA) reporting the studies on the ESS Tantalum target-moderator-reflector system as a stationary target with 4 moderators and 18 beam tubes. Different cooling concepts were studied. He cooling for 1 MW beam at 5 bar Helium pressure

and with 2 cooling circuits was studied. He cooling for 1 MW beam at 5 bar Helium pressure and for 2 MW at 10 bar Helium pressure seems to be feasible. At higher beam power (5 MW) H_20/D_20 cooling is demanded. The adaption of the Tantalum target dimensions to those of the ESS Mercury target was demonstrated.

The sixth paper was given by T. Broome (RAL) on the performance of ISIS targets and Methane moderators. The used Tantalum target gives no significant problem in operation. The main reason for removing the first Tantalum target was to make it available for material studies as part of the ESS studies. It is planned to dismantle this target and make detailed examinations of the condition of the tantalum. The Uranium targets used upto now failed by swelling and many of the target plates buckled. The discussion about Uranium target failure came to the conclusion that there is a growth of the Uranium grains during the proton irradiation, however, to start with smaller grains implies that this is not the dominant process leading to failure. It seems that the effect of Hydrogen in both Zircaloy and Uranium is to form hydrides and this causes embrittlement. The future use of Uranium targets at ISIS depends on establishing the detailed cause of failure. The Methane moderators still suffer from effects of irradiation which lead to the production of hydrogen gas and formation of solids in the moderator can. The minimum lifetime should be 500 mA/h. A development programm is underway concentrating on two main topics, the fluid regime in the moderator and the irradiation chemistry of the methane. There is some indication that the formation of the hydrocarbons which lead to the blockage could well be reduced by the addition of chemical agents. The chemistry is based of the recombination of free radicals in ethane-methane systems.

The seventh and eighth papers were from our Russian colleagues V.G. Miroshnichenko (INR) and S.F. Sidorkin (INR) proposing multiplying targets with Ga-cooling and concepts of Uranium targets for the Moscow meson factory. Concepts for Tungsten targets as an alternative were also diccussed. The multiplying target RIN-10 is designed as a fast critical assembly with uranium nitride fuel and liquid Ga-cooling having a $k_{eff} < 0.95$. The question was raised about the critically safety of those target systems and the licensing in Western Europe of a spallation facility using multiplying targets. A good overview about different possible Uranium alloys was given. Target characteristics for various fuel compositions (e.g. for W, U-233, U-235, Pu-239) are also studied. The performance of the RIN-10 neutron source compared to ESS was discussed. Fuel elements on the basis of U_3Si with natural Uranium and Tungsten and other main components for the RIN-10 facility have already been manufactured.

The final paper was from K. Ziegler (HMI) about FFAG-accelerator options for spallation sources. The status of the FFAG-evaluation and physics studies was reported. The main problem is the technical experience with a proton FFAG; an electron machine worked very well. In general a FFAG design looks very promising, however, there are still problems in the design with the injection and extraction scheme.

A good session, some interesting challenges with Mercury as target material for high power pulsed target systems beyond 1 MW beam power relating to safety, cooling and nuclear physics; great progress in the engineering of stationary 5 MW beam power target systems, but nevertheless there are open problems concerning damage, lifetime, stress waves and corrosion questions.

ICANS-XIII
13th Meeting of the International Collaboration on
Advanced Neutron Sources
October 11-14, 1995
Paul Scherrer Institut, 5232 Villigen PSI, Switzerland

TARGET-MODERATOR-REFLECTOR SYSTEMS: COMPONENTS

T A Broome

ISIS Facility, Rutherford Appleton Laboratory, CCLRC, Chilton, Didcot, UK

The presentations in these two sessions combined to give a varied programme covering several aspects of target station design. These included a new concept for a long pulse spallation source target station (F. Mezei), detailed work on moderator performance, both by experiment (N. Watanabe and Y. Kiyanagi) and Monte Carlo Simulation (G. Russell), a new approach for engineering solid methane moderators (T. Lucas), the cryogenic cooling system design for the ESS hydrogen moderators (K. Stendal) and the practical realisation for handling target station components constructed at SINQ (W. Wagner).

It is relatively rare for reactor engineers and physicists to address the problems of designing a spallation source. It was thus particularly welcome that the concept presented for a long pulse spallation target station arose from a deliberate collaboration with the reactor community. Starting with a typical large D2O tank which acted as moderator reflector and coolant the design incorporated rotating targets and small moderators in flux trap geometry to give a source capable of operating at high power with the prospect of high neutron fluxes. As shown in the presentation of coupled moderator neutronic calculations the incorporation of additional reflector components would then allow the pulse shape and intensity to be optimised.

The experimental work using the electron linac at Hokkaido university is aimed at developing high efficiency cryogenic moderators for spallation sources. The programme includes the study of the three classes of moderator those designed to produce the highest possible intensity beams of cold neutrons (regardless of pulse width), those for narrow neutron pulses with highest possible peak intensity and moderators cooled to extend the slowing down region to low energies. The experimental arrangement utilises an electron beam directed into a lead target as the primary neutron production mechanism. The performance of a wide variety of moderator assemblies in a graphite reflector has been studied by measuring both the intensity and pulse shape of the produced neutron beams at different wavelengths. In particular the work focuses on the effects of different arrangements of water premoderators, beam hole geometry in the reflector, decouplers and poisons. Detailed measurements showed that by a suitable choice of premoderator configuration combined with poisoning or decoupling the premoderator it is possible to get significant gains in intensity without sacrificing a good pulse shape. The coupled moderator studies measured the effects on intensity of different beam extraction geometries and the effect of adding a cooled beryllium reflector/filter. This is a unique experimental programme which is providing invaluable data for the spallation source community. It would be very desirable for the results to be used as benchmark data for the Monte Carlo simulation codes.

The Monte Carlo calculations presented were directed towards an understanding of the performance of coupled moderators on a long pulse spallation source. The effects on the pulse shape and intensity of reflector geometry and material and ortho to para hydrogen fraction were discussed. Of particular interest was way in which peak intensity and brightness could be adjusted by a suitable choice of geometry and material taking into account their effect on the decay time of the pulse. Also the calculations showed the gains possible by taking advantage of the spatial variation of flux across the moderator face. The calculations demonstrated the value to the moderator designer of the huge increase in computer power now available in modern workstations. Calculations to examine subtle effects (~ few per cent changes in intensity) which were not practical a few years ago are now a routine activity. The challenge remains to demonstrate the ability of the calculations to simulate the detail becoming available in the experimental data.

It is accepted that the best material for a cold moderator is solid methane. Operational experience, has shown that radiation damage to the methane is a formidable operational problem. The concept presented may allow the possibility of high power operation. The basic idea is to form the methane as solid pellets in a flow of liquid hydrogen which serves as the coolant. The pellets are formed in a continuous stream and removed after passage through the moderator volume. The solid methane is melted, purified and returned to the pellet source. There is a need for a detailed research and development programme to investigate this idea and solve the engineering problems which should not be underestimated. However, the prospect of solid methane as a high power cold moderator material is most exciting.

Use of liquid, or supercritical, hydrogen is the more conventional approach to providing cold moderators. The supply system required for the proposed ESS moderators was presented. The design was fully detailed and the options of a siphon system or a pumped loop considered. Layout considerations strongly favoured the latter approach. The scale of the systems for supplying 15 kW of cooling to each target station at 25 K and their complexity was clearly demonstrated including large compressor buildings, joint boxes and supplementary cooling to allow the source to run even if there were problems with the cryogenic plant.

In arriving at a practical operational design for a target station a vital consideration is the ability to insert and remove complex equipment on the target station especially when activated. The equipment design for this purpose for SINQ was presented. This included the equipment designed to handle moderator inserts, guide bundles and standard beam tubes. The equipment described (and seen operating in the tour of SINQ during the meeting) has to move tonnes of shielding with great precision and allow remote connection of services and flanges. The presentation clearly demonstrated the considerable technical challenge and high quality detailed mechanical engineering required to for this activity.

ICANS-XIII
13th Meeting of the International Collaboration on
Advanced Neutron Sources
October 11-14, 1995
Paul Scherrer Institut, 5232 Villigen PSI, Switzerland

COMPUTATIONAL METHODS

Philip Seeger, Loma del Escolar, Los Alamos 87545 NM, USA

The work reported in the session on "Computational Methods" ran the gamut from accelerator pulses through target calculations and instrument design to data acquisition and reduction. Such diversity, which is typical of ICANS, made the session very interesting. And with one paper being delayed for two days, this was certainly one of the longest sessions. This summary works backwards from the user toward the source.

W. Schmidt *et al.* reminded us that it not always appropriate - or even correct - to treat the resolution of an experiment just by combining standard deviations of the contributing terms and then applying the central-limit theorem. For one example, there may be very significant asymmetric terms such as moderator pulse response which must be treated in more detail. Another situation which is too often ignored is that there are correlations between the terms, *e.g.* angular divergence of the incident neutron beam is correlated with position of interaction in the sample, and the correlations may either increase *or decrease* the width of the resolution function. The solution is to convert all variables to a common coordinate system (the authors use sample coordinates) to unmask the correlations, and then to integrate the convolution of the terms. To make analytic integration easier, they expand all functions as sums of Gaussians or error functions in one or two dimensions. This level of approximation should be quite adequate for resolution calculations, but should be tested using Monte-Carlo integration of the actual distributions.

The paper of Yu. A. Astakhov *et al.*, presented by V. I. Prikhodko, discussed specifications of hardware and software for an upgrade of the Measurement and computational complex at the Frank Laboratory of Nuclear Physics. The present electronics are old and have little standardization. making maintenance difficult. They also anticipate a large increase in data rates as new instruments and new detectors come on-line. Their new generation of electronics involve the VME system and workstations integrated into their local computer network. Control and management of the apparatus will generally be through simple input/output registers from the VME processor. Individual detector systems will not be standardized to the same extent, but encoding and histogramming modules will be standard. To minimize dead time and to leave the VME bus free for other tasks, the accumulation of spectra occur directly in the memory module. Data formats and archiving, graphical user interfaces, and mathematical processing packages will also become standardized for all experiments at FNLP.

Two papers were concerned with the MCLIB library of Monte Carlo subroutines for instrument design. P. A. Seeger described the structures used in the library to define the

geometry and various types of beam elements; types include moderator source functions, uniform materials, single-crystal filters, multilayer reflectors, monochromators, choppers, various scattering samples, detectors, *etc.* The written report includes complete subroutine descriptions, a sample problem, and a description of the process by which either experimental flux measurements or detailed moderator source calculations are included in the code. The library is now available to the public. In its present form the user is required to write a specific program to set up the geometry for each class of instrument. The second paper, by T. Thelliez *et al.* (presented by R. P. Hjelm), concerned the development of a graphical user interface (GUI) to overcome this difficulty. Early prototypes of the GUI can already reduce the time to implement certain instrument classes from days of programming to minutes of selecting options. It was noted that the GUI itself is appropriately written in an object-oriented language, but that the Monte Carlo code would remain in Fortran for speed of execution.

N. U. Sobolevsky presented the paper by A. V. Dementyev *et al.* on the universal Monte Carlo hadron transport SHIELD, which has evolved from HETC (High-Energy Transport Code), in particular extending it to energies up to (at least) 100 GeV. At such high energies the code depends on hadron-nucleus interaction models developed in Russia, and it gives an excellent fit to experimental data on neutron production from a Pb target (20-cm diameter, 60-cm length) between 0.5 GeV and 70 GeV. Computed heat deposition in Pb and U for 1-GeV protons is also in excellent agreement with calorimetric measurements. Radiation damage and isotope production may also be inferred from the code. The author concludes that although the specific neutron production (n/MW) falls off at proton energies above about 1.2 GeV (due to increasing pion production), engineering aspects of the energy deposition might favor the use of such energies.

J. N. Carpenter wanted to consider in detail the effect of the shape of the proton pulse on the final result, with the aim of extracting the maximum possible information in the range of higher neutron energies where the moderated pulse is intrinsically narrow. He first considered the ISIS "double-pulse" problem (i.e., accelerator operating at harmonic number 2), and showed that the intuitive result can also be found using Laplace transforms. Since the individual extracted pulses are not delta functions, general pulse-shape broadening must also be considered. The experimental data C(t) may in principal be "deconvoluted" by convoluting with the inverse Laplace transform of the reciprocal of the forward Laplace transform of the broadening function; note that this is done using a model function which is mathematically precise. The example shown was a truncated parabolic function, which generated an embarrassing cubic in the inverse Laplace transform, which can be avoided by taking the third derivative of the data. Since the data are histograms, derivatives are estimated by difference operators, and the integrations of the convolution become matrix multiplications. Thus the effects of different model functions on the recovery of data from counts for different classes of experiments can be estimated on a case by case basis to evaluate accelerator options.

ICANS-XIII
13th Meeting of the International Collaboration on
Advanced Neutron Sources
October 11-14, 1995
Paul Scherrer Institut, 5232 Villigen PSI, Switzerland

SUMMARY OF THE SESSION ON SOURCE CONCEPTS

Rex P. Hjelm, Neutron Scattering Center, Los Alamos Neutron Science Center, Los Alamos National Laboratory, Los Alamos, NM 87545 USA

The session on source concepts had contributions dealing with long (LPSS) and short (SPSS) pulsed neutron spallation sources, as well as a proposal for a new reactor facility in Canada.

Ferenc Mezei started off the session with a discussion of the relative merits of LPSS and SPSS sources in "Complementarity of LPSS and SPSS Facilities". His conclusion was that an SPSS is best for high resolution neutron scattering, using the slowing down spectrum of thermal or cold moderators, while an LPSS is more effective for work that uses fully moderated thermal or cold neutrons. His arguments were based on the need to match the time structure of the proton pulse with the response of the moderator-reflector (MR) system, the resulting penalties of this on the total and peak intensity of the moderated neutron pulse of an SPSS, and on cost considerations. He pointed out that the realization of the full potential of the LPSS concept would require new concepts in instrument design, which if successfully implemented would likely remove the need for a low resolution SPSS target station.

Roger Pynn with Luc Daemen of Los Alamos in "Long-pulse Spallation Sources in Perspective" continued the discussion of the relative merits of LPSS and SPSS. They expanded on the argument that matching proton pulse time structure to MR system response leads to intensity penalties for an SPSS. This factor and consideration of SPSS and LPSS instrument frequency responses lead them to conclude that an LPSS is may be a better option than an SPSS for lower resolution scattering measurements. They also reviewed the conclusions of a recent workshop on LPSS instrumentation held at Lawrence Berkeley Laboratory that there are a number of cold neutron spectrometers and diffractometers that could be build at a 1 MW LPSS that would match or exceed the performance of the best instruments available.

Details of the design and performance of the Los Alamos concept for the target-moderator-reflector system for a 1 MW LPSS was presented in "LANSCE LPSS Target System Neutron Performance" by Eric Pitcher, Gary Russell and Phil Ferguson. The reference design is a split tungsten target, with three cold (liquid hydrogen) moderators. Two of the moderators are in wing geometry and one in flux-trap geometry, giving six viewed moderator surfaces. The optimized 10 x 10 cm upstream wing moderator with an all beryllium reflector gave fluxes about one-quarter of those from CS2 cold source at the ILL over a wavelength range above 2 Å.

Plans are afoot for a new reactor source to replace the aging Chalk River facility. Although the primary purpose of the new facility is for reactor materials and fuel element research, the "Proposal for a New Research Neutron Source in Canada AEC" described by Tom Holden will be outfitted with tangential neutron beam lines and two cold neutron source inserts. Present plans call for six guides to transport the beam from one of the cold inserts to an experimental hall. The reactor has a concentrated, split core design for high uniform irradiation near the core center (ϕ = 2-3 x 10^{14} n/cm^2/s).

The session ended with two papers describing LINAC upgrades and the construction of a compressor ring to service the new neutron research facility, IN-06, at the Moscow Meson Factory. The LINAC upgrade was described by L.V. Kravchuck in "Proton linear Accelerator for Pulsed Neutron Research". Presently the LINAC produces a beam with an energy of 100-130 MeV and 17 mA peak current. The completed LINAC will give a 700 MeV beam with a peak current of 50 mA and a 0.34 duty factor. LPSS operation of the water cooled uranium target at IN-06 is expected in 1996 using a 500 MeV proton beam. SPSS operation of the facility is planned with the completion of a compressor ring in 1998 as described by M.I. Grachev in "Proton Storage Ring for IN-06 Pulsed Neutron Source". With the ring the IN-06 target is anticipated to produce neutron pulses with a peak flux of 5×10^{15} n/cm^2/s over 35 μs, at 50 Hz, with an average flux of 8×10^{12} n/cm^2/s.

ICANS-XIII
13th Meeting of the International Collaboration on
Advanced Neutron Sources
October 11-14, 1995
Paul Scherrer Institut, 5232 Villigen PSI, Switzerland

TARGET MODERATOR SYSTEM - NEUTRONICS

Gary J. Russell
Los Alamos National Laboratory

Presentations in this session touched on both broad and specific issues associated with spallation target-system design, including: a) radioisotope production and their influence on radioactivity release, disposal issues, corrosion, and effects on component lifetime; b) experimental measurement of neutrons per proton versus proton energy; c) benchmark measurements of thermal neutron fluxes from a reference SPSS target system; d) neutronic studies for a ESS reference target system; e) basic neutronic studies of wing and flux-trap moderator geometries; and e) benchmark neutronic calculations of some reference LPSS target systems.

The temporal production/destruction of radionuclides from a spallation target system are important for analyzing accident scenarios, estimating waste streams, determining long-term disposal requirements, appraising corrosion issues, and evaluating component lifetimes. The choice of proton energy for a spallation source needs continued study; the issues include energy deposition, radiation damage, neutronic and geometric coupling between targets and moderators, and accelerator requirements. Neutronic data and results demonstrate the neutronic advantage of Hg compared to Ta and W as a target material for the ESS SPSS. The issues of a Hg target for an SPSS rests not in neutronics, but with engineering, materials, and (perhaps) safety details.

The choice between wing-moderator and flux-trap moderator geometry is buried in the neutronic details of the target system and the specifics of the target station layout. Neutronic brightness from a wing moderator is hard to beat. Flux-trap moderators respond to bulk neutron production more so than wing moderators. Flux-trap moderator performance in backscattering geometry holds some promise compared to transmission geometry. Compromises must be made to balance neutron intensities between fore and aft moderators in wing geometry. The neutronic performance of an LPSS flux-trap moderator can be significantly altered by the choice of reflector materials and geometry.

Keywords: Target, Moderator, Reflector, Target System

ICANS–XIII
13th Meeting of the International Collaboration on
Advanced Neutron Sources
October 11–14, 1995
Paul–Scherrer–Institut, 5232 Villigen PSI, Switzerland

SCATTERING METHODOLOGY – INSTRUMENT COMPONENTS

Harald Conrad

Institut für Festkörperforschung, Forschungszentrum Jülich GmbH
Postfach 1913, 52425 Jülich, Germany

In the contribution **Morphology of Glass Surfaces** by P.Böni, D.Clemens, H.Grimmer and H.Swygenhowen (ETH Zürich and PSI), **Peter Böni** impressively showed the effort which had gone in the past years into the improvement of the performance and reproducibility of supermirrors. He presented the results of reflectivity measurements of supermirrors using four different types of glasses. In 385 runs with all together 90 m^2 of supermirrors it was found that the reflectivity depended on the type of glass but was fairly reproducible for each type. The average reflectivities varied from $\langle R \rangle = 86.6$ % for polished Calcite, $\langle R \rangle = 86.8$ % for float Ni–guide (this type showed the largest data scatter from about 82 % to 92 %), $\langle R \rangle = 88.1$ % for polished Borkron to a remarkable $\langle R \rangle = 91.1$ % for float glass from a local supplier. Interestingly, in this latter case with glass batches purchased over a period of 10 months from the same supplier, the results were consistently reproducible at this high level. Another important performance aspect discussed was the dependence of the reflectivity on the critical angle. It was found that for a supermirror aimed at a critical angle of four times that of Nickel ($m = 4$), the reflectivity decreased from about 1 for $m = 1$ to acceptable 0.7 for $m = 3$, whereas it was down to 0.3 at $m = 4$. It was therefore concluded that in this case a much better glass quality is required.

In a talk on **Remanent Multilayers for Polarized Neutron Instrumentation** presented by **Daniel Clemens** (ETH Zürich and PSI), after remarks on the history of FeCo mirrors and the problem of matching the scattering length densities, it was shown that by using non–stoichiometric $Ti_{1-x}N_x$ the scattering length for $|\downarrow\rangle$ – neutrons in magnetized $Fe_{0.5}Co_{0.48}V_{0.02}$ could be matched. On this basis a supermirror could be fabricated which had a number of useful properties such as a high reflectivity of 87 % at 2.1 times the critical angle of bulk Nickel and a flipping ratio $R > 40$. It was found that these supermirrors are operational in zero field, which were important for neutron spin echo application. No clear evidence for 'magnetically dead' layers in these multilayer structures was found. Furthermore, they are thermally stable, i.e. no interdiffusion of the layers are to be expected. SQUID hysteresis curve measurements with a 28 nm $Fe_{0.5}Co_{0.48}V_{0.02}$ film, which was produced by stationary sputtering with oblique incidence of the sputtered particles, showed that a 'hard' magnetization was obtained.

Laszlo Cser (RISSP Budapest) contributed **Three Remarks on Wide Band Devices.** Firstly, he proposed a much broader use of supermirror (SM) guides for source utilization in order to more efficiently exploit the precious neutrons. With SM guides it were much easier to multiply use the individual beam holes due to the possible wider lateral instrument separation. Then he presented and advocated a proposal of Y.M.Ostanevich and Y.Y.Nikitenko (Dubna) for a wide–spectrum polarizer for pulsed sources on the basis of a set of rotating magnetized mirrors. The main feature of such a

device is a sequence of differently inclined mirrors passing a beamhole, whereby neutrons of different wavelengths are reflected according to their time of flight. Technically the device might resemble a mechanical velocity selector or a set of conical tubes of different diameters assembled on a common axle. A possible advantage of these moving polarizing devices ($P \simeq 0.9$, $T = 0.5$) might be the higher overall polarization in a set–up with polarization analysis after the sample ($P_{eff} \simeq 27$ %) as compared to a polarizer/analyzer system consisting of ^{3}He components only ($P \simeq 0.3$, $T = 0.5$, $P_{eff} \simeq 10$ %). Finally the use of statistical choppers at pulsed sources was discussed for a better source utilization in trying to separate weak inelastic lines from nearby strong elastic contributions.

A talk on the recent development within the EU–sponsored NEREIDE collaboration of **Two–dimensional Neutron Detectors** was given by **Roland Gähler** (TU München). He presented the effort in selecting the adequate scintillator material from choices with widely varying and partly unwanted properties (γ–sensitivity, quantum yield, hygroscopicity etc.). A ^{6}Li–glass now seems to be superior to the formerly used hygroscopic ^{6}LiJ. It was impressive to see the enormous progress in improving the spatial resolution of the two–dimensional detectors, which is particularly important for neutron radiography. As a lucid example the radiographic picture of a small electric motor was shown displaying minute details. An example of a set–up was presented, where the light from the scintillator was reflected from a mirror into the camera in order to get out of the direct radiation field. The difficulties with the readout of the CCD cameras were pointed out in this context, which are due to the fact that the size of the image within the camera is of the order of 1 cm^2 only.

The final contribution on **Sputtering Method for Improving Composite Germanium Monochromators** by G.Böttger, A.Dönni, P.Fischer, S.Fischer, M.Koch, M.Medarde, J.Schefer, U.Staub and R.Thut was presented by **Jürg Schefer** (ETH Zürich and PSI). After some remarks on the reasons for using Germanium as a monochromator and the necessity to enlarge the mosaic spread of natural Ge crystals for use in high resolution powder as well as single crystal diffractometers, the audience was reminded that the demanded mosaic spread can only be achieved by forming stacks of properly treated wafers. The slow and complicated bending and flattening procedures in a vacuum furnace generating the necessary lattice defects in the wafers and the cleaning, sputtering and soldering steps were explained. It was pointed out that, in further developing the method originally introduced at Brookhaven, the replacement of the tin foils by sputtered material as a soldering agent sandwiched between the wafers considerably improved the alignment of the individual wafers. Good neutron results and a constant quality of the produced composite monochromators were obtained at the cost of an extensive manpower.

ICANS-XIII
13th Meeting of the International Collaboration on
Advanced Neutron Sources
October 11-14, 1995
Paul Scherrer Institut, 5232 Villigen PSI, Switzerland

ICANS on the World Wide Web

John M. Carpenter and John P. Hammonds

Intense Pulsed Neutron Source, Argonne National Laboratory, Argonne, IL 60439

ABSTRACT

This paper describes our entry of ICANS information on the World Wide Web.

Description of the ICANS entry on the World Wide Web

In July 1995 we created a site on the World Wide Web[1] to provide information about the International Collaboration of Advanced Neutron Sources (ICANS)[2]. The World Wide Web provides a means of distributing and updating (in an on demand method) information to the neutron scattering community using the Internet services. Information is distributed on the Web using a client server format. A host computer stores the original document and clients access it using software on the requester's computer. Client software addresses information on the server (host) using a Uniform Resource Locator (URL)[3]. The URL for the ICANS Web is http://www.pns.anl.gov/icans/icansdescript.html. The ICANS entry is available through a link from the IPNS home page[4]. Other sites can add a reference to it by adding a link to the URL above. The ICANS Web server is located at IPNS. At present, the site contains

- a brief history of ICANS
- a statement of the goals of ICANS
- a list of member organizations with names of ICANS contacts

and

- an annotated list of meetings and proceedings reports.

Future plans for this site include

- announcements of upcoming events
- references to other items of interest to the neutron scattering community

and

- electronic copies of conference reports.

We encourage ICANS members to provide corrections, changes, and suggestions for additional information to either author via e-mail[5][6].

A copy of the current contents of the ICANS World Wide Web entry follows. All underlined text in the Web document indicates a hypertext link to a site containing information about that text. All of the references in this paper are in the form of URLs since most of the information about the Web is available as on-line documentation.

Keywords: ICANS, History, Meetings, Proceedings

ICANS

International Collaboration on Advanced Neutron Sources

ICANS is an informal network of laboratories whose scientists are involved in developing pulsed neutron sources and accelerator based spallation neutron sources.

Brief history of ICANS

ICANS originated in discussions that took place in 1977 at Argonne National Laboratory among John M. Carpenter of Argonne National Laboratory, Rex G. Fluharty of Los Alamos Scientific Laboratory, Leo C. W. Hobbis of Rutherford Laboratory, and Motoharu Kimura, representing Tohoku University and the Japanese National Laboratory for High Energy Physics (KEK). They formulated the goals and structure of the Collaboration, described below as they have since been slightly modified. T. O. Brun and J. M. Carpenter share blame for the "ICANS" acronym.

ICANS meetings began in 1977 with a gathering at Argonne. A second was held at Rutherford Laboratory in 1978, and a "mini-ICANS" meeting, held jointly between KEK and Rutherford Laboratory scientists, took place at Rutherford Laboratory in 1979. None of these sessions was reported in any published document. Subsequent meetings have all been reported in proceedings. Altogether there have been twelve major ICANS meetings up to 1994. About 125 scientists have attended each of the recent ICANS meetings.

Related similar topical collaborations and series of meetings have recently been established, the Advanced Pulsed Neutron Sources (PANS) conferences convened by the Frank Laboratory of Neutron Physics, JINR, Dubna, and the International Group on Research Reactors (IGORR) meetings.

Goals and structure of ICANS

The attention of the Collaboration is on the subjects of accelerator development, source (target) and moderator development, and neutron scattering instrumentation development. The collaboration has the following goals:

to facilitate the exchange of technical information
to provide for review of results and designs
to reduce duplication of efforts
to identify areas for collaborative efforts, and
to provide means for informing participants about plans for activities relating to pulsed and steady spallation source development.

Meetings are normally of four or five days duration and are held about every two years. Efforts are made to coordinate ICANS meetings with other events in order to minimize the costs and other impacts of travel. Usually, meetings address two of the three subject areas, always including the topic of targets and moderators. Meetings are only loosely structured, including brief status reports from each of the active laboratories, contributed papers from the participants, and sometimes poster sessions. Ideally, meetings provide substantial time for workshop sessions and informal discussions. Always, meetings end with "how did we do?" discussions and planning for forthcoming meetings.

It is the tradition within the Collaboration that each of the participating laboratories identifies an "ICANS Contact" who serves to communicate with the Collaboration on behalf of the laboratory. Normally responsibility for playing host to meetings rotates among the participating laboratories and is decided by discussions among the contacts one or two cycles before the planned meeting. Responsibility for coordinating events rests with the host of the next

upcoming meeting, and the host laboratory takes responsibility for timely publication of proceedings and for supporting other conference costs. Otherwise, the Collaboration is quite informal. For early meetings, there was no fee for participation in ICANS meetings. This policy was changed as of ICANS XIII (1995) due to the growing burden on the host laboratory because of participants from non-member laboratories. Attendance is by invitation from the host through the member laboratory ICANS Contacts.

The tradition is that the directors of the member laboratories send a letter to the director of any new laboratory that wishes to join in the Collaboration; these are shepherded by the ICANS Contacts. A new member laboratory must be willing to accept host responsibilities. Initial expressions of interest should be addressed to the ICANS Contact of the next-host laboratory.

ICANS Contacts for current member laboratories

V. L. Aksenov - Laboratory of Neutron Physics, Joint Institute for Nuclear Research, Dubna, Russia
B. R. Appleton - Oak Ridge National Laboratory, Oak Ridge, Tennessee, USA
G. S. Bauer - Paul Scherrer Institute, Villigen, Switzerland
J. M. Carpenter - Argonne National Laboratory, Argonne, Illinois, USA
G. J. Russell - Los Alamos National Laboratory, Los Alamos, New Mexico, USA
I. M. Thorsen - TRIUMF, Vancouver, British Columbia, Canada
~~N. Watanabe~~ H. Ikeda - National Laboratory for High Energy Physics, Tsukuba, Japan
W. G. Williams - Council for the Central Laboratory of the Research Councils, Chilton, Oxon, UK

ICANS meetings and proceedings

Following is a list of ICANS meetings, dates, venues, and references to proceedings. The list includes full titles of the proceedings volumes, sources for obtaining copies (availability is not certain) , and suggested short forms for use in journal references.

ICANS I Argonne National Laboratory, December 12-15, 1977

ICANS II Rutherford Laboratory, July 10-14, 1978

ICANS III Los Alamos Scientific Laboratory, March 19-22, 1979

International Collaboration on Advanced Neutron Sources ICANS III: Conference on Target Stations and Accelerator Technology. Los Alamos Scientific Laboratory, March 19-22, 1979. Compiled by Gary J. Russell. (ring bound, 136 pages)

Unnumbered internal report of Los Alamos Scientific Laboratory, September, 1979.

ICANS III, Los Alamos, March, 1979; unnumbered internal report of Los Alamos Scientific Laboratory, (September, 1979).

ICANS IV National Laboratory for High Energy Physics, Tsukuba, Japan, October 20-24, 1980

Proceedings of the 4th Meeting of International Collaboration on Advanced Neutron Sources (ICANS IV) KEK, Tsukuba, October 20-24, 1980, KENS Report II, March, 1981. Edited by Yoshikazu Ishikawa, Noboru Watanabe, Yasuo Endoh, Nobuo Niimura and John M. Newsam. (perfect bound, 776 pages)

Unnumbered internal report of the Japanese National Laboratory for High Energy Physics, 1-1 Oho-Machi, Tsukuba-gun, Ibaraki-ken, 305 Japan.

ICANS IV, KEK, October, 1980, unnumbered internal report of the Japanese National Laboratory for High Energy Physics, (March, 1981).

ICANS V KFA Jülich and KfK Karlsruhe, Germany, June 22-26, 1981

ICANS-V: Proceedings of the 5th Meeting of the International Collaboration on Advanced Neutron Sources, Plenary Sessions and Target Station Workshops, Jülich, June 22-26, 1981. Editors: G. S. Bauer and D. Filges. ISSN 0344-5789. KFA report Jül-Conf-45, Kernforschungsanlage Jülich GmbH, October, 1981. (perfect bound, 664 pages)

Printed by Berichte der Kernforschungsanlage Jülich GmbH. Available through ZENTRALBIBLIOTEK der Kernforschungsanlage Jülich, Postfach 1913 D-5170, Jülich, Germany.

ICANS V, Jülich, June, 1981, KFA report Jül-Conf-45, (1981).

and

ICANS-V: Proceedings of the 5th Meeting of the International Collaboration on Advanced Neutron Sources, Workshop on High Intensity Accelerators and Compresor Rings, Karlsruhe, June 22-26, 1981. Editor: M. Kunze. ISSN 0303-4003. KfK report KfK 3228, Kernforschungszentrum Karlsruhe, October, 1981. (perfect bound, 254 pages)

Printed by Kernforschungszentrum Karlsruhe

ICANS V, Karlsruhe, June, 1981, KfZ report KFZ 3228, (1981).

ICANS VI Argonne National Laboratory, June 28-July 2, 1982

ICANS VI: Proceedings of the Sixth Meeting of the International Collaboration on Advanced Neutron Sources, Argonne National Laboratory, June 29-July 2, 1982. Editor J. M. Carpenter. Argonne National Laboratory report ANL-82-80. January, 1983. (perfect bound, 662 pages)

Available from National Technical Information Service, U. S. Department of Commerce, 5285 Port Royal Road, Springfield, VA 22161.

ICANS VI, Argonne, June, 1982, Argonne National Laboratory report ANL-82-80, (1983).

ICANS VII Chalk River Nuclear Laboratory, September 13-16, 1983

ICANS-VII Proceedings of the Seventh Meeting of the International Collaboration on Advanced Neutron Sources, Chalk River Nuclear Laboratories, September 13-16, 1983. Edited by S. O. Schriber. Atomic Energy of Canada Limited report number AECL-8488, September, 1984. ISSN 0067-0367 (perfect bound, 292 pages)

Scientific Document Distribution Office, Atomic Energy of Canada Limited, Chalk River, Ontario, Canada K0J1J0. Document number 3003-84. $11.00 per copy

ICANS VII, Chalk River, September, 1983, Atomic Energy of Canada Limited report number AECL-8488

ICANS VIII Rutherford-Appleton Laboratory, July 8-12, 1985

Proceedings of the Eighth Meeting of the International Collaboration on Advanced Neutron Sources, 8-12 July 1985. Editor George C. Stirling. Volume I, Status reports, Target systems, Moderators; Volume II, Neutron-scattering instruments; Volume III, Neutron-scattering techniques. Rutherford Appleton Laboratory report RAL-85-110, November, 1985. (perfect bound, 3 volumes, 831 pages)

Published by the Science and Engineering Research Council, Rutherford Appleton Laboratory, Chilton, Oxon, OX 0QX, UK.

ICANS VIII, Rutherford-Appleton Laboratory, July, 1985, Volumes I, II, III, Rutherford-Appleton Laboratory report RAL-85-110, (1985).

ICANS IX Swiss Institute for Nuclear Research, September 22-26, 1986

ICANS IX: Proceedings of the 9th Meeting of the International Collaboration on Advanced Neutron Sources, Villigen, September 22-26, 1986. Editors F. Atchison and W. Fischer. SIN report number 7 87 180 40926; ISBN 3-907998-01-4, July, 1987. (perfect bound, 657 pages)

Produced by the Information Services, Public Affairs Office, Swiss Institute for Nuclear Research, CH 5234 Villigen/Switzerland. Document number 7.87 180 40926.

ICANS IX, Villigen, September, 1986, SIN report number 7 87 180 40926, (1987).

ICANS X Los Alamos National Laboratory, October 3-7, 1988

Advanced Neutron Sources 1988, Proceedings of the 10th Meeting of the International Collaboration on Advanced Neutron Sources (ICANS X) held at Los Alamos, 3-7 October, 1988, Edited by D. K. Hyer. Institute of Physics Conference Series Number 97, Institute of Physics, Bristol and New York. CODEN IPHSAC 97 1-890 (1989), ISBN 0-85498-053-9. (hard cover, 890 pages)

IOP Publishing Ltd, Techno House, Radcliffe Way, Bristol BS1 6NX, England; 335 East 45th Street, New York, NY 10017-3483, USA.

ICANS X, Los Alamos, October, 1988, Institute of Physics Conference Series Number 97, Institute of Physics, Bristol and New York, (1989).

ICANS XI National Laboratory for High Energy Physics, Tsukuba, Japan, October 22-26, 1990

ICANS-11: Proceedings of the 11th Meeting of the International Collaboration on Advanced Neutron Sources, KEK, Tsukuba, October 22-26, 1990. KEK report 90-25, March, 1991 AMRD. Editors M. Misawa, M. Furusaka, H. Ikeda and N. Watanabe. (2 volumes, perfect bound, 1159 pages)*

Technical Information and Library, National Laboratory for High Energy Physics, 1-1 Oho, Tsukuba-shi, Ibaraki-ken, 305 Japan.

ICANS XI, Tsukuba, October, 1990, Japanese Laboratory for High Energy Physics, KEK report 90-25, (1991).

ICANS XII Rutherford Appleton Laboratory, Abingdon, Oxfordshire, UK, May 24-28, 1993.

Proceedings of the Twelfth Meeting of the International Collaboration on Advanced Neutron Sources, ICANS-XII, held at the Cosener's House, Abingdon, Oxfordshire, UK, 24-28 May, 1993. Volume 1, New Science at Pulsed Sources, Instrumentation Workshop; Volume 2, New Sources, Accelerator Workshop, Target Station Workshop; Facility Status Reports, Abstract Booklet. Rutherford-Appleton Laboratory report 94-025, 1994. Editors Ushchi Steigenberger, Tim Broome, Grahame Rees and Alan Soper. (perfect bound, Volume 1, 384 pages; Volume 2*, 392 pages; Status Reports, 56 pages; Abstracts, 112 pages)

Published by the Science and Engineering Research Council, Rutherford Appleton Laboratory, Chilton, Oxon, OX 0QX, UK.

ICANS XII, Rutherford-Appleton Laboratory, May, 1993, Volume 1, Volume 2, Status Reports, and Abstracts, Rutherford-Appleton Laboratory report 94-025, (1994).

Next ICANS Meeting, ICANS XIII

To be held in Switzerland, October 11-14, 1995, in sequence with the third ESS Plenary Meeting. Host, Paul Scherrer Institute. Contact, G. S. Bauer.

* Contains list of attendees' names, addresses, and telephone numbers.

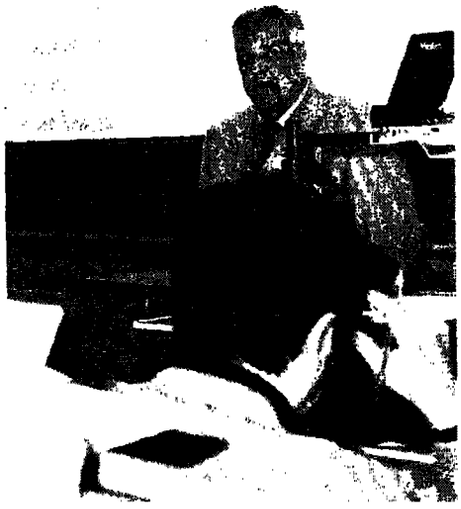

Body

Language

News from Existing ICANS-Facilities

ICANS-XIII
13th meeting of the International Collaboration on
Advanced Neutron Sources
October 11-14, 1995
Paul Scherrer Institut, 5232 Villigen PSI, Switzerland

ISIS: THE FIRST 10 YEARS

A D Taylor

ISIS Facility, Rutherford Appleton Laboratory, Chilton, OXON OX11 0QX, UK

ABSTRACT

Recent progress at ISIS is reviewed.

1 Introduction

At 7.16 pm on the 16 December 1994, ISIS celebrated its 10th Anniversary of first producing neutrons. These first 10 years have been a period of remarkable growth both in terms of the source performance and of the scientific exploitation of the source. ISIS is now widely acknowledged as being one of the foremost neutron sources in the world, and has played a major part in establishing the pulsed spallation technique as the technology of choice for the next generation of neutron sources for condensed matter research. A major achievement has been the expansion of science capabilities from acknowledged areas such as powder diffraction and high energy spectroscopy to the exploitation of cold neutrons for reflectometry, diffraction and high resolution inelastic studies. Recently significant advances in studying coherent excitations in single crystals using time-of-flight techniques have also been made.

The scientific progress made in these first ten years has been remarkable, with almost all of the science anticipated in the original ISIS proposal being realised. What was not anticipated has been a source of great satisfaction: the whole field of reflectometry, the use of muons for condensed matter research, the quality of information available from powder diffraction on a pulsed source, diffuse studies using white beams, very detailed information on the liquid state, stress measurements on engineering components, magnetic excitations in single crystals and the power of cold neutrons -- all of which are now established as major components of the ISIS programme -- were not even mentioned in the original proposal.

2 Source

The ISIS accelerator now routinely operates at currents of 180 μA, averaged over a 28 day cycle, with an efficiency between 85% and 90%. (Whilst currents in excess of 200 μA are possible, the increased beam loss jeopardises hands-on maintenance of key accelerator components). In six operational cycles in 1994 ISIS delivered some 653 mA-hr of protons onto a tantalum target. At

Keywords: ISIS, Pulsed Spallation Source, Instruments, Science

these power levels, radiation damage in methane severely limits the lifetime of the 100K methane moderator. Improved flow characteristics in the latest design and regular flushing of the methane to limit the build up of higher hydrocarbons has extended operation of the moderator to an acceptable 2-3 cycles before it is necessary to replace it. The lifetime of the new micrograined uranium target is, however, at one cycle, unacceptable. A tantalum target will be used routinely until the damage problem in uranium is better understood. The performance of the accelerator is summarised in Figure 1.

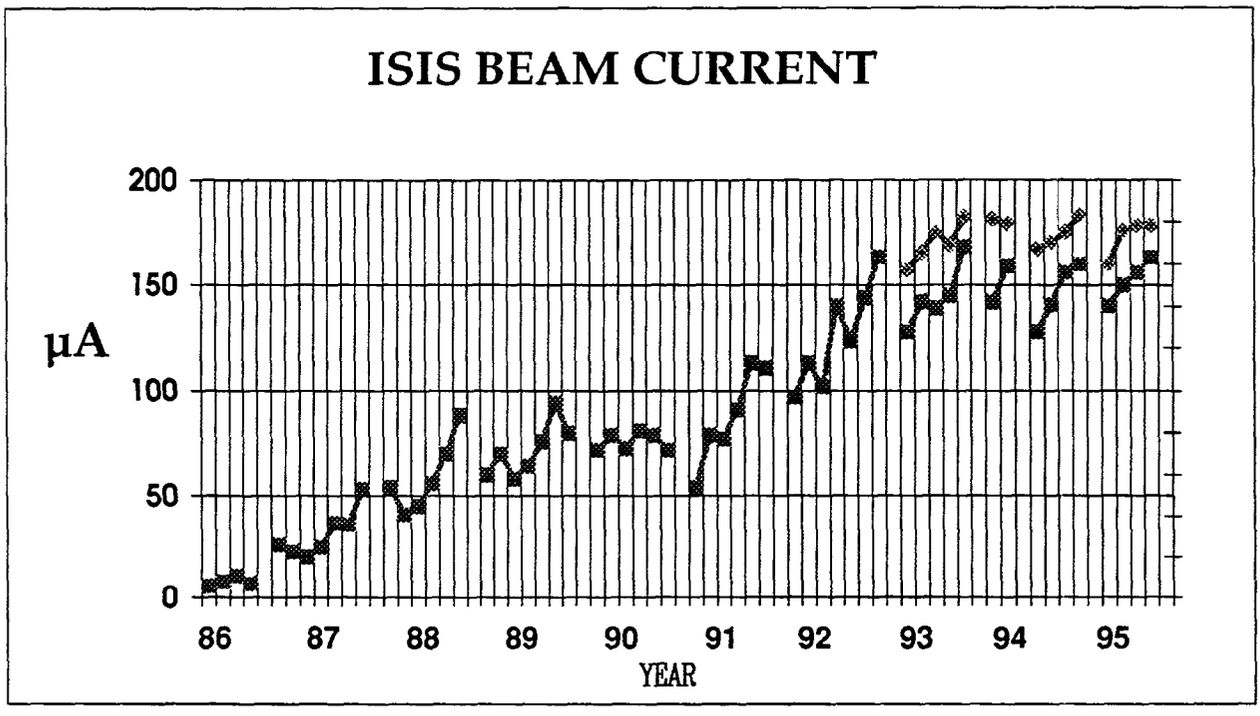

Figure 1 ISIS beam current. The main trace is the current averaged over each cycle as perceived by the end user. The upper trace for 1993 - 1995 is the actual beam current on target.

3 Instruments

Sixteen neutron and three muon instruments are now available to the ISIS community (Figure 2), and the RIKEN beamlines are being commissioned for muon catalysed fusion research as well as fundamental and condensed matter studies using both positive and negative muons.

Recent advances in instrumentation include a major pressure cell development programme based on the Paris-Edinburgh cell. Pressures of 100 kbar are routinely available to the user programme, and high quality diffraction data at pressures in excess of 250 kbar have been achieved by the development team. A time-of-flight strain scanner ENGIN has also been developed as part of an EU-funded programme. From 1996, the present TEST beam will be shared between the pressure diffraction programme and the strain programme. An increasing fraction of the beamtime on the direct geometry chopper spectrometers HET and MARI has been devoted to the study of coherent magnetic excitations in single crystals. The development of sophisticated visualisation and analysis routines, together with imaginative exploitation of the time-of-flight techniques, have shown that, in addition to the success already demonstrated in lower dimensions, the technique is immensely powerful for three dimensional systems, even at modest energy transfers.

A healthy instrument development programme has now been funded through the Collaborative Research Grant mechanism. A new reflectometer, SURF, is in its commissioning phase, and will

Figure 2 *The ISIS Facility*

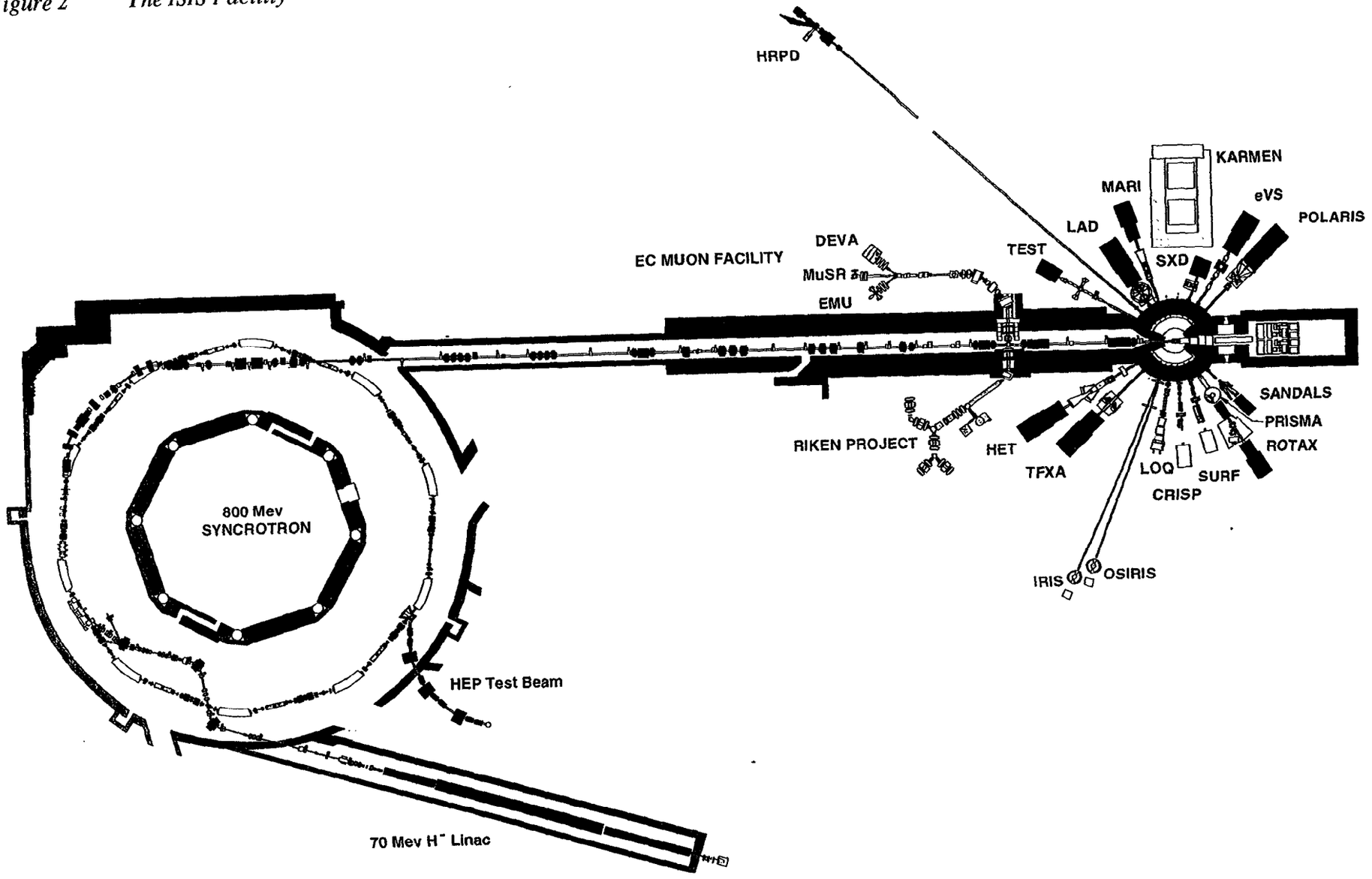

be fully scheduled from 1996. SURF is optimised to study surfactants at the air-liquid interface and has an intensity gain of a factor 7 over its sister reflectometer CRISP. A second cold neutron guide will be extracted through the IRIS shutter to provide a beam for OSIRIS, which will serve as a testbed for developing several aspects of cold neutron instrumentation on a pulsed source. The initial phase will include a long wavelength diffractometer some 100 times more effective than IRIS and will be available in 1997. Later stages will develop polarisation analysis and μeV spectroscopy. Building on the success of the single crystal excitation programme on HET and MARI, a new chopper spectrometer, MAPS, is in the initial stages of engineering design (Figure 3). MAPS, with its large array of position sensitive detectors will be commissioned in 1998. A state-of-the art diffractometer, the General Materials Diffractometer GEM is the latest of these GRG-funded instrument. GEM will replace LAD, the first of the ISIS instruments, in early 1999 and will be particularly powerful for kinetic studies

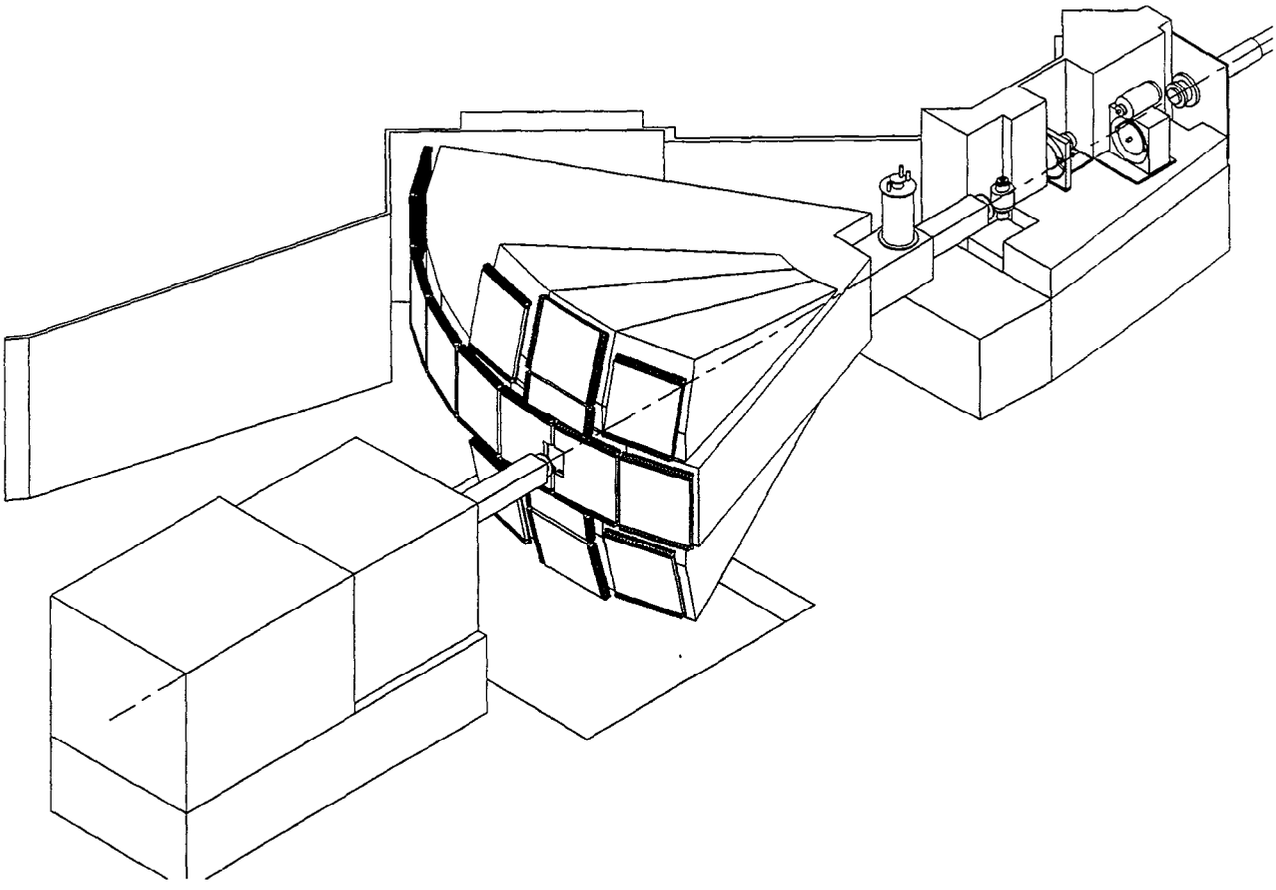

Figure 3 A preliminary layout of the MAPS spectrometer. The secondary flight path is 6 m and the detector area covers 14 m^2.

4 Science

The output of the ISIS source and instruments in the 2½ years between ICANS-XII and ICANS-XIII has been greater that the integral over all time up to the last meeting. This, combined with the increase in the sophistication of the user community who are now actively exploiting the features of pulsed sources in a very creative way, helps to explain the quality and quantity of science which can be found in the latest ISIS annual report.

It is not appropriate in these proceedings to single out a few of the five hundred experiments reported in ***ISIS 95***, nor is it appropriate to highlight any one of the ISIS instruments. The interested reader is referred to the latest annual report where details of the science programme and the instrumental and technical developments are given.

ICANS-XIII
13th Meeting of the International Collaboration on
Advanced Neutron Sources
October 11-14, 1995
Paul Scherrer Institut, 5232 Villigen PSI, Switzerland

NEWS FROM IPNS

B. S. Brown

Argonne National Laboratory, IPNS Division, Argonne, IL 60439, USA

ABSTRACT

Under the Scientific Facilities Initiative, IPNS is planning to double its operation to 32 weeks/yr. Additional scientific and technical support staff will be added for the greatly expanded user program. The IPNS Upgrade Feasibility Study was published in April, 1995 and is a thoroughly documented study on a 1-MW pulsed spallation neutron source at Argonne, including cost and schedule. A new booster target (^{235}U-Mo alloy) has been designed that will increase the neutron flux by a factor of ~3 and construction will begin soon. A new small angle diffractometer (SAND) is in the final stages of commissioning, a prototype inelastic scattering spectrometer for Chemical Excitations (CHEX) was recently constructed and an upgraded quasielastic spectrometer (QENS) has been designed. IPNS has gained considerable operating experience with solid methane moderators, including controlled heating at periodic intervals in order to anneal the accumulated radiation induced stored energy.

1. Scientific Facilities Initiative (SFI)

A highly coordinated effort was put forth by the national labs to obtain funding for a range of Department of Energy (DOE) facilities that are operating well below their optimum level. For a relatively small increase in operating funds, facilities for physical sciences, high energy physics and nuclear physics research can significantly increase their operating effectiveness. IPNS, along with the other DOE neutron, synchrotron and electron microscope facilities, is scheduled to receive a significant increase in funds for the next year and beyond. Although the final bill has not been passed, the SFI has wide support and is very likely to succeed.

Under the SFI, IPNS will double its operating time. There are also funds for a significant increase in operating personnel for both the accelerator and neutron source groups and support personnel for the neutron scattering instruments. The goal is to have an instrument scientist, support person and post doc for each IPNS instrument. In addition, support personnel will be hired for ancillary equipment, data analysis and detectors/electronics. The goal is to operate 28 weeks in 1996 vs. 16 weeks in 1995, and to ramp up to 32 weeks/yr. operation.

2. IPNS Upgrade

Over the last 20 years, the United States has fallen alarmingly behind other scientific communities in the availability of up-to-date neutron sources and instrumentation. In June 1992, the DOE requested the formation of a panel to report on key issues concerning possible new sources, emphasizing especially the comparison of reactors and pulsed spallation neutron sources. The Panel, chaired by Professor Walter Kohn (UCSB) organized a broad Review of Neutron Sources and Applications, with the participation of 70 national and international

experts, in Oak Brook, Illinois. The Kohn Panel's report was published in January 1993[1] and the Oak Brook findings and conclusions were published in January 1994.[2]

After reviewing the capability and cost-effectiveness of different alternatives, the Kohn Panel concluded that the United States urgently needed to construct a complementary pair of neutron sources: a next-generation research reactor, the Advanced Neutron Source (ANS), and a powerful pulsed spallation source (PSS). Unfortunately, the ANS was canceled in February, 1995. The Kohn Panel's second recommendation was to "immediately authorize the development of competitive proposals for the cost-effective design and construction of a 1-MW PSS." The cancellation of the ANS puts even more emphasis on the development of PSSs for the nation's future. Subsequent to the Kohn Panel recommendations, two workshops took place in the United States within the PSS community. One workshop further evaluated accelerator prospects (Santa Fe, February 1993)[3]; the other addressed technological and scientific applications of a 1-MW PSS (Argonne, May 1993).[4]

Argonne National Laboratory (ANL) has recently completed a feasibility study for a 1-MW PSS dedicated for slow neutron scattering in response to the Kohn Panel's recommendation for a cost-effective design and construction of a dedicated 1-MW PSS, the IPNS Upgrade.[5] The project leader for the accelerator, cost and schedule was Y. Cho; for the target stations it was J. Carpenter; and for the instruments it was K. Crawford. The development of the design and preparation of the Feasibility Study greatly benefited from the expertise in the Advanced Photon Source project. The methodologies used for this study were essentially identical to those used for the APS and greatly enhance the quality and reliability of this study. Details of the IPNS Upgrade Feasibility Study are given in other papers at this meeting by Y. Cho and J. Carpenter.

The Argonne proposal is for a 400 MeV, 500 mamp linac and rapid cycling synchrotron system operating at 30 Hz. The beam will be injected into two target stations for neutron scattering, each of which has 18 beam lines. The proposal uses buildings and infrastructure of the former Zero Gradient Synchrotron (ZGS) facility. The ZGS Ring Building can house the synchrotron, about 200 meters in circumference, and has enough radiation shielding to accommodate a 1-MW accelerator system. Two of the former ZGS experimental buildings can house the neutron-generating target stations and associated neutron beamlines. It is estimated that the use of existing buildings saves about $175 million in construction costs.

If the project is initiated in FY 1997, the total estimated construction cost (TEC) is $478 million (in 1995 dollars), or $559 million in inflated dollars for the year in which they are spent. The facility commissioning would start at the beginning of FY 2001. Construction of new components and refurbishment of existing facilities will not interfere with the present IPNS operations, except for reworking and relocation of the scattering instruments. An interval as short as a few months will be required to rework the scattering instruments and install them in their new locations. The accelerator commissioning period will be followed by commissioning of the target stations and instruments. Details of the cost and schedule appear in the IPNS Upgrade Feasibility Study[5].

The IPNS Upgrade is a 1-MW source that can easily be upgraded to 5-MW by injecting the beam from the 2-GeV RCS into a 10-GeV RCS. Studies on this option have been underway since the 1-MW Feasibility Study was completed and a feasible concept, including siting, has been developed, the details of which are discussed in another paper at this meeting. This design has the very large advantage of permitting full operation of the 1-MW source while the 10-GeV ring and target areas are under construction. Connecting the 2- and 10-GeV rings can be done quite quickly. In addition, no additional capabilities need to be built into the 1-MW facility for future enhancement to 5-MW, thereby avoiding any extra costs for the 1-MW source.

3. Booster Target

IPNS operated with a 77% enriched uranium target from 1988-1991, and measured a factor of ~3 increase in neutron beam current over the depleted uranium target. This target failed (as determined by the presence of fission gases) and the depleted uranium target that had been in use from 1981-1988 was reinserted. It failed approximately 6 months later and metallurgical inspection revealed that the failure mechanism was anisotropic growth of the uranium metal which caused cracks in the Zircaloy cladding.[6] It is quite reasonable to assume that this was the same failure mechanism for the failed booster target. With this in mind, the design for the new booster target uses an alloy that does not have anisotropic growth under irradiation or fatigue, ^{235}U-10 w/o Mo. The target has been fully designed and safety documentation has been written. At the request of the U.S. Department of Energy (DOE), an additional study was done to determine if significant corrosion occurred during a loss of coolant accident (LOCA) that would contribute to the radiation released during the LOCA. The study showed only a minor contribution and this report is now undergoing an independent review. We have been in close communication with the DOE during the review process and are confident that the final report will be quickly approved when submitted following this final internal review. The target will be built at the Y-12 plant at Oak Ridge, TN, as was the first booster target. It is anticipated that fabrication will take approximately one year.

4. Instrument Development

4.1 New Small Angle Diffractometer (SAND)

A new small-angle neutron diffractometer SAND at IPNS is now being commissioned. This instrument builds upon the more than 15 years experience with pulsed neutron small-angle diffraction at IPNS, and incorporates many new features to improve both Q_{min} and Q_{max} as well as improving the ease of instrument operation. The present small-angle diffractometer SAD at IPNS has been severely oversubscribed for several years, with proposals exceeding operating time by a factor of 2 to 3. Because of this, and because experience led us to believe we could now build a significantly improved instrument, consideration of a second SANS instrument at IPNS was begun in 1986. Work on SAND has proceeded slowly, as permitted by concurrent commitments to other, higher-priority projects, but the instrument is now near completion. Figure 1 shows the SAND layout and details are discussed elsewhere in these proceedings.

SAND is designed to make a value of Q_{min} down to 0.002 $Å^{-1}$ readily accessible for those experiments which require it. SAND includes a chopper to allow operation with much longer wavelengths (up to 28 Å), and will eventually have a second set of collimators having smaller angular divergence, both of which will serve to reduce Q_{min} from the ~0.005 $Å^{-1}$ available on SAD. A second goal is to increase the maximum Q value accessible, and to provide better counting statistics for the higher-Q data where the scattering cross-section is usually quite small. This goal is achieved by using a larger area detector (40x40 cm^2) for SAND, and by including an array of linear position-sensitive detectors (LPSDs) at higher scattering angles.

Based on experience with SAD, SAND incorporates features to facilitate the alignment of the instrument components and of the sample, to improve access for various types of sample environment equipment, and to permit in situ calibration of the area detector.

The area-detector portion of SAND is expected to be operational with the coarse soller collimators in late 1995. The chopper is being bench-tested and will also be incorporated in the instrument in 1995. It is expected that SAND will be placed in the user program in this configuration in Spring, 1996. The schedule calls for bringing the LPSD bank on line in late 1996. The last item to be added will be the set of fine soller collimators, and the schedule for these will depend on the outcome of the efforts to develop the appropriate fabrication technology. Details are discussed in another paper at this meeting by K. Crawford.

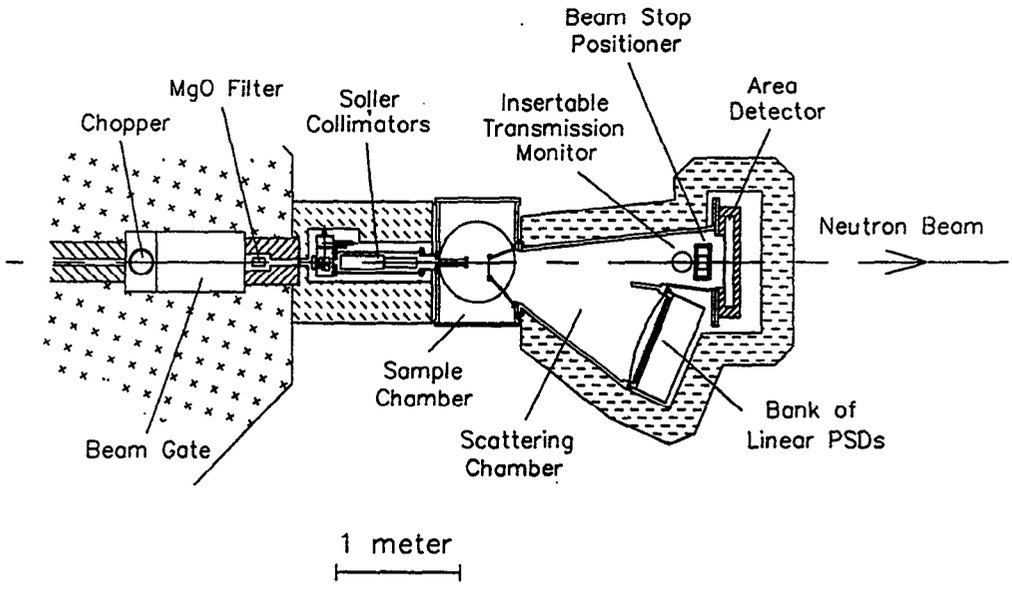

Figure 1: Small Angle Neutron Diffractometer (SAND)

4.2 Chemical Excitations Spectrometer (CHEX)

A prototype inelastic scattering spectrometer for Chemical Excitations (CHEX) was recently constructed at IPNS. The first data were taken in early October, 1995. The instrument is based on well known time focusing principles and the expected dynamic range is 0-500 meV. The instrument views the liquid methane moderator at 100 K, which provides a higher flux of short wavelength neutrons than the solid methane moderators. Chemical spectroscopy such as hydrogen bonding and vibrational density of states will be studied at CHEX. Details are discussed in another paper at this meeting by F. Trouw.

5. New Instruments

5.1 Upgraded Quasielastic Neutron Spectrometer (QENS)

QENS is a crystal-analyzer spectrometer at IPNS optimized to provide ~ 70 μeV resolution for quasielastic scattering, but it also has very good resolution for chemical spectroscopy at excitation energies up to ~150 meV. The "white" beam from the source is incident on the sample, so a separate detector can be mounted to monitor diffraction from the sample. This allows a careful following of phase changes, in situ sample growth or modification, etc., concurrently with the quasielastic- and inelastic-scattering measurements. QENS has three focused-crystal-analyzer arms mounted on a rotating table so that a wide range of scattering angles can be covered. For the past year QENS has been viewing a solid CH_4 moderator at 25K, and this has resulted in a factor of ~5 increase in data rate for most experiments, when compared to the previous liquid CH_4 moderator which operated at ~100K. This higher intensity has made the instrument even more attractive, and demand is rapidly increasing.

The upgrade of QENS, now in the planning stage, will replace the rotating instrument table having 3 detector banks with a fixed instrument having 16 analyzer-detector banks plus 2 diffraction detector banks. Figure 2 shows this planned arrangement. Quasielastic resolution will be kept at ~70 μeV for each of the banks. The incorporation of 16 analyzer banks will allow sampling of the full angular range (~15°- 165°) for inelastic scattering without rotating the instrument. Eliminating the need to rotate will allow the use of improved shielding and will simplify the types of sample environment required. The upgrade will also result in a factor of ~5 increase in the analyzer solid angle, leading to an additional factor of ~5 increase in useful data rate. It is expected that this upgraded version of QENS will be operational in about 2

years. Both QENS and the QENS Upgrade are discussed in further detail elsewhere in these proceedings by F. Trouw.

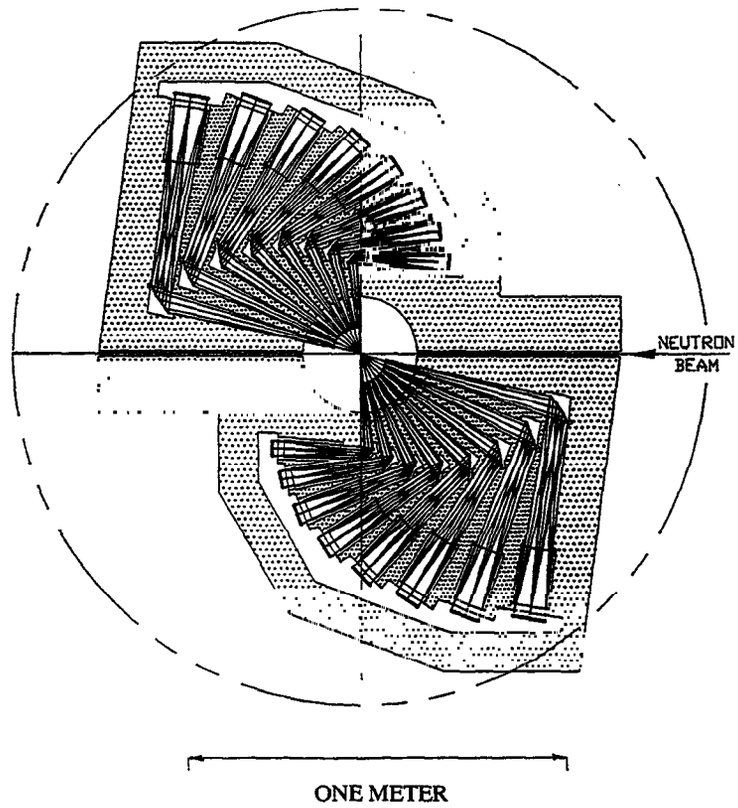

Figure 2: Upgrade of QENS

5.2 Powder Diffractometer

Two new powder diffractometers are being considered for construction at IPNS and eventual transfer to the IPNS Upgrade. The first of these is a 50-meter, multiple-scattering-angle diffractometer which would achieve a resolution of about 1×10^{-3} in back scattering. This diffractometer would be optimized for state-of-the-art structure refinement. A high count rate (comparable to the present GPPD, which is on a 20 meter flight path) would be maintained by the use of a neutron guide along the incident flight path, large detector areas, and multiple scattering angles in order to make optimum use of the full 30-Hz repetition rate. Bandpass choppers would prevent frame overlap, while making use of the highest-intensity part of the spectrum. Such a design was first described by J. Jorgensen at a workshop at Los Alamos in 1986.[7]

Another instrument under consideration is a dedicated high-pressure diffractometer based on the Nelmes-Besson opposed-anvil pressure cell. This new pressure cell design has achieved excellent results in experiments at ISIS and LANSCE. Our plan is to share the neutron beam of SCD, using the beam after it passes through the SCD sample position. By constructing a dedicated instrument, almost a full circle of detectors at a scattering angle of 90° could be employed. This would give excellent count rates at IPNS. This instrument would also be useful for small samples.

6. IPNS Operation

6.1 Accelerator

The IPNS accelerator system has maintained its excellent operating record. Figures 3 & 4 show availability and average target current.

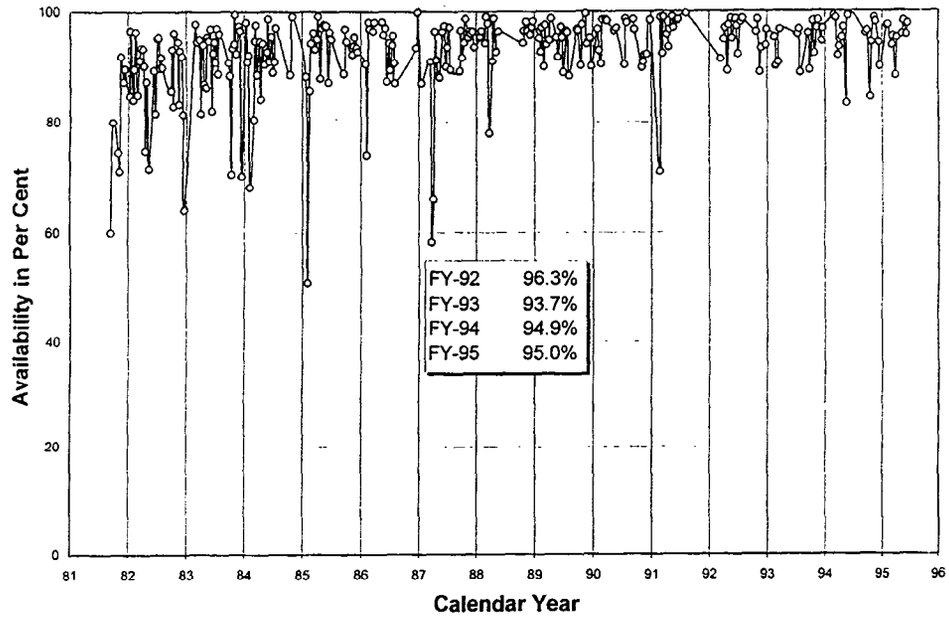

Figure 3: IPNS Accelerator System Availability

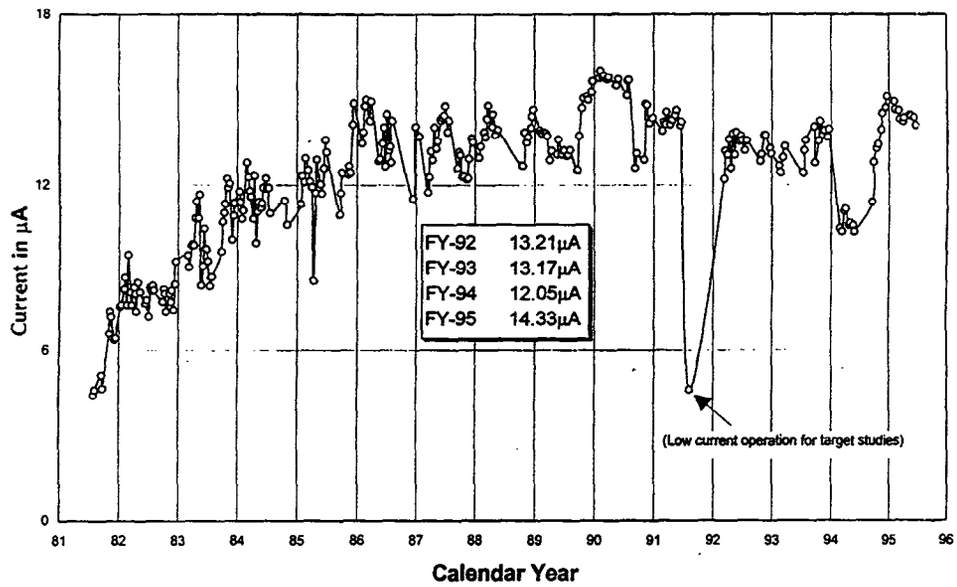

Figure 4: IPNS Accelerator Average Target Current

6.2 User Program

IPNS continues to run one of the most active user programs at a U.S. neutron scattering source. Table 1 below shows the results since IPNS began operation. Fiscal year (FY) 1995 finished at the end of September, 1995, and the data have not been fully tabulated, but they will show a slight increase over FY 1994. The decrease in number of experiments performed following

1989-90 was due to the removal of the booster target and a decrease in operating time. As discussed above, it is anticipated that both of these situations will be reversed soon. In May, 1996, IPNS will mark the 15th Anniversary of the first proton beam on target and a celebration is being planned. Argonne National Laboratory will also be celebrating its 50th Anniversary during 1996.

TABLE 1: IPNS USER PROGRAM

	FY82	FY83	FY84	FY85	FY86	FY87	FY88	FY89	FY90	FY91	FY92	FY93	FY94
NO. OF EXPERIMENTS PERFORMED	94	110	210	180	212	223	257	323	330	273	210	248	281
VISITORS TO IPNS FOR AT LEAST ONE EXPERIMENT:													
ARGONNE	37	41	49	44	52	55	57	60	61	60	53	48	49
OTHER GOV. LABS	8	9	8	7	11	15	18	16	19	15	14	18	13
UNIVERSITIES	27	33	45	51	79	78	89	94	120	92	62	64	63
INDUSTRY	5	5	9	7	13	24	20	24	36	18	20	16	15
FOREIGN	12	18	39	35	27	24	17	26	18	27	14	25	32
	89	106	150	143	182	196	201	220	254	212	163	171	172

6.3 Cold Moderator Development

In September, 1994, a new cold solid methane moderator was installed in the "H" position, which serves three instruments: GLAD, QENS, and HRMECS. We continue operating the grooved solid methane moderator in the "C" position and the liquid methane moderator in the "F" position. The new "H" moderator contains Aluminum foam for heat transfer and Gadolinium poisoning (17 w/o Gd in Al, 0.5 mm thick) 2.5 cm beneath the viewed surface. Both solid methane systems are operated at about 25 K and melted at approximately 60 hour intervals to anneal out the stored energy and remove accumulated Hydrogen. The schedule is dictated by the observation of unprogrammed "burps" that take place irregularly at somewhat less than three day intervals in the "C" moderator.

Figure 5 shows a spontaneous burp of the "C" moderator that took place after 47 hours irradiation with about 15 μA proton current on the depleted Uranium target. It was determined that such a spontaneous burp does not remove all the stored energy, because subsequent scheduled annealing produces another energy release even following a relatively short irradiation. We also find that little Hydrogen gas evolves during warming up to about 65 K, but that the gas comes off rapidly as warming takes place through this temperature (recall that methane melts at about 90 K.) We recently increased the moderator temperature slightly in an effort to eliminate the unscheduled "burps".

The colder moderator, compared to the previous liquid methane "H" moderator (~100 K) not only produces a greater flux of long-wavelength neutrons, but also extends the sharp slowing-down pulse shape to lower energies (with sacrifice of some flux in the ~10 meV region.) This extends the useful range of HRMECS to E_0 below 4 meV, where it achieves about 150 μeV elastic resolution. The counting rate in QENS in the near-elastic range (E_f = 3.7 meV) has increased by about a factor of 5 with little resolution change, so that the typical measuring time for quasielastic scattering from hydrogenous samples is now 2-3 hours. GLAD enjoys cleaner resolution in the longer-wavelength range. The systems have operated with little trouble in recent times.

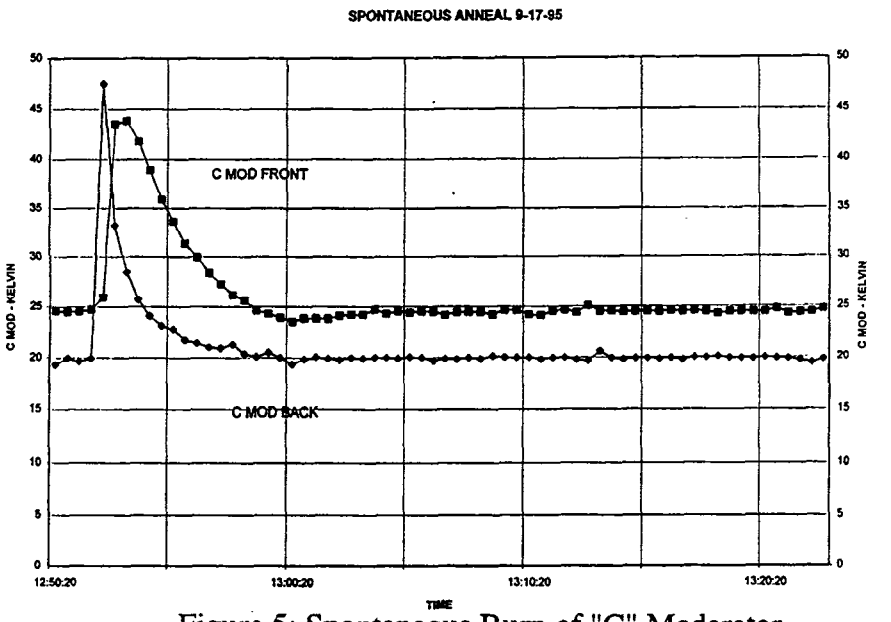

Figure 5: Spontaneous Burp of "C" Moderator

7. New Procedure for Fast Access to the IPNS Powder Diffractometers

Beginning in October, 1995 a procedure will be implemented for obtaining fast turn-around on the Special Environment and General Purpose Powder Diffractometers. A small fraction of the operating time on each of these instruments will be available on a first-come first-served basis, without the need to write the standard four page proposal. A short, one-page form will need to be completed indicating any potential hazards. Interested users should contact the instrument scientists, J. Jorgensen (SEPD) or J. Richardson (GPPD), to learn the backlog for each instrument. Samples will be shipped to IPNS and data collection will be done when time becomes available without requiring the user to come to IPNS. The raw data can then be accessed on the instrument computer. Similar to other experiments performed at IPNS, users will be responsible for data analysis. This service will be limited to short (less than one-day) experiments involving only room-temperature data collection for samples that present no special handling problems. The time allocated to a single user will be limited to allow access for as many different users as possible.

Jim Jorgensen
Phone: 708/252-5513
FAX: 708/252-7777
e-mail: Jim_Jorgensen@qmgate.anl.gov

Jim Richardson
Phone: 708/252-3554
FAX: 708/252-4163
e-mail: JWRichardson@anl.gov

8. Computing at IPNS

IPNS still uses DEC VMS computers for data acquisition and analysis, although most of the staff have personal computers or workstations for other tasks. Some Unix workstations have been introduced for special needs and we have converted our accelerator control system to EPICS, running on Sun workstations. File sharing among personal computers is handled by a Windows NT server. We are investigating the use of Windows NT for data analysis using MS Powerstation Fortran and Visual C++. Windows NT is also used for the IPNS Web-Server (http://pnsjph.pns.anl.gov).

Graphics applications at IPNS were converted several years ago from CA-DISSPLA to GKS using a library of routines called GPLOT. We have now converted many of our graphics applications to PGPLOT, a free graphics library available from Cal Tech which runs on many different computer systems. PGPLOT has been extended with some routines written here, and we are looking at PGPLOT extensions from other laboratories.

A visualization package has been developed, called TOF_VIS, which can be used to quickly survey the experimental data and to analyze detector performance. This started as an application for the GLAD spectrometer and has been generalized for use by other instruments, including some at ISIS. Development will continue on TOF_VIS. For more general data visualization we have purchased IDL software and for analyzing powder diffraction data, we have adopted GSAS.

IPNS has been helping to initiate a number of proposals to increase computing cooperation and collaboration within the neutron scattering community. We hosted the first Workshop on Software Development at Neutron Scattering Sources (SoftNeSS'94) in October, 1994. Following the recommendations of that workshop, we have set up a Web server for neutron scattering in general (http://www.neutron.anl.gov) and a neutron scattering mailing list which now has over 400 subscribers. To subscribe to this list, send an E-mail message to "neutron-request@anl.gov" with the word "SUBSCRIBE" as the first line of the message and you will receive further instructions. We also helped to initiate a follow-up workshop to establish a standard format for the exchange of neutron and X-ray data (SoftNeSS'95) and are currently involved in implementing the new format using NCSA's HDF.

9. Acknowledgments

Almost all of the work discussed in this article and many of the words of the article are the result of effort by other members of IPNS, the neutron scattering group and the APS at Argonne. The operation of IPNS is funded by the U.S. Department of Energy, BES-Materials Science, under contract W-31-109-ENG-38, and the National Science Foundation (DMR-91-20000) through the Science and Technology Center for Superconductivity.

10. References

[1] *Neutron Sources for America's Future*, Report of the DOE Basic Energy Sciences Advisory Committee Panel on Neutron Sources, W. Kohn, Chair, USDOE Report ER-0576P (1993).
[2] *Neutron Sources and Applications*, eds. J. J. Rush and D. L. Price, Report of review held at Oak Brook, IL., Sept. 8-10, 1992, USDOE Report ER-0607P (1994).
[3] *Proc of Workshop on Accelerators for Future Spallation Neutron Sources* , eds. R. J. Macek and H. A. Thiessen, (Santa Fe NM, Feb. 16-20, 1993), LANL Report LA-UR-93-1356 (1993).
[4] *Technology and Science at a High Power Spallation Source*, eds. G. Aeppli and B. S. Brown, Proc of Workshop held at ANL, May 13-16, 1993, ANL Internal Report (1994).
[5] *IPNS Upgrade Feasibility Study,* ANL Report ANL-95/13 (1995).
[6] R. Strain memo to J. Carpenter.
[7] J. Jorgensen, Proc of 1986 Workshop on Advanced Time-of-Flight Neutron Powder Diffraction, LANL Report LA-10824-C (1986).

ICANS-XIII
13th Meeting of the International Collaboration on
Advanced Neutron Sources
October 11-14, 1995
Paul Scherrer Institut, 5232 Villigen PSI, Switzerland

PROGRESS ON THE PSR/LANSCE UPGRADE*

Robert J. Macek†

AOT-Division
Los Alamos National Laboratory
MS-H848
Los Alamos NM, 87544, USA

ABSTRACT

A two-phased improvement program for the spallation neutron facilities at LANSCE is underway and scheduled to be completed early in 1998. The primary goals are a beam reliability or availability of 85% or greater, a capability for routine and sustained beam operations for eight months per year, access to the experimental room (ER-1) closest to the neutron production target with beam on, and 100 μA average beam current from PSR. Many reliability improvements are included in the project along with implementation of direct H^- injection into PSR and a major upgrade of the target/moderator system.

1. Introduction

The winding down of the nuclear physics program at LAMPF (the Los Alamos Meson Physics Facility) presented an opportunity to redeploy these high-intensity accelerator assets at modest cost for a revitalized neutron science program. To this end, the US Congress allocated funds in two phases commencing in 1994 to upgrade the spallation neutron facilities at the LAMPF site and to facilitate the transition to the new LANSCE (the Los Alamos Neutron Science Center). This paper will discuss the objectives, plans, results and progress on both phases of the PSR/LANSCE improvement (upgrade) project undertaken with these funds [1].

2. Goals and Requirements

The primary objective of the upgrade is to improve the research productivity of the neutron facilities and establish LANSCE as a premier center for neutron science. Much of the effort is aimed at improving the reliability and availability of high-intensity neutron beams. Other

* Work performed under the auspices of the US Department of Energy.
† Presented on behalf of the entire LANSCE Upgrade Team.
Key Words: LANSCE Upgrade Project

issues raised by the neutron scattering community are also addressed including a) the need for personnel access to the experimental room (ER-1) while beam is on, b) operation for a significantly larger fraction of the time than the present 3-4 months per year, and c) routine operation of the proton storage ring (PSR) at the design current of 100 μA.

2.1 Reliability/Availability Issues

A key issue for the upgrade is to address the user concern with relatively poor beam reliability and availability at the Manuel Lujan Jr., Neutron Scattering Center (MLNSC). A very significant improvement to ~85% beam reliability/availability (with respect to scheduled beam time) is needed to make the facility attractive to the majority of potential users.

Data on past performance shown in Figure 1 reveal that the average beam availability in the years 1989 through 1993 was 69%. During this same period the availability of PSR (proton storage ring) equipment (including the H- ion source, pre-accelerator and low energy beam transport) was 84% and the availability of the linac was 83%. Of perhaps more significance is length of downtime intervals. In the years 1992 and 1993, for which we have data on the length of downtime intervals, the beam to MLNSC was down 33.4% of the schedule and most (~2/3) of this was due to intervals longer than 8 hours. In fact, the beam was off 20% of the scheduled time for periods of 8 hours or longer. Downtimes longer than a shift are particularly disruptive to the short experiments (around 3 days) typical at a spallation neutron scattering facility.

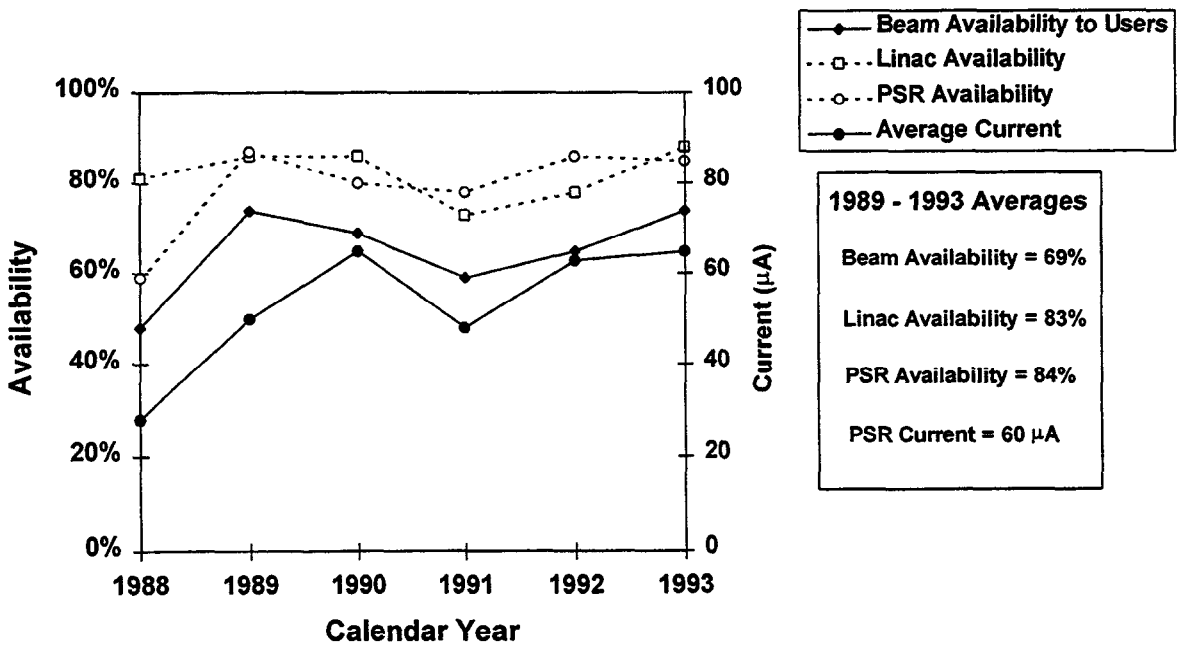

Figure 1. PSR/MLNSC Beam Statistics 1989-1993

Yet another aspect of the general issue of beam availability is the limited amount of beam time per year that has been available in the past. A viable neutron science program requires beam for more than the 3-4 months per year that has been reality for much of the time that PSR has been in operation. While this underutilization is primarily the result of limited budgets for accelerator operations, the goal of operating for about eight months per year is

more than just a question of additional funds for accelerator operations. The long down-times between beam cycles have been utilized to advantage for cool-down of activated components before servicing of both the PSR and the target/moderator systems. In the future, it will be necessary to carry out yearly maintenance activities in much less time. Thus, another important goal of the upgrade is a capability for routine and sustained beam operations for up to eight months per year.

2.2 Personnel Access to ER-1

Safety concerns over the high radiation levels possible in experimental room ER-1 under unmitigated worst-case beam spill accident scenarios have prevented personnel access to this room while beam is on either to the neutron production target or in the beam channel passing over ER-1. As a result of this safety policy, entries are scheduled on a daily basis through negotiations with all affected users on the floor at the time. While the downtime for such entries is scheduled and thus removed from the calculations of beam delivery equipment availability it still has a serious impact on user effectiveness and satisfaction. Access to this area with beam on is very high on the list of goals for the upgrade project.

2.3 Beam current from PSR

The original design goal for PSR was 100 μA of average current at a low (12 Hz) repetition rate. Average beam current in PSR is limited, not by our ability to generate and accumulate the beam intensity, but rather, by beam losses in the ring and the resulting radioactivation of certain ring components. In fact, average currents of 95 μA for periods of one hour or so were demonstrated years ago. As a result of the accumulative effects of beam losses, PSR has a long-term, practical limit of ~ 70 μA average current at 20 Hz.

The causes of the slow losses at PSR are well understood as is the remedy, direct injection of H^- into PSR [2],[3], [4]. What has been missing until the upgrade project is the resources and priority to carry it out. Phase II will include the PSR injection upgrade. It is aimed as much at the reliability and availability improvements that flow from reduced beam loss rates as it is at the opportunity to raise the average current.

3. Phase I

Phase I has focused on the most urgent, short lead-time reliability/availability issues plus measures to assure access to ER-1 with beam on the neutron production target. Measures to mitigate the causes of the longer downtime intervals received the highest priority. A long list (2-3 times more than could be implemented with the combined resources of phase I and II) of meritorious improvement projects was considered and items were selected for the upgrade primarily on the basis of cost/benefit considerations.

3.1 Technical Goals

Specific technical goals for phase I were adopted early in the project and are enumerated below:

- Capability for routine and sustained 8 months/year operation of LANSCE (by end of Phase II)
- Beam availability to LANSCE users > 80% (w.r.t. schedule) by 1996
- Less than 10% down-time from intervals > 8 hours by 1996
- Personnel access to ER-1 with PSR beam on to the MLNSC target
- Reduced beam delivery operating costs
- Reduced radiation exposure

3.2 Main Accomplishments

Phase I was 90% complete as of July 1, 1995 and on time for the start-up activities preceding the beginning of 1995 beam operations. After about 50 days of scheduled beam operations for the MLNSC users the accumulated beam availability was 78% and down-time from intervals longer than 8 hours was 8.5%. While the statistics for 50 days are too limited to claim complete victory, we are encouraged that beam availability is close to the goal set for phase I. The reduction by more than a factor of two in the down time from intervals longer than 8 hours is very encouraging but is also the aspect most limited by the available statistics.

It would be inaccurate to suggest that the hardware improvements alone are responsible for the improved performance. Due credit must be given to the operating and maintenance staff who gave highest priority to improving availability in all of their activities. Both the upgrade and operating teams had improved reliability/availability as a main goal.

The complete list of improvements successfully implemented in phase I is too long to include in this paper. However, the more significant ones are enumerated below:

- Several H^- Source, Injector and Chopper reliability improvements
- Better understanding of RFQ-Injector Options for the H^- beam and the difficulties in chopping such beams to meet existing WNR time structure requirements [4]
- Soft-vacuum upgrade for Tank 1 of the 201 MHz Linac
- Several Linac RF Reliability/Availability improvements
- DC Beam Switching (H^-) to Line D (the beam line transporting beam to PSR and WNR)
- Several PSR Reliability/Serviceability improvements
- PSR Pulsed-Power improvements
- Extraction line BPM upgrade
- Some PSR controls converted to EPICS
- Design Studies for the PSR Injection Upgrade and the Target/Moderator Upgrade
- Improved operability and serviceability of the MLNSC target/moderator cooling systems
- Improved Target Cell Shielding permitting access to ER-1 with beam on the MLNSC target
- LANSCE Hazard Classification and Safety Assessment Document completed and submitted to DOE
- Completed design of an improved, site-wide Radiation Security System (RSS interlocks)

The improvements range from deferred maintenance items and deferred incremental improvements to complete systems redesigned for reliability and maintainability. The reconfiguration/redesign of the highly radioactive extraction septum region in PSR for ease of

maintenance and replacement is an example of the latter. Several design studies for systems to be implemented in phase II were also carried out. The overall flavor is one of a concerted attack on a broad front.

4 Phase II

Phase II consists principally of two longer-term, large projects i.e., direct H^- injection for the PSR and a major upgrade of the MLNSC target/moderator system. The PSR injection upgrade aims at a large reduction (factor of 3-5) in beam loss rates in PSR while the target upgrade seeks to reduce the time to replace the target/moderators from the present 10 months to 3 weeks. The target upgrade also seeks to increase the intensity limit (arising from target constraints) from the present 70 μA to 200 μA.

4.1 Technical Goals

Specific and, where applicable, quantitative technical goals for phase II are enumerated below:

- Beam Availability > 85% by 1998
- Less than **5%** downtime from intervals > 8 hours by 1998
- Access to ER-1 with WNR beam on
- Add capability for more neutron beam lines and neutron scattering instruments
- 100 μA routine operating current @ 20 Hz by 1998

4.2 PSR Injection Upgrade

Beam losses at PSR and the resulting radioactivation of ring components are the dominant factor limiting average beam current, a major factor in equipment repair times and a significant cause of equipment failure. Reducing the beam loss rate is key to any significant increase in the performance of PSR whether it is increased reliability, availability or higher average beam current that is desired.

Stored beam losses in PSR are primarily caused by nuclear and Coulomb scattering in the foil when traversed by stored protons. [2],[4] Large angle scattering leads to immediate loss whereas smaller angles lead to growth of beam halos which can be lost later as synchrotron motion moves the protons to higher momenta and thus larger displacements. Stored beam loss can be reduced by keeping the stored beam off the foil as much as possible. The present two-step injection process (H^- to H0 in a stripper magnet then H0 to H+ in the stripper foil) leads to significant emittance growth in the bend plane of the stripper magnet and a large mismatch at the injection foil. Both factors severely limit the use of various injection "painting" methods to keep the stored beam off the foil.

Direct H^- injection does not suffer the emittance growth from a stripper magnet and offers the capability to focus the beam for optimal painting. Our implementation of direct H^- injection shown in the layout of Figure 2 makes use of a low field magnet (low enough to avoid field stripping of the H^-) to merge the incoming H^- beam with the stored H+. A stripper foil after

the merging magnet strips the H^- primarily to H^+ which is captured in PSR. A small amount of H^- and H^0 beam is present just after the stripper foil. The residual H^- strips to H^0 in the fringe field of the first down stream dipole magnet. Both H^0 beams, the one produced in the foil and the one resulting from field-stripping the residual H^- are converted to H^+ in another foil and transported to a beam dump.

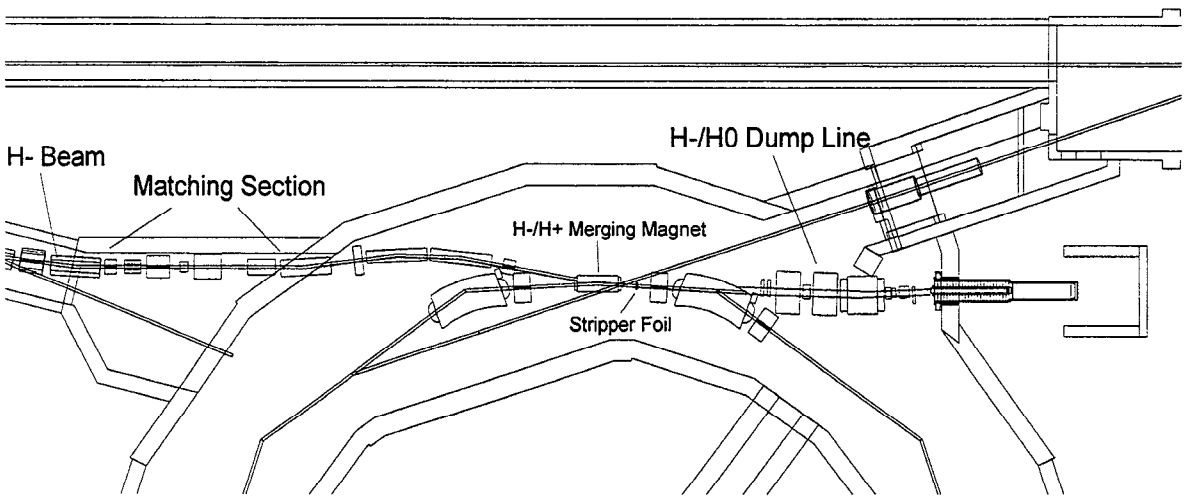

Figure 2. PSR Injection Upgrade (Direct H- Injection Beam Line) Layout

Simulations of an optimized direct H^- injection as configured in layout of Figure 2 and with a programmed closed orbit bump in the vertical plane show a factor of 10 reduction in the number of foil hits per turn. [5]. Some of the gain from reduced foil hits is given up in making the foil thicker (by ~ a factor of 2) to reduce production of excited states of H^0 in the stripper foil and their contribution to "first turn" losses when the excited states strip part way into the first bend magnet downstream from the stripper foil. The final foil thickness is chosen to minimize the sum of stored beam and first turn losses. Thus, the overall reduction in total beam losses, compared with the present injection system, is estimated to be 3-5.

4.3 MLNSC Target Upgrade

Beam operations are at significant risk from target/moderator failures because of the long down time (~ 10 months) needed to make major repairs or replacement. Target failure rates are difficult to predict but the best educated guesses are life-times of order 5 years at present intensities and for 6-8 months of beam operations per year. The liquid hydrogen moderator has failed twice. The most recent failure (September 1995) occurred five years after installation and with no more than 15 months of beam operation. The vulnerability to infrequent but costly failures is clear.

The present target/moderator system takes about 10 months of down-time to replace because many pieces of equipment and shielding must be removed piece-by-piece by personnel working in the target cell. Three to four months of radiation cool-down with beam off are needed before is practical have people working for extended periods of time in the target cell removing components.

The present approach for the target upgrade is a design concept of concentric cylindrical vertical inserts enabling quick access to the failed components. It is illustrated below in Figure 2. The paper presented by Gary Russell at this conference will discuss the target upgrade including this concept in more detail.

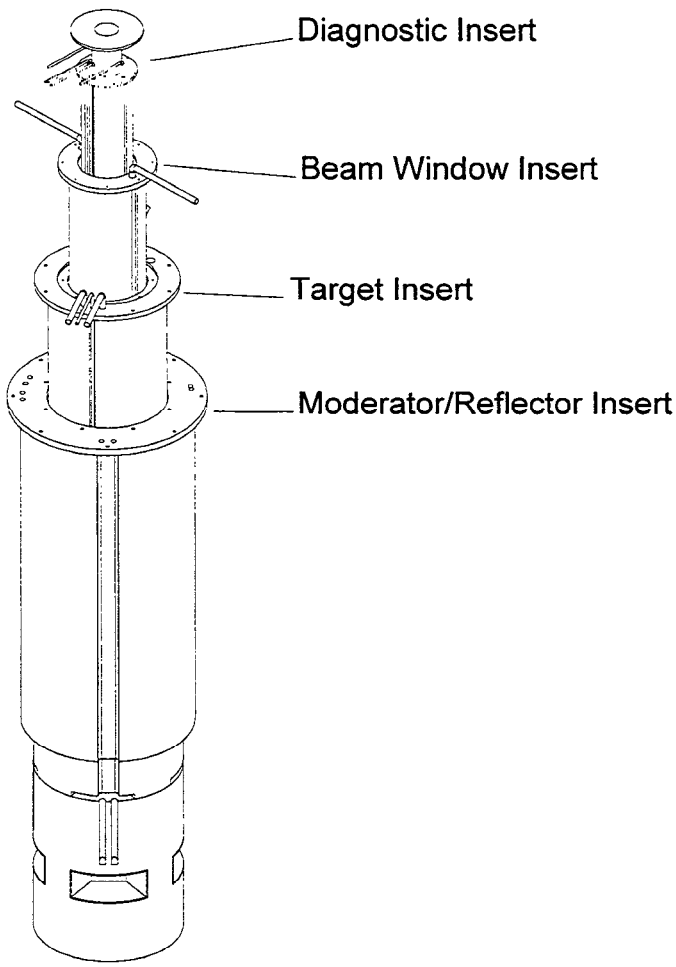

Figure 2. Concept for MLNSC Target/Moderator Assembly Inserts

4.4 ER-1 Access

The added shielding in the MLSC target cell along with RSS-rated beam current limiters in the H^- beam lines to PSR were sufficient protection (under the existing authorization basis) to permit access to ER-1 with PSR beam on to the MLNSC target. The problem of access while WNR beam is on remains to be solved in phase II. The RSS interlock system will be upgraded to full compliance with the latest LANL and DOE standards. With these in place, the case will be made with the regulators that the residual risk from a worst-case beam spill accident is acceptable. Prompt-radiation accidents leading to doses of 25 rem or more in an hour in ER-1 require simultaneous failures of several systems including 3 functionally distinct safety systems.

4.5 Schedule and Status

The target date for completion of phase II is February 1998. One of the drivers is the need for 8 months of down time in one stretch to install the target upgrade. Other than this requirement, phase II will work around the planned beam schedule of 5 months operation in calendar year 1996 and 3-5 months in 1997.

Phase II began in July of 1995 with detailed planning of the work. Design studies of direct H^- injection and the target upgrade began in phase I. Detailed design work is underway in phase II. A first baseline detailed plan for phase II is expected to be finished by November of 1995. An external review of the PSR injection upgrade design is scheduled for October 30-31, 1995. Reviews of the target upgrade and the project cost and schedule are planned for early in 1996.

5. References

[1] R. J. Macek, *A Proposal for Performance Improvements to the Los Alamos Neutron Science Center*, **LANL R-1339-94-2**, July 11, 1994 and R. J. Macek, *LANSCE Performance Improvements, Phase II*, **LANL R-1339-95-0**, May 3, 1995.

[2] R. Macek, et al, *Analysis of Beam Losses at PSR*, **Proceedings of the European Particle Accelerator Conference, Rome, June 7-11, 1988**, p1252-1254.

[3] R. Hutson and R. Macek, *First-Turn Losses in the LAMPF Proton Storage Ring (PSR)*, **Proceedings of the 1993 Particle Accelerator Conference**, p363-365, May 1993.

[4] R. J. Macek, et al, *Status of the PSR Improvement Program*, **Proceedings of the 1993 Particle Accelerator Conference**, p3739-374, May 1993.

[5] A. Browman, et al, *Evaluation of the Existing H- Injector/LEBT for an RF Upgrade*, **PSR Technote 94-016**, November 28,1994.

[6] F. Neri, private communication to be documented as a PSR/LANSCE tech note.

ICANS-XIII
13th Meeting of the International Collaboration on
Advanced Neutron Sources
October 11-14, 1995
Paul Scherrer Institut, 5232 Villigen PSI, Switzerland

NEWS FROM KENS

Hironobu Ikeda

National Laboratory for High Energy Physics
1-1 Oho, Tsukuba, Ibaraki 305 Japan

ABSTRACT

The present status of the KENS Facility is reported and the recent progress in instrumentation is described. A brief outline of the present status of the future program (Japan Hadron Project) is also given.

1. Outline of the KENS Facility

The KENS Facility has been successfully operated since the last ICANS meeting at Abingdon. The operation time of the 500 MeV Booster synchrotron in the past year was about 3500 hours, and the beam time allocated for neutron experiments was about 1500 hours. The average proton-beam intensity was about 1.5 $\times 10^{12}$ protons per pulse (ppp). Figure 1 shows the record of the beam intensity in protons per pulse over the past six year. Since the repetition rate of the accelerator is 20 Hz, the average proton beam current was about 5 μ A.
Although the depleted uranium target has been operated trouble-free since the beginning of its operation in 1985, it was replaced with new uranium target on September, 1995. This is due to the detection of a small amount of Xe-135 in a cover-gas of primary cooling water (8000 atoms / liter). We experienced no serious problems with the cryogenic moderator (solid methane at 20 K) since 1988 because solid methane is renewed every two days before a "burp" can occur.
During the last financial year, 106 experiments including 13 large proposals by groups responsible for the instruments were carried out. Scientists who visited the KENS facility spent about 5000 man-days. The oversubscription has become more serious in recent years; especially for LAM-40, SAN, WINK and VEGA.
A construction of a new cold-guide experimental hall (1200m^2 in area) was financially approved last May, and a construction will start on November 1995. At the same time, we will install a high-resolution multi-purpose diffractometer in the new experimental area (Fig.1).

2. Instrumental Developments

There are currently 16 instruments in the KENS Facility as listed in Table I. We have seen appreciable progress in instrumentation since the last ICANS meeting.
The construction of a new high-resolution powder diffractometer, VEGA, was completed, and HRP was replaced. Although the HRP is a prototype instrument equipped with only 12 normal

^{3}He counters, it has been very productive and busy. VEGA was designed to have large counter banks, comprising many 1D-PSD's at the backward, 90 degrees, and lower angles in order to improve the data-rates (about 5 times higher than the HRP) and the resolution ($\Delta d/d \sim 0.002$) and to increase the range of the d-spacing covered. Figure 2 shows the detector layout of VEGA.

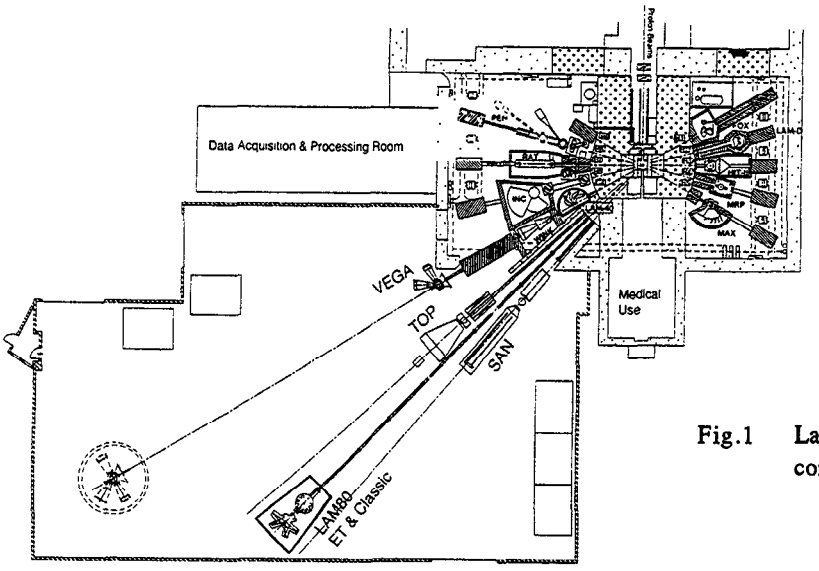

Fig.1 Layout of new KENS Facility to be completed in June, 1996

The development of polarized ^{3}He as broad-band neutron polarizing filter from thermal to epithermal energy region is in progress. Rubidium atoms are polarized by irradiation of circularly polarized photons. Atomic polarization is transferred to ^{3}He nuclei upon atomic collision. A ^{3}He polarization of about 50% was achieved for a 8-cm length and 2.5 cm diameter cell at 3-atm ^{3}He pressure. High power diode-laser system for the optical pumping is used to polarized higher pressure cell, 8 atm. The result will be reported elsewhere.
We are also making progress on the development of pulsed high magnetic field equipment for scattering experiments. The highest field (up to 20 T) in the horizontal direction has already been achieved, and we started, in 1993, the construction of a new magnet and very recenty we achieved 30T. This instrument will provide new opportunity for the sudy of magnetic phase transition.

Table 1. KENS neutron scattering instruments

Instrument Name		Range of Q & E		Resolution	
Liquid and Amorphous Diffractometer	HIT	$0.2 \le Q \le 100$	A^{-1}	$\Delta Q/Q = 0.006 - 0.05$	
Small-Angle Scattering Instrument	SAN	$0.003 \le Q \le 4$	A^{-1}	$\Delta Q/Q \approx 0.1$	
Small-/Medium-Angle Diffractrometer	WINK	$0.015 \le Q \le 20$	A^{-1}	$\Delta Q/Q \approx 0.1$	
Multi-Purpose Diffractrometer	MRP	$1 \le d \le 5$	A^{-1}	$\Delta Q/Q = 0.015 - 0.03$	
High Resolution Powder Diffractrometer	VEGA	$0.3 \le d \le 13$	A^{-1}	$\Delta Q/Q = 0.002$	
Single Crystal Diffractrometer	FOX	$0.2 \le Q \le 40$	A^{-1}		
Polarized Cold Neutron Spectrometer	TOP	$0.02 \le Q \le 0.6$	A^{-1}		
Polarized Epithermal Neutron Spectrometer	PEN	$0.02 \le E \le 100$	eV		
Ultra-Cold Neutron Machine	UCN				
High Resolution Quasi-Elastic Spectrometer	LAM-80ET	$E \le 0.3$	meV	$\Delta E = 1-5$	μeV
Quasi-Elastic Spectrometer	LAM-40	$E \le 10$	meV	$\Delta E = 100$	μeV
Molecular Spectrometer	LAM-D	$E \le 200$	meV	$\Delta E = 300$	μeV
High Resolution Spectrometer under Extrime Condition	LAM-80C	$E \le 1$	meV	$\Delta E = 5-20$	μeV
Sub-eV Spectrometer	CAT	$3 \le E \le 1000$	meV	$\Delta E/E = 2$	%
Coherent Inelastic Scattering Spectrometer	MAX	$0 \le E \le 100$	meV	$\Delta E = 2.5 - 10$	meV
eV Spectrometer	RAT	$E \le 100$	eV	$\Delta E = 50$	meV
Chopper Spectrometer	INC	$2 \le E \le 1000$	meV	$\Delta E/E = 2-4$	%

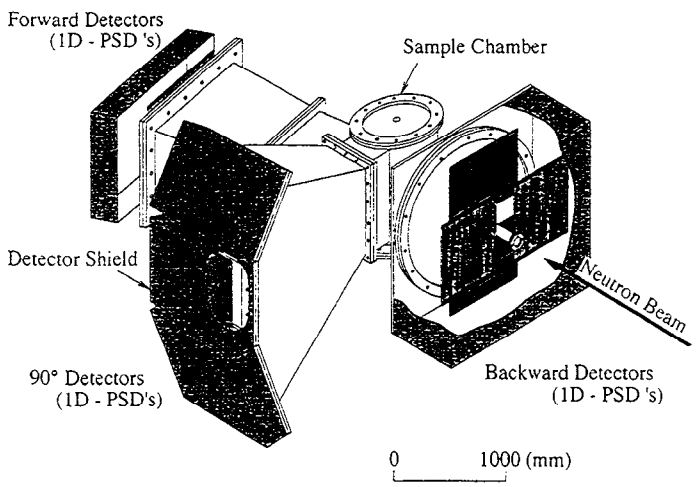

Fig.2 Detector layout of VEGA

3. Neuron Scattering Experiments

The determination of self-similar structure in the system near the percolation threshold in the diluted antiferromagnet, $RbMn_{0.34}$ $Mg_{0.66}F_3$, has been made on HRP using a single-crystal sample. As the magnetic concentration (0.34) is very lose to, but above, the percolation threshold (0.312), a crossover from a resolution-limited Gaussian shape near q=0 to a power-law decay function with a fractal dimension of 2.48 has been observed in the elastic magnetic scattering near the Bragg position.

Critical inelastic scattering measurement has been made on high-resolution spectrometer LAM-80ET with an energy resolution of 5 μ ev of Mica (004) reflection. Experiments on a single-crystal sample of a two-dimensional Ising antiferromagnet, Rb_2CoF_4, have been made at q=0 as a function of temperaturen. From these measurements, dynamical critical exponent, z, was determined to be 2.0 $\pm$0.05 (Γ (q=0,T) $\propto \kappa_1(T)^z$), where Γ is a damping constant at q=0 and κ_1 is the inverse thermal correlation length (Fig.3).

One of the current topics in the research of amorphous materials is dynamics near the glass transition. Neutron scattering measurements on the fast process of polybutadien have been performed with LAM-40 (energy resolution is about 200 μ ev) (Fig.4). It was made clear, from the observation of the damping constant of a quasi-elastic component as a function of q and T, that the fast process is related to the localized cage motion.

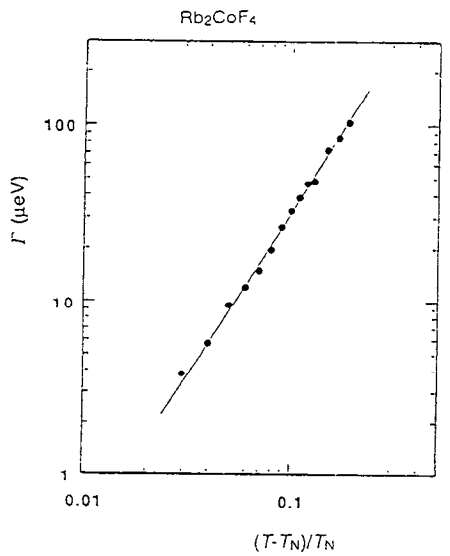

Fig.3

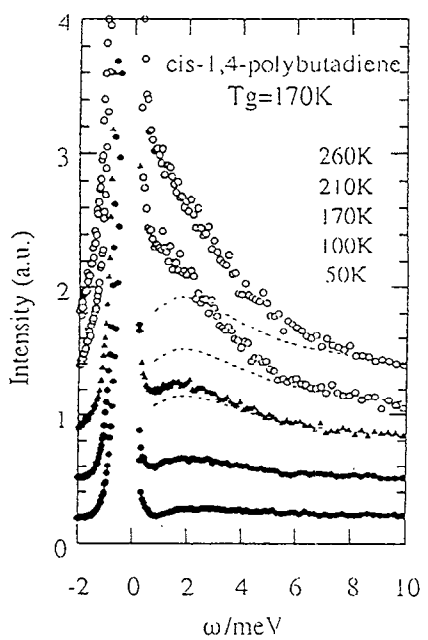

Fig.4

The hexagonal $CsCuCl_3$ has linear chains of Cu^{2+} ions along the c-axis and it makes triangular lattices in the c-plane. It shows 120° magnetic structure in the c-plane due to the imterchain antiferromagnetic interaction. In such a magnetic system, if an external field is applied parallel to the c-axis, the magnetic moments tilt from the c-plane and the magnetization is supposed to be linear up to saturation with respect to the field intensity. However. the change of the umbrella-like structure at low fields to the coplanar one at high fields was observed at about 12 T in the field-dependence of the magnetic elastic intensities (Fig.5). The result is explained as a transition due to the quantum effect in the system with one-diumensionality and S = 1/2.

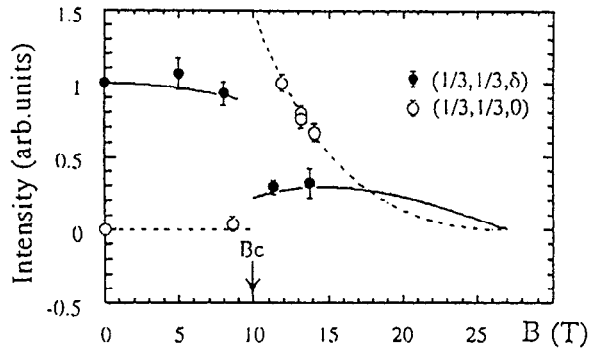

Fig.5 Field dependence of diffraction intensities as a function of field intensity.

Great prgress in P,T violation study in neutron nucleus resonance is realized. Parity-violating neutron-spin rotation was firstly observed in a neutron-nucleus p-wave resonance. A compound nucleus resonance theory predicts large enhancement in the p-wave resonance in eV region and a dispersion like shape for the parity violating effect as a function of the neutron energy. The experiment verified the theoretical prediction. For the T-violation study, a large lanthanum nuclear polarization is realized for the measurement of T-odd triple correlation, $\sigma \cdot k \times I$. σ is the neutron spin, k the neutron momentum and I the lanthanum nuclear spin.

4. Future Program

For a long time we have been anticipating funding for Japan Hadron Project (JHP). Within these several months great advance in the JHP was seen. At this moment, discussions are being made on the governmental base. Institute of Nuclear Science (INS), University of Tokyo, which has been a leading institute of JHP, will move to KEK-area and be reconstructed together with KEK. This reorganization will hopefully start on April, 1997, and a construction of new proton acclerator will be started in 1998. New organization will have a responsibility for the construction of JHP and scientific activities of high energy physics, synchrotron radiation sciemce, nuclear science and neutron scattering. In the present program, a 200 MeV proton linac and 3GeV and 50 GeV proton synchrotrons are being considered for neutron science, muon science, nuclear science. For neutron scattering facility, 3GeV-200 μ A (25 H_z, 0.6 MW) proton beam is injected to a neutron target, and as the second stage of JHP there exists possibility of upgrading to 1.2 MW (50 H_z).

ICANS-XIII
13th Meeting of the International Collaboration on
Advanced Neutron Sources
October 11-14, 1995
Paul Scherrer Institut, 5232 Villigen PSI, Switzerland

NEWS FROM IBR-2

V.L.Aksenov

Frank Laboratory of Neutron Physics, Joint Institute for Nuclear Research, 141980 Dubna, Moscow region, Russia

ABSTRACT

The IBR-2 nuclear reactor is the most intense pulsed neutron source for condensed matter physics in the world. The present status and trends of reactor development and instrumentation for physical research are described.

1. Introduction

The IBR-2 reactor is the pulsed reactor of periodic operation (pulsing reactor) which has been operating in a regular mode with a mean power of 2 MW and a pulse repetition rate of 5 Hz since 1984. The power in the pulse is 1500 MW and the neutron flux in the pulse is 10^{16} n/cm^2/s. Detailed description of the IBR-2 reactor structure is given in the monography[1]. Later developments of the reactor and its instrumentation are detailed in reviews[2-5].

The main original feature of the IBR-2 reactor consists of the mechanical modulation of reactivity which is accomplished with the help of a movable reflector. Because of a low mean power and as a result, lower activation of equipment and slower burnup of the core the IBR-2 reactor is an extremely economical and relatively inexpensive machine. For 2500 hours of regular operation per year the service life of the core is 20 years and of the movable reflector 5 to 7 years.

On March 27, 1995 the IBR-2 reactor resumed operation with a new movable reflector with a rated service life of 7 years. At the same time, after 2001 the resource of the core currently in use will be exhausted. In this connection, it seems expedient to simultaneously replace the reactor jacket, fuel, stationary reflectors, control and emergency system mechanisms, and water moderators in the period from 2002 to 2004. So, this year we started work to prepare the IBR-2 modernization in the period from 1995 to 2001. In principle, the

Keywords: Pulsed reactor, Instrumentation

new reactor will have the same structure and mean power as the IBR-2, but improving all reactor elements following accumulated experience of reactor operation will, as we hope, help upgrading the reactor characteristics and, in particular, permit a 2 times increase in the neutron flux and a 1.5 to 2 times decrease in the pulse width. More detailed information on the programme of the development of the neutron sources in Dubna is published in[6].

This contribution gives information on the recent main results of upgrading the IBR-2 reactor and development of spectrometers in the period after the last ICANS meeting.

2. Cold moderator for IBR-2

At present, work on upgrading the IBR-2 reactor concentrates on manufacturing the cold methane moderator[7,8].

Over a period of several years work to create a cold neutron moderator for the IBR-2 reactor has been carried out by the Frank Laboratory of Neutron Physics. In 1992, a cold moderator prototype was manufactured and installed in place of the cock water moderator on channels 4 to 6 for short-term investigations of the thermotechnical and physical characteristics of the cold moderator at a reactor power of 1 MW. In December 1992 - January 1993 a long-term investigation of cold methane behavior under irradiation was conducted with the URAM facility at a reactor power of 2 MW.

In February 1994, investigations of the cold moderator prototype completed. The basic possibility of using solid methane as a neutron moderator at a reactor power of 2 MW was demonstrated. A 15 to 25 times increase in the cold neutron flux in comparison with the regular water moderator was obtained. The obtained results formed the basis for creating a regular cold moderator for IBR-2 using solid methane at 20-60 K.

In 1995, work on the creation of a regular cold moderator for IBR-2 continued. Designing of the cryogenic moderator was executed. Development of the project for the technological systems of the cryogenic moderator is approaching its final stage. The project for temporal siting the cold moderator was elaborated. The project of a system for parameter measurements and control and measuring devices is in the stage of realization. A contract for investigating strength characteristics of the cryogenic moderator was concluded. Contracts for manufacturing the cryogenic moderator were concluded and are due to payment by the end of 1995. We hope that the cold methane moderator will be ready for regular operation at the end of 1996.

3. Instruments

At present 13 spectrometers for physical research are operating on the beams of the IBR-2 with 6 of them serving experiments on diffraction studies, 1 - on small-angle scattering, 2 - on reflectometry, and 4 - on elastic scattering. Detailed information about the parameters of these spectrometers is given in[5].

Two new spectrometers were reported on at the last ICANS meeting: the NERA-PR Multicrystal Inverted Geometry Spectrometer[9] and the HRFD High Resolution Fourier Diffractometer[10]. These spectrometers, especially the HRFD, are of significant importance for IBR-2 because they give the same resolution as the ISIS instruments. Recent comparison of parallel measurements with TFXA ISIS and NERA-PR is given in[11]. A special session of this meeting will be devoted to Fourier diffractometers, where detailed information on the HRFD will be presented.

In this contribution I will focuse on the other two new spectrometers which recently started operations.

3.1. Time-of-flight neutron spectrometer for micro-sample studies under high pressures (DN-12 spectrometer)

The DN-12 spectrometer is placed in channel 12 of the IBR-2 reactor and consists of the following main systems: neutron beam chopper phased with the power pulse of the reactor, beam collimating system, multicounter circular detector system, information management, and a registration and processing system.

The DN-12 spectrometer is specifically intended for work with high-pressure cells based on sapphire anvils. A well collimated neutron beam passes through the sapphire single crystals, between which a sample is placed. Scattered neutrons are registered by the detector consisting of small counters positioned around the circle of a vertically standing ring. The ring as a whole can be moved relative to the sample along the beam direction, providing scattering angles from 45° to 135°.

In Table 1 the essential parameters of the DN-12 spectrometer are given.

Table 1. The main characteristics of DN-12

	1994	1997
1. Thermal neutron flux at the sample position	$1 \cdot 10^6$ n/cm^2/s	$2 \cdot 10^6$
2. Distances: moderator-sample	31.8 m	27.0 m
sample-detector	0.4 m	0.4 m
3. Range of:		
wavelength	1 - 4 Å	0.8 - 10 Å
scattering angle	45° - 135°	45° - 135°
d_{hkl}	0.8 - 5.2 Å	0.6 - 13 Å
4. Resolution ($\Delta d/d$, d=2 E):		
for 2θ=90°	0.022	0.022
for 2θ=135°	0.012	0.012
5. Solid angle of the detector system	0.125 sr	1.0 sr
6. Pressure range:		
with sapphire anvils	10 GPa	25 GPa
with diamond anvils	20 GPa	50 GPa

Table 2 gives the list of some experiments performed with DN-12 since the start of its operations.

Table 2. Experiments performed with DN-12 from November 1993. Pressure is given in GPa, sample volume in mm^2

Sample	Pressure	Volume	Anvils	Main result
Hg-1212	3.6	1	sapphire	equation of state, struct. changes
DyD_3	10.0	0.01	diamond	equation of state
ND_4Cl	2.5	2	sapphire	structural changes
NH_4Cl	4.0	2	sapphire	libration and lattice mode changes
Fe_2O_3	4.7	1	sapphire	new magnetic phase above 3 GPa

Results of the investigations of the vibrational spectrum and structure variations in NH_4Cl are published in[13], the results of the structural studies of high-temperature superconductors are published in[14].

Several experiments have been carried out to determine the minimal quantity of substance from which it would be possible to obtain a diffraction pattern with DN-12 within a reasonable amount of time (not more than 50-100 hours). For this purpose, a $^{164}DyD_3$ sample with a maximal coherent scattering cross-section was used ($\sigma_{coh}\approx250$ b). This sample was placed in the diamond anvil cell. The sample volume was 0.027 mm^3, the pressure was about 10 GPa, and it was possible to increase the pressure up to 20 GPa. One can see in Fig.1 the clear diffraction pattern, which was obtained in 24 hours.

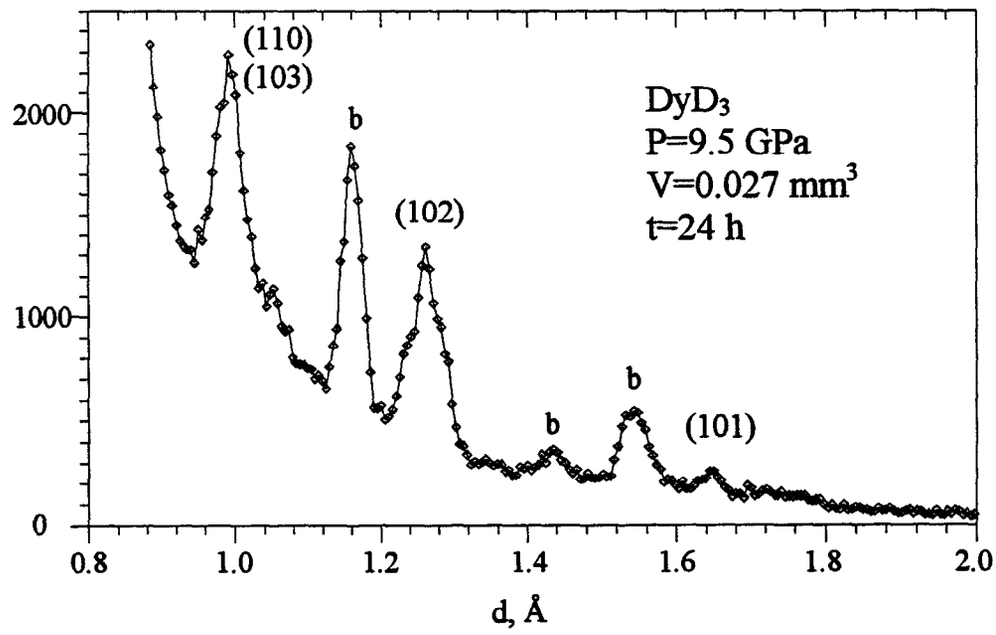

Fig.1 Diffraction pattern of DyD_3 powder (the isotope ^{164}Dy was used) measured in a diamond anvil cell in 24 hours. The sample volume was 0.027 mm^3, the pressure was 9.5 GPa. The Miller indices of diffraction lines from the sample and background lines (b) are shown.

It is planned to develop the DN-12 in the following directions:

- improvement of the detector system, including the creation of a data acquisition system in VME standard;
- substitution of the vacuum neutron guide tube by a mirror neutron guide tube;
- moving of the neutron beam chopper to another position. (It will be placed 4.5 m between the moderator and chopper instead of 8.9 m at this moment);
- creation of special equipment for loading the pressure cell with the optical spectrometer measurement of pressure;
- widening of experimental possibilities (use of new materials for the anvils, getting low and high temperatures at the samples.

The experiments carried out at the DN-12 spectrometer have shown its advantages in comparison with similar devices in such centres as RAL, RRC KI, ANL, LANL. Putting the

new detector system into operation, building the mirror neutron guide tube and a beam chopper will improve the device characteristics significantly, increase its efficiency and will make it more attractive and beneficial for users.

3.2. REFLEX complex

This instrument having been designed with account for experience acquired by the neutron laboratories over the world has some original features making it different from the like instruments. The design of the instrument is described in[15]. The incident neutron splits into two beams in the collimator system. Then one of the beams passes through a polarizing and the other through a nonpolarizing mirror systems which focuse neutrons on two samples, where each of the two beams again splits into two. So, the REFLEX complex consists of two independent reflectometers: REFLEX-N with an unpolarized neutron beam and REFLEX-P with a polarized neutron beam and a horizontal geometry arrangement.

In 1994-early 1995, the main units of the REFLEX complex were installed, adjusted and the first test experiments on REFLEX-P were performed. The REFLEX-P uses the unique, highly efficient Korneev spin-flipper with an extended spin-reverse area. The polarization reflectometer also has an original magnetic system: a solenoid with a special electromagnet which can be rotated about the neutron beam axis to create an arbitrary oriented field up to 1 KOe on the sample. The essential parameters of the REFLEX-P spectrometer are given in Table 3.

In Fig.2 the polarization of the incident beam as a function of the wavelength, as measured by the FeCo/TiGd analyzer, is shown.

The detector system for each reflectometer consists of four PC-controlled movable ^{3}He detectors. The REFLEX-P is also equipped with a helium cryostat for 1.5 K, a helium refrigerator for the temperatures above 9 K, and a vacuum furnace for up to 500°C.

Table 3. The main characteristics of the REFLEX-P

Moderator	water at 320 K
Neutron wavelength	1.2-8 Å
Polarizer	two parallel FeCo/TiGd mirrors 1.6 m long adjusted for twofold impindge of neutrons
Incident beam polarization averaged over the spectrum	98%
Q range	0.005-0.1 1/Å
ΔQ/Q (for a grazing angle of 7 mrd)	2%
Spin-flipper efficiency	99.6%

Test experiments with the REFLEX-P reflectometer have demonstrated high efficiency and a ready state of the instrument for the realization of the physical program whose first priority is the study of microscopic magnetic properties of superconductors, inhomogeneities in magnetics, and multilayer polymer structures. It is planned to carry out complete equipping the REFLEX-N in 1996.

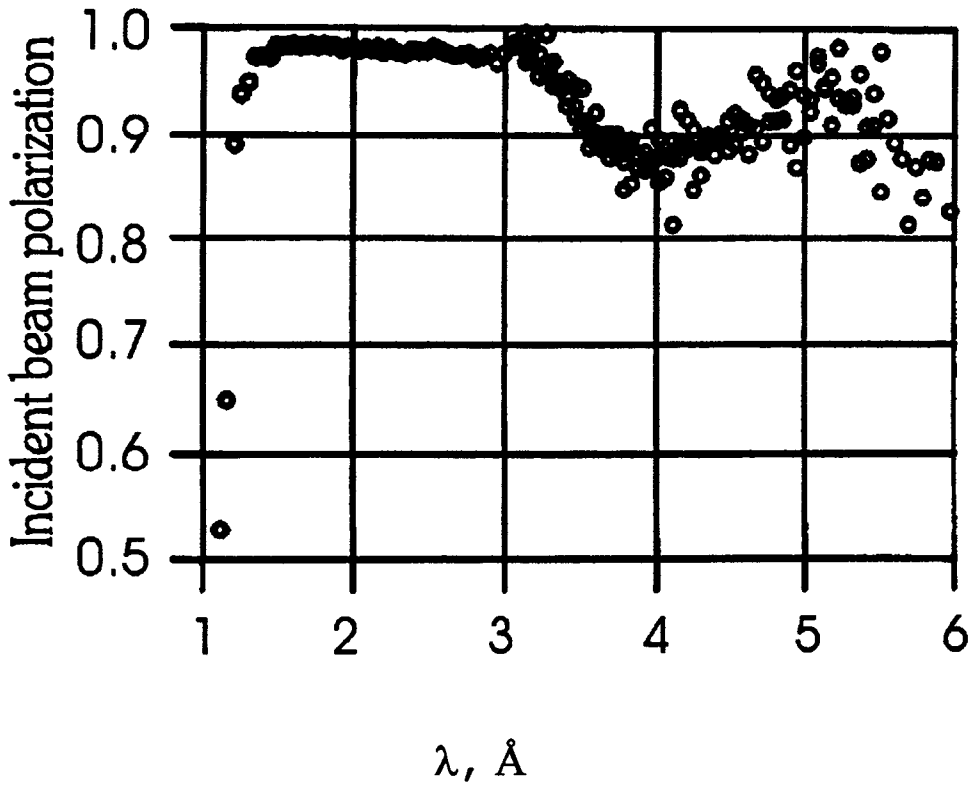

Fig.2. Neutron beam polarization by REFLEX-P as a function of the wavelength

4. Conclusion

The third field of activity around the IBR-2 reactor (besides upgrading the reactor and development of spectrometers) is the development of the experimental infrastructure, including upgrading sample environments and the computational and data acquisition systems of the Laboratory. The major goal of these projects is to create a system for performing experiments which will be user friendly and similar to what scientists find in western or international neutron centers. This system will also allow effective data storage and easy transfer of data between Dubna and other institutions.

So, in the last two years much effort was made by the Laboratory staff to make all IBR-2 experimental facilities open to the world scientific community.

In conclusion, I would like to emphasize that the IBR-2 high flux pulsing reactor with a large neutron pulse duration (~300 μsec) really gives physicists the possibilities which are very close to those provided by spallation sources nowadays. The operational experience with IBR-2 shows that the width of the neutron pulse is not crucial in achieving a good quality source and to have a higher flux is more important. I believe the above conclusion from the IBR-2 experience could be helpful in discussions on the prospects of neutron sources in condensed matter physics.

5. References

[1] E.P.Shabalin, *Fast Pulsed and Burst Reactors* (Pergamon Press, Oxford, 1979)
[2] A.V.Belushkin, *Neutron News* **2** (1991) 14

[3] V.L.Aksenov, *Physica B* **174** (1991) 438
[4] V.L.Aksenov, in *Large Facilities in Physics,* ed. M.Jacob and H.Schopper (World Scientific, Singapore, 1995)
[5] A.M.Balagurov, *Neutron News* (1995) in press
[6] *FLNP - Programme of Research and Development 1996-1998,* ed. V.L.Aksenov and Yu.V.Taran (JINR, Dubna, 1995)
[7] A.A.Belyakov, V.G.Ermilov, V.L.Lomidze et al., in *Proc. of ICANS-XII,* RAL Report 94-025 (1994), vol.II, p.144.
[8] A.A.Belyakov, V.V.Melikhov, Yu.N.Pepyolyshev and E.P.Shabalin, *J. of Neutron Research* (1995) in press
[9] I.Natkaniec, S.I.Bragin, J.Brankowski and J.Nayer, in *Proc. of ICANS XII,* RAL Report 94-025 (1994), vol.1, p.89
[10] V.L.Aksenov, A.M.Balagurov, V.G.Simkin et al., ibid, p.124
[11] R.Baddour-Hadjean et al., Chemical Phys. **197** (1995) 81
[12] V.L.Aksenov, A.M.Balagurov, B.N.Savenko et al., *High Pressure Research* **14** (1995) 181
[13] A.M.Balagurov, B.N.Savenko, A.V.Borman et al., ibid, p.55
[14] V.L.Aksenov, A.M.Balagurov, B.N.Savenko et al., ibid, p.127
[15] V.L.Aksenov, D.A.Korneev, L.P.Chernenko, in *Neutron Optical Devices and Applications,* ed. Charles F.Majkrzak, James L.Wood. *Proc. SPIE,* **1738** (1992) 335

ICANS-XIII
13th Meeting of the International Collaboration on
Advanced Neutron Sources
October 11-14, 1995
Paul Scherrer Institut, 5232 Villigen PSI, Switzerland

SPALLATION NEUTRON SOURCES AT THE INR RAS: PRESENT STATUS AND PROSPECTS

Y.Y.Stavissky

Institute for Nuclear Research RAS

60th Anniversary of October Ave., 117322 Moscow, Russia

ABSTRACT

The paper presents the program of development of spallation neutron sources for research in nuclear and solid state physics, radiation damage physics, problems of the weapon plutonium utilization and nuclear waste transmutation.

1. Introduction

The INR RAS is developing the program of creation of intensive neutron sources driven with the high-current proton linac of the Moscow Meson Factory for studies in nuclear and solid state physics and for applied studies.

The program relies on the Monte Carlo simulation of spallation and fission neutron generation and interaction with medium [1, 5].

The construction of the intensive pulsed slow neutron source IN-06 [4] based on the proton linac [2], storage ring [3] and tungsten or natural uranium silicide targets is near completion (1996). It is primariliy intended for studies in nuclear and solid state physics.

The multiplying uranium target with gallium cooling is under development (RIN-10, [5]). It will allow the slow neutron fluxes with peak and average densities as high as 10^{17} and 10^{14} n/cm^{2}s to be achieved.

This year the construction of the proton beamstop with the irradiation channel [6] should be completed. The fast neutron flux density as high as 10^{15} n/cm^{2}s·mA is to be achieved.

The super sensitive neutron spectrometer based on the neutron slowing-down in lead is under development. The spallation neutron generation rate in it will constitute $\sim 10^{16}$

n/s. Its prototype "Python" [7] with the intensity of $5 \cdot 10^{13}$ n/s is now being used for studying actinide's fission.

Certain efforts are directed towards the problems of efficient utilization of weapon plutonium and transmutation of long-lived fission products with high-current proton accelerators [8,9].

2. Methods for calculating the spallation neutron source characteristics

For calculations of neutron yield, heat deposition, nuclide production and radiation damages in targets and shielding under the proton beam in the energy range 0.1 - 100 GeV the transport codes SHIELD [10] and RADDAM [11] are used. The SHIELD code is intended for statistical simulation of hadronic cascades in targets of arbitrary geometry and composition. Effects considered include transport of nucleons, antinucleons, pions, kaons and muons upto 100 GeV, ionization losses, straggling. The SHIELD's hadronic generator provides for exclusive description of nuclear reactions for all the energy and target nucleus mass ranges. As an example, the specific neutron leakage (E < 10 MeV) from the large lead target as a function of the incident proton energy is given in Fig. 1 [12].

Low-energy (below 10 MeV) neutron transport in optimization studies is simulated with the Monte Carlo code NeuMC [5].

3. Pulsed neutron source IN-06 ond possibilities of its development

The neutron source consists of the target irradiated with the proton beam accelerated by the linac and compressed in the storage ring and of the moderator system (Figs.2,3).

At the first stage, before the storage ring will be in operation, it is supposed to use the linac's proton beam with pulse duration 0.2-1 μs for nuclear physics studies and 30-150 μs for solid state physics studies. Pulse shaping is performed with the chopper in the linac's injector [13].

Presently, the accelerator is completely assembled and is capable of producing proton pulses with the energy 423 MeV, pulse current 20 mA, duration 0.2-70 μs and repetition rate 50 pps.

The bending magnets of the storage ring has already been manufactured. Mounting the magnet and vacuum systems of the storage ring is scheduled on the second half of 1997.

Initially the neutron source will operate with water-cooled tungsten and natural uranium silicide targets [4]. Rod fuel elements made of uranium silicide (γ = 16.1 g/cm^3) canned in stainless steel (1X18H9T - similar to 316 steel) tubes and distantiated with wire constitute a hexagonal lattice. 1.5-6 cm thick wing-type water moderators are placed above and below the target inside the vessel made of the Al-Mg alloy AMG-3 (Fig.4). Four neutron guides are directed at the upper moderator and three - at the lower one (Fig.5).

The tungsten target is assembled of 5-10 mm thick plates made of metal tungsten with density 18.9 g/cm^3 and coated with titanium.

Presently the most of neutron source construction is completed: cast-iron and heavy concrete shielding with netron channels and cavities for targets, collimators, choppers

and gates; the targets and cooling circuit equipment are manufactured; the mounting is in progress.

Tungsten and uranium target elements have been tested in the core of the light-water research reactor.

Start of the source operation under the proton beam is scheduled late in 1996.

At the initial stage it is planned to conduct research works in the following directions:

- studying fission of heavy nuclei aligned at low temperatures (~0.1 K) with polarized resonant neutrons - collaboration of the Institute of Physical Energy (Obninsk), LNP JINR (Dubna), ITEP (Moscow), INR RAS;
- studying dynamics of solids and liquids using the inverse geometry spectrometer KDSOG - INR RAS in collaboration with LNP JINR [14];
- studying dynamics and structure of solids and liquids using the multifunctional spectrometer of Lebedev's Physical Institute RAS;
- properties of matter under high pressure - Institute of High-Pressure Physics RAS, Troitsk.

4. Multiplying targets

Further gain in slow neutron fluxes may be achieved by using multiplying targets [15]. High spallation neutron generation rate allows the deeply subcritical targets with the gain factor not exceeding 20 to be used. Even if the target will be surrounded by a thick reflector (upto 50 cm), prompt neutron lifetime in such a system will not exceed 100 ns [4, 5], and, as a consequence, power and fast neutron pulses will be 1.2 - 1.5 μs long.

The cumulative effect of neutron multiplication, comparatively soft spectrum of fission neutrons and slowing-down of neutrons due to elastic and inelastic scattering in a reflector results in achieving the peak and average values of slow neutron flux density as high as 10^{17} and 10^{14} n/cm^{2}s respectively [5]. The values given correspond to the 0.3 MW beam of 0.7 GeV protons. It is worth mentioning, that a neutron source using a non-multiplying target will require a 5 MW proton beam to achieve the same performance.

Preliminary study made by the INR RAS in collaboration with EDBMB (Nizhny Novgorod), Bochvar's ARSRIIM, RDIPE (Moscow), ARSRIEP (Arzamas-16) and IPE (Obninsk) has shown the possibility of creating a pulsed neutron source with such characteristics (project RIN-10). The source will have a multiplying target made of highly enriched U^{235} (U^{233},Pu^{239}) nitride and cooled with liquid gallium and will be driven with the proton beam of the MMF's linac compressed in the storage ring. The linac needs to be upgraded: the proton energy should be rised to 0.7 GeV and pulse duration - to 350 μs at the pulse current 50 mA.

The project requires the accelerator's equipment to be upgraded without any additional construction [2] and the new experimental hall with the target facility to be constructed (Fig.6).

Currently an intermediate design (RIN-3) is being considered which does not require neither accelerator's upgrading, nor any construction and can be implemented using the existing shielding and water cooling system (Figs. 7, 7a).

Some characteristics of the neutron source IN-06 for the first (1996-1998) and subsequent stages of its operation (storage ring, multiplying target) are given in Table 1.

5. Radiation studies

This year the construction of the beamstop with the core assembled of tungsten plates and cooled by water (Fig.8) should be finished. The existing system provides adequate cooling of the core and thermal shielding at the proton current upto 1 mA. The beamstop core has a channel for radiation studies of materials used under conditions of irradiation by protons and spallation, fusion and fission neutrons. The fast neutron flux density inside the channel as estimated by displacement rate will be about 10^{15} n/cm^{2}s at full proton current[16]. The energy spectrum can be estimated by the ratio of displacement rate to He production rate (Fig.9). Radiation studies are being prepared by collaboration of the INR, Kurchatov Institute, Bochvar's Institute of Inorganic Materials and R&D Institute for Power Engineering [17].

6. Lead slowing-down neutron spectrometry

Neutrons slowing down in lead tend to be phocused, at any given moment of time, in a comparatively narrow energy range with the half-width of 30-40 % of the average energy. This effect provides the possibility of the very sensitive neutron spectrometry in the energy range from thermal to 70 keV neutrons (with limited energy resolution).

Employing for generating the primary neutrons the spallation process induced by protons from the storage ring will allow the neutron source intensity as high as 10^{16} n/cm^{2}s to be achieved that is 8 orders of magnitude higher than that for the usual lead spectrometer based on the d-T reaction. This spectrometer will be capable of measuring actinide's fission cross sections for 10^{-12} g micro samples.

At present, the experiments are conducted on the small-scale prototype spectrometer "Python" (Fig.10) installed in the linac's tunnel on the direct proton beam. Proton pulses with the duration 0.2 μs and average current up to 1μA are shaped by a chopper in the linac's injector [13].

7. Applied studies

The following topics concerning the practical employment of the spallation process induced by ~1 GeV protons for transmutation of actinides and fission products are considered now:

- experimental studies based on the proton and H- beams of the MMF's proton linac and equipment of the neutron source IN-06 [8] concerning efficient utilization of plutonium in subcritical channel-type nuclear reactors (RBMK, Russia; CANDU, Canada);
- transmutation of long-lived fission products under proton irradiation [9].

8. Acknowledgements

The author would like to acknowledge helpful discussions with V.Aksenov, G.Bauer, V.Lobashev, M.Markov, V.Matveev, F.Mitenkov, V.Orlov, Y.Osipyan, Y.Petrov, L.Ryabev, A.Skrinsky, T.Springer. The author is grateful to Y.Bulkin, Y.Cherkashev, V.Fedchenko, Y.Gabrielyanz, M.Grachev, M.Kazarnovsky, V.Khmelshikov, A.Kirushin, V.Kolesov, L.Kravchuk, S.Lebedev, Y.Likhachev, A.Lubivy, V.Miroshnichenko, V.Sazanov, S.Sidorkin, N.Sobolevsky, O.Shvedov, V.Trushkin, M.Voronzov, S.Votinov for helpful discussions and their participation in activity reported here.

9. References

1. N.M.Sobolevsky et al., this Meeting.
2. L.V.Kravchuk, this Meeting.
3. M.I.Grachev et al., this Meeting.
4. S.F.Sidorkin et al., this Meeting.
5. V.G.Miroshnichenko et al., this Meeting.
6. E.A.Koptelov et al., *On the possibility of using 600 MeV protons for research of radiation damage of thermonuclear reactor materials*, Plasma Devices and Operations, 1993, v.2, pp. 141-143.
7. A.A.Alekseev et al., *High-luminosity lead slowing-down neutron spectrometer driven by linac of Moscow Meson Factory*, 2nd Int. Seminar on the Interact. of Neutrons with Nuclei, April 26-28, 1994, Dubna, Russia.
8. Y.Y.Stavissky, *Subcritical nuclear reactors driven with high-current proton accelerators*, Preprint INR-0893/95, June 1995, to be published in NIM.
9. V.G.Semenov, N.M.Sobolevsky, *Estimation of transmutation of long-lived fission products by proton beam*, Int. Meeting on Intermediate Energy Nuclear Data, Paris, May 31 - June 2, 1994.
10. A.V.Dementyev, N.M.Sobolevsky, *SHIELD - a Monte Carlo Hadron Transport Code*, Preprint INR-0874/94, Nov. 1994, Moscow.
11. S.G.Lebedev, O.N.Smirnova et al., *RADDAM - a Code for Simulation of Radiation Damage by High-Energy Nucleons*, to be published J. Nucl. Mater.
12. A.V.Dementyev et al., *Neutron yield from extended lead target under incident protons of 0.1 to 100 GeV*, Preprint INR-0880/95, Feb. 1995, to be published in NIM.
13. A.V.Novikov et al., *Fast chopper for creating intermediate time structure for proton and H- beams of the linac of the Moscow Meson Factory*, to be published in J. for Instr. and Exp. Techniques, in Russian.
14. A.Belushkin, V.Kazimirov, this Meeting.
15. Y.Y.Stavissky, *Intensive pulsed neutron sources based on proton beams of meson facility*, Preprint PEI-389, Obninsk, 1973, in Russian.

16. S.E.Boriskin et al., *Radiation damage of materials at Moscow Meson Factory*, Preprint INR P-0431, Moscow, 1985, in Russian.

17. E.A.Koptelov, S.G.Lebedev et al., *Radiation experimental facility based on the beam stop of MMF*, Int. Conf. on Thermonucl. Materials, Oct. 1995, Obninsk, Russia.

Pulse Neutron Source IN-06 / RIN-10

mode	f,pps	$\theta_P, \mu s$	$\theta_T, \mu s$	$\hat{\Phi}_T \frac{neutr}{cm^2 s}$	$\bar{\Phi}_T$	W_T, MW	W_{beam}, MW
1. Accelerator,	50	40	50	3.2×10^{14}	0.8×10^{12}	0.08	0.06
U-target	50	150	160	4×10^{14}	3×10^{12}	0.3	0.22
2. Accelerator,	50	40	50	7.2×10^{15}	1.8×10^{13}	1.6	0.06
Multipl.target	25	150	160	7.7×10^{15}	2.9×10^{13}	3.3	0.11
3. Storage ring, U-target	50	0.35	30	2.1×10^{15}	3×10^{12}	0.3	0.22
4. Storage ring, Multipl.target	25	0.35 (1.2)	35	3.5×10^{16}	2.9×10^{13}	3.3	0.11
5. Upgrade ACC, SR, Mult.target	25	0.35 (1.2)	35	9.6×10^{16}	7.9×10^{13}	9.1	0.3

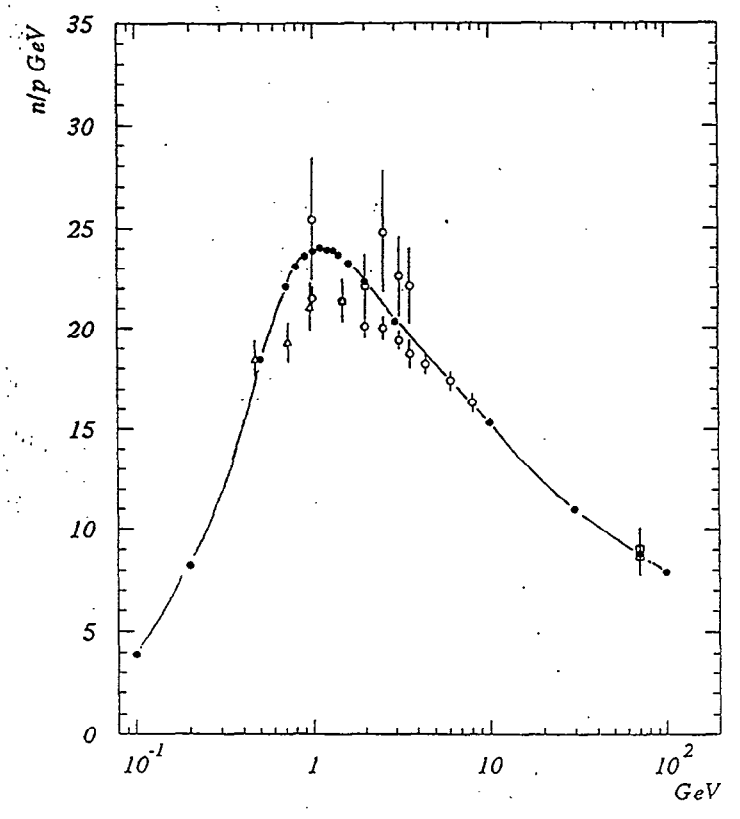

Figure 1: Yield of neutrons with energies below 10.5 MeV from total surface of cylindric lead target (D=20 cm, L=60 cm) in dependence on incident proton energy.

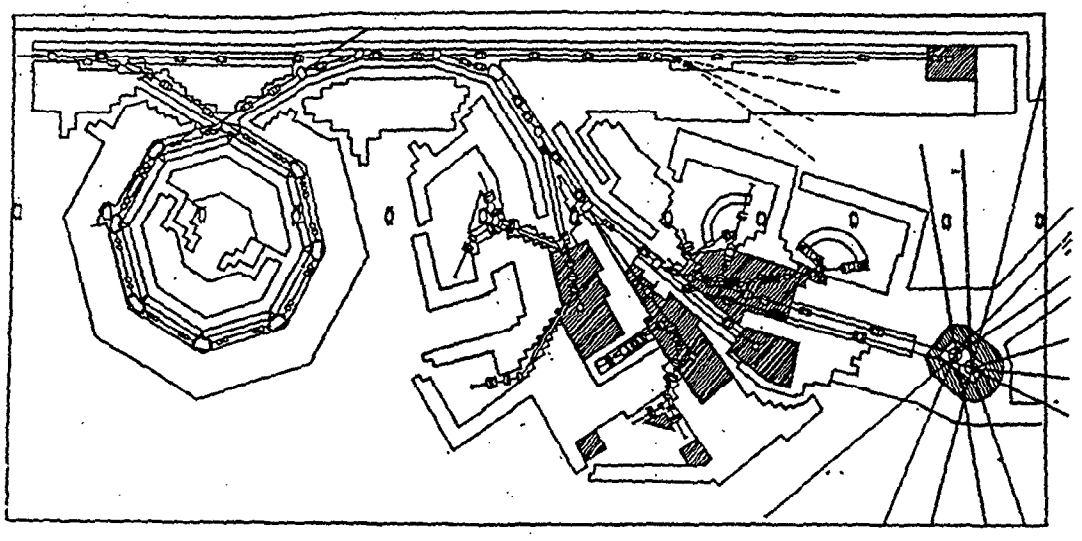

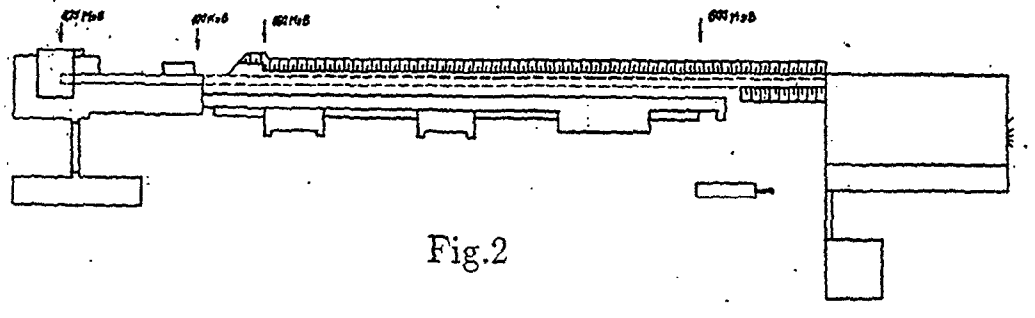

Fig.2

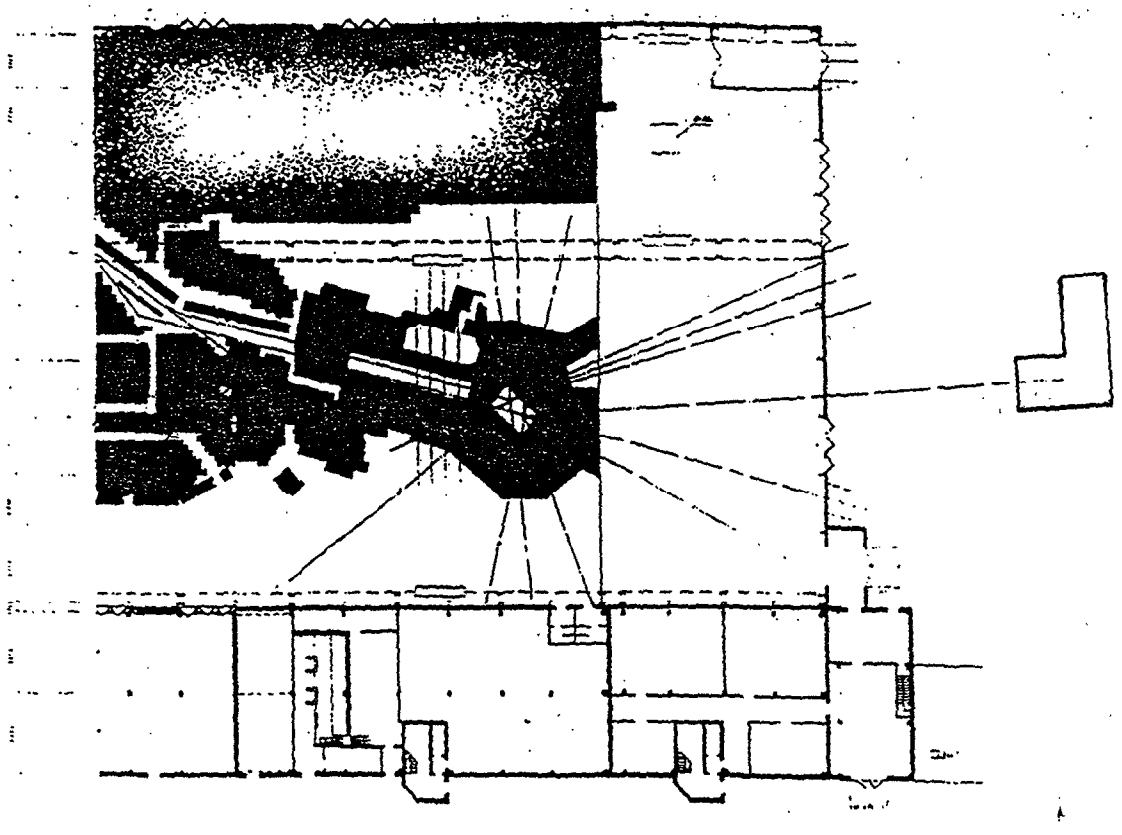

Fig.3

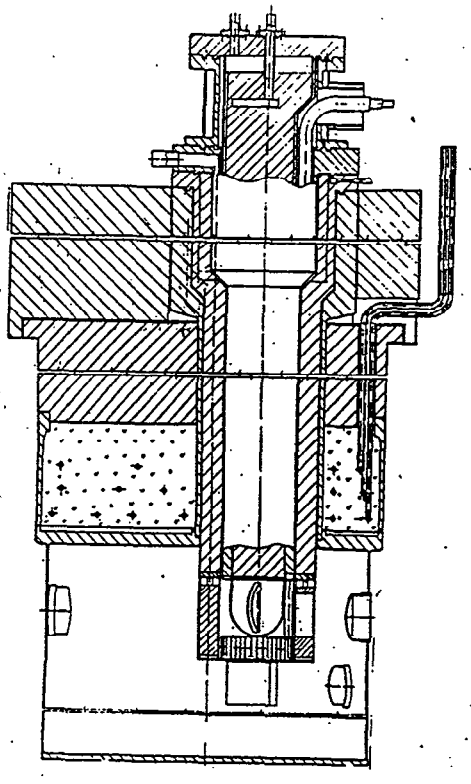

Fig.4

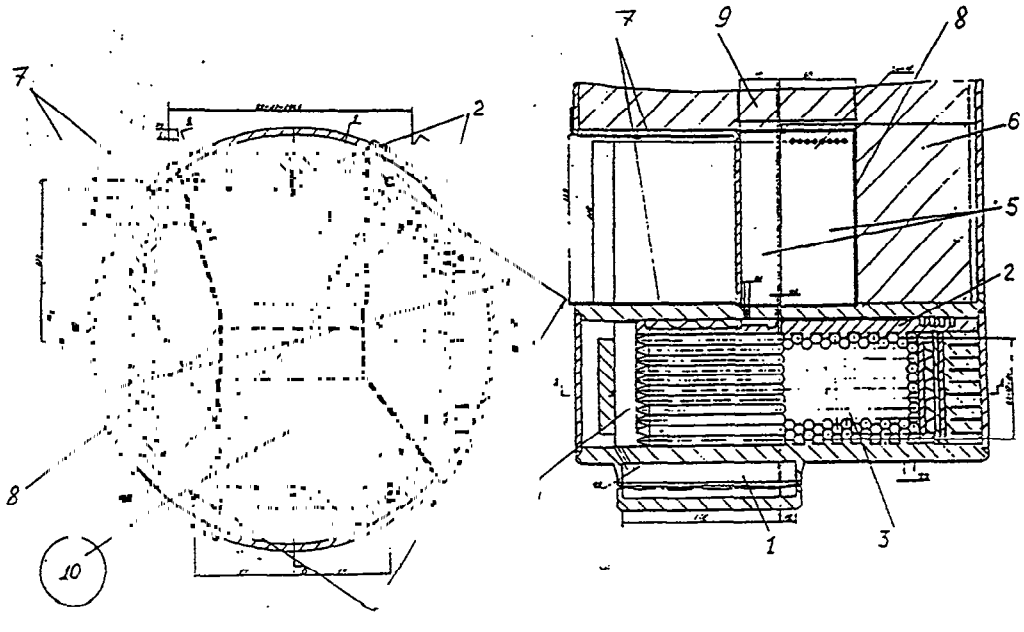

238 USi3 target

1 - lower moderator; 2 - Ti-Gd decoupler; 3 - core; 4 - coolant inlet and outlet;
5 - upper moderator; 6 - reflector; 7 - Gd decoupler; 8 - Ti-Gd insertion;
9 - Be plug; 10 - fuel element.

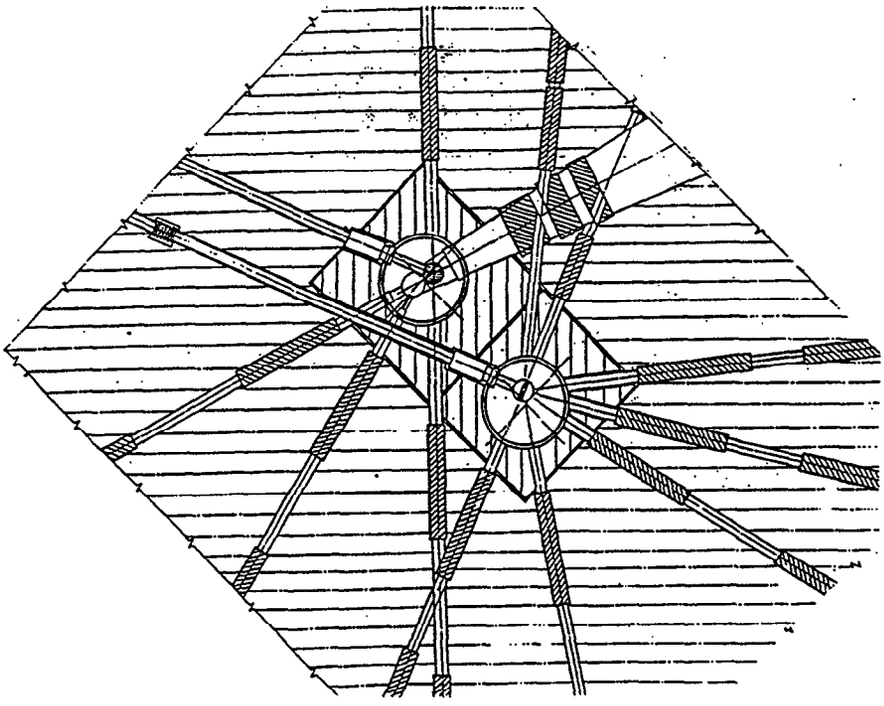

Fig.5

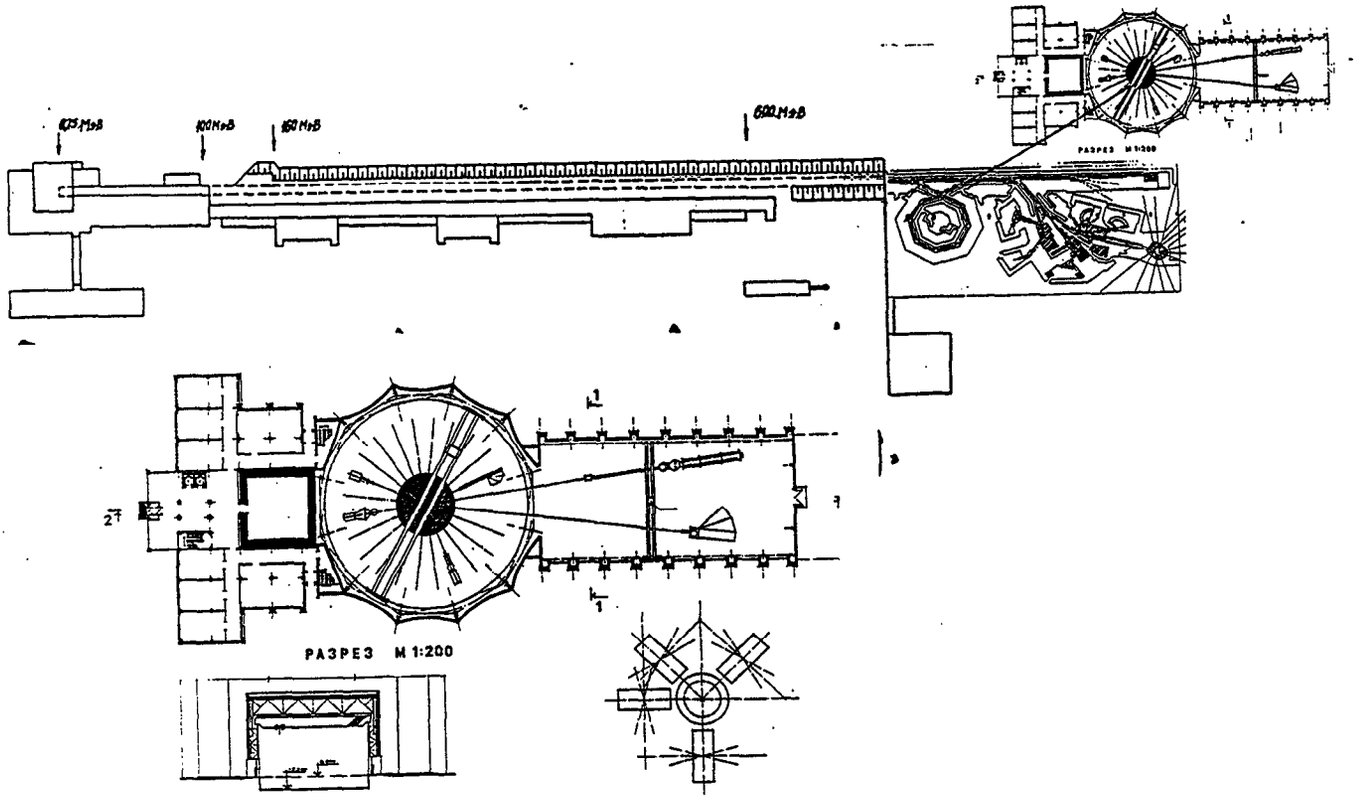

Fig.6

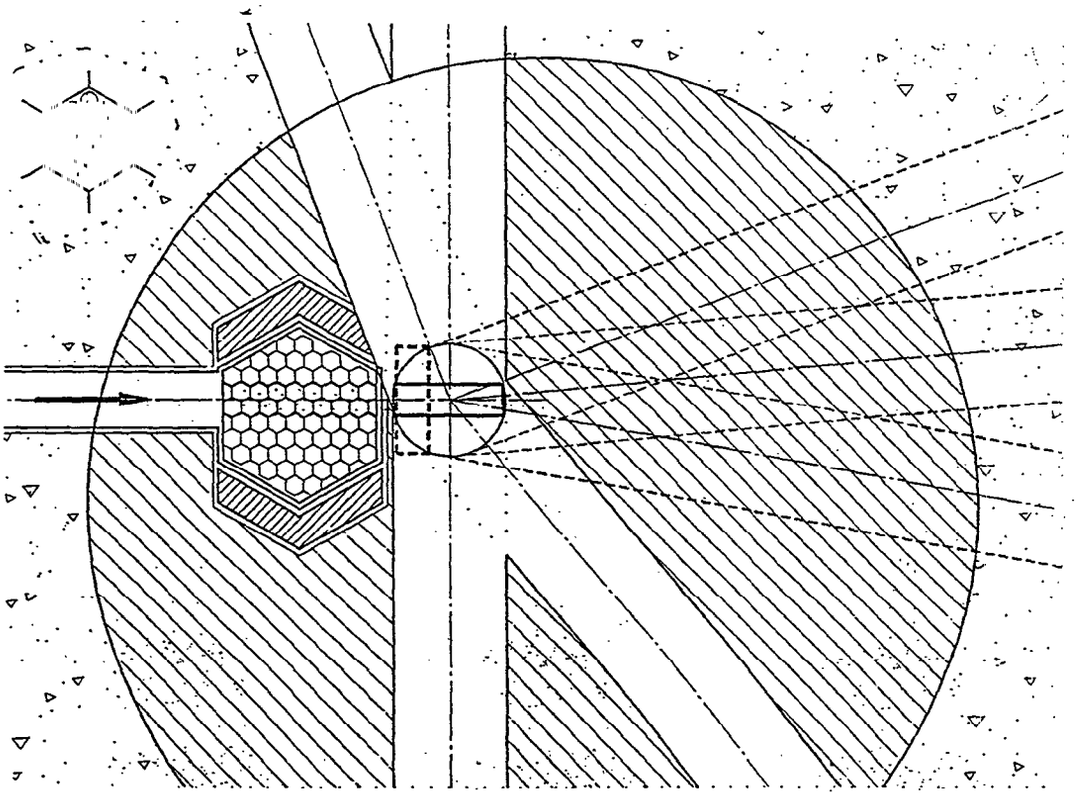

Fig.7

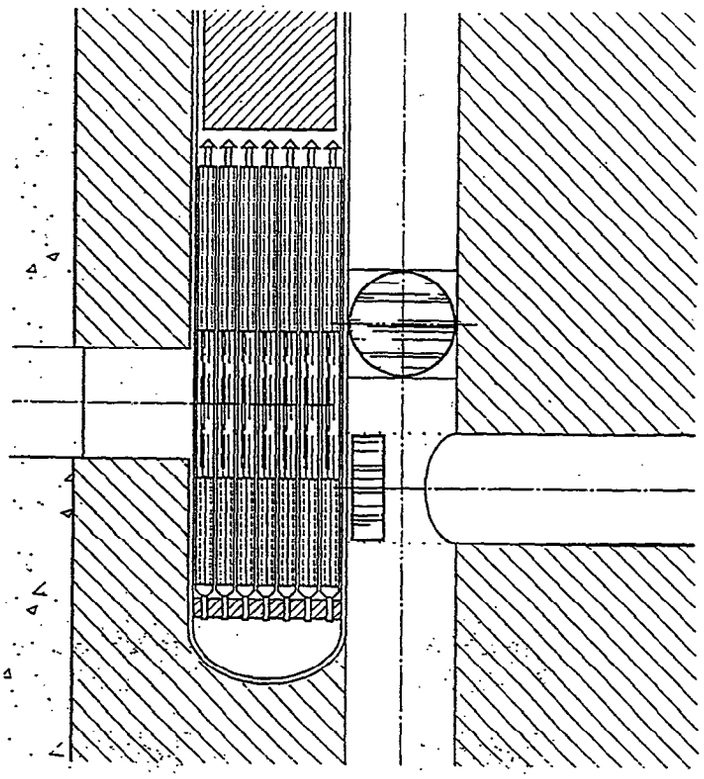

Fig.7a

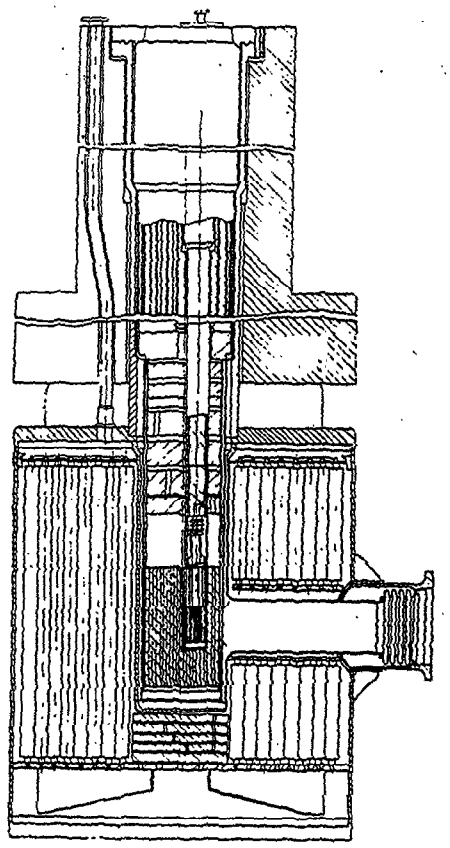

Fig.8

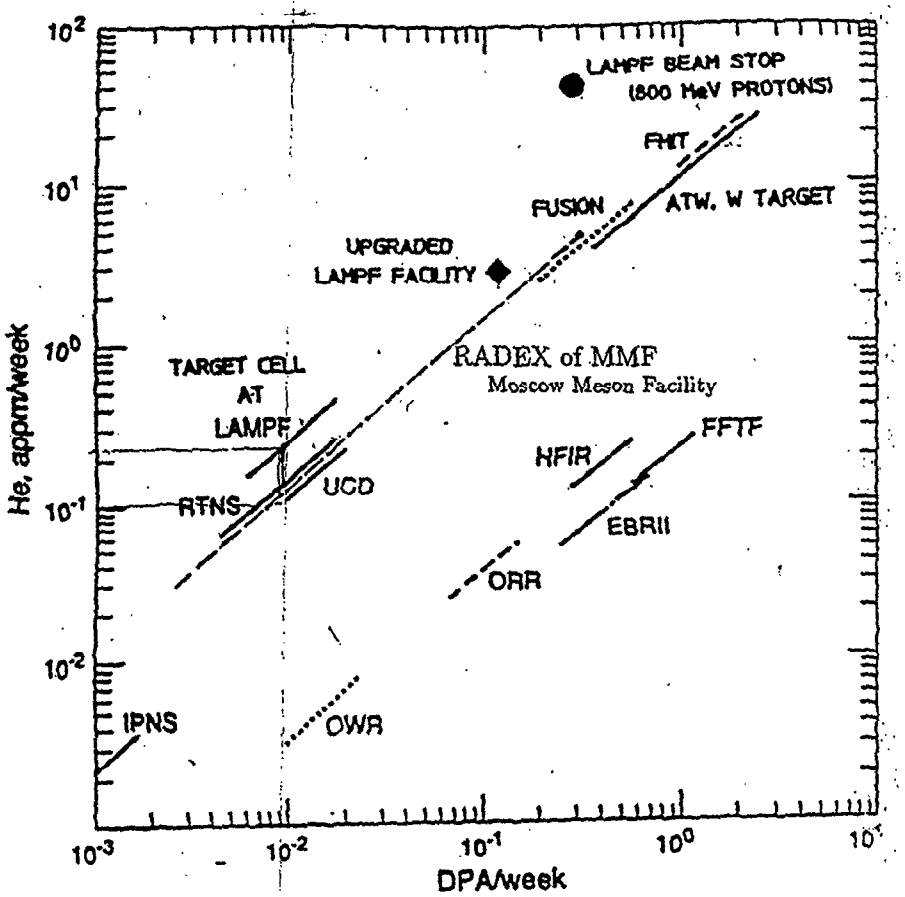
LAMPF BEAM STOP
(800 MeV PROTONS)
FHT
FUSION
ATW, W TARGET
UPGRADED
LAMPF FACILITY
RADEX of MMF
Moscow Meson Facility
TARGET CELL
AT
LAMPF
UCD
RTNS
HFIR
FFTF
EBRII
ORR
IPNS
OWR
He, appm/week
DPA/week

Fig.9

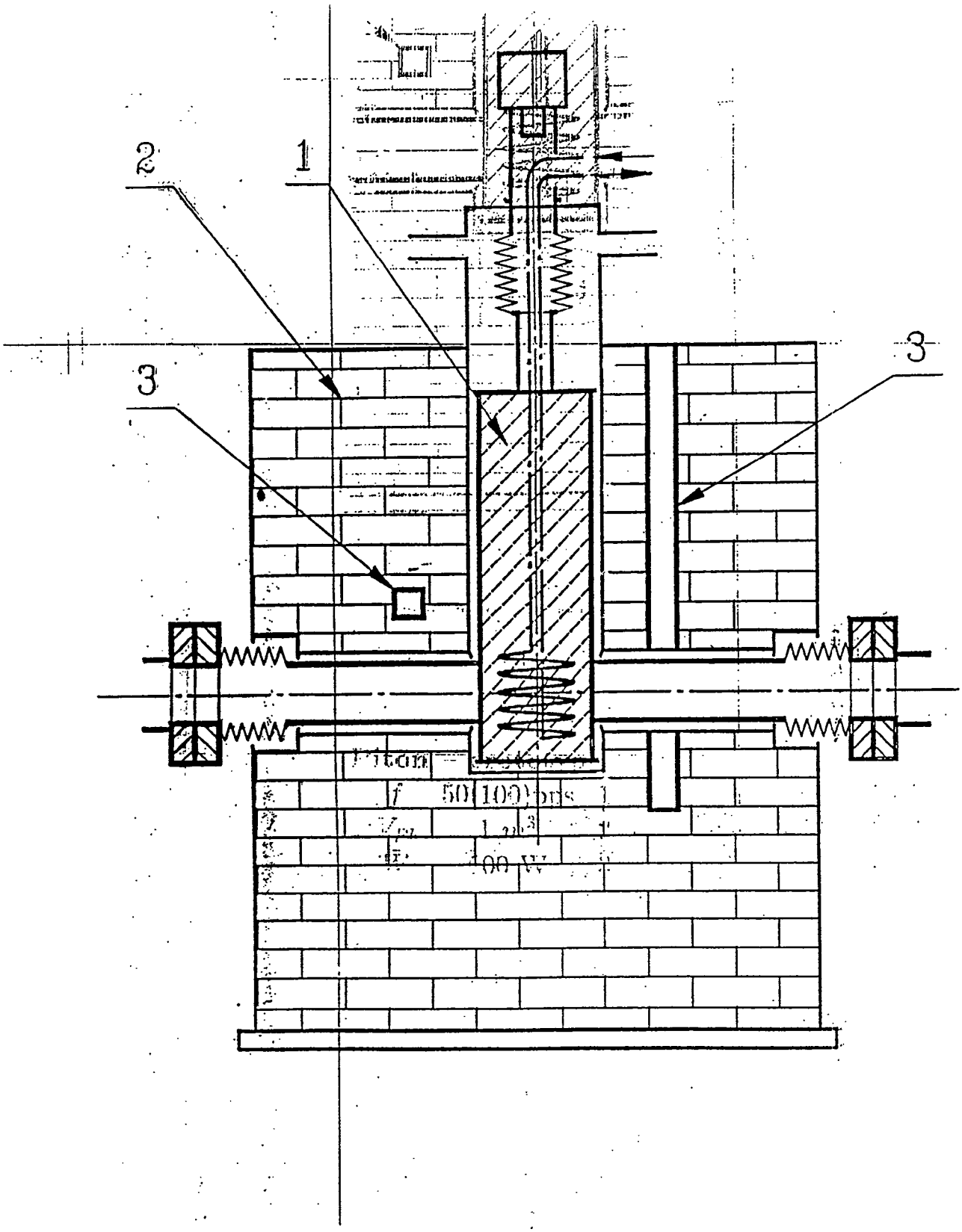

Fig.10 **Piton – prototype of SLS**

$\bar{J}$	$\sim 6 \times 10^{13}$	f	50(100)pps	1 – Target (Pb)
$\bar{i}_p$	$1\ \mu A$	V_{Pb}	$1\ m^3$	2 – Lead laying
θ_p	$0.2 \div 0.5 \mu sec$	$\bar{W}$	600 W	3 – experimental channels

ICANS-XIII
13th Meeting of the International Collaboration on
Advanced Neutron Sources
October 11-14, 1995
Paul Scherrer Institut, 5232 Villigen PSI, Switzerland

SINQ - A CONTINUOUS SPALLATION NEUTRON SOURCE (AN APPROACH TO 1 MWATT OF BEAM POWER)

Walter E. Fischer (for the project team of SINQ)

Paul Scherrer Institut, 5232 Villigen PSI, Switzerland

ABSTRACT

In this status report we describe the continuous spallation neutron source at PSI, which will come into operation in fall 1996. We present the present state of the construction work and review the expected performance of the source.

1. The accelerator system

Fig. 1 shows the layout of the experimental facilities at PSI together with its accelerator system. Today it is used for particle/nuclear physics, medical applications and an ever increasing portion of physics of condensed matter and material science. The experimental program using the muon spin resonance technique, by now traditional at PSI, gained significance through its contributions to the investigation of high temperature superconductors and heavy fermion systems. The spallation neutron source which is in construction and should go into operation next year obviously amplifies this trend.

The PSI-accelerator system consists of two isochronous cyclotrons fed by a Cockcroft-Walten preaccelerator with a 860 keV proton beam. The time structure of the accelerated beam from the cyclotorns is determined by the frequency of the acceleration cavities which is 50 Mc. Hence the beam has a pulse microstructure of 20 ns (which is irrelevant for the production of thermal neutrons) and no "macro" time structure. Hence SINQ is a continuous spallation neutron source and has strong similarities with a beam tube research reactor.

Properties of the Proton Beam

extraction energy	590 MeV
energy spread (FWHM)	1.5 ‰
beam emittance	2 π mm x mrad
beam current	1.5 mA
time between pulses	19.75 ns
bunch width	1 ns

Table 1:

Keywords: SINQ

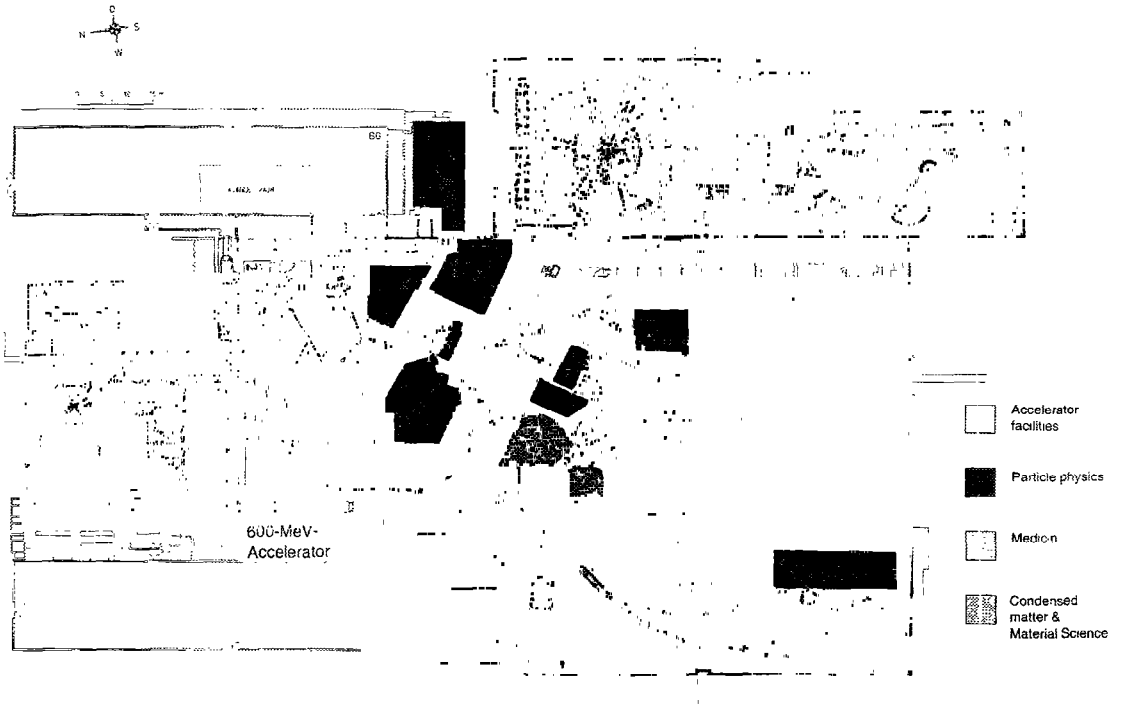

Figure 1: Layout of the experimental facilities of PSI at the accelerator system

2. On the target station

Since SINQ is a steady state neutron source, its concept should be optimized for the highest possible neutron flux that can be generated from the available beam power. Furthermore, with our emphasis on cold neutrons, we aimed at an optimal position for the cold moderator and at maximal possible space for the instruments. Together with a liquid metal spallation target as ultimate concept these are reasons for the choice of an arrangement of the target station with vertical beam injection from below (Fig. 2). The whole circumference of the target station is then accessible for neutron beam extraction. This concept also provides for a multiple containment of all potentially volatile radioactivity produced inside the target block. For this purpose a double-walled steel tank with contained atmospheres will surround the target and the moderator tank (Fig. 3).

The target block will surround a 2 m diameter heavy water tank in whose axis the target with essentially cylindrical geometry is positioned. Fig. 4 shows a cut through this inner region of the target block. The double walled moderator tank with two meter diameter and height is readily visible. This tank has in its axial center a central tube, containing (from below) the collimator for the injected proton beam, the target and a shielding and heat transport zone. A cooled beam tube plug (tangential to the target) and the horizontal part of the installation for the cold D_2-moderator are also shown. A perspective view of the moderator tank is shown in Fig. 5. The manufacture of this tank turned out to be a formidable task of casting and welding - all in aluminum (Fig. 6).

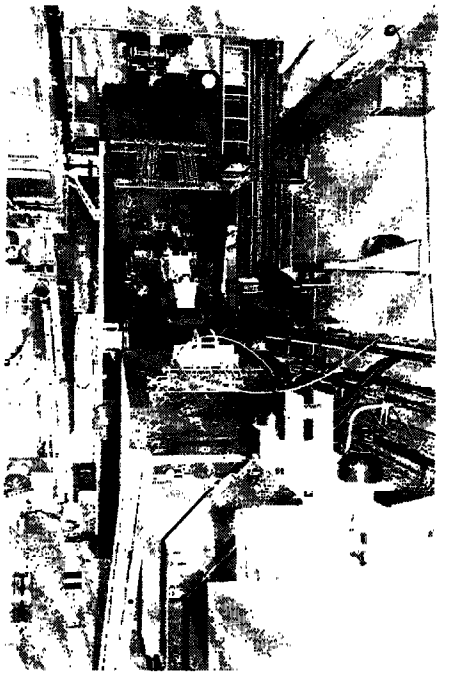

Figure 2: View of the proton beam line in the ditch below the floor of the neutron hall. The bending magnet for vertical injection is visible in the back.

Figure 3: Deposition of the double-walled containment tank in an early phase of construction at the target station. Two - already positioned - boxes for beam tubes are also visible.

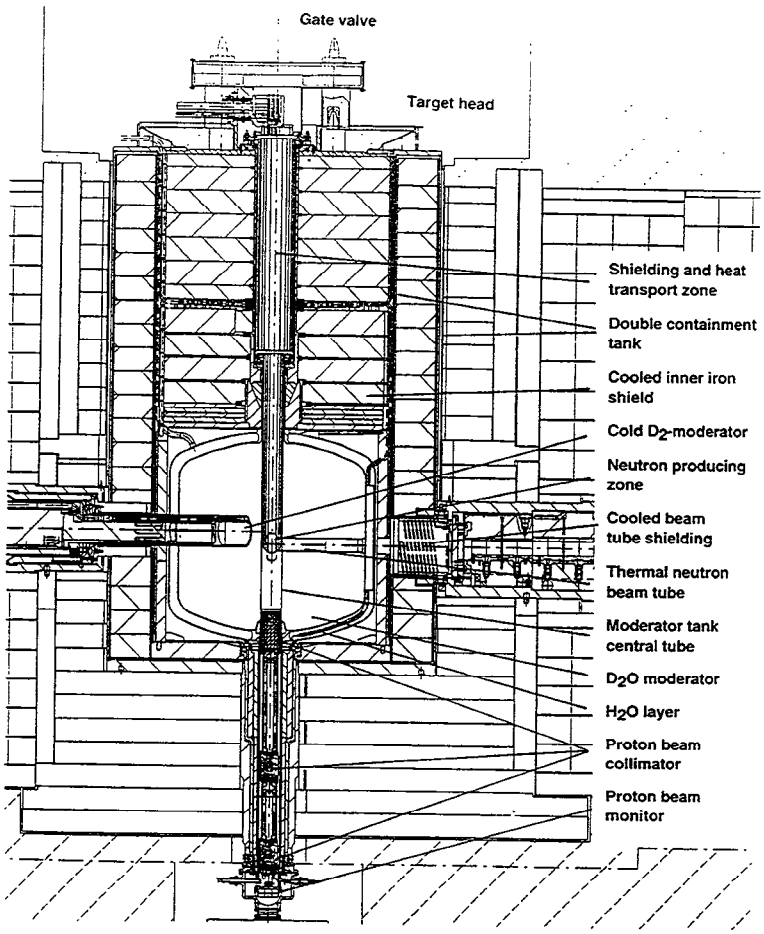

Figure 4: Cut through the inner region of the target block

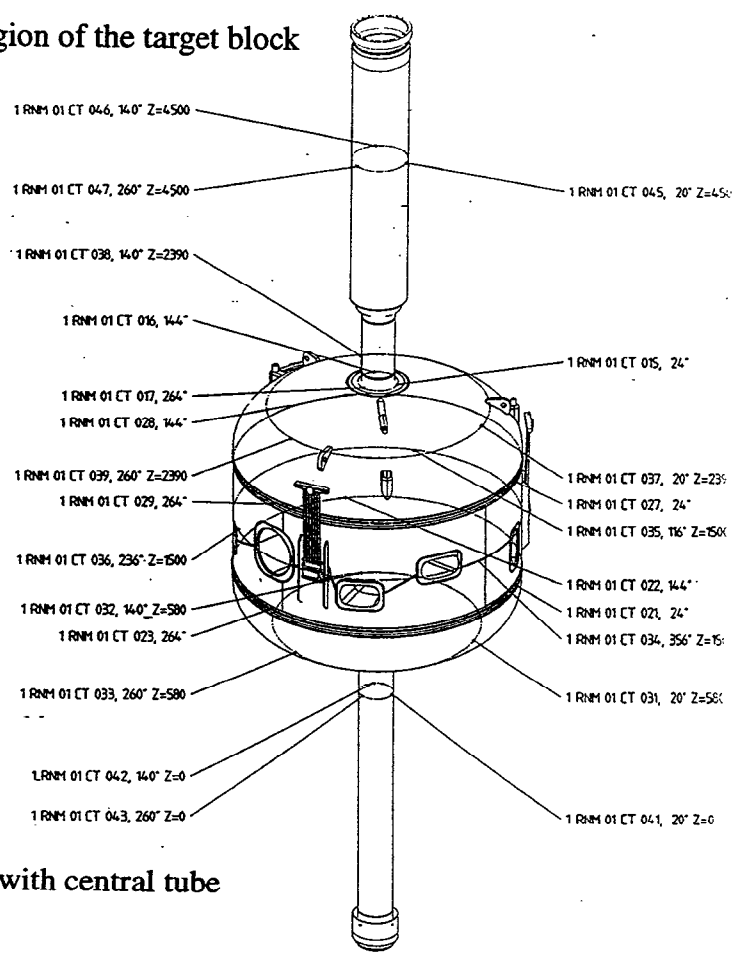

Figure 5: The D_2O-moderator tank with central tube

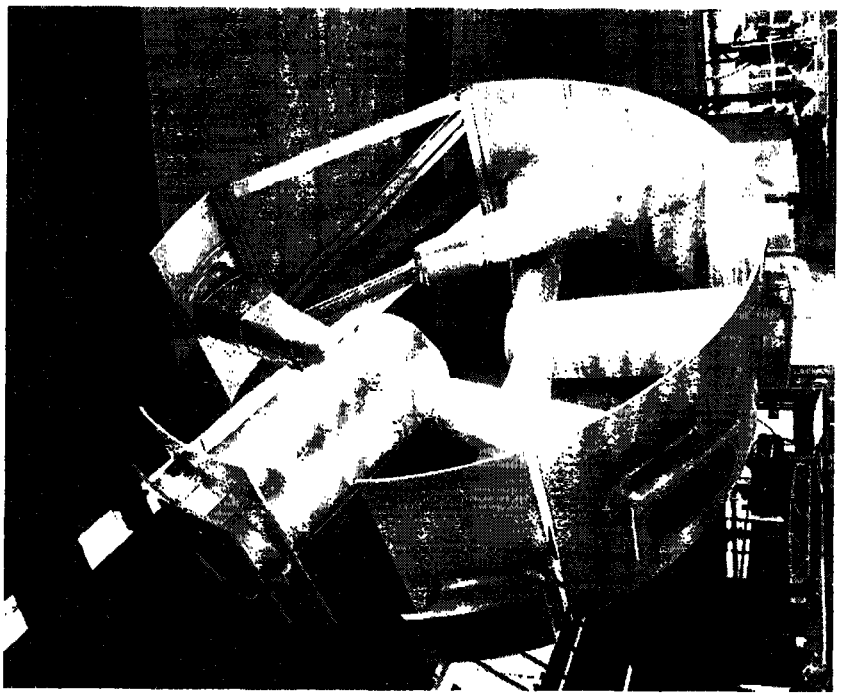

Figure 6: Welded beam tube inserts in the moderator tank. The T-frames for the cold D_2-source and for the scatterer (later second cold source) are already attached.

3. On the target

Safe and reliable operation of a target at the anticipated beam power of 1 MW is a prime concern. The proton current density will be 25 $\mu A/cm^2$ under normal conditions. In view of the lack of experience world-wide with targets at this power density we shall start with a relatively simple design of a target made up of zircaloy rods, cooled by D_2O. The concept of this target is shown on the right side of Fig. 7. For safety a double walled aluminium container with water cooling will surround the target proper. We hope to proceed to a target with higher neutron yield within a year by replacing the zircaloy rods by lead filled zircaloy- (or aluminium-) tubes. These targets, while producing neutrons for the users of the source, serve as a demonstration of the integrity of the safety hull under real operational conditions.

The concept of the liquid metal target is shown on the left side of Fig. 7. The realization of this concept will remain a focus of the development work for SINQ. Apart from a favourable neutronic performance, this target is self shielding and heat is transported away from the reaction zone of the proton beam by convective motion of the target material. Hence the target cooling water is not intercepted by the proton beam, thus avoiding radiolysis - and part of the activation problems in the secondary circuit.

4. Cold source and neutron guides

The cold source has been built up on a test rig and is essentially ready for first operational tests. The stability of the stationary states and the behaviour of the thermo-syphon during transients have to be tested before moving and integrating the installation to the target station.

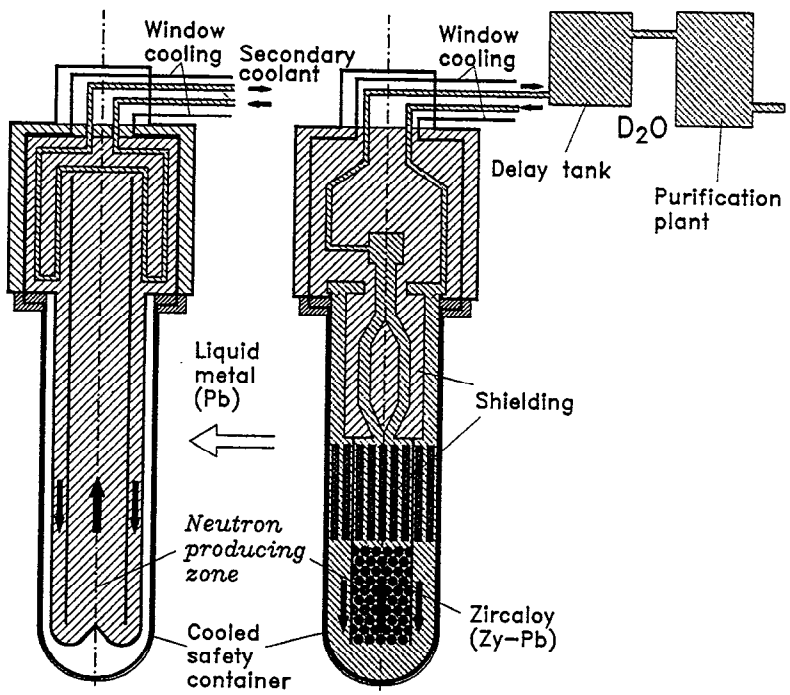

Figure 7: Concepts of the SINQ-target, right: rod target; D_2O-cooled, left: convectively cooled liquid metal target

The mounting of the neutron guide system is near completion. According to the emphasis we give to the production of cold neutrons at SINQ, most of the guides (depending on the kind of instrument attached to them) are of the supermirror type. A supermirror with m=2 times the critical angle of bulk Ni-coating consists typically of 40 bilayers of Ni and Ti. The thickness of the single layers varies continuously between 70 Å and 1000 Å. All the pieces have been tested on a test spectrometer at reactor "Saphir" at PSI and later on at "Orphée" in Saclay. A transmission profile for about nine reflections near m=2 is shown in Fig. 8. As can be seen in Fig. 9, by means of the transport properties of these guides, the neutron flux can be increased by more than a factor of three and the spectrum of the transmitted neutrons through curved guides can be extended to shorter wave length (e.g. below 2 Å).

5. Performance and Instrumentation

Fig. 9 shows the expected (calculated) performance of SINQ for a primary proton current of 1 mA on the spallation target. The spectral flux data is given at positions of the user, that is either at the monochromator for a thermal beam tube or at the exit of a 50 m long neutron guide. The benefit from use of supermirrors is clearing visible, if the data of "cold beam tube" (3.5 x 12) is compared with "cold guide m=2".

Table 2 lists the instruments which are under preparation at SINQ. Their location at beam ports or neutron guides can be seen in Fig. 10.

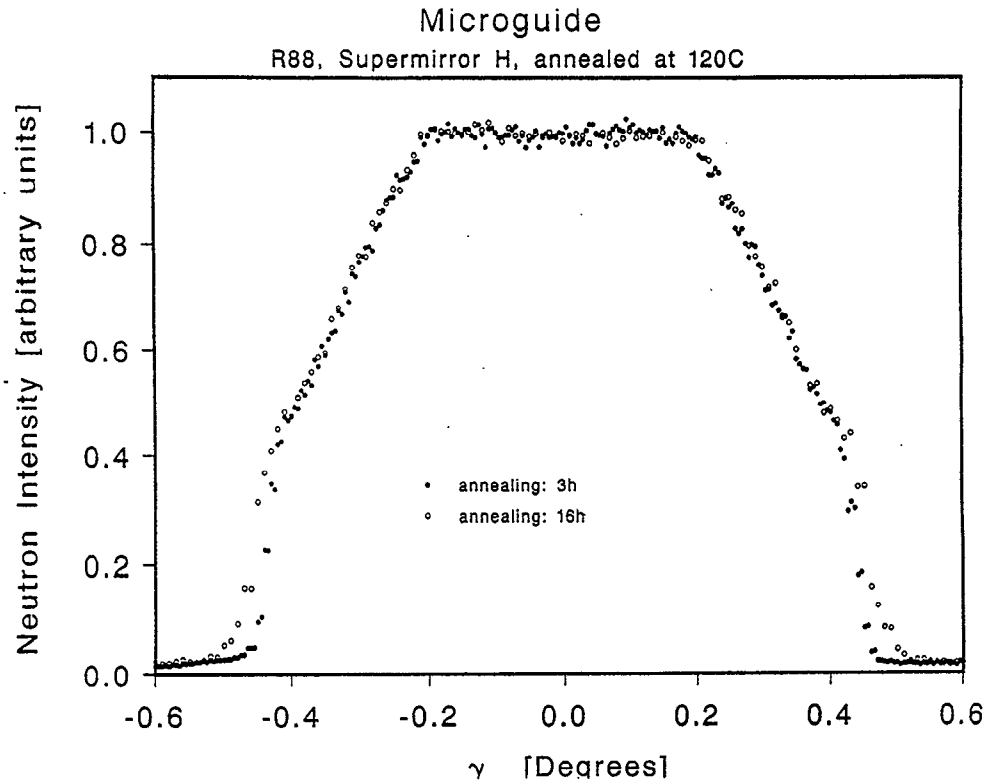

Figure 8: Transmission profil for about nine reflections at a supermirror plate of the neutron guide system.

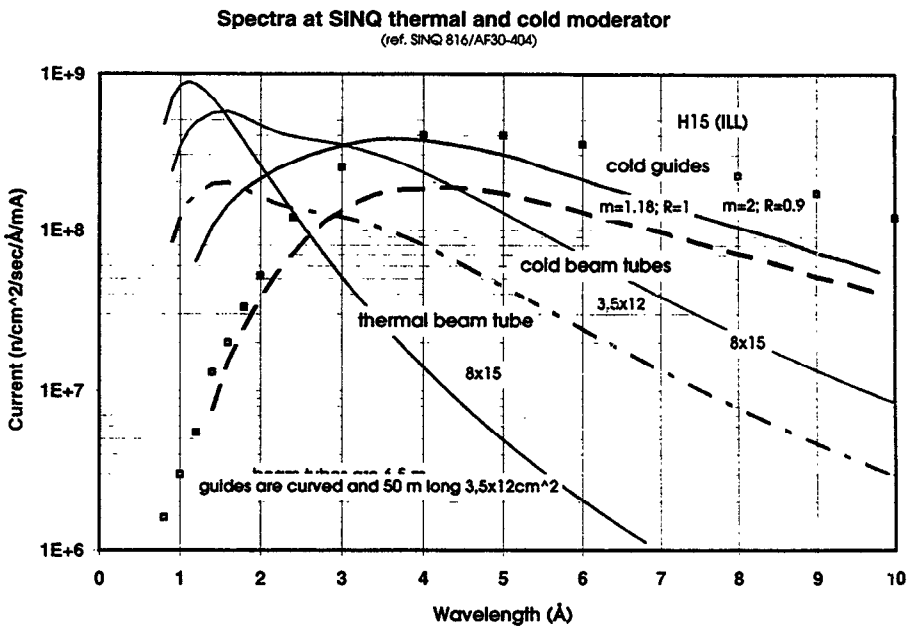

Figure 9: Spectral flux at various user positions for SINQ

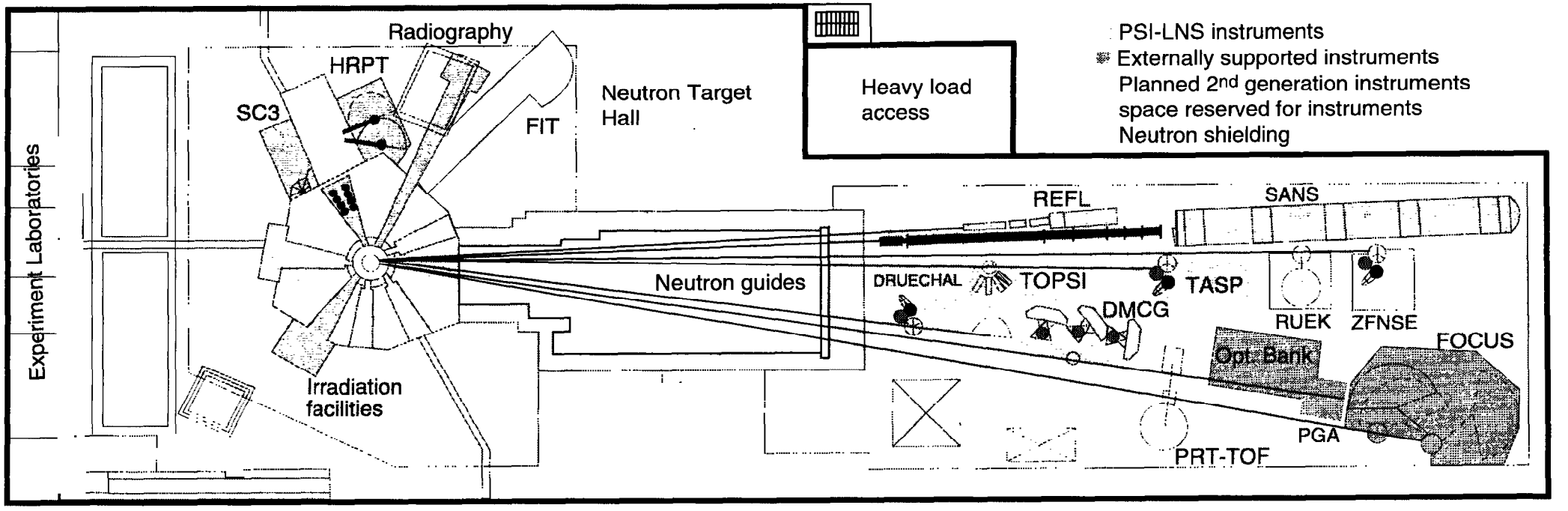

Figure 10: Layout of the instruments and spectrometers at the beam ports and neutron guides of SINQ

Instruments under preparation for SINQ

Gen.	Design.		Avail.	Suppl.
		New PSI-LNS-Instruments		
{1}	HRPT	High resolution diffractometer (thermal neutrons)	So 96	ETHZ/UGe
{1}	SC3	4-circle diffractometer (thermal neutrons)	So 96	PSI
{1}	DrüchaL	Three axis spectrometer (cold neutrons)	So 96	ETHZ
{1}	TASP	Three axis spectrometer (polarized cold neutrons)	So 96	PSI
{1}	SANS	Small angle scattering camera, 40 m (cold n.)	So 96	PSI
{1}	(REFL)	Neutron reflectometer (cold neutrons)	Wi 96	PSI
		Transfer from SAPHIR (LNS-Instr.)		
{1}	DMCG	Powder diffractometer (cold neutrons)	So 96	PSI/ETHZ
{1}	TOPSI	Test spectrometer (cold neutrons), NSE-option	So 96	PSI/TUM
{1}	NTR	Neutron radiography facility (thermal neutrons)	So 96	PSI
{2}	T3AX	Triple axis spectrometer (thermal neutrons)	Wi 96	PSI/ETHZ
		Instruments with outside support {Country}		
{1}	FOCUS	Time of flight spectrometer (cold neutrons) {D}	Sp 97	BMFT/PSI
{2}	ITOF	Inverted time of flight instr. (cold neutrons) {D}	Sp 97	PSI/ETHZ
{1}	NOB	Neutron optical bench (cold neutrons) {A}	Wi 96	Al-Wien
{1}	PGA	Prompt gamma activation analysis (cold n.) {CH}	Au 96	UFb/PSI
		New developments considered		
{2}	FTOF	Fourier diffractometer (for radioactive samples)		PSI/ETHZ
{2}	PST-TOF	Phase space transformation time-of-flight		PSI
{2}	LADI	Laue Diffractometer		PSI/?
{2}	(DENS)	Instrument for diffuse-elastic scattering		PSI/?
{2}	PTBS	Phase space transformation back scattering		PSI/?
		Non-beam facilities		
{1}	PNA	Isotope production stringer (2 thimbles)	So 96	PSI
{1}	NAA	Neutron activation analysis (2 thimbles)	So 96	PSI
{1}	GJA	Fission product gas jet	So 96	UBe/PSI

Table 2:

Instruments, Methods and Components

ICANS-XIII
13th Meeting of the International Collaboration on
Advanced Neutron Sources
October 11-14, 1995
Paul Scherrer Institut, 5232 Villigen PSI, Switzerland

SETUP AND OPERATION MODE OF A PULSED WHITE BEAM ANGLE-DISPERSIVE TOF-TEXTURE-DIFFRACTOMETER

W. Schäfer, E. Jansen, W. Kockelmann, H. Tietze-Jaensch, G. Will

Mineralogisches Institut, Universität Bonn, D-53115 Bonn, Germany

ABSTRACT

The paper reports on the setup and texture operation mode of the redesigned ROTAX instrument at ISIS. Pulsed white beam time-of-flight diffraction, a one-circle sample goniometer and a linear position-sensitive detector are used to assemble the neutron texture diffractometer. Sets of complete pole-figures can be measured in a minimum of different sample orientations due to the fact that the conventional pole-distance scanning of the sample becomes unnecessary. Test results on copper specimens are reported. Data collection times are reduced up to a factor 50 compared to those at a continuous reactor source with monochromatic neutrons.

1. Introduction

Despite the advantages of using neutrons for volume texture analysis, e.g. the high penetration capability of neutrons and the possibility of using rather large samples, those of irregular shape and coarse grained material, the measurement of neutron diffraction pole-figures often fails because of the time consumptive experimental procedure and the demand of beam time. This is due to the fact that Bragg intensities have to be measured for a large number of different sample orientations for adequate pole-figure resolution. When using monochromatic neutrons, the sample scanning is usually performed on a two-circle Eulerian cradle with rotation axes ϕ and χ for azimuth and pole-distance scanning, respectively. Depending on the crystalline constitution, i.e. mainly on the grain size of the crystallites, the number of different sample orientations varies roughly between 100 and 1000 to stepscan one hemisphere of the sample. Depending on the scattering power of the sample, i.e. mainly on size, composition and structural symmetry, measuring times of about 1 to 10 min per pole-figure data point are necessary; this is experienced, when working with monochromatic neutrons at a conventional reactor diffractometer (see e.g. [1]). Thus, the total measuring time for a set of pole-figures lies between approximately half a day for high-symmetry metallic samples and one week for low-symmetry multiphase geological samples.

Keywords: TOF-diffraction, Texture diffractometer, Pole-figure scanning, ROTAX

It is the merit of position-sensitive detector (psd) installations to obtain several or a multitude of individual pole-figures simultaneously during one pole-figure scan [2]. The so-called 'blind area' arising for those pole-figures, which are registered under non-bisecting scattering conditions at the outer parts of the psd, can be overcome by a few additional sample orientations [3]. When using the linear JULIOS-psd of 70 cm sensitive length, for instance, one needs only one additional sample orientation to fill the blind area [4]. When installed in the horizontal scattering plane, the psd saves measuring time only with respect to the measurement of more than one pole-figure, but it cannot reduce the number of individual sample orientations during the pole-figure scanning procedure. When installed under $2\Theta = 90°$ in the vertical scattering plane, the psd allows a reduction of different sample orientations, but only one hkl pole-figure can be measured during one sample scan. [5].

This situation will change, when using polychromatic neutrons at a pulsed spallation source. Here, the psd fulfils two objects simultaneously: (1) the simultaneous measurement of a multitude of hkl pole-figures <u>and</u> (2) an essential reduction of sample orientations in the course of the pole-figure scanning. Furthermore, angle-dispersive TOF-measurements will reduce the measuring time per data point because of the better exploitation of the primary neutron spectrum [6]. Method, instrumental setup and experimental tests will be described in the following.

2. Scheme of pole-figure scanning

The angle-dispersive, white beam pole-figure scanning is based on the fact that Bragg reflection conditions are fulfilled for different wavelengths at different positions of the linear position-sensitive detector. One and the same Bragg reflection,

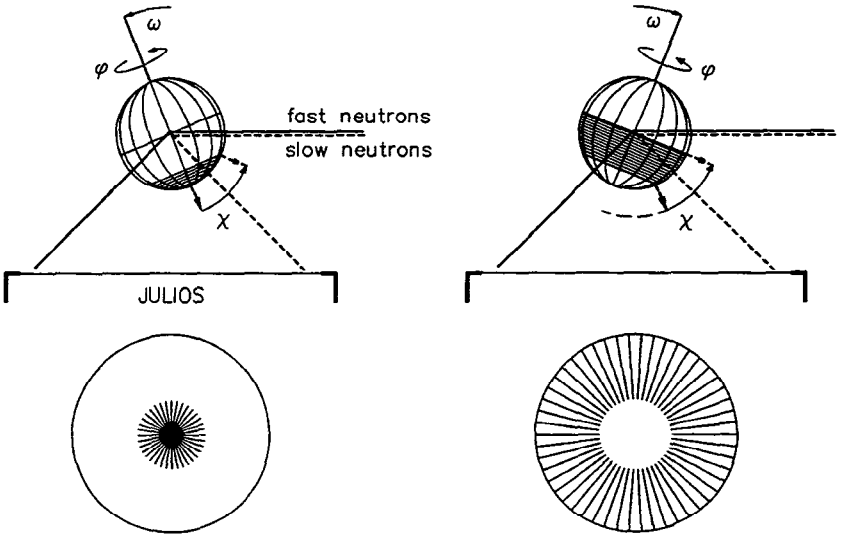

Fig. 1: Reference pole-spheres around the sample mounted in two different ω-positions (top: left and right resp.). The limiting scattering vectors (arrows) of one Bragg plane are shown for the shortest and the longest neutron wavelength diffracting at the left (solid line) and right hand side (dashed) of the linear JULIOS detector, resp.; accessory Δχ-coverages in stereographic projection (bottom), when applying Δφ step scanning in steps of 10° (left) and 7.2° (right). Pole-distances from 0° to 45° (left) and 45° to 90° (right) are covered simultaneously.

which appears along the detector, originates from differently oriented crystallites each. Thus, different orientations of a Bragg plane within a sample can be registered simultaneously in a fixed sample position. This is illustrated in Fig. 1. The angular width of different cystallite orientations expressed by the width of the pole-distance $\Delta\chi$, which can be registered simultaneously, depends on the linear extension of the position-sensitive detector and its simultaneous 2Θ-coverage. A $\Delta 2\Theta$ of 180° corresponds to a $\Delta\chi$-coverage of 90°; this means the complete coverage of one hemisphere of the sample in one fixed ω-setting with respect to the primary neutron beam. The pole-figure scanning procedure is reduced to a $\Delta\phi$ azimuth stepscanning, the grid of which is selected according to the desired pole-figure resolution. The complete $\Delta\chi$-scanning, indispensible for complete pole-figures when using monochromatic neutrons, is substituted by means of the position-sensitive detector and the exploitation of the white neutron spectrum. The $\Delta\lambda$-window accessible by the instrument determines the d-spacing coverage and thus the number of hkl pole-figures registered simultaneously.

Obviously, this method of pole-figure scanning is not confined to the ideal conditions of a 180°-scattering angle detector system. When using detector installations of smaller extensions, however, more than one fixed ω-setting of the sample is needed to cover the complete pole-distance of one hemisphere around the sample. Two ω-settings are sufficient for a 90°-detector instrument. A $\Delta 2\Theta$-coverage of 90° corresponds to a $\Delta\chi$-coverage of 45°. First and second ω-position are selected according to individual scattering geometry realizing that the two settings correspond to pole-distance coverages $\Delta\chi$ from 0° to 45° and from 45° to 90° (see Fig. 1). The shorter the detector dimensions or the simultaneous 2Θ-coverage, respectively, the more different ω-settings are necessary, where the 360° $\Delta\phi$ scanning procedure has to be performed each time. In case of using an arrangement of several counting tubes instead of a psd, each counting tube position defines one fixed χ-value and measures one concentric ring of the pole-figures [7].

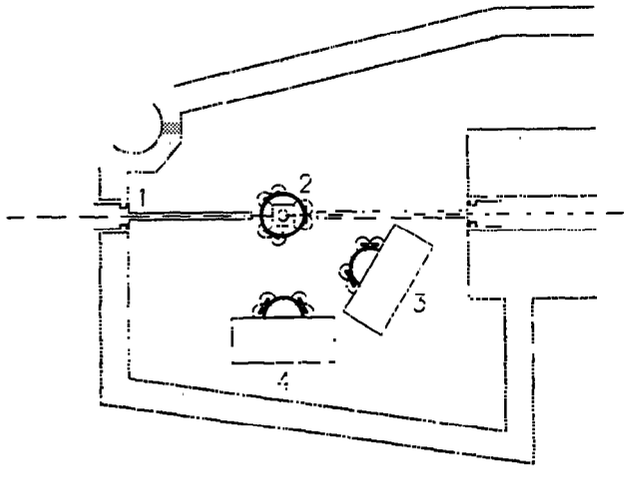

Fig. 2: The ROT/DIFF-setup in the ROTAX-blockhouse (shaded); primary beam (1), sample position and goniometer support module (2), JULIOS detector units to be positioned on air pads (3 and 4)

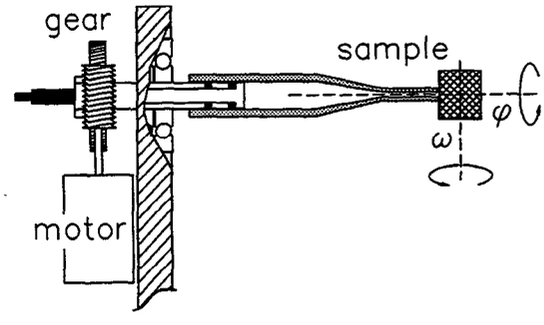

Fig. 3: One-circle goniometer with horizontal ϕ-axis and sample to be centered in the vertical ω-axis of the turn-table (see (2) in Fig. 2)

3. ROT/DIFF instrumental setup

The instrumental setup of a pulsed white beam angle-dispersive time-of-flight texture diffractometer is being realized at the ROTAX instrument at ISIS. The ROTAX spectrometer [8] has been redesigned into a versatile neutron powder diffractometer ROT/DIFF [9], which is characterized by the flexible installation of several linear psd-units of the JULIOS-type [10] (Fig. 2). The detector positions can be varied with respect to different 2Θ-settings and with respect to variable distances between sample and detector. One detector unit of 682 mm sensitive length and 2.3 mm spatial resolution covers a $\Delta 2\Theta$-section of about 38° in 100 cm distance. In minimum distance the $\Delta 2\Theta$-coverage is approximately 90°, thus allowing the scanning of complete pole-figures in two ω-settings of the sample as is shown in Fig. 1. The wavelength band used is from 0.4 Å to 4.0 Å. The d-spacing coverage of the instrument is from 0.2 Å in backscattering to about 60 Å at small scattering angles. The neutron flight path from the moderator to the sample is 14 m.

In its operation mode for pole-figure measurements, the instrument is equipped with an additional goniometer device, which is installed on the sample-table of the diffractometer. A stepping motor drive at the turn-table allows different ω-settings of the goniometer with respect to the primary beam. The goniometer itself (Fig. 3) is constructed with a horizontal rotation axis to perform the $\Delta\phi$ pole-figure scanning. The ϕ-axis is driven by a stepping motor combined with a reduction gear of 100 steps per one degree rotation. The texture sample can be glued on a glass-capillary at the end of the rotation axis. Flexible lengths are adjustable to enable the centering of samples of different size within the vertical ω-axis of the turn-table.

4. Test measurements and results

Pole-figure test measurements have been performed during the reconstruction of the ROTAX-instrument by transferring one unit of the linear JULIOS-detector and the sample goniometer to the TESTbeam facility at ISIS. The provisional experimental setup allowed flexible ω-settings, $\Delta\phi$-stepscanning and a JULIOS installation of 90° 2Θ-coverage. The neutron flight path from the moderator to the sample was 12 m at TEST; i.e. 2 m shorter than at ROTAX with the consequence of improved primary intensity and slightly reduced d-spacing resolution.

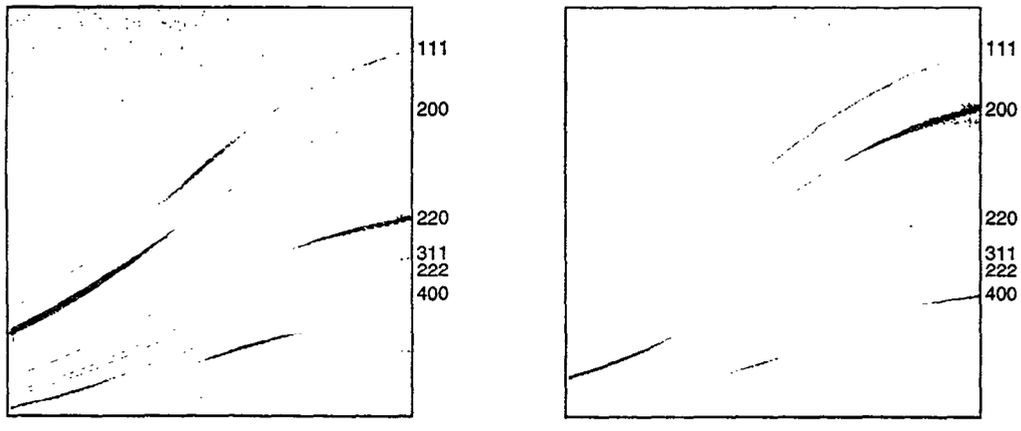

Fig. 4: Images of the detector matrix with 2Θ-channels (horizontal) and λ-channels (vertical) showing traces of simultaneously registered Bragg reflection intensities of the recrystallized copper specimen for sample orientations ω_1 = +22.5°, ϕ_1 = 0° (left) and ω_2 = −22.5°, ϕ_2 = 0° (right).

Pole-figure scans have been performed on cube-shaped copper specimens. The samples had been prepared by cutting plates of 0.9 mm thickness into pieces of 1 cm^2 and glueing them on top of each other in the same orientation. The one specimen was made from cold rolled copper sheets, the other from recrystallized ones. [8]. The central detector position during the angle-dispersive time-of-flight measurements was $2\Theta = 90°$, the wavelength band used was from 0.6 Å to 4.2 Å resulting in a simultaneous experimental d-spacing coverage from about 0.4 to 5.0 Å, where all relevant Bragg-reflections of the fcc-structure of copper are contained. According to the 90° $\Delta 2\Theta$-coverage of the detector the pole-figure scanning was performed in two ω-settings of each sample: $\omega_1 = +22.5°$ to cover pole-distances $\Delta\chi$ from 0° to 45° and $\omega_2 = -22.5°$ for $\Delta\chi$ from 45° to 90°. The grid of the 360°-azimuth stepscanning was $\Delta\phi_1 = 7.2°$ and $\Delta\phi_2 = 10.0°$ for the ω_1- and ω_2-setting, respectively. Fig. 4 shows the variation of Bragg intensities for two different (ω, ϕ)-orientations of one texturized sample. The real counting time for one sample orientation was 40 sec; the total experimental time, i.e. positioning and counting, was approximately 1 h for one sample.

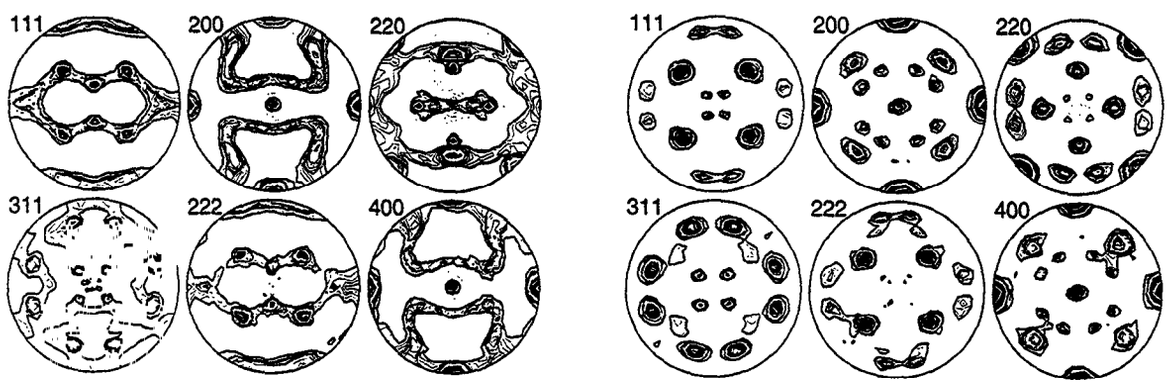

Fig. 5: Experimental pole-figures of the rolled copper specimen (left) and of the recrystallized copper specimen (right).

A total of 86 individual angle-dispersive time-of-flight diffraction patterns per sample have to be analysed for pole-figure representation. The experimental data, which are stored in (2Θ, λ)-channels, have to be rearranged for a proper allocation of (ϕ, χ)- and hkl-parameters. The orientation dependent hkl intensity variations are plotted as usual as hkl pole-figures in stereographic projections of the sample hemisphere. A selection of the simultaneously measured pole-figures is shown in Fig. 5. The pole-figures show the typical appearence of rolling and recrystallization textures.

5. Discussion and prospects

The copper specimens have been chosen for this methodical test of white beam angle-dispersive pole-figure scanning, because the identical samples had already been measured in conventional constant-λ technology at the JULIOS-equipped diffractometer SV7 at the FRJ-2 reactor [8]. The identical material and the identical detector system form a favourable basis for a direct comparison of both technologies. The quality of the pole-figures, which is defined on the one hand by the resolution width and the density of the mesh of data points and on the other hand by the measurement statistics, is found almost the same for both measurements.

This is revealed by a direct comparison of the reactor and spallation source pole-figures [9]. The constant-λ $\Delta\phi$- and $\Delta\chi$-pole-figure scanning had been performed with a total of 800 sample orientations and 3 min measuring time each. The total experimental time was about 48 h per sample. Thus, a gain factor of roughly 50 in experimental beam time can be stated in favour of the angle-dispersive time-of-flight technology at ISIS. This gain may be splitted into a factor 10 obtained by the reduction of different sample orientations (86 instead of 800) and a factor 5 resulting from the general advantage of pulsed white beam time-of-flight diffraction and its exploitation of the primary neutron spectrum (compare [6]).

The substantial reduction of neutron beam time is of special interest in geological texture analysis. The low structural symmetry of most natural mineral constitutents and the multiphase character of many geological specimens cause complex diffraction patterns and the distribution of Bragg intensities over a multitude of comparatively weak reflections. This involves rather long measuring times to guarantee adequate statistics in the diffraction patterns during pole-figure scanning. Furtheron, geologists are interested in the study of texture variations involving large series of many individual samples to be analysed. The decisive factor of beam time, which often prevents people from doing neutron diffraction texture measurements, becomes less important when using the technology described here.

Acknowledgement This work has been funded by the German Federal Government (BMBF) under contract-nos. 03-WI4BO2 and 03-WI4BO3.

6. References

[1] W. Schäfer, S. Höfler and G. Will, Textures and Microstructures **8 & 9** (1988) 457

[2] W. Schäfer, P. Merz, E. Jansen and G. Will, Textures and Microstructures **14-18** (1991) 65

[3] H.J. Bunge, H.R. Wenk and J. Pannetier, Textures and Microstructures **5** (1982) 153

[4] G. Will, W. Schäfer and P. Merz, Textures and Microstructures **10** (1989) 375

[5] D.J. Jensen and J.K. Kjems, Textures and Microstructures **5** (1983) 239

[6] W. Schäfer, E. Jansen and G. Will, J. Appl. Cryst. **26** (1993) 660.

[7] K. Helming, W. Voitus and K. Walther, Physica B **180 & 181** (1992) 1025

[8] H. Tietze-Jaensch, W. Schmidt and R. Geick, Proc. ICANS-XII 1993, eds. U. Steigenberger, T. Broome, G. Rees and A. Soper, RAL-Report 94-025 (1994) Vol. I, p. I-97

[9] W. Schäfer, E. Jansen, R. Skowronek, G. Will, W. Kockelmann, W. Schmidt and H. Tietze-Jaensch, Nucl. Instr. and Meth. A (1995), in press

[10] W. Schäfer, W. Kockelmann, E. Jansen, W. Schmidt, H. Tietze-Jaensch and G. Will, Proc. of EPDIC-IV, Chester, 10-14 july 1995, to appear in Physica B

[11] O. Engler, J. Palacios, W. Schäfer, E. Jansen, K. Lücke and G. Will, Textures and Microstructures **21** (1993) 195

[12] E. Jansen, W. Schäfer, G. Will and K.S. Knight, Proc. of EPDIC-IV, Chester, 10-14 july 1995, to appear in Physica B

ICANS-XIII
13th Meeting of the International Collaboration on
Advanced Neutron Sources
October 11-14, 1995
Paul Scherrer Institute, 5232 Villigen PSI, Switzerland

NEUTRON TIME-OF-FLIGHT DIFFRACTOMETER FOR INVESTIGATIONS OF MICROSAMPLES UNDER HIGH EXTERNAL PRESSURE

V.L.Aksenov*, A.M.Balagurov*, S.L.Platonov*, B.N.Savenko*, D.V.Sheptyakov*
V.P.Glazkov†, I.V.Naumov†, V.A.Somenkov†, G.F.Syrykh†

* Frank Laboratory of Neutron Physics, Joint Institute for Nuclear Research, 141980, Dubna, Russia
† Russian Scientific Center "Kurchatov Institute", 123182, Moscow, Russia

ABSTRACT

A new neutron time-of flight diffractometer for investigations of microsamples structure under high external pressure in diamond and sapphire anvils cells with the use of elastic neutron scattering is described. The diffractometer is operating at the IBR-2 pulsed reactor at JINR. The time-of-flight method and ring-shaped multicounter detectors technique are used to register the scattered neutrons. Parameters and methodical peculiarities of the device are given.

1. INTRODUCTION.

Progress in the study of substances under high pressure by direct methods is closely connected with the use of diamond anvils, providing pressures up to 400 GPa, and synchrotron radiation which allows the study of very small amounts of substance due to high illumination. At the same time a whole set of important problems, such as magnetic transitions, structural phase transitions in systems containing atoms with small or similar numbers demands for the use of neutron methods. But the range of neutron methods application was usually limited to the value of several GPa. This was connected with the use of relatively large sample volumes (~1 cm^3) and cylinder-piston type pressure cells. The use of diamond anvils for this purpose seemed to be impossible because of the small (~10^{-3} mm^3) amounts of substance and the relative weakness of neutron source fluxes. During the last ten years, however, a new method of neutron investigations at high pressures was developed.

Keywords: time-of-flight, high pressure, sapphire, anvil

It was based on the successful composition of diamond and sapphire anvil techniques and high-illumination, low-background neutron diffractometry [1]. This allowed the range of available pressures to be increased up to several tens GPa.
As inelastic neutron scattering experiments demand larger amounts of substance than diffraction ones, they were carried out only in of piston-cylinder type systems in a limited range of pressures. The first work on inelastic coherent neutron scattering investigations with the use of sapphire anvils was carried out just recently [2], and the possibilities of using this technique for inelastic incoherent neutron scattering has not been studied yet.
A new time-of-flight neutron diffractometer (DN-12) is described in this work. It is destined for elastic neutron scattering studies of polycrystal samples under high pressures in pressure cells based on sapphire and diamond anvils. The diffractometer is installed at a high-flux pulsed neutron source - the IBR-2 reactor of JINR. The parameters and methodical peculiarities of the device are discussed in this paper.

2. CONSTRUCTION OF THE DIFFRACTOMETER

A view of the DN-12 diffractometer is shown in fig.1. It is placed in the 12th channel of the IBR-2 reactor and consists of the following main systems: neutron beam chopper phased with the power pulse of the reactor, beam collimating system, multicounter circular detectors system, information management, registration and processing system.

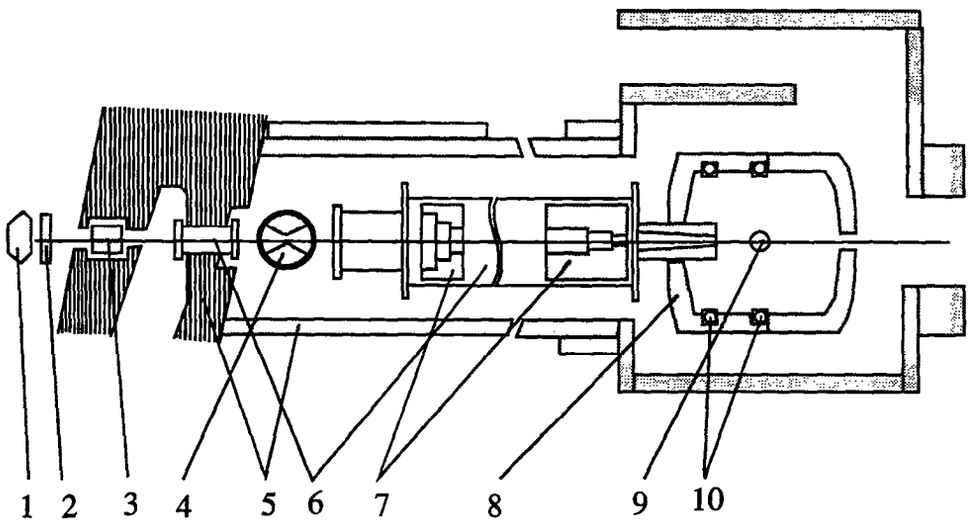

fig. 1. Lay-out of the DN-12 diffractometer at the IBR-2 pulsed reactor.
1 - active core, 2 - moderator, 3 - beam damper, 4 - chopper,
5 - fast neutron shield, 6 - vacuum neutron guide, 7 - beam collimators,
8 - shielding, 9 - sample position, 10 - ring-shaped detectors.

The DN-12 diffractometer is specifically intended for works with high-pressure cells based on sapphire anvils. A well collimated neutron beam passes through the

sapphire single crystals, between which a sample is placed (Fig.2). Scattered neutrons are registered by the detectors consisting of small counters positioned around the circles of a vertically standing rings. The rings as a whole can be moved relative to the sample along the beam direction providing scattering angles from 45° to 135°.

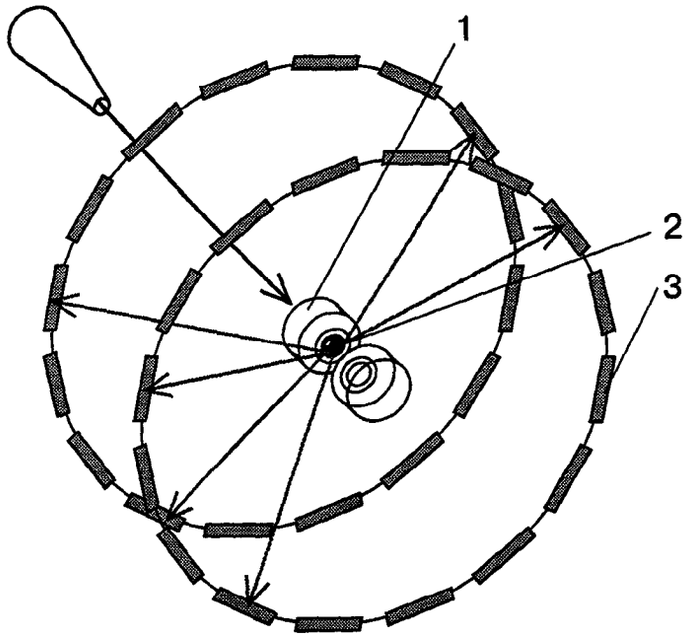

fig.2. Position of the high-pressure cell with the sample and the detector at the DN-12 diffractometer. The neutron beam passes through the sapphire single crystals 1. The neutrons scattered from the sample 2 are registered by the ring-shaped detectors 3 assembled of separate counters.

3. DN-12 PARAMETERS

TABLE 1. *The main characteristics of DN-12.*

Parameters	1994	1997
1. Thermal neutron flux at the sample position ($n/cm^2/s$)	$1 \cdot 10^6$	$2 \cdot 10^6$
2.Distances: moderator - sample sample - detector	31.8 m 0.4 m	27.0 m 0.4 m
3.Range of: wavelength	1 ÷ 4 A	0.8 ÷ 10 A
scattering angle	45° ÷135°	45° ÷ 135°
d_{hkl}	0.8 ÷ 5.2 A	0.6 ÷ 13 A
4.Resolution ($\Delta d/d$, d=2A): for $2\theta=90°$	0.022	0.022
for $2\theta=135°$	0.012	0.012
5. Solid angle of the detector system	0.125 sr	1.0 sr
6.Pressure range: with sapphire anvils	5 GPa	5 GPa
with diamond anvils	20 GPa	20 GPa

4. EXPERIMENTS ON DN-12

TABLE 2. Experiments performed with DN-12 during November 1993 to March 1994. Pressure is given in GPa, sample volume in mm^3.

Sample	Pressure	Volume	Anvils	Main result
DyD_3	10.0	0.01	diamond	equation of state
Hg-1212, Hg-1201	3.6 3.2	1	sapphire	structural changes
ND_4Cl	2.5	2	sapphire	structural changes
Fe_2O_3	4.7	1	sapphire	new magnetic phase above 3 GPa

4.1 The lowest limit of the sample volume.

Several experiments have been carried out in order to determine the minimal quantity of substance from which it would be possible to obtain a diffraction pattern at our facility within a reasonable amount of time (not more than 50 - 100 hours). For this purpose, the $^{164}DyD_3$ sample with a maximal coherent scattering cross-section was used ($\sigma_{coh}\approx250$ b). This sample was placed in the diamond anvil cell. The sample volume was 0.027 mm^3, the pressure was about 10 GPa, and it was possible to increase the pressure up to 20 GPa. It took 24 hours to obtain a clear diffraction pattern.

4.2 Structural experiments

We have already used our diffractometer to carry out several structural experiments.

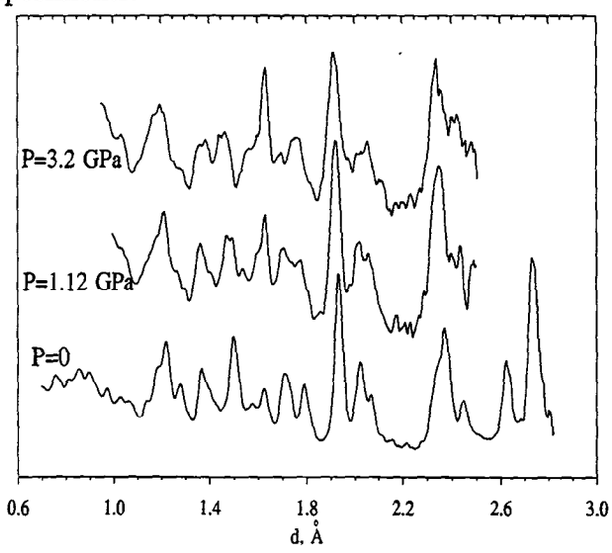

fig. 3. Typical view of raw neutron diffraction patterns obtained at the DN-12 diffractometer - patterns of hg-1201 structure under high external pressure

For example, the pressure dependences of lattice parameters and interatomic distances of some representatives of the recently discovered series of mercury-based superconductors were investigated [3]. We performed the studies of $HgBa_2CaCu_2O_{6.3}$ (Hg-1212) and $HgBa_2Cu_1O_{4.2}$ (Hg-1201) (see raw experimental spectra on the fig.3). The results including lattice parameters and interatomic distances (within the accuracy of 0.005 A) appeared to be in good agreement with the data obtained at another devices [4].

5. DEVELOPMENT OF THE DN-12

As the DN-12 is a new device, it is constantly developed and modified. The fig.4 shows the probable plan of the DN-12 diffractometer layout as it will be in a few months probably.

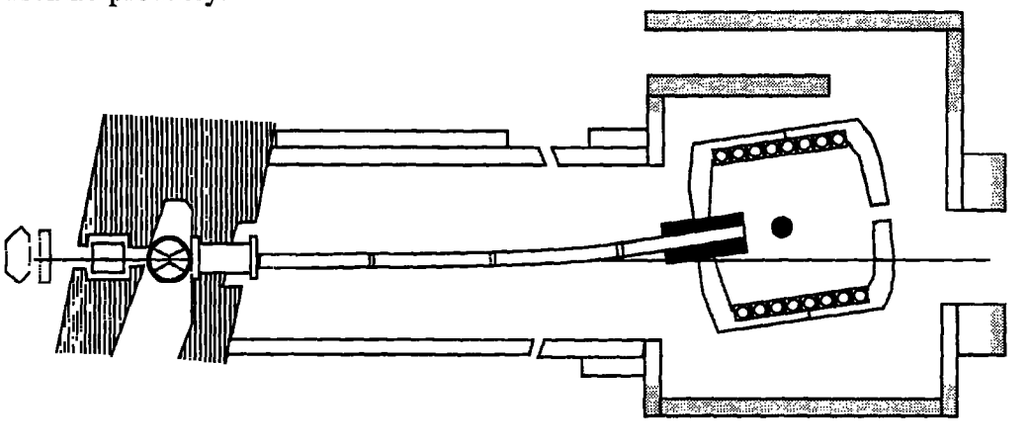

fig.4. Probable lay-out of the DN-12 diffractometer at the IBR-2 pulsed reactor after improvement.

It is planned to develop the DN-12 in the following directions:

- moving of the neutron beam chopper to another position (The distance will be 4.5 m between moderator and chopper instead of 8.9 m at the moment);
- substitution of the vacuum neutron guide tube by the curved mirror neutron guide tube;
- increasing of the number of the detector rings to 8 instead of 2.
- improvement of detector system, including the creation of data acquisition system in the VME standard;
- creation of the special equipment for loading the pressure cell with the optical spectrometer measurement of pressure;
- widening of experimental possibilities (using of new materials for the anvils, getting low and high temperatures at the samples).

CONCLUSION

The experiments carried out at the DN-12 have shown its compete-ability with the similar devices in such centres as RAL, RRC-KI, ANL, LANL. Putting of new detector system into operation, building of mirror neutron guide tube and moving of the beam chopper will allow to improve the device characteristics significantly, will increase the efficiency of its using and will make it more lovely for the users.

PUBLICATIONS

1. V.L.Aksenov, A.M.Balagurov, B.N.Savenko, S.L.Platonov, V.P.Glazkov, I.V.Naumov, V.A.Somenkov and G.F.Syrykh.
High Pressure Research, 1995, v.14, N1-3, p.181-191.

2. A.M.Balagurov, B.N.Savenko, A.V.Borman, V.P.Glazkov, I.N.Goncharenko, V.A.Somenkov, G.F.Syrykh.
ibid., p.55-60.
3. V.L.Aksenov, A.M.Balagurov, B.N.Savenko, V.P.Glazkov, I.N.Goncharenko, V.A.Somenkov, E.V.Antipov, S.N.Putilin and J.-J.Capponi.
ibid., p.127-137.
4. B.A.Hunter, J.D.Jorgensen, J.L.Wagner, P.G.Radaelli, D.G.Hinks, H.Shaked and R.L.Hitterman, Physica C 221 (1994).

ICANS-XIII
13th Meeting of the International Collaboration on
Advanced Neutron Sources
October 11-14, 1995
Paul Scherrer Institut, 5232 Villigen PSI, Switzerland

THE NEW SMALL-ANGLE DIFFRACTOMETER SAND AT IPNS*

R. K. Crawford, P. Thiyagarajan, J. E. Epperson, F. Trouw, R. Kleb, D Wozniak, D. Leach
Argonne National Laboratory, Argonne, IL 60439 USA

ABSTRACT

A new small-angle neutron diffractometer SAND is undergoing commissioning at IPNS. This paper provides details of the design and expected performance of this instrument.

1. Introduction

In 1980, a prototype time-of-flight (TOF) small-angle diffractometer was operated at the prototype pulsed neutron source ZING-P' at Argonne National Laboratory, and this instrument was later upgraded and operated at the IPNS pulsed source from 1982 through 1984. In late 1984, this instrument was further upgraded to become the current Small Angle Diffractometer (SAD) at IPNS. Many experiments have been performed on the SAD by Argonne and outside users, and these have resulted in a number of publications to date. The quality of this work as well as that at other pulsed source small-angle neutron scattering (SANS) instruments clearly demonstrates that SANS using the TOF method at a pulsed source is now an established technique, capable of producing data of quality comparable to those taken on the more mature reactor instruments.

The SAD instrument at IPNS has been severely oversubscribed for several years, with proposals exceeding operating time by a factor of two to three. Because of this, and because experience led us to believe we could now build a significantly improved instrument, consideration of a second SANS instrument at IPNS was begun in 1986. Design of this second small-angle diffractometer and development of the necessary components has proceeded with relatively low priority, but the new instrument (named SAND) is now beginning commissioning. A number of related studies have also been completed during this period.[1-8]

* Work supported by U.S. Department of Energy, BES, contract No. W-31-109-ENG-38.

Keywords: Small-angle, Instrument, Collimation

The new instrument SAND is designed to provide all the capabilities now provided by SAD, and to enhance those capabilities by extending the dynamic range and improving the ease of operation and the instrument reliability. One goal is to make a value of Q_{min} down to 0.002 $Å^{-1}$ readily accessible for those experiments which require it. Since for small scattering angles ϕ

$$Q \approx \frac{2\pi\phi}{\lambda} \tag{1}$$

the minimum Q which can be reached is

$$Q_{min} \approx \frac{2\pi\phi_{min}}{\lambda_{max}} \tag{2}$$

Thus to reduce Q_{min} from that on SAD (~0.005 $Å^{-1}$), one must either use tighter collimation of the incident beam (to reduce ϕ_{min}) or longer wavelengths (to increase λ_{max}) or both. The new instrument includes a chopper to allow operation with much longer wavelengths, and will eventually have a second set of collimators having smaller angular divergence, both of which will serve to reduce Q_{min}.

A second goal is to increase the maximum Q value accessible, and to provide better counting statistics for the higher Q data where the scattering cross-section is usually quite small. For a given wavelength, Q_{max} can be increased only by increasing the maximum scattering angle which can be used. This goal has already been partially addressed by procuring a 40 cm × 40 cm detector for the new instrument. This is twice the linear dimensions of the SAD detector (4 times the area). An array of linear position-sensitive detectors (LPSDs) at higher scattering angles is also included to provide large additional increases in Q_{max}.

Experience with SAD has suggested a number of improvements which would enhance the instrument operation. Based on these suggestions, SAND includes features to facilitate the alignment of the instrument components and of the sample, improved access for various types of sample environment equipment, and design features to permit *in situ* calibration of the area detector.

This paper presents details of the SAND instrument, indicating differences from SAD where appropriate. Some examples of SAD data are presented, and expected improvements with SAND are discussed.

2. SAND Design

2.1 Overview

Figure 1 shows SAND in its location on the C3 beamline, and indicates its relationship to its neighbors. Figures 2 and 3 show portions of the instrument in greater detail, indicating the geometry and relative placement of major components of the instrument. Major components include the moderator, incident beam filter, background chopper, collimation system, sample chamber, area detector, high-angle detector bank, and beam monitors and beamstops. Specifications for various components and the reasoning behind their designs are discussed below. Table 1 summarizes the instrument parameters for SAND.

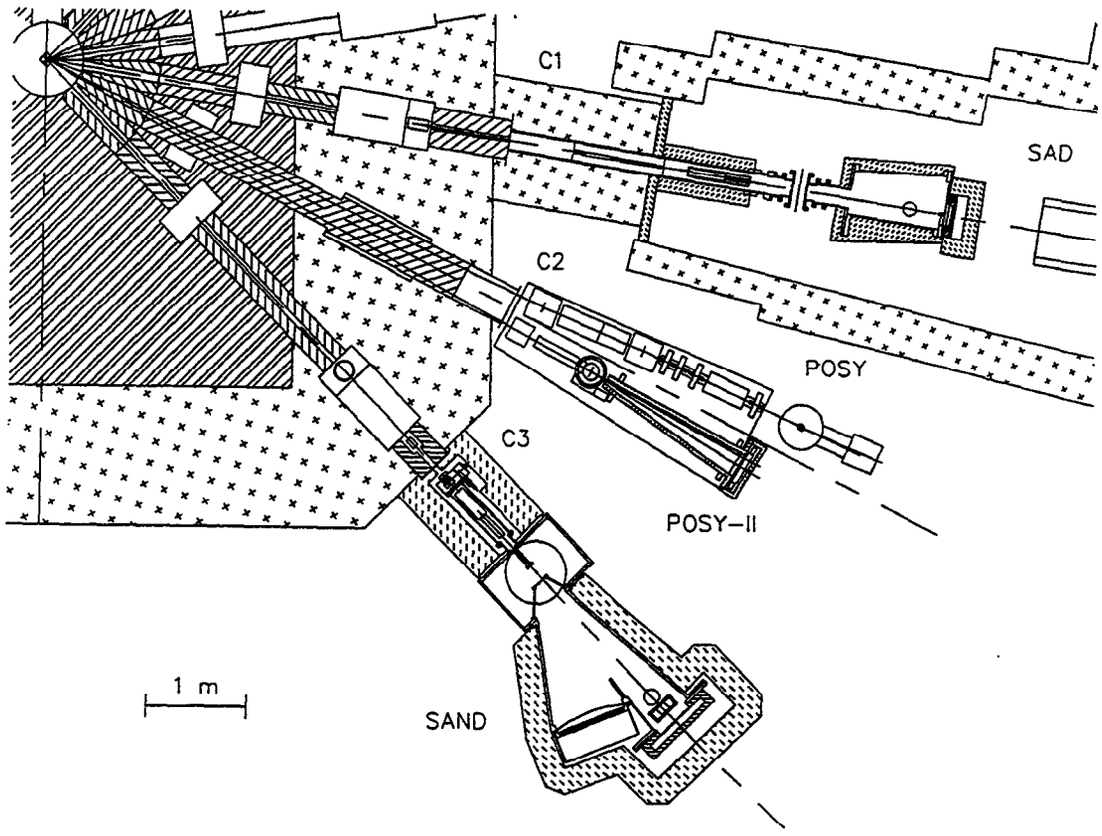

Figure 1. Top view of a portion of the IPNS experiment hall, showing SAND and adjacent instruments.

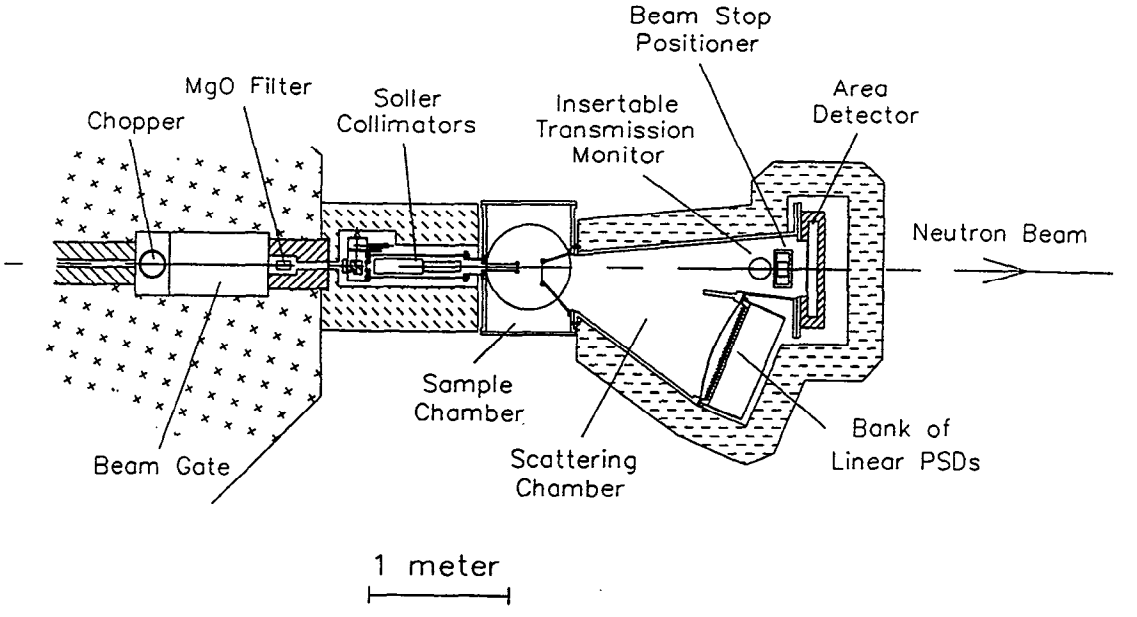

Figure 2. Top view of SAND, showing major instrument components.

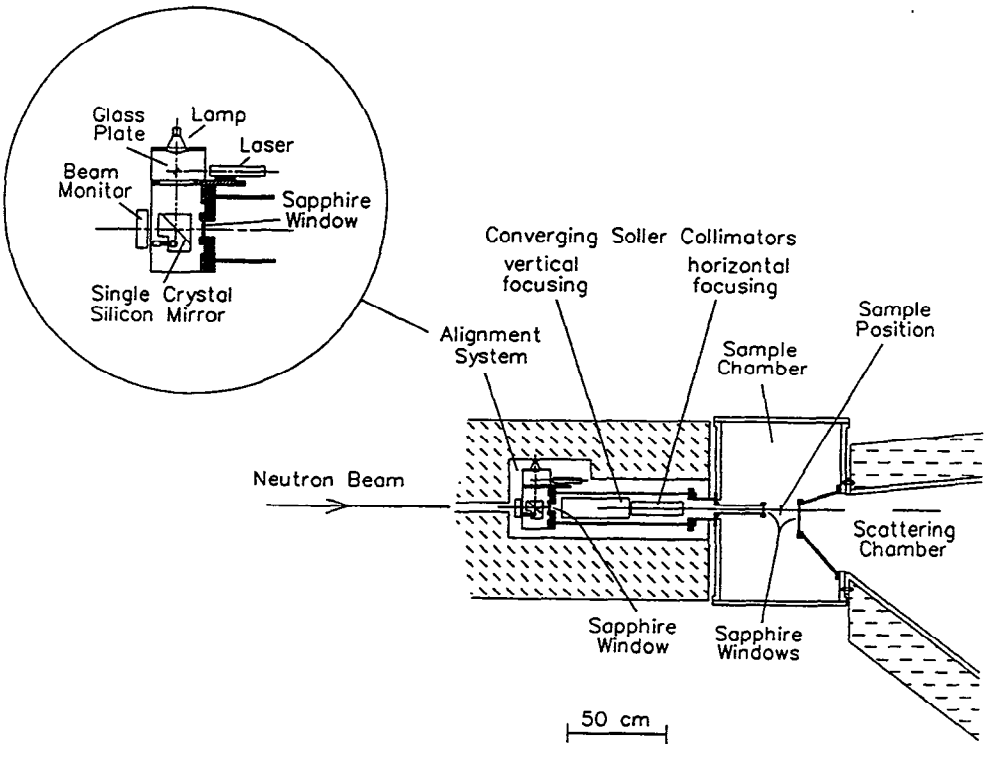

Figure 3. Details of the collimation and alignment systems on SAND. The inset shows a ×2 magnification of the optical alignment system and the incident beam monitor.

Table 1. Parameters for SAND

Parameter	Value
Source frequency	30 Hz
Moderator	decoupled solid CH_4
Source-to-sample distance	7.0 m
Sample-to-area-detector distance	2.0 m
Collimator-to-sample distance	0.5 m
Sample-to-LPSD distance	1.524 m
Beam size at moderator	9.0-cm diameter
Maximum beam size at sample	2.0-cm diameter
Area detector	
active area	40×40 cm^2
active thickness	2.5 cm
resolution	4-6 mm
fill	2.6 atm ^{3}He plus 1.4 atm CF_4
encoding	rise time, 256×256 pixels
max. scattering angle	~9°
LPSD	
active volume per detector	1.1 cm diameter $\times$ 60 cm long
number of detectors	65
resolution	1-2 cm along detector
fill	~10 atm ^{3}He
encoding	charge division, 64 segments/ detector
max. scattering angle	36°
Focusing collimators	
coarse	0.0034 radians fwhm
fine	0.0014 radians fwhm
Wavelength range	1-14 Å (5-14 Å for crystalline samples)
Q_{max}	
λ_{min} = 1.0 Å (noncrystalline)	>2.0 Å^{-1}
λ_{min} = 5.0 Å (crystalline)	~0.6 Å^{-1}
Q_{min} (λ_{max} = 14 Å)	
coarse collimation	~0.005 Å^{-1}
fine collimation	~0.002 Å^{-1}
Q_{min} (λ_{max} = 28 Å, using chopper)	
coarse collimation	~0.003 Å^{-1}
fine collimation	~0.001 Å^{-1}

2.2 Moderator

The C3 beamline where SAND is located is one of three beamlines viewing the same cold moderator. SAD on beamline C1 also views the same moderator, as do POSY and POSY-II. From early 1985 until late 1988, and again since 1994, these beamlines have viewed a grooved solid CH_4 moderator (physical temperature ~ 20 K) which is an excellent source of long-wavelength neutrons. During the other operating periods, the moderator can was filled with liquid H_2 instead. Measurements shown in Fig. 4 indicate that over most of the wavelength range of interest for small-angle diffraction the solid CH_4 moderator provides a factor of ~3.5 more intensity than did the liquid H_2 moderator.

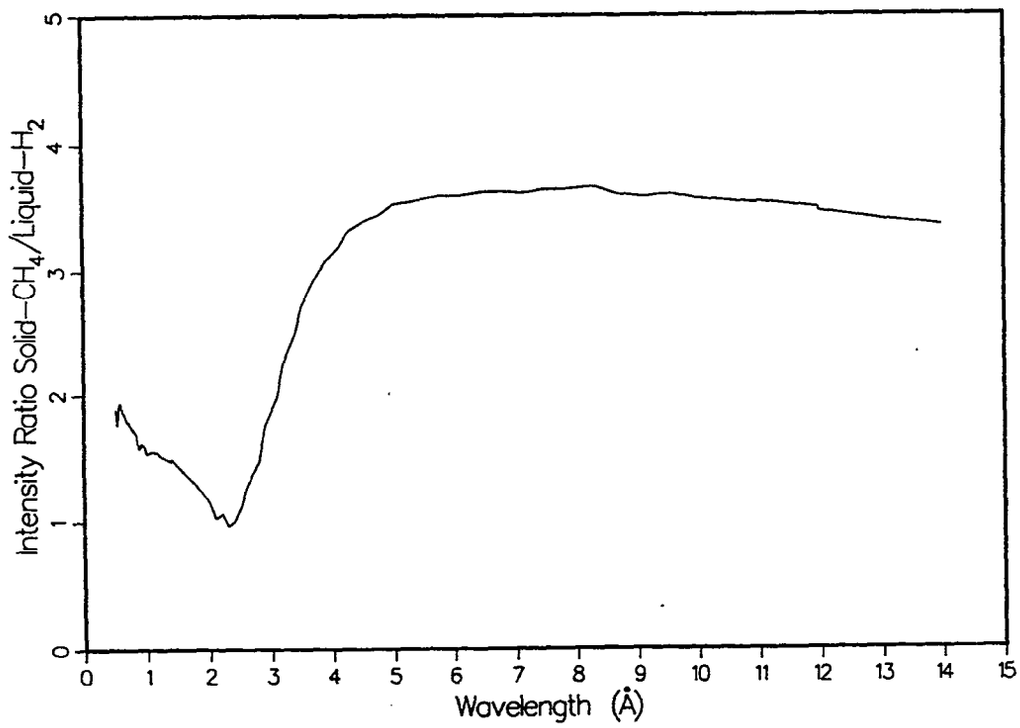

Figure 4. Ratio of the spectral intensities of solid CH_4 and liquid H_2 moderators. The same moderator can was used in both cases, and all geometry was the same.

2.3 Filter to Remove Fast Neutrons

In an instrument in which the moderator, sample, and detector are in a direct line, the very fast neutrons from the moderator can reach the detector directly. The multiple-aperture collimation used on SAND has inadequate stopping power to fully collimate such fast neutrons, so these contribute to a background halo about the main beam. Also, a very large number of such fast neutrons arrive almost simultaneously at the detector immediately after the protons strike the target, and these can produce an overload of the area detector and its

associated electronics that can affect subsequent area detector performance throughout the time frame (depending on the overload recovery time of the area detector and electronics). In SAND, a 10 cm long filter made of oriented single-crystal MgO cooled to ~80 K is located in the incident beamline. A similar MgO filter has been used on SAD for a number of years. This filter reduces the fast neutron flux by roughly two orders of magnitude, while having a transmission of ~0.5-0.7 for most of the neutrons of interest (roughly 1-14 Å). Figure 5 shows the measured transmission of the SAND MgO filter at room temperature. The cryostat for this filter is under construction, and experience with the SAD filter [4] indicates that the transmission will increase to above ~0.7 over the wavelength range of ~2-14 Å when the filter is cooled.

The MgO filter on SAND is refrigerated by a closed-loop system (CryoTiger, APD Cryogenics, Inc., Allentown, PA), and the filter and the cold head of the refrigeration system are located just inside the monolith in the outermost beamline shield block, as shown in Fig. 2. This location makes considerable use of the bulk shielding monolith for shielding against the neutrons scattered by the filter, thus minimizing the amount of external shielding which must be added. This location also allows relatively easy access to the filter and its cryostat and refrigerator for maintenance.

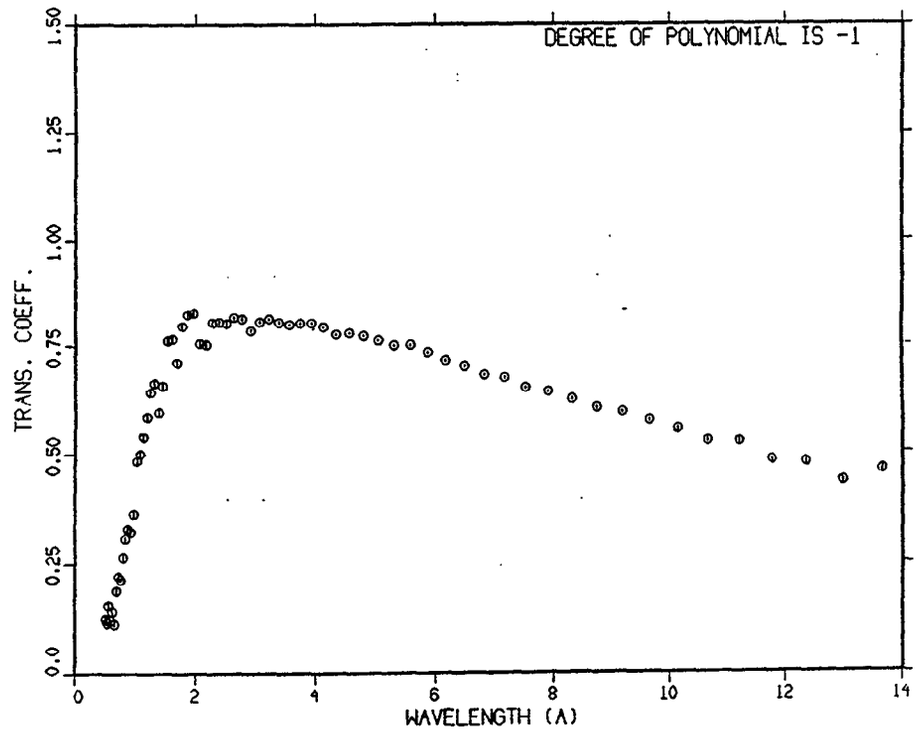

Figure 5. Transmission of the SAND single-crystal MgO filter at room temperature. Several sharp dips in the transmission in the 1-3 Å range are due to Bragg scattering in the filter.

2.4 Background Chopper

A detailed analysis [6] showed that the use of a low-speed drum chopper similar to those on the IPNS powder diffractometers SEPD and GPPD could be quite effective on the new instrument if the chopper were reduced in size and placed in the gate cavity on the C3 beamline. This chopper can be rotated at 7.5 Hz (opening twice per revolution, for a 15 Hz effective chopping frequency) in a "frame-elimination" mode to eliminate alternate prompt pulses from the 30 Hz IPNS source, providing an effectively 15 Hz operation of the instrument. In this mode the chopper also eliminates those delayed neutrons which contaminate the very-long-wavelength portion of the spectrum, so that ~16-28 Å neutrons in addition to some of the short-wavelength neutrons can be used cleanly with this chopper setting. Alternatively, the same chopper can be operated at 15 Hz (30 Hz effective chopping frequency), allowing full 30 Hz operation of the instrument, and in this mode it eliminates the delayed neutrons which normally contaminate the data from ~8-14 Å. At wavelengths below 8 Å the spectrum is sufficiently intense that delayed neutron contributions are negligible, so with this mode of operation no delayed neutron correction is required over the entire data range. The net effect is to eliminate a large background component from the long-wavelength portion of the data, thus greatly improving the signal-to-noise ratio for data over this range (delayed neutrons contribute roughly half the signal measured at TOF values corresponding to a nominal wavelength of 14 Å). Based on these simulations, an ~18.5 cm diameter drum chopper with a ~1 cm thick B_4C shell as the chopping material has been fabricated and will soon be installed in a cutout portion of the beam gate on the C3 beamline, as indicated in Fig. 2.

2.5 Collimation, Path Lengths, and Q_{min}

To achieve the necessary angular collimation in the incident beam while utilizing most of the full moderator size (~ 10 cm square) and a reasonable sample size (~ 1-2 cm diameter) requires the use of either a very long total flight path or else the use of converging multiple-aperture collimation.[2] Because of frame-overlap conditions, the maximum wavelength which can be utilized on a pulsed-source TOF instrument is

$$\lambda_{max} = \frac{3955.4}{f L_{md}} \tag{3}$$

where λ is in Å, f is the effective source frequency in Hz, and L_{md} is the total moderator-detector distance in m. A large λ_{max} helps in reaching small Q_{min}, so L_{md} must be kept as small as possible. This leads to relatively low intensities if pinhole collimation having the desired angular divergence is used, but much higher counting rates are achieved with the same angular divergence by using converging multiple-aperture collimation. If the collimation channels are all focused to the same point on the detector, then even with a short sample-to-detector distance the sample size will not affect Q_{min} or the Q-resolution.[9] Both SAD and SAND have L_{md} = 9 m, but are still able to use samples of 1 cm diameter or larger and to use neutrons from nearly all of the moderator face because of this type of collimation.

In both SAD and SAND such focusing multiple-aperture collimation is done with crossed converging Soller collimators,[2,3] as shown schematically in Fig. 6. The collimators presently available for SAND define ~ 400 converging beam channels with essentially no "dead" space between them, and provide ~0.0034 radian fwhm angular divergence (~0.007 radian full divergence) of the incident beam. The entire collimator system occupies a distance of only ~ 60 cm along the incident flight path. Figure 3 shows the physical arrangement of the collimators in their independent vacuum space, and also shows the optical system used for initial collimator and sample alignment.

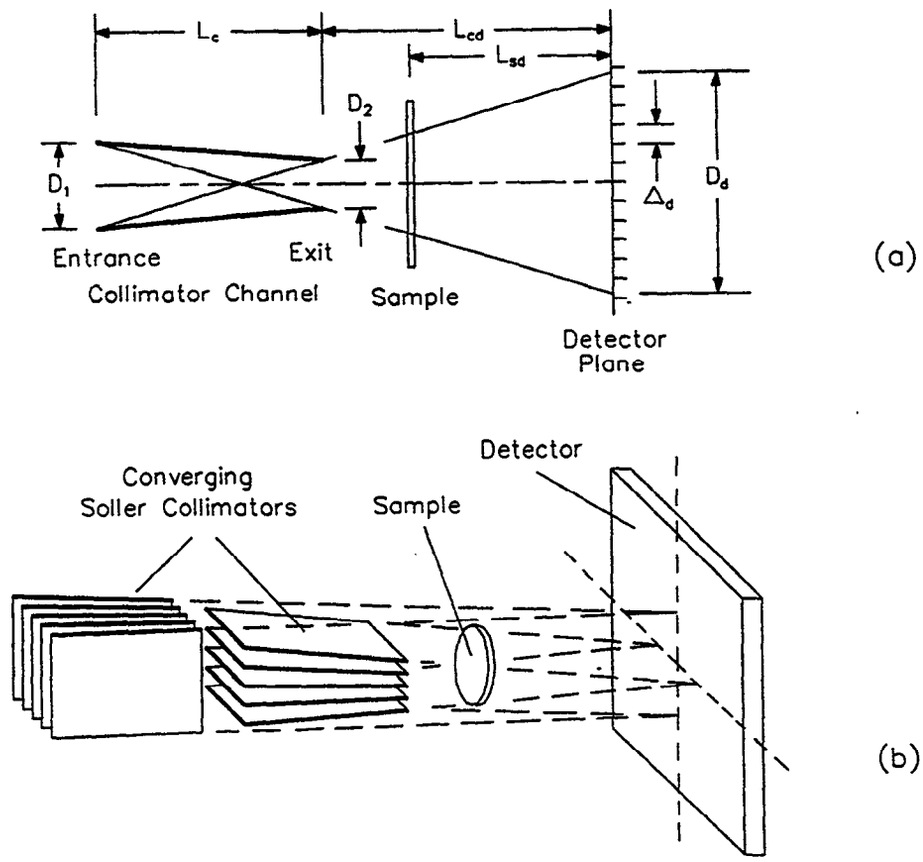

Figure 6. Schematic diagram of crossed converging soller collimators. (a) Geometry of a single collimator channel, defining some of the parameters used in the text. (b) Schematic arrangement of the crossed converging soller collimators.

The soller collimator blades are of the standard form made of stretched mylar, with ^{10}B in a suitable matrix deposited on each surface of each blade. [All collimators were purchased from Cidic, Ltd., Cheltenham, UK.] Similar collimators have been used on SAD for a number of years, and have worked quite well once the proper technique was devised for fabricating a non-reflective coating on the collimator blades.[3] It was found to be very

important to have the ^{10}B coating deposited with a rough (matte) finish in order to minimize surface reflections from the blades. Over the normal SAD operating range of 0.5-14 Å these collimators provide very low backgrounds (10^{-6} to 10^{-7} of the incident beam intensity) and produce resolutions in good agreement with the calculated values. Recent tests at IPNS with 15 Hz accelerator operation indicated that these collimators also perform well at wavelengths up to 28 Å. The multiple-aperture collimation must focus on the detector, as shown in Fig. 6, so different collimators would be needed for a different sample-to-detector distance and there is no point in having a continuously variable sample-to-detector distance in this instrument.

Upstream from the collimators, the incident beam is shaped with a series of apertures which define a circular beam with an umbra that converges from ~9 cm diameter at the moderator to a point at the detector. These apertures follow standard IPNS practice and consist of boron carbide cast with minimum epoxy. Between these apertures are thick segments of lead shot cast in epoxy containing borax and having slightly larger aperture diameters. With these apertures and the soller collimators, and with the MgO filter attenuating the fast neutrons, the resulting collimated beam has clean edges defined by the nominal geometric penumbra of the soller collimators. There is no measurable fast-neutron halo when the area detector pulse-height discrimination levels are properly set.

All channels in each soller collimator are equivalent and focus to the same spot on the area detector. Figure 6a shows the geometry associated with the focusing from a single channel of one of the soller collimators. The minimum useful scattering angle is given approximately by

$$\phi_{min} \approx \frac{\frac{B}{2} + \Delta_d}{L_{sd}} \tag{4}$$

where B is the diameter of the beamstop, Δ_d is the fwhm spatial resolution of the detector, and L_{sd} is the sample-detector distance. The beamstop must have a diameter larger than the beam penumbra diameter D_d at the detector, or

$$B = D_d + \delta \tag{5}$$

where δ is small (~2 mm or less), so this leads to

$$Q_{min} = \frac{2\pi}{\lambda_{max}} \frac{\frac{D_d + \delta}{2} + \Delta_d}{L_{sd}} \tag{6}$$

The beam penumbra size at the detector is given by

$$D_d = \frac{D_2 (L_{cd} + L_c) + D_1 L_{cd}}{L_c} \tag{7}$$

and the fwhm angular divergence of the incident beam is

$$\alpha = \frac{D_1}{L_c} \tag{8}$$

where D_1 and D_2 are the dimensions of the entrance and exit apertures of the collimator, respectively, L_{cd} is the distance from the collimator exit to the detector, and L_c is the length of the collimator, as defined in Fig. 6a.

Table 2 summarizes the values of these collimation parameters for SAD and for the current "coarse" SAND collimators. For SAND it is also intended to provide a set of "fine" soller collimators once suitable fabrication techniques can be developed. Approximate values for these collimators are included in the table as well. The measured Q_{min} for the present SAD collimators is ~0.005 $Å^{-1}$, in good agreement with the calculated value in the table, so the calculated values for SAND are expected to be fairly accurate as well. Values of Q_{min} down to ~0.003 $Å^{-1}$ and ~0.001 $Å^{-1}$ should be possible with the coarse and fine collimators for those experiments where the chopper permits useful operation with wavelengths out to 28 Å.

Table 2. Collimation Parameters for SAD and SAND[a]

		SAD[b]	SAND (coarse)[b]	SAND (fine)[c]
λ_{max}	(Å)	14	14	14
L_{sd}	(m)	1.5	2.0	2.0
L_{cd}	(m)	2.0	2.5	2.5
L_c	(m)	0.25	0.25	?[d]
D_1	(mm)	0.844	0.844	?[d]
D_2	(mm)	0.750	0.767	?[d]
D_d	(mm)	13.5	16.9	5.6[e]
α	(radian fwhm)	0.00338	0.00338	0.0011[e]
B	(mm)	15.5	19.0	8[e]
Δ_d	(mm)	~6	~6	~4[f]
Q_{min}	($Å^{-1}$) -- calculated	0.0041	0.0035	0.0022[e,f]

a. Parameters are given for the downstream (x) collimator in each case. The upstream (y) collimator parameters are somewhat different because of the different L_{cd} required, but are chosen to provide the same value of D_d as the downstream collimators.

b. Presently available.

c. Planned.

d. Final values will depend on the design and fabrication techniques selected.

e. Values in table are approximate and are based on the desired collimator performance.

f. Assumes that the nominal detector resolution can be achieved.

When both sets of collimators for SAND are available, they will be mounted on an automatic changer so that they can be easily interchanged depending on the experiment. An automated beamstop insertion mechanism has been provided on SAND to allow the use of a different beamstop size when the collimators are interchanged, in order to utilize the corresponding minimum scattering angles. This device also allows removal of the beamstop for measurements of detector sensitivity and resolution. Cadmium beamstops are used, and have adequate stopping power so long as the MgO filter is in the beam to attenuate the higher-energy neutrons.

2.6 Area Position-Sensitive Detector

SAND uses a two-dimensional rise-time-encoded position-sensitive gas-proportional-counter detector of 40×40 cm^2 active area, 2.5 cm thick and having nominally 4×4 mm^2 resolution (Ordela, Inc., Oak Ridge, TN). This detector covers the smallest scattering angles and can be operated centered on the direct beam or offset by 10 cm to increase the angular range. A gas detector was chosen because of its excellent intrinsic background characteristics, rejection of fast neutrons and gammas, and commercial availability. This detector is filled with a mixture of ^3He and CF_4 at 4 atm to provide an efficiency of ~65% at 2 Å and an intrinsic gas contribution to the position resolution of ~1.7 mm. Position and time encoding electronics for this detector duplicate those used on the present SAD. At present the measured spatial resolution is ~6 mm fwhm so there is still room for improvement in the electronics. Pulse height discrimination is used to reject any remaining fast-neutron halo around the main beam, and to eliminate the signals from gammas and electronic noise.

2.7 High-Angle LPSDs

The minimum usable wavelength with the MgO filter in the beam is ~ 1 Å. This yields usable intensity at a Q_{max} of ~ 0.5-0.6 $Å^{-1}$ when the area detector is centered on the beam. With the detector operated 10 cm off center, this is increased to Q_{max} ~ 0.8-0.9 $Å^{-1}$, at some cost in intensity at the smaller Q values. (For reference, the usable Q_{max} for SAD is ~ 0.35 $Å^{-1}$.) It is frequently desirable to have Q_{max} even larger than this, and in most cases it is desirable to sum data from a wide range of wavelengths to improve the statistics in the high-Q data. Therefore the ability to cover even higher scattering angles is incorporated into SAND by including an array of linear position-sensitive detectors (LPSDs) at higher angles. The glass-liquids-and-amorphous diffractometer (GLAD) recently built at IPNS is based entirely on such LPSDs, so the technology for position- and time-encoding a large number of such detectors is already developed.[10] This bank of LPSDs is mounted as shown in Fig 2, and will extend the range of scattering angles out to 36°. As on GLAD, a motorized absorbing bar can be driven past the upstream side of these detectors for periodic recalibration of the position encoding and resolution. Even when the wavelength range must be restricted to $\lambda > 5$ Å, as is necessary to avoid multiple-Bragg scattering for many crystalline samples, these LPSDs it should make it possible to collect good data at Q values up to ~0.7 $Å^{-1}$. Wavelengths down to 1 Å can be used for most experiments, and in this case good counting statistics should be possible at Q values up to 1 $Å^{-1}$ or more.

2.8 Beam Monitors and Measurement of Sample Transmissions

The incident beam monitor is a low-efficiency BF_3 ionization chamber, similar to that used on most of the other IPNS instruments. It is located just upstream from the soller collimators (see Fig. 3).

Sample transmissions are measured by means of a gas proportional counter detector having an efficiency of ~0.1 for 2 Å neutrons. For transmission measurements this detector is automatically lowered into the transmitted beam just in front of the beamstop (see Fig. 2), while for scattering measurements it is automatically raised outside the path of the scattered neutrons.

Development is underway on a small detector which can be placed just upstream from the beamstop. This monitor detector is smaller than the diameter of the beamstop, so that it is totally masked from the area detector by the beamstop. If this detector proves successful it will replace the insertable transmission monitor, making it possible to measure transmissions concurrently with the scattering measurements.

2.9 Alignment and Calibration

An optical alignment system has been built into SAND in order to facilitate alignment of the soller collimators, beamstop, and transmission monitor. This system, shown in Fig. 3, includes a halogen lamp as a broad white-light source and a low-power laser for finer alignment. Both are directed along the surveyed axis of the instrument by a thin (3 mm thick) single-crystal silicon wafer permanently mounted in the neutron beam upstream from the soller collimators, and inclined at 45° to the beam. This wafer has minimal effect on the neutron beam. . The laser beam is first reflected by a thin glass plate in front of the halogen lamp (see Fig. 3), and then directed along the instrument axis by the silicon mirror. The vacuum windows at the entrance and exit of the soller collimator chamber, and at the entrance to the scattering chamber are all made of high-quality single-crystal sapphire (HEMEX quality, from Crystal Systems, Inc., Salem, MA). These windows have good neutron transmission and are optically transparent, so the light from the halogen lamp or from the laser can be transmitted all the way to the area detector.

The broad white-light source illuminates all the slits of the soller collimators, and so provides a good representation of the entire collimated beam. Either this light source or the laser can be used to align the soller collimators so that the transmitted beam is centered on the sample position and on the optical axis at the detector. The laser is then used to provide the initial centering of the beamstop and the transmission monitor, before their alignment is fine-tuned using the neutron beam. This optical system has reduced the alignment process to a matter of a few minutes.

The white-light source provides good images of any apertures placed near the sample, so the exact portion of the sample being illuminated by the light, and hence by the neutron beam,

can be determined. For non-standard sample equipment, the laser and white-light sources provide a means for quick centering of the sample in the beam.

The encoding of the area detector and LPSDs is periodically checked for linearity and resolution by measurement of uniform flood patterns with and without masks in front of the detectors. This is usually done with a moderated Pu-Be source at the sample position. The beamstop and transmission monitor can be withdrawn so that the entire area detector can be illuminated by this source. A hinged mask can be swung into place in front of the area detector, and a motorized absorbing bar can be driven in front of the LPSDs, and patterns measured with these masks in place enable the position encoding and the resolution of the detectors to be indexed on an absolute scale.[8,10] All of these measurements can be made during scheduled accelerator down time, so that no beam time is wasted.

2.10 Effects of Gravity

Because of gravity a neutron beam of wavelength λ traveling a distance L falls a distance

$$y = \frac{gt^2}{2} = \frac{g}{2}\left(\frac{m}{h}\right)^2 L^2 \lambda^2 = 3.132 \times 10^{-4} L^2 \lambda^2 \qquad (13)$$

where $g = 980$ cm·sec^{-2}, and y is in cm, L in m, and λ in Å. For L = 2.5 m, the distance from the collimator exit to the area detector on SAND, the maximum fall is y = 0.38 mm at λ = 14 Å. Thus for 30 Hz operation all gravitational effects are small enough to be ignored. If the chopper is operated in frame-elimination mode to allow use of neutrons out to 28 Å, then the maximum gravitational fall will reach 1.5 mm for the longest wavelengths, necessitating the use of slightly elongated beamstops and minor wavelength-dependent corrections to the scattering angle to account for this drop.

2.11 Sample Environment

A large sample region is provided in the instrument, with proper alignment fixtures so that a wide variety of sample environments can be easily interchanged in the instrument. Included among these are cryogenic capabilities, temperature-controlled sample changers, furnace capabilities with the sample in vacuum or a controlled atmosphere, high pressure cells, and magnetic fields.

Figure 3 shows details of the sample chamber. The incident flight path has its own independent vacuum, which is terminated downstream from the last soller collimator by a single-crystal sapphire vacuum window. A second sapphire window at the entrance to the scattering flight path isolates the scattering flight path vacuum from the sample area, while introducing little additional background in the scattering pattern. The use of sapphire windows permits optical alignment of the various instrument components. For most samples, the path between these windows will be in air. Both of the sapphire windows can be removed and the sample area can be evacuated when it is desired to minimize the window and air scattering, or when bulky sample-environment equipment is in use. The top flange

on the sample chamber conforms to IPNS standards, and ensures precise centering of the sample in the beam when top-mounting sample equipment (e.g., closed-cycle refrigerator) is used.

2.12 Data Acquisition System

The data acquisition system is essentially a duplicate of other IPNS data acquisition systems,[10,11] with some modifications to allow operation of both the area detector and the LPSDs on the same system.

2.13 Data Analysis

Because it is necessary to use the TOF technique at pulsed sources, data are collected as functions of the x and y coordinates on the detector and of the time-of-flight t, which is proportional to the neutron wavelength. The resulting x-y-t data sets can contain on the order of a million elements, or even considerably more when LPSDs are used to supplement the angular range, so considerable attention must be given to data collection and analysis. Analysis programs for reducing the TOF SANS data from SAD have been in routine use for a number of years, and are currently used to analyze data from the SAND area detector. Development of the software to smoothly combine the area detector and LPSD data is now underway.

3. Performance

SAND is just now being commissioned, so its measured performance can not yet be discussed in detail. However, at least in the initial stages it is expected to have performance similar to or better than SAD. Therefore we discuss briefly the operation of SAD and the quality of data obtained, and then indicate areas in which SAND will likely provide improvements.

3.1 Data Reduction

In a typical scattering experiment at the SAD, prompt neutrons with wavelengths between 0.5 and 14 Å are used. The scattering data are binned in 67 time slices, with $\Delta\lambda/\lambda = 0.05$, and for each time slice the data are stored in a 64×64 spatial array. These binning parameters, however, may be altered at the discretion of the user, depending on the resolution requirement. In order to express the SANS data in terms of the sample's absolute differential cross section, one needs the scattering data from the sample and its background, the wavelength-dependent transmission coefficients for the sample and its background, thickness of the sample, the detector sensitivity and nonlinearity of the pixels of the area detector, spectral distribution of the probing neutrons and a scale factor to account for certain unscaled parameters.

Because one wishes to combine the information from the different wavelength bands (time slices) into the more conventional S(Q) array, it is necessary to determine the wavelength distribution of neutrons in the beam for use in normalization. This measurement is carried

out using the area detector, with the beam stop removed and with the incident beam intensity attenuated by a cadmium mask filled with tiny holes. This mask protects the detector by attenuating the beam intensity, without altering the spectral character of the neutron beam.

The wavelength-dependent sample transmission coefficient is defined as the ratio of the sample attenuated neutron beam to that of the unattenuated beam. It is determined in a separate measurement by inserting a high-efficiency transmission monitor detector in front of the beam stop.

The data on the wavelength dependent transmission coefficients for the sample and the background, efficiency-weighted source spectrum, relative detector sensitivity, and the measured raw scattering data for the sample, background, and cadmium blank are sufficient to determine the net normalized scattering data in each encoded detector element. The full measured time spectrum for each pixel provides the necessary information to correct the data for the effects of delayed neutrons,[5] if this is important. Dividing the net scattering values by the thickness of the sample and multiplying by a scale factor converts the measured scattering of the unknown sample to absolute cross sections. The scale factor is determined from measurements of a standard sample whose absolute scattering cross-section is available. At IPNS we use a polymer melt sample (Bates poly) which consists of a 50:50 volume mixture of hydrogenous and deuterated high molecular weight polystyrene for this purpose. The data can then be remapped as S(Q) by using the known values of the bin widths of the encoded cells and the wavelengths corresponding to each of the time slices. These resulting S(Q) values are on an absolute scale in the units of cm^{-1} per steradian.

3.2 Example of SAD Data

As an example, Figure 7 shows data measured for a 5.5 mM GroEL in D_2O measured at the 30m SANS instrument at ORNL and at SAD at IPNS.[12] GroEL is a chaperonin which identifies and binds with proteins denatured under stress. The SAD data have been reduced and placed on an absolute scale using the procedure described above. While the SANS data from the ORNL instrument has been measured at 12 m and 3 m sample-to-detector settings for a total of 5.5 hr in a 0.5 cm thick Suprasil cell, the SAD data was measured in a single setting for 4 hr in 0.2 cm thick Suprasil cell. There is excellent agreement, on an absolute scale, between the low-Q ORNL data and that from SAD, although the density of points in the low Q region in the ORNL data is about 3 times larger than that in the SAD data.

However, this example illustrates the importance of measuring over the full Q range in a single experiment whenever time-dependent variations can occur in the sample. This protein complex in solution can change with time due to a change in the subunit-complex equilibrium,[12] depending on the handling and storage conditions. Since SAD data for other, stable, samples agree with ORNL data over the entire Q range, the small discrepancies at higher Q in these particular data sets suggest a possible time-dependent change in the sample between the measurements with the two different settings on the ORNL instrument. Thus the SAD data were necessary in order to be able to properly assess the relative magnitudes of the low-Q and high-Q portions of the scattering.

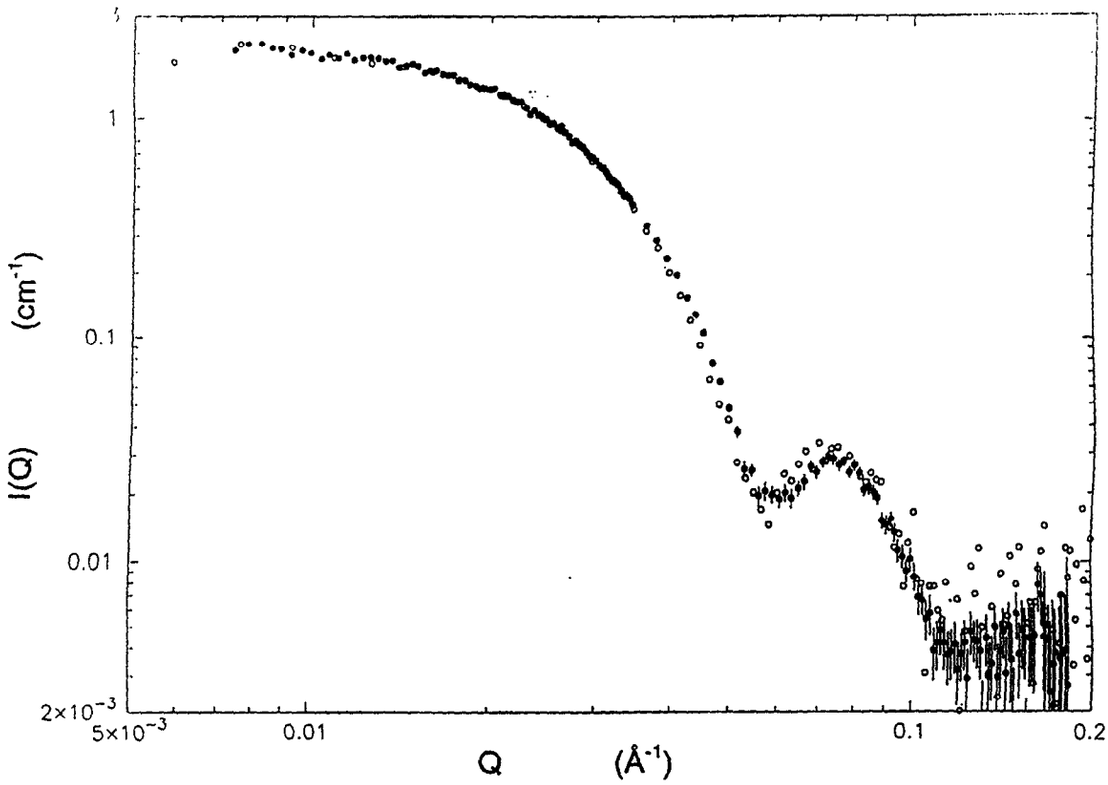

Figure 7. SANS data for E. coli GroEL from SAD (open circles) and from the 12-m and 3-m settings of the 30 m SANS instrument at ORNL (closed circles).

3.3 Expected Improvements with SAND

As is suggested in Fig. 7, much of the interesting data lies at the higher Q values, above 0.1 $Å^{-1}$. The present SAD already provides data in this region comparable to that from ORNL. Even so, the statistics are too poor to do much with the data above 0.1 $Å^{-1}$ in this example. More and more of the experiments being proposed are of this type, and would greatly benefit from an extension of the Q range to higher Q values. The larger area detector on SAND will lead to factors of 2-4 increase in measured intensity in this Q range, and the inclusion of the LPSDs on SAND will provide as much as an order of magnitude additional intensity at these and even higher Q values. This should open up an exciting new range to further exploration.

At present, SAD cannot reach Q values below 0.005 $Å^{-1}$, as can be seen in Fig. 7. This low-Q range is also important for many experiments. When SAND is fully operational, the capability to use wavelengths out to 28 Å and the availability of a set of fine soller collimators should extend the range down to 0.002 $Å^{-1}$ or possibly even to 0.001 $Å^{-1}$.

4. Summary

A new small-angle neutron diffractometer SAND at IPNS is now being commissioned. This instrument builds upon the more than 15 years experience with pulsed neutron small-angle diffraction at IPNS, and incorporates many new features to improve both Q_{min} and Q_{max} as well as improving the ease of instrument operation. The area-detector portion of SAND is expected to be operational with the coarse soller collimators in late 1995. The chopper is being bench-tested, and will also be incorporated in the instrument in 1995. It is expected that SAND will be placed in the user program in this configuration in Spring, 1996. The schedule calls for bringing the LPSD bank on line in late 1996. The last item to be added will be the set of fine soller collimators, and the schedule for these will depend on the outcome of the efforts to develop the appropriate fabrication technology.

Acknowledgments

The authors would like to thank the National Science Foundation and Professor S.-H. Chen of the Massachusetts Institute of Technology for a grant which aided in the development of some of the instrument concepts for SAND, and would also like to thank the Texaco Corporation for a grant that funded part of the construction of SAND.

References

[1] J. M. Carpenter, U. Walter, and D. F. R. Mildner. Proceedings of the 9th Meeting of the International Collaboration on Advanced Neutron Sources (ICANS IX), Swiss Institute for Nuclear Research, Villigen, Switzerland, Sept. 22-26, 1986. Swiss Institute for Nuclear Research report ISBN 3-907998-01-4, 1987, pp. 279-303.

[2] R. K. Crawford and J. M. Carpenter. *J. Appl. Cryst.* **21** (1988) 589-601.

[3] R. K. Crawford, J. E. Epperson, and P. Thiyagarajan. *Advanced Neutron Sources 1988*, Proceedings of the 10th Meeting of the International Collaboration on Advanced Neutron Sources (ICANS X), Los Alamos National Laboratory, Oct. 3-7, 1988. Institute of Physics Conference Series Number 97, IOP Publishing Ltd, New York, 1989, pp. 419-426.

[4] J. M. Carpenter, D. F. R. Mildner, S. S. Cudrnak, and R. O. Hilleke. *Nucl. Instrum. Methods* **A278** (1989) 397-401.

[5] J. E. Epperson, J. M. Carpenter, P. Thiyagarajan, and B. Heuser. *Nucl. Instrum. Methods* **A289** (1990) 30-34.

[6] R. K. Crawford, J. E. Epperson, P. Thiyagarajan, and J. M. Carpenter. Proceedings of the 11th Meeting of the International Collaboration on Advanced Neutron Sources (ICANS XI National Laboratory for High Energy Physics, Tsukuba, Japan, Oct. 22-26, 1990. KEK report 90-25, 1991, pp. 873-889.

[7] J. M. Carpenter, D. F. R. Mildner, J. W. Richardson, Jr., and W. C. Dimm. Proceedings of the 11th Meeting of the International Collaboration on Advanced Neutron Sources

(ICANS XI), National Laboratory for High Energy Physics, Tsukuba, Japan, Oct. 22-26, 1990. KEK report 90-25, 1991, pp. 1044-1053.

[8] R. K. Crawford, P. Thiyagarajan, and J. Chen. Proceedings of the 12th Meeting of the International Collaboration on Advanced Neutron Sources (ICANS XII), Abingdon, UK, May 24-28, 1993. Rutherford Appleton Laboratory report 94-025, 1994, pp. I208-I215.

[9] A. C. Nunes. *Nucl. Instrum. Methods* **119** (1974) 291-293.

[10] R. K. Crawford and J. R. Haumann. *IEEE Trans. Nucl. Sci.* **NS-37** (1990) 72-81.

[11] J. R. Haumann and R. K. Crawford. *IEEE Trans. Nucl. Sci.* **NS-34** (1987) 948-953.

[12] P. Thiyagarajan, S. J. Henderson, and A. Joachimiak. *Structure*, (1995) in press.

ICANS-XIII
13th Meeting of the International Collaboration on
Advanced Neutron Sources
October 11-14, 1995
Paul Scherrer Institut, 5232 Villigen PSI, Switzerland

NOVEL TENDENCIES IN DEVELOPING SMALL-ANGLE NEUTRON SCATTERING METHODS FOR STUDYING THE STRUCTURE OF BIOLOGICAL MACROMOLECULES

Igor Serdyuk

Laboratory of Neutron Physics, Joint Institute of Nuclear Research,
141980 Dubna, Moscow Region, Russia

ABSTRACT

In recent 20 years thermal neutron scattering has been acknowledged an important instrument for structural studies in molecular biology. The methods of neutron diffraction of high resolution, which are not discussed in this paper, have already permitted to obtain a detailed representation of the course of proteolytic reactions and have arisen a number of new problems connected with the localization of water molecules and the H-D exchange. The methods of low resolution widely used due to a relative simplicity of the experiment have been successfully applied for both solving structural problems per se and investigating the changes in the structure when macromolecules perform their biological functions. The most promising are novel experimental approaches: the triple isotopic substitution method and the method of spin dynamic polarization. These methods ensure solving structural problems at a higher resolution than the dimensions of the macromolecules studied. Installation of new experimental instruments makes neutron measurements more accessible, and development of direct methods for interpretation of experimental data using the apparatus of spherical harmonics opens new possibilities for small-angle neutron scattering making it a necessary element for interpretation of diffraction data of monocrystals of intricate biological macromolecules.

The paper presents a brief account of the tendencies in theoretical development and practical use of small-angle scattering for studying biological macromolecules. Special attention is given to the studies carried out in the Laboratory of Neutron Physics on a unique pulse IBR-2 reactor.

1. Modern Small-angle Spectrometers

The development of experimental methods and possibilities in neutron physics have always been determined by the accessible power of neutron sources. By 1969 these possibilities had been developed to such an extent that it became possible to use neutrons for investigation of real biological macromolecules. In 1972 such an attempt was successfully realized on hemoglobin on a FRJ-2 reactor by a group of German physicists (Schelten, Schlecht, Schmatz and Mayer) in Julich [1]. The interest to the

Keywords: Neutron scattering, Direct methods, Macromolecules

studies was explained by a number of advantages of neutron investigations over X-ray ones: much higher "sensitivity" of neutrons to the presence of light atoms in the structure and, in the first place, of hydrogen atoms, and unique isotopic and spin "sensitivity" of neutrons. At the same time, the neutron method has certain disadvantages. They are a high level of incoherent neutron scattering in hydrogen-containing molecules and appreciable stiff neutron scattering. However, the main disadvantage of neutrons is low intensity and limited accessibility of neutron beams which is explained by the technical possibilities of the existing neutron sources and their high cost. Therefore the first studies of hemoglobin were made at very high concentrations of the protein (up to 144 mg/ml) [1].

The usage and accessibility of neutron sources has noticeably increased. First of all this can be said about Europe where the International Laue-Langevin Institute in Grenoble (France) is the leading center of neutron studies. The installation of a new small-angle D22 spectrometer and modernizing of the small-angle D11 spectrometer by substituting the wave rate selector have essentially enhanced the capabilities of neutron diffraction for studying biological macromolecules. The recently adopted decision to construct a new powerful reactor in the suburbs of Munich will make such measurements far more accessible. Now the concentrations of biomacromolecules required for measurements vary from 2 to 20 mg/ml at the volume of the measuring cell 0.2-0.3 ml.

At present a small-angle "YUMO" spectrometer located in the fourth canal of the pulse IBR-2 reactor is successfully operating in Dubna [2]. The average heat flux of neutrons in the sample is about $4 \cdot 10^7$ neutrons/cm$^2 \cdot$s that is only two times lower than the flux in the sample of the D11 spectrometer (prior to modernizing). The low pulse frequency of the IBR-2 reactor (5 Hz) makes it possible to apply the time-flight method with high efficiency. Eight angular detectors provide for automated radial averaging. A comparative study of particles of large molecular dimensions (ribosomes with a molecular weight of about $2 \cdot 10^6$ and the radius of gyration of 90 Å) and particles of average molecular dimensions (the protein of the translation apparatus with a molecular weight of about $43 \cdot 10^3$ and the radius of gyration 24 Å) has shown that the pulse IBR-2 reactor with a heating retarder (Dubna) and the stationary HFR reactor with a cooling retarder (Grenoble) allows to obtain results comparable in the following parameters: the absolute values of the scattering intensity and the calculated radii of gyration coincide within the limits of statistical errors [3]. It was shown on tetramethyl urea that the YUMO spectrometer is highly efficient for studying weakly scattering samples (=0.05 cm^{-1}) [4]. The high transmission of the spectrometer is combined with a good three-dimensional resolution which is illustrated by the scattering curve for a protein particle possessing a spherical symmetry (apoferritin) [3].

The installation of a new sliding reflector and improvement of the infrastructure of the YUMO spectrometer allow us to expect that in the nearest years the spectrometer will be the main instrument for carrying out neutron studies of biological macromolecules for users from the states of the CIS, East Europe and Germany.

2. New Experimental Approach

Recently two additional experimental schemes have been added to the existing three ones traditionally used in SANS studies: contrast variation by changing the scattering properties of the solvent or particle (isotopic substitution [5]), contrast variation by using a mixture of protonated and deuterated particles (double isotopic substitution [6]), the method allowing us to determine the distance between the marked sites (the triangulation method). The first is based on using three types of particles and is called a triple isotopic substitution method (the TIS-method) [7, 8]. In this scheme, the difference between the scattering of two solutions is considered. One solution contains a mixture of normal (undeuterated) and deuterium labelled particles, and the other contains intermediately deuterated particles only. A necessary condition for the application of the TIS-method is that the two solutions are identical in all respects except for the extent of the deuterium label. The main properties of the TIS-method are elimination of interparticle effects, "invisibility" of the isotopically non-substituted parts of the particle and independence of the TIS scattering curve on the buffer isotopic content (D_2O:H_2O ratio). Recently unique possibilities of the TIS-method were illustrated in the study of the polypeptide elongation factor Tu (EF-Tu) from *E.coli* associated with GDP and within the ternary complex EF-Tu·GTP·aminoacyl-tRNA [9]. The minimal part of the macromolecular assembly whose structure can be obtained by the TIS-method is close to several percent. It was demonstrated that the radius of gyration of protein S4 within the 30S subunit can be really measured by the TIS-method [10]].]

The second experimental scheme called spin contrast variation is based on a great change in the scattering amplitude of hydrogen when polarized neutrons are scattered by polarized protons. The scattering length of hydrogen varies from $-18.3 \cdot 10^{-12}$ cm, when the polarization direction of the neutron beam is antiparallel to that of the proton spins, to $+10.82 \cdot 10^{-12}$ cm, when the interacting spins have the same direction with respect to the external magnetic field. In a strong magnetic field (B=2.5 T) and at low temperatures ($T < 1$ K), irradiation of 4 mm microwaves will align the nuclear spin system parallel (or antiparallel) to the polarized electronic spins of added paramagnetic centers [11].

Recently this idea has been used for determining the structure of ribosomal proteins from the large (50S) ribosomal subparticle. The position and shape of the two proteins, L3 and L4, were determined [12].

3. Small-angle Scattering in Solution and Diffraction in Crystal

Between an ideal solution and an ideal monocrystal there exists an intermediate region of structural arrangement from which it would be possible to obtain, in a general case, structural information with a resolution intermediate between the dimensions of the macromolecule and the atom. Great ambiguity of the shapes of the structural arrangement in this region makes it impossible to obtain a general solution of the structural task. However, in the cases when this ambiguity is removed, the task becomes structurally sensitive. In particular, such an approach can be used not only for studying the distance and position of the particles

in specifically bound dimers and more complicated macromolecular complexes, but also for obtaining information on their shape and internal structure. The practical realization of such an approach is complicated due to the fact that the scattering curve of a certain biological particle always consists of three contributions: the contribution of the shape, the contribution of the internal structure and the contribution of the intersecting member. To isolate each of the contributions, the neutron scattering curve is measured at different contrasts (it is evident that the minimal number of contrasts is three), and the scattering curve of a "homogeneous" particle is obtained by extrapolation to infinite contrast. The envelope of a globular particle can be described by the angular function $F(\omega)$ which is parametrized using the multipole expansion

$$F(\omega) = \sum_{l=0}^{L} \sum_{m=-1}^{1} f_{lm} Y_{lm}(\omega).$$

In this formula, the highest value of L determines the resolution (the angular resolution is $\pi/(L+1)$ and the spatial resolution is $R_o\pi/(L+1)$, where R_o is the radius of the equivalent sphere), f_{lm} are complex numbers, $Y_{lm}(\omega)$ are spherical harmonics, and (r,ω) are spherical coordinates. The partial amplitudes $A_{lm}(Q)$ in the corresponding scattering intensity

$$I(Q) = 2\pi^2 \sum_{l=0}^{L} \sum_{m=-1}^{1} |A_{lm}(Q)|^2$$

are expressed in terms of a power series with coefficients that are non-linear combinations of the shape coefficients f_{lm}. Recently this approach has been successfully applied to study the tertiary structure of protein (pyruvate decarbozylaze [13]) and the 50S subunits of *E.coli* [14]. The model for the 50S subunit (the spatial resolution being about 40 Å) is in good agreement with electron microscopic studies.

The possibility to construct such models opens principally new perspectives for a joint use of the data of small-angle neutron scattering and X-ray diffraction. Let us define these possibilities for the 50S ribosomal subparticle whose crystals diffracting up to 10 Å are obtained in some laboratories, but the phase problem is far from its solution. To construct a model of the 50S ribosomal subparticle at a resolution of ~20 Å, it is necessary to get scattering curves in a maximally possible range of scattering vectors (from 0.007 to 0.30-0.35 Å). This can be done only in conditions when the contribution of incoherent scattering of the solvent is minimal, in other words, all measurements should be done in 100% D_2O. In this case, the contrast can be varied by reverse contrast using particles with a different contribution to the scattering of the RNA and protein components. Such particles are isolated from the bacterial mass grown on a specific combination of protonated and deuterated substrates. The developed three-dimensional model of the 50S subunit with a resolution of 40 Å will be used for obtaining the function of packing in the crystal, and the resolution will be increased using a diffraction set. The data in the range of transmitted pulses from 0.15 to 0.35 Å will serve as a base for refinement and interpretation of reflexes corresponding to the resolution of 40-20 Å. A group of physicists from our laboratory jointly with representatives from a number of foreign laboratories have been working on realization of this project in which for the first time small-angle scattering in solution is combined with diffraction in crystal.

References

[1] J.Schelten, P.Schlecht, W.Schmatz and A.Mayer, *J. Biol. Chem.* **247** (1972) 5436

[2] Yu.Ostanevich, *Macromol. Chem. Macromol. Symp.* **15** (1988) 91

[3] I.N.Serdyuk, *Physica B* (accepted for publication) (1995)

[4] V.Yu.Bezrabotnov, L.Czer, T.Grosz, G.Jancsó and Yu.M.Ostanevich, *J. Phys. Chem.* **96** (1992) 976

[5] Yu.M.Ostanevich and I.N.Serdyuk, *Uspekhi Fizicheskikh Nauk* (in Russian) **137** (1982) 85

[6] A.Z.Akcasu, G.C.Summerfield, S.N.Jahshan, C.C.Han, C.Y.Kim and H.Yu, *J. Polym. Sci. Polym. Phys.* **18** (1980) 863

[7] I.N.Serdyuk and M.Yu.Pavlov, *Macrom. Chem. Macrom. Symp.* **15** (1988) 167

[8] M.Yu.Pavlov, I.N.Rublevskaya, G.Zaccai, R.Leberman and Yu.M. Ostanevich, *Appl. Cryst.* **24** (1991) 243

[9] I.N.Serdyuk, M.Yu.Pavlov, I.N.Rublevskaya, G.Zaccai and R.Leberman, *Biophys. Chem.* **53** (1994) 123

[10] D.H.Harrison, R.P.May and P.B.Moore, *J. Appl. Cryst.* **26** (1993) 198

[11] W.Knop, H.-J.Schink, H.B.Stuhrmann, R.Wagner, M.Wenkow-Es-Souni, O.Schärpf, M.Krumpolc, T.O.Ninikovski, M.Rieubland and A.Rijllart, *J. Appl. Cryst.* **22** (1989) 352

[12] H.B.Stuhrmann, *Physica Scripta* **T49** (1993) 644

[13] S.König, D.I.Svergun, M.H.J.Koch, G.Hubner and A.Schellenberger, *Eur. Biophys. J.* **22** (1993) 185

[14] D.I.Svergun, M.H.J.Koch, J. Scov. Pedersen and I.N.Serdyuk, *J. Mol. Biol.* **240** (1994) 78

ICANS XIII
13th Meeting of the International Collaboration on
Advanced Neutron Sources
October 11-14, 1995
Paul Scherrer Institut, 5232 Villigen PSI, Switzerland

SURF - A Second Generation Neutron Reflectometer

DG Bucknall[§], J Penfold[§], JRP Webster[§], A Zarbakhsh[§], RM Richardson[‡], A Rennie[‡], JS Higgins[‡], RAL Jones[‡], P Fletcher[‡], RK Thomas[‡], S Roser[‡] and E Dickinson[‡]

§ Rutherford Appleton Laboratory, Chilton, Oxon, OX11 0QX
‡ CRG Member

Abstract

The SURF neutron reflectometer has been built at the ISIS Facility at the Rutherford Appleton Laboratory. It is a reflectometer optimised for the surface chemistry of soft condensed matter research. The instrument has been built with almost total computer control, allowing a high degree of reproducibility and accuracy of the data. Unique to the instrument is a focusing supermirror which focusses the beam at the sample position. In addition the instrument has a 2D area detector. Some of the results from the commissioning period by RAL staff and the CRG are described.

1. Introduction

Over the eight years that the CRISP neutron reflectometer has been in operation it has been applied to numerous but completely varied interfacial and surface studies. This reflectometer is a general purpose reflectometer that is designed to be as flexible and adaptable as possible and can work in the non-polarised and also polarised mode. The instrument is located at the ISIS facility at RAL which provides a white beam of neutrons. The beam on CRISP is inclined at 1.5° to the horizontal to allow the easy application to liquids. The white beam TOF method of reflectivity has several advantages with constant illumination and resolution and due to the white beam provides all the reflectivity curve simultaneously. The motivation for SURF was 2 fold, firstly to make an instrument designed specifically for surface chemistry and secondly to help the pressure of demand of instrument time on CRISP. The basic instrumental requirements were:

- Optimise for surface chemistry
- Provide a large wave-vector transfer, Q
- Ensure a high degree of accuracy and reproducibility on absolute scale
- Provide a good signal to background noise ratio
- Have full control of reflectometer using sophisticated instrumentation
- Have sophisticated and controlled environment
- Increase flux at sample with the capability of relaxed resolution

2. SURF Design

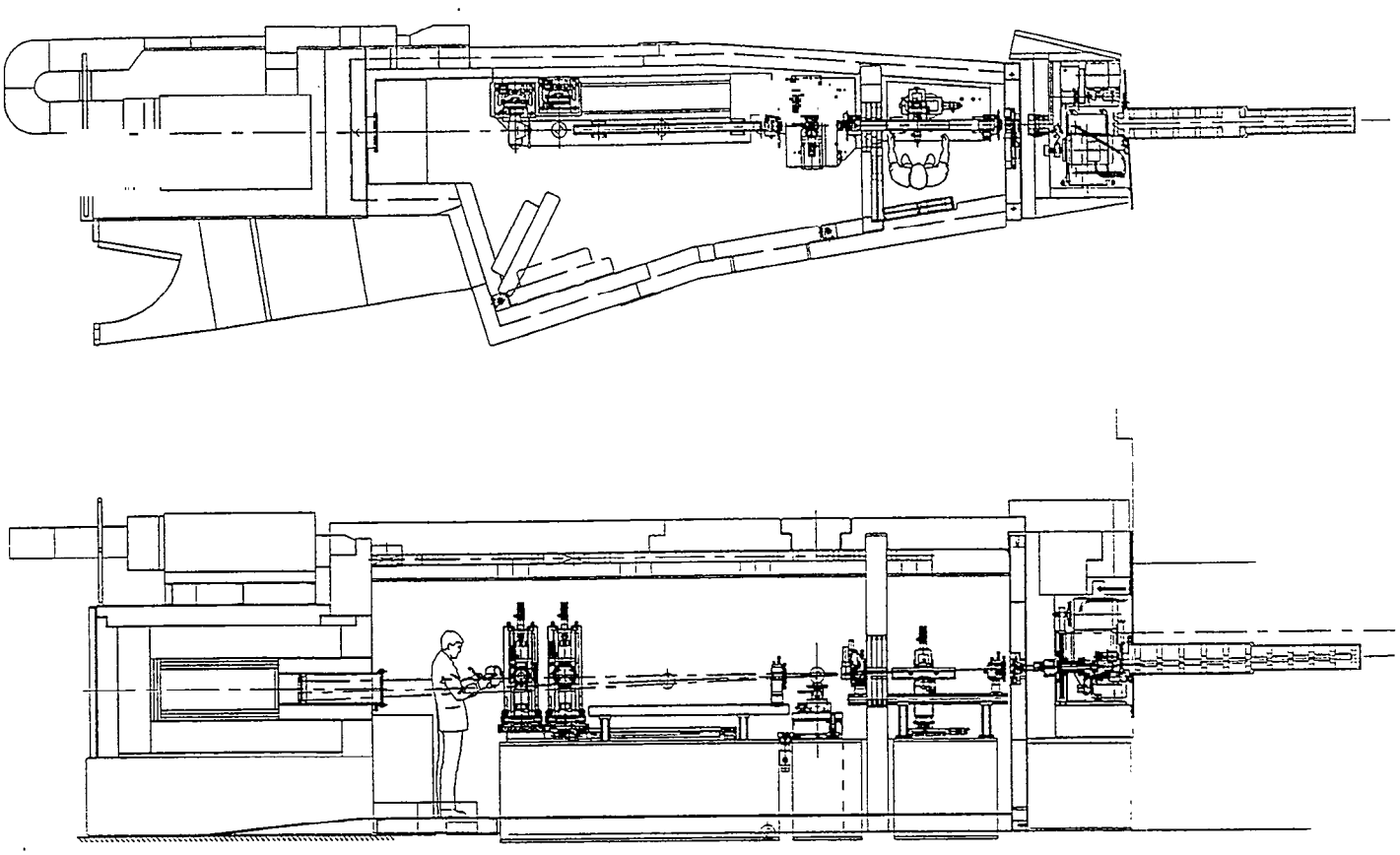

Figure 1: A schematic layout of the SURF neutron reflectometer in plan and side cross-sections.

The SURF neutron reflectometer has been installed at the ISIS facility viewing the liquid hydrogen moderator, a schematic layout is shown in Figure 1. The beam is guided down a neutron absorbing shielded collimation tube which defines the 1.5° inclined beam to the horizontal. The beam is defined using a nimonic chopper to remove the fast neutrons and gammas from the beginning of every pulse as well as a wavelength selective double disc chopper. Both choppers are located in a which is well shielded enclosure providing high quality shielding from the target but also from the instruments on either side and the rest of the SURF instrument. The choppers can operate at either 25 or 50 Hz giving a wavelength selection between 0.5 and 13 Å depending on the chopper frequency and disc aperture selected. After further collimation via a pair of coarse collimation jaws a beam of dimension of approximately 60 × 10 mm is obtained, which after passing through a low efficiency scintillator monitor, enters the block house. Great care has been taken in the design of the block house to try and reduce background noise, for this purpose the frame overlap mirrors (FOMs) and focusing supermirror have been separated from the sample area by incorporation of a shielding wall just before the sample position. Accurate computer controlled beam defining slits before the FOMs and also at the sample position allow the illuminated length and resolution to be defined. The sample position has a full set of movements available to it, including height, lateral translation and the possibility of angular motion via 2 perpendicular goniometer arcs. Post sample there is

the option of 2 detectors either a single detector or a 2D area detector (to be installed at the end of October 1995). Both detectors are based on a scintillator design. Both these detectors sit on height and rotation stages, and these assemblies are mounted on a translation stage which allows variable sample to detector distances of 1 - 2.43m. At the sample position there is a growing number of sample environment equipment, from the basic goniometer platform, static and dynamic (Nima) liquid troughs, solid sample changer, liquid-solid cells and liquid-liquid cells. The whole instrument enclosure is a controlled environment.

The focusing supermirror is a unique feature of the SURF reflectometer. The mirror has a supermirror coated reflecting surface of 600 × 60 mm, but it has a 2000m radius of curvature. This gives a focusing effect of the beam so that the effective illuminated length is reduced by 3 without loss of neutron flux. (This option has not been installed at time of writing, but the mirror has been purchased and awaits supermirror coating to be deposited.) The supermirror has the option to deflect the beam so that the beam either comes from above but now no longer at 1.5° to the horizontal, or from below. This will allow extreme flexibility of operation for various systems. Without the supermirror there is an approximate seven fold increase in the neutron flux over the reflectometer CRISP. This increase comes from a combination of an increased view of the hydrogen moderator, increased beam size and hence a relaxed resolution specifically for liquids and a shorter moderator to sample distance with respect to CRISP. Optical ray tracing calculations have demonstrated that the use of the focusing mirror will reduce the footprint at the sample by 3 times.

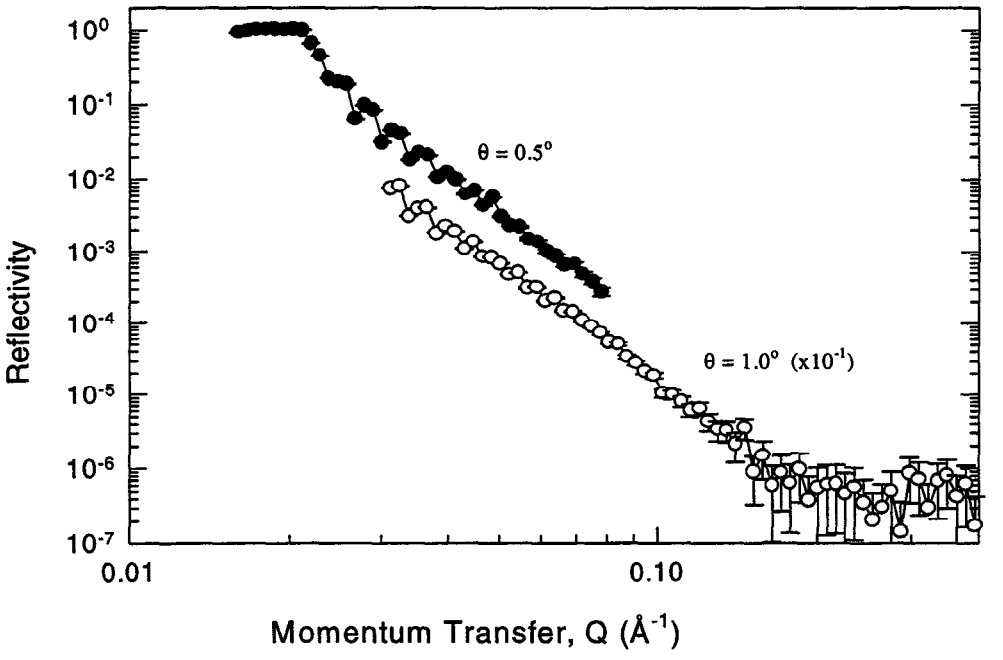

Figure 2: *Reflectivity profile of a NiC film on quartz. The closed circles are the reflectivity profile obtained at an incident angle of θ = 0.5°. The profile obtained at θ = 1.0° is translated by a factor of 2 for clarity.*

3. Science on SURF

Although the SURF reflectometer is not fully operational since not all its beamline components installed it has nevertheless been through a vigorous commissioning period during which members of RAL staff and the CRG have been able to push the instrument into areas not previously accessible to the CRISP. Here we present some of the elegant work that has been contributed so far to demonstrate the power of the reflectometer.

Perhaps the place to start is at the beginning with the first data from the reflectometer. It is of a NiC film deposited on quartz. The film is a well characterised sample and shows in Figure 2, the reflectivity profile taken at 2 angles, which are displaced for clarity. The beam defining slits before the sample were varied between the runs to keep a constant illuminated length and resolution. The interference fringes are well pronounced even though the sample was run under a modest resolution of $d\theta/\theta = 5\%$. Although not apparent in this plot the data from both angles overlaps extremely well and indicates the control and precision of the beamline components. Another standard sample used for calibration is the surface of pure D_2O, as seen in Figure 3. The open circles is the specular reflectivity of a D_2O using the single detector, showing a background of better than 2×10^{-6} in reflectivity. By moving the single detector off the specular position and measuring the off-specular background it is clear that the background observed in the specular reflectivity plot is indeed the true sample dependent background. These data were measured using a resolution of $d\theta/\theta = 10\%$ allowing the data to be collected extremely quickly of the order of 10 of minutes.

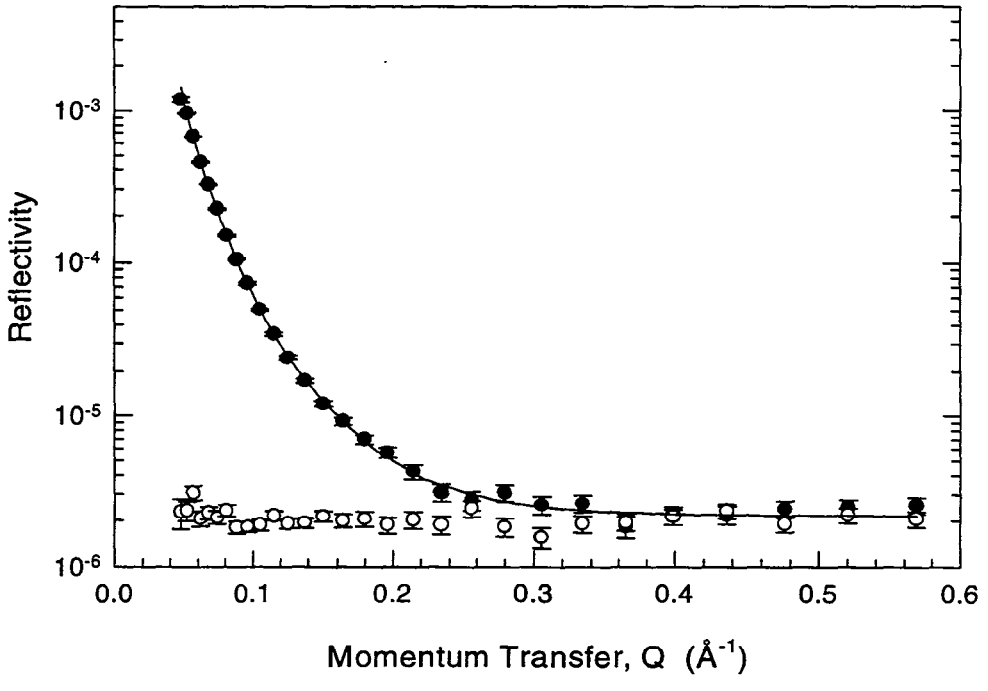

Figure 3: Plot of the specular reflectivity profile (closed circles) of the surface of D2O with an icident angle of $\theta = 1.5°$. The off-specular profile of the D2O surface obtained by moving the detector off the specular position to 1.65°.

Instrumental backgrounds have been reduced to the absolute minimum on the reflectometer by careful incorporation of neutron shielding, not only in the design of the blockhouse but also by incorporation of neutron absorbing materials in slits and detector housing. Typically the background for the instrument is below 10^{-7} in reflectivity, as can be seen in Figure 4, where the surface of Si has been measured at 3 angles, which have been over plotted. This decrease in background noise has provided a good signal to noise ratio. This has been seen for a hydrogenous thermotropic liquid crystal monolayer on a silicon substrate. The minima of the interference fringe is visible at a reflectivity of approximately 10^{-6} which would perhaps not have been possible to observe without all the enhanced signal to noise ratio.

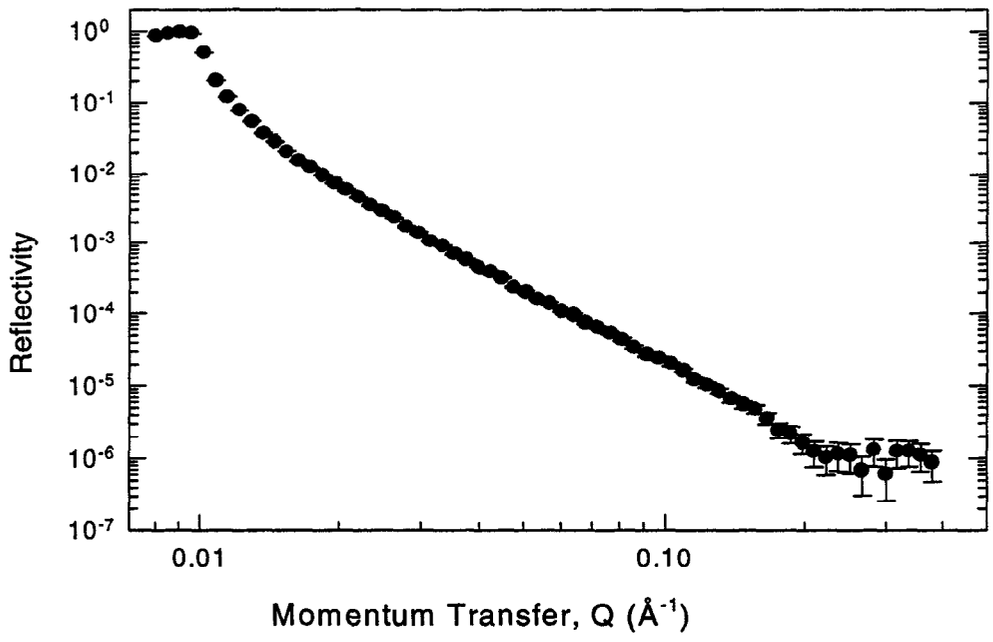

Figure 4: *Reflectivity profile of the surface of Si with its natural oxide in air. The profile was obtained by combining the reflectivity profiles from 3 incident angles of* θ *= 0.25, 0.7 and 2.0°.*

Of course, the reflectometer is not restricted to relaxed resolution measurements and in fact a large proportion of the data collected so far has used resolution down to $d\theta/\theta$ = 2 or 3%. There is of course a flux loss penalty over the relaxed resolution case but this is still a significant flux gain over similar measurements on CRISP. An example of the high resolution work is shown in Figure 5. This is a solid polymer film of polystyrene which incorporates a deuterated end-functionalised telechelic polystyrene. The reflectivity profiles shown are for the unannealed as made sample and also after annealing to equilibrium above the glass transition temperature. The interference fringes are well defined and the fits to the data suggest that there is segregation of the deuterated telechelic polystyrene to both the air-polymer interface as well as the polystyrene-Si substrate interface.

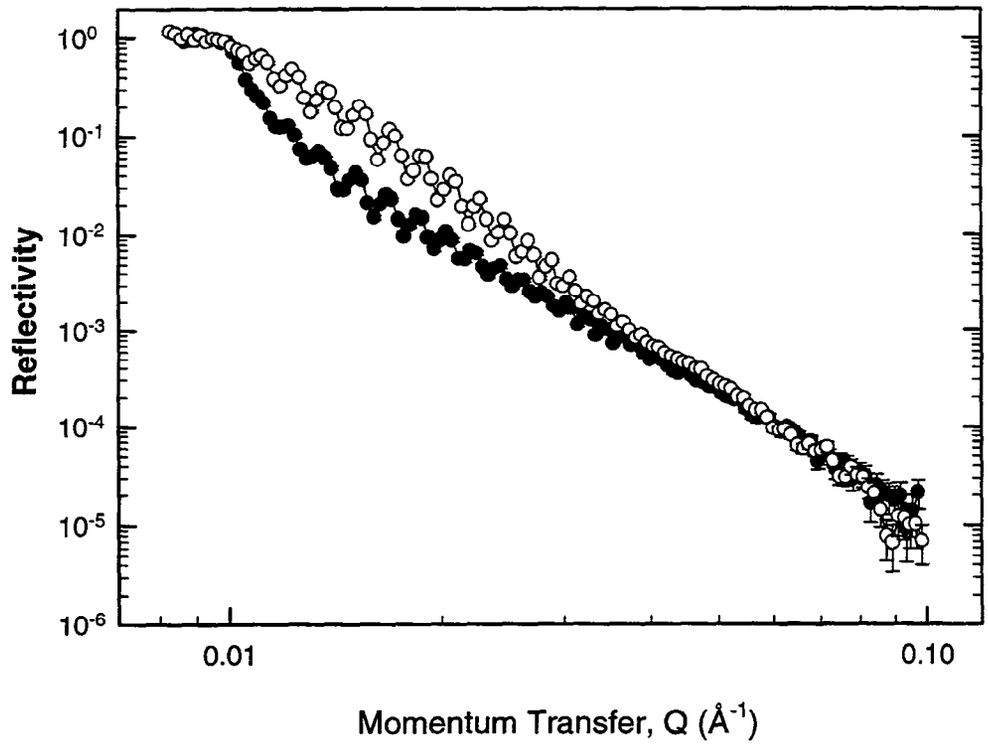

Figure 5: Two reflectivity profiles over-plotted obtained from a thin polystryrene film with a small percentage of end-functionalised telechelic polymer, in the as made state (closed circles) and after annealing above the glass transition temperature (open circles).

Perhaps the most stunning result of the commissioning period has been the speed at which meaningful data can now be collected due entirely to the increase in flux. The best demonstrations of this have been using the instrument to its full design potential with wide beam defining slits giving maximum beam dimensions at a relaxed resolution. From work on monolayers on water are 2 examples, which perhaps shows that now truly kinetic effects can be observed. As shown in Figure 6, an insoluble monolayer on D_2O has been measured as a function of time at fixed surface pressure. Each of the lines represents a reflectivity profile collected in 20 minute scans. The obvious change in the reflectivity is due to the monolayer collapsing and from this data it is possible to extract useful data about the layer thickness and density. In an even more stunning example measurements on a different system were allowed the adsorbed monolayer thickness and adsorbed amount to be determined from reflectivity profiles each collected in 5 minutes.

4. Future work

The commissioning period of the SURF reflectometer will be completed after the installation of the focusing supermirror (late November 1995) and 2D area detector (in late October 1995). The instrument will become a fully scheduled instrument after at the end of the ISIS 1995

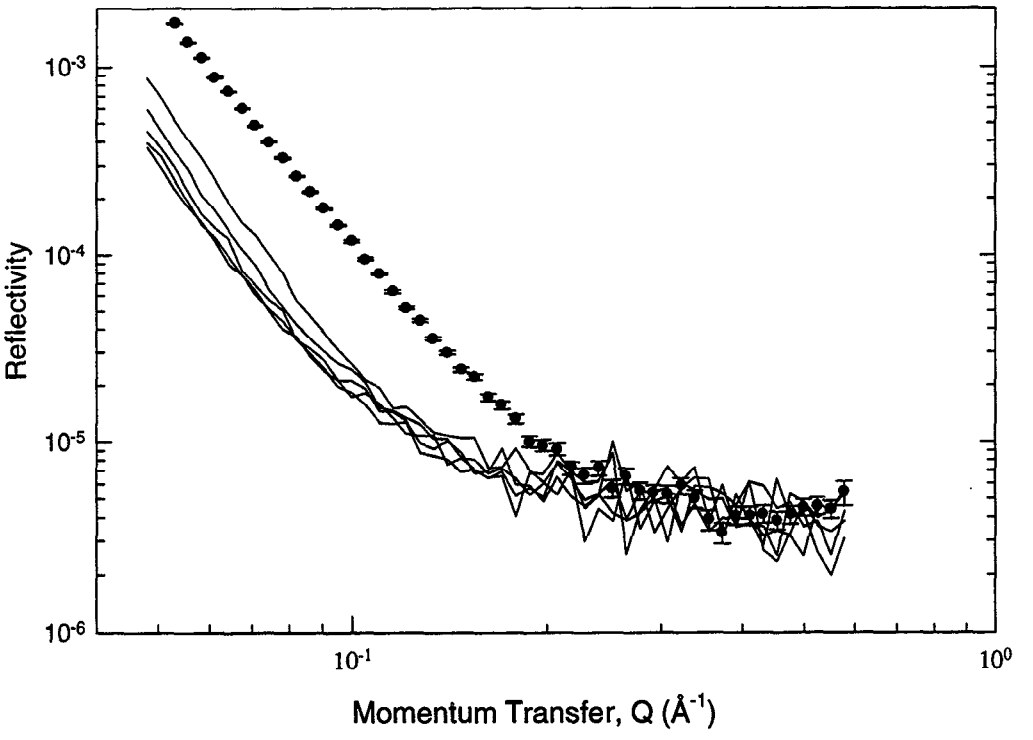

Figure 6: Kinetic reflectivity profiles obtained from a collasping polymer monolayer (lines) on D_2O (closed circles). Each line represents a reflectivity profile of the monolayer obtained in 20 minute measurements.

schedule. At the time of writing the instrument is accepting its first set of proposals for scheduling and will become fully incorporated into the suite of instruments at ISIS available to the user community. With the installation of the focusing supermirror it will be possible to push areas not fully exploited as yet. Kinetic studies will now become reality as has already been observed for some systems, but also more exotic systems will be achievable since it will mean smaller sample volumes. In addition the 2D area detector with start to really test some of the newer theories of off-specular scattering which are emerging in literature.

5. Acknowledgements

The authors acknowledge the financial backing of the EPSRC for funding the SURF CRG project, as well as additional contributions from ANSTO, Australia. We also gratefully acknowledge the help from the technical staff at ISIS in the design and construction of the reflectometer, especially the project design engineer Richard Coleman. In addition we acknowledge the help in commissioning the instrument from I McLure, A Burgess, E Staples, J White, M James.

ICANS-XIII
13th Meeting of the International Collaboration on
Advanced Neutron Sources
October 11-14, 1995
Paul Scherrer Institut, 5232 Villigen PSI, Switzerland

EVALUATION OF ROTAX

H Tietze-Jaensch[1,2], W Schmidt[2,3], R Geick[4] and G Will[5]

1 ISIS Facility, Rutherford Appleton Laboratory, Chilton OX11 0QX, U.K.
2 KFA Forschungszentrum Jülich GmbH, D-52425 Jülich, Germany
3 ILL Grenoble, Centres des Tri, F-38042 Grenoble, France
4 Physikalisches Institut, Universität Würzburg, Am Hubland, D-97074 Würzburg, Germany
5 Mineralogisches Institut, Universität Bonn, Poppelsdorfer Schloß, D-53115 Bonn, Germany

ABSTRACT

After the ROTAX spectrometer has been devised and installed at ISIS it is now time to conclude on its merits and problems. We are able to show that practical scans in (Q,ω) space with a nearly arbitrary scan direction, i.e. polarisation of $\vec{q}$ vs. $\vec{Q}$ are possible and feasible with no compromises on the resolution. In addition, valuable technological and methodological knowledge has been compiled, namely in the field of digitally controled and fast acting gear-less direct drives. However, ROTAX faces difficulties from an unexpectedly weak neutron flux of its beam. We shall discuss the consequences of this outcome and briefly mention its modified new application field.

1. Introduction

The principle ideas of the rotating crystal analyser spectrometer ROTAX were presented for the first time at ICANS IX held at PSI Villigen in 1986. Since then ROTAX has been devised and installed at ISIS and we gained a lot of experience.

The method of inelastic neutron spectroscopy by using the rotating analyser principle has proved to work out feasible experimental scans through (Q,E) space, and in-hand with a much enhanced scan versality. We shall emphasize once more the benefits and improvements of the rotating analyser technique when compared with triple axis, direct geometry chopper and MAX-type inverted time-of-flight spectrometers. No compromises on the resolution with respect to the spinning analyser had to be made. As for the ESS instrumentation discussions already started, we feel that rotating analyser technique deserves a serious consideration to use it at a new intense short pulsed neutron source. We shall sketch here the proposed out-line of a very promissing ROTAX '2000.

2. Comparison with other spectrometers

2.1 general

One of the major advantages of ROTAX has always been its superior flexibility designing a time-of-flight scan in (Q,ω) space [1,2]. All neutron scattering takes place under the rules of momentum and energy conservation. The simultaneous satisfaction of both laws

$$\hbar\omega = (\hbar^2/2m)\,(k_i^2 - k_f^2)$$

and

$$\vec{Q} = \vec{k}_i - \vec{k}_f$$

is described by any point on the surface of the "scattering paraboloid" (cf. fig. 1). With a triple axis spectrometer it is, in principle, possible to view any of these scattering points which, however, needs a high-flux DC-source and all sorts of flux enhancing ancillary devices like (double)-focussing monochromators and analysers etc. for an up-to-date spectrometer. The corresponding key-word on time-of-flight machines is "multiplexing" as neighbouring tof-channels may be detected quasi-simultaneously in the course of time the neutrons take for travelling through the instrument. By using a time resolved detection electronics one will obtain tof-scans penetrating an anticipated scattering point P in (Q,ω) space on the surface of the scattering paraboloid. The specific scan direction is fixed by the instrument's geometry and set-up, only on ROTAX one may temper the scan direction [1,2,3].

On all tof-machines the time step-width may well be less than one unit of the resolution, thus encounting for a real scan profile of the envisaged point P. This is measured simultaneously instead of step-by-step in the consecutive mode of a triple axis instrument.

2.2 chopper spectrometers

Fig 1a illustrates the scattering paraboloid and the tof trajectory of a direct geometry chopper spectrometer like HET/MARI or MAPS at ISIS; these intruments operate with a fixed incident neutron energy E_i. Considering one designated point P in (Q,ω) space, a probe crystal can be aligned in such a way that one detector is viewing at a scattering angle Φ and tof-scanning through P from the bottom towards the top. Using a detector array covering a whole range of $\Phi \pm n\Delta\Phi$ will enable to measure a pixelised map of $(\Delta\Phi,\Delta t)$ digits of the whole vicinity of P. All detectors view at the same scattering paraboloid because of the fixed common incident energy E_i. Certain cuts and regrouping/rebinning out of this 2-dimensional picture enable to calculate specific scans, however, a real constant-$\vec{Q}$ scan will not be possible.

2.3 inverted spectrometers

On an inverted geometry tof-spectrometer like PRISMA at ISIS [5] or elswhere [6,7] the picture becomes much more complicated (fig 1b). n scattering arms are set to constant final energies $E_f(n)$ under certain scattering angles $\Phi_0 \pm n\Delta\Phi$, whereas the sample is bathed in a white neutron beam. Hence, every arm has got its own and inverted scattering paraboloid culminating at $-E_f(n)$. Geometric constraints to avoid clashing of adjacent detectors confine the tof-trace along a line $Q_\parallel$ parallel to k_i. The

component $Q_\perp$ is kept constant for all spectrometer arms and for all time channels, thus all paraboloids focus at a point ($Q_\perp$, $-\hbar\, Q^2_\perp/\, 2m$) in (Q,ω) space where $Q_\parallel = 0$. Every detector counts the scattered intensity along its attached tof-parabola and one will obtain a tof-profile through the point P under consideration. The adjacent detector arms may be used to coarsely map the vicinity, but no further adjustment of the scan direction can yet be made. For practical purposes of single-crystal spectroscopy $Q_\perp$ must be chosen in units modulo $2\pi/d_{hkl}$ and together with the geometric range of the instrument this means, in practice, a considerable limitation of the feasibility of an experiment on Prisma. This problem is being discussed in more detail by Dorner [8].

2.4 ROTAX in particular

This problem is overcome by the use of a non-uniformly rotating analyser crystal like on ROTAX. A rotating analyser means as much as a continuous modification of the final energy $E_f(t)$. Thus one is no-longer dealing with a discrete set of scattering paraboloids rather with a whole continuum. And, as there is only one analyser, there is no clash condition, of course, like on Prisma. This means that the Prisma-constraint $Q_\perp = \text{const}$ is no longer required. The Q-trace of the tof-scan is parameterised by the Q-value of the centre-axis of the scattering paraboloids and because it may move freely on ROTAX this may be regarded as yet another illustration of the feasibility of the various tof-scans of ROTAX. In the first place we have introduced the const-$\hbar\omega$ and the const-$\vec{Q}/|Q|$ or const-Ψ scan [1,2]. And there is a generalisation of the const-Ψ scan to the whole class of "linear-Q" scans [3]. These are scans where the Q-trace of the tof-scan forms a straight line.

Technical limitations to the performance of Rotax scans is only dictated by the time frame, i.e. incident flight path L_i, and the achievable angular acceleration that is needed to move the analyser from one point to another, i.e. the power resources of the analyser drive system. The analyser does not neccessarily have to follow an analytic curve, as the analyser drive control is working on an entirely digital basis. Further, we may emphasize that we observe the vicinity of the tof-scan, thus the vicinity of the point P under consideration too, with a very high degree of pixeling resolution. This is because we employ a linear JULIOS detector array [9] of high angular/spatial resolution. This is very essential for evaluating the 2-dimensional multiplex advantage and it is the reason why ROTAX can in principle achieve more, i.e. acquire more usefull data with only one analyser than a Prisma-type machine can do with n analyser-detector assemblies.

3. Results

3.1 inelastic scattering

Starting an experiment on ROTAX has been described in detail elsewhere [10]. A ROTAX scan is designed by an interactive software package and, of course, the experimenter is required to provide his sample parameters and experimental set-up. The experimental results are then displayed as intensities vs. a 2-dimensional pattern in detector coordinates of position and time-of-flight (x,t). Every detector pixel (x,t) is uniquely related with a corresponding pixel in (Q,ω) space. The latter can be projected onto the (x,t) plane together with the Rotax analyser scan and intensity contours of the data. Fig. 2 presents an example of longitudinal LA[110] phonons of an Al crystal as

sample. Cuts at a fixed time-of-flight or detector position channel reveal const.-k_i and const.-k_f peak profiles, respectively (fig. 3), and the FWHM time width can be used to determine the energy resolution. As an alternative the detector coordinates can be transformed into (Q_1, Q_2, $\hbar\omega$) [11] from which cuts resemble the peak profiles in Q_1, Q_2 or $\hbar\omega$ direction instantaneously. This is made possible because of the high resolution 2-dimensional data acquisition with the time-resolved Julios detector. The results yields highly "TAS-like" data. As an example we present inelastic data from a Cu crystal: fig. 4a shows the LA[110] phonon dispersion with the trace of a ROTAX const-Ψ scan in extended and reduced zone schemes. The numbers are tof-tickmarks in msec. The corresponding data and the (Q,e) projection in (x,t) coordinates is shown in fig. 4b. The enlargement shows the inelastics data around the (200) Γ-point in more detail. The approx. 25% contour of the resolution is sketched as a solid line. After transforming the data into a (Q_1=[h00], Q_2=[0k0]) projection the enlargements of fig. 4b is shown in fig. 5. A profile along [110] scan direction which is almost a const.-energy scan is shown in fig 6a with the error bars on the energy axis to denote approximately the resolution; const.-k_f profiles are shown in fig. 6b.

3.2 multiplex advantage

The multiplex potential is immediately obvious from the raw data: the number of pixels used to form the scan profiles (fig. 6b) is 21, i.e. 21 TAS-like setting would be neccessary to obtain the same picture. Not mentioned the simultaneous acquisition from higher order Brillouin zones that would add-on another factor of 3 in this particular case. The scattering intensity within the limits of a resolution unit is formed from approx. 50 pixel cells. So an average overall multiplex advantage of a factor of 50 may well be regarded as realistic. This, however, is still not sufficient to compete well with TAS machines based at typically 40 times more intense reactor sources equipped with additional flux enhancing devices like focussing monochromator etc as mentioned earlier.

3.3 enhanced efficiency: PG analyser

Nevertheless, the multiplex advantage of 50 obtained on ROTAX is a very promissing figure for the instrument itself. In fact, an additional efficiency enhancement of 3 has been achieved since we were able to install a pyrolythic graphite (PG) analyser crystal of 3.5 x 5 cm^2 (w x h) size on ROTAX at the end of 1993. The graphite is framed in a dur-aluminium clamp that is itself mounted onto the analyser motor shaft directly. The height of that analyser must not exceed much of the given size to avoid fatigue and shear-off of the Al-clamp. The electronic regulation stiffness had only been reduced to 90% of the former value used for the cylindrically shaped Ge-analyser crystal [12].

3.4 resolution

From the results achieved so far we can compile the experimentally obtained values for the energy resolution in tab. 1. The figures correspond quite well to what can be achieved on Prisma [13]. In fact, ROTAX used with a fixed, non-rotating analyser is the same as Prisma with only 1 scattering arm, and since we achieve the same resolution figures we can conclude that no resolution compromises whatsoever or any other

coarsening is observed as the result of spinning the analyser. This is made possible from the improved scan regulation electronics to work hand-in-hand with a fine tuning of the synchronisation with the ISIS sync-pulse on a μsec scale (cf. fig. 4 in [17]).

Table 1: ROTAX energy resolution:

	Ge-(220)			PG-(002)			PG-(004)		
E_i (meV)	14	50	100	13	50	100	20	75	170
$\hbar\omega$ (meV)	1.8	6.5	14	1.7	7	13	2	7	16
ΔE (meV)	0.6	3.2	10	0.6	2	8	0.5	2.6	10
$\%E_i$	4%	6%	10%	5%	4%	8%	2%	3.5%	6%

4. Technical problems and solutions

It sounds ironical, but earlier results with a temporary ROTAX set-up on the ISIS test beam were easier to achieve than with the real instrument after its commissioning had started in early 1993. An evaluation of the instrument must not miss out some comments on this fact. First of all there has been approx 3-4 times more neutron flux on test beam than on than N2a position behind Prisma. Secondly, the resolution conditions (collimation and regulation band width) on the test assembly were relaxed in order to find inelastic scattering intensities easily. So much of our time in 1993 was spent tackling bugs in the regulation software of the signal processor control. And all the other odds and bits had to be set straight. Then, it was the attempt of proper cabeling and geometric positioning of the various units that caused much of the technical difficulties we faced in the course of 1994.

4.1 fault condition

The general fault-picture was a severely diminished live-time (some 10's of minutes only) of the analyser motor's induction coils with subsequent electrical flashes and short cuts in the power unit. With a power change of up to 2 GigaWatt/sec the analyser system came to an immediate halt that could not be fused properly in the short period of time. The damaging result was that not only the servo-motor of the analyser drive was burnt to scrap but the costy power-mosfets (IGBT: insulated gate bipolar transistors) in the main amplifier unit were blown-up, too; a major electrical repair was needed every time. The regulation accuracy and running properties of the motor, while still alive, were fine and over-heating could be ruled out for the shortness of the livetime. Never before during development and thorough laboratory tests this problem had ever occurred.

4.2 technical solution

An industrial report [14] on the sensitive frequency behaviour of fast acting servo-drives running on pulse-width modulated (PWM) inverters (like our system) brought us to the correct error analysis: In fact, the length of the cable between the main amps and the motor was far too high resulting in a far too high cable capacity. Operating the system at a pwm-frequency of 10kHz ment to produce over-voltages of up to 2.5

kV between the phycically spliced cables of the 3 motor induction coils. The cable insulation was not strong enough to withstand that for long and the synchronised running mode of the motor inevitably caused hot-spots to occur persistantly at the same angular position of the coils where the motor took-up maximum power. In order to avoid this, the cable length and with it its electrical capacity had to be limited drastically back to the former length of 5-10m at the period of laboratory testing. On the other side the fibre optic communication link between the signal processor and the main inverter unit was increased to 20 m. In addition we have installed specifically made choking coils in each of the 3-phase circuits. They have an inductance of 0.5mH each in the frequency range of 0-20 kHz, a much higher value above that range and, thus, act as low-pass filters.

4.3 improvements

In fact, the temperature behaviour of the analyser motor has much improved since these modifications were introduced. The operating temperature of the ROTAX scan of fig. 6, for example, was subsequently reduced from 85°C to only 47°C only. The regulation behaviour was found to be even better, because all the high frequency rippels were filtered out. Apperently they did not contribute to any decent mechanical rotation anyway. After all, the introduction these choking coils has proved to be very vital and must not be overseen in any future design. Long term running tests on the analyser motor have been performed since May 1995 with no such problem having occurred again. Fig. 7 sketches the recent modified set-up of the ROTAX analyser hardware components.

5. Future use as a diffractometer

Despite the technical and methodological success ROTAX will predominantly be used as a conventional time-of-flight diffractometer ROTAX/Diff [15]. The main reason for this is that the neutron flux is too weak to perform successfully many interesting inelastic experiments. As a diffractometer, however, ROTAX/Diff can comply much easier with recently existing demand.

5.1 time-of-flight diffraction and data processing

The set-up and operation as a diffractometer is straight forward (fig. 8). There is no need for a time-focussing set-up of the detector geometry: This becomes evident from the tof-Bragg equation and the geometric parameters of our Julios detector (fig.9a):

$$t(x) = \frac{2\, m\, d_{hkl}}{h} \; (L_i + L_f(x)) \; \sin \Phi/2$$

with (cf. fig. 9a):

$$x - x_0 = L_{f0} \; \mathrm{tg} \; (\Phi(x) - \Phi(x_0))$$

the total time-of-flight reads:

$$t(x) = \frac{2\, m\, d_{hkl}}{h} \; (L_i + L_{f0}) \; \sin 1/2 \left[\mathrm{tg}^{-1} (x-x_0)/L_{f0} + \Phi(x_0) \right]$$

Every powder line of const d_{hkl}-value is imaged as a curved line on the detector dis-

play (fig. 10a). Yet again we image a complete mask of the detector coordinates in (x,t) onto the (elastic) Q-space or d-space. In other words, one unique d_{hkl}-value of the powder line is attached to every single pixel in (x,t). Integration of powder diffraction lines along d-values is then obtained by rebinning a histogramm of d-value pixels (fig. 10b).

5.2 time focussing

A time focussed set-up of the Julios detector (fig.9b) would not gain anything, because the powder lines of fig. 10 would appear as horizontal lines only. It would rather worsen the (spatial) resolution because the exact position of the neutron count would be determined less accurately. Last not least, the detector is simply not long enough for a time-focussed set-up at scattering angles $\Phi > 30°$.

5.3 enhanced data acquisition

Recently, a second Julios detector unit has been installed, now capable to address a 14bit (time) by 8 bit (position) and 4 byte deep data memory array of 16 MB total size [16]. With respect to the specific application this raw data field will subsequently be reduced to handable size of some 100 kB but the data acquisition is now capable to encount for the full physical time resolution of 1 μsec for the whole time window of a neutron frame.

6.) Conclusion and sketch of ROTAX '2000

6.1 neutron scattering

The rotating analyser technique has been proved successfully by experiments. Disregarding its beam flux, ROTAX performes better than its pulsed source competitors if the experimental purpose is more to look at detailed structures in (Q,ω) space. The widely arbitrate choice of scanning through a particular point P (cf. fig. 1c), with the possibility of real transverse or longitidunal polarisation of $\vec{q}$ vs. $\vec{Q}$, is advantageous for investigating structural and magnetic excitations, in particular.

The Q and energy resolution were proved to be equal to what is achieved on other spectrometers. Setting up a scan and correctly interprete the data is achieved in a similar way and not more sophisticated than on other spectrometers. ROTAX takes best advantage of the pulsed peak-flux because of its dynamics synchronisation with the source.

The use of the rotating analyser has also proved to be a very efficient filter against spurious and off-channel background. The condition for neutrons to have the "right" energy and flight direction $(\vec{k}_f)$ at the appropriate time channel t_A when the analyser allows them to be scattered is simply much harder to be met. For experimental details about this dynamic background filtering confer fig. 3 in [17].

6.2 technical

Not saying that the ROTAX-technique is yet fully matured but the major technical problems seem to be solved now and the reliability and durability in the analyser drive has been achieved, eventually. There was, admittedly, the long and painful period of

bug-fixing and fine tuning of all sorts of technical bits and pieces. The whole system is fully software-controled and runs on standardised hardware. A complete copy of the analyser drive system would now cost not more than ca. 70 thousand Deutschmarks. Indeed, ROTAX is the first instrument to use active real-time components.

6.3 present limitation

At present, the performance of ROTAX scans is limited by the following factors:

1.) the power resources of the motor is limited by its electro-magnetic force (emf) and the limit of converting electric power into mechanic power or torque. Consider that the mechanic load of mounting an analyser crystal is negligible with respect to self-momentum and mechanic inertia of the motor's rotor shaft. That means the motor basicly runs free. Replacing the existing CoSm magnets by stronger and smaller $Nd_2Fe_{14}B$ magnets would increase the magnetic energy density and enable smaller and less inert rotors giving a higher power/torque ratio. This would require R&D efford in new servor-motors.

2.) The other most critical limiting factor is, indeed, the time scale or the level of average speed on which all other dynamic actions are to be performed. Consider a reduction of the time scale by a factor of 2. That would reduce the speed by 2, the acceleration by 4 and the total electric power by 8, yet enable the perfomance of many more scans on ROTAX which are at present limited purely by technical reasons.

6.4 what to do better?

1.) How to stretch the time scale? Simply by increasing the incident flight path by the same factor. This would bring ROTAX down to a position ca. 30 m off the moderator and would, inevitably push ROTAX into the domain of colder or cold neutrons. A primary path neutron guide should be used instead of a pin-hole tube not to give away too much incident flux.

2.) The analyser would then turn at only half the average speed. Yet there is a serious possibility of introducing frames to mount at least a vertically curved analyser for secondary focussing.

3.) More than one secondary flight arm may be installed, however, we don't believe that more than 2 (max. 3) could be employed reasonably.

4.) More promissing would be to install another rotating analyser on the one existing scattering arm. It could be made moveable around one analyser's axis and would give access to two simlutaneous and closely related scans. One or two detector assemblies may be used. Fig. 11a sketches an example of 2 correlated const.-Ψ scans, fig. 11b illustrates the real space geometry of such a ROTAX '2000.

5.) The pulsed source repitition frequency should not be at 50 Hz, rather adapted to avoid frame overlap at a 30 m position and allow sufficient time to rephase the analyser for the next pulse. This repositioning time is typically 2/3 of the physical scan time, i.e. the time for the neutrons to travel accross the instrument.

6.) A neutron beam-line with full flux should be made available.

6.5 promissing future?

Why not considering such an instrument for the ESS at its 10 Hz target with a cold moderator ?

Acknowledgment

We are indebted to a great number of people who have advised and helped us to develop and install the ROTAX instrument at ISIS. They can't be named all explicitly but their contribution has been very valuable. ROTAX was initiated under the hospices of the University of Würzburg and been transferred recently to be administered and further developed by the University of Bonn. Financial support was given by the German Minister for Education and Research BMBF under contract no.s 03-ge3-wue and 03-wi3-bon. The collaboration with the ISIS Facility of the Rutherford Appleton Laboratory is gratefully acknowledged. Thanks to Peter Fabi for inspiring discussions on this manuscript.

references

[1] R Geick and H Tietze, Nucl. Inst. & Meth. A 249 (1986) 325

[2] H Tietze and R Geick, Proc. ICANS IX, PSI 1986, SIN-rep. 40926 (1987) 389

[3] W Schmidt, H Tietze-Jaensch and R Geick, Proc. ICANS XII, Abingdon 1993, RAL rep. 94-025, p. I-293

[4] R S Eccleston and R Osborn, RAL rep. 94-117
S M Bennigton and R S Eccleston, RAL rep. 94-102
T G Perring, A D Taylor, R Osborn, D Mc Paul, A T Boothroyd and G Aeppli; Proc. ICANS XII, Abingdon 1993, RAL rep. 94-025, p. I-60

[5] U Steigenberger, M Hagen, R Caciuffo, C Petrillo, F Cilloco and F Sacchetti; Nucl. Instr. & Meth. B53 (1991) 87-96

[6] E Maliszowski, V V Nite, I Sosnowska and J Sosnowska; Inel. Neutron Scattering (IAEA, Vienna 1968) vol. 2, p. 313

[7] K Tajima, Y Ishikawa, K Kanai, C G Windsor and S Tomiyoshi; Nucl. Instr. & Meth. A254 (1987) 333

[8] B Dorner, J Neutron Research 2.3 (1994) 115-127

[9] E Jansen, W Sch'fer, A Szepesvary, G Will, R Reinartz, K D M[ller, H Tietze and U Steigenberger; Physica B 180 & 181 (1992) 917-919

[10] H Tietze-Jaensch, W Schmidt, R Geick and U Steigenberger; Physica B 213 & 214 (1995) 878-880

[11] W Schmidt, H Tietze-Jaensch and R Geick; Physica B 213 & 214 (1995) 881-883

[12] A Freund and C Petrillo, internal unpublished report, ISM Frascati (1987)

[13] M Hagen and U Steigenberger, Proc. ICANS XII 1993, RAL rep. 94-025, p. I-314

[14] P Hansen and F Petersen, Danfoss Drives and Controls, Graasten, Denmark 1993

[15] W Schäfer, E Jansen, R Skowronek, G Will, W Kockelmann, W Schmidt and H Tietze-Jaensch, Nucl. Inst. & Meth A (1995), in press

[16] K D M[ller, R Reinartz, R Engels, P Reinhart, J Schelton, W Sch'fer, E Jansen and G Will, Proc. workshop "new tools f. neutron instrumentation", Les Houches 1995, J Neutron Research, submitted

[17] H Tietze-Jaensch, W Schmidt and R Geick, Proc. ICANS XII, Abingdon 1993, RAL rep. 94-025, p. I-97

figure captions:

Fig. 1: scattering paraboloids at point P in (Q,E) space for a direct geometry chopper spectrometer like MAPS and the inverted geometry spectrometers PRISMA and ROTAX. Tof-trace and the same scattering triangles for P and an imaginate Q-lattice are shown in all 3 cases.

Fig. 2: Inelastic neutron scattering with a ROTAX scan along (100) direction of Al.

Fig. 3: const-k_i and const-k_f profiles of the phonons denote in fig. 2.

Fig. 4: ROTAX inelastic scattering from copper (110) direction: (a) Rotax scan parabola in extended and reduced zone scheme, (b) plot of the data and (Q,$\hbar\omega$) lattice together with the scan trace in (x,t) detector coordinates; the insert enlarges the area around the (200) Γ point.

Fig. 5: Transform of the enlargement of fig 4b into (Q_1=(h00),Q_2=(0k0)) coordinates with trace of energy transfer $\hbar\omega$ and scan trace.

Fig. 6: Scan profiles of the close-up of fig. 4b: (a) along Q=(110), which is almost at constant energy transfer; (b) const. k_f profiles through either phonon peak.

Fig. 7: Hardware of the ROTAX analyser drive after the 1995 improvements.

Fig. 8: Sketch of the ROTAX / Diff time of flight diffractometer after removal of the analyser tower.

Fig. 9: (a) real space detector coordinates as used for calibration and d-value line integration of powder patterns; (b) potential alignment for time-focussing set-up: All neutron energies scattered from one powder line would arrive at the same time in all position channels. As discussed in text, this set-up is obsolete on ROTAX/Diff.

Fig. 10: Example of a Ni-powder pattern obtained on ROTAX/Diff: (a) original raw data in (x,t) detector coordinates; (b) after powder-line integration discussed in text.

Fig. 11: Correlated scans of a double-ROTAX set-up for simlutaneous scanning at 2 different scattering angles Φ_1 and Φ_2.
(a) (Q,E)-parabolas of the tof traces and scattering triangles; (b) real space shape of the instrument and sketch of detector raw data.

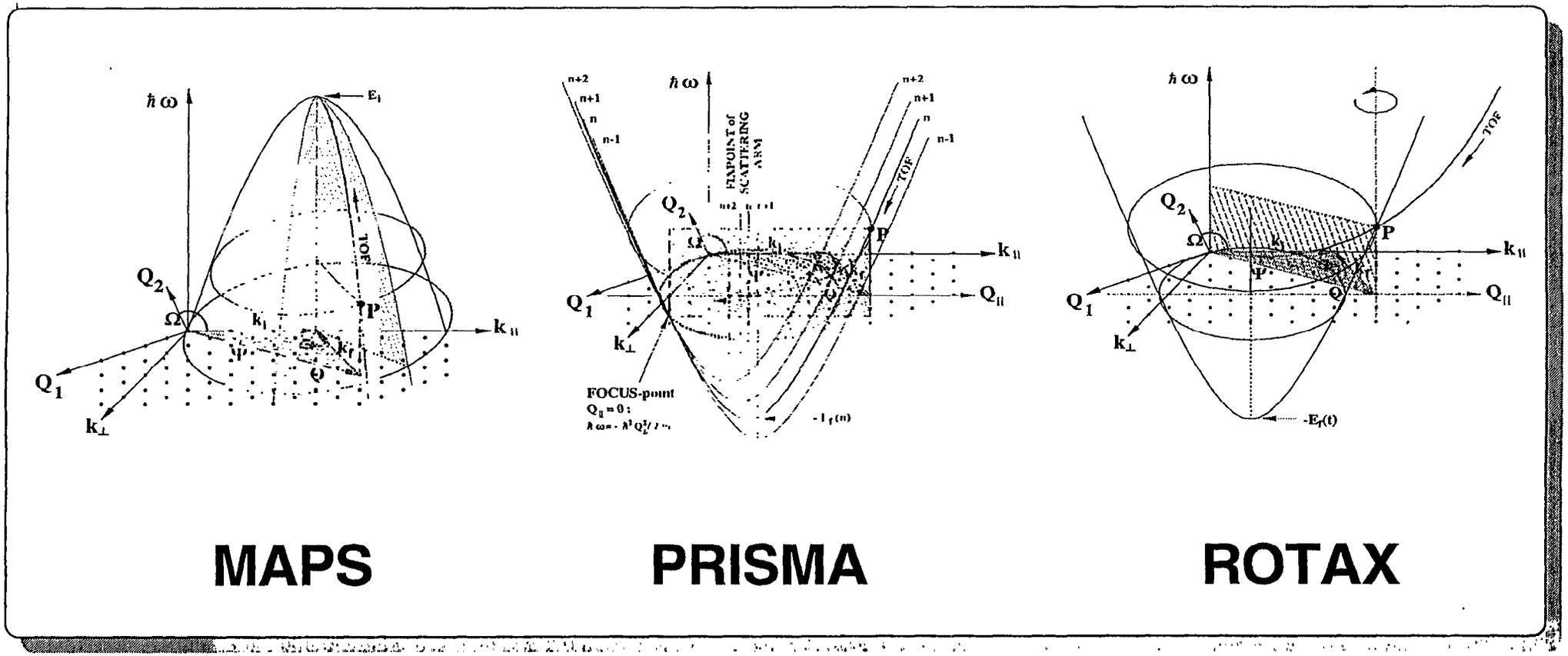

Fig. 1: scattering paraboloids at point P in (Q,E) space for a direct geometry chopper spectrometer like MAPS and the inverted geometry spectrometers PRISMA and ROTAX. Tof-trace and the same scattering triangles for P and an imaginate Q-lattice are shown in all 3 cases.

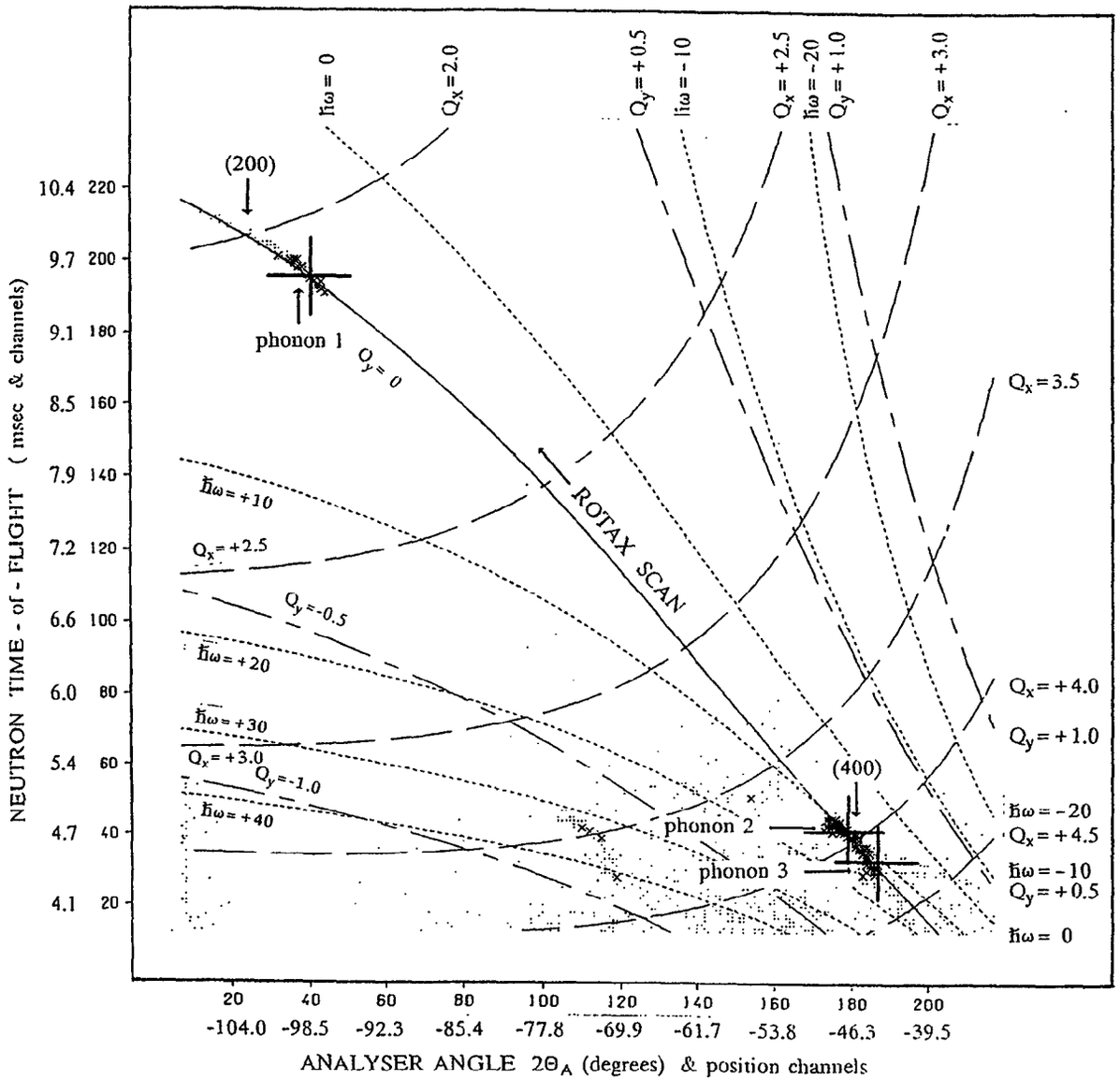

Fig. 2: Inelastic neutron scattering with a ROTAX scan along (100) direction of Al.

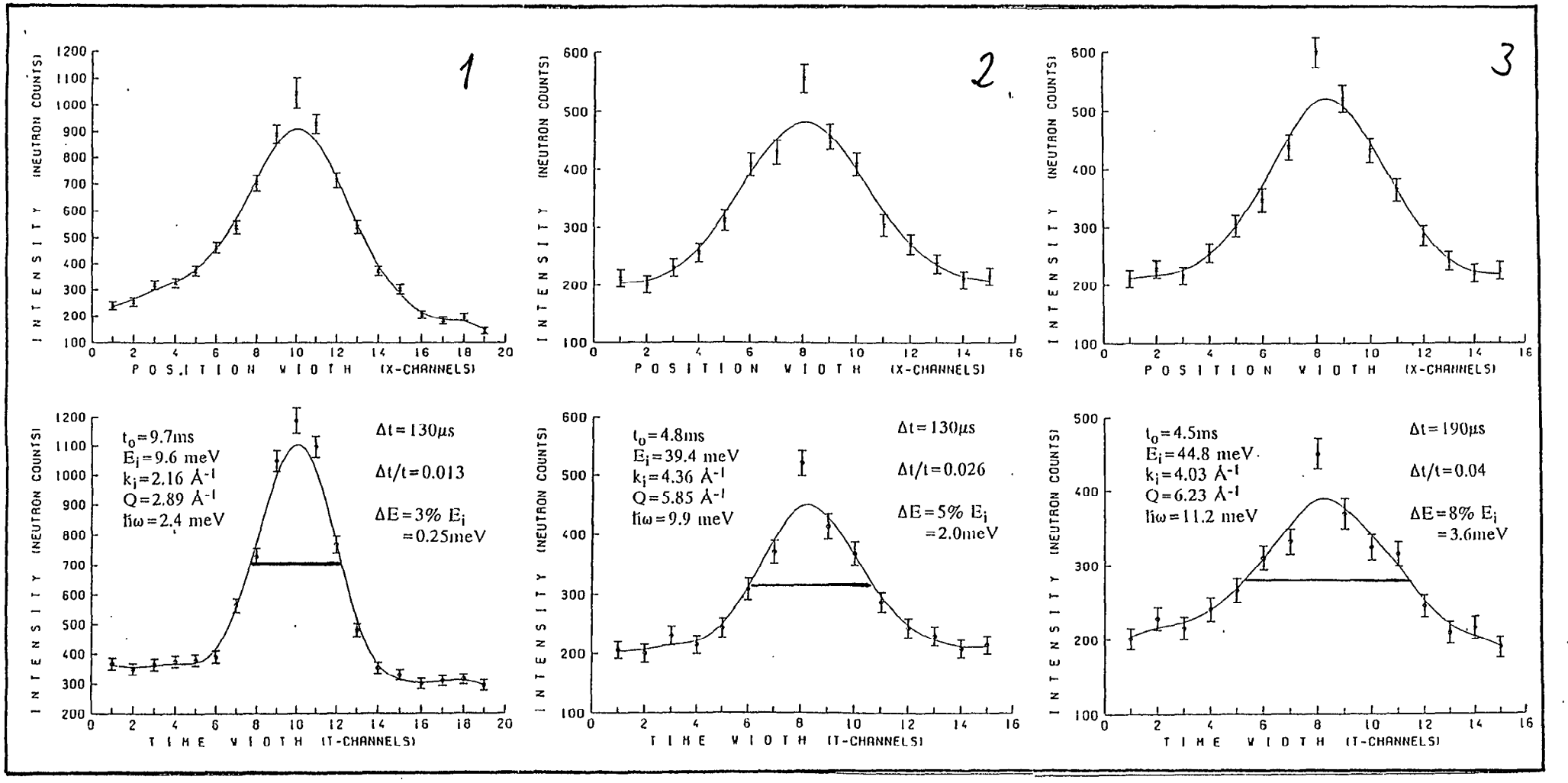

Fig.3: Intensity profiles of the phonons 1,2,3 (cf. fig.2) along position and time channels of the detector units.

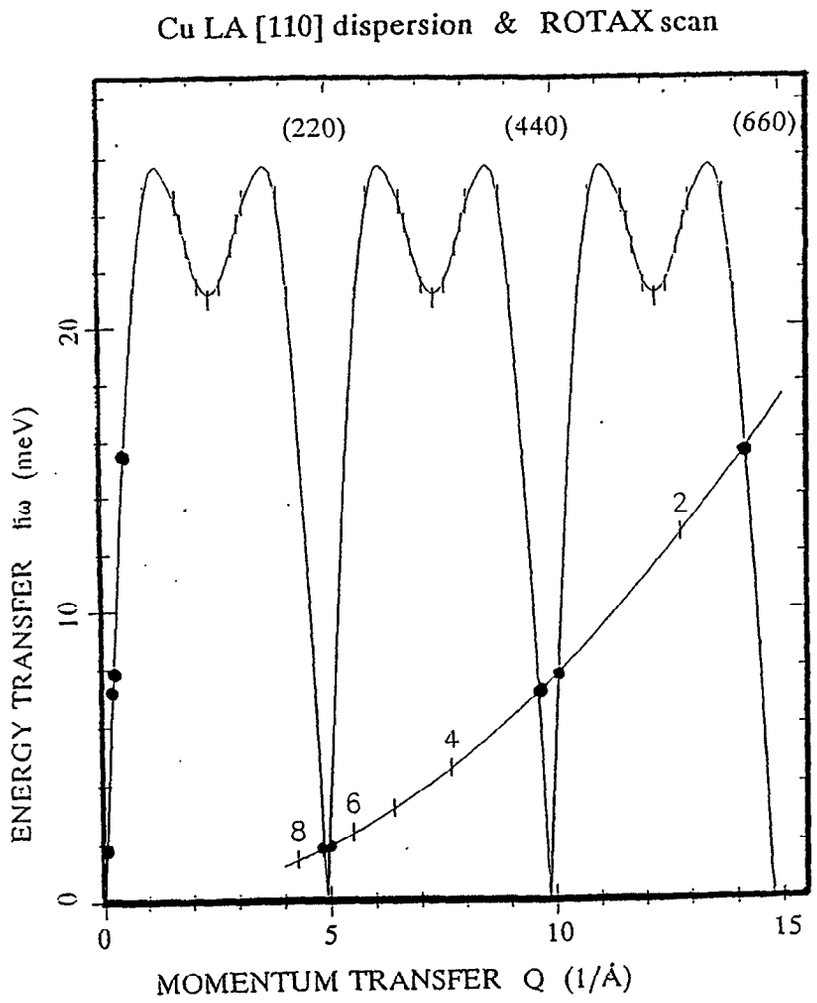

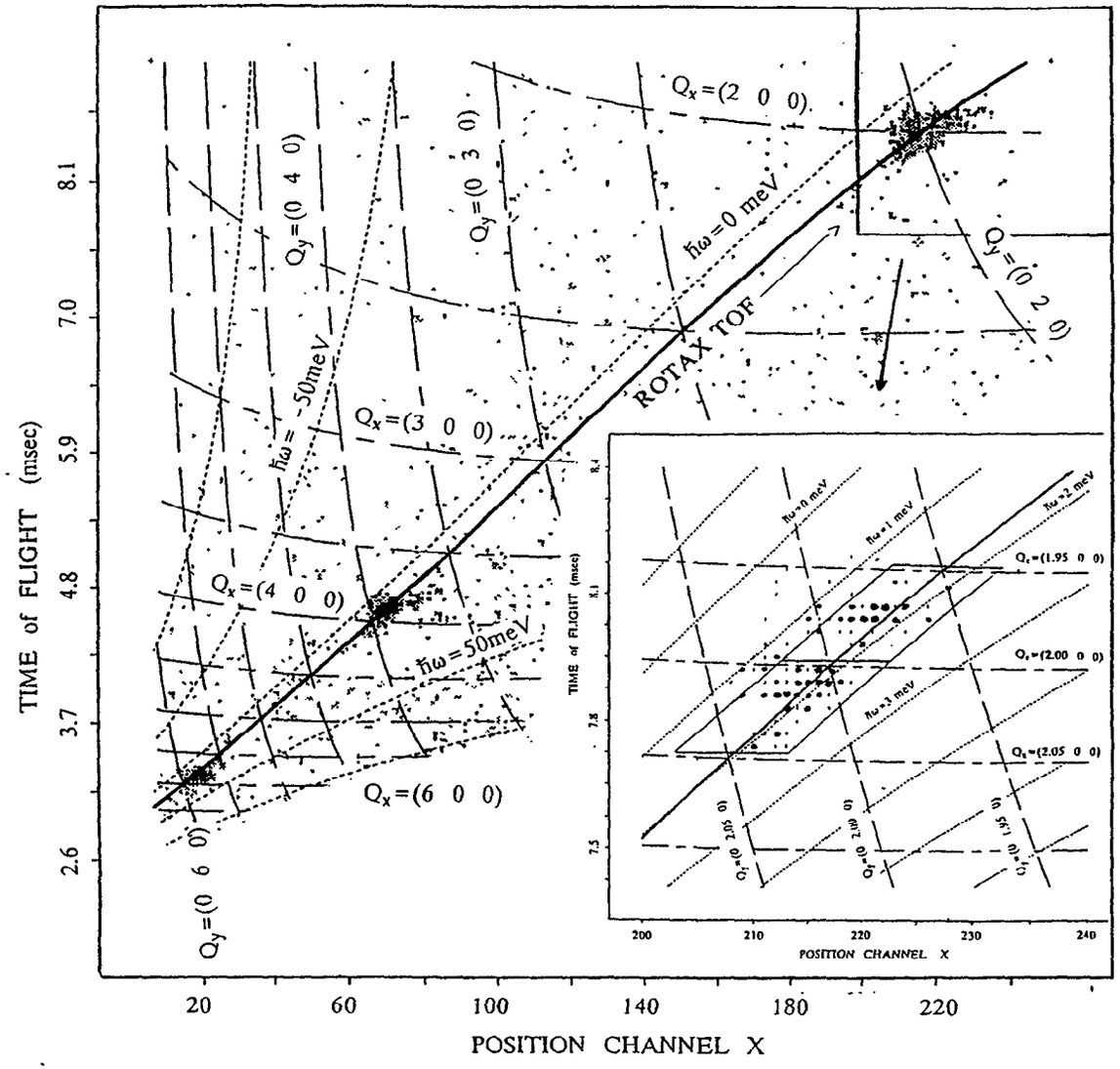

Fig. 4: ROTAX inelastic scattering from copper (110) direction: (a) Rotax scan parabola in extended and reduced zone scheme, (b) plot of the data and (Q,ħω) lattice together with the scan trace in (x,t) detector coordinates; the insert enlarges the area around the (200) Γ point.

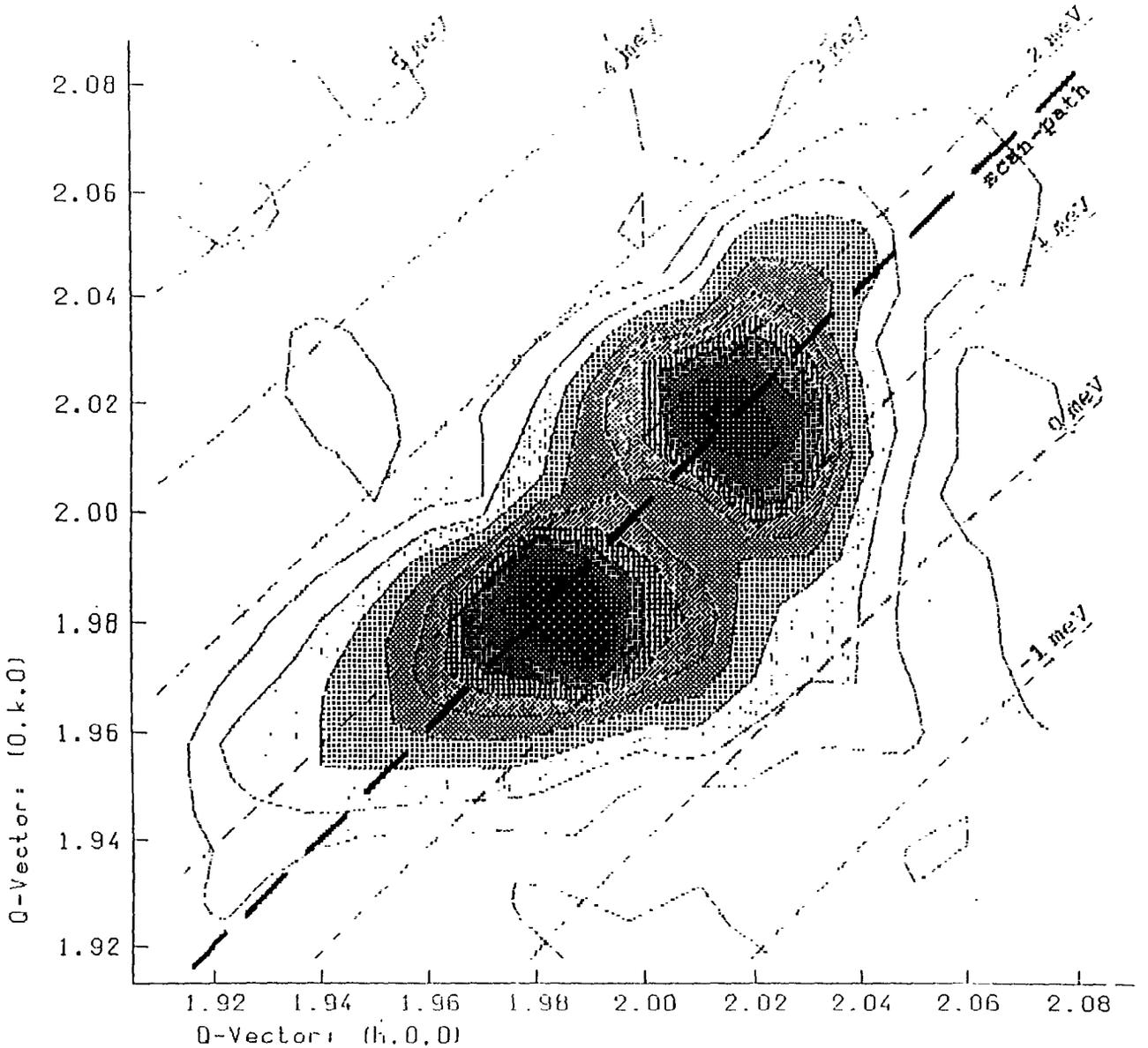

Fig. 5: Transform of the enlargement of fig 4b into (Q_1=(h00),Q_2=(0k0)) coordinates with trace of energy transfer $\hbar\omega$ and scan trace.

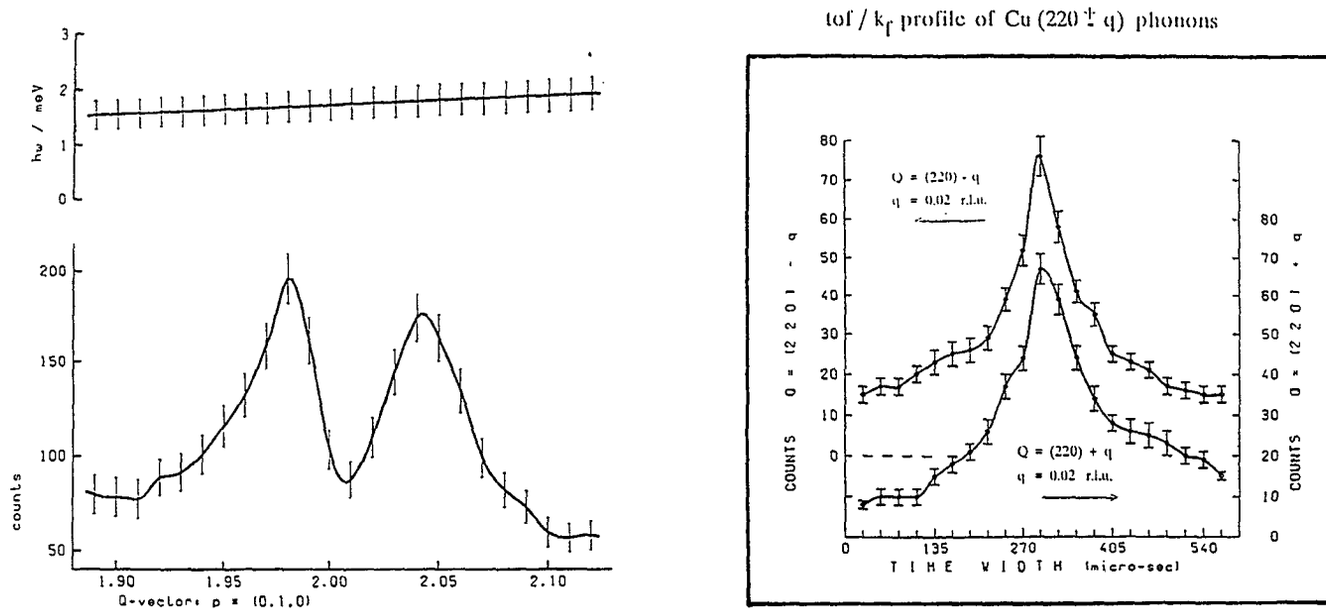

Fig. 6: Scan profiles of the close-up of fig. 4b: (a) along Q=(110), which is almost at constant energy transfer; (b) const. k_f profiles through either phonon peak.

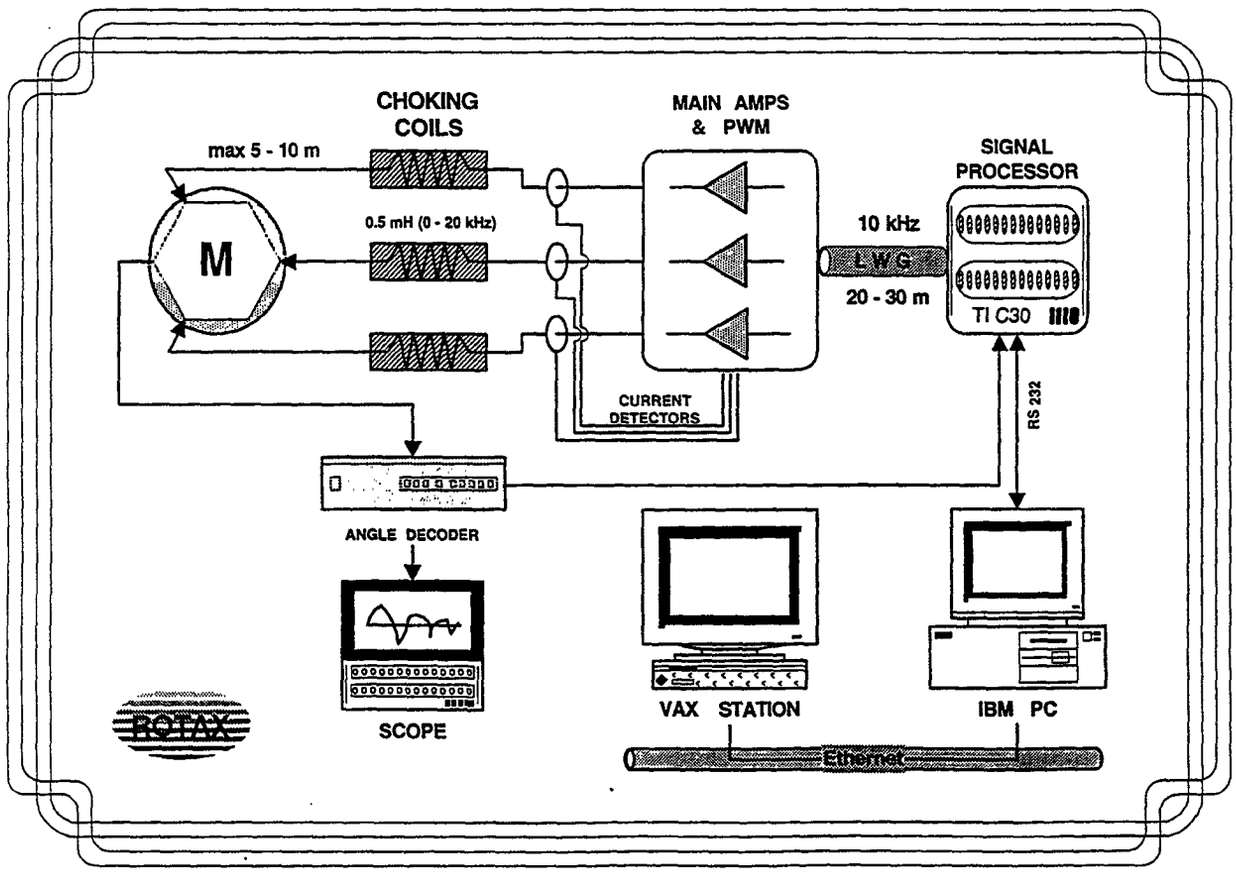

Fig. 7: Hardware of the ROTAX analyser drive after the 1995 improvements.

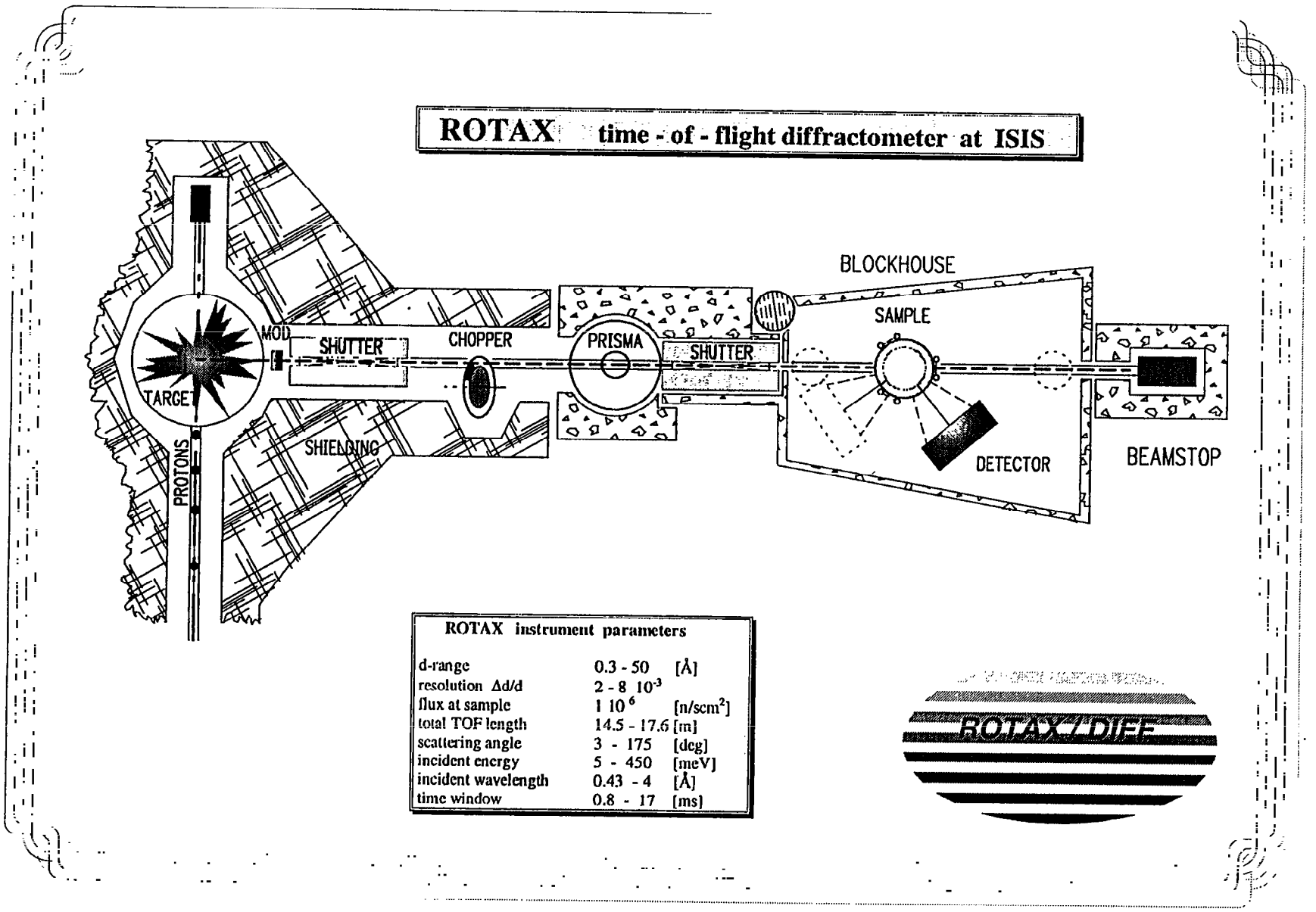

ROTAX instrument parameters

d-range	0.3 - 50	[Å]
resolution Δd/d	2 - 8 10^{-3}	
flux at sample	1 10^{6}	[n/scm^2]
total TOF length	14.5 - 17.6	[m]
scattering angle	3 - 175	[deg]
incident energy	5 - 450	[meV]
incident wavelength	0.43 - 4	[Å]
time window	0.8 - 17	[ms]

Fig. 8: Sketch of the ROTAX / Diff time of flight diffractometer after removal of the analyser tower.

A

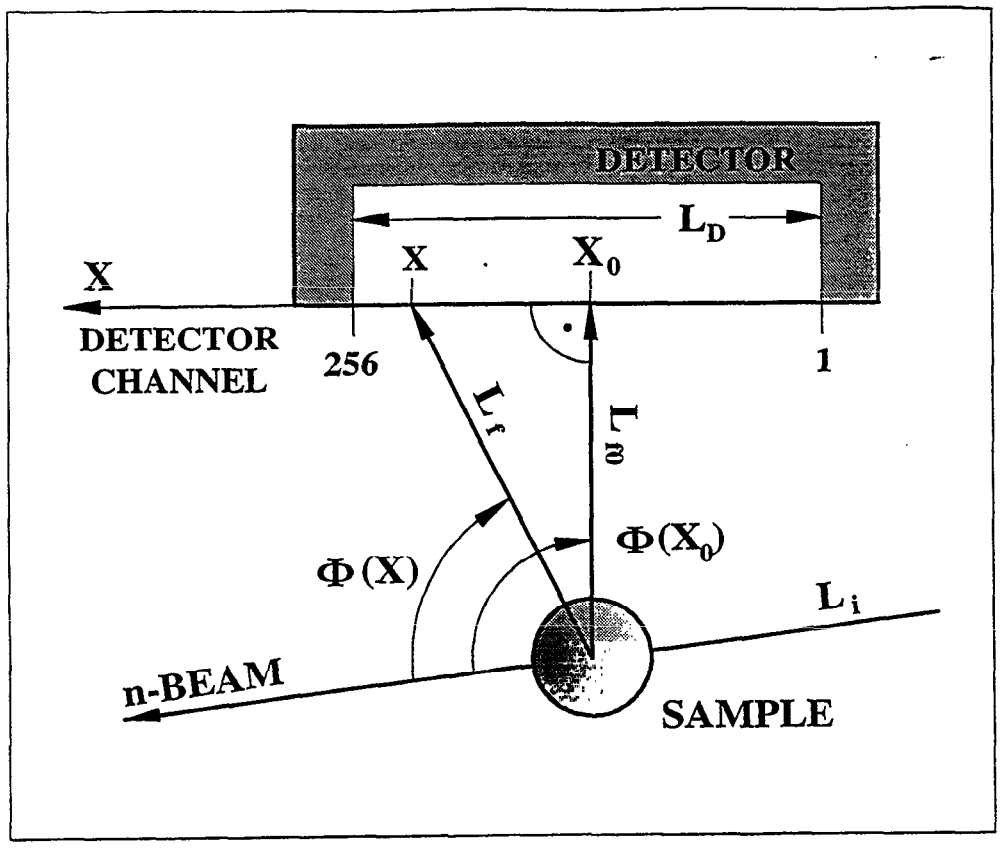

B

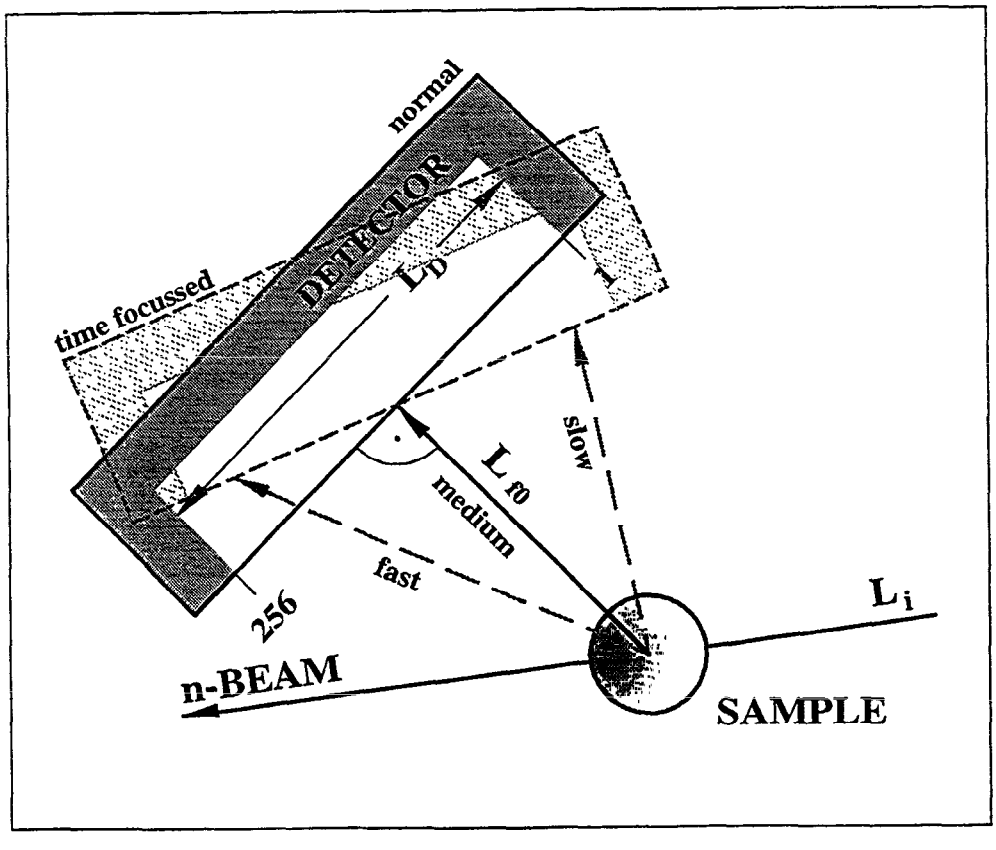

Fig. 9: (a) real space detector coordinates as used for calibration and d-value line integration of powder patterns; (b) potential alignment for time-focussing set-up: All neutron energies scattered from one powder line would arrive at the same time in all position channels. As discussed in text, this set-up is obsolete on ROTAX/Diff.

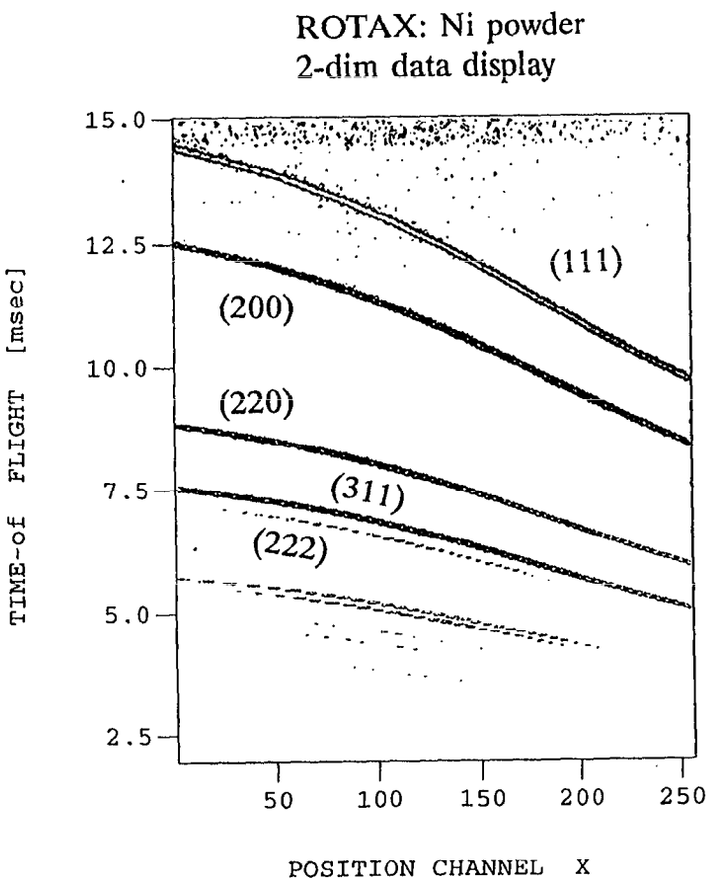

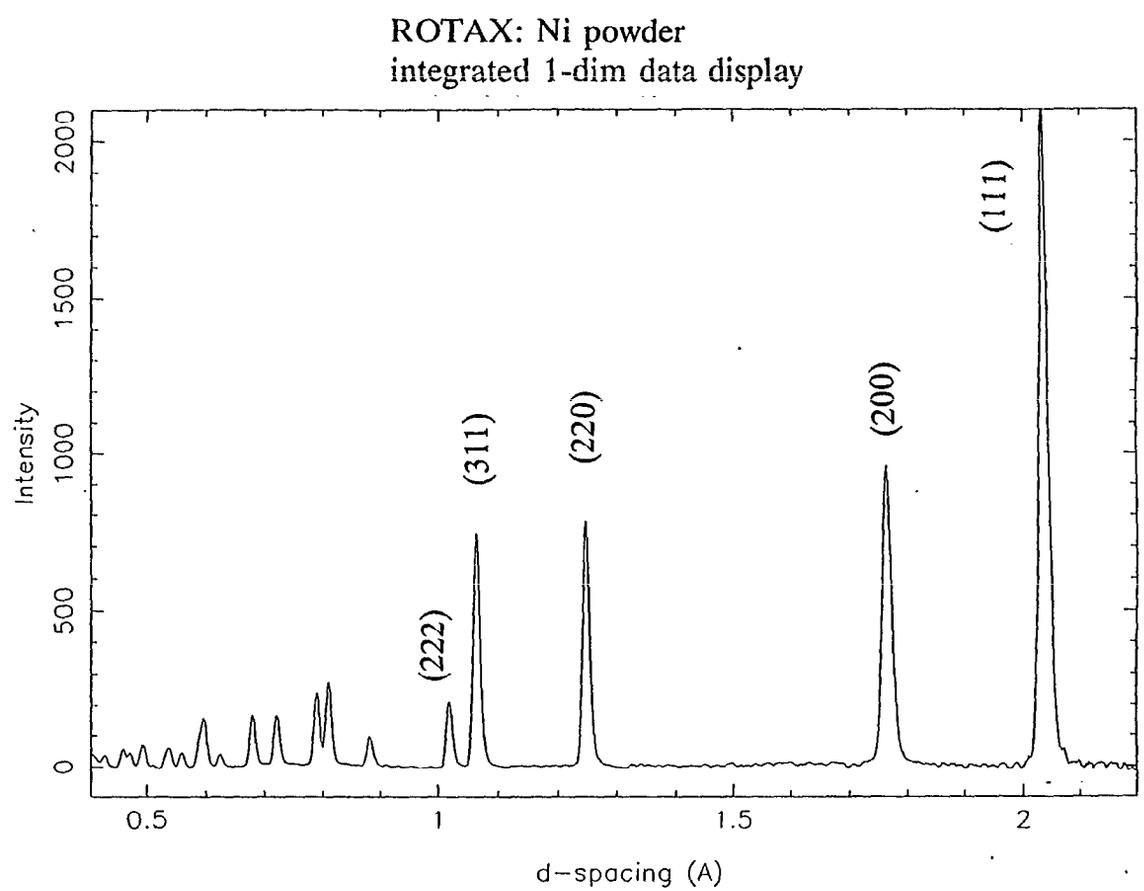

Fig. 10: Example of a Ni-powder pattern obtained on ROTAX/Diff: (a) original raw data in (x,t) detector coordinates; (b) after powder-line integration discussed in text.

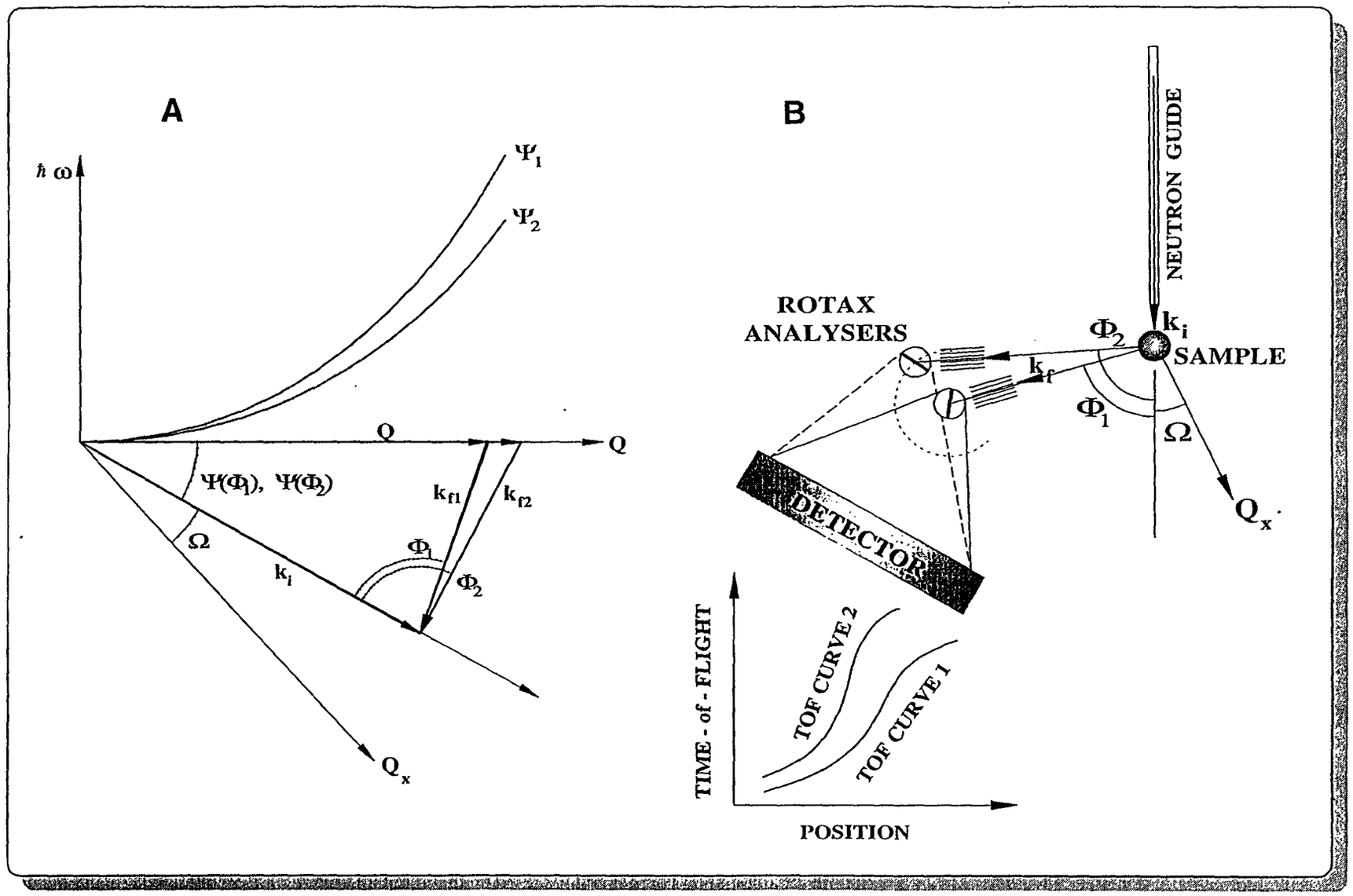

Fig. 11: Correlated scans of a double-ROTAX set-up for simlutaneous scanning at 2 different scattering angles Φ_1 and Φ_2.
(a) (Q,E)-parabolas of the tof traces and scattering triangles; (b) real space shape of the instrument and sketch of detector raw data.

ICANS - XIII
13th Meeting of the International Collaboration on
Advanced Neutron Sources
October 11-14, 1995
Paul Scherrer Institut, 5232 Villigen PSI, Switzerland

FOCUS: A NEW TIME OF FLIGHT SPECTROMETER AT THE NEUTRON SPALLATION SOURCE SINQ/CH

J. Mesot[1], S.Janßen[2,1], L. Holitzner[2,1], M. Prager[3], D. Richter[3], and R. Hempelmann[2]

1) Labor für Neutronenstreuung, Paul Scherrer Institut, Switzerland
2) Physikalische Chemie, Universität des Saarlandes, Germany
3) IFF, Forschungszentrum Jülich, Germany

ABSTRACT

The design of the time-of-flight (TOF) spectrometer FOCUS to be built at the SINQ at the Paul Scherrer Institute is presented. The main purpose is to provide a versatile TOF machine well suited for a large variety of applications. The concept of the instrument consists in the combination of a doubly- and variably-focusing monochromator with a Fermi chopper. By changing the optical conditions FOCUS will have the option to be operated either in time- or monochromatic-focusing mode, for quasielastic and inelastic scattering measurements, respectively. The expected performances of FOCUS are presented and compared to the existing IN6-TOF spectrometer at the Institute Laue-Langevin (ILL).

1. Introduction

The Swiss spallation neutron source SINQ is expected to produce the first neutrons at the end of '96. FOCUS (Focusing Crystal University Spectrometer) is the project of a new time of flight (TOF) spectrometer for cold neutrons at this source. It is being built in cooperation between the 'Universität des Saarlandes, FRG', the 'Forschungszentrum Jülich, FRG' and the 'Paul Scherrer Institut, CH'.
Within the 'day-1' instrumentation FOCUS will be the only TOF spectrometer. Therefore the physical design should provide a versatile and highly flexible instrument to be suited for a wide range of applications. The concept of FOCUS consists in a hybrid TOF spectrometer combining a crystal monochromator focusing both horizontally and vertically with a Fermi chopper. Equipped with two interchangeable monochromators (pyrolithic graphite and mica) the spectrometer will continuously cover a band of incoming energies 0.25 meV $\leq E_i \leq$ 20 meV, thus touching also the thermal neutron regime.
The spectrometer will be located at the end of the curved guide RNR11 viewing the cold D_2-source.

Keywords: Time of Flight Spectrometer, Focusing, Fermi Chopper, SINQ

2. Components

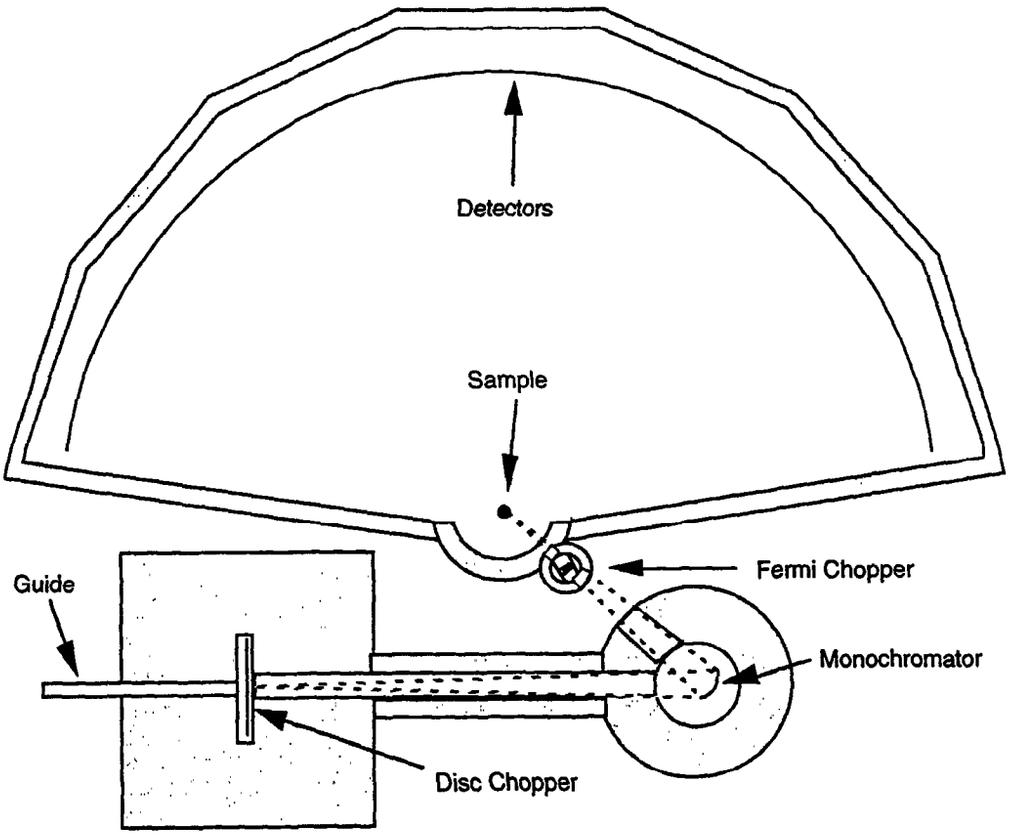

Fig. 1 Schematic drawing of FOCUS and its main components

Table 1: Relevant spectrometer parameters

Component		Dimension
guide	horizontal	5 cm
	vertical	12 cm
converg. guide	vertical	12 cm →10 cm
distance	guide - disc chopper	0.2 m
	guide - monochromator d_{gm}	1.5 - 3 m
	monochromator - sample d_{ms}	1.5 - 3 m
	Fermi chopper - sample	0.5 m
	sample - detectors	2.5 m
monochromator	horizontal	16 cm
	vertical	21 cm
	mosaic η (PG)	$(0.8\pm0.1)^\circ$
	Take-Off Angle	$35^\circ < 2\theta < 140^\circ$
Fermi chopper :	frequency ν :	<330 Hz
	window: horizontal	6 cm
	vertical	10 cm
	collimation Σ :	1-3°
disc-chopper:	diameter:	70 cm
	frequency:	<165 Hz

Figure 1 presents a schematic drawing of the spectrometer layout. By means of a vertically converging guide (G), the white beam is first reduced from 12 x 5 cm^2 (h x w) to 10 x 5 cm^2 and then chopped by a disc chopper (DC). The horizontally and vertically focusing monochromator (M) with variable curvature in both directions focuses the beam through a Fermi chopper (FC) onto the sample. The disc chopper will also prevent higher order contamination and frame overlap. At the sample (S) position the beam has the dimension 6x3 cm^2. In its first stage FOCUS will be equipped with 200 ^3He counter tubes (D) of rectangular cross section, covering a scattering angle range from -34^0 to 130^0. Two further banks of detectors can be added so that FOCUS will run on 600 counter tubes in its final stage. In between sample position and detectors a He-filled box is placed to prevent scattering from air. For incident energies $E_i \leq 4.8$ meV optionally a cooled Be-Filter can be placed in the monochromator shielding. The dimensions of FOCUS are listed in table 1.

3. Time- versus monochromatic-focusing

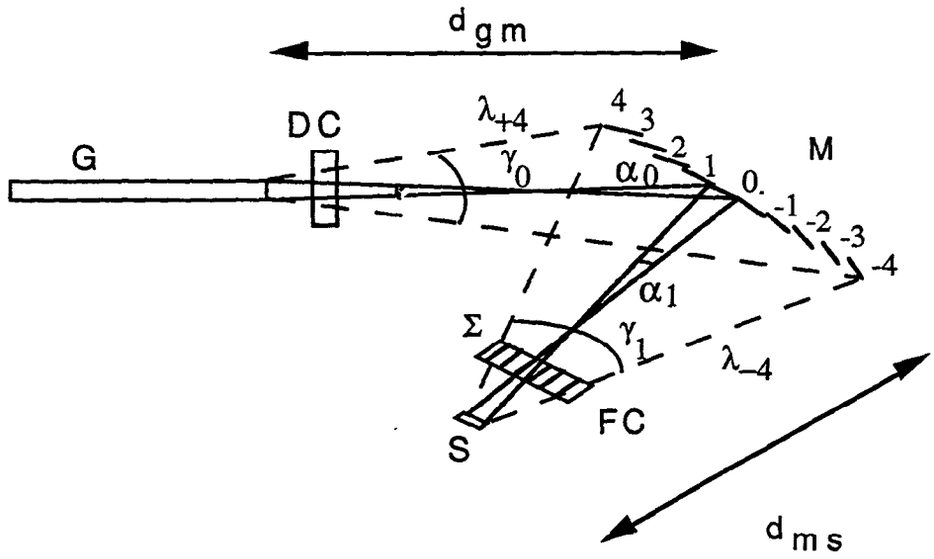

Fig. 2 Horizontal cut of the focusing monochromator

A copy of the existing IN6 (ILL)[1, 2] spectrometer would not be appropriate at the SINQ. Indeed the high divergence and the large size of the beam available at the end of the guide RNR11 would have a detrimental effect on both the energy resolution and the intensity.

Consider an arrangement in which the distance d_{gm} between the end of the guide and the monochromator can be increased (Fig. 2). Thus, for each individual piece of the monochromator, the wavelength uncertainty decreases since the local collimation α_0 decreases. On the other side the intensity at the sample position remains almost unaffected if the horizontal and vertical curvature of the monochromator are adjusted to focalise the beam onto the sample.

The overall wavelength band delivered by a curved monochromator is given by[3]

$$\Delta\lambda = |\lambda_{-n} - \lambda_n| = (\lambda_i/2)\cot(\Theta)|\gamma_1 - \gamma_0| \qquad (1)$$

Where λ_i is the incident wavelength, θ is the monochromator angle and γ_0, γ_1 are the aperture angles of the monochromator. Clearly, two configurations are possible:

3.1 Monochromatic focusing

If one desires a good resolution over a wide energy-transfer range, it is necessary to focus monochromatically ($\Delta\lambda = 0$). For that purpose the distances d_{gm} and d_{ms} have to be equal. This arrangement allows to work with a relaxed collimation Σ of the Fermi chopper. This means a large intensity gain since firstly, the cross-section is directly proportional to Σ [4] and secondly, the dynamic transmission is improved (especially for long wavelengths and high frequencies).

3.2 Time focusing

$\Delta\lambda \neq 0$ ($\gamma_1 \neq \gamma_0$ or $d_{gm} \neq d_{ms}$) and the time-focusing principle has to be used, i. e., the Fermi chopper allows the slow neutrons to start before the fast ones in such a way that they will reach the detectors at the same time. The Fermi-chopper frequency is determined by the time focusing condition and the Fermi-chopper collimation has to be adjusted such that the sample is viewing only one monochromator piece. Unfortunately the time focusing mode is valid for one energy transfer only, thus being inadequate for scattering processes over a large energy transfer range.

4. Expected performances of FOCUS

Intensities and energy resolutions for several spectrometer configurations have been calculated for the proposed spectrometer as well as for IN6-ILL. We used both analytical expressions[4] and a modified version of a Monte Carlo simulation program developed by H. Mutka[3]. The results using both methods are very similar and Table 2 gives the values obtained for an incident wavelength of 6 Å. The first solid target at the SINQ should deliver a flux $\partial\sigma/\partial\Omega$ at the end of the guide RNR11 of the order of one third of the flux measured at the IN6-ILL guide. The next generation targets (either solid or liquid) should allow to increase the flux by a factor of 3. Therefore, considering these uncertainties, the flux $\partial\sigma/\partial\Omega$ has been set to unity in all calculations.

Table 2: calculated performances of FOCUS for several configurations. The values obtained for the IN6 spectrometer at the ILL and an IN6-type spectrometer at the SINQ are also included.

	λ=6 Å Instr. Type	$I/(\partial\sigma/\partial\Omega)$	Resol. (μeV) ΔE=-2 meV	Resol. (μeV) ΔE=0 meV	Resol. (μeV) ΔE=10 meV	Comments
	IN6-ILL					
1	145 Hz	1.00	66	45	850	Time-foc.
	FOCUS					
	d_{gm} / d_{ms} / Σ / ν					
2	3.0/ 1.5/ 1/ 260	0.26	47	35	690	Time-foc.
3	3.0/ 1.5/ 1/ 160	0.67	46	54	1140	
4	1.5/ 1.5/ 3/ 160	1.82	26	85	1060	Monochr.
5	3.0/ 3.0/ 3/ 330	0.86	26	47	580	Monochr.
6	3.0/ 3.0/ 3/ 330	0.42	13	46	580	Monochr.

All intensities are given relatively to the instrument IN6-ILL and we included in our intensity calculations an anti-overlap condition for Fermi-chopper frequencies higher than 160 Hz. For comparable resolutions at the elastic position, FOCUS (row 3 (R3) and R5) will reach about 80% of the intensity of IN6-ILL (R1).
The best resolution of FOCUS, at the elastic position, is achieved in the time focusing mode (R2). The monochromatic configurations (R4-R6) of FOCUS are the most attractive ones since it is possible to work either in high intensity mode (R4) or in high resolution mode (R6), with a good resolution over a large energy transfer range.

5. Conclusions

The physical design of the new hybrid TOF-spectrometer FOCUS in construction at the Swiss spallation source SINQ has been presented. By changing the optical conditions FOCUS will have the option to be operated either in time- or monochromatic-focusing mode, for quasielastic and inelastic scattering measurements, respectively. This flexibility is necessary since FOCUS will be the only "first generation" TOF instrument. The energy resolution has been calculated for several spectrometer configurations using a Monte Carlo algorithm and the expected performances of FOCUS should be very comparable to those of IN6 at the ILL. The flux at the sample position will be directly related to the performance of the target. For the 'day-1' experiments, the expected flux will be one third of the flux measured at the IN6-ILL guide.

6. Acknowledgements

The necessary funds of the project "FOCUS" are provided by the German "Bundesministerium für Bildung und Forschung (BMBF, project nr. 03-HE4SA2-2)" and by the Swiss "Paul Scherrer Institut". The authors are very grateful for this support. Furthermore, we thank A. Furrer and W. Bührer (PSI), H. Mutka (ILL), as well as M. Prager and D. Richter (Jülich) for fruitful and stimulating discussions.

7. References

[1] R. H. Scherm, C. J. Carlile, J. Dianoux, J. Suck, J. White, ILL Report 76S235
[2] Y. Blanc, *Le spectromètre à temps de vol IN6*, ILL Report 83-BL21G
[3] H. Mutka, *Nucl. Instr. and Meth. in Phys. Res.* A **338**, 144 (1994)
[4] J. Mesot , *A Time of Flight Spectrometer at the SINQ*, PSI Report 895/MJ33-401

ICANS-XIII
13th Meeting of the International Collaboration on
Advanced Neutron Sources
October 11-14, 1995
Paul Scherrer Institut, 5232 Villigen PSI, Switzerland

INELASTIC NEUTRON SCATTERING SPECTROMETER FOR THE IN-06 NEUTRON SOURCE AT THE MOSCOW MESON FACTORY

V.Yu.Kazimirov*, A.V.Belushkin†

* *Laboratory of Pulsed Neutron Sources, Institute for Nuclear Research of RAS, Moscow, Russia*

† *Frank Laboratory of Neutron Physics, Joint Institute for Nuclear Research, Dubna, Russia*

ABSTRACT

In the spectrometers in which the so-called inverse geometry of scattering is used, the scattering neutron energy, E_2, is fixed and the initial neutron energy, E_1, is determined by source to sample time of flight. The inverse geometry method is a unique reliable means for determination of the absolute intensity of spectral lines. It is possible because this method allows experiments in a wide range transferred energies to be carried out without changing the experiment geometry. Such spectrometers possess a good definite dependence of the transfer energy on momentum transfer. This allows one to extract complementary to optical methods information from the experimental data.

The KDSOG-M spectrometer was created at the IBR-2 pulsed reactor of JINR for investigation of the lattice dynamics of solids and simultaneous analysis of the phase structure of samples. For analysis of the scattering neutron energy polycrystal filters and single crystals are used.

Creation of the IN-06 neutron source based on the proton accelerator of the Moscow meson factory leads to the necessary formation of a scientific research program for condensed matter physics. Re-equipment of the KDSOG-M spectrometer for use at the IN-06 neutron source includes preparation of an instrumental basis for carring out experiments in solid state physics and other fields (biophysics, applied science and so on).

This work is a project for transfer and updating the inverse geometry inelastic neutron scattering spectrometer KDSOG-M for use at the IN-06 neutron source of Moscow meson factory.

Keywords: Inelastic scattering, Inverse geometry

1. The IN-06 neutron source

The principle of operation of the IN-06 slow and fast (spallation) neutron source for neutron investigation in the branches of condensed matter physics and nuclear physics is based on use of the pulsed proton beam and accelerator-storage complex of the Meson factory of the State Scientific Centre Institute for Nuclear Research of the Russian Academy of Science and uranium targets [1].

The neutron source is planned to be put into operation in stages. In the first stage, the use of 4 experimental channels inside the experimental hall (neutron channel N1-N4) is planned. Flight paths in the first stage will be up to 30 m. In 1998 another three channels with flight paths up to 100 m, which terminate in experimental pavilions, will be in use.

The layout of the IN-06 experimental hall is shown in Fig. 1. Basic parameters of the IN-06 neutron source in the first stage is as follows: thermal neutron peak flux ~4×10^{14} n/см^2/s, thermal neutron average flux ~0.8×10^{12} n/см^2/s, thermal neutron pulse width ~50 μs at a frequency of 50 Hz.

In addition, changing the non-multiplying target to a multiplying target is supposed. It will increase the thermal neutron flux density by 1-2 orders of magnitude. Creation of a storage ring will decrease the thermal neutron pulse width.

Since the length of flight paths in the first stage are limited to 30 m (channel N1), creation of spectrometer with moderate resolution and high luminosity is the optimum version. A spectrometer like the KDSOG-M

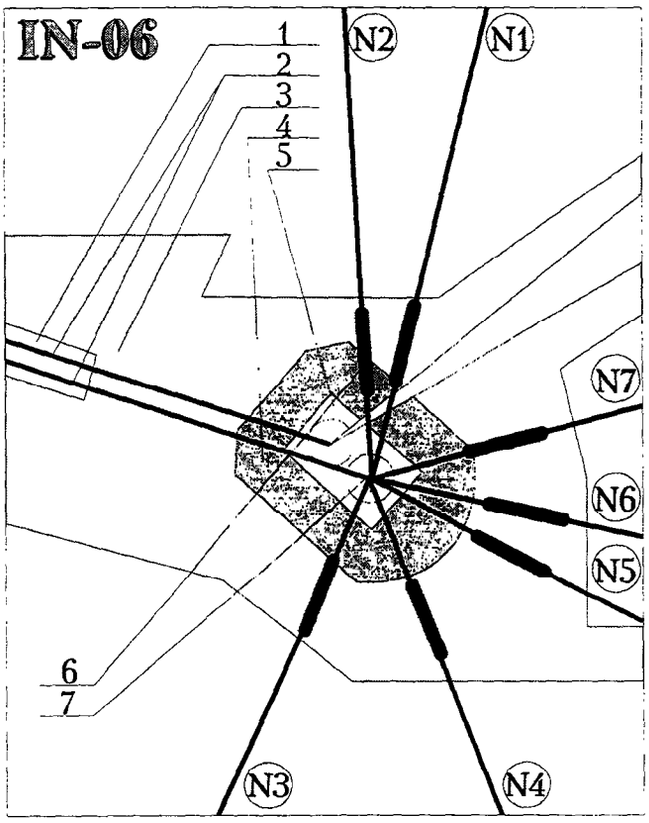

Fig. 1. The layout of the IN-06 neutron source experimental hall:

1. Accelerator
2. Proton beams
3. Shield
4. Concrete
5. Thermal shield
6. Channel gate
7. Neutron target

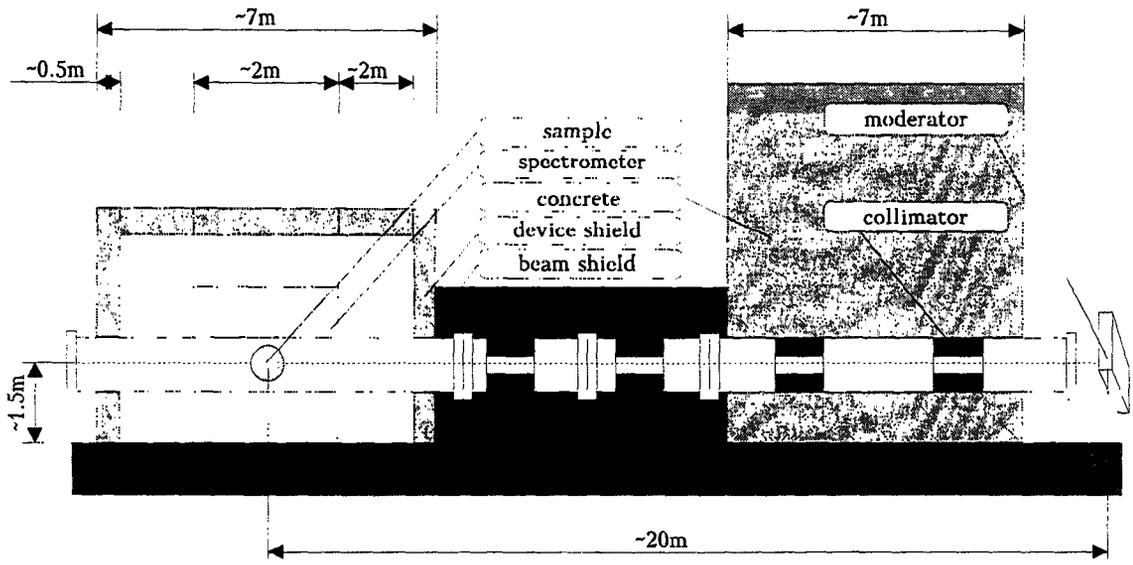

Fig. 2. Scheme of equipment and arrangement of shields.

spectrometer satisfies these requirements. Moreover, the smaller (compared to IBR-2) thermal neutron pulse width will allow an increase in spectrometer resolution. The scheme of spectrometer modernisation described below allows the use of time focusing and gives possibilities for step-by-step equipping of the spectrometer by supplementary section for investigation of inelastic neutron scattering.

Equipment and shielding for normal operation of the spectrometer, which must be placed in the IN-06 experimental hall, are shown in Fig. 2.

2. The KDSOG-M spectrometer

In 1984 the inelastic neutron scattering spectrometer using inverse geometry (see Fig. 3), KDSOG-M, was put into operation at the IBR-2 pulsed reactor [2]. The KDSOG-M spectrometer was designed for investigations of crystal lattice dynamics by inelastic scattering and for neutron diffraction studies simultaneously. That gave the possibility to investigate the phase composition of the sample which sufficiently increased the volume of information obtained from experimental data.

The most convenient conditions for carring out the experiments in condensed matter physics using the KDSOG-M spectrometer are available in the region of energy transfer below 50 meV (see Fig. 4). The composition of the low background level in this region of energy transfer, medium resolution and high luminosity allows the study of crystal lattice dynamics, its changes at phase transitions, vibration spectra of amorphous substances and low frequency intramolecular vibrations in molecular crystals. The values of the transition energies between the levels of paramagnetic ions in the crystal fields also lie in the same range.

At higher values of energy transfers (up to 500 meV) despite the background increases and the resolution becomes worse, it is still possible to

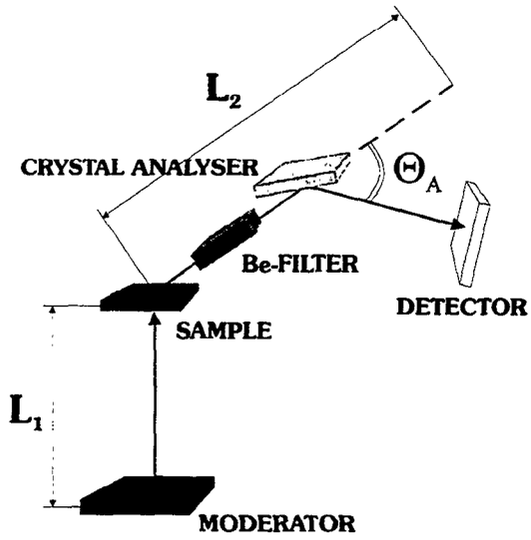

Fig. 3. The inverse geometry method.

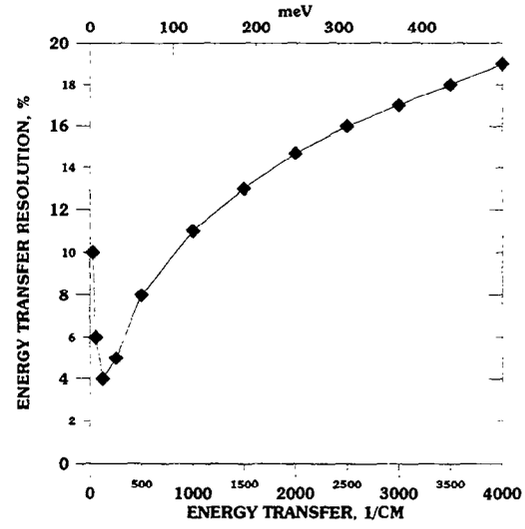

Fig. 4. Relative resolution of the KDSOG-M spectrometer.

investigate hydrogen vibrations in the lattices of metal hydrates due to the high luminosity of the device.

It is possible to conclude that the most straightforward directions for using the KDSOG-M spectrometer are the investigations of hydrogen containing crystals, molecular crystals and crystal field effects.

While discussing the possibilities of reconstruction of the spectrometer for use at the IN-06 neutron source of Moscow meson factory, it is necessary to take into account peculiarities of this neutron source. Such includes the considerably lower thermal neutron pulse width and several orders of magnitude lower background of fast neutrons in comparison with the IBR-2 reactor. Consequently, the creation of a spectrometer which would take into account these peculiarities of the source and at the same time include all the advantages of the KDSOG-M spectrometer (high luminosity, possibility of sample phase composition control) seems to be the most prospective.

3. The MAINS spectrometer

The inelastic scattering inverse geometry MAINS (Multy Analyser Inelastic Neutron Scattering spectrometer) spectrometer is being designed on the basis of the KDSOG-M spectrometer. It is intended for solid state dynamics investigations and is planned for use at the IN-06 neutron source.

3.1 The construction

The MAINS spectrometer is similar to the MODES spectrometer at ISIS, which is projected as an upgrade of the time focusing TFXA spectrometer. The MAINS spectrometer is different from that one in its neutron scattering analysis and detector systems. Due to the peculiarities of the IN-06 neutron source, the most reasonable construction of the spectrometer is the following (see Fig. 5):

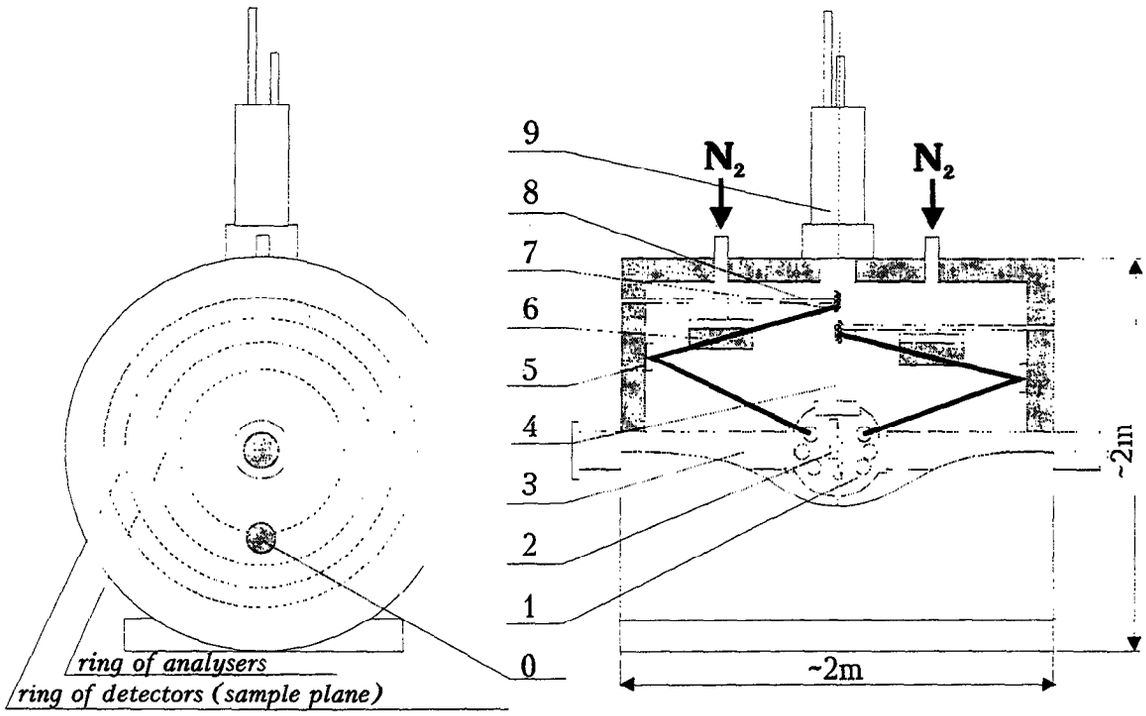

0	*Diffraction detector*	5	*Single-crystal analyser*
1	*Vacuum bank*	6	*Beryllium filter*
2	*Sample*	7	*Inelastic scattering detector*
3	*Neutron guide*	8	*Detector holder*
4	*Well for sample insertion*	9	*Vacuum valve*

Fig. 5. The MAINS spectrometer

The inner vacuum volume of device is limited by the cylinder tank. Crystal-analysers 5 for inelastic scattering investigation are ring-shaped and are made of Zn- or PG-single crystals (see Fig. 6). Crystal-analysers are mounted on the side walls of the cylinder tank from inside. After being reflected from analysers 5, neutrons pass through beryllium filter 6 (the construction of which is shown in Fig. 7) and fall on detectors 7. The detector system consists of two detector rings of different radii which are located in the same plane with the sample. One of the

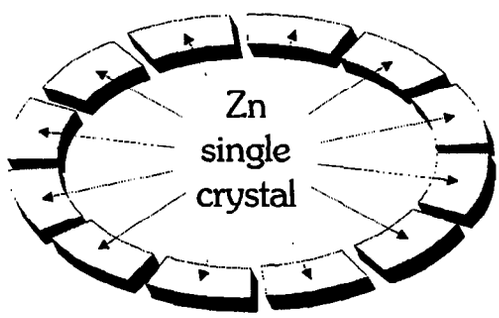

Fig. 6. Ring of analysers

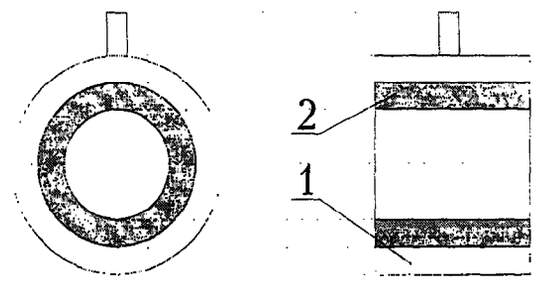

Fig. 7. Beryllium filter:
1. Liquid nitrogen bonjo
2. Polycrystal beryllium

detector rings is designed for registering neutrons scattered in the reflection geometry. Another is designed for the transmission geometry. Inelastic scattering sections are symmetrical relative to the neutron guide tube. The arrangement of the detectors in the same plane with the sample gives the possibility to use time focusing while collecting data.

The diffraction part of the spectrometer is the SNM-17 counter placed in the backscattering geometry and surrounded by a Cd-shield.

3.2 Resolution

For estimation of the resolution ability of the inelastic scattering spectrometer we will use the general formula:

$$\frac{\Delta\varepsilon}{\varepsilon} = \frac{1}{\varepsilon}\sqrt{R_1^2 + R_2^2 + R_3^2 + R_4^2} \qquad (1),$$

where

$$R_1 = \frac{\partial\varepsilon}{\partial E_2}\Delta E_2 = \left(1 + \frac{L_2}{L_1}\left(\frac{E_1}{E_2}\right)^{3/2}\right) \times \Delta E_2 \qquad (2),$$

$$R_2 = \frac{\partial\varepsilon}{\partial L_2}\Delta L_2 = \frac{4E_1^{3/2}}{L_1 E_2^{1/2}} \times \Delta L_2 \qquad (3),$$

$$R_3 = \frac{\partial\varepsilon}{\partial t}\Delta t = \frac{2E_1^{3/2}}{AL_1} \times \Delta t \qquad (4),$$

$$R_4 = \frac{\partial\varepsilon}{\partial L_1}\Delta L_1 = \frac{2E_1}{L_1} \times \Delta L_1 \qquad (5).$$

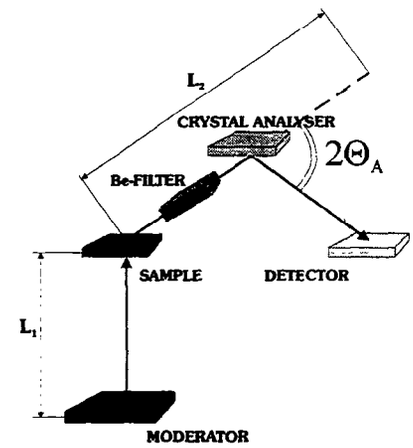

Fig. 8. Principle of the time focusing method.

Here

E_1, ΔE_1, E_2, ΔE_2	-	*the energies of neutrons before and after scattering and corresponding uncertainties;*
L_1, ΔL_1, L_2, ΔL_2	-	*first and second flight paths and corresponding uncertainties;*
$\varepsilon = E_1 - E_2$, $\Delta\varepsilon$	-	*energy transfer and uncertainty of energy transfer;*
$A = 2286.4$	-	*constant.*

The use of time focusing means (see Fig. 8) that all neutrons at the detector have one and the same secondary flight time. In the first order of approximation, mosaicity of the crystal analyser does not affect the focusing and the derivative (2) is reduced to $\partial\varepsilon / \partial E_2 = 1.0$ in this geometry. The uncertainty of the neutron energy after the scattering is defined by the expression $\Delta E_2 = 2E_2 \coth\Theta_A \times \Delta\Theta_A$. So we have:

$$R_1 = 2E_2 \coth\Theta_A \times \Delta\Theta_A \qquad (6).$$

Besides that, time focusing on the second flight path eliminates all the terms in the resolution connected with limitations of the beam collimation. Consequently, the term in resolution due to the uncertainty of the second flight path is connected only with the finite thickness of the sample, analyser and the detector. Let us define the effective uncertainty of thicknesses Δl as:

$$\Delta l = (\Delta s^2 + \Delta a^2 + \Delta d^2)^{\frac{1}{2}} \qquad (7),$$

where Δs, Δa, Δd are thicknesses of the sample, analyser and the detector. When $\Delta L_2 = \Delta l / \sin\Theta_A$ and:

$$R_2 = 4E_1^{3/2} \times \Delta l / L_1 E_2^{1/2} \sin\Theta_A \qquad (8).$$

In the third term of formula (1) we will define the time uncertainty as $\Delta t = \sqrt{\Delta t_{th} + \Delta t_{ch}}$, where Δt_s is the thermal neutron pulse width, Δt_{ch} is the time channel width.

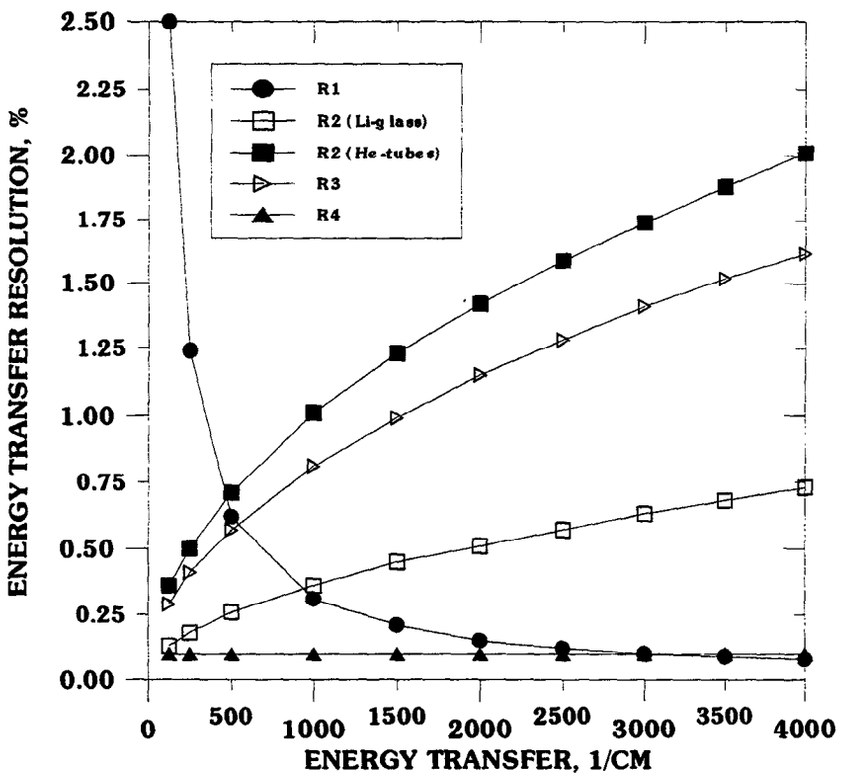

Fig. 9. Contributions to the resolution of the MAINS spectrometer from different terms of formula (1).

In the fourth term of formula (1) the uncertainty of the first flight path ΔL_1 is low (see Fig. 9) and the contribution of R_4 is also low. Neglecting these we obtain the final expression for the resolution of the spectrometer:

$$\frac{\Delta\varepsilon}{\varepsilon} = \frac{1}{E_1 - E_2}\sqrt{(2E_2\coth\Theta_A \times \Delta\Theta_A)^2 + \left(\frac{4E_1^{3/2} \times \Delta l}{L_1 E_2^{1/2}\sin\Theta_A}\right)^2 + \left(\frac{2E_1^{3/2}\Delta t}{AL_1}\right)^2} \qquad (9).$$

From Fig. 9 it is obvious that the R_2 term is most valuable, after the R_3 term, which depends on the thermal neutron pulse width or even exceeds it. So the question about the type of detectors for the detector system of the spectrometer seems to be the most interesting. The use of scintillation detectors made of Li-glass (of 2 mm thickness) gives sufficient improvement in resolution compared to the He^3-detectors (of 8 mm thickness) and allows MAINS to reach the level of the TFXA and MODES (ISIS) devices.

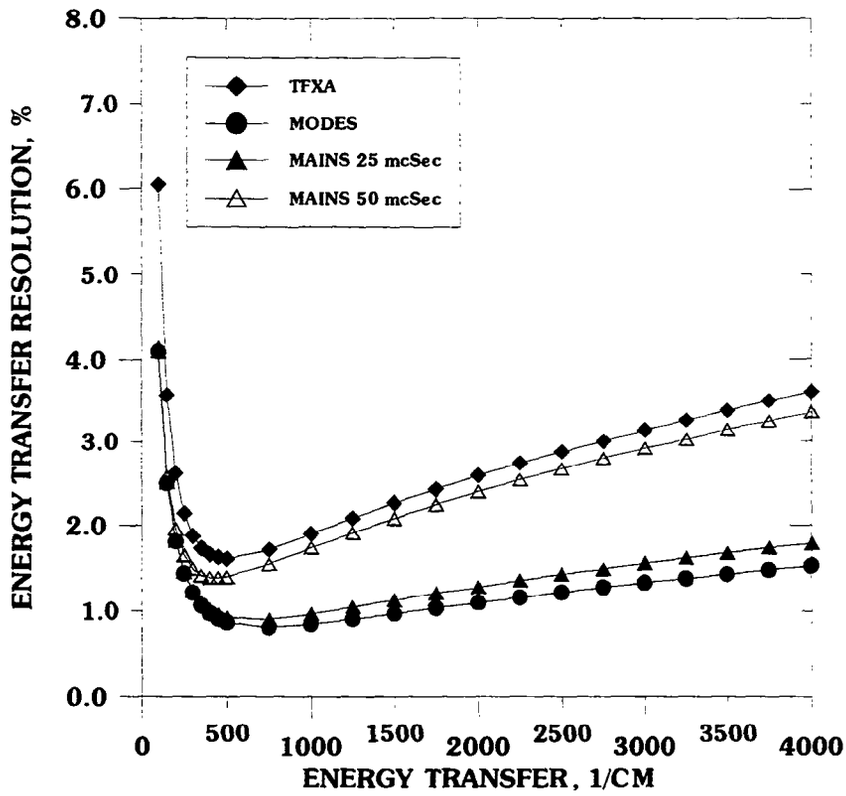

Fig. 10. Resolution of the MAINS spectrometer

Assuming the spectrometer parameters are equal to the following:

Primary flight path	L_1	30 m
Secondary flight path	L_2	0.7 m
Initial neutron energy	E_1	0-4000 cm^{-1}
Scattering neutron energy	E_2	3 meV
Angle of incidence	θ	45°
Beam divergence	$\Delta\theta$	0.064 rad
Sample thickness	Δs	1 mm
Analyser thickness	Δa	2 mm
Detector thickness	Δd	2 mm
Pulse width	Δt	25, 50 μs

we obtain estimations of resolution at different energy transfer (see Fig. 10).

Comparing the resolution of the MAINS spectrometer with the resolutions of the TFXA spectrometer [3] operating at ISIS and designed on its base MODES

spectrometer [4] shows that the use of Li-glass detectors compensates for the differences in the widths of the thermal neutron pulses. The creation of a storage ring will allow a decrease in the thermal neutron pulse width. The substitution of the non-multiplying target by the multiplying one gives the possibility for a sufficient increase in the peak flux and consequently for enlargement of the first flight path without any intensity loss.

3.3 Sample environment

The sample environment of the MAINS spectrometer must contain the standard set of systems including "ORANGE" He-cryostats, a high pressure cell, closed cycle refrigerator. Thus will provide a wide range of possibilities for investigations of the crystal lattice dynamics of different substances, including high temperature superconductors, molecular crystals, non-ideal crystals and alloys.

4. Conclusion

The described MAINS spectrometer is designed for carring out investigations in condensed matter physics and gives possibilities to study the structure and dynamics of substances. Due to specific features of the device and of the IN-06 neutron source, the most straightforward directions of investigations with this spectrometer are the following:

◊ investigations of the vibration spectra of hydrogen containing materials;
◊ investigations of catalysis process;
◊ investigations of molecular crystals;
◊ investigations of the lattice dynamics of novel materials.

Improvement of the experimental data quality and widening the range of scientific problems demands the development of neutron source, precise inspection of the detector system of the spectrometer and the creation of an advanced software for treatment of experimental results.

5. Aknowledgements

The authors are grateful to Prof. V.L.Aksenov and Prof. Yu.Ya.Stavissky for their constant interest and help in this work, and, also, to G.D.Bokuchava for useful discussions.

6. References

[1] Proceedings of the ICANS-XII, RAL94-025, vol.2, T71, 1994.
[2] G.Baluka et al. Preprint of JINR, R13-84-242, 1984.
[3] J.Penfold and J.Tomkinson: Report RAL-86-019, Rutherford Appleton Laboratory, Chilton, UK, 1986.
[4] R.E.Hester, P.C.H.Mitchell, K.Prassides. Research proposal for MODES, EPSRC, Polaris House, November 1994.

ICANS XIII
13th Meeting of the International Collaboration on
Advanced Neutron Sources
October 11-14, 1995
Paul Scherrer Institut, 5232 Villigen PSI, Switzerland

Future Opportunities and Present Possibilities for Coherent Inelastic Single Crystal Measurements on Pulsed Neutron Sources

Mark Hagen [1], Uschi Steigenberger [2], Caterina Petrillo [3] and Francesco Sacchetti [3]

[1] Physics Department, University of Keele, UK
[2] ISIS Facility, Rutherford Appleton Laboratory, UK
[3] University of Perugia, Italy

This paper is available as **RAL Report RAL-95-006** and is accepted for publication in **Journal for Neutron Research.**

Pulsed Magnetic Fields and Pulsed Neutron Sources

Further information from this workshop which was held 29 - 30 June 1995 can be obtained from :

Uschi Steigenberger
ISIS Facility
Rutherford Appleton Laboratory
e-mail : USM@isise.rl.ac.uk

and

Keith McEwen
Department of Physics
Birkbeck College, London
e-mail : K.McEwen@physics.bbk.ac.uk

ICANS-XIII
13th Meeting of the International Collaboration on
Advanced Neutron Sources
October 11-14, 1995
Paul Scherrer Institut, 5232 Villigen PSI, Switzerland

TIME COLLIMATION FOR ELASTIC NEUTRON SCATTERING AT A PULSED SOURCE

V.L.Aksenov and Yu.V. Nikitenko

Frank Laboratory of Neutron Physics, JINR, 141980 Dubna, Moscow Region, Russia

ABSTRACT

Conditions for carrying out elastic neutron scattering experiments using the time-of-flight technique are considered. It is shown, that the employment of time dependent neutron beam collimation in the source-sample flight path increases the luminosity of the spectrometer under certain resolution restrictions. Time collimation modes are proposed for small-angle scattering and neutron reflection.

Introduction

A traditional design of the elastic neutron scattering spectrometer (Fig.1) implies angle collimation of the neutron beam on the source-sample flight path and detection of neutrons scattered at different angles. For fixed neutron wavelengths, which is the case for a steady-state neutron source, the dependence of the scattering cross-section on the q scattering vector is measured at a definite q resolution. At a pulsed neutron source, a wide range of neutron wavelengths is used, thus, making it possible to measure the scattering cross-section over an interval of scattering vector values an order of magnitude greater than at a steady-state source. At the same time, however, conditions of measurements on the scattering vector interval differ greatly. This implies that the ratio of the value for distortions of the scattering law (the scattering cross-section) to the statistical precision in measuring the scattering law greatly depends on the scattering vector. This, in fact, may be considered equal to a narrowing of the measuring interval with a given reliability.

At the same time, at pulsed neutron sources, the possibility exists of changing the neutron phase volume on the sample with time in the interval between power pulses of the neutron

source. In the present paper we propose changing the solid angle at which the neutron source is visible and the cross-section of the neutron beam on the sample with time (starting from the moment of initiation of the source pulse) following certain laws. This will be considered for three types of spectrometers: the small-angle diffusion scattering spectrometer, the small-angle diffractometer and the reflectometer.

2. Optimization criteria

We shall consider the optimization criteria at length for the small-angle scattering spectrometer. Figure 2 presents the scheme of the small-angle scattering spectrometer with axial geometry. The main functional elements of the spectrometer are: the first and the second diaphragms used for angle collimation of the incident beam, placed at distances of L_0 and L_0+L_1, respectively, from the source; the sample position (made coincident with the second diaphragm) and scattered neutron detector placed at a distance $L_0+L_1+L_2$ from the neutron source. The dependence of the scattering cross-section $d\sigma(q)/d\Omega$ (the scattering law is $F(q)$) on the scattering vector $q = 4\pi\sin(\theta/2)/\lambda$ is measured with the spectrometer, where λ is the neutron wavelength and θ is the scattering angle. For the intensity of the scattered beam, $J(\lambda,q)$, and the root-mean-square deviation, $\sigma_q(\lambda)$, the following relationships apply [1]:

$$J(\lambda,q) = j_0(\lambda)\, R_1^2R_2^2F(q)R\Delta R/L_1^2/L_2^2,$$

$$\sigma_q(\lambda) = \pi/\lambda((R_1/L_1)^2+R_2^2(1/L_1+1/L_2)^2+(\Delta R/L_2)^2/3+(R/L_2)^2(\Delta\lambda/\lambda)^2/3)^{1/2}, \quad (1)$$

where $j_0(\lambda)$ is the neutron flux before the first diaphragm, R_1 and R_2 are the radii of the first and second diaphragms, respectively, R and ΔR are the radius and width of the detecting element in the detector and $\Delta\lambda$ is the wavelength uncertainty.

The well-known approach in optimization [1,2] involves the achievement of maximum intensity at fixed values for the root-mean-square deviation of the scattering vector, the scattering vector itself, neutron wavelength and total flight path, L_1+L_2. This can be attained if the following relationships are satisfied [2]:

$$L_1 = L_2\,,\ R_1 = 2R_2 = (2/3)^{1/2}\Delta R = (2/3)^{1/2}R\Delta\lambda/\lambda. \quad (2)$$

Conditions should be stated, however, appropriate for the whole interval of scattering vector values. It is apparent that the scattering intensity should be represented in relation to the scattering vector [3]:

$$J = \int j_0(q)\ \Phi(q)\ dq, \quad (3)$$

where $j_0(q)$ is the scattering intensity at a definite value of q and unit value of scattering law, $\Phi(q)=\int F(q')R(q,q')dq'$ is the scattering law distorted by the resolution of scattering vector;

$R(q,q')$ is the resolution function. For $j_0(q)$ and $R(q,q')$ the following relationships should be satisfied:

$$j_0(q) = q \int j_s(\lambda)d\lambda \quad \text{and} \quad R(q,q') = \int R(q,q',\lambda)\, j_s(\lambda)\, d\lambda \,/\, \int j_s(\lambda)d\lambda, \qquad (4)$$

where $j_s(\lambda) = \lambda^2 R_1^2 R_2^2 j_0(\lambda)$, $R(q,q',\lambda)$ - resolution function at a definite value of λ, $\lambda_{max}=2R_{max}/qL_2$, $\lambda_{min}=2R_{min}/qL_2$ are the integration limits, R_{max} and R_{min} are the maximal and minimal radii of the detecting area of the detector.

We introduce a deviation of the scattering law $\delta F(q) = |(\Phi(q) - F(q))|$ and a root-mean-square deviation of the scattering law $\delta F_{st}(q)$, caused by the statistics of counting scattered neutrons. Now we can write the optimization conditions as follows:

$$A = \int \delta F(q) \,/\, F(q)\, dq = \text{const}$$

$$B = \int (\delta F_{st}(q) \,/\, \delta F(q))^2\, dq = \int (F(q)/\delta F(q)^2/(j_0(q)F(q))dq = \min \qquad (5)$$

Additional conditions are the fixed neutron spectrum and fixed wavelength interval, as well as measuring time, total neutron flight path and detector size. The relationship between the flight paths, $a=L_1/L_2$, and the relationship between the radii of the diaphragms in relation to time, starting from the moment of initiation of the pulse, $b(t)=R_1(t)/R_2(t)$, should be determined. Since the time of neutron flight from the source to the diaphragm is directly proportional to the neutron wavelength, $b(t)$ can be transformed to $b(\lambda)$.

3. Diffusion small-angle scattering

The resolution function in a certain approximation may be represented by a Gaussian [3] with a variance of the scattering vector, $D_q(q)$:

$$D_q(q) = \int \sigma_q^{-1}(\lambda) j_s(\lambda) d\lambda \,/\, \int \sigma_q^{-3}(\lambda) j_s(\lambda) d\lambda. \qquad (6)$$

In this case in the first approximation for the distortion of the scattering law, we obtain $\delta F(q) = 1/2 dF^2(q)/dq^2 D_q(q)$. Then we choose the approximations $\Delta R = 0$ and $\Delta\lambda = 0$, at which $\delta\sigma_q(\lambda)$ is inversely proportional to the neutron wavelength and it is possible under certain conditions to obtain an analytical solution. This takes place in practice and is realised for the case of high luminosity, when the resolution is determined only by the sizes of the neutron source and the sample. Let us next represent the diaphragm radii as $R_1 = R_{10}(\lambda/\lambda_{min})^n$ and $R_2 = R_{20}(\lambda/\lambda_{min})^n$. The problem can be formulated as follows: optimal values of the a,b and n parameters should be determined so that conditions (5) are fulfilled. To this end the equation $dB/dX = 0$, where $X = a,b,n$, should be satisfied. This gives us $a=1$ and $b=2$.

To determine the optimal value of the n parameter, numerical calculations should be made. Figure 3 presents the results of these calculations. When carrying out the calculations, the Maxwellian spectrum with a characteristic wavelength $\lambda_t = 1.8$ A was taken. The following parameter values were chosen: $L_1 = L_2 = 40$m, $R_{min} = 5$cm and $R_{max} = 50$cm. The wavelength interval 0.5 - 10A corresponds a scattering vector interval 0.0008 - 0.16A^{-1}. The dependence of parameter $\eta(n) = B(n=0)/B(n)$ for different scattering laws is given in Fig.3. From this figure we notice that for the 1/q law (curve 1) the maximum for $\eta(n)$ is achieved at n = -0.98. For the $\exp(-pq^2)$ law the maximum for $\eta(n)$ is at positive values of the n parameter (curves 2 and 3). As an illustration, Fig.4 shows the dependence $\delta F_{st}^2(q)/\delta F^2(q)$ for the scattering law $F(q) = \exp(-100(A^2)q^2)$ for n=0 and n=1/4. One can see that the curve 2 (n=1/4) runs integrally below curve 1 (n=0). We also notice that at large q the statisticaling accuracy decreases.

4. Neutron reflection

Figure 5 presents the scheme of the reflectometer. The neutron beam is incident on the sample at the θ angle of slide. Two diaphragms, placed in the ZX plane at distances L_1 and L_2 from the source, are used to collimate the beam. Suppose that in the X-axis direction the diaphragm sizes are considerably greater than in the Z-axis direction. Then for the variance of the scattering vector (reflection vector) we have ($\Delta\lambda$ is assumed to be 0):

$$D_q(q)= k^2 \cos^2(\theta)(z_1^2+ z_2^2)/3L_0^2, \qquad (7)$$

where k is the wave vector, z_1 and z_2 are the diaphragm sizes in the direction of the Z-axis, $L_0 = L_2 - L_1$.

The following relation holds for $j_0(q)$:

$$j_0(q) = j_0(\lambda)z_1(\lambda)x_1z_2(\lambda)x_2/ L_0^2/q^2 \quad , \qquad (8)$$

where x_1 and x_2 are the diaphragm sizes in the direction of the X-axis. Let us represent z_1 and z_2 as $z_1 = z_2 =z_0 (\lambda/\lambda_{min})^n$. Figure 6 gives the $\eta(n)$ dependence for different scattering laws at the angle of reflection $\theta = 6$ mrad and wavelength interval 0.7 - 10A. It can be seen that, as in the case of the small-angle spectrometer, the optimal n value may be either positive or negative depending on the type of scattering law.

5. Small-angle diffraction

Let us consider the case of small-angle powder diffractometry. In this connection we choose a diffractometer scheme identical to the scheme for small-angle diffusion scattering

(Fig.2). Depending on the scattering vector, the scattering law for the Bragg diffraction, as is well-known, is a delta-function. Therefore, the employment of conditions (5) presents difficulties. Because of this, let us formulate a simplified (though universally used) criteria:

$$C = \int \delta q(q)/q \, dq = \text{const} \quad \text{and} \quad E = \int j_0(q)\Phi(q)dq = \max \qquad (9)$$

The dependence $\delta q(q)/q$ for different values of the n parameter is given in Fig.7. Compared to the case when n = 0, at n = 1 $\delta q/q$ increases at small q and decreases at large q. At n = -1 the pattern of the $\delta q/q$ behaviour, compared to the case when n = 0, appears to be the reverse. From this it follows that if a higher resolution of reflexes at small (large) q is required, it is more preferable to use the power law of diaphragm radius variation with an exponent of n = -1 (n = 1). Figure 8 presents the dependence of the $\eta = E(n)/E(n = 0)$ parameter for the scattering law $F(q) = \sum_\tau \delta(q-q_\tau)$, where q_1=7.94E-04, q_2=8.16E-04, q_3=8.7E-4, q_4=1.0E-03, q_5=1.35E-03, q_6=2.2E-03, q_7=4.345E-03, q_8=9.7E-03, q_9=2.31E-02, q_{10} =5.65E-02. It is apparent that negative values of the n parameter are the most optimal for the ten reflexes given.

6. Conclusion

In the present paper the time-of-flight mode of neutron beam collimation on the source-sample flight path is considered. The calculations show that at a fixed distortion of the scattering law and following certain collimation laws, the statistical accuracy of measurements increases many-fold. The proposed operating regime for the elastic scattering spectrometers is rather simple to realise. Its use is the most effective at low-frequency pulsed sources where a broad wavelength interval is available. This method makes it possible to form an optimal (according to neutron wavelength) phase volume on the sample and it is suitable for both hot and cold neutron sources.

7. Acknowledgements

The authors are grateful to L. Cser and B.N. Savenko for usefull discussions and to T.V. Prikhodko and A. Shaeffer for preparing the English translation of this report.

8. References

[1] R.W. Hendricks, *J. Appl. Cryst.* 11 (1978) 15
[2] D.F.R. Mildner, J.M. Carpenter, *J. Appl. Cryst.* 17 (1984) 249
[3] D.F.R. Mildner, J.M. Carpenter and D.L. Worcester, *J. Appl. Cryst.* 19 (1986) 311.

$$V_{phase} = d^3p \times d^3r \propto \Omega \times S_{beam} / \lambda^3$$

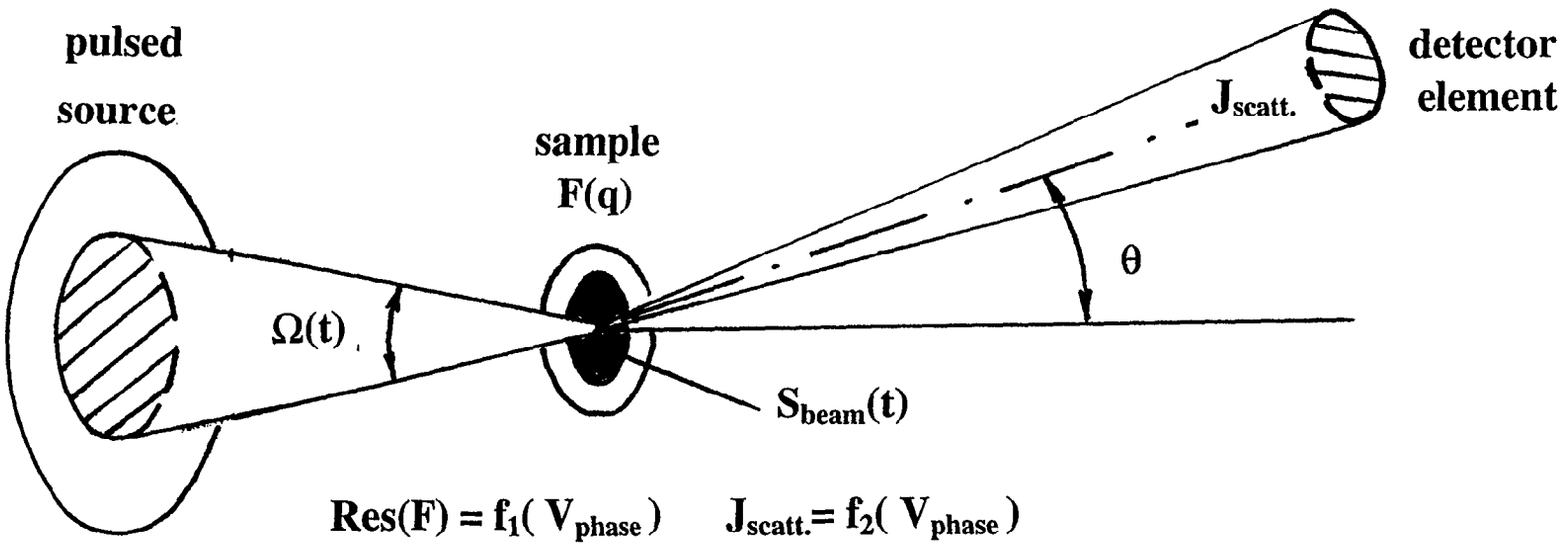

$$Res(F) = f_1(V_{phase}) \qquad J_{scatt.} = f_2(V_{phase})$$

$$V_{phase} \times \lambda^3 = f(t \propto \lambda)$$

Fig. 1. Layout of the elastic scattering neutron spectrometer with a time-of-flight collimation of the neutron beam;

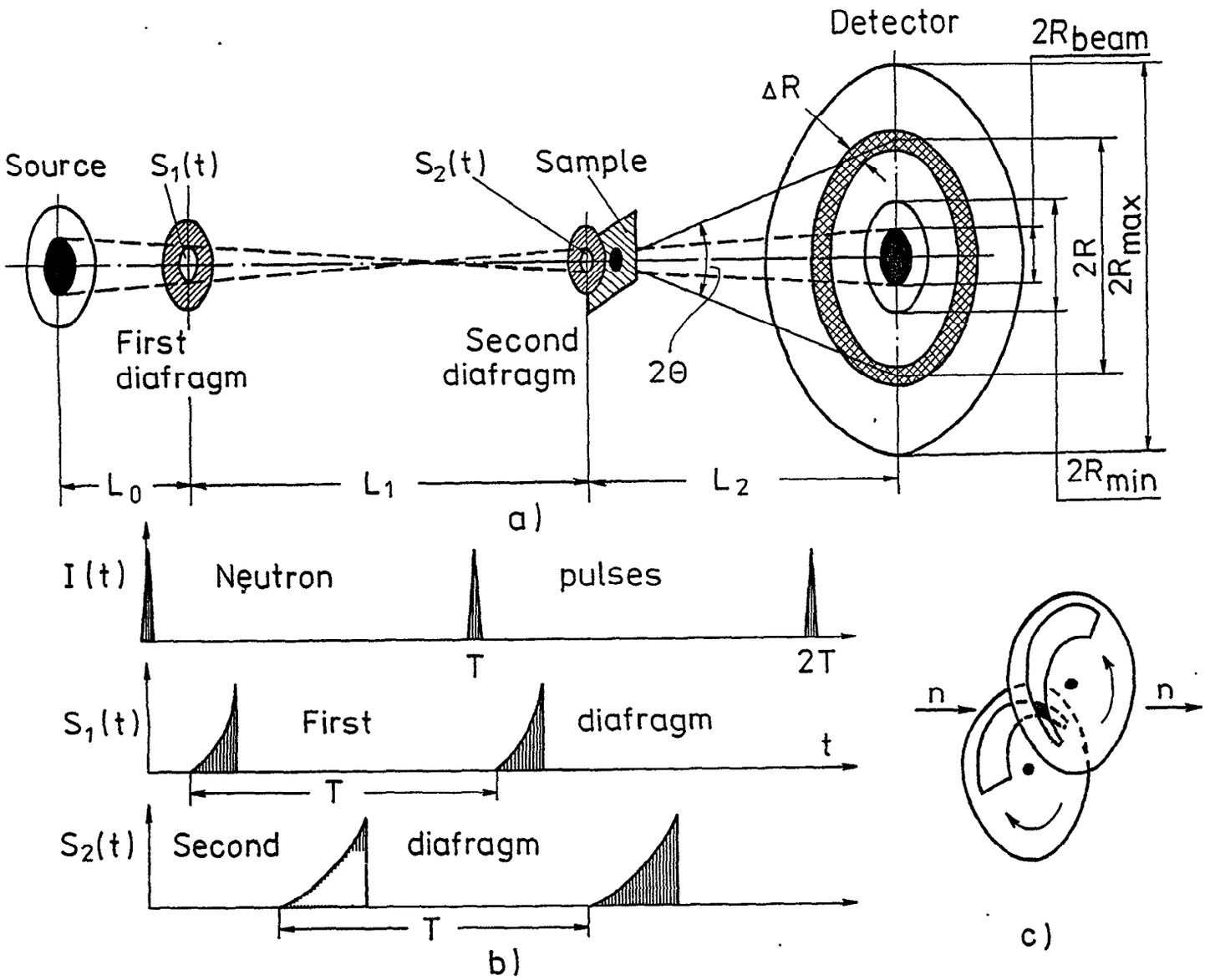

Fig. 2. a) Scheme of the small-angle neutron scattering spectrometer with a time-of-flight collimation of the neutron beam: two diaphragms on the flight path to the sample have an area of S1(t) and S2(t) which change with time starting from the moment of initiation of the source pulse;

b) time diagram which explains the operation of the spectrometer for the period T of recurring power pulses of the neutron source;

c) a possible version of the diaphragm design in the form of two disks made of absorbing neutron material, rotating at the frequency of the power pulses. Slots in the disks meet in mutually perpendicular directions;

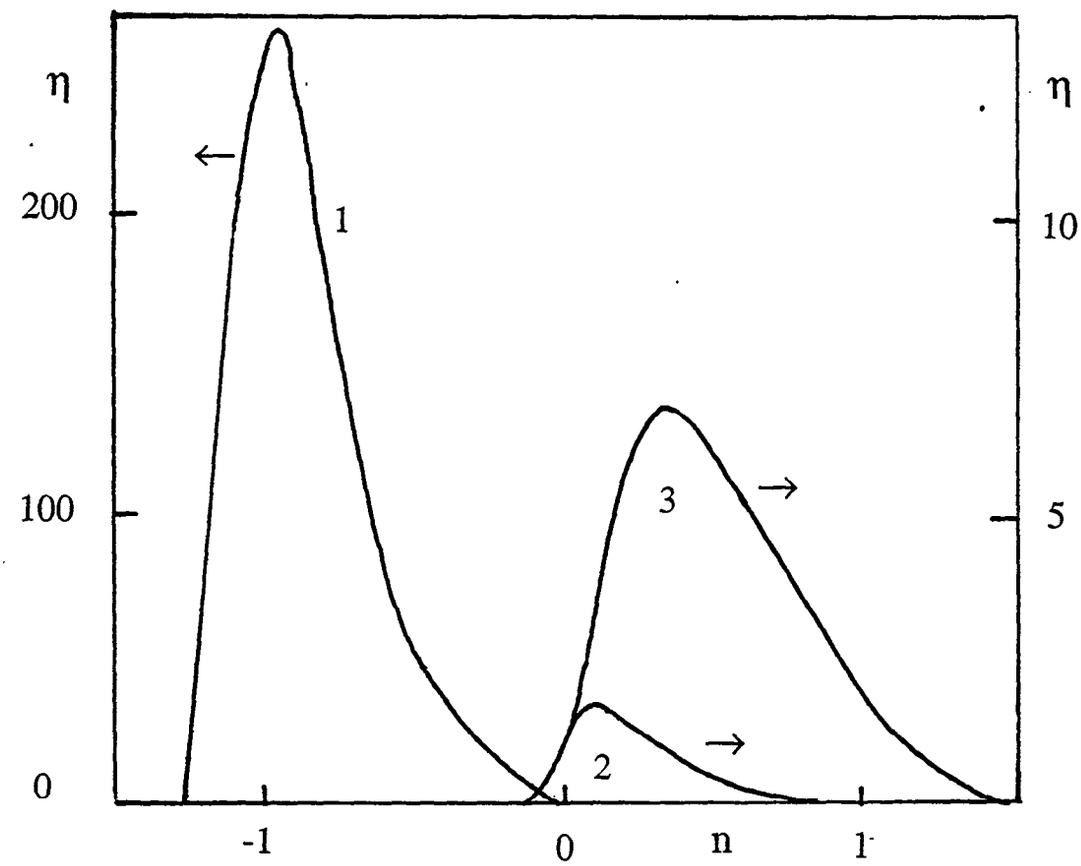

Fig. 3. Dependence of the η(n) parameter for different small-angle diffusion neutron scattering laws: F(q) = 1/q - curve 1; F(q) = exp(-pq^2) and p=10A^2 - curve 2, p=100A^2- curve 3;

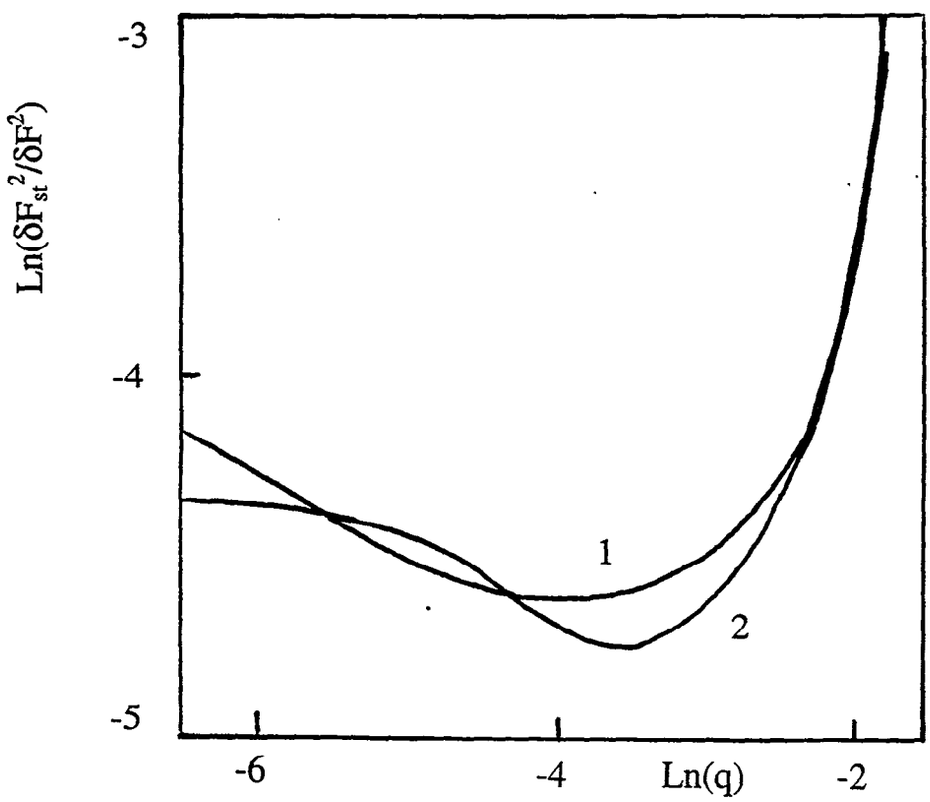

Fig. 4. Dependence of δF$^2_{st}$(q)/δF^2(q) for the scattering law F(q) = exp(-100q^2) at different values for the n parameter: 1- n=0; 2 - n=1/4;

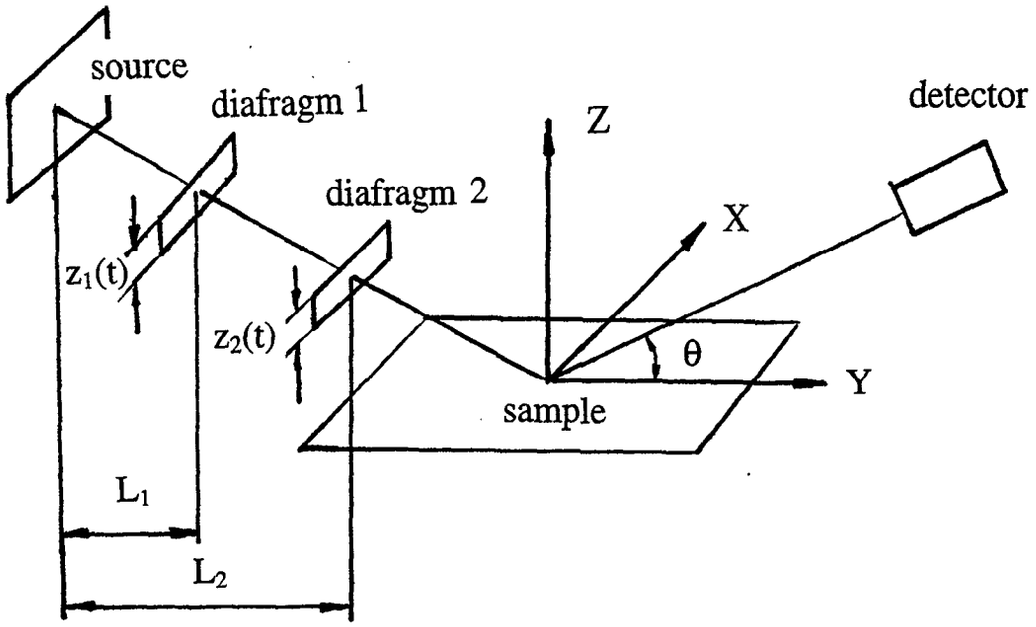

Fig. 5. Neutron reflectometer with a time-of-flight collimation of the neutron beam;

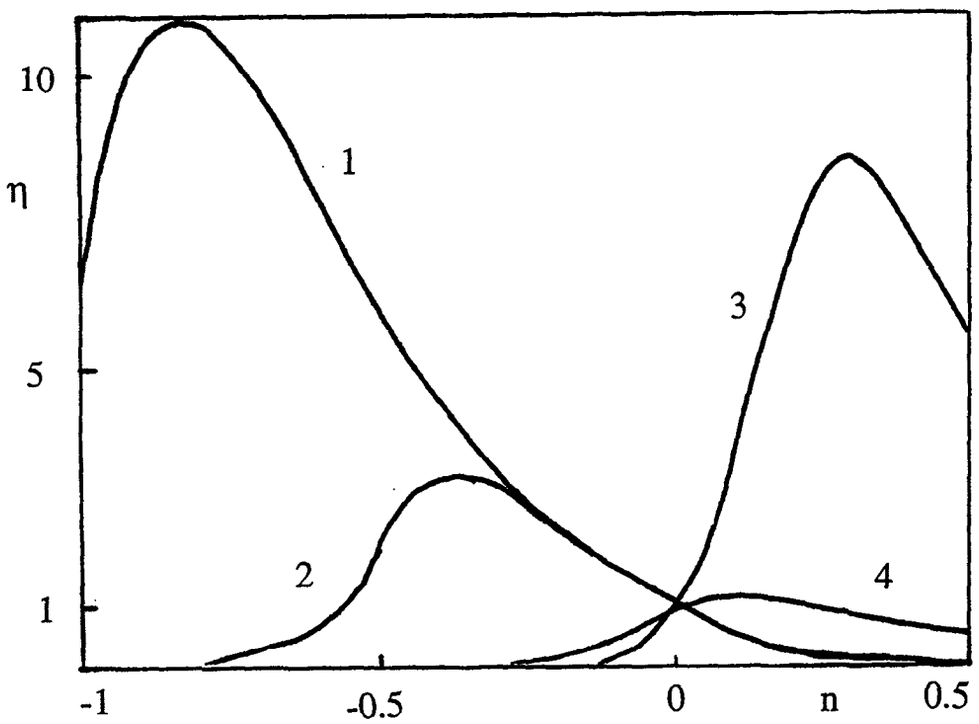

Fig. 6. Dependence of the η(n) parameter for different neutron reflection laws: $F(q) = q^{-4}$ - curve 1; $F(q) = q^{-1}$ - curve 2; $F(q) = \exp(-rq)$ and r = 50 A - curve 3, r = 100 A - curve 4;

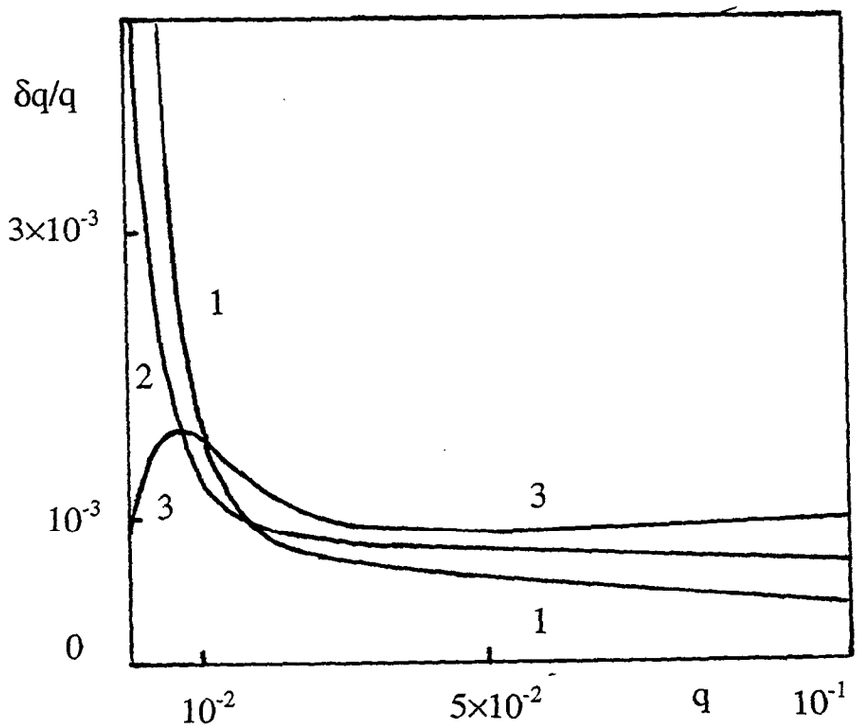

Fig. 7. Dependence of $\delta q(q)/q$ at different values of the n parameter: 1- n=1, 2 - n=0, 3 - n=-1;

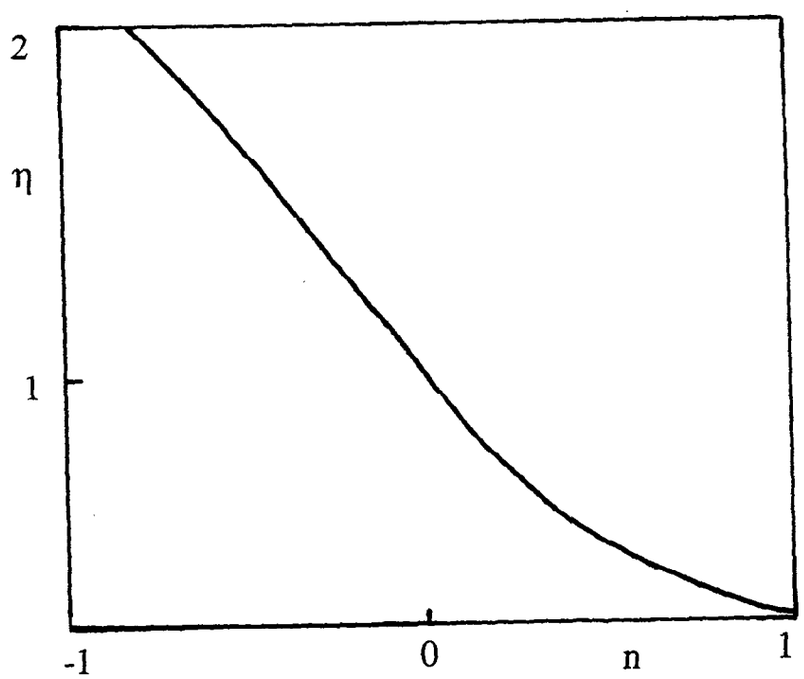

Fig. 8. Dependence of the $\eta=E(n)/E(n=0)$ parameter for the case of ten reflexes in the Bragg neutron diffraction.

ICANS-XIII
13th Meeting of the International Collaboration on
Advanced Neutron Sources
October 11-14, 1995
Paul Scherrer Institut, 5232 Villigen PSI, Switzerland

DECONVOLUTING SOURCE PULSE BROADENING IN PULSED SOURCE TIME-OF-FLIGHT MEASUREMENTS

John M. Carpenter

Intense Pulsed Neutron Source, Argonne National Laboratory
Argonne, IL 60439, USA

ABSTRACT

This paper describes the development of closed form expressions for deconvoluting several types of source pulse broadening, that due to double pulses, and those due to square-wave, triangular, and parabolic-shaped source pulses.

1. Introduction

An option exists within synchrotron design for first harmonic (h=1) or second harmonic (h=2) design. With h=1, single pulses will be delivered to the target at the system cycling frequency; with h=2, two pulses will be delivered per machine cycle, each of which would be narrower than the single h=1 pulse, but separated in time such that together the two pulses represent a broader pulse than that for h=1. The question is, which is more desirable from the standpoint of use by time-of-flight neutron scattering instruments. By way of background, operating pulsed spallation sources IPNS, KENS and LANSCE operate with single pulses, while ISIS operates in the double-pulse mode.

Narrow pulses are desirable from the point of view of instrument resolution; this makes a difference only in the range of higher neutron energies where the moderated pulse is intrinsically narrow. However, not to be ignored is that even for low neutron energies, the rising side of the pulse is quite sharp even though the falling side descends slowly from the peak. Therefore, judgments need to be made which respect the impact of proton pulse shape on the rise time of the moderated pulse, not simply on the basis of overall pulse width, since in this sense the shape of the proton pulse affects spectroscopy using even modestly low energy neutrons.

The general problem is one of deconvoluting broadening effects from measured data. Here, there are two effects to deal with, broadening due to the double pulse and broadening due to the time structure of individual pulses. The mathematical treatments of the two effects are similar, but the latter is substantially more complicated than the former. This paper draws no universal conclusions, however, the results can be used either to model specific cases or to perform model-independent deconvolutions of data. In this last sense, the results are complementary to maximum-entropy treatments.

The submitted manuscript has been authored by a contractor of the U. S. Government under contract No. W-31-109-ENG-38. Accordingly, the U. S. Government retains a nonexclusive, royalty-free license to publish or reproduce the published form of this contribution, or allow others to do so, for U. S. Government purposes.

Keywords: Deconvolution, Pulse broadening, Data treatment, Accelerator design

2. The General Problem

Say $C(t)$ is the observed counting rate at time t, $I(t)$ is the proton current at time t, $M(t)$ is the neutron current from the moderator at time t per unit of proton charge at time 0, and $R(t)$ is the counting rate in the detector of an instrument at time t after a neutron emerges from the moderator at time 0. Then, suppressing reference to certain details,

$$C(t) = I(t)*M(t)*R(t) \quad , \qquad (1)$$

where * represents convolution in time,

$$f(t) = g(t)*h(t) = \int_0^t g(\tau)h(t-\tau)d\tau \quad . \qquad (2)$$

3. The Double Pulse Problem

Say protons appear as pairs of pulses of the same shape,

$$I(t) = i(t) + \alpha i(t-\delta) = H(\alpha,\delta;t)*i(t) \quad , \qquad (3)$$

where $i(t)$ describes the intensity distribution of one pulse, δ is the time delay between the first and the second pulses, and α is the ratio of the total charge in the second pulse to that in the first pulse. α and δ are known. $H(\alpha,\delta;t)$ is the double pulse function

$$H(\alpha,\delta;t) = \Delta(t) + \alpha\Delta(t-\delta) \qquad (4)$$

where $\Delta(x)$ is the Dirac delta function. (One expects $\alpha \approx 1$ but we carry $\alpha \neq 1$ for generality.) With appropriate definition of the time scale, causality arguments require $i(t) = I(t) = C(t) = M(t) = R(t) = 0$ for $t < 0$. All functions are well behaved for large t.

The response to a single pulse can be derived exactly from the response observed to the double pulse, for which we can write

$$C(t) = c(t) + \alpha c(t-\delta) = H(\alpha,\delta;t)*c(t) \quad , \qquad (5)$$

where $c(t)$ is the response to a single pulse

$$c(t) = i(t)*M(t)*R(t) \qquad (6)$$

and $c(t) = 0$ for $t < 0$. Equation (5) is a "difference equation"

$$c(t) = \left\{ \begin{array}{ll} C(t); & 0 < t \leq \delta \\ C(t) - \alpha c(t-\delta); & t > \delta \end{array} \right\}. \qquad (7)$$

Thus $c(t)$ can be calculated sequentially starting from $t=0$, and could be computed and stored on the fly during measurement if desired. A closed form result for $c(t)$ in terms of

$C(t)$ can be derived trivially by induction from iterative use of (7) for sequential ranges of t, or elegantly by Laplace transform techniques[1]

$$c(t) = \sum_{n=0}^{[t/\delta]} (-\alpha)^n C(t-n\delta) \quad , \qquad (8)$$

where $[t/\delta]$ is the greatest integer less than or equal to t/δ (e. g. $[1.9] = 1$). The result can also be expressed as a convolution in terms of a resolvent kernel

$$H^{-1}(\alpha,\delta;\tau) = \sum_{n=0}^{\infty} (-\alpha)^n \Delta(\tau-n\delta) \quad . \qquad (9)$$

Then

$$c(t) = \int_0^t H^{-1}(\alpha,\delta;\tau)C(t-\tau)d\tau \quad . \qquad (10)$$

The figure illustrates the situation for $\delta < t < 2\delta$.

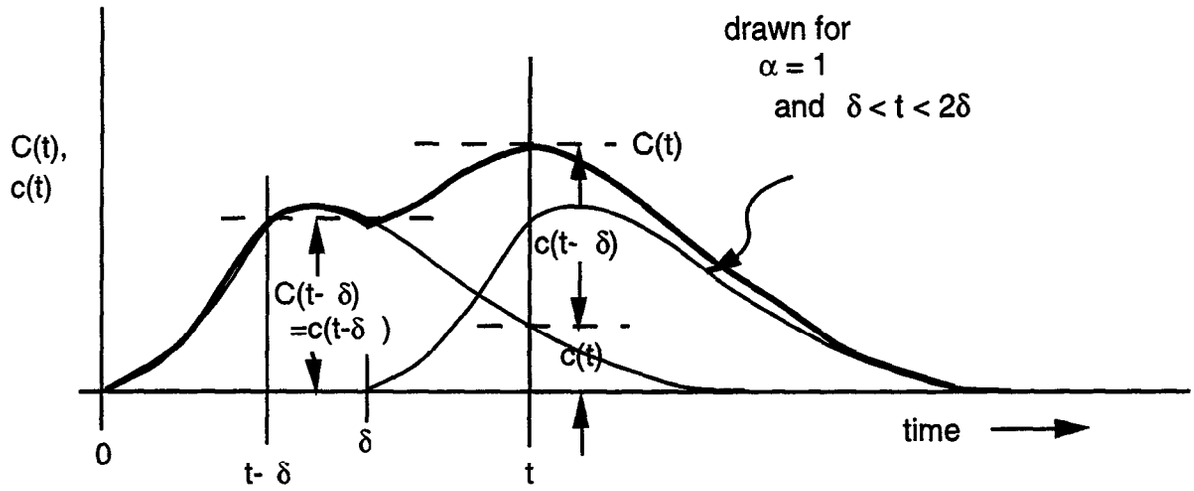

The equations recorded so far are relationships among the expected values of measured functions. The measured values are subject to uncertainties, that is, they are statistically distributed quantities, but the expected-value relationships are always used to extract results from data. Assuming time binning on small time intervals so that t represents a discrete variable, then the statistical distribution of $C(t)$ for any time t is independent of the distribution of $C(t')$ for any other time $t' \neq t$. In particular, the distributions of the $C(t)$ are independent, Poisson-distributed counting errors. Extracted results $c(t)$ are also statistically distributed quantities but these typically have correlated errors. It will be necessary to deal with the results in these terms in order to come to conclusions concerning the effects of the double pulse and of the single pulse broadening of experimental results.

4. Pulse Shape Broadening

Now what can be said about the general problem of broadening due to the shape of the proton pulse $i(t)$? Recall

$$c(t) = i(t)*P(t) \quad , \qquad (6)$$

where we define

$$P(t) = M(t)*R(t) \quad . \qquad (11)$$

The object is to recover $P(t)$. Equation (6) is just an integral equation for $P(t)$, whose solution we seek. Such equations are Volterra integral equations of the first kind, with the special property that the kernel is a function of the difference between the inner and outer variables. Thus they are of the form of "faltung" (folding) integrals, formally amenable to solution by Laplace transform methods. The Laplace transform of (6) is

$$\tilde{c}(s) = \tilde{i}(s)\tilde{P}(s) \qquad (12)$$

where $\tilde{f}(s)$ is the Laplace transform of a function $f(t)$,

$$\tilde{f}(s) \equiv \int_0^\infty e^{-st} f(t)dt \quad . \qquad (13)$$

Then

$$\tilde{P}(s) = \frac{\tilde{c}(s)}{\tilde{i}(s)}, \qquad (14)$$

where ordinary division of functions is implied. Finally, formally, the result is the convolution, a faltung integral,

$$P(t) = i^{-1}(t)*c(t) \quad , \qquad (15)$$

where $i^{-1}(t)$ is the inverse Laplace transform of $\frac{1}{\tilde{i}(s)}$. $i^{-1}(t)$ may not be a well-behaved function but is expected to be an integrable density distribution. It turns out that this leads to problems in real cases such that it is not possible to express results in the form (15). In view of these complications of the Laplace inversion, we won't get much further without becoming specific about $i(t)$. Consider several cases, progressively more realistic.

4.1 Top Hat Distribution

$$i(t) = \frac{Q}{2b}\begin{Bmatrix} 1; & 0 \le t \le 2b, \\ 0; & t < 0, t > 2b \end{Bmatrix}, \qquad (16)$$

$$\tilde{i}(s) = Q\, e^{-sb} \left(\frac{\sinh(sb)}{sb}\right). \qquad (17)$$

4.2 Triangular Distribution

$$i(t) = \frac{Q}{2b}\left\{\begin{array}{ll} 1 - \left|\frac{t-2b}{2b}\right|; & 0 \le |t-2b| \le 2b \\ 0; & |t-2b| > 2b \end{array}\right\}, \qquad (18)$$

which is just (16) convoluted with itself. The transform

$$\tilde{i}(s) = Q\, e^{-2sb} \left(\frac{\sinh(sb)}{sb}\right)^2, \qquad (19)$$

is the square of (17). Having found the inversion function for the top hat distribution, the solution for the triangular distribution only involves convoluting the same function into itself, therefore we do not treat this case at any further length.

4.3 Parabolic Distribution

$$i(t) = \frac{3Q}{2b}\left\{\begin{array}{ll} 1 - \left(\frac{t-b/2}{b/2}\right)^2; & 0 \le t \le b \\ 0; & |t-b| > b \end{array}\right\} \qquad (20)$$

$$\tilde{i}(s) = 12Q\, e^{-sb/2} \left(\frac{(sb)\cosh(sb/2) - 2\sinh(sb/2)}{(sb)^3}\right). \qquad (21)$$

5. Worked Examples

5.1 The Top Hat Distribution

Taking the relatively simple top hat distribution as an example, the Laplace inversion of $\frac{1}{\tilde{i}(s)}$ gives

$$i^{-1}(t) = \frac{b}{Q}\int_{\gamma - i\infty}^{\gamma + i\infty} e^{st}\frac{se^{sb}}{\sinh sb}\, ds \qquad (22)$$

in which the integral is closed in the left half of the complex s-plane (standard Laplace transform theory.) A problem becomes clear, in that the integrand of (22) does not have the properties usually required of a Laplace transform; it is of order $|s|$ as $|s|$ becomes large, while, in order that it represent the transform of a well-behaved function, it must decrease more rapidly than $|s|^{-1}$ in that limit. Consequently any results gleaned from a formal pursuit of the inversion cannot be guaranteed.

We can obtain a result by differentiating the original equation, so that the top hat problem reduces to a particularly simple and familiar form; if $t > b$,

$$c(t) = \int_0^t i(\tau)P(t-\tau)\,d\tau = \frac{Q}{b}\int_0^b P(t-\tau)\,d\tau = \frac{Q}{b}\int_{t-b}^t P(u)\,du \qquad (23)$$

$$c'(t) \equiv \frac{dc(t)}{dt} = \frac{Q}{b}\left[P(t) - P(t-b)\right] \qquad (24)$$

and if $t < b$

$$c'(t) = \frac{Q}{b}P(t)\,. \qquad (25)$$

This is of the same form as the two pulse problem with $\alpha = -1$ and $\delta = b$ and the answer is of the same form,

$$P(t) = \frac{b}{Q}\sum_{n=0}^{[t/b]} c'(t-nb) \qquad (26)$$

although it involves the derivative $c'(t)$ rather than the function $c(t)$.

5.2 The Parabolic Distribution

The parabolic distribution (18) is a realistic description of the pulse broadening. Differentiation reduces the original problem to a simpler equation, but we are forced to more elegant methods than used above to obtain a result. We have

$$c'(t) = \int_0^t i'(t-\tau)P(\tau)d\tau \qquad (27)$$

where

$$i'(t) = 12\,\frac{Q}{b^3}\left\{\begin{array}{ll} (b/2 - t); & 0 \le t \le b \\ 0; & t > b \end{array}\right\}. \qquad (28)$$

Twice more differentiating gives a difference-differential equation with constant coefficients that is tractable by Laplace transform methods

$$c'''(t) = 6\,\frac{Q}{b^2}\left[P'(t) + P'(t-b) - 2\,\frac{}{b}\left(P(t) - P(t-b)\right)\right]. \qquad (29)$$

Since $P(-b) = P(0) = 0$, Laplace transformation gives

$$\widetilde{c'''}(s) = 12\,\frac{Q}{b^3}\left(\frac{sb}{2}(1 + e^{-sb}) - (1 - e^{-sb})\right)\tilde{P}(s)$$

$$\widetilde{c'''}(s) = 24\,\frac{Q}{b^3}e^{-sb/2}\left(\frac{sb}{2}\cosh sb/2 - \sinh sb/2\right)\tilde{P}(s)\,, \qquad (30)$$

familiar from (21). Thus

$$\tilde{P}(s) = \frac{b^3}{24Q} \frac{e^{sb/2}}{\left(\frac{sb}{2} \cosh sb/2 - \sinh sb/2 \right)} \widetilde{c'''}(s) \ . \tag{31}$$

Inverting (32) as is leads to a slowly converging Fourier series which is difficult to recognize. However, the Laplace transform is similar to ones found in some problems of one dimensional heat flow[2] where a suggestive trick is used that produces a <u>closed form</u> result when we apply it here.

Write

$$\frac{e^z}{\left(z \cosh z - \sinh z \right)} = \frac{2e^z}{(z-1)(1 + \frac{z+1}{z-1} e^{-z})} \tag{32}$$

which for large $Re\ z$, as required of the Laplace inversion, can be expanded

$$\frac{e^z}{\left(z \cosh z - \sinh z \right)} = \frac{2e^z}{z-1} \sum_{n=0}^{\infty} (-1)^n \left(\frac{z+1}{z-1}\right)^n e^{-nz} \ . \tag{33}$$

Then the Laplace inversion becomes

$$f(b;t) = \frac{4}{b} \int_{\gamma - i\infty}^{\gamma + i\infty} e^{\frac{2t}{b}z} \frac{e^z}{\left(z \cosh z - \sinh z \right)} dz =$$

$$= \frac{4}{b} \sum_{n=0}^{\infty} (-1)^n \int_{\gamma - i\infty}^{\gamma + i\infty} e^{\frac{2t}{b}z} \frac{(z+1)^n}{(z-1)^{n+1}} e^{-(n-1)z} dz \ . \tag{34}$$

With the substitution $z \rightarrow z + 1$ this becomes

$$= \frac{4}{b} \sum_{n=0}^{\infty} (-1)^n e^{\frac{2t}{b} - (n-1)} \int_{\gamma' - i\infty}^{\gamma' + i\infty} e^{\left(\frac{2t}{b} - (n-1)\right)z} \left(\frac{(z+2)^n}{z^{n+1}} \right) dz \ .$$

(35)

Expanding the numerator

$$= \frac{4}{b}\sum_{n=0}^{\infty}(-1)^n e^{\frac{2t}{b}-(n-1)}\sum_{k=0}^{n}\binom{n}{k}2^{n-k}\int_{\gamma'-i\infty}^{\gamma'+i\infty} e^{\left(\frac{2t}{b}-(n-1)\right)z}\left(\frac{1}{z^{k+1}}\right)dz\ ,$$

(36)

where $\binom{n}{k}$ is the binomial coefficient, leaves the simple inversion integral

$$\int_{\gamma'-i\infty}^{\gamma'+i\infty} e^{z\tau}\left(\frac{1}{z^{k+1}}\right)dz = \left\{\begin{array}{c}\tau^k/k!\ ;\ \tau \geq 0\\ 0\ ;\ \tau < 0\end{array}\right\} \equiv U(\tau)\tau^k/k! \qquad (37)$$

so that

$$f(b;t) = \frac{4}{b}\sum_{n=0}^{\infty}(-1)^n e^{\frac{2t}{b}-(n-1)}\ U\left(\frac{2t}{b}-(n-1)\right)\ \sum_{k=0}^{n}\binom{n}{k}2^{n-k}\left(\frac{2t}{b}-(n-1)\right)^k/k!\ . \quad (38)$$

The result is not as horrifying as it might at first seem, since the step function (37) limits the otherwise-infinite n-sum to a maximum $n \leq 2t/b + 1$, while the k-sum is only a finite series. Thus, finally,

$$f(b;t) = \frac{4}{b}\sum_{n=0}^{[2t/b+1]}(-1)^n 2^n e^{2t/b-(n-1)}\ \sum_{k=0}^{n}\frac{1}{k!}\binom{n}{k}\left(\frac{2t/b-(n-1)}{2}\right)^k . \quad (39)$$

This result enables deconvolution of the parabolic pulse broadening from measured data,

$$P(t) = f(b;t)*c'''(t) = \int_0^t f(b;\tau)c'''(t-\tau)d\tau\ . \qquad (40)$$

6. The Derivatives

The results above involve derivatives of observed data, $C'(t)$, $c'(t)$, and $c'''(t)$ which arise naturally when they refer to functions of the continuous variable. However, we refer to measured, binned data, that is, functions of a discrete variable so that, strictly, derivatives do not exist. However, finite differences of discrete data can represent derivatives as can derivatives of fitted functions. Say time binning is on equispaced intervals ε. Then, for example, the central finite difference representation of the derivative $c'(t)$ for interval t is

$$c'(t) = \frac{1}{2\varepsilon}\left(c(t+\varepsilon) - c(t-\varepsilon)\right) \qquad (41)$$

and of the third derivative $c'''(t)$ is

$$c'''(t) = \frac{1}{(2\varepsilon)^3}\left(c(t+3\varepsilon) - 3c(t+\varepsilon) + 3c(t-\varepsilon) - c(t-3\varepsilon)\right), \qquad (42)$$

which are linearly related to the $c(t)$. Similarly, the derivatives could be represented in terms of the coefficients of an unweighted sliding cubic polynomial fit to the nearby data,

$$c(t) = a_0 + a_1 t + a_2 t^2 + a_3 t^3 \quad , \tag{43}$$

$$c'(t) = a_1 \ , c'''(t) = 6a_3 \quad , \tag{44}$$

which lead to forms similar to (41) and (42), in general, for the nth derivative,

$$c^{(n)}(t) = \sum_{t'} d^{(n)} c(t - t') \quad , \tag{45}$$

where the $d^{(n)}$s are constants which, with the range of summation depend on the specific choice of method of differentiation. Formally, at least, we can connect such methods of differentiation into the results above, in terms of differentiation operators

$$D^{(n)}(t) \equiv \sum_{t'} d^{(n)} \Delta(t - t') \tag{46}$$

so that

$$c^{(n)}(t) = \int_0^\infty D^{(n)}(t-\tau) c(\tau)\, d\tau \quad . \tag{47}$$

7. Assembling the Results

From (40)

$$P(t) = \int_0^t f(b;\tau) c'''(t-\tau) d\tau \quad = \int_0^t f(b;\tau) \int_0^\infty D^{(3)}(t-\tau-\tau') c(\tau')\, d\tau d\tau'$$

$$= \int_0^\infty \left[\int_0^t f(b;\tau)\, D^{(3)}(t-\tau-\tau') d\tau \right] c(\tau')\, d\tau' \, . \tag{48}$$

Using this result, put in finite-interval form, it is possible to model the effects of recovering the desired function $P(t)$ from data $c(t)$ or similarly from $C(t)$ for different model functions representing different classes of measurements. That exercise remains to be done, but the results here provide the basis for that work.

8. References

[1] A. Erdélyi, W. Magnus, F. Oberhettinger, and F. G. Tricomi, Tables of Integral Transforms, McGraw-Hill, New York, 1954. Volume 1, page 243, line 22.

[2] H. S. Carslaw and J. C. Jaeger, Conduction of Heat in Solids, Second Edition, Oxford University Press, 1986. See § 3.10, § 9.4, esp. §12.5 IV.

ICANS-XIII
13th Meeting of the International Collaboration on
Advanced Neutron Sources
October 11-14, 1995
Paul Scherrer Institut, 5232 Villigen PSI, Switzerland

IMPROVEMENTS IN RESOLUTION CALCULATION FOR TRIPLE AXIS AND TIME-OF-FLIGHT

W. Schmidt [1,3], H. Tietze-Jaensch [2,3], R. Geick [4], G.Will [5], H. Grimm [3]

1) Institute Laue Langevin, BP 156, 38042 Grenoble, France
2) Rutherford Appleton Laboratory, ISIS Facility, Chilton OX11 0QX, UK
3) KFA Forschungszentrum Jülich, IFF, 52425 Jülich, Germany
4) Universität Würzburg, Physikalisches Institut, Am Hubland, 97074 Würzburg, Germany
5) Universität Bonn, Mineralogisches Institut, Poppelsdorfer Schloß, 53115 Bonn, Germany

ABSTRACT

In the calculation of the resolution function for a neutron spectrometer the scattering probabilities for the various components (moderator, monochromator, sample, etc.) are usually described separately by Gaussian functions. We will show how to extend the resolution calculation to non-Gaussian (e.g. asymmetric) probability functions. In addition, we present a refinement of the formalism by including the mutual dependencies between the probability functions of different components. These improvements can be applied both on triple-axis and time-of-flight instruments. As an example the procedure will be discussed on the resolution function of a diffractometer at a pulsed source (ROTAX-Diff. at ISIS). In particular we will focus on the treatment of the asymmetric time distribution of the methane moderator, leading to asymmetric peak shapes in the measured spectra.

1.) Introduction

Browsing through publications concerning resolution calculation of neutron spectrometers it is common sense that all probability distributions are approximated by Gaussian functions. In most cases this approximation is quite sufficient if not accurate. In some cases, however, it is not appropriate at all. The well defined edges of diaphragms or detector channels or the sample itself are examples of rectangular distributions, poorly approximated by Gaussian functions. Further we must deal with asymmetric functions like the temporal distributions of the incoming neutrons on a pulsed source arising from the properties of the moderator. A correct treatment of the asymmetry is crucial in the time-of-flight analysis of the measured peaks. In this paper we will present some ideas how to use non-Gaussian functions in the resolution function so that the calculation can still be carried out analytically. These calculations are mainly based on the use of the error-function erf(x) and Gaussian expansion. The latter has been used successfully for the description of Lorentzians in an analytical 4d-convolution [1].
Further we will show a refinement in the algorithm of resolution calculation. All probability distributions (Gaussian or non-Gaussian) will be expressed in terms of the basic coordinates in space and time of the various components of the spectrometer. In the process of integration over these variables all

Keywords: resolution function, triple-axis, time-of-flight

mutual dependencies between different distributions (i.e. different probability functions contain the same variable) are automatically included.
As a first step we have carried out this algorithm for ROTAX-Diff. [2,3], a diffractometer at the pulsed source ISIS, including the asymmetric pulse shape of the moderator. The principles of this calculation can be well demonstrated on this comparatively simple example. A comparison with experimental results as well as more complicated calculations for the ROTAX-spectrometer and triple-axis instruments including focusing techniques are in progress.

2.) Non-Gaussian distributions

For this subject we will demonstrate the analytic treatment of non-Gaussian functions in the resolution calculation. Two different methods will be discussed: Gaussian expansion and the use of the error-function erf(x). As examples we have chosen rectangular distributions and, as an asymmetric case, the moderator time structure on a pulsed source. In addition, a Gaussian expansion for $\exp(-x^4)$-terms is shown as well.

a) Rectangular distributions

For the definition of these function we use the unit-step function $\theta(x)$:

$$\theta(x) := \begin{cases} 1, x \geq 0 \\ 0, x < 0 \end{cases} \tag{1}$$

A rectangular distribution *w(x)* is then created by:

$$w(x) := \theta(x+1) - \theta(x-1) \tag{2}$$

Many components can be described by this function, like the shape of sample or analyser or detector channels. A rectangular sample with the dimensions *a* and *b* then reads:

$$p_S(x,y) = w(2x/a) \cdot w(2y/b) \tag{3}$$

i) Use of erf(x)

For further mathematical treatment it is much more convenient not to use this discontinuous function but to deal with the continuous error-function:

$$w\left(\frac{x}{a}\right) = \frac{1}{2} \lim_{\varepsilon \to 0} \left[\operatorname{erf}\left(\frac{x+a}{\varepsilon}\right) - \operatorname{erf}\left(\frac{x-a}{\varepsilon}\right) \right] \tag{4}$$

Products of these functions can be expressed as sums:

$$\lim_{\varepsilon\to 0}\left[\operatorname{erf}\left(\frac{x-a_1}{\varepsilon}\right)\cdot\operatorname{erf}\left(\frac{x-a_2}{\varepsilon}\right)\right]=\lim_{\varepsilon\to 0}\left[\operatorname{erf}\left(\frac{x-a_1}{\varepsilon}\right)-\operatorname{erf}\left(\frac{x-a_2}{\varepsilon}\right)\right]\cdot\operatorname{erf}\left(\frac{a_1-a_2}{\varepsilon}\right)+1 \tag{5}$$

Together with Gaussian distributions we end up with single products of these two kinds of functions. Therefore we have to deal with integrals of the following type, easily solved analytically:

$$\int_{-\infty}^{\infty}\exp\left(-a^2x^2\right)\cdot\operatorname{erf}(b\pm x)\,dx=\frac{\sqrt{\pi}}{a}\cdot\operatorname{erf}\left(\frac{ab}{\sqrt{a^2+1}}\right) \tag{6}$$

ii) Gaussian expansion

With this method we approximately describe an (almost) arbitrary function by a sum of Gaussians. Fitting parameters can be height, width and centre of the Gaussians. In most cases restrictions will be made on the parameters to simplify the fitting procedure. For a function like $p_S(x,y)$ we use equidistant 2-dimensional Gaussians of the same height. This restriction drastically simplifies the calculation of the parameters with little loss of accuracy. Fig.1 shows a plot of a rectangular structure approximated by 3x10 Gaussians.

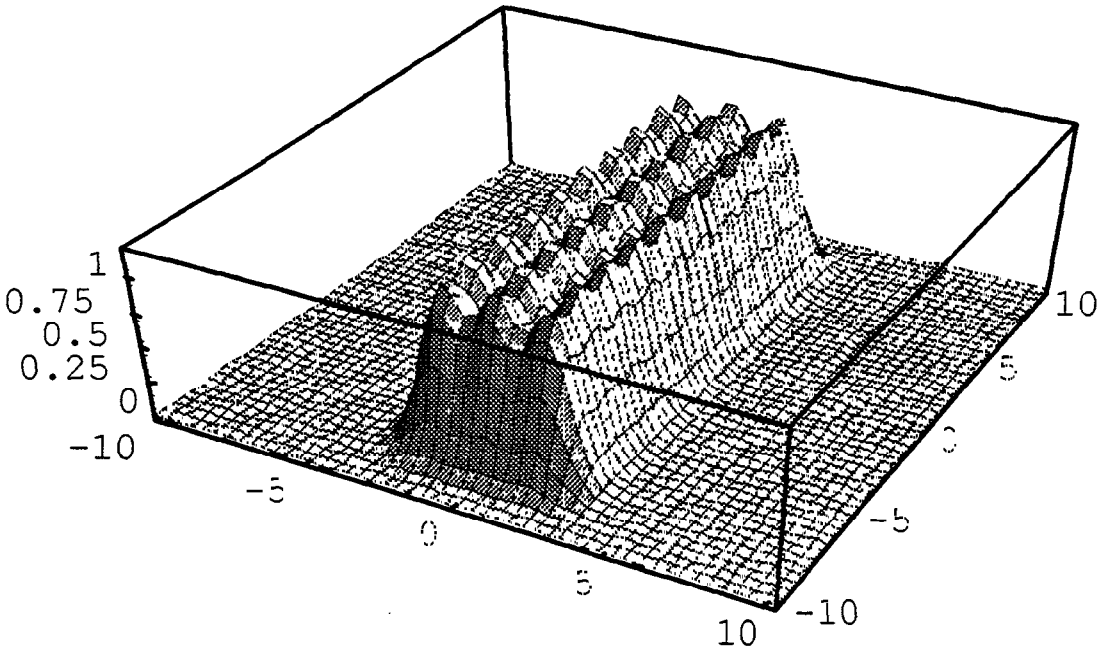

*Fig1: Gaussian expansion for a 2-dim. rectangular distribution with 3*10 peaks*

The equation for this approximation reads

$$w(2x/a)\cdot w(2y/b)\approx A\cdot\sum_{i=1}^{m}\exp\left[-\mu_1^2\cdot(x-x_i)^2\right]\cdot\sum_{j=1}^{n}\exp\left[-\mu_2^2\cdot(y-y_j)^2\right] \tag{7}$$

with

$$x_i = x_0 + i \cdot \Delta x; \quad y_j = y_0 + j \cdot \Delta y \tag{8}$$

From symmetry considerations the final number of parameters can be further reduced to five. They can be determined in general, only depending on n and m, by non-linear least-square methods.

b) Moderator Time Structure

For a mathematical model of these type of functions we follow the guidelines given in [4]. For the methane moderator at the spallation source ISIS we end up with the following equation:

$$\begin{aligned} p_M(\Delta t_M) = & \left[2\tau_1 R + 2\tau_2(1-R)\right]^{-1} \cdot \left[R \cdot \exp\left(\kappa_1^2 - \Delta t_M / \tau_1\right) \cdot \mathrm{erfc}\left(\kappa_1 - \Delta t_M / \sigma\right) + \right. \\ & \left. (1-R) \cdot \exp\left(\kappa_2^2 - \Delta t_M / \tau_2\right) \cdot \mathrm{erfc}\left(\kappa_2 - \Delta t_M / \sigma\right)\right]; \\ & \kappa_{1,2} = \sigma / 2\tau_{1,2}; \\ & R(\lambda) = \frac{1}{2}\mathrm{erfc}\left(\frac{c}{\lambda_0} - \frac{c}{\lambda}\right) \end{aligned} \tag{9}$$

with
$\tau_1 = 32.0$ µsec; $\tau_2 = 2.5$ µsec /Å; $\sigma = 1.5$ µsec/Å; $c = 3.4$ Å; $\lambda_0 = 2.45$ Å
and the complementary error-function
erfc(x) = 1 - erf(x) .

The time structure $p_M(\Delta t_M)$ is given normalised so that the integration over Δt_M will yield 1.

i) Use of erf(x)

Since the function $p_M(\Delta t_M)$, defined by eq.9, is already given in terms of Gaussians and error-functions it can be directly used in the resolution calculation. We get integrals like eq.6 and the calculation is straight forward.

ii) Gaussian expansion

Despite the nice mathematical description we have got in eq.9 we have to consider that this is the result of theoretical predictions and the parameters are based on Monte-Carlo-Simulations. Therefore, the real time structure may look a little different due to circumstances in the set-up of the moderator which are not included in the calculations. Considering a case where the function would just be determined experimentally by a series of data-points the Gaussian expansion will deliver a very accurate and easy way to handle those functions in the resolution calculations.

$$p_M(\Delta t_M) \approx \sum_{j=1}^{n} c_j \cdot \exp\left[-a_j^2 \cdot \left(x - b_j\right)^2\right] \tag{10}$$

Fig.2 shows the result of a 7-peak Gaussian expansion for eq.9 and neutron energy of 50 meV. It demonstrates that a small number of Gaussians is already sufficient to describe a function like eq.9 with

high accuracy. It should be mentioned that this particular function just serves as an example, the expansion will work equally well throughout a wide range of functions.

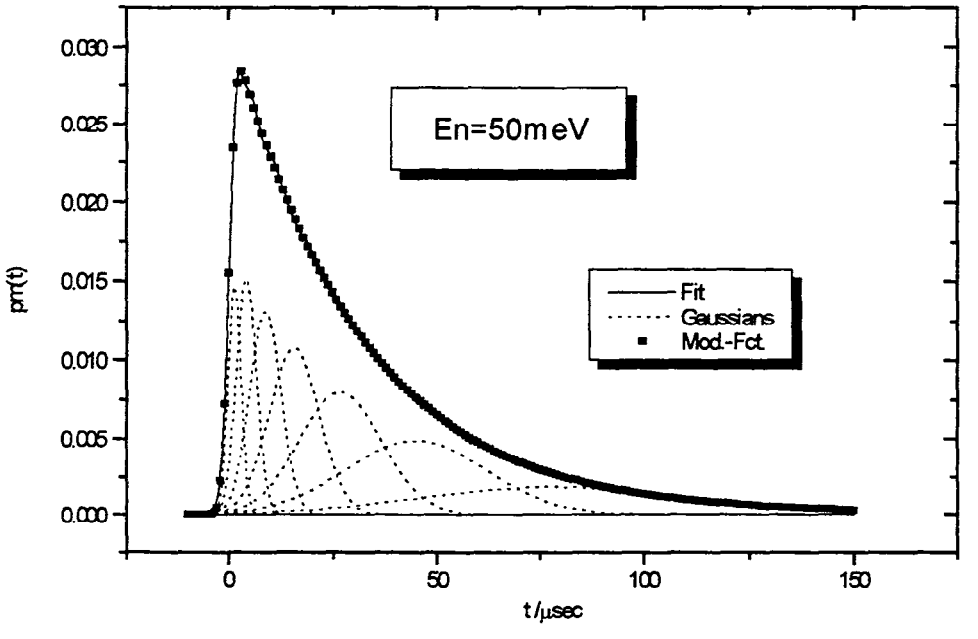

Fig.2: 7-peak Gaussian expansion of a moderator time structure

c) Expansion for exp(-x⁴)- terms

The function exp(-x^4) shall be a final example for a non-Gaussian distribution. Why this function? We will mention two cases:

i) Quadratic Terms:
If the linearisation which is usually carried out for all variables in the resolution calculation is not sufficient quadratic terms may be used in addition. Putting them into Gaussian distributions will result in exp(-x^4)-terms.

ii) Dispersion Relations
For the general use of quadratic terms from a dispersion relation in the convolution with the resolution function we need to deal with q^4-terms in the exponentials. Also in this case the following expansion shows an analytic way to do the calculation with sufficient accuracy.

$$\exp\left(-x^4\right) \approx c_1 \cdot \exp\left[-a_1 \cdot (x+b)^2\right] + c_2 \cdot \exp\left(-a_2 \cdot x^2\right) + c_1 \cdot \exp\left[-a_1 \cdot (x-b)^2\right] \tag{11}$$

with
$a_1 = 5.6064$; $a_2 = 2.7981$; $b = 0.66432$; $c_1 = 0.55693$; $c_2 = 0.91027$;

A plot is shown in Fig.3. We will use this expansion for a generalisation of the 4d-convolution in [1]. Calculations are in progress.

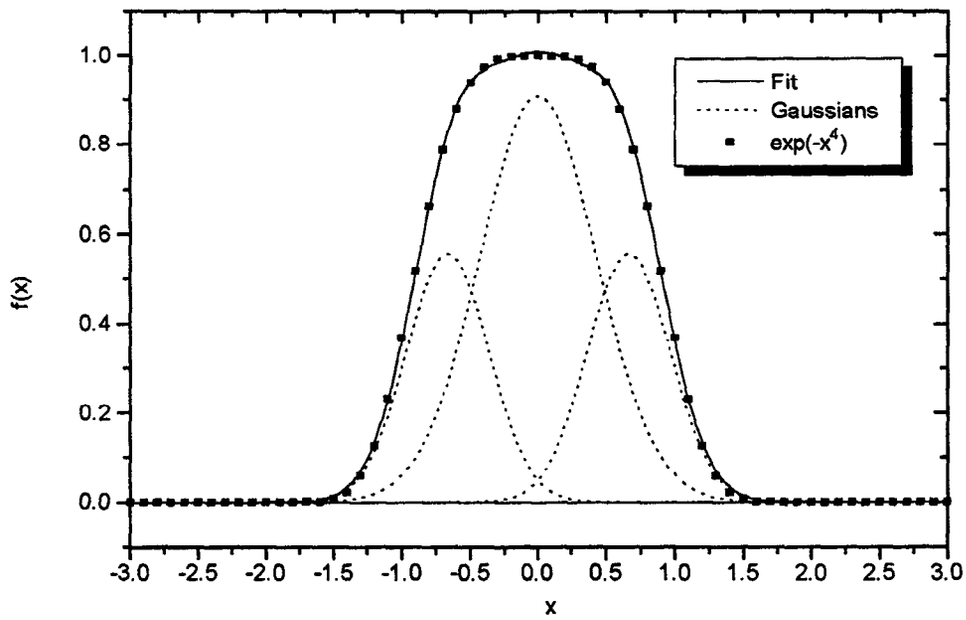

Fig.3: 3-peak Gaussian expansion for the function exp(-x⁴)

3) Refined resolution formalism

The principle of the refinement is the use of the basic coordinates in space and (if applicable) in time for all components so that all misfits and their probability distributions are expressed in terms of the coordinates of sample, analyser, detector, etc. Integrations are then performed on these variables and therefore *simultanuously* on all distributions which are depending on them. This includes automatically all dependencies between distributions treated separately otherwise. Two short examples shall be given:

i) Time-of-flight:

Let us assume an angular misfit γ_i of incoming neutrons at the sample. It is clear that neutrons with $\gamma_i>0$ will preferably arrive at one side of the sample and vice versa (cf. fig.4a). Thus the misfit of the secondary length ΔL_f (and the corresponding time-of-flight) is directly related to γ_i because both are functions of the sample coordinates x_S and y_S. Two separate distributions for γ_i and ΔL_f will not take in account this mutual dependency. In the refined formalism the integration coordinates will not be γ_i and ΔL_f but the coordinates x_S and y_S instead.

ii) Triple-axis:

For this instrument we consider a focusing analyser. Depending on the angular misfit of the incoming neutrons they will find a mosaic spread centred on different values η_0 (cf. fig.4b). Therefore η_0 is directly connected to the coordinate y_A. Assuming a Gaussian distribution of width σ for the mosaic spread η this fact can easily be expressed by a probability function for η depending on y_A .

$$p(\eta) = \exp\left[-\left(\eta - \eta_0(y_A)\right)^2 / \sigma^2\right] \tag{12}$$

Again, the mutual dependencies between mosaic spread and angular misfit are included in the refined formalism by using the basic coordinates. In addition, this kind of treatment provides a straight forward way to include focusing techniques at triple-axis machines into the resolution calculation .

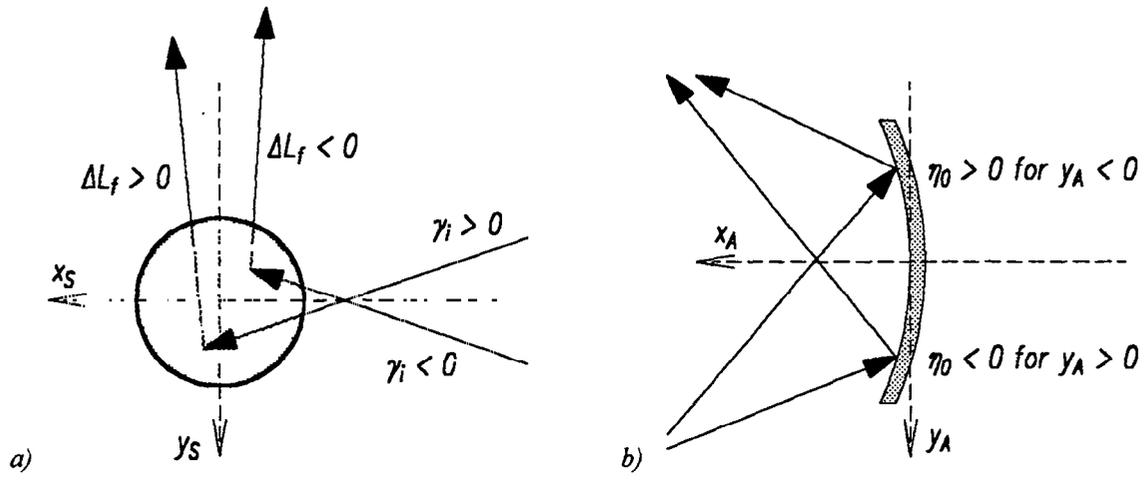

Fig.4: Schematic diagrams of misfit combinations for time-of flight and triple-axis machines

4) Resolution function of ROTAX-Diff.

Using the formalism described above we have calculated the resolution function of ROTAX-Diff., i.e. the diffraction mode of the ROTAX spectrometer installed at ISIS [2,3]. Fig.5 shows the set-up with the relevant variables and coordinate systems.

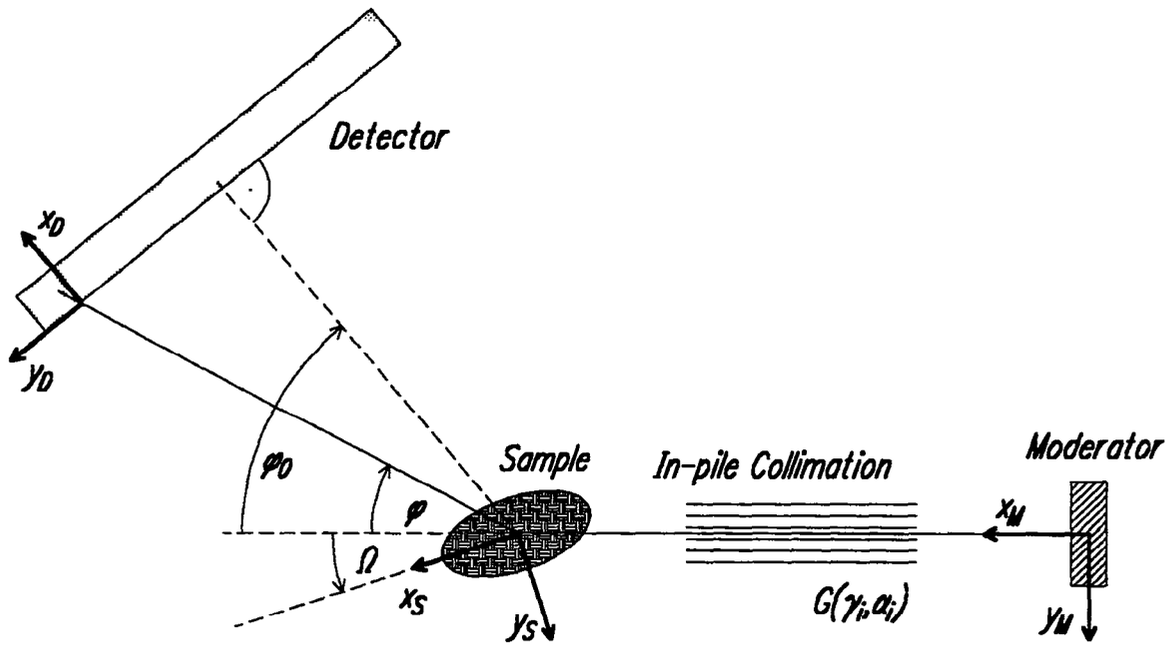

Fig.5: Set-up of ROTAX-Diff. with definitions of variables and coordinates

So far we have used the Gaussian approximation for all probability distributions except the time structure of the moderator. It is very important to include this asymmetric function since it leads to correspondingly asymmetric peaks in the measured spectra as well. Further improvements beyond the Gaussian approximations will be made where the experimental data show that improvements are necessary. Tests are planned for the near future.
The calculation includes the in-pile collimation (α_i), size of moderator (b_M), sample (a_S, b_S) and detector channel (a_D, b_D) as well as the moderator time structure $p_M(\Delta t_M)$ and the time width of the detector channels (τ_D). The resolution function is then given by

$$
\begin{aligned}
p(\Delta d) = \int & \delta(\Delta d + d_0 \cdot \Delta k / k_0 + \Delta\theta \cdot d_0 \cdot \cot\theta) \\
& \cdot \delta(\gamma_i - (x_S \cdot \sin\Omega + y_S \cdot \cos\Omega - y_M) / L_i) \\
& \cdot \mathrm{G}(\gamma_i, \alpha_i) \cdot \mathrm{G}(y_M, b_M) \cdot \mathrm{G}(x_S, a_S) \cdot \mathrm{G}(y_S, b_S) \cdot \mathrm{G}(x_D, a_D) \cdot \mathrm{G}(y_D, b_D) \cdot \mathrm{G}(\Delta t_D, \tau_D) \\
& \cdot p_M(\Delta t_M) dy_M\, dx_S\, dy_S\, dx_D\, dy_D d\Delta t_D\, d\Delta t_M \\
= & \frac{t_0 \cdot V_M}{\sqrt{\pi} \cdot \tau_D \cdot d_0 \cdot Y_M} \cdot \int \exp\left[-\frac{V_M^2}{Y_M^2} \cdot \left(\frac{\Delta d}{d_0} - \frac{\Delta t_M}{t_0} \right)^2 \right] \cdot p_M(\Delta t_M) d\Delta t_M
\end{aligned}
\tag{13}
$$

with

$$
\mathrm{G}(x,a) := \exp(-x^2 / a^2) \tag{14}
$$

and the time structure of the moderator as defined in eq.9. For the calculation all coordinates are transformed into the sample coordinate system. The corresponding equations and definitions of all misfits and abbreviations can be found in the appendix. The final integration is carried out according to eq.6.

5) Conclusion

In this paper we have introduced some ideas to improve the resolution calculation with mathematical methods to go beyond the Gaussian approximation but still keep the calculation analytical. Both the error-function and Gaussian expansion are the keys to perform this task. Further, we have shown a refined formalism to achieve a more accurate description of the dependencies for the probability distributions among each other. The formalism works for both Gaussian and non-Gaussian distributions. As an example it has been used for a time-of-flight diffractometer fully including the asymmetric time structure of the moderator. For the future we plan to present complete calculations for triple-axis machines including flux enhancement techniques like focusing devices and, on the time-of-flight sector, the resolution function for the ROTAX-spectrometer with its non-uniformly spinning analyser which will really emphasize these new techniques in resolution calculation.

Acknowledgement

This work has been funded by the German Minister for Education and Research under contract numbers 03-GE3-WUE, 03-WI3-BON and 05-300-CJB6 .

References

[1] W.Schmidt, D.Sieger, H.Tietze-Jaensch, R.Geick, Nucl. Inst. & Meth. **A316** (1992) 364

[2] H.Tietze-Jaensch, W.Schmidt, R.Geick, G.Will, Proc. ICANS XIII, Villigen, PSI, Switzerland

[3] W. Schäfer, E.Jansen, R.Skowronek, G.Will, W.Kockelmann, W.Schmidt, H.Tietze-Jaensch, Nucl. Inst. & Meth. **A**, in press

[4] A.D.Taylor, RAL Report 84-120

Appendix

Basic equations, definitions and abbreviations for the resolution calculation (eq.13):

Detector coordinates in sample coordinates:

$$\begin{pmatrix} x_{D(\hat{S})} \\ y_{D(\hat{S})} \end{pmatrix} = L_f \cdot \begin{pmatrix} \cos\varphi \\ \sin\varphi \end{pmatrix} + \begin{pmatrix} \cos\varphi_0 & -\sin\varphi_0 \\ \sin\varphi_0 & \cos\varphi_0 \end{pmatrix} \begin{pmatrix} x_D \\ y_D \end{pmatrix} \tag{15}$$

Moderator coordinates in sample coordinates:

$$\begin{pmatrix} x_{M(\hat{S})} \\ y_{M(\hat{S})} \end{pmatrix} = -L_i \cdot \begin{pmatrix} 1 \\ 0 \end{pmatrix} + \begin{pmatrix} x_M \\ y_M \end{pmatrix} \tag{16}$$

Sample axis rotation:

$$\begin{pmatrix} x_{\hat{S}} \\ y_{\hat{S}} \end{pmatrix} = \begin{pmatrix} \cos\Omega & -\sin\Omega \\ \sin\Omega & \cos\Omega \end{pmatrix} \begin{pmatrix} x_S \\ y_S \end{pmatrix} \tag{17}$$

Deviations in lengths and angles:

$$\Delta L_i = x_S \cdot \cos\Omega - y_S \cdot \sin\Omega - x_M \tag{18}$$

$$\Delta L_f = -x_S \cdot \cos(\Omega - \varphi) + y_S \cdot \sin(\Omega - \varphi) - x_D \cdot \cos(\varphi_0 - \varphi) - y_D \cdot \sin(\varphi_0 - \varphi) \tag{19}$$

$$\begin{aligned} \Delta\varphi = & \frac{1}{L_f} \cdot \left[-x_S \cdot \sin(\Omega - \varphi) - y_S \cdot \cos(\Omega - \varphi) + x_D \cdot \sin(\varphi_0 - \varphi) + y_D \cdot \cos(\varphi_0 - \varphi) \right] \\ & + \frac{1}{L_i} \cdot \left[-x_S \cdot \sin\Omega - y_S \cdot \cos\Omega + y_M \right] \end{aligned} \tag{20}$$

$$\gamma_i = \frac{1}{L_i} \cdot \left(x_S \cdot \sin\Omega + y_S \cdot \cos\Omega - y_M \right) \tag{21}$$

Deviations in wave vector and d-spacing:

$$\frac{\Delta d}{d_0} = -\frac{\Delta k}{k_0} - \Delta\theta \cdot \cot\theta \tag{22}$$

$$\frac{\Delta k}{k_0}=\frac{1}{L_0}\cdot\Big[2x_S\cdot\sin\theta\cdot\sin(\theta-\Omega)-2y_S\cdot\sin\theta\cdot\cos(\theta-\Omega)-x_M$$
$$+x_D\cdot\cos(\varphi_0-\varphi)-y_D\cdot\sin(\varphi_0-\varphi)\Big]-\frac{\Delta t_D+\Delta t_M}{t_0} \tag{23}$$

Abbreviations:

$$L_0=L_i+L_f;\quad t_0=\frac{m\,L_0}{\hbar\,k_0};\quad \theta=\frac{\varphi}{2};\quad d_0=\frac{k_0}{\pi\cdot\sin\theta} \tag{24}$$

$$V_M^2=\left(A_i^2V_S^2+B_M^2\hat{V}_S^2\right)\cdot V_D^2$$
$$Y_M^2=B_M^2Y_S^2+\left(K_0^2K'^2+A_i^2Y_D^2\right)\cdot V_S^2+\left(A_i\overline{K}_c-A_{ic}K_0K'\right)^2\cdot A_S^2+\left(A_i\overline{K}_s-A_{is}K_0K'\right)^2\cdot B_S^2$$
$$Y_S^2=\left(Y_D^2+V_D^2\right)\cdot\hat{V}_S^2-V_D^2\overline{V}_S^2/V_S^2$$
$$V_S^2=A_S^2B_S^2$$
$$\hat{V}_S^2=A_{ic}^2A_S^2+A_{is}^2B_S^2+V_S^2$$
$$\overline{V}_S^2=A_{is}B_S^2\overline{K}_s+A_{ic}A_S^2\overline{K}_c$$
$$V_D^2=A_D^2B_D^2$$
$$Y_D^2=V_D^2+A_D^2\hat{K}_c^2+B_D^2\hat{K}_s^2$$
$$A_M=1/a_M$$
$$B_M=1/b_M$$
$$A_S=1/a_S$$
$$B_S=1/b_S$$
$$A_D=1/a_D$$
$$B_D=1/b_D$$
$$A_i=1/a_i$$
$$A_{is}=A_i\cdot\sin\Omega$$
$$A_{ic}=A_i\cdot\cos\Omega$$
$$\hat{K}_s=K\cdot\sin(\varphi_0-\varphi)+\cos(\varphi_0-\varphi)$$
$$\hat{K}_c=K\cdot\cos(\varphi_0-\varphi)-\sin(\varphi_0-\varphi)$$
$$\overline{K}_s=K\cdot\sin(\Omega-\varphi)+\cos(\Omega-\varphi)+K'\cdot\sin\Omega-\cos\Omega$$
$$\overline{K}_c=K\cdot\cos(\Omega-\varphi)-\sin(\Omega-\varphi)+K'\cdot\cos\Omega+\sin\Omega$$
$$K=\frac{\cot\theta}{2\nu}$$
$$K'=\frac{\cot\theta}{2(1-\nu)}$$
$$\nu=\frac{L_f}{L_i}$$

ICANS-XIII
13th Meeting of the International Collaboration on
Advanced Neutron Sources
October 11-14, 1995
Paul Scherrer Institut, 5232 Villigen PSI, Switzerland

THE MCLIB LIBRARY: MONTE CARLO SIMULATION OF NEUTRON SCATTERING INSTRUMENTS

Philip A. Seeger

239 Loma del Escolar, Los Alamos, NM 87544, USA
E-mail: PASeeger@aol.com

ABSTRACT

This report describes the philosophy and structure of MCLIB, a Fortran library of Monte Carlo subroutines which has been developed to test designs of neutron scattering instruments. A pair of programs (LQDGEOM and MC_RUN) which use the library are shown as an example.

1. Introduction

Monte Carlo is a method to integrate over a large number of variables. Random numbers are used to select a value for each variable, and the integrand is evaluated. The process is repeated a large number of times and the resulting values are averaged. For a neutron transport problem, we first select a neutron from the source distribution, and project it through the instrument using either deterministic or probabilistic algorithms to describe its interaction whenever it hits something, and then (if it hits the detector) tally it in a histogram representing where and when it was detected. This is intended to simulate the process of running an actual experiment (but it is *much* slower). Monte Carlo is a useful supplement to analytical treatment of an instrument, in particular to check and demonstrate "non-intuitive" focusing arrangements.

The present MCLIB library has been derived from codes written by Mike Johnson at the Rutherford Laboratory [1]. Significant additions and revisions were made by this author in 1984 [2], and the entire code was rewritten in a structured form in 1994 [3]. Whenever the code has been applied to new problems, additions have been made. Thus significant contributions to the present library have been made by Richard Heenan (Rutherford-Appleton Laboratory), and by Glenn Olah, Bob VonDreele, Greg Smith, and Luke Daemen (Los Alamos neutron Science Center, LANSCE). Mike Fitzsimmons and Joyce Goldstone have contributed greatly to the debugging process. Several applications of the code were presented at an instrument design workshop [4]. A new collaboration with Larry Passell and Uli Wildgruber (Brookhaven National Laboratory) is also producing improvements.

The process is carried out in two stages. First a program must be generated to describe the geometry of the specific instrument being simulated; for example, the program LQDGEOM may be used to define a small-angle scattering instrument with pinhole collimation, up to three

Keywords: MCLIB, Monte Carlo, simulation, instruments

choppers, and an on-axis 2-dimensional position sensitive detector. Essentially all of the user interaction occurs in this stage. The output is a geometry file containing the complete problem definition. That file is then passed to a second-stage program, for example MC_RUN, which transports neutrons and tallies results in histograms. Principal outputs are a file with a statistical summary, and a data file with histograms of the spectrum and detector. A third stage, which is not part of the Monte Carlo process, is to perform whatever data reduction is appropriate to the experiment being simulated. Some measure of the information content (or a "figure of merit") is then used to evaluate the design of the instrument.

Features of MCLIB which are different from other Monte Carlo libraries include

- Simplified transmission through materials. Rather than compute microscopic interaction in a simple (amorphous unpolarized) region, attenuation of the transmitted neutron is calculated.
- Optics at surfaces. When a neutron reaches a surface, the (complex) index of refraction is computed to decide whether the neutron will reflect or refract.
- Time-dependent devices. There are element types to describe moving devices such as choppers or a gravity focuser.
- Acceleration of gravity is included in transport.
- Scattering functions. Each kind of scattering sample is an element type. The scattering algorithm may be deterministic (reflectometry), probabilistic (hard-sphere scatterer), or a combination (Bragg reflection into a Debye-Scherrer cone).

2. Geometry Description by Surfaces and Regions

The geometry of a system is described by surfaces and regions. A *surface* is defined by a general 3-dimensional quadratic equation of the form

$$A x^2 + B x + C y^2 + D y + E z^2 + F z + G + P xy + Q yz + R zx = 0 \qquad (1)$$

with 10 coefficients, plus a roughness parameter (*BETA*). The surface divides 3-dimensional space into two parts, which are called the + and – sides of the surface depending on whether the left-hand side of eq. (1) evaluates to a positive or a negative value. For example, a plane perpendicular to the z-axis at z = 1 can be expressed by the equation

$$z - 1 = 0,$$

i.e., $F = 1$ and $G = -1$ (all other coefficients zero). Then all points with $z < 1$ are on the – side and all points with $z > 1$ are on the + side of the surface. The scaling of eq. (1) is arbitrary, but we tend to evaluate it as m^2, so that coefficients A, C, E, P, Q, and R are dimensionless, coefficients B, D, and F are in m, and G is m^2. The parameter *BETA* is the length of a randomly oriented 3-dimensional vector which is added to the unit vector normal to the mathematical surface to determine the surface orientation when a particle interacts. For a perfect smooth surface, $BETA = 0$; for $0 < BETA < 1$, *BETA* is the sine of the maximum angular deviation of the surface normal from smooth. If $BETA < 0$ (or $BETA >> 1$), the surface is completely random.

Note that the coordinate system being used is left handed: the instrument axis is the positive z-direction, the x-axis is horizontal and positive to the right, and the y-axis is vertical with the acceleration of gravity in the negative y-direction.

The geometric shape of each *region* is defined by its relationship to all of the defined surfaces. A positive or negative integer is placed in the region definition if every point in the region is on the + or – side of the corresponding surface, and surfaces which do not bound the region are set to zero. Special characteristics of the boundary are given by the value of the integer: ±1 for an ordinary surface with roughness *BETA* and the possibility of refraction or critical reflection; ±2 for total reflection; ±3 for diffuse scattering (independent of *BETA*); ±4 for total absorption; and ±5 for cases requiring special action (such as a coordinate transformation) whenever a particle enters or leaves the region. Generally, no surface may be used as a boundary of a region if any part of that surface is inside the region, because then some points in the region would be on the + side and some on the – side of that surface. Concave (reentrant) shapes are allowed when using quadratic surfaces as in fig. 1a, but the shape in fig. 1b requires that two regions be defined. Another method to define a reentrant region is to exclude embedded regions, which is accomplished by adding 10 to the surface type number in the definition of the enclosing region (*e.g.*, "4" becomes "14" or "–1" becomes "–11"). Such surfaces are *not* tested as part of the definition of being inside the region. When the trajectory of a particle inside the region intersects the surface, it will exit if a valid region exists on the other side, but will otherwise remain in the enclosing region. This method must be used with care, since particles within the embedded regions also pass the test for being within the enclosing region.

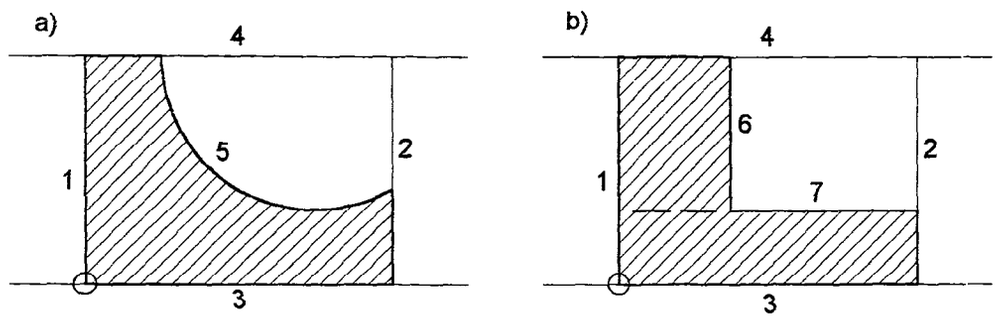

Figure 1. Concave regions.

Equations of the numbered surfaces are

1:		x				$=$	0	
2:		x			-4	$=$	0	
3:				y		$=$	0	
4:				y	-3	$=$	0	
5:	x^2	$-6x$	$+y^2$	$-6y$	$+14$	$=$	0	or $(x-3)^2 + (y-3)^2 = r^2 = 4$
6:		x			-1.5	$=$	0	
7:				y	-1	$=$	0	

The shaded area in a) can be expressed unequivocally as a single region:

+1 –1 +1 –1 +1 0 0

To avoid ambiguity, the area in b) requires two regions, divided as shown by surface 7 (or alternatively by surface 6).

+1 –1 +1 0 0 0 –1
+1 0 0 –1 0 –1 +1

The unshaded area in either case requires 5 regions for a complete unambiguous definition. (One choice of region boundaries is shown by the faint lines.) If the upper right corner

0 –1 0 –1 0 +1 +1

is considered an embedded region, then the shaded area may also be defined as

+1 –1 +1 –1 0 –11 –11

3. Instrument Elements

Each region is also an *element* of the instrument. Every element has a *NAME* and a pointer (*INDEX*). For a void drift region, *INDEX* = 0, and for every element which is not a void

INDEX points to a location in a `REAL*4` parameter block which contains the element type number, possibly followed by additional parameters. Future development of the library should be accomplished by defining new element types and implementing the corresponding algorithms for how a neutron interacts in such regions. Presently defined types and their parameters are listed below; file `MC_ELMNT.INC` (Appendix A) includes definitions of mnemonic symbols for all the parameters, with values equal to the address offset from the *INDEX* pointer.

type 0 = total absorber; no parameters
type 1 = amorphous unpolarized material; 4 parameters
Real and Imaginary scattering-length density ($10^{10}/cm^2$)
macroscopic scattering cross section (1/m)
velocity-dependent cross section, at 1 m/μs (1/μs)
type 2 = aluminum, including Bragg edges; no parameters
type 3 = hydrogenous, including multiple scattering
type 4 = supermirror represented by trapezoidal reflectivity; 4 parameters
Real & Imaginary scattering-length density ($10^{10}/cm^2$) (see type 1)
Supermirror multiplier
Reflectivity at maximum supermirror limit
type 5 = beryllium at 100K, including Bragg edges; no parameters
type 6 = single-crystal filter, Freund formalism; 3 parameters

$$\Sigma = \Sigma_{free} \times \{1 - \exp(-C_2/\lambda^2)\} + \Sigma_{abs} \times \lambda$$

Σ_{free} = limiting (short wavelength) free-atom macroscopic cross section (1/cm)
$C_2 = -\ln\{1 - (\Sigma(1Å) - \Sigma_{abs})/(\Sigma_{free} - \Sigma_{abs})\}$ ($Å^2$)
Σ_{abs} = sum of 1/v macroscopic cross sections at 1Å (1/cm/Å)
type 10 = multi-aperture collimator
type 11 = multi-slit collimator, vertical blades; 3 or 5 parameters
Note: the type 11 region must be followed immediately by up to 5 additional regions defining the center passage and the bounding blades, and the entrance/exit surfaces must be surface type 5.
Spacing of slits, centerline-to-centerline (m)
Rate of convergence (>0) or divergence (<0) of one slit
Z at entrance of the region, where spacing is measured (m)
For a curved system (bender),
sine of half the angle of bend
cosine of half the angle of bend
type 12 = multi-slit collimator, horizontal blades; 3 or 5 parameters
Same parameters as type 11 (see *Note* under type 11)
type 13 = crystal monochrometer; 10 parameters
Twice the crystal plane spacing (Å)
Nominal Z position for rotation of instrument axis (m)
Sine and cosine of take-off angle
X-, Y-, and Z-components of mosaic spread, rms of sines of angles
rms spread of plane spacing, σ_d/d
max number of loops (or microcrystal orientations) to try
probability normalization factor per try, derived from reflection probability at peak wavelength: $1 - (1 - \text{max_prob})^{(1/\text{trys})}$
types 20.n = chopper (disk or blade); 6 parameters
20.0 or 20.2 for motion in x-direction, 20.1 or 20.3 for y-direction

20.2 or 20.3 is counter-rotating (fully closed when edges at 0)
Linear velocity of opening crossing beam centerline (m/μs)
Time to cover or uncover half the width of the moderator (μs)
Nominal time at which opening chopper edge crosses zero (μs)
Nominal time at which closing chopper edge crosses zero (μs)
Phase jitter of chopper, rms (μs)
Period of chopper (μs)

type 21 = Fermi chopper (not implemented)

type 22 = gravity focuser; 5 parameters
Note: the type 22 region must be followed immediately by 2 additional regions defining the aperture, and the entrance/exit surfaces must be surface type 5.
acceleration (m/μs^2), and rms phase jitter (μs)
nominal times for start and top of upward stroke (μs)
time between pulses (μs)

type 23 = removable beamstop; no parameters

type 30 = sample which scatters at constant Q; 2 parameters
–ln(transmission at 1 Å)
value of Q for scatter (1/Å)

type 31 = scattering sample of hard spheres; 2 parameters
–ln(transmission at 1 Å)
hard-sphere radius for scatter (Å)

type 32 = isotropic scatterer with fixed energy change; 2 parameters
–ln(transmission at 1 Å)
inelastic energy change (0 if elastic) (meV)

type 34 = inelastic scattering kernel; no parameters; *NAME* is '[path]filename' of $S(\alpha,\beta)$ file in MCNP Type I format

type 35 = scattering from layered reflectometry sample; 1 + 4 *N* parameters
number of layers, including substrate
parameters for each layer, starting with substrate:
4π x Real and Imaginary scattering-length density (1/Å^2)
Thickness of layer (zero for substrate) (Å)
Roughness, 2 σ^2 of outer surface of this layer (Å^2)

type 36 = scattering from isotropic polycrystalline powder; 6 parameters + 2 × table length
number of Bragg edges included
limiting (short wavelength) macroscopic total xsection (1/cm)
macroscopic incoherent scattering cross section (1/cm)
macroscopic 1/v scattering cross section at 1 Å (1/cm/Å)
macroscopic 1/v absorption cross section at 1 Å (1/cm/Å)
table of d-spacings of Bragg edges (Å), followed by explicit 0 and table of cumulative macroscopic cross sections at 1 Å (1/cm/Å^2)

type 40 = detector; 9 parameters
surface number
–ln(1 – efficiency at 1 Å)
time-of-flight clock parameters:
minimum and maximum times (μs)
number of time channels
if logarithmic, dt/t (otherwise dt/t = 0)
minimum clock tick in determining log scale (μs)

electronic delay of detector events (μs)
repeat period of data-acquisition electronics (μs)
Note: if t-o-f is logarithmic, *TMAX* is overridden

type 41 = vertical linear detector; 14 parameters
surface number
–ln(1 – efficiency at 1 Å)
time-of-flight parameters (7)
locations of bottom and top of detector (m)
number of detector elements
size of detector element (m)
root-mean-square encoding error of detector (m)

type 42 = horizontal linear detector; 14 parameters
surface number
–ln(1 – efficiency at 1 Å)
time-of-flight parameters (7)
locations of left and right ends of detector (m)
number of detector elements
size of detector element (m)
root-mean-square encoding error of detector (m)

type 43 = 2-D rectilinear detector; 18 parameters
surface number
–ln(1 – efficiency at 1 Å)
time-of-flight parameters (7)
locations of left and right edges of detector (m)
number of detector elements in the horizontal direction
width of detector element (m)
root-mean-square X encoding error of detector (m)
locations of bottom and top edges of detector (m)
number of detector elements in the vertical direction
height of detector element (m)
root-mean-square Y encoding error of detector (m)

type 44 = longitudinal linear detector; 14 parameters
surface number
–ln(1 – efficiency at 1 Å)
time-of-flight parameters (7)
locations of upstream and downstream ends of detector (m)
number of detector elements
size of detector element (m)
root-mean-square encoding error of detector (m)

type 50 = scattering chamber, void-filled. No parameters, but other regions may be embedded, indicated by surface types with 10s digit on.

types 90.n = source size and phase space to be sampled; 14-18 parameters
edges of rectangular moderator face (m)
location and radius (half-width) of apertures which define beam (m)
additional vertical space to sample for gravity focus (m)
min and max neutron energy to be sampled (eV)
time between beam pulses and square pulse width (μs)
offset to parameter block with spectrum and line shape parameters
(optional) half-heights of apertures, type 90.1 or 90.2 (m)

(optional) vertical offsets of apertures, type 90.4 (m)

type 91 = source energy distribution table and line shape parameters; 12 parameters plus length of table

number of entries in energy table (1 is special case)

location in table of center of normal distribution (index units)

or value of nominal neutron velocity (m/μs) (if number of entries = 1)

standard deviation of normal distribution (table index units)

or relative fwhm of velocity selector (if number of entries = 1)

source brightness, summed over limits of *E_TABLE* (n/ster/m^2/MW/s)

1 or 2 exponential time constants in thermal (low-energy) limit (μs)

probability of 2nd exponential

epithermal (high energy) time constant proportional to λ (μs/Å)

or mean (t/λ) parameter of Ikeda-Carpenter form (μs/Å) (if width < 0)

Gaussian delay and width proportional to λ (μs/Å) (width<0 is special case)

switching function 1/e point (Å) and power (slope)

origin of table of cumulative energy distribution (weighted by λ^2) of source spectrum on equally spaced normal-curve values of log(E / 1 meV)

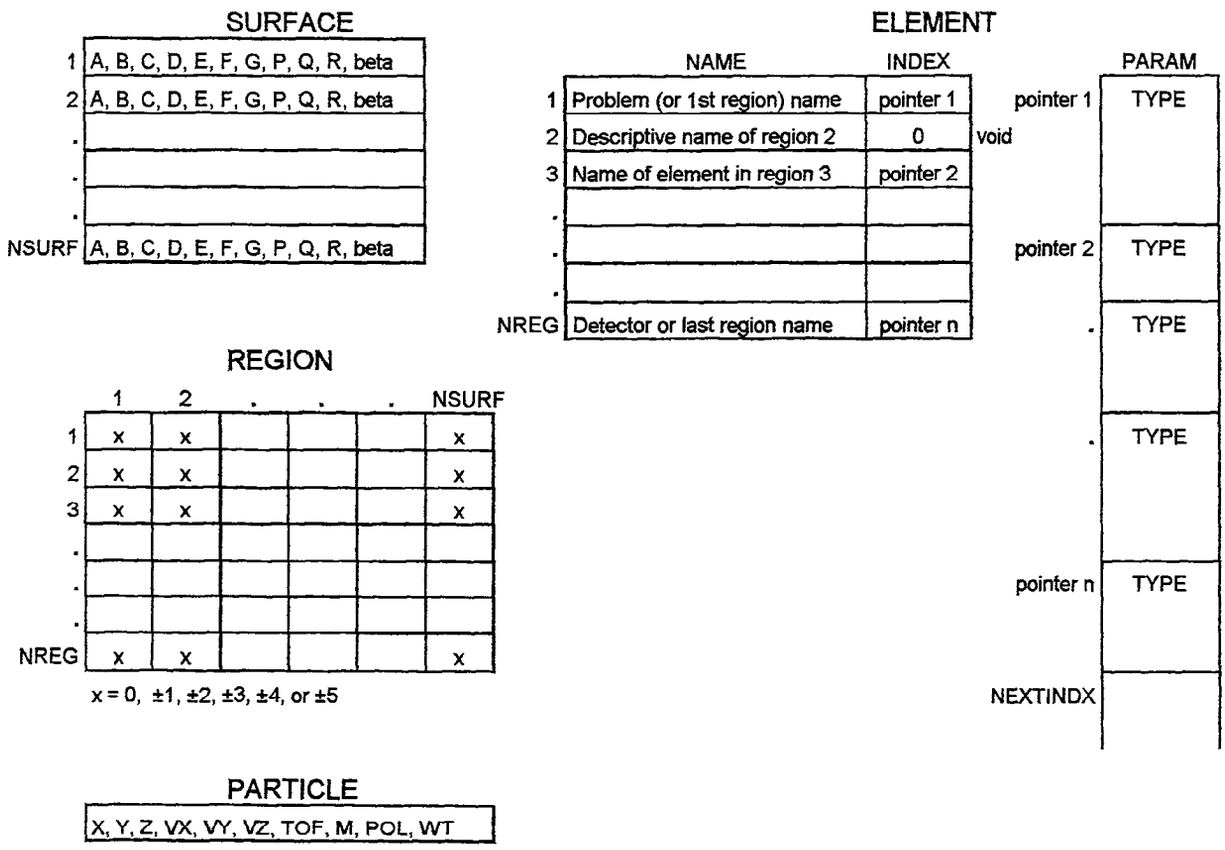

Figure 2. Structures used in MCLIB.

4. Program Structures

The relationships of the structures are shown schematically in fig. 2. The library source code is available in Fortran 77 with VAX structure extensions (F77/VAX), and also in Fortran 90 (F90). Unfortunately the F90 syntax did not adopt the relatively widespread F77/VAX standard, most distressingly by using "%" instead of "." as the member pointer in a structure!

In F77/VAX, each surface is a RECORD of type /SURFACE/, and elements are referenced as (*e.g.*) SURFACE.G. In F90, the surfaces are defined as derived TYPE (SURFACE), and element references are of the form SURFACE%G. Similarly, a geometric region is a RECORD of type /REGION/ or a derived TYPE (REGION); the structure in either case is a vector *IGEOM* of 2-byte integers, of length equal to the maximum allowed number of surfaces. An additional structure, MC_GEOM, contains the numbers of surfaces and regions in the problem, *NSURF* and *NREG*, and arrays of surface and region structures. Information about elements is contained in a structure called MC_ELEMENT which includes *NAME* and *INDEX* arrays, the parameter block *PARAM*, and the pointer *NEXTINDX* to the next available location in *PARAM*.

The final structure is PARTICLE, which includes the position, velocity, time of flight, mass (1 for a neutron), polarization (not yet implemented in the code), and statistical weight of a particle. A purely "analog" Monte Carlo traces each individual neutron until it is either lost or detected. MCLIB uses "weighted" neutrons, and in many of the processes the statistical weight is multiplied by the probability of survival instead of using a random number to decide whether to terminate the history ("Russian Roulette"). This is especially beneficial when scattering probability is small, as in subcritical reflection. To track more long-wavelength neutrons (which in general have larger scattering probability), the source distribution used is $\lambda^2 I(\lambda)$ instead of $I(\lambda)$ and the initial weight is proportional to $1/\lambda^2$. The tallied results are then the sum of detected neutron weights. The relative error in each bin, however, depends on the number of histories recorded.

The F77/VAX and F90 structure definitions follow. As compiled, the dimensions of the arrays are *MAXS* = 150, *MAXR* = 100, and *MAXP* = 800. For use in coding, all structure definitions are included in file MC_GEOM.INC (Appendix A).

F77 / VAX

```
STRUCTURE /SURFACE/
   REAL*4 A,B,C,D,E,F,G,P,Q,R
   REAL*4 BETA
END STRUCTURE

STRUCTURE /REGION/
   INTEGER*2 IGEOM(MAXS)
END STRUCTURE

STRUCTURE /MC_ELEMENT/
   CHARACTER NAME(MAXR)*40
   INTEGER*4 NEXTINDX, INDEX(MAXR)
   REAL*4    PARAM(MAXP)
END STRUCTURE

STRUCTURE /MC_GEOM/
   INTEGER*4 NSURF,NREG
   RECORD /SURFACE/ SURFACE(MAXS)
   RECORD /REGION/  REGION(MAXR)
END STRUCTURE

STRUCTURE /PARTICLE/
   REAL*4 X, Y, Z, VX, VY, VZ
   REAL*4 TOF, M, POL, WT
END STRUCTURE
```

F90

```
TYPE SURFACE
   SEQUENCE
   REAL 4:: A,B,C,D,E,F,G,P,Q,R
   REAL 4:: BETA
END TYPE SURFACE

TYPE REGION
   INTEGER 2:: IGEOM(MAXS)
END TYPE REGION

TYPE MC_ELEMENT
   CHARACTER   NAME(MAXR)*40
   INTEGER 4:: NEXTINDX, INDEX(MAXR)
   REAL 4::    PARAM(MAXP)
END STRUCTURE

TYPE MC_GEOM
   SEQUENCE
   INTEGER 4:: NSURF,NREG
   TYPE (SURFACE) SURFACE(MAXS)
   TYPE (REGION)  REGION(MAXR)
END TYPE MC_GEOM

TYPE PARTICLE
   SEQUENCE
   REAL 4:: X, Y, Z, VX, VY, VZ
   REAL 4:: TOF, M, POL, WT
END TYPE PARTICLE
```

5. Subroutine Library

Complete descriptions, calling sequences, revision history, and externals of all of the library subroutines are given in Appendix B. The following listing divides the subroutines into (somewhat arbitrary) categories, and includes the latest modification date and an abbreviated description. Note that if the operating system does not include the function `RAN(ISEED)`, then the function must be provided as part of the library.

Vector analysis and transport

ANGLI	03 Feb 94	angle of incidence
DIST	23 Mar 95	distance to a surface
DTOEX	06 Mar 95	distance to nearest boundary
ELSCAT	26 Aug 95	do elastic scattering
LIGHTRFL	19 Mar 85	light reflection probability
LMONOCRM	21 Sep 95	reflection by crystal monochromator
LREFLCT	07 Jan 85	neutron reflection probability
MOSAIC	27 Jan 95	angle of incidence with mosaic spread
MOVEX	19 Apr 94	move a particle
NEXTRG	29 Jun 95	find region across boundary
N_SOURCE	29 Sep 95	get source neutron
GET_SPACE		get phase space of source
OPERATE	26 Aug 95	find what happens to particle within region
EXIT_REG		find what happens to particle leaving region
OPTICS	03 Feb 94	photon at region boundary
RFLN	03 Feb 94	do reflection
SNELL	03 Feb 94	apply Snell's law
TESTIN	29 Jun 95	find if within region
WHICHR	03 Feb 94	find what region particle is in
WOBBLE	03 Feb 94	angle of incidence at wavy surface

Material properties and scattering functions

ATTEN_Al	28 Jan 93	attenuation of Al
ATTEN_Be	25 Jan 95	attenuation of Be
ATTEN_X	14 Aug 95	attenuation of single-crystal filter
KERNEL	03 Apr 95	inelastic scattering kernel
PLQSPHR	06 Mar 95	probability from spherical scatterer
POWDER	14 Jul 95	scatter from polycrystalline powder
REFLAYER	07 Feb 95	reflection probability from multiple layers

Random distributions

IKDACARP	27 Sep 95	random sample from Ikeda-Carpenter
ORRAND	11 Mar 95	random unit vector
PLCNVL	11 Mar 95	probability from convolution of top-hats
PLEXP	16 Feb 95	probability from exponential
PLNORM	11 Mar 95	probability from normal
PLNRMTBL	13 Feb 95	probability from table vs. normal distribution
PLPOISSN	18 Mar 95	probability from Poisson
PLTIME	05 Sep 95	probability from parametrized emission time
PLTRNGL	04 Jan 85	probability from triangle
RAN	various	random number; platform dependent
RAN0	86	desequentialized random number
RNDCRCL	11 Mar 95	random point in unit circle

General utilities

DIGITS	05 Dec 87	convert number to string
GAMMLN	92	$\ln(\Gamma(x))$

GET_BINS	26 Jul 95	find detector/time bins
GET_RHO	16 Oct 95	find scattering-length density
GINI	05 Feb 92	standard deviation by Gini statistic
HUNT	13 Apr 87	find index in array
INTERP	84	interpolate in array
NORM	78	normalize unit vector
READ_1D	26 Jul 95	read 1-D block ASCII data file
READ_2D	21 Sep 95	read 2-D block ASCII data file
REALOUT	16 Aug 95	output array of REAL*4 numbers in block ASCII

Time-dependent devices

GRAV_FOC	07 Apr 94	gravity focuser
XCHOPPER	15 Mar 93	disk or blade chopper

Subroutine OPERATE and its other entry point EXIT_REG play special roles in the transport process. As can be inferred from the abstract in Appendix B, if this subroutine is called when a neutron enters a new region, then the routine will determine what happens. Possible results on exit from OPERATE include detection or loss of the neutron, exiting the region with reduced statistical weight (partial absorption), splitting the neutron into a transmitted and a scattered particle with the sum of statistical weights equal to the original weight, or a transform of the coordinate system of the problem. Coordinate transforms are applied for element types made up of sub-regions (*e.g.,* Soller slits and benders), elements which change the beam direction (benders and monochromaters), and time-dependent devices (gravity focuser). In order to assure that the coordinate system is properly restored when the neutron leaves the region, EXIT_REG must be called; this is flagged by using ±5 as the integer defining all exit surfaces from such a region.

6. Neutron Source Functions

Subroutines NSOURCE and PLTIME are called to generate source neutrons, using table lookup to select the velocity and a parametrized model to select the emission time. (If the length of the lookup table is 1, the velocity is a triangular or delta-function distribution; if the thermal decay constant is ≤ 0, emission time is 0.) The table and parameters are generally read from a file derived either from experimental measurements or from a detailed Monte Carlo simulation of a target/moderator/reflector system. The example given below uses a coupled liquid H_2 moderator with a 40-cm thick Be reflector on a spallation source, computed with MCNP [5], but the procedure would be the same for an experimental spectrum measurement. The energy spectrum from the MCNP output is shown in fig. 3. Program MKNRMTBL is provided to convert the spectrum. To improve sampling at long wavelengths, the data are multiplied by λ^2 before the cumulative sum is formed (the neutron is given an initial statistical weight proportional to $1/\lambda^2$ to account for this). The cumulative sum of the weighted table is compared to the integral of a Gaussian (*vs.* log E) fitted to the weighted data to form the table; that is, for equal steps in the argument of the Gaussian, its integral is evaluated and the cumulative sum is interpolated to find the corresponding neutron energy, which is then tabulated as $\log_{10}(E\ /$ 1 meV). To sample the neutron energy, a random deviate is chosen from a Gaussian distribution and that value is used to interpolate in the table ("transform" method [6]). This provides sharp detail over the peak of the spectrum and coarser interpolation in the wings, which may extend to more than 5 standard deviations.

The model for the time distribution is the sum of an epithermal and a thermal term convoluted with a Gaussian, added using a switch function [7,8] of the form $\exp[-(\lambda_0/\lambda)^P]$. This form was

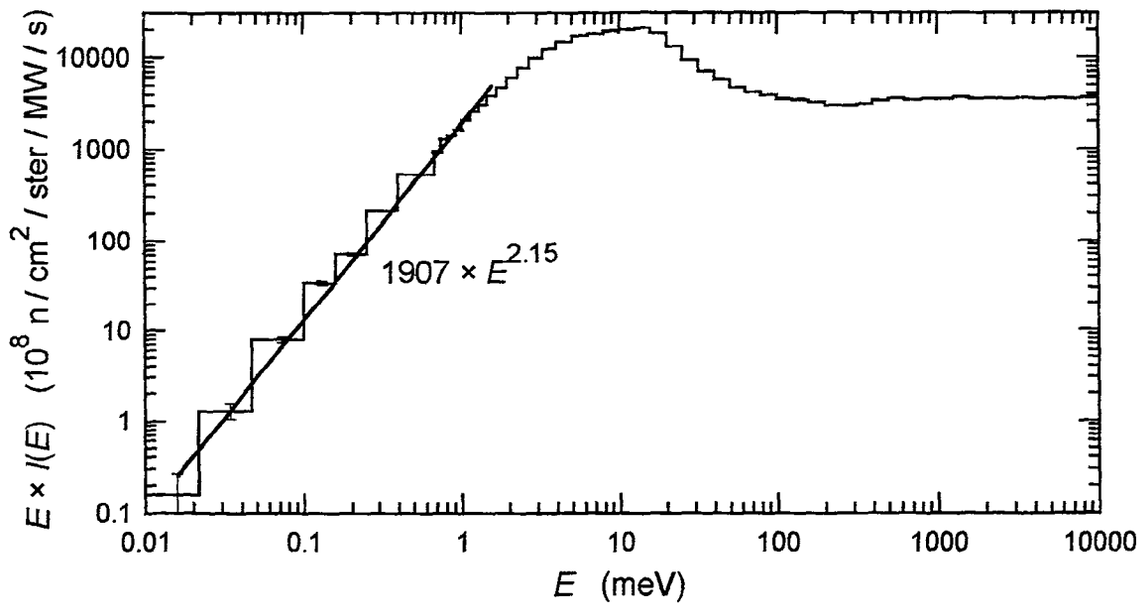

Figure 3. Neutron source energy distribution, as computed with the MCNP code.
Coupled liquid hydrogen moderator (equal fractions ortho and para), flux-trap geometry, 40-cm Be inner reflector, and Pb outer reflector (both reflectors are D_2O cooled). A power law was fitted to the low-energy regime to interpolate the histogram.

chosen because the convolution is easy in Monte Carlo; note however that a function to sample an Ikeda-Carpenter pulse shape distribution [7] has now been added to the library. Adequate fits can be made to most source terms using two exponentials; the epithermal (and the two parameters of the Gaussian) are proportional to wavelength, and the thermal time constant is independent of wavelength. Including the switch function, the total number of parameters in the model is then six. For the hybrid Be/Pb reflector case shown here, however, the fit with just two exponentials is not adequate and the thermal term itself must be a linear combination of two exponentials, for a total of eight parameters. Neutrons escaping from the moderator surface in the MCNP run [5] were tallied *vs.* time for 18 (logarithmic) wavelength bins from 0.09 to 15 Å; fig. 4 shows the data for one such bin, from 0.9 to 1.2 Å. Since the exponential decay after 1000 μs is constant for all wavelengths, the data from 0.9 to 15 Å were summed and a least-squares fit was made over the time range 1200–6000 μs, giving a thermal time constant τ_1 = 610 μs. Since the early (epithermal) parameters are all proportional to λ, the early-time data can be summed after binning *vs.* (t/λ). (The variable t/λ is equivalent to the reduced time vt used in ref. [7].) A least-squares fit in the t/λ range 1–30 μs/Å gave the values epithermal exponential η = 8.67 μs/Å, delay Δ = 5.68 μs/Å, and width σ = 2.08 μs/Å. Given these fits to the early and late times, the additional exponential term was estimated (τ_2 = 170 μs, ratio R = 2/3). Then the ratios of thermal to epithermal terms were extracted, and the two parameters of the switch function determined (λ_0 = 0.86 Å, P = 2.63). The line in fig. 4 is an example of the resulting fit, evaluated at λ = 1.0 Å where all three components are significant.

7. Sample Program Output

Sample program source codes `LQDGEOM.FOR` and `MC_RUN.FOR` will be distributed with all copies of the library, but because of their lengths are not included in this report. Communication between the two programs is through a geometry file, such as the following example, `LPSS.GEO`. The first part of the file is not used by the succeeding program, but contains text to identify the problem and to give the parameters entered by the user.

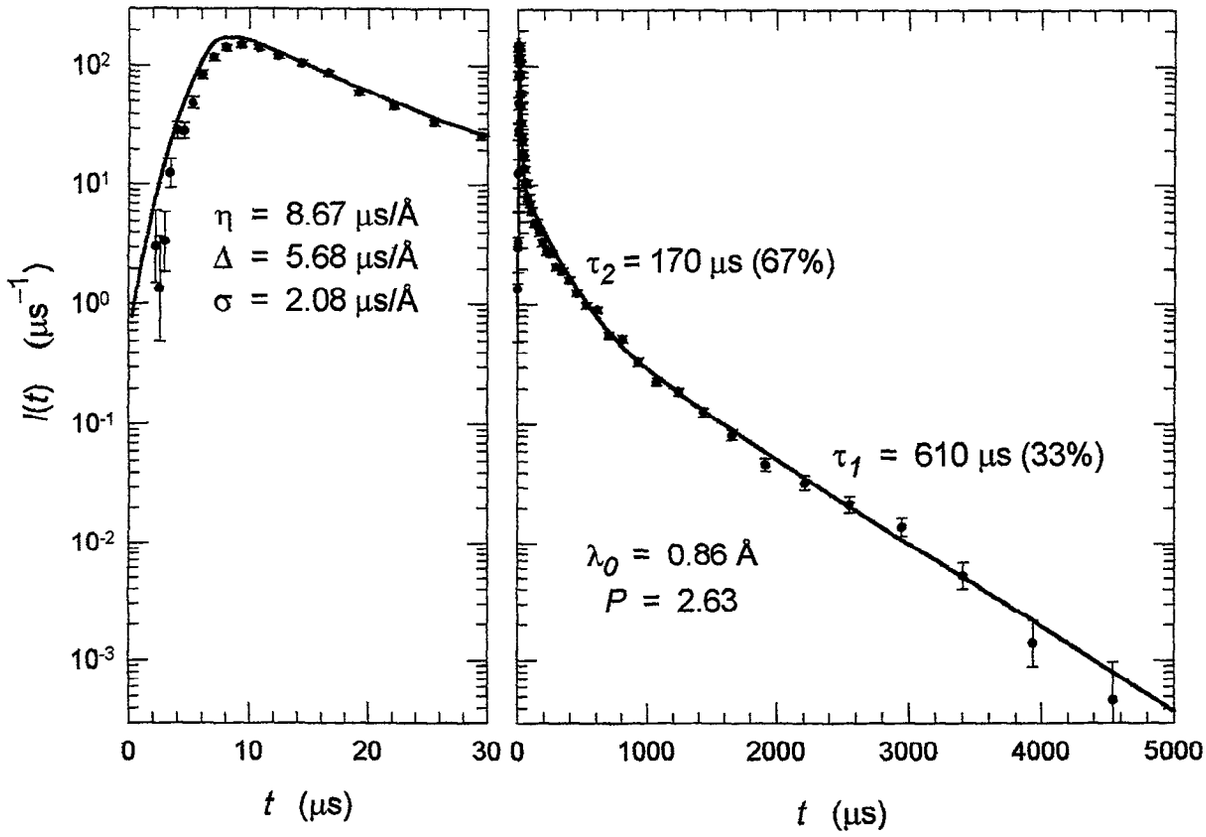

Figure 4. Source time distribution at 1.0 Å.
Points are the MCNP "data," and the line is the model fit. At this wavelength, near the midpoint of the switch function, the early "epithermal" and the two late "thermal" exponential terms are all seen.

```
Geometry code version: F90, June 30, 1995, P.A.Seeger
LQD Geometry file: lpss.geo
Proton pulse rate = 60.0 Hz, width = 1000.0 us, max wavelength 15.1 A
Sample at  7.00 m, Detector at 13.00 m from moderator
Sample diameter = 10.00 mm
Spectrum and lineshape file: \mclib\Pb40Be13.tbl
   T0 Chop at  2.60m, open 0.827ms, close 14.839ms, rms  40.0us, v 56.55m/s
O'lap Chop at  3.10m, open 7.257ms, close 12.281ms, rms  20.0us, v 94.25m/s
Frame Chop at  6.00m, open 16.253ms, close 22.874ms, rms  20.0us, v 94.25m/s
Collimation:  entrance aperture radius  7.53 mm at position  2.500 m
              exit                      4.44 mm              6.800 m
Moderator half-width and half-height = 0.050 m
          spot radius  9.32 mm, penumbra radius 14.48 mm
Time range  34370.0 -  49665.1 us
Sample Transmission at Lmax (15.11 A) is 0.600
Total thickness of Al = 12.0 mm
Detector half-width 0.320 m,  pixel 5.00 mm,  rms 3.40 mm
         penumbra radius 21.70 mm,  min angle 4.78 mr
Q-range:  0.00200 - 0.03134 /A
Gravitational droop  2.21 -   4.62 mm
```

The next three lines give the numbers of surfaces and regions and the length of the parameter block. They are required, and the remainder of the file must follow in order:

```
SURFACES     25
REGIONS      28
PARAMETERS  189
```

Each surface definition is given on one line; zero entries may be left null:

`,,,,,1/`	PZ (plane perpendicular to z-axis) at z = 0
`1,,1,,,,-.0036/`	CZ (cylinder on z-axis), radius 60 mm
`,,,,,1,-2.498/`	PZ at z = 2.498 m
`486749,,486749,,-1,15.5,-60.0625/`	Cone on z-axis
`,,,,,1,-2.5/`	PZ at z = 2.5 m
`,,,,,1,-2.6/`	PZ at z = 2.6 m
`1,,1,0.6,,,-.2025/`	Cylinder parallel to z-axis, offset y = –0.3 m, radius 0.335 m
`,,,,,1,-2.9/`	PZ at z = 2.9 m
`1,,1,,,,-.0036/`	CZ, radius 60 mm
`,,,,,1,-3.1/`	PZ at z = 3.1 m
`1,,1,0.6,,,-.2025/`	Cylinder parallel to z-axis, offset y = –0.3 m, radius 0.335 m
`,,,,,1,-3.102/`	PZ at z = 3.102 m
`,,,,,1,-6/`	PZ at z = 6.0 m
`1,,1,0.6,,,-.2025/`	Cylinder parallel to z-axis, offset y = –0.3 m, radius 0.335 m
`,,,,,1,-6.002/`	PZ at z = 6.002 m
`,,,,,1,-6.8/`	PZ at z = 6.8 m
`585518,,585518,,-1,6.8,-11.56/`	Cone on z-axis
`,,,,,1,-6.802/`	PZ at z = 6.802 m
`,,,,,1,-7/`	PZ at z = 7.0 m
`,,,,,1,-7.001/`	PZ at z = 7.001 m
`,,,,,1,-7.013/`	PZ at z = 7.013 m
`1,,1,,,,-0.25/`	CZ, radius 0.5 m
`,,,,,1,-13/`	PZ at z = 13.0 m
`,,,,,1,-12.95/`	PZ at z = 12.95 m
`1,,1,,,,-5.6169E-4/`	CZ, radius 23.7 mm

Each region is a line with an entry for each surface:

```
-1  0  0  0  0  0  0  0  0  0  0  0  0  0  0  0  0  0  0  0  0  0  0  0  0
-1  0  0  0  0  0  0  0  0  0  0  0  0  0  0  0  0  0  0  0  0  0  0  0  0
 1 -4 -1  0  0  0  0  0  0  0  0  0  0  0  0  0  0  0  0  0  0  0  0  0  0
 1  4 -4  0  0  0  0  0  0  0  0  0  0  0  0  0  0  0  0  0  0  0  0  0  0
 0  0  1 -4 -1  0  0  0  0  0  0  0  0  0  0  0  0  0  0  0  0  0  0  0  0
 0  0  1  4 -4  0  0  0  0  0  0  0  0  0  0  0  0  0  0  0  0  0  0  0  0
 0  0  0  0  1 -1  0  0  0  0  0  0  0  0  0  0  0  0  0  0  0  0  0  0  0
 0  0  0  0  0  1 -4 -1  0  0  0  0  0  0  0  0  0  0  0  0  0  0  0  0  0
 0  0  0  0  0  1  4 -4  0  0  0  0  0  0  0  0  0  0  0  0  0  0  0  0  0
 0  0  0  0  0  0  0  1 -4 -1  0  0  0  0  0  0  0  0  0  0  0  0  0  0  0
 0  0  0  0  0  0  0  1  4 -4  0  0  0  0  0  0  0  0  0  0  0  0  0  0  0
 0  0  0  0  0  0  0  0  0  1 -4 -1  0  0  0  0  0  0  0  0  0  0  0  0  0
 0  0  0  0  0  0  0  0  0  1  4 -4  0  0  0  0  0  0  0  0  0  0  0  0  0
 0  0  0  0  0  0  0  0 -4  0  0  1 -1  0  0  0  0  0  0  0  0  0  0  0  0
 0  0  0  0  0  0  0  0  4  0  0  1 -4  0  0  0  0  0  0  0  0  0  0  0  0
 0  0  0  0  0  0  0  0  0  0  0  0  1 -4 -1  0  0  0  0  0  0  0  0  0  0
 0  0  0  0  0  0  0  0  0  0  0  0  1  4 -4  0  0  0  0  0  0  0  0  0  0
 0  0  0  0  0  0  0  0 -4  0  0  0  0  0  1 -1  0  0  0  0  0  0  0  0  0
 0  0  0  0  0  0  0  0  4  0  0  0  0  0  1 -4  0  0  0  0  0  0  0  0  0
 0  0  0  0  0  0  0  0  0  0  0  0  0  0  0  1 -4 -1  0  0  0  0  0  0  0
 0  0  0  0  0  0  0  0  0  0  0  0  0  0  0  1  4 -1  0  0  0  0  0  0  0
 0  0  0  0  0  0  0  0  0  0  0  0  0  0  0  0  0  1 -1  0  0  0  0  0  0
 0  0  0  0  0  0  0  0  0  0  0  0  0  0  0  0  0  0  1 -1  0  0  0  0  0
 0  0  0  0  0  0  0  0  0  0  0  0  0  0  0  0  0  0  0  1 -1  0  0  0  0
 0  0  0  0  0  0  0  0  0  0  0  0  0  0  0  0  0  0  0  0  1 -4 -1 -11 14
 0  0  0  0  0  0  0  0  0  0  0  0  0  0  0  0  0  0  0  0  1  4 -4  0  0
 0  0  0  0  0  0  0  0  0  0  0  0  0  0  0  0  0  0  0  0  0  1  0  0  0
 0  0  0  0  0  0  0  0  0  0  0  0  0  0  0  0  0  0  0  0  0 -1  1 -4
```

The *NAME* associated with each region; the first *NAME* is the problem title, and the second is the title of the source file:

```
 7m, 13m, 15A, 60Hz (1000us), Q=0.01/A
H2 (50/50,64/16), Fluxtrap, 40-cm Be, Pb
Shutter penetration
Bulk shield
Circular entrance aperture
Collimator entrance
Drift to T0 chopper
T0 Chopper
T0 chopper shielding
Collimator pipe
Collimator shielding
Frame-overlap chopper
Overlap chopper shielding
Collimator pipe
Collimator shielding
Frame-definition chopper
Frame-definition chopper shield
Collimator pipe
Collimator shielding
Circular exit aperture
Collimator exit
Drift to Sample
Sample
Aluminum
Secondary Flight Path
Secondary flight Path shielding
Detector
Beamstop
```

Next is the list of *INDEX* pointers into the parameter block:

```
   1   18    0  133    0  134    0  135  142    0  143  144  151    0  152
 153  160    0  161    0  162    0  163  166  167  168  169  189
```

Finally, the parameter block, including the source wavelength distribution:

```
90,-0.05,0.05,-0.05,0.05,2.5,.007525,6.8,.00444333,,8.95436-5,.0818145,16666.67,-1000,18,,,
91,102,47.6,11.24,5.83333E16,610,170,.667,8.67,5.68,2.08,.86,2.63,
  -1.700001,-1.698674,-1.69677,-1.694059,-1.69023,-1.684864,-1.677405,-1.667116,-1.653036,
  -1.633922,-1.608176,-1.579874,-1.544875,-1.49911,-1.453015,-1.394889,-1.336073,-1.27017,
  -1.198053,-1.128077,-1.054727,-.978697,-.90117,-.828609,-.75508,-.680891,-.608064,
  -.540398,-.472038,-.403717,-.342582,-.2799292,-.2202448,-.1641208,-.1068591,-.0565061,
  -.00302955,.0482707,.0975991,.1475286,.1969256,.2461485,.2951157,.341733,.387269,.432616,
  .475812,.519135,.56161,.603647,.645207,.685663,.727038,.767961,.808221,.852178,.893306,
  .937217,.978778,1.020489,1.062588,1.100546,1.141591,1.177922,1.213727,1.252556,1.286119,
  1.326629,1.370402,1.412875,1.467081,1.520122,1.581781,1.650554,1.722381,1.800968,
  1.889334,1.981707,2.078442,2.177055,2.278023,2.383607,2.487587,2.585048,2.668664,
  2.739018,2.795598,2.847828,2.88669,2.918281,2.943239,2.960935,2.973372,2.982054,2.988064,
  2.992237,2.995075,2.996995,2.998247,2.999082,2.999666,3,,,
20,9.42478E-5,117.0279,7257.36,12280.94,20,16666.67,,,
20,9.42478E-5,82.747,16253.48,22874.19,20,16666.67,,,,
30,.0337991,0.01,2,50,,
43,23,1.89712,34370,49665.1,37,0.01,0.1,,16666.67,-0.32,0.32,128,0.005,.0034,
   -.3231944,.3168057,128,0.005,.0034,23/
```

The program MC_RUN asks the user for the geometry file name, the number of histories to be detected, and a starting value for the random-number generator. The user chooses whether the recorded monitor spectrum is to represent a sample-in or a sample-out measurement. Options

are also given to convert the final output histograms, which are sums of weights, to integers. There are two ways to do this. If one wishes the error bars on the output to be similar to a Poisson distribution so they look like real data, and if the error from the number of histories is small, then the value for each bin can be replaced by a sample from a Poisson distribution with mean equal to the tally for that bin. If the error bars are already appropriate, then a simple Russian roulette procedure is to add a random number (on the range 0 – 1) and truncate the result to an integer. The following file is the output using the above geometry file. The running time to detect 300000 neutron histories (5.4×10^6 starts) was 4.55 hours on a 486/66 PC; the estimated experiment time is 10.5 seconds (at 1 MW proton beam power).

```
MONTE CARLO SIMULATION OF A NEUTRON SCATTERING INSTRUMENT
 MC_RUN code version: PC, September 17, 1995, P.A.Seeger
```

(At this point the text from the front of the geometry file is reproduced)

```
 Successfully read input file with  25 surfaces,  28 regions,
                                and 189 element parameters.
```

A test particle is sent along the instrument axis as a simple sanity check:

```
 Beam elements along the instrument axis:
 Surf  1, Z =   .000 m, enter reg  3, Shutter penetration
 Surf  3, Z =  2.498 m, enter reg  5, Circular entrance aperture
 Surf  5, Z =  2.500 m, enter reg  7, Drift to T0 chopper
 Surf  6, Z =  2.600 m, enter reg  8, T0 Chopper
 Surf  8, Z =  2.900 m, enter reg 10, Collimator pipe
 Surf 10, Z =  3.100 m, enter reg 12, Frame-overlap chopper
 Surf 12, Z =  3.102 m, enter reg 14, Collimator pipe
 Surf 13, Z =  6.000 m, enter reg 16, Frame-definition chopper
 Surf 15, Z =  6.002 m, enter reg 18, Collimator pipe
 Surf 16, Z =  6.800 m, enter reg 20, Circular exit aperture
 Surf 18, Z =  6.802 m, enter reg 22, Drift to Sample
 Surf 19, Z =  7.000 m, enter reg 23, Sample
 Surf 20, Z =  7.001 m, enter reg 24, Aluminum
 Surf 21, Z =  7.013 m, enter reg 25, Secondary Flight Path
 Surf 24, Z = 12.950 m, enter reg 28, Beamstop
 Surf 23, Z = 13.000 m, enter reg 27, Detector
 ** No exit found from Detector
```

Having found the source, the sample, and the detector, it is safe to proceed:

```
 Number of detector bins = 128 x 128 ( 90 radial), and    37 spectrum slices
 Output data forms: T       RT
 Initial random number = 075BCD15,  300000 neutrons to be detected
 Moderator phase space to be sampled =    .00060 mm**2-ster
                                       x 6.82 e-fold of energy
 Source brightness = 5.833E+16 n/ster/m**2/MW/s
```

A tally is kept of how much neutron statistical weight was absorbed in each element:

```
t     7m, 13m, 15A, 60Hz (1000us), Q=0.01/A   MC__951002_112859
Summary of neutron losses by region:
   11.77% lost in region  3, Shutter penetration
     .02% lost in region  6, Collimator entrance
   13.30% lost in region  8, T0 Chopper
   73.62% lost in region 12, Frame-overlap chopper
     .80% lost in region 16, Frame-definition chopper
     .00% lost in region 20, Circular exit aperture
     .00% lost in region 23, Sample
     .06% lost in region 24, Aluminum
     .00% lost in region 25, Secondary Flight Path
```

```
    .00% lost in region 27, Detector
    .00% lost in region 28, Beamstop

Beam is centered at (   -.02,  -3.19) mm, with rms (  7.7,   7.7) mm
 Total histories tracked:  5421391 (3.665E+08 neutrons)
 Detected in Transmission:  303763 (9.975E+05,    .27%)
 Detected in Scatter Mode:  300000 (5.191E+05,    .14%)
 Beam power on target:       10.5      Mw-s
 Bad-Frame neutrons passed:          0.000E+00
 Bad-Frame neutrons detected:        0.000E+00
 Final random number: 0FB3ECE2
```

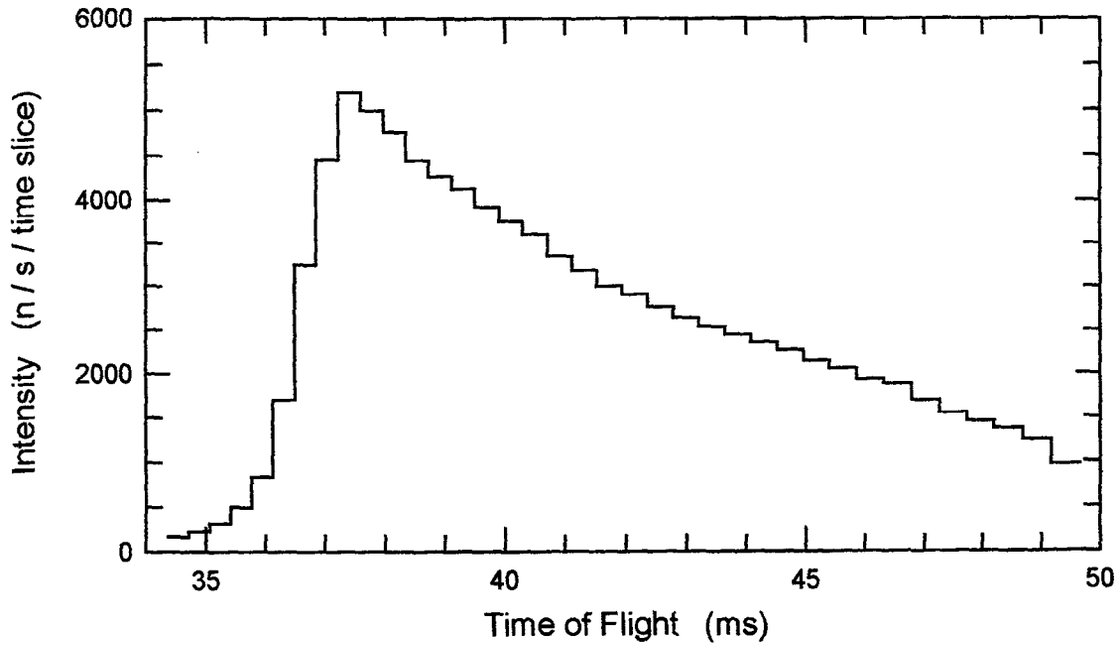

Figure 5. Time-of-flight spectrum of transmitted neutrons for LPSS test case.
At 13 m flight path length, the corresponding wavelength range is 10.5–15.1 Å. The source is a 1-MW spallation source with a coupled liquid H_2 moderator, pulsed at 60 Hz.

The output data files include header information and blocks of ASCII data for bin boundaries, data, and standard deviations. The values in the blocks are "," separated and "/" terminated as in the geometry file shown above. Data include the transmitted spectrum histogram (fig. 5) and a 2-dimensional histogram of counts integrated in radial zones on the detector for each time slice (fig. 6). By converting the radial data to Q for each individual wavelength (time slice) before combining, the time-of-flight wavelength resolution is maintained. The final result for this test case is shown in fig. 7.

8. Future Directions

It is the intention of the author that MCLIB remain in the public domain (see copyright notice in Appendix B). The most recent versions of the library and auxiliary codes as described above will continue to be available to any interested users from the author or from the Los Alamos Neutron Science Center (LANSCE) *via* Internet file transfer. Input of ideas, algorithms, and/or (public) code modules to expand the library is requested and encouraged, and will be acknowledged. Element types 70 through 79 are reserved for individual non-standard use; please contact the author for assignment of permanent type numbers.

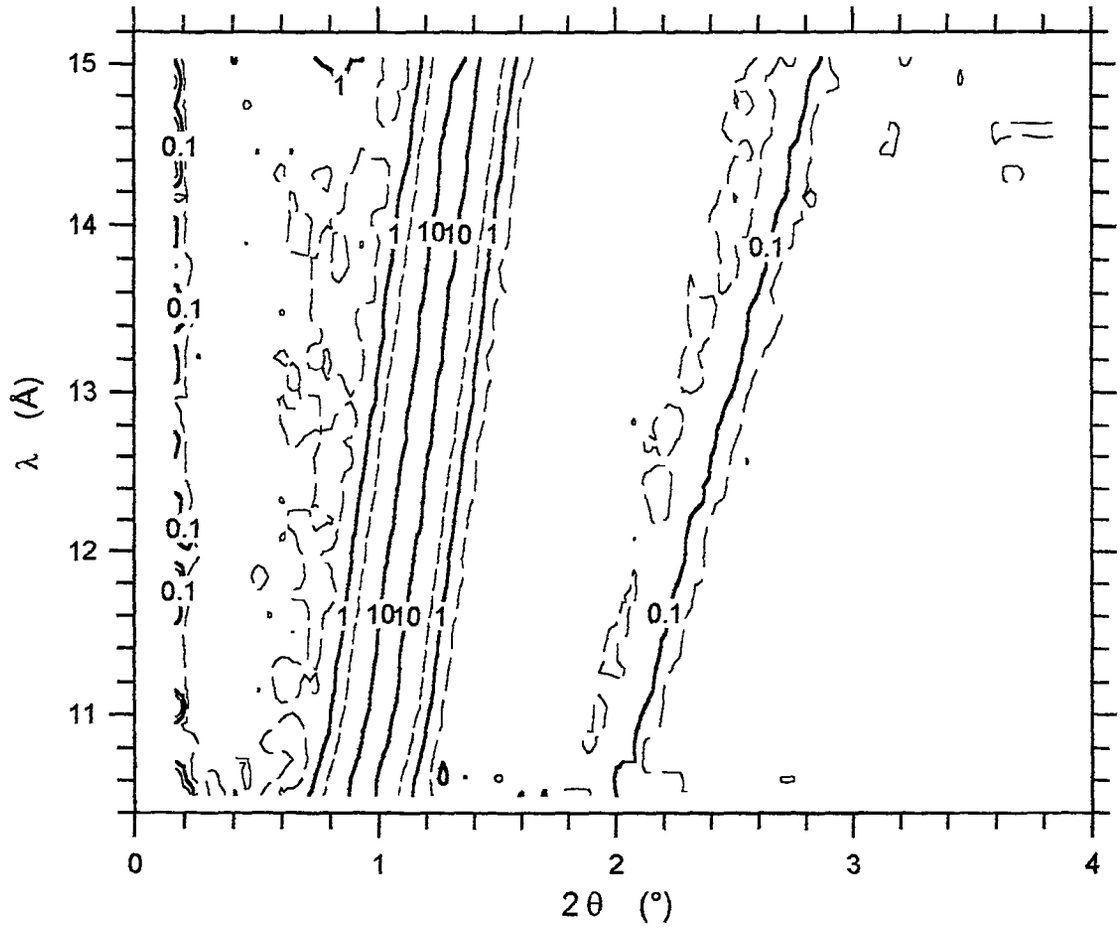

Figure 6. Relative count rate in detector *vs.* radial position and time of flight, for test case.
Time of flight has been converted to wavelength and detector radial zone to scattering angle (2θ). Contour intervals are logarithmic.

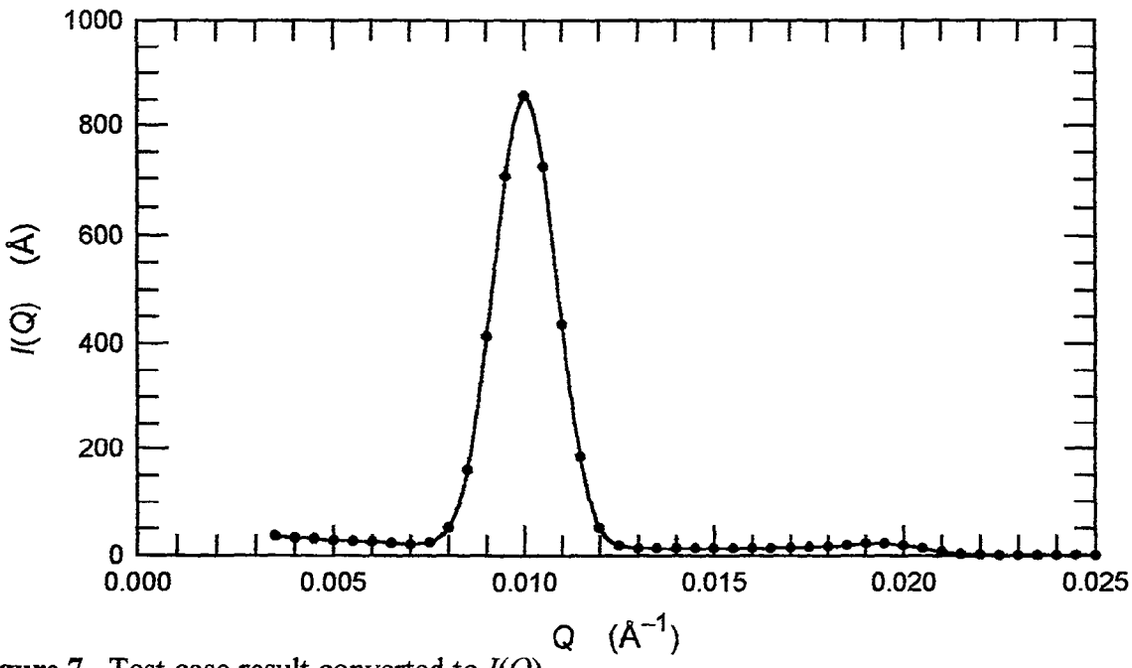

Figure 7. Test case result converted to $I(Q)$.
The scattering "sample" was a δ–function in Q at $Q = 0.010$ Å^{-1}. The standard deviation of the result is thus the resolution of the instrument at this value of Q; in this case $\sigma = 0.0009$ Å^{-1}.

A parallel (but separate) effort at LANSCE is developing a user interface (based on the Smalltalk language) which will greatly simplify design of new instrument configurations by facilitating creation of the geometry file [9]. The MCLIB library will be modified as necessary to support this project, and to include new features, such as polarization.

9. Acknowledgments

This effort has been supported historically by the U. S. Department of Energy under contract W-7405-ENG-36, and the author is grateful to the Los Alamos Neutron Science Center for their continued interest and support. Many (hopefully *most*) of the individuals who have contributed directly are listed in the text. I am also grateful to Jack Carpenter and Kent Crawford (IPNS) for making comments and suggestions for this manuscript.

10. References

[1] M. W. Johnson and C. Stephanou, "MCLIB: A Library of Monte Carlo Subroutines for Neutron Scattering Problems," Rutherford Laboratory report RL-78-090, September, 1978; M. W. Johnson, "MCGUIDE: A Thermal Neutron Guide Simulation Program," Rutherford and Appleton Laboratories report RL-80-065, December, 1980.

[2] P. A. Seeger and R. Pynn, "Resolution of Pulsed-Source Small-Angle Neutron Scattering," *Nucl. Inst. Methods* **A245** (1985) 115–124.

[3] P. A. Seeger, "Monte Carlo Calculations for the Optimisation of the Beam Optics of the LOQ Spectrometer," report to Rutherford Appleton Laboratory, 28 April, 1994.

[4] P. A. Seeger, G. S. Smith, M. Fitzsimmons, G. A. Olah, L. L. Daemen, and R. P. Hjelm, Jr., various contributions, Instrumentation for a Long-Pulse Spallation Source Workshop, Lawrence Berkeley Laboratory, Berkeley, CA, April 18–21, 1995.

[5] E. J. Pitcher, G. J. Russell, P. A. Seeger, and P. D. Fergusson, "Performance of long-pulse source reference target-moderator-reflector configurations," Proceedings of the 13th Meeting of the International Collaboration on Advanced Neutron Sources, October 11–14, 1995, Paul Scherrer Institut, Villigen, Switzerland.

[6] W. H. Press, S. A. Teukolsky, W. T. Vettering, and B. P. Flannery, *Numerical Recipes,* 2nd Edition (Cambridge University Press, 1992), section 7.3.

[7] S. Ikeda and J. M. Carpenter, "Wide-energy-range, high-resolution measurements of neutron pulse shapes of polyethylene moderators," *Nucl. Inst. Methods* **A239** (1985) 536–544.

[8] R. A. Robinson and J. M. Carpenter, "On the use of switch functions in describing pulsed neutron moderators," *Nucl. Inst. Methods* **A307** (1991) 359–365.

[9] T. G. Thelliez, L. L. Daemen, P. A. Seeger, and R. P. Hjelm, Jr., "A user-friendly geometry interface for the Monte Carlo neutron optics code MCLIB," Proceedings of the 13th Meeting of the International Collaboration on Advanced Neutron Sources, October 11–14, 1995, Paul Scherrer Institut, Villigen, Switzerland.

Appendix A
Files MC_GEOM.INC, MC_ELMNT.INC and CONSTANT.INC

Appendix B
Subroutine Abstracts

Editors' note:
In view of the length of these appendices, the author has agreed to our request to omit them from the published proceedings. The author has assured us that he will be pleased to provide a copy to anyone who is interested (see e-mail address on the title page). In particular, the file MCLIB.TXT containing a copy of the text of this article including the appendices may be obtained by anonymous ftp from

```
azoth.lansce.lanl.gov/pub/mclib.txt
```

The copyright notice referenced as being in Appendix B follows.


```
C
C         Copyright, 1995,  The  Regents  of the University of California.
C     This software was produced under a U.S. Government contract (W-7405-
C     ENG-36)  by the Los Alamos  National  Laboratory,  which is operated
C     by the University of  California for the U. S. Department of Energy.
C     The U. S. Government  is licensed to use,  reproduce, and distribute
C     this software.  Permission is granted  to the public to copy and use
C     this  software  without charge,  provided  that  this notice and any
C     statement  of authorship  are reproduced on  all copies. Neither the
C     Government nor the University makes any warranty, express or implied,
C     or assumes any liability or responsibility for the use of this soft-
C     ware.
C
```


See also late submission paper I-26

ICANS-XIII
13th Meeting of the International Collaboration on
Advanced Neutron Sources
October 11-14, 1995
Paul Scherrer Institut, 5232 Villigen PSI, Switzerland

DEVELOPMENT OF THE FLNP MEASUREMENT-AND-COMPUTATIONAL COMPLEX

Yu.A.Astakhov*, A.A.Bogdzel*, F.V.Levchanovsky*, B.Michaelis**, V.E.Novozhilov*, A.I.Ostrovnoy*, V.I.Prikhodko*, V.E.Rezaev*, A.P.Sirotin*, G.A.Sukhomlinov*, Yu.A.Volkov***

* Frank Laboratory of Neutron Physics, JINR, 141980 Dubna, Moscow reg., Russia
** Technical University Otto von Guerike, Magdeburg, Germany
*** Moscow Engineering Physics Institute, Moscow, Russia

ABSTRACT

In the present paper consideration is given to the problems connected with creation of a new generation of systems for experiment automation at the IBR-2 and IBR-30 pulsed reactors at the Frank Laboratory of Neutron Physics (FLNP).

1. Introduction

The purpose of this work is radical innovation of the electronics and software for spectrometers as well as development of the informational and computational infrastructure (ICI) of the FLNP, to make it possible to carry out experiments in the fields of condensed matter physics and of neutron nuclear physics at an up-to-date level at the IBR-2 and IBR-30 reactors and, in the future, at the IREN installation.

The implementation of a number of technical proposals [1-6] has laid down the basis for large-scale transition of the measurement and control systems of the FLNP spectrometers to a new generation of electronics, computational hardware and software involving the VME system and workstations integrated into the local computational network (LCN).

Keywords: Data acquisition, Electronics, Networks, Workstations

These systems, as compared with those already in operation (based on PCs and CAMAC devices), should exhibit qualitatively new measurement (this, for example, concerns IREN) and operational parameters and provide for parallel (including remote) control over data acquisition and accumulation, over variation of conditions at a sample, over information processing and visualization.

An essentially new requirement voiced by physicists-users is the requirement to create a unified set of hardware and software means for the entire complex of the Laboratory spectrometers, centralized archives of experimental data and unified means for analyzing data and for their graphical presentation. Implementation of this requirement will result in simplifying service of the spectrometers and essentially facilitate transition to the user policy at the experimental setups.

The overall problem of developing systems for the automation of experiments and for the Laboratory measurement-and-computational complex involve several independent ranges of activities, each of which is worth being examined individually.

2. Measurement and control systems for the spectrometers.

Recently, there have been purchased over 10 standard crates of the VME equipment, each of which comprises the following:

- a crate together with the power supply;
- a CPU based on the Motorolla 68020/30/40 processor with a RAM of 4 Mbytes;
- a HDD with a capacity of 100-300 Mbytes;
- a floppy disk driver;
- an ETHERNET card;
- an ADC and DAC block;
- input/output registers;
- a serial interface module.

Creation of a system for automation of the spectrometers requires developing and purchasing electronics for the readout, amplification, analog processing and transformation of signals from the detectors, for registration and accumulation of spectra, for control and management of the detector equipment (devices for substituting and positioning irradiated samples - step motors, goniometers etc.; devices for changing conditions at samples - the temperature, pressure, magnetic field, etc.).

The actual measurement-and-control spectrometer systems in operation were developed during various periods of time and in accordance with individual technical assignments. This has resulted in the electronics exhibiting an extremely low level of standardization, which hinders its operation and development and practically renders impossible any unification of the software. Moreover, a significant part of the electronic blocks have become obsolete and their parameters do not meet present-day enhanced requirements (thus, for experiments to be performed with the IREN installation a time

encoder will be needed operating at a rate of 10^6 pulses/sec with a minimum channel width of 50 ns, amount of channels up to 16384 and with up to 16 detector inputs; a spectrometric ADC with up to 8192 channels and conversion time of $3 \div 5$ μs will also be needed). Therefore, in transition to VME systems we cannot just copy the electronics operating within the CAMAC standard; what are needed are a radical innovation of the component base and of circuitry-and-engineering solutions, an improvement of the measurement characteristics, a reasonable limitation of the nomenclature of blocks to be developed and to be purchased, and, in certain cases, a revision of the techniques adopted for data readout and registration. When choosing a technical solution, such factors as the experience of other physical centers [7-10], standards accepted in JINR and available material base, are taken into account.

We shall now consider the main tasks and approaches in developing the electronics.

2.1. Detector electronics

Various types of detectors are utilized in the FLNP spectrometers:

- semiconductor detectors (Ge(Li)- and Si- detectors, high resolution Ge- detectors);
- scintillation detectors (detectors with Na(J) crystals, multi-section detectors with a liquid scintillator and with Li-glass windows);
- ionization and proportional chambers, including fission chambers;
- helium and boron neutron counters;
- position-sensitive neutron detectors (linear and two-coordinate PSD).

Each type of detector requires its own special electronics for the readout and optimum filtration of signals.

Most of the equipment for the semiconductor detectors is to be purchased at the market (probably, with the exception of the above-mentioned ADC).

The electronics for the scintillation detectors requires significant updating. The disadvantages of this equipment include the following: only current signals are read out, a low degree of integration, and, consequently, difficulties in production and adjustment. We propose to develop a preamplifier for the readout of charge signals as well as charge-to-digital converters based on up-to-date components. Thus, at present joint work is under way together with the Moscow Engineering Physics Institute (MEPI) for developing fast electronics for the scintillation detectors, making use of analog matrix crystals. The planned introduction of a large amount of detectors with Li-glass requires the development of standard multi-channel blocks of fast amplifiers and shapers. From a methodical point of view, an important task consists in suppression of the γ-background applying methods for analyzing the shape of pulses from these detectors, i.e. the creation of electronics for n-γ separation.

Owing to large differences in the operating conditions, in the constructions, and the gas fillings of ionization and proportional chambers, standardization of the analog electronics for this group of detectors is difficult. A new generation of preamplifiers

involving the readout of current and charge pulses must be developed. Unification must concern such blocks as amplifiers, discriminators, shapers, etc.

The amount of point-like neutron detectors continuously increasing necessitates the development of new electronic blocks extensive involving integral microcircuits (chips). The degree of integration necessary is such that the electronics for 16 or more detectors must occupy a single card. At present, work has started on testing a series of domestic and of imported microcircuits (chips) for the readout electronics from these detectors. A unified circuitry solution is under development for the entire electronics channel.

The spatial resolution of the linear PSD utilized in the FLNP is far from being up-to-date. One of the reasons is the low quality of the readout and processing electronics, which requires serious modernization and, also, probably, development of another method for signal readout, for example, making use of delay lines. The planned startup, at the DN2 spectrometer, of a high precision two-coordinate PSD (a neutron chamber with gas filling) will require the development of time-to-digital converters in the nanosecond range.

The nanosecond electronics, comprising discriminators, shapers, precise timing devices coupled with pulses from the detectors, coincidence circuits, summators, splitters of logical signals, etc., also requires up-dating.

Most of the detector electronics will be located in available CAMAC and NIM crates, which are most suitable for analog devices. Amplitude encoders, realizing the transformation of signals from the detectors may be located both in a CAMAC crate or incorporated in VME. In both cases the ADC digital codes are transmitted to the blocks producing event codes or to the histogram memory via connectors on the front panels of these blocks without making use of the VME bus.

2.2. Control and management systems of the equipment for the spectrometers

A large amount of equipment is used in experimental installations for positioning samples and detectors and for varying the conditions at the sample. The executive mechanisms of these devices, which include step motors, asynchronous motors of neutron beam choppers, furnaces, refrigerators, current/voltage supplies for producing constant and pulsed magnetic fields, high-voltage supplies for the detectors etc., exhibit great variety at various spectrometers, which significantly complicates unification of the electronics. For this reason, a decision has been adopted, now, to provide for maximum standardization of this equipment and, correspondingly, of the control-and-measurement equipment, of the regulators, and of the sensors. The whole complex of these problems and the technical solutions proposed are dealt with in separate work. Herein we only raise certain issues of the development and unification of electronics for the equipment mentioned, relevant to the utilization of VME systems.

The general functional control-and-management scheme for the executive mechanisms (EM) is presented in Fig.1.

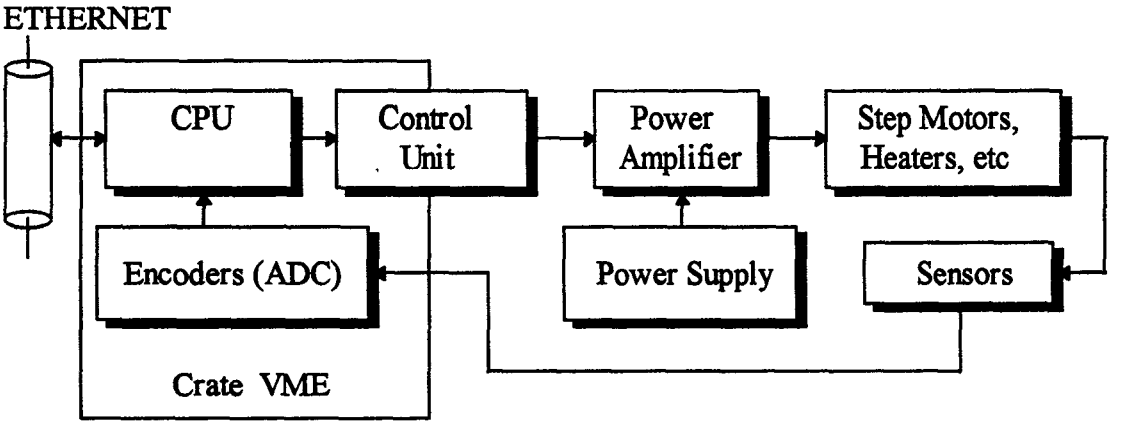

Fig.1. General functional control-and-management scheme for the executive mechanisms.

One of the main problems consists in the choice of a control block corresponding to the entire EM variety. This is evidently possible only if control is realized by means of software, i.e., if all the specific features exhibited in the concrete EM operation are taken into account in its control system. Two versions are possible for constructing such a block:

- involving an incorporated "intellect" (microcomputer);
- utilizing simple input/output registers and control from a VME processor.

The second version is preferable owing to its simplicity and to utilization of the same software environment OS-9 for the entire automation system. The first experience in application of the VME system at the NSVR high resolution neutron spectrometer has revealed that not more than 3-5% of the CPU resources are taken up in running EM control tasks [2]. Utilization of autonomous microprocessor blocks is justified, when the EM are sufficiently far away from the control crate (> 20 m) or when the equipment of the spectrometer is purchased together with the control block.

Unification of power amplifiers for the step motors is done quite simply. At present a power amplifier for alternate control of the motors is under development. The connection of the amplifiers with the control block is also to be developed in a unified form, suitable for connecting the amplifiers both to the input/output registers and the microprocessor blocks. The connection scheme is consistent with the scheme provided by the company Middex, whose equipment is utilized in many FLNP spectrometers.

At present, practically none of the spectrometers has a comprehensive system for acquisition of analog information on the state of the physical setup. The task of accumulating analog parameters and of producing control influences for the regulator is to be performed using ADC blocks with multiplexors at the input and multichannel DACs. Preamplifiers for each sort of sensor and power amplifiers for the regulators will have to be developed individually owing to the contradictory requirements of their input and output parameters, although even here standard solutions may be suggested. Anyhow, a significant part of these problems will be resolved in the course of standardization of the equipment surrounding the sample.

2.3. Data acquisition and accumulation

Figure 2 presents the general scheme for data acquisition and accumulation in experiments in condensed matter physics. From the Figure it can be seen that the encoding device assigns each detected event a time channel number and a detector number in the multidetector system (SCD point detectors, scintillation detectors, neutron detectors) or in the position group involving PSD, which are combined into a sole event code. This code is input to the histogram buffer memory, which interprets it as an address code and by hardware means increments by "1" the content of the respective memory cell. Thus, accumulation of spectrometric data proceeds directly inside the histogram memory without participation of the processor, which permits freeing the VME bus from performing routine operations continuously and provides for a minimum dead time.

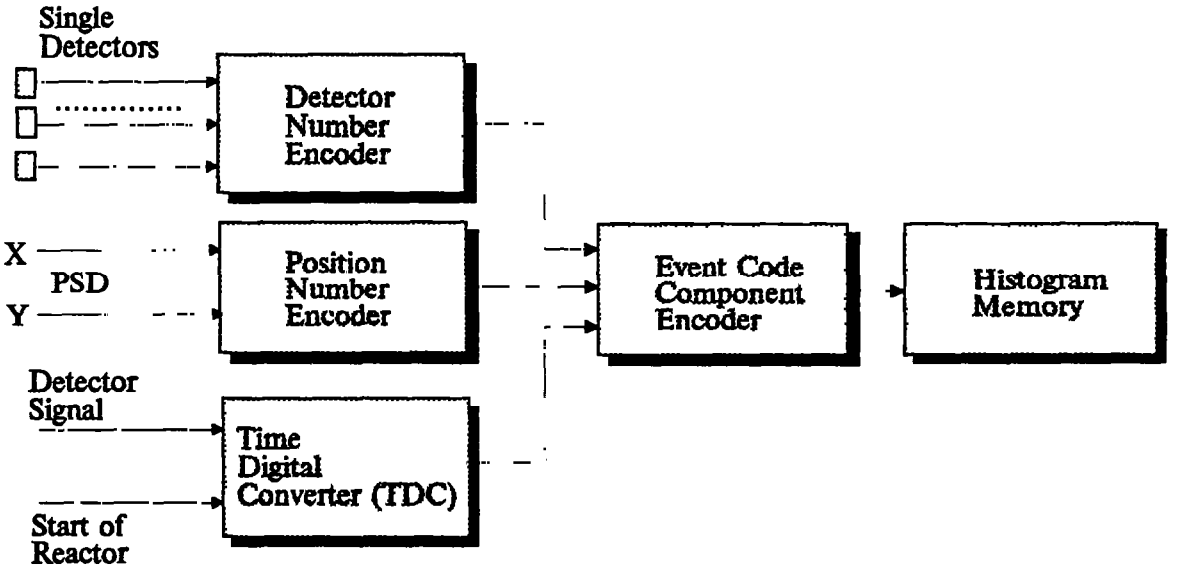

Fig.2. General scheme for data acquisition and accumulation

The number of point detectors utilized in experiments may be up to 128; the number of positions in linear PSD up to 64, and in two-coordinate PSD up to 128 x 128; the number of channels in TDC up to 1K ÷ 4K (up to 16K are planned). Thus, an information word (address) in present-day experiments may occupy from 10 up to 26 bits. A memory volume of 64 Mwords is required for accumulation of this amount of information. However, utilization of information re-encoders, involving the selection of events with the aid of "digital windows", makes possible reduction of the number of bits occupied by the event code and, accordingly, of the required memory volume. Another way of reducing the required memory volume consists in the application of a programmable scale in the TDC, i.e., in division of the time interval into several subintervals with channel widths differing from each other. In real experiments both methods are applied and in most cases a memory of 1 M sixteen-bit words turns out to be sufficient for data accumulation. Such a memory has been developed earlier in the VME standard [4], it represents a dual-port memory with an operation cycle of 350 ns.

The code of an event comes via connector on the front panel of the block. As viewed from the bus, this VME block represents an ordinary RAM, which is available to the processor at any moment (even during accumulation of spectra). If several detector systems are used in the experiment, then an appropriate number of encoders and memory blocks is required for data accumulation.

Now two VME modules are under development: a unified TDC (with the parameters indicated above) and a histogram memory based on SIMM modules, foreseeing the possibility of varying its volume from 1 to 64 Mbytes, depending on the concrete requirements of the experiment, with 32-bit words and a FIFO memory at the input for smoothing out the intensity peak.

In multiparameter experiments in neutron nuclear physics the information on an event represents a set of codes arriving from spectrometric ADC and TDC, which are stored in sequence in the buffer memory and, when it has been filled up, rewritten on magnetic carriers (hard disks, streamers etc.). The number of parameters registered in these experiments is from 3 to 8, while the maximum address space amounts to 10^{19} (the CASCADE spectrometer). These data cannot be sorted on-line, even taking into account that a significant part is discarded at the stage of accumulation.

Modernization of the existing equipment for multiparameter analysis will be carried out by improving the methods of selection and of data accumulation, and also by performing operations for sorting out on-line integral spectra over individual parameters for establishing control of the experiment. The electronic blocks for these purposes will be realized on the basis of digital signal processors (DSP) or transputers, which are to be utilized both at the stage of data accumulation and during subsequent (or parallel) processing. These blocks will have a large volume of dual-port memory available to the VME processor, and data transfer via the bus will be realized in arrays, as the memory is filled up. In order not to overload the network, raw data will be accumulated on a local disk and written to the archive in an off-line mode.

A prototype of a DSP-based [12] RTOF correlator costing nearly two orders of magnitude less, than correlators of the parallel type [13], has been developed for the High Resolution Fourier Diffractometer (HRFD), where correlation analysis of the inverse time of flight is applied. At present, a correlator is under development in the form of an autonomous VME module, in which data accumulation and processing is performed without participation of the VME processor. All four detector systems of the spectrometer will be equipped with such correlators.

The development of unified electronics for the automation systems of the spectrometers will be based on broad application of software-controlled microprocessor techniques (DSP, transputers) intended for real-time operation and of programmable logic matrices (ALTERA, XILINX).

3. The general concept underlying the organization of experiment automation systems

Control over the experiment as a whole and over the equipment of the spectrometer is performed by a computer in a VME crate, which provides for the following: data

acquisition and accumulation; control of the equipment of the spectrometer and implementation of the experimental program; interaction with the Graphic User Interface (GUI); storage of the data on a local disk or in the file-servers of the ETHERNET network. The VME manager crate has a built in disk, a multiprogram real-time operation system OS-9, TCP/IP and NFS network software.

For effective work the VME processor is assumed to have sufficient productive capacity and the VME bus is freed as much as possible from routine operations of accumulating spectra capable of loading it completely or nearly so. Note that data are exchanged via the VME bus between built in disks, streamers, and other programmable control blocks, and a broad range of network operations is performed too.

From the point of view of organization, the software for the automation systems is divided into the interface part GUI and the control part. Control and monitoring of an experiment and of the entire system is implemented by the user from GUI based on a workstation within the X-Windows environment and included in the ETHERNET. It represents combination of menus, windows, on-line help etc., i.e. programs providing interaction with the control system in the style adopted for the Windows system. Individual application programs of the graphics interface allow setting the configuration of the system, provide interactive control over separate devices of the spectrometer, testing the efficiency of its subsystems, and also control over the operation conditions of measurements. Realization of the user's interface in the Windows environment makes possible the presentation of information on the screen in text, numerical, and graphical forms at the same time.

The user's commands are transmitted via the GUI for implementation by the control part. Connection between the GUI and the control software is realized by means of the software of the ETHERNET network supporting the TCP/IP protocol. Since a personal computer (X-terminal) or a workstation can be included into the local network at any site, then, upon realization of such a user's interface, we acquire the possibility both of remote control over the spectrometer and of control from a computer located directly at the experimental setup.

The control part of the software is realized in the VME system and its operation is controlled by the OS-9 system. It performs all the functions, essential for carrying out the experiment, of direct control of the equipment of the spectrometer, acquisition and accumulation of information, preliminary data processing and storage in archives. The organization of software is discussed in greater detail in [1].

Thus, the VME electronics and software fully realize all the functions relevant to performing the experiment. The workstation is utilized as a user's graphic terminal during the dialogue between the user and the experiment automation system, i.e. it performs service functions and is intended for the organization of readily mastered and modern in style means of communication between the experimenter and the system. An essential point in this approach consists in the achievement of high reliability of the measurement systems, which is due to the VME computer being capable of monitoring the experiment

and accumulating data even in the case of failure of the equipment of the network, the file-servers and the workstations.

When the experiment is being performed, the physicist must have the possibility to carry out at the same time data analysis and processing, examination of the experimental information represented in graphical form. This can be done at any computer incorporated in the network, since during the experiment the data are recorded and stored by network file-servers in standard format.

4. Data formats

The representation of data within the automation systems may vary for different spectrometers and depend on the equipment and method of transforming information during the experiment, but the results of measurements and of subsequent processing must be written down in unified format. This is necessary for creating a unique software complex permitting, without additional transformations, to process and analyze data from different experimental installations, and also for convenience in comparison of the results of processing, obtained for the given sample under other conditions or at another setup. Essential also are the problems of unification in the processes of archive creation, searching for, and identification of collected data and of compatibility at the data level when various types of computers are utilized. The problem of choosing the data format should be resolved together with the problem of choosing the data base, the control system of the data base, and the software packages for the data processing and analysis. Commercially supported systems, being universal, exhibit significant superfluity, so at many centers specialized systems are under development. Obviously, it would be expedient to define the laboratory format, which would be economical for concrete tasks in the FLNP, and to develop programs for transforming it into international formats [14] or into formats adopted in collaborating organizations.

5. Creation of data archives

An archive is divided into two levels. The first is operational and has short access time (on hard disks) for files written in the archive at the current run. The second level is for long-term storage of data on rewrittable laser disks.

The amount of data obtained in experiments at IBR-2 and IBR-30 is constantly rising. Thus, for instance, during the period from November 1992 to June 1993, when 9 two-week cycles were carried out, data were obtained for ~ 450 samples [11] with the 11 spectrometers of the IBR-2. On the average, the volume of data accumulated during one IBR-2 cycle exceeded 1 Gbyte. This figure will increase significantly, when the spectrometer REFLEX are put into operation, new detectors for some of the spectrometers are established (a two-coordinate PSD for the DN-2 spectrometer, two large multi-section scintillation detectors for HRFD, a PSD for the MURN small-angle scattering spectrometer), and the nomenclature is expanded of devices for variation of the conditions at the sample.

The spectrometers at IBR-30 provide less information (~ 0.3 Gbyte per cycle), but it must be noted that in multiparameter experiments the volume of information is artificially restricted (selection using "digital windows") owing to the low capacity of the accumulating systems. The situation will become even more complicated, when the IREN setup is installed, the expected enhancement in the neutron flux intensity being of about an order of magnitude.

Determining the volume requirements of disk memory for organization of the archive and, in a broader sense, for supporting the entire information-and-computational infrastructure of the Laboratory, is a complex problem, the solution of which must involve taking into account a great number of inter-related and inter-dependent parameters, many of which are difficult to predict.

Theoretically, the capacity of the archive should be planned starting from maximum possible information flows from the spectrometers, although more precise estimations are based on the actual amount and conditions of experiments to be carried out during the period predicted. The memory volumes of the first and second levels of the archive depend, also, on the rate and profundity (degree) of data processing, which, in turn, depend on the efficiency of the computers utilized, on the quality of available software, on the existence of local computational facilities at the spectrometers, on the organization of data accumulation and processing, and on a number of subjective factors.

It must be pointed out that the operational archive and ICI make use of the same memorizing environment shared between the users, spectrometers, and system problems. Therefore, in estimating the resources of disk subsystems required it is necessary to take into account the constantly and rapidly rising demands related to development of the infrastructure (the appearance of new software, the creation and utilization of various data bases, enhancement of the number and activity of users, expansion of communications with other centers, improvement of the informational service, the constant rise of intrasystem overhead expenses etc.).

Finally, the world experience reveals that in normal conditions the computational facilities and volumes of disk space must double at least every three years [7]. When new setups, spectrometers, detectors etc. are put into operation the doubled figures indicated must be accordingly increased. It is also well-known that the requirements of disk memory cannot be overestimated, since users are capable of filling up any informational space in relatively short time. At present, somewhat over 30 Gbytes are at the disposal of the FLNP SUN-cluster. Taking into account the above mentioned factors we plan significant enhancement of the disk capacity both for operational and long-term data storage. Specifically, the Jukebox archive system on rewrittable magnetic-optical disks of total capacity 40 Gbytes was purchased a few months ago.

6. Software packages

As a rule, each scientific research center makes use of some software package for analyzing and processing experimental information. Thus, for instance, RAL applies GENIE, the center for nuclear physics in Rossendorf uses AVS, HMI (Berlin) applies

PV-wave, and CERN uses PAW. But, besides this, often packages of more general purpose are applied, since the problems dealt with by physicists in planning an experiment or in designing an experimental setup may include general mathematical calculations, simulation, etc. It is expedient to let the users choose the graphics package or processing program most appropriate for the concrete case. First of all, this implies the graphics software packages intended for utilization in data processing and analysis with application of computer graphics. Effective application of any of the packages with the purpose of analysis and processing experimental information in FLNP requires the development of specialized application software (such as for standard operations with spectra: summation, normalization, background subtraction, decomposition of peaks, calculation of measurement errors, etc.), besides the facilities provided by the package itself.

The packages listed above are all organized in the same way, from the point of view of the user. They provide the user with a set of programs for processing and transforming data, a set of graphics programs and an interpreter, which makes possible easy utilization of available graphical facilities and of means for data processing, and, also, the construction, without any detailed knowledge of computer graphics, of applications in the form of interpretable programs for integrating the graphics and processing. Such packages, as a rule, permit creating C and FORTRAN programs, which are specialized for a concrete range of applications, and utilizing them in interpretable programs together with standard commands.

The libraries of programs for data processing and the graphical facilities of packages determine their lines of application, although they may overlap to a certain extent. There also exist differences in the resources required and in the operation speed (the more sophisticated the package, the slower it is and the more disk and operational memory it needs).

At the FLNP for the first step, GENIE and PV-Wave packages are to be installed and mastered.

7. Network and computer infrastructure

As one can see from the above, performing experiments at an up-to-date level, as well as normal activity in the Laboratory, are practically impossible without reliable operation of LCN, its continuous development, and enhancement of resources.

Until recently, many of the FLNP LCN parameters have not even satisfied the everyday demands of users, first of all owing to the low reliability of the network equipment, to the capacity of the disk subsystems being insufficient, to the inadequate physical and logical configuration of the network, to the absence of many software products, to the bad service etc.

In 1994-95 significant efforts have been undertaken for the ICI development, new workstations (two of the SPARCstation 10 type and four SPARCstation 20), additional disks, four network HP LaserJet 4Si/MX printers, two colour HP DeskJet 1200 C/PC printers, five X-terminals, etc. have been purchased and installed. The new configuration

of the network resources and its logical organization are presented in Fig.3. Measuring systems of spectrometers and PCs in physicists' offices are included into LCN. The SUN-cluster, which consists of servers and workstations, holds a central position in the network. At present, more than 150 PCs, 2 servers and 14 workstations are incorporated into the network. Twenty three PCs of the total number are placed in the experimental halls and pavilions of the IBR-2 and IBR-30 reactors. These computers are connected to the CAMAC equipment and provide for data acquisition and accumulation, as well as for control over the experiment. They are run by the MS-DOS system and the PC-NFS network software. In addition, PCs in users' offices make use of the MS-Windows system.

The SUN-cluster includes different models of SPARCstation computers, all of them are run by the SunOS 4.1.3 system and network software supporting the TCP/IP protocol. The NFS (Network File System) is used for organization of the distributed file system of the cluster. More than 230 users are registered in the SUN-cluster. The X-Windows system (version 5), installed in the computers of the SUN-cluster, allows the user to work with any computer (or with several computers simultaneously) both in a remote mode and at the console of the workstation.

At the moment the NQS (Network Queue System) is being installed on the SUN-cluster computers for automatic distribution of tasks between the computers in the cluster, and also in order to provide for even workload and to increase the rate of running non-interactive tasks. This system enables the user to put the task on the queue to be executed, and the NQS system will send it to a less loaded computer of the cluster. NQS periodically autosaves the task context and this makes it possible to continue its execution in case of a failure in the cluster operation. It is of importance for time-consuming tasks.

The shared resources of the SUN-cluster computers include: disk space and computational resources; CD-ROM; devices for storing information on the EXABYTE magnetic tape of capacity 2.3 Gbytes and 10 Gbytes; devices for reading/writing data to rewrittable magnetic-optical disks; the JukeBox archive system.

Figure 3 also presents information on "specialization" of the SUN-cluster computers, i.e., it indicates the main tasks which should be executed by this or that computer, the content of software packages which require considerable amount of the disk and RAM memory and high performance of the processor. In spite of the mentioned specialization, the users may work on all the cluster computers in a usual computational mode.

Part of the workstations are intended to exercise control over the experiment, to perform an on-line analysis and processing of the accumulated data, therefore the names of the spectrometers to which these computers are assigned, are given in this figure. At the HRFD, NERA-PR and NSVR spectrometers, the greater part of the work connected with transition of electronics to the VME-based equipment, will be completed by the end of 1995.

Today, from a logical point of view, all the computers are connected to a single segment of the network (physically to several lines interconnected with repeaters), which,

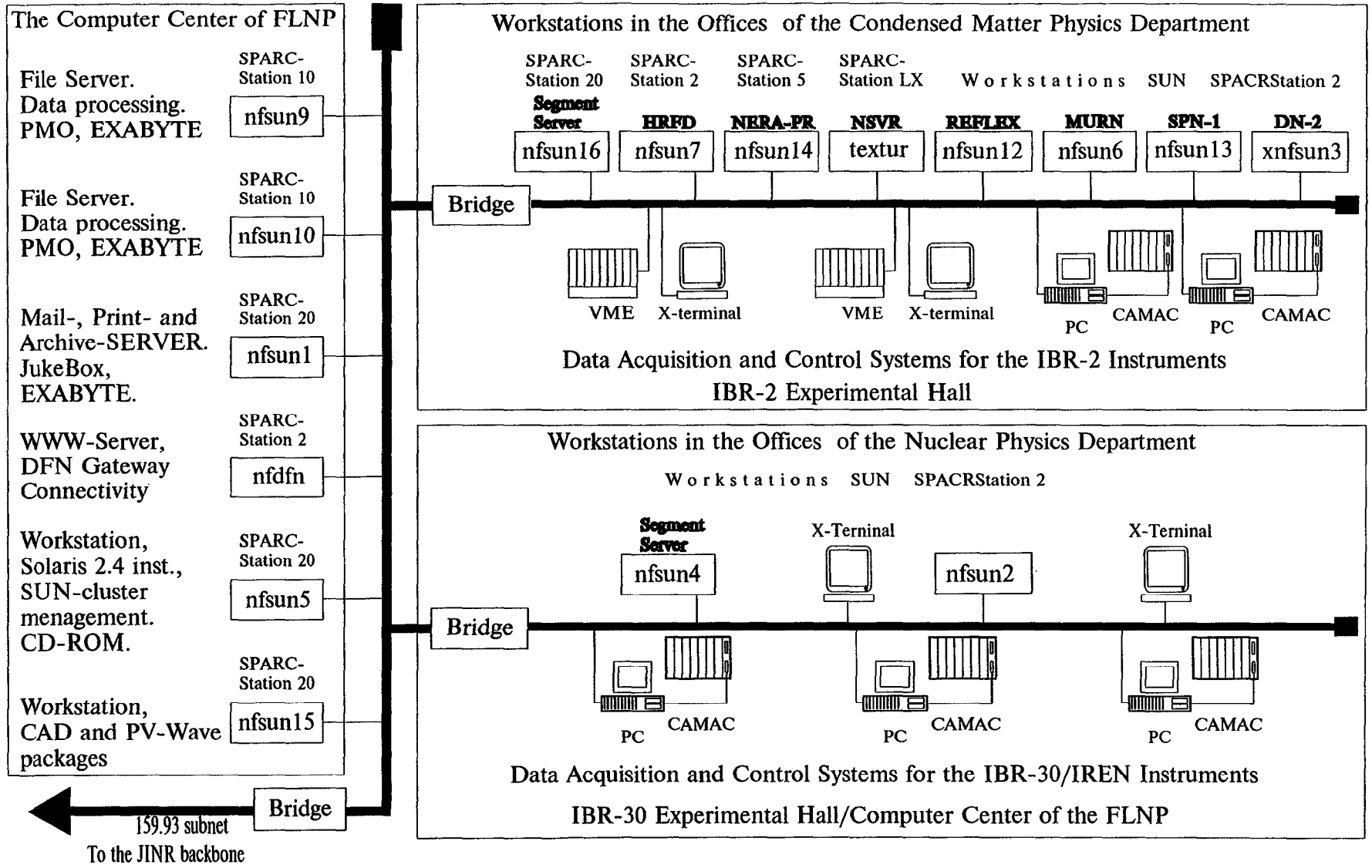

Fig. 3. Structure of the local area network of the FLNP.

in turn, is one of the segments of the JINR network and is separated from it by a network bridge. A network of the ETHERNET type is known to function effectively when its load does not exceed 30%, after which its capability of operation drops drastically. From general LCN construction principles it follows that the elements of the network, including sources of information and accumulation means (i.e. actually representing a closed information system) must represent an individual segment and be separated from the rest of the network by a bridge connecting the information flows inside this segment. Outside such segments one finds, as a rule, equipment which itself does not generate large information flows and to which access must exist from all segments. Such are the system of archiving for long-term storage, file-servers with general-purpose software (translators, libraries etc.), powerful computational servers for operation in the package processing mode, etc. Usually, at the central segment there are located computational means of distributive or administrative services, which must have the same easy access to all the other network segments and which, also, do not create large flows of information.

At the end of 1995 we shall complete the work aimed at dividing the single FLNP network segment into a central segment and segments of physics departments, and also for incorporating into the network the computers located in all the Laboratory buildings [15]. Thus, all the computational means of the measurement systems of the spectrometers at the IBR-2 and IBR-30 and the computational means serving the reactor equipment directly and practically operating independently of each other will be divided into two separate segments.

Ideally, each spectrometer or, which is more realistic, each group of similar spectrometers with common means for generation, storage and processing of information should be made to represent an individual segment. This means that it is necessary to concentrate, as much as possible, the data storage and processing at the place where the data were obtained, and thus to essentially reduce the load of the network. For financial reasons, however, this work is postponed. The problem of current concern is to replace the section of the ETHERNET network which includes servers and computers providing service for the Laboratory, for the ATM type network to provide more effective operation of servers.

8. Conclusion

The FLNP spectrometers have much in common and at the same differ essentially from each other in the amount and type of detectors, in the equipment used for varying the conditions at the sample, in the volume and speed of data accumulation, in the control algorithms, etc. Accordingly, the automation systems of the experiments also have their own specific features, although attempts are made in developing them to achieve maximum unification of both the electronics and the software. At the same time the problems of data formats and archive creation, of developing the graphic user interface, of applying standard mathematical processing packages and of graphical representation of the data, of integrating local computational means of the spectrometers into the LCN are common in nature and will be resolved in the same way for all the experiments carried out in the Laboratory.

9. References

[1] V.E.Novozhilov et al., Organization of a distributed system within the VME standard for automation of experiments at the IBR-2 reactor (JINR, P10-94-8, Dubna, 1994)

[2] Zen Yen Ken et al., Management and control system for the HRNS spectrometer within the VME standard (JINR, P13-94-73, Dubna, 1994)

[3] A.I.Ostrovnoy et al., Programmable blocks for management and control of the parameters of experimental installations at the IBR-2 and IBR-30 reactors in the CAMAC and VME standards (JINR, P13-94-76, Dubna, 1994)

[4] V.E.Rezaev, Spectrometric memorizing device in the VME standard. *Talk at the XVI International Symposium on nuclear electronics* (Republic of Bulgaria, Varna, 12 -18 September, 1994) [to be published]

[5] D.A.Balagurov et al., System for experiment automation at the High Resolution Fourier Diffractometer (JINR, P10-94-91, Dubna, 1994)

[6] Yu.A.Astakhov et al., Development of the FLNP network infrastructure and SUN-cluster [to be published]

[7] W.C.A.Pulford, Future Strategy for Computing at ISIS, *ICANS-XI International Collaboration on Advanced Neutron Sources* (KEK, Tsukuba, October 22-26, 1990)

[8] G.Herdam et al., Time-of-Flight Data Acquisition Unit (DAU) for Neutron Scattering Experiments. Specification of the Requirements and Design Concept (HMI-B-478, Berlin, 1984)

[9] P.Ziem, The Design of VME Based Data Acquisition Systems, *Proc. of the International Symposium "Electronic Instrumentation in Physics"* (Dubna, 14-17 May 1991, JINR, E13-91-321, Dubna, 1991)

[10] H.Schwab, RTA, Remote Task Activation (ILL, SI Internal Grenoble, 1991)

[11] Frank Laboratory of Neutron Physics, *Report of Activity 1992-1993* (JINR, E13-94-191, Dubna, 1994)

[12] V.A.Butenko et al., RTOF-correlator based on the TMS 320C25 digital signal processor for a high-resolution Fourier diffractometer (JINR, P10-94-87, Dubna, 1994)

[13] P.Hiismaki, H.Poyry, A.Tiitta, *Appl. Cryst.* **21** (1988) 349-354

[14] M.Konnecke, Proposal for a European Neutron Scattering Data Exchange Format

[15] A.V.Alfimenkov et al., Priority measures for development of the FLNP information-and-computational infrastructure [the FLNP project].

ICANS-XIII
13th Meeting of the International Collaboration on
Advanced Neutron Sources
October 11-14, 1995
Paul Scherrer Institute, 5232 Villigen PSI, Switzerland

PRINCIPLES OF REVERSE TIME-OF-FLIGHT METHOD AND FOURIER TECHNIQUE

P. Hiismäki
Technical Research Centre of Finland
P.O.Box 1404, FIN-02044 VTT, Finland

ABSTRACT

A general lay-out and principle of operation of the reverse time-of-flight measurement is given, applicable particularly to studying diffraction at powdered samples and predictively also to coherent exitations at single crystal samples, both characterized by spectra made up of peaks. Conclusions on the applicability of the method at steady state sources and pulsed sources of short or long pulse duration are presented[1] .

1. Introduction

The interest in the reverse time-of-flight (RTOF) method, introduced in 1972 [1], has only recently started to grow outside of the small core of pioneers. The major impact forwards took place in 1992, when the first implementation at a pulsed neutron source, the high-resolution Fourier diffractometer HRFD was completed in Dubna and started its successful operation [2]. Powder diffraction has so far been the sole area of applications. The first successor of the early demonstrations was the mini-SFINKS diffractometer, jointly built by PNPI, Russia and VTT, Finland in Gatchina [3]. It has already been used some ten years for extensive studies on crystallography. The next installation FSS, the Fourier strain spectrometer, started its operation in Geesthacht in 1988 [4]. Currently there is an on-going project for constructing a time-of-flight Fourier diffractometer at the ET-RR-1 reactor in Cairo, Egypt [5].

Most of the published litterature on the subject deals with experiments at steady state sources. It seems, however, that best performance and widest spectrum of applications can be expected at
pulsed sources [2,6], coinciding with the trend of planned future neutron sources. There the trade between resolution and intensity has led to short pulse moderators, suffering

[1] Keywords: Fourier, Reverse TOF, Diffraction, Phonons

from severe losses in intensity and to intensity optimized, long pulse moderators, suffering from poor inherent resolution. A spallation neutron source can normally have both type of moderators simultaneously, while a pulsed reactor lacks the short pulse option. If the source pulse is not short enough, the desired resolution is most advantageously provided by Fourier choppers, operated in the RTOF-mode. Yet, the information on the on-state of the source is very useful in screening out the "wrong" neutron histories and thereby markedly increasing the signal to noise ratio. In the RTOF-method this screening can be achieved in a very flexible manner.

Complying with the workshop character of session T3, the strategy from general to specific, rather than vice versa, was considered more appropriate for dealing the subject and arriving at specific conclutions to be assigned to different types of neutron sources. It should be realized, however, that while some of the concepts to be presented are well established already, some are at a very embryotic state lacking experimental verification or quantitative simulation. The experimental arrangement to be considered is shown in Fig. 1.

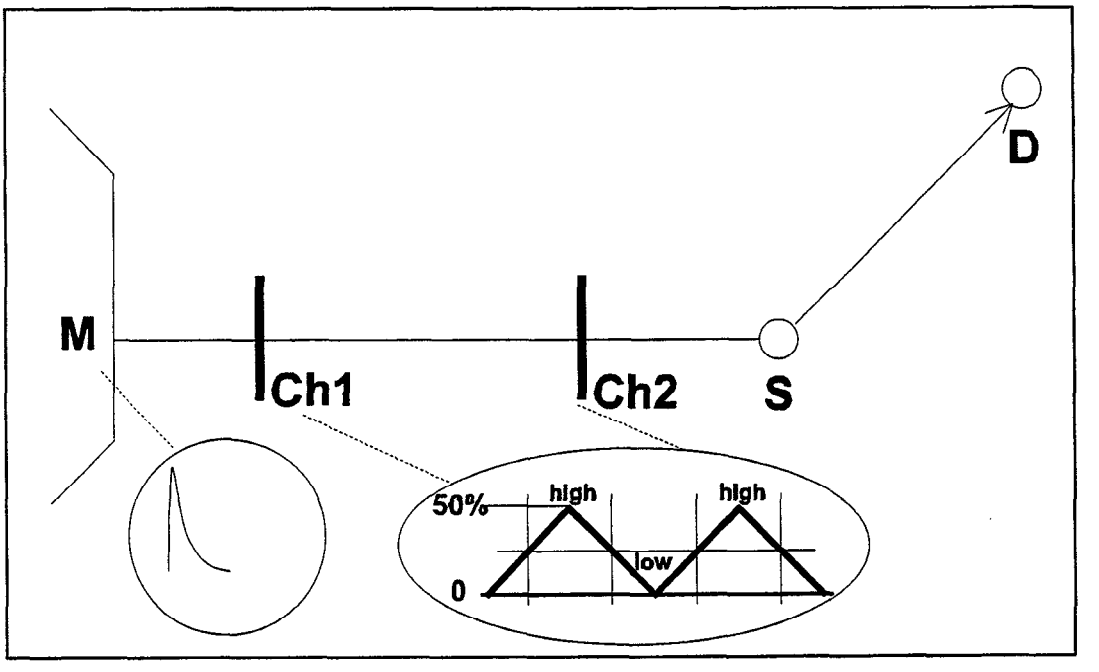

Figure 1. The schematic lay-out of the experiments under consideration. M is moderator of the source, Ch1 and Ch2 two Fourier choppers, S sample and D detector. Inserts show the time-dependence of the moderator intensity and chopper transmission.

2. RTOF-plot

The basic idea of the RTOF-method is to check for each neutron detected, whether certain postulated neutron histories have high or low probability of occurrence based on the knowledge on the actual state of the source or of the time-dependent selectors installed in the flight path. Because neutron detection occurs at the very end of its flight, checking must act on instants of the immediate past extending to the longest time-of-flight

expected. Therefore the history of the states of the source and of the neutron selectors must be made available as continuously updated arrays for real time classification between the high or low probability histories. Such arrays are conveniently obtained from discrete time shift registers, provided with parallel outputs for every time channel.

The trajectories of neutrons as the travelled path length versus time-of-flight are conveniety presented in a RTOF-plot shown in Fig. 2. The figure shows the largest conceivable number of

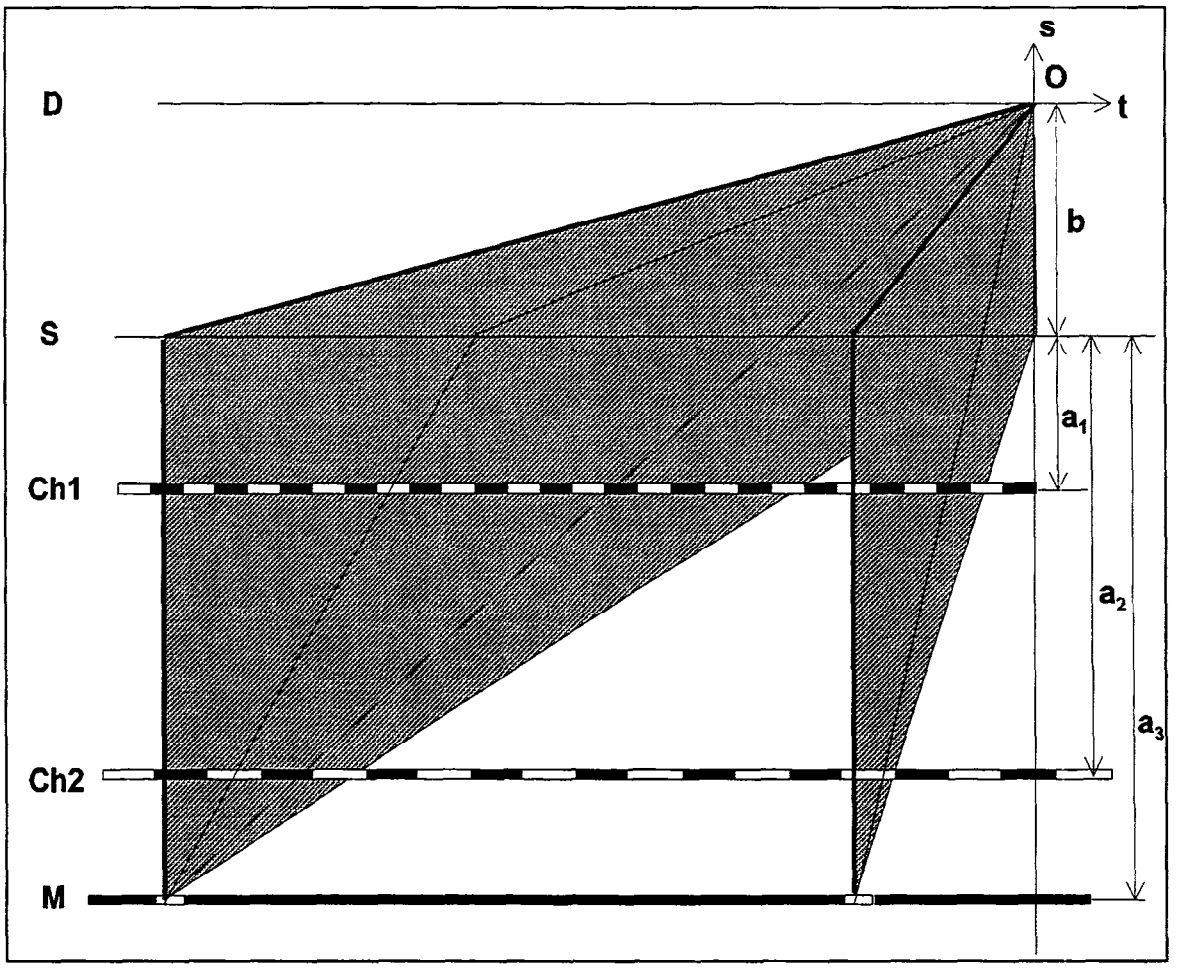

Figure 2. RTOF-plot for a pulsed source and two Fourier choppers. Horisontal lines labelled with D, S, Ch1, Ch2 and M are the locations of detector, sample, chopper1, chopper2 and moderator. Origin is fixed at the detector at the instant of neutron detection.

neutron selectors to be used for classification of neutron histories. Depending on the neutron source and on the purpose of the experiment the picture can be much simpler. The binary moderator delay line, labelled with M, is shown as the black horizontal ribbon, most of the time off, but shortly interrupted by the white on-states, as the burst of neutrons are emitted. The two black and white ribbons labelled with Ch1 and Ch2 are binary delay lines of two Fourier choppers. White colour indicates the high-transmission state and black

colour the low-transmission state of the chopper. The grey quadrangles are the allowed time-of-flight frames associated with two most recent moderator pulses. Each frame is divided by the straight, elastic scattering line into the down-scattering regime to its lef and up-scattering regime to its right. Presented in reversed time order the allowed neutron histories start from the origin as a straight line within the grey frame to any point of the sample line S and continue from there as another straight line staying within the grey frame to any white point at the moderator delay line.

Screening means that certain neutron histories are considered as impossible and are not classified or recorded at all. This applies to histories with the moderator in the off-state or, in the case of two choppers, also to histories with one of the choppers in the on-state and the other in the off-state, such as the elastic line in the most recent frame of Fig.2.

Measuring means classification of the unscreened histories in the high-probability and low-probability records. The down-scattering history in the most recent minus one frame must be classified as a high-probability event, since all selectors were in white on-state along its path. The elastic history of the same frame must be classified as the low-probability event, since both choppers were in black off-state along its path.. As the choppers are rotated according to one of the common frequency windows used in Fourier synthesis taking care that all phases of the choppers are uniformly covered without any mutual correlation, the signal or an estimate of the time-of-flight distribution is obtained by subtracting the low-probability record from the high-probability record and an estimate of its variance by adding the two together. Because the local Fourier codes of two time-of-flights outside of the resolution width are practically orthogonal, frame-overlap disappears from the signal, but is present in the variance part.

Considering now powder diffraction or one-phonon scattering at a single crystal along a chosen line in the momentum space the time-of-flight scan for one detector is allways one-dimensional. This means that one has to connect every time channel of the moderator delay line to one and only one time channel of each chopper delay line according to some simple rule chosen according to the experiment. For this adjustmet two parameters for each delay line n are available, namely the channel width $\Delta t^{(n)}$ and the predelay $d^{(n)}$. Three different scans can be accomplished namely $\{k_i = \text{const.}\}$, $\{k_f = \text{const.}\}$ and $\{ k_i / k_f = \text{const.} \}$ with the last scan containing the elastic scan as a special case. The choice of parameters for each of the three scans are compiled in Table 1.

Table 1. Choice of the delay line parameters for the three different scans. $T^{(1,3)}{}_i$ is the incident neutron time-of-flight between components (1,3), e.t.c.

	k_i = const.	k_f = const.	$k_i / k_f = r_k$ =const.
channel width condition	$\Delta t^{(1)}=\Delta t^{(2)}=\Delta t^{(3)}$	$\frac{\Delta t^{(1)}}{a_1} = \frac{\Delta t^{(2)}}{a_2} = \frac{\Delta t^{(3)}}{a_3}$	$\frac{\Delta t^{(1)}}{a_1 + r_k b} = \frac{\Delta t^{(2)}}{a_2 + r_k b} = \frac{\Delta t^{(3)}}{a_3 + r_k b}$
predelay condition	$d^{(1)} = d^{(3)} - T^{(1,3)}{}_i$ $d^{(2)} = d^{(3)} - T^{(1,2)}{}_i$	$d^1 = d^2 = d^3 = T^{(S,D)}{}_f$	$\frac{d^{(1)}}{a_1 + r_k b} = \frac{d^{(2)}}{a_2 + r_k b} = \frac{d^{(3)}}{a_3 + r_k b}$

3. TOF scans in momentum space

A simple FCC lattice of Fig. 3 was chosen as a frame of reference for illustrating in the momentum space the three TOF-scans introduced above for a single detector. Scan 1 with $\{k_i = \text{const.}\}$ is not very interesting, because only one detector can measure along the same line for fixed orientation of the sample. Modifying scan 2 from $\{k_f = \text{const.}\}$ to $\{k_f\sin(2\theta) = \text{const.}\}$, brings scans 2 of all detectors, independent from θ, to coincide in the momentum space differing in their energy transfer versus momentum transfer relationship, as well known from TOF-operating spectrometers. Scan 3 is a very interesting scan directed right to the origin of the

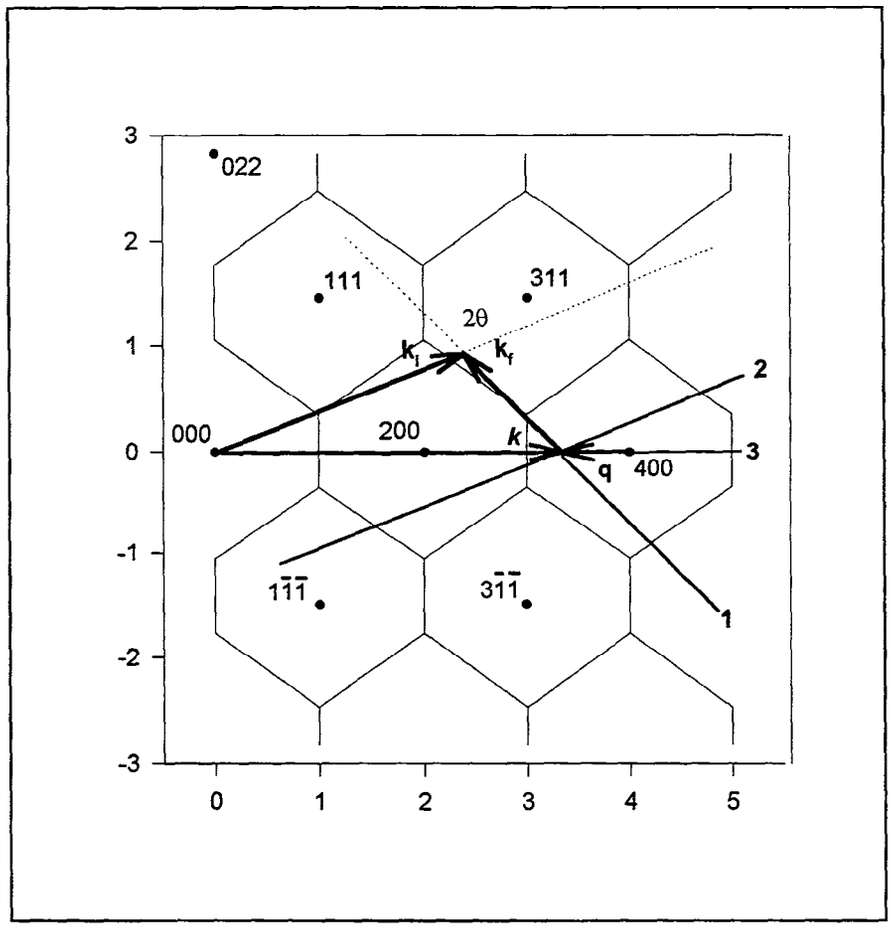

Figure 3. Reciprocal lattice plane of an FCC-crystal, perpendicular to (01$\underline{1}$)-axes, with 1 labelling the $\{k_i = \text{const.}\}$-scan, line 2 the $\{k_f = \text{const.}\}$ scan and line 3 the $\{ k_i / k_f = \text{const.} \}$-scan.

momentum space. If this scan is adjusted to go through any of the neighbouring reciprocal lattice points, only longitudinal phonons will get exited. Like before scans of detectors at different scattering angles can be adjusted to coincide in the momentum space, while their energy transfer versus momentum transfer relationship follows parabolic law. A certain scattering angle corresponds to elastic scattering allowing one to

accomplish a very simple diffractometer with inelasticity discrimination leading to definite signal-to-noise ratio benefit compared to the total scattering instruments, almost exclusively used to day.

3. Applicability of RTOF-method at different neutron sources

A general guide for the applicability of the RTOF-method for studies on diffraction and on phonons or magnons at different neutron sources is outlined in Table 1. The prospects of the steady state source case are limited because screening of "wrong" neutron histories implies installing an extra pulsed chopper with severe intensity losses compared to a

Table 2. Applicability of RTOF-method versus neutron source type.

	STEADY STATE	LONG PULSE	SHORT PULSE
DIFFRACTION for crystallography	*Well established* Total scattering Instrument with one chopper, applicability: samples with less than about 50 parameters	*Well established* Total scattering Instrument with one chopper+ inelasticity discrimination applicability: samples upto more than 50 pameters	Only benefit could be achieving inelasticity discrimination, but not competitively with long pulse source
for residual strains	*Well established*	*Established*	No benefit
PHONONS & MAGNONS: three scans with the same instrument!	Implementation requires one Fourier chopper and one pulsed chopper. Applicability depends on comparison with TAS	Probably competitive. Low resolution with one chopper, high resolution with two choppers and modif. data acquisition	Probably competitive. High resolution with one chopper only and simple data acquisition

pulsed source. On the other hand powder diffraction studies on samples of "medium complexity" seems to be very competitive compared to the other alternatives available at steady state sources.

Considering powder diffraction at pulsed sources one should notice that due to time-focussing and large detector a whole range of wavelengths are contributing to the same Bragg reclection. Focussing condition can be met for one neutron selector at a time only. If another one is used for inelasticity discrimination, its time aperture must be made large enough, roughly matching the duration of the long pulse source, in order to avoid

reduction of the effective area of the detector. Therefore intensity optimized, long pulse source seems to be the best choice for achieving inelasticity discrimination, useful especially for hydrogenous samples.

Residual strain application characterized by precise determination of small shifts of the positions of relatively few peaks fits ideally with the strengths of the RTOF-method. There high resolution and also good neutron economy are essential, because very small sample volumes are desirable. The unique possibility of synthetizing the diffraction peaks in antisymmetric shape has turned out to be very effective in precise detrermination of the peak shifts. [4]

Application of the RTOF method to phonon or magnon spectroscopy is still at a conceptual study stage. The next step needed is a simulation study for finding the latitude in the choice of the main parameters of such an instrument as well as a quantitative assessment of the expected performance.

4. References

[1] P. Hiismäki, Neutron Inelastic Scattering, Proceedings of A Symposium Grenoble 1972, (IAEA Vienna 1972) p. 803

[2] V.L. Aksenov, A.M. Balagurov, V.G. Simkin, Yu.V. Taran, V.A. Trounov,

V.A. Kudrjashev, V.A. Bulkin, V.G. Muratov, P. Hiismäki, A. Tiitta, and O. Antson, International Collaboration on Advanced Neutron Sources, ICANS-XII, Oxfordshire,

U.K., Proceedings of The Twelth Meeting ICANS-XII 1994, Vol.1 p. 124

[3] O. Antson, A.P. Bulkin, P. Hiismäki, T.K. Korotkova, V.A. Kudryashev, H. Kukkonen, V.G. Muratov, H. Pöyry, A.F. Schebetov, A. Tiitta, V.A. Trounov and V.A. Ulyanov, International Conference on Neutron Scattering, ICNS'88, Grenoble 1988, Physica B (1988) p.

[4] J. Schröder,V.A. Kudryashev, J.M. Kreuter, H.G. Priesmeyer, J. Larsen, A. Tiitta, Journal of Neutron Research **2** (1994) p. 129

[5] R.M.A. Maayouf, H.-G. Priesmeyer, V.A. Kudryashev, GKSS 91/E/65, GKSS-Forschungszentrum, Geesthacht GmbH, (1991)

[6] P. Hiismäki, Journal of Neutron Research (to be published)

ICANS-XIII
13th Meeting of the International Collaboration on
Advanced Neutron Sources
October 11-14, 1995
Paul Scherrer Institut, 5232 Villigen PSI, Switzerland

PERFORMANCE OF THE HIGH RESOLUTION FOURIER DIFFRACTOMETER AT THE IBR-2 PULSED REACTOR; LATEST RESULTS

V.L.Aksenov*, A.M.Balagurov*, V. A. Trounov†, P.Hiismaki‡

* Frank Laboratory of Neutron Physics, JINR, Dubna, Russia
† St.-Petersburg Nuclear Physics Institute, Gatchina, Russia
‡ Technical Research Center of Finland, Espoo, Finland

ABSTRACT

The High Resolution Fourier Diffractometer (HRFD) was designed for neutron powder structural studies and was realized at the IBR-2 pulsed reactor in Dubna. The RTOF method is used at HRFD for gathering diffraction spectra. High $\Delta d/d$ resolution, close to 0.001, and high neutron flux at the sample position, ~10^7 n/cm^2/s, make HRFD one of the best diffractometers in the world intended for the structural studies of polycrystalline materials and studies of internal stresses in bulk samples.

1. INTRODUCTION

HRFD is a neutron reverse time of flight Fourier-diffractometer intended for diffraction experiments with polycrystalline materials at a resolution level of about 0.001 or better [1]. It operates at the high flux pulsed reactor IBR-2 in Dubna and is a spin-off of the cooperation between JINR (Dubna), PNPI (Gatchina) and VTT (Espoo). The main special feature of HRFD, distinguishing it from other Fourier-diffractometers, such as mini-SFINKS [2] and FSS [3], operating at steady state reactors, is the analysis of the triple correlations between signals from the neutron source, Fourier-chopper and detector. As a result, the neutron intensity measured with HRFD is:

$$I(t) \sim \int R_s(t-\tau)R_c(t-\tau)\sigma(\tau)d\tau + c\int R_s(t-\tau)\sigma(\tau)d\tau + B(t), \qquad (1)$$

where R_c is the resolution function of the Fourier chopper, R_s is the source pulse, σ is the scattering cross section of the sample, B is the conventional background and c is a certain constant close to 1. The second term, which can be called "the correlation background" is proportional not to the total detected intensity as in the case at steady state reactors, but to the intensity measured in short time intervals equal to the width of the source pulse (~350 μs for IBR-2). This leads to a substantial decrease of that

correlation background, better quality of the diffraction patterns and permits the useful wavelength interval to be extended.

The first experiments with HRFD were performed in 1992 and the results from them were reported at the ICANS XII conference [1]. Since, the development of HRFD has continued, first of all with the detectors, data acquisition system and data analysis procedure. In early 1994 regular experiments were started at HRFD, mainly in two directions: structural studies of new materials and of residual stress in bulk samples [4]. Here we report the current situation with HRFD performance and some results of recent experiments.

2. THE EXPERIMENTAL SET-UP

The HRFD diffractometer is installed on one of the beam-lines of the IBR-2 pulsed reactor (Fig.1). Immediately behind the reactor shielding a background chopper is placed as a filter for fast neutrons and γ-rays. The distance between the moderator and the Fourier chopper is about 9 m. The neutron beam before the Fourier chopper is formed by a straight mirror neutron guide, and after it, by a focusing, horizontal and vertical, curved neutron guide 19 m in length. This guide tube acts both as the forming element for the neutron beam and an additional filter of fast neutrons and γ-rays. Having passed through the choppers and the neutron guide, the neutron flux at the sample position is close to 10^7 n/cm^2/s. Currently, only two of the four detectors planned for operation are working, at the scattering angles of +152° and +90°. The RTOF electronics of the HRFD is based on a dual-delay-line correlator [2] of special design. At present, two 8192-channel analyzers operate simultaneously with the Fourier chopper pickup signals, in opposite phases. For a back-scattering detector these analyzers cover the 3.2 Å *d*-spacing interval, usually from 0.6 Å to 3.8 Å, if the channel width is equal to 4 μs. For the 90°-detector a new DSP-TMS320C25 based correlation analyzer has recently been designed and tested [5].

3. INSTRUMENT PERFORMANCE

Usual experiments with standard samples have been performed with HRFD. They revealed the main parameters of the diffractometer to be close to the computed ones [6]. The resolution function of HRFD depends on the maximum modulation frequency of the neutron beam and on geometrical uncertainties. In principle, the value of 0.00035 is accessible at HRFD for both terms and then $R=0.00035\sqrt{2}=0.0005$ (for d=2 Å). Usually, however, experiments are performed with $R\approx0.0010$ (Fig.2). The effect of such high resolution is shown in Figure 3. The *d*-spacing scale of HRFD is very linear (Fig.4) and that offers the possibility of obtaining lattice parameters of powders with an accuracy close to 10^{-5}.

HRFD Layout

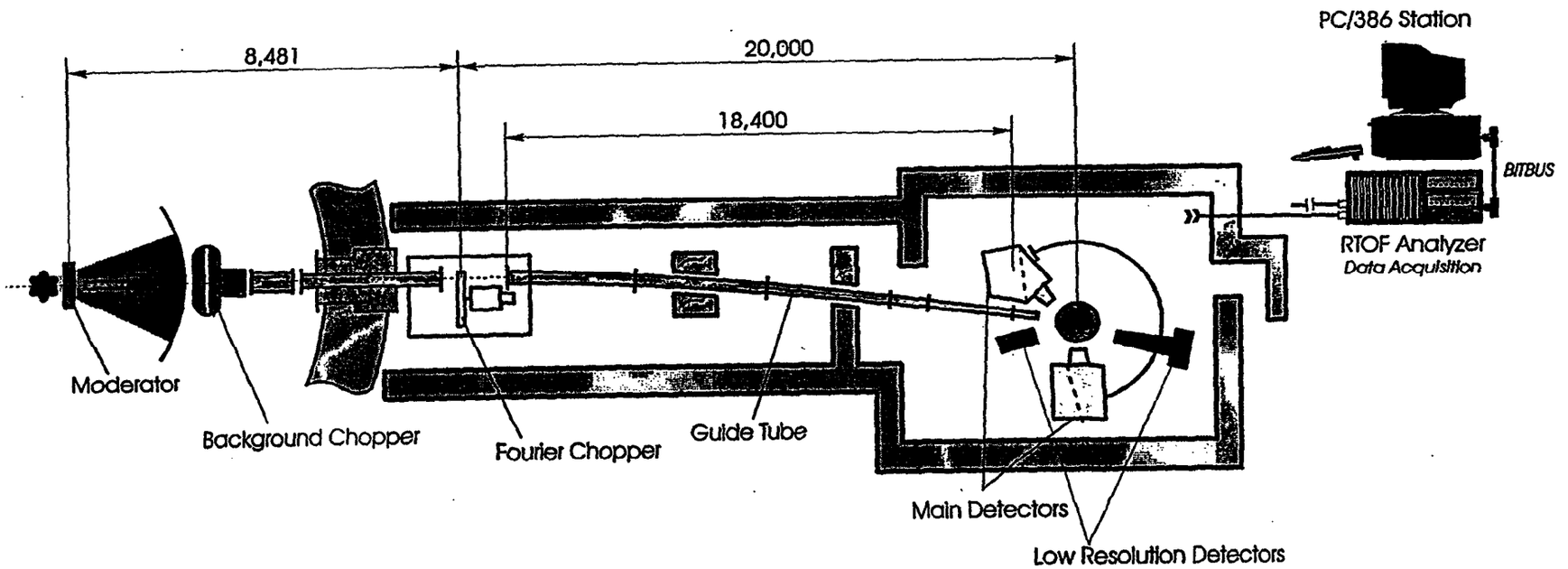

Fig. 1

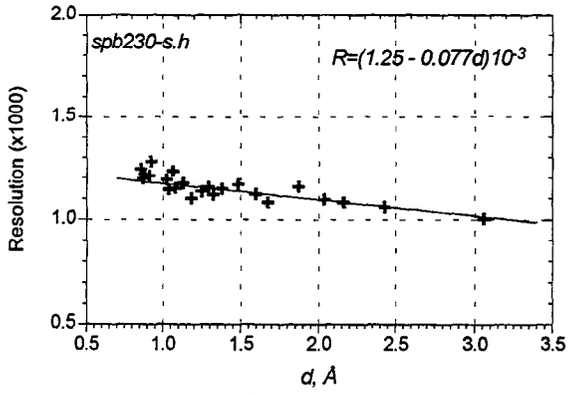

Fig.2. The resolution function of HRFD as a function of d-spacing measured on a high quality powder sample $Bi_{1.7}Mg_{0.3}Nb_{0.7}O_{6.5}$ (SPB) with pyrochlor-type cubic structure.

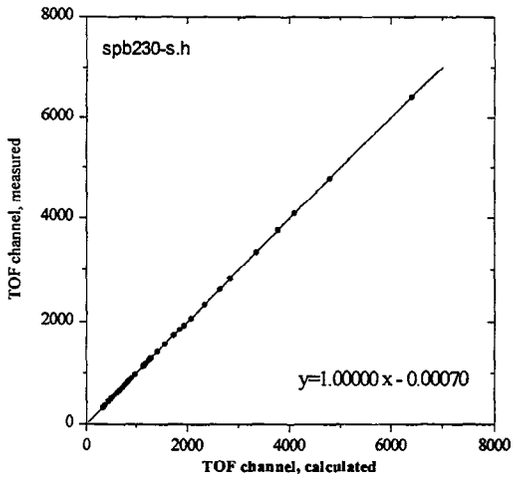

Fig.4. Measured versus calculated TOF channel positions of diffraction peaks of the SPB sample demonstrating the very linear TOF-scale of HRFD.

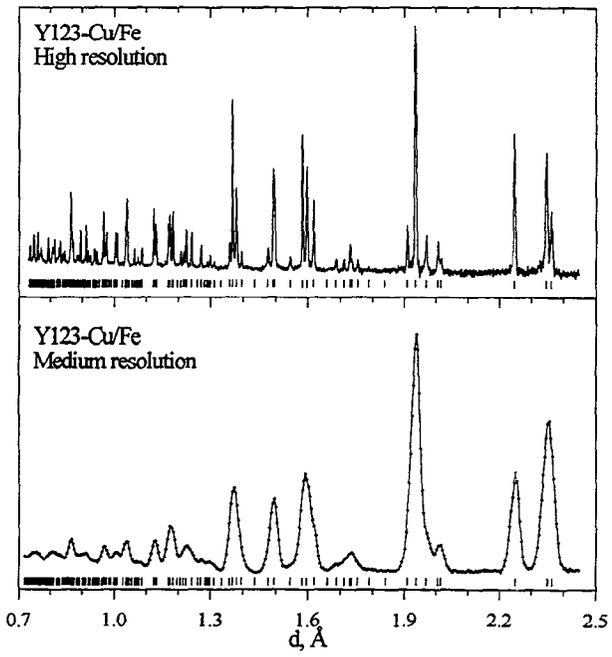

Fig.3. Comparison of $YBa_2Cu_{2.7}{}^{57}Fe_{0.3}O_{6.3}$ diffraction patterns measured with HRFD in conventional and high resolution modes.

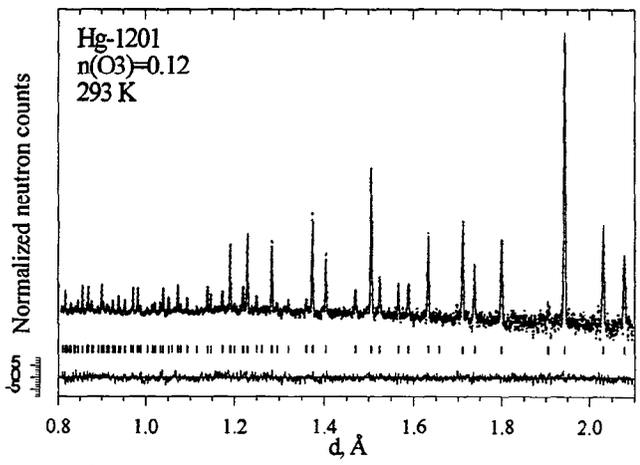

Fig.5. Diffraction spectrum from $HgBa_2CuO_{4.12}$ measured with HRFD and processed by the Rietveld method.

4. EXAMPLES OF EXPERIMENTAL STUDIES

Among the physical experiments performed at HRFD, the following HTSC compounds were studied: $Y(^{44}Ca)Ba_2Cu_4O_8$, $YBa_2{}^{65}Cu_{2.7}Zn_{0.3}O_7$ and several $HgBa_2CuO_{4+y}$ (Hg-1201) samples with various oxygen contents. As an example, in Figure 5 the diffraction pattern of $HgBa_2CuO_{4.12}$ is shown after Rietveld refinement.

In this study [7] the precise structural data for Hg-1201 system were obtained and the real dependence of the superconducting phase transition temperature on oxygen content was found. The very high resolution of HRFD helps the realistic values of experimental structure factors to be obtained for many diffraction peaks of a sample under study and to calculate experimental and difference Fourier maps for the scattering density (Fig.6).

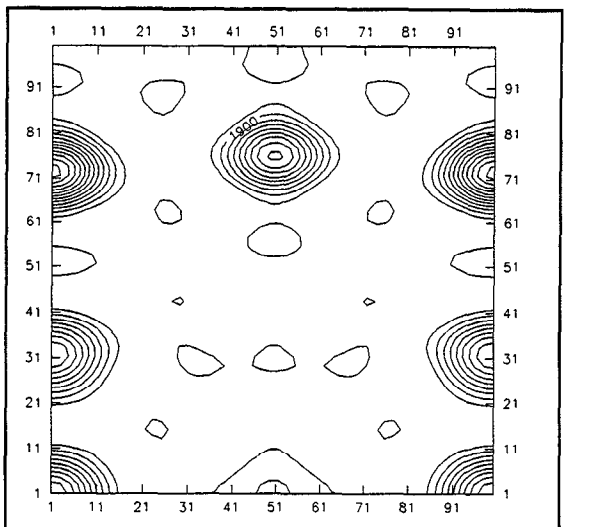

Fig.6. Experimental Fourier map of the y=0 plane of $YBa_2Cu_{2.7}{}^{57}Fe_{0.3}O_{6.3}$, containing Cu1, O4 atoms in chain, Cu2, O2/O3 atoms in plane and apical oxygen O1. The Cu1 and Cu2 sites occupied partly by iron atoms.

5. CONCLUSION

In [2] it was supposed that the Fourier technique at a pulsed neutron source can successfully be used to refine low-symmetry crystal structure with much improved signal-to-noise ratio compared with a steady state source case. The present experience fully confirmed that supposition.

The further development of HRFD includes setting up two large detectors at $2\theta=90°$ and doubling the solid angle of the back scattering detector. The sample environment equipment which includes a cryostat down to 4 K and a He-refrigerator for $8 \leq T \leq 300$ K will be complemented by a furnace up to 900 K and gas high pressure cells up to 1 GPa.

REFERENCES

1. V.L.Aksenov, A.M.Balagurov, V.G.Simkin et al., *ICANS-XII, RAL Report 94-025*, v.I, p.124, Abingdon, 1993.
2. P.Hiismaki, H.Poyry, A.Tiitta, *J.Appl.Cryst.*, 21 (1988) 349.
3. J.Schroder, V.A.Kudryashev, J.M.Keuter et al., *Neutron Research*, 2 (1994) 129.
4. A.M.Balagurov, V.G.Simkin, Yu.V.Taran, *Materials Science Forum*, 166-169 (1994) 257.
5. V.A.Butenko et al., *JINR Communications*, P10-94-87, Dubna, 1994.
6. A.M.Balagurov, *Material Science Forum*, 166-169 (1994) 261.
7. E.V.Antipov, A.M.Balagurov, S.N.Putilin et al, to be published.

ICANS-XIII
13th Meeting of the International Collaboration on
Advanced Neutron Sources
October 11-14, 1995
Paul Scherrer Institut, 5232 Villigen PSI, Switzerland

The Fourier-RTOF neutron diffractometer FSS at the 5 MW research reactor FRG-I

Hans Georg Priesmeyer
Institut für Reine und Angewandte Kernphysik,
- Angewandte Neutronenphysik -
Christian-Albrechts-Universität Kiel
c/o GKSS Research Center
Max-Planck-Str.1, D-21502 GEESTHACHT, Germany
e-mail: Hans-Georg.Priesmeyer@GKSS.DE

Introduction

At the GKSS research center new experimental facilities have been built around the FRG-I reactor to cover a wide variety of different aspects of materials science, which will help to understand the macroscopic behaviour of materials by studying their microstructure. This covers also the non-destructive measurement of strains within polycrystalline materials and the subsequent calculation of the internal stresses, which are important both from the technical as from the basic research point of view.
The concept and layout of the FSS spectrometer - which stands for *Fourier Strain Spectrometer* - was therefore optimized for this purpose.
From comparison of the positions of Bragg reflections in strained and unstrained specimens the lattice strain is detemined as the relative difference between the two. The fact that the elastic constants of most materials are crystal-orientation dependent and that texture may considerably influence their intensities, led to the decision to use time-of-flight diffractometry to measure the positions of Bragg reflections. Any variations of peak intensities at different angles of observation indicate the presence of texture, the knowledge of which is important in order to calculate stress factors, using the orientation distribution function. Stress factors replace elastic constants when stresses are calculated from strains for textured samples. Since the duty cycle of a high-resolution chopper is too low to allow to perform time-of-flight spectroscopy at a steady state reactor source economically, only a correlation spectrometer can be used. In this case the two competing properties „neutron intensity" and „resolution" are decoupled: the resolution in a time-of-flight Fourier spectrometer is determined by the three components: angular resolution (divergent neutron beams), flightpath resolution (sample sizes and aperture outlines) and time resolution (e.g. the maximum frequency of beam modulation and time channel width in this case). If this latter component is further decreased by using a higher modulation frequency, this will not affect the intensity of the neutron beam. There is another advantage of a Fourier spectrometer which becomes important, when the widths of Bragg reflections have to be measured. Peakbroadenings in general can be caused by size effects or microstrain effects. If they need to be analysed, the shape of the resolution function must be accurately known. Using the calculations of V.Kudryashev, we can choose adequate rotor rotational frequency programs to make the resolution function Gaussian, or the first or second derivative of it, so that any deviation from these shapes leads to information about the physical phenomenon which caused the broadening. ([2], [3], [4],).

Technical details of the FSS design

The main features of the spectrometer have been described in [1]. The instrument is operating in a stable and reliable manner over the periods of time necessary at a low power neutron source to arrive at the statistics requested. According to the materials investigated, standard rotor speed programs, delay times and channel widths have emerged from the growing experimental experience, so that a standardized data evaluation can be performed on a PC. The sample positioner control system is connected to the control of the experiment, so that scan measurements (like through-thickness scans or measurements across the full geometrical extension of a sample) can be performed automatically.
Figure 1 is a schematic of the RTOF diffractometer at this time, while there is hope to be able to install an second detector opposite to the existing one, in order to do simultaneous measurements in the directions of two mutually orthogonal scattering vectors. This will reduce the measuring times for tensor determinations by more than a factor of two.

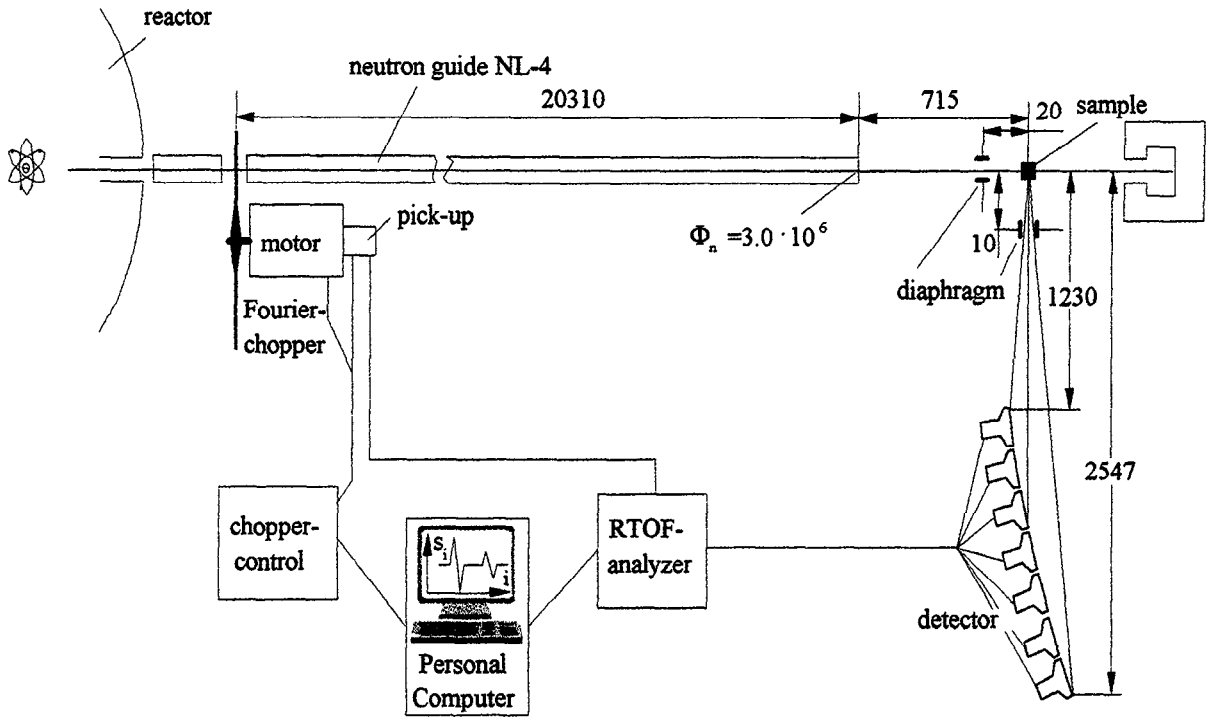

Fig.1: Schematic outline of the FSS setup (dimensions given in mm)

The detector bank is equipped with 16 ^{6}Li-glass sintillator/photomultiplier units (5" diameter), aligned according to the optimization calculations described in [2]. Figure 2 shows, how the detectors were lined up with a certain tilt from the ideal time-focussing curve to achieve a larger area coverage of the detectors. So a typical run in our case for a 4x4x25mm^3 scattering volume can be done in about 3 hours for steel.

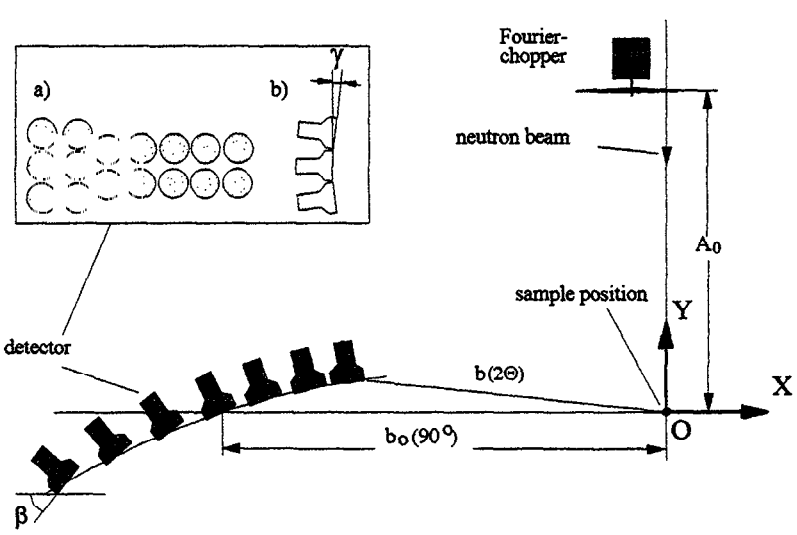

Fig.2: The detector positions are optimized for maximum neutron capture probability at minimum deviation from the time-focussing curve

The nominal spectrometer resolution is determined by three components: the angular and the flight path uncertainties - combined as the geometric component and the time component. It has been calculated and experimentally veryfied, as can be seen in Figure 3.

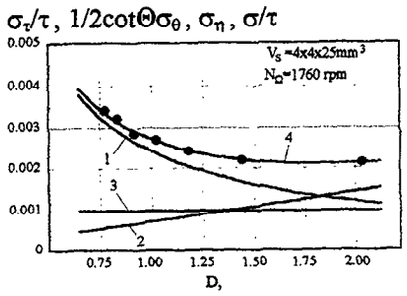

Fig. 3: Components and the resulting relative resolution σ/τ of FSS for a G_1 - shape reflection
1- time component σ_τ/τ,
2- term $1/2\cot\Theta\sigma_\theta$ of the geometric component
3- term σ_η of the geometric component
4- resulting relative resolution σ/τ and experimental values.

The following figure shows the three modes, in which the spectrometer can be used.
Row *a* shows the time vs. frequency functions (u is normalized to the maximum frequency Ω_{max}) , which lead to the reflexion peak shapesshown in row *b* and *c*. The measured peaks in row *c* were fitted and the residues (multiplied by a factor of ten) are also shown.

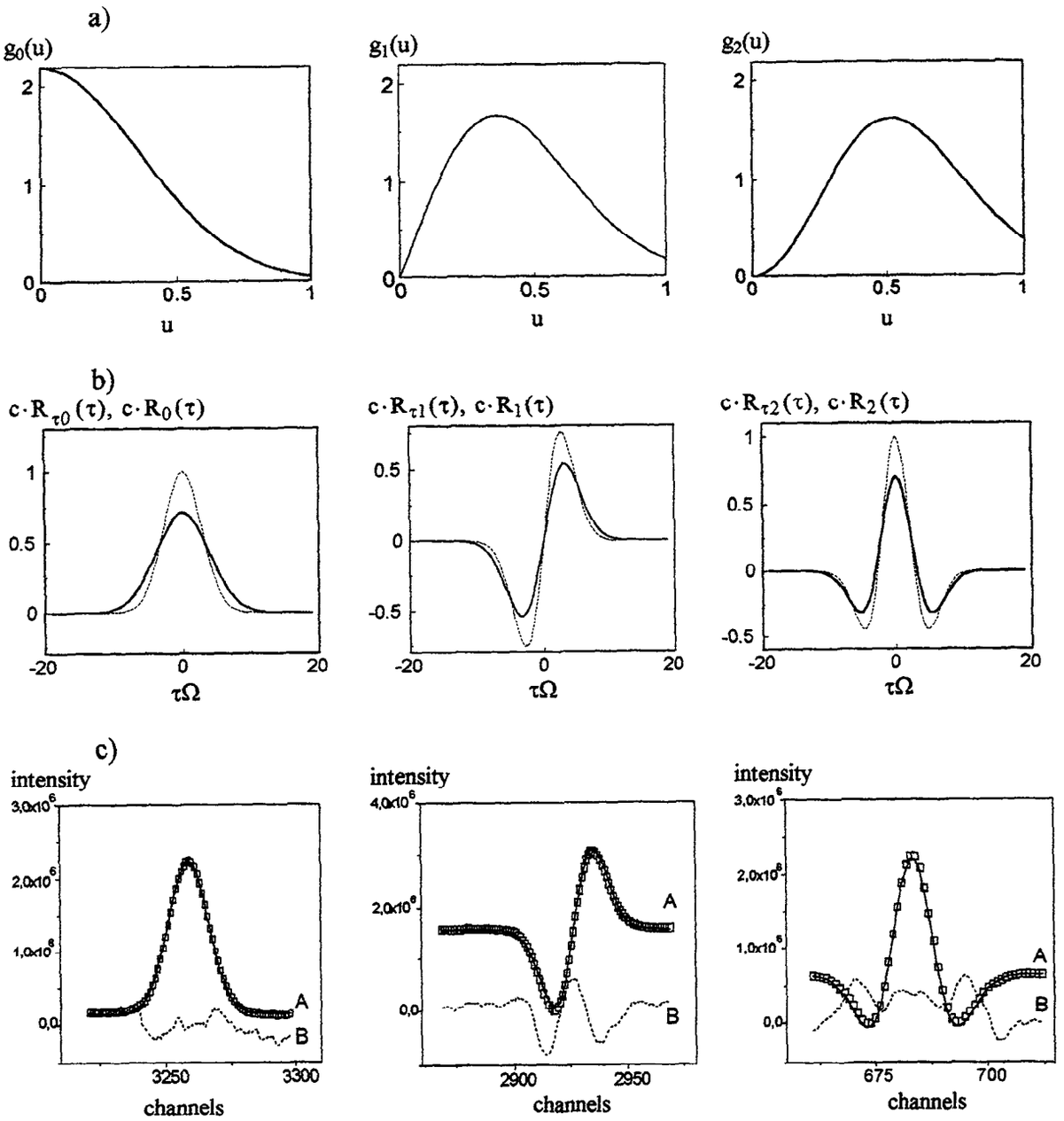

Fig. 4: Main rotor frequency programs and resulting peakshapes (b.) = calculated, c.) = measured and fitted) used at FSS

The development of Rietveld refinement software is underway; it has to be adopted to the $g_1(u)$ rotor frequency program

Ancillary equipment that has been developed and used is a stress rig to apply tensile forces in-situ to the samples measured, which includes a calibrated strain gauge setup to check the applied forces and an x,y,z,ω_1,ω_2 positioner, which is PC-controlled and can be adapted to different experimental tasks. A furnace, which will allow to measure specimens under uniaxial stress while heated, is under construction.

Experiences and experimental results

The predominant frequency program used for the strain measurements is the $g_1(u)$-window, which produces the first derivative of a Gaussian as peak shapes. The reason for trying other than Gaussian shapes was the basic idea that the contribution of low frequencies beginning from zero is the „DC component" and long-period „AC components", which have no or at least negligible influence on the peak positions and can therefore be cancelled to the advantage of more measuring time for the spectrum. The calculations [3] have then shown that for a given period of measurement time the „first derivative Gaussian" peak shape mode gives the highest precision for the peak position and is therefore the most suitable form for the type of measurements the FSS spectrometer was designed for.

An example is given in the next figure, which shows the measured shift in peak position in a tensile stress experiment on TMCP steel, a material used in offshore applications.

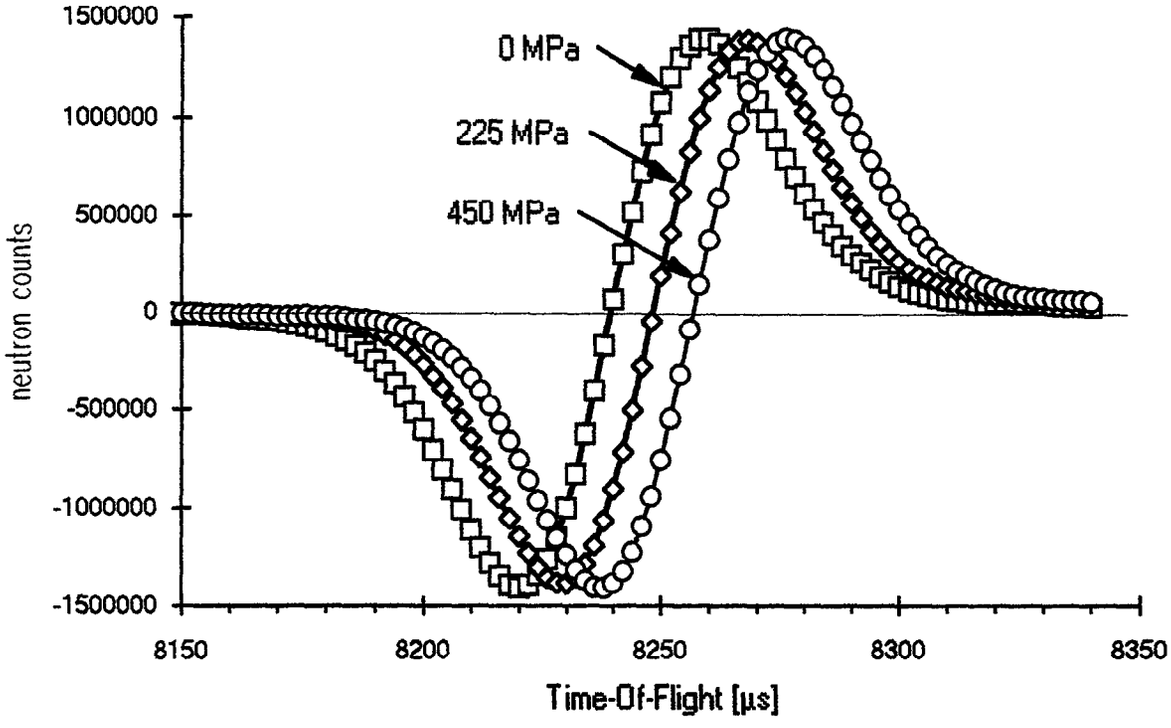

Fig. 5: Measured peakshift in a uniaxial-tension experiment (first derivative of Gaussian)

A fixed phase relationship between the opening of the neutron chopper and the optical pickup must be guaranteed. The experience with FSS has shown that the peak parameters „position" and „width" depend on the stability of this phase. Deviations from the ideal phase angle result in an asymmetry of the peak shape. Measurements done with very high statistical accuracy show, that a phase angle of zero degrees strictly can only be achieved for a certain part on the neutron diffraction spectrum, since the flighttime of the neutrons between the rotor and the stator already in principal causes phase differences: for the fast neutrons, the full opening is not yet reached, while the slow neutrons arrive at the stator only after the maximum opening. In practise the asymmetry due to this effect may be tolerated, if the distance between rotor and stator is less than 5 mm. In order to appreciate the influence of phase errors, calculations have been made, which resulted in a fitting function, which takes these errors into account, so that they can be eliminated in the peak position determination [5].

The following figure is included here as an example for the simultaneous determination of reflections from different phases, a task for which time-of-flight experiments are most suitable. The specimen was a composite steel containing both fcc and bcc structures.

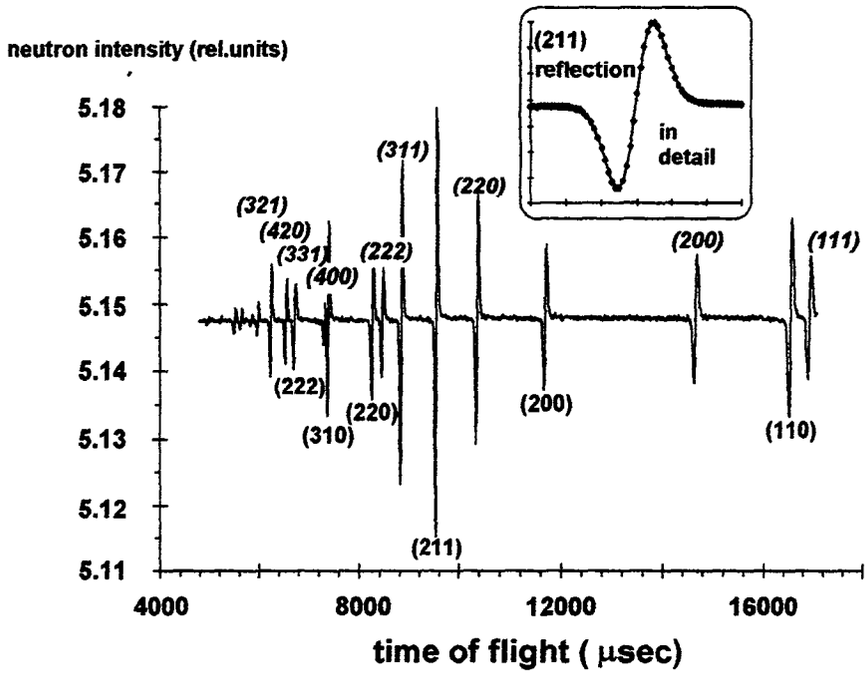

Fig. 6: Simultaneous measurement of α- and γ- phase in composite steel

Our research program concentrates on the validation of finite-element calculations of residual stresses by nondestructive neutron diffraction, in order to arrive at reliable theoretical predictions which can be verified experimentally at a few representative points. The following figure shows the results of measurements on a quenched steel cylinder of 100 mm length and 30 mm diameter, which was a non-transforming austenitic material. Residual stresses in this case are pure thermal stresses. The specimen and the FE calculations were supplied by Prof.Dr.Hougardy of the Max-Planck-Institut für Eisenforschung in Düsseldorf. Calculations and measurements are in good agreement.

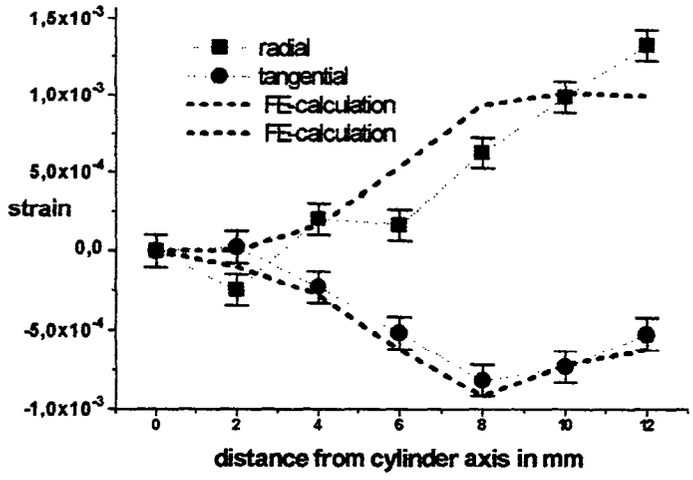

Fig. 7: Radial and tangential strains in a quenched steel cylinder, compared to FE calculations

An experiment on quenched cylinders which contain phase transformation stresses due to the formation of martensite is ongoing.

The last figure shows the result of a recent experiment on a steel plate, which was plastically deformed by 10% and released afterwards. The residual stresses induced by this plastic deformation cause compression in the direction of the tensile force applied and tension in the two orthogonal directions. By plotting the strains as a function of the orientation factor Γ, the crystalline elastic anisotropy is accounted for. The Reuss model predicts a linear relation between collinear stress and strain for the plain strain case:

$$\varepsilon_{\parallel} = \sigma_{\parallel} \cdot (s_{11} - 2\,S \cdot \Gamma)$$

$$\text{where} \quad S = s_{11} - s_{12} - \frac{s_{44}}{2}$$

$$\text{and} \quad \Gamma(hkl) = \frac{\left(h^2k^2 + h^2l^2 + k^2l^2\right)}{\left(h^2 + k^2 + l^2\right)^2}$$

A uniaxial tensile experiment therefore results in a linear relation, when the strains derived for different peaks (with Miller indices hkl) are plotted against Γ(hkl). On the other hand, from the slope of this linear curve, the existance of tensile or compressive residual stresses may be concluded. As shows the formula, a positive slope indicates tension, while a negative slope indicates compression. The errors on the strain values in the following figure are below 1×10^{-4}.

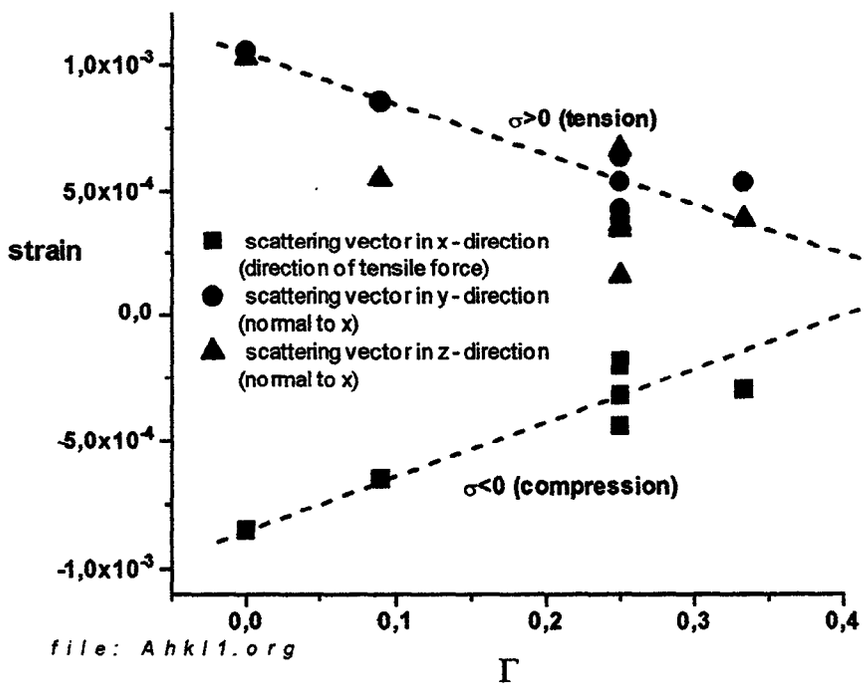

Fig. 8: Plain residual stresses in a plastically deformed steel plate

The specimen was investigated under seven different aspect angles, in order to arrive at seven independent linear relations to be able to calculate the full strain tensor. The analysis of this experiment is not yet completed.

Summary

The FSS RTOF- diffractometer, which was designed and optimized for residual stress measurements, has proven to be a reliable precision instrument. Examples of recent experiments are given.
When residual stress states in polycrystalline materials are to be measured, neutron time-of-flight spectrometry offers a number of unique advantages:
Since a large number of reflexions can be observed simultaneously, which originate from the same scattering volume, this method is especially useful in the investigation of multiphase materials like modern MMC's (metal matrix composites). By choosing a scattering angle of 90°, the optimal scattering volume is defined. A fixed geometry simplifies the setup of different sample environments considerably: heavy loads, furnaces or cryostats can be installed within short times.
With increasing operating experience it is likely, that progress in even better neutron untilization can be expected.

Acknowledgements

The work reported here is supported by GKSS Research Center, Geesthacht/Germany. Special thanks are therfore due to Prof.Dr.R Wagner and R.Kampmann.
Direct contributions came from Ch.Bittorf, H.Glöde, J.M.Keuter, Dr. V. Kudryashev, Th.Kulak, J.Larsen, Dr.K.Meggers, A.Mohr, C.Ohms, Dr.J.Schröder, S. Schwarz and Dr.G.Wiener.

References:

[1] J.Schröder, V.A.Kudryashev, J.M.Keuter, H.G.Priesmeyer, J.Larsen, A.Tiitta
FSS - A novel RTOF - diffractometer optimized for residual stress investigations
J.Neutron Research 2 (1994) 129 - 141

[2] V.A.Kudryashev, H.G.Priesmeyer, J.M.Keuter, J.Schröder, R.Wagner, V.Trounov
Optimization of detectors in time-focussing geometry for RTOF neutron diffractometers
Nuclear Instruments and Methods B 93 (1994) 355-361

[3] V.A.Kudryashev, H.G.Priesmeyer, J.M.Keuter, J.Schröder, R.Wagner
On the shape of the diffraction peaks measured by Fourier reverse time-of-flight spectrometry
Nuclear Instruments and Methods B 101 (1995) 484 -492

[4] J.Larsen, Die röntgenographischen Elastizitätskonstanten (REK) eine Grad 450 TMCP - Stahls für Offshore Anwendungen
Diplomarbeit, Kiel 1993

[5] V.A.Kudryashev, H.G.Priesmeyer, J.M.Keuter, J.Schröder, R.Wagner
Phase errors and their influence on the RTOF-Fourier-Method
accepted for publication in NIM B 728 (1995)

ICANS-XIII
13th Meeting of the International Collaboration on
Advanced Neutron Sources
October 11-14, 1995
Paul Scherrer Institute, 5232 Villigen PSI, Switzerland

M.SFINKS DIFFRACTOMETER AT GATCHINA REACTOR.

V.A.Trounov
St.-Petersburg Nuclear Physics Institute, Gatchina, Russia

ABSTRACT

Some details of design and technical parameters of the neutron Fourier diffractometer "M.SFINKS" installed at Gatchina (Russia) reactor are presented. Some achieved scientific results are presented also.

1. Introduction

The present time is characterized by the development of new technologies and new materials accordingly. In the next order this situation have stimulated the development of new methods and modernization of using ones especially nondestructive types. The diffraction methods based on penetrating rays are ones of the most significant in long list of such methods. The neutron diffraction is occupied very significant complementary niches to *x*-ray one. The main reason of this definition is a great advantage of the luminosity of *x*-ray sources. For compensation of this situation the creation of the powerful and perfect neutron sources is continuing in the world.

Design and construction of new high flux neutron sources have stimulated development of advanced instruments for carrying out research at these sources. A good example illustrating the above statement is the building of a high flux reactor at ILL (France) whose instrument suit costs much more than the expenditure of money on the reactor itself. This stems from the fact that reactors are expensive and one should take care of their most effective exploitation.

So the new Fourier diffractometer was designed for the steady state reactor PIK, the construction of which started in 1976 in the town of Gatchina (about 40 km south from St.-Petersburg) and is continued up to present time. By 1978 the list of instruments was formed for the realization of the research program being developed for this reactor. It included a number of diffractometers for experiments with powder samples. By that time became known successful applications of the Rietveld profile analysis method [1] and high resolution diffractometers [2,3]. This tendency in neutron diffractometry development and application received confirmation in a detailed consideration of the bright prospects opening with the use of high resolution neutron powder diffraction methods [4].

Keywords: Neutron, Diffraction, Structure properties

In 1979 during the visit of Prof. P. Hiismaki to the Petersburg Institute of Nuclear Physics in Gatchina a decision was reached to build a Fourier diffractometer at the steady state reactor PIK. During the 1980 year design plans and specification were executed. This file of documents were submitted for approval of the experts from the United Kingdom, Norway and Sweden and being given it. The work started on design of particular units and elements of the diffractometer.

To the greatest majority of improvements was subjected the electronic system. The one that served the diffractometer model in Finland [5] executed a successive mode of signal transferring with a very large dead time and could not be used with high intensity beams. Therefore, a new analyzer was to be designed operating in a parallel mode of signal transferring. Two versions were considered: a multicomputer and a microprocessor system. The latter one has won the competition. Special chips with internal logic were created. Now we use a 32-channel one for building the analyzer. By 1983 we were ready to start assembly of the new diffractometer on a neutron beam. However, as the completion date of the PIK construction was postponed to after 1986 acuteness became the question of what to do with the newly built equipment. After long and difficult discussions it was decided to install it on the old reactor. In 1984 works started on the preparation to operation of this new diffractometer "M. SFINKS", the given name, on beam 9 of the WWR-M reactor at Gatchina [6]. On Fig.1 the scheme of this diffractometer and steps of its modernization are presented. Its upgrading was finalized with the installation of a four-element neutron detector schematically shown in Fig.2. The surfaces of the converters (lithium glass elements pasted on light guides) were adjusted most close to the time focusing geometry. The time-focusing conditions are defined by the following formula:

$$b(\theta_B) = \frac{(a+b_0)}{\sin\theta_B} - a \quad ,$$

a - distance chopper-sample
$b(\theta_B)$ - distance sample-points on the time focusing surface.
b_0 - distance sample-time focusing surface when $\theta_B = 90^\circ$.
The aperture of the detector was 0.09 sterad.
As is seen on Fig.1 the "M.SFINKS" diffractometer is machine with fixed geometry the mostly matched to structural investigations of materials under extreme conditions being included in the scientific program of reactor PIK. Also such instruments are giving the general preference in realization of structural studies as they are capable of providing more rich uncorrelating experimental information for the application of the Rietveld method. The distance between uncorrelating points in the diffraction spectrum is defined by the resolution of the instrument.
This is conditioned by the shape of the dispersion curves $\Delta d/d_{hkl}=f(d_{hkl})$ for the time-of-flight technique and the constant wavelength method. They are illustrated in Fig.3. As is seen from this figure the time-of-flight method covers with high resolution a much wider range of d_{hkl} (interplane spacings) than the constant wavelength method does. Figure 3.1 shows the resolution function of the time-of-flight diffractometer of M.SFINKS installed at the WWR-M reactor at Gatchina. Figure 3.2 illustrates the resolution function of the multidetector diffractometer D1A (ILL, Grenoble), which immediately followed by questions of its selection.

The time-of-flight diffractometer requires time-dependent periodicity of the steady state neutron intensity and its main parameters (resolution, luminosity, geometrical size) depends on the time characteristics of the beam.

There are several ways of producing pulsed neutron beams at steady state reactors. The most popular is the use of mechanical systems (choppers). The chopper consists of two parts. One of them is the fast rotating disk (rotor) and the other is a fixed element (stator) with one or more neutron opaque slits. In the periphery of the rotor in some way or another there are also made neutron opaque slits. If these slits are arranged with some periodicity the chopper is called the Fourier chopper. If the arrangement of these slits is random, the chopper is called the pseudo-random chopper. The one with few (2 or 4) equidistant slits in the periphery of the rotor has got the name of the Fermi chopper. There exist other methods for pulsed neutron beam production, but they are not the topic of the present paper.

From the viewpoint of the main parameters of diffractometers (luminosity and resolution) the Fourier and pseudo-random versions are equivalent. However, it is cheaper to build a Fourier and pseudo-random techniques one needs some special procedures to be performed to restore the studied spectrum. The Fourier and pseudo-random techniques are efficient in measuring spectra with well pronounced lines. Spectrum refinement with a Fourier or pseudo-random method requires exact knowledge of the phase of the neutron wave passing through the chopper. This is the principal problem the solution of which determines success of practical realization of these techniques.

2. Diffractometer "M.SFINKS" - ideas and realization

This solution was found and tested by the group of Prof. P Hiismaki at VTT (Finland). They have developed the so-called Reverse Time-of-Flight Fourier Method. What does this method consist in Figure 4 gives schematic illustration. The scheme comprises the Fourier chopper, the detector, the phase shifting register, the transferring logic unit and the analyzer. The Fourier chopper performs time modulation (Fig.4) of the beam described by the function:

$$x^w = \sum_{1}^{\infty} p_r e^{irwt}$$

where p_r are corresponding Fourier coefficients.

The detector intensity $Z^w(t)$ can be given at each rotation speed as integral over time-of- flight span T_S where the scattering cross sections of samples give non-zero contribution:

$$Z^w(t) = \int_0^{T_S} S_0(\tau) x^w(t-\tau) d\tau + b_0$$

where b_0 - describes the unmodulated background.

$S(\tau)$ is the time-of-flight primary spectrum incident on the sample. $S_0(\tau)$ is convolution of the primary beam spectrum incident on the sample and scattering function of the sample. The rotor rotation frequency changes following $G(w)$. This function must satisfy the condition $G(w)dw=dt$, that determines the time interval dt

within which the frequency changes from w to dw. The frequency is changed from 0 to w_{max}. The function $G(w)$ is normalized to unity, i.e.

$$\frac{1}{T^{w_{max}}}\int_0^{w_{max}} G(w)dw = 1$$

The total time for running the chopper from 0 to w_{max} is marked by $T^{w_{max}}$, then the time spent near the speed w is given by $dT^w = G(w)dw$.

A device is mounted on the chopper to generate a pick-up signal, e.g., in the form of a rectangular pulses. This signal is also described by the Fourier series expansion:

$$y^w(t) = \sum_{r=-\infty}^{\infty} q_r e^{irwt} \ .$$

The pick-up signals come to the shifting register, through which they are step-wise transmitted with step period Δ by a special generator, that synchronizes the work of all electronic systems. Phase determination accuracy in the shifting register depends on stable operation of this generator and the value of the step period Δ. This is the principal moment hard to be accomplished in the direct method. Such a distribution of phases from the shifting register comes to the analyzer via the transferring logic unit at the moment of neutron registration by the detector. Thus the transferring probability is proportional to the neutron intensity of the detector $Z^w(t)$ and accumulated data in the analyzer can be represented by help of following formula:

$$Z(\tau) = \int_0^{w_{max}} \Delta Z^w dw = C\int_0^{T_s} d\tau' S_0(\tau')R(\tau-\tau') + (S_0\overline{x} + B_0)\overline{y},$$

where

$$\Delta Z^w(\tau) = \Delta T\int_0^{T_s} d\tau' S_0(\tau')(\overline{xy} + 2\sum p_r q_r e^{irw(\tau-\tau')}) + b_0\overline{y}\Delta T^w$$

Here the bar indicates time average. As results

$$Z(\tau) = C\int_0^{T_s} d\tau' S^0(\tau)R(\tau-\tau') + (S_0\overline{x} + B_0)\overline{y}$$

The symbols have the following meanings:

$S^0(\tau) = T_m S_0(\tau)$, $S_0 = \int_0^{T_s} S_0(\tau)d\tau$, $B_0 = T_m b_0$,

T_m - the time of the measurement.

$$R = \frac{2}{C}\sum_{1}^{\infty} p_r q_r G(rt) .$$

$$G(t) = \int_{0}^{w_{max}} G(w)\cos(wt)dw$$

The function $G(t)$ is the Fourier transformation of the frequency window. The function x, y, $G(w)$ can be selected so that R will have the form close to δ-function and its width will determine the resolving power of the instrument. Then $Z(\tau)$ will be the studied spectrum. A brief account of the technique and the possible ways of its realization can be found in [5] and a more detailed description [7].
Table 1 summarizes the technical parameters of the diffractometer after the last modernization in 1986 in comparison with the parameters of the analogous instruments.

Table 1

parameter	D1A, ILL	GPBD, Argone	M.SFINKS Gatchina	D2B, ILL	HRPD RAL, England
λ, Å	1.2-6	0.5-6	1-5	1-6	1-12
Φ_s, n/cm²sec	$2\cdot10^6$	$\sim10^5$	$1.5\cdot10^7$	$\sim10^7$	10^6
V_s, cm	3	5	5	5	2
R, %	0.2	0.25	0.25	~0.05	0.05
Ω, sterad	0.004	0.1	0.09	0.008	0.1
$\Phi_s V_s \Omega$	$2.4\cdot10^4$	$5\cdot10^4$	$f_k\cdot6\cdot10^6$	$4\cdot10^5$	$2\cdot10^5$

λ , Å - the wavelength range attainable in the experiment;
Φ_s , n/cm²sec - is the neutron flux at sample site;
V_s , cm - the maximum sample volume;
R , % - the resolution;
Ω , sterad - the detector aperture;
$f_k \approx 0.02$ - the effective correlation coefficient.

So installation of the M.SFINKS diffractometer on an average flux reactor is superior the DIA on the high flux reactor of ILL (old version). M.SFINKS test measurements were performed with standard samples $Zr_{1-\delta}$ Hf_δ O_2, recommended by the Crystallography Community Committee. Figure 5 shows the experimental spectrum and the difference with the theoretically calculated one. Table 2 lists the extracted parameters. They are in good agreement with the results of investigations performed at the other research centers.

Table 2

$Zr_{0.98}Hf_{0.02}O_2$ Sp. gr. $P2_1/c$ No.14 setting 2,
a= 5.1447(1), b= 5.2099(2), c= 5.3117(1), β=99.219.

Atom	Occupation	x	y	z	B_{iso}
Zr/Hf	0.98/0.02	0.2756(2)	0.0407(2)	0.2082(2)	0.12(1)
O1	1	0.0695(3)	0.3333(3)	0.3433(2)	0.33(2)
O2	1	0.4185(2)	0.7562(2)	0.4794(2)	0.16(1)

3. Review of scientific studies

From the structural investigations performed with the wide use of the isotopic contrast method emphasis should be laid on the following compounds:
$Re(DCOO)_3$, Re=Y, Ce, Sm, La, Tm [8, 9, 10];
$Re B_6$, Re=La, Ce, Nd, Sm, Y [11, 12, 13, 14];
$Re_2 Cu O_4$, Re=La, Nd, Sm [15, 16, 17];
$Re Ba_2 Cu_3 O_7$, Re=Y, Sm, Gd, Eu [18, 19, 20, 21];
1-2-4-type superconductors $Y_{1-x} Ca_x Ba_2 Cu_4 O_8$ [22, 23].

1. $Re(DCOO)_3$ list of compounds is rather interesting due to non-linear optical properties and its possible relation with structure. It was discussed some phases related with optical peculiarities, also it was discussed the changing of the optical properties along the list of rare earth-elements [8, 9].

As result of our studies we didn't observe significant structural difference in all list of formates from Y to Tm. Isostructural list was interrupted on Tm. We observed the hydrogen bonding in all isostructural list [8, 9]. We optimized the sensitivity of diffraction experiment by help of isotope "0"-matrix of Sm [10] for the study possible temperature changing in structure near temperature of decomposition which starts from Re-0-bonding. Some models of decomposition might be discussed.

2. The hexaborides in frame of long list of rare earth elements and Y are very interesting. Along this list it can be observed the different physical properties from superconductivity to Condo-behavior. We started from the problem of the distribution of vacancies in hexaboride structure. By help of using "0"-matrix of Sm [11] we have observed the location of the vacancies in boron sublattices. We have defined temperature dependence of Debay-Waller factor for both sublattice of hexaborides (Re and B) [12], also we observed the steady-state Debay-Waller factor and have fixed the type of thermal vibration model, Einstein model for Re-sublattice and Debay model for boron one [12, 13]. We calibrated "M.SFINKS" diffractometer by help single crystal x-ray measurements and neutron powder ones. We have observed a good correspondence between both methods, Fig.6. Also we observed the softening of the phonon acoustic mode along list rare-earth hexaborides [14]. Now we are starting the modeling of the dynamical properties of hexaborides using valence

force field method. On the first stage of such treatment we have a good agreement between experimental data and theoretical simulation. These results which confirmed high resolution of M.SFINKS diffractometer will be published soon.

3. The structure of $Re_2 Cu O_4$ was studied. We fixed phase-diagram of ortho-tetra transition for $La_{1-x} Sr_x Cu O_4$ compound by help of temperature dependence of the Bragg-peak splitting [15]. Also we observed some structural effects due to oxygen content[16]. In time of the study Sm_2CuO_4 it was observed the non - linear temperature dependence of the lattice parameter which might be related with a fluctuation of Sm valence. May be it is one of the main reason for explanation of the difference in T_c between $Nd_{1-x}Sr_xCuO_4$ and $Sm_{1-x}Sr_xCuO_4$ [17].

4. We have actively participated in research of high-T_C superconductive ceramics type 1-2-3. One of most reliable results concerning structure of Y 1-2-3-compound was achieved by help of study carried out on "M.SFINKS" [18]. We paid attention on some possible anomalous behavior of the structure of 1-2-3-compounds. We have optimized experiment by help of "0"-matrix of Sm and ^{63}Cu. We observed anomalous kink in temperature dependence of unit cell parameters near T_C [19]. Also we used this compound for the "M.SFINKS" calibration by help of direct comparison with D2B (ILL) and DMC (Villigen, Swizerland). Fe-Cu substitution was carefully studied in complex research by using of "M.SFINKS", D2B, DMC [20]. For systematic research of 1-2-3 compounds [21] Sm, Gd, Eu versions were attested on "M.SFINKS" diffractometer preliminary.

5. We have prolonged our collaboration with Villigen in the study of Ca-substituted 1-2-4-system [22, 23]. We have observed that the Ca substituted Y in structure [22]. Also phase transition near 155K was observed [23].

4. Conclusion

The numeral physical results to be achieved by help of "M.SFINKS" diffractometer have confirmed a high reliability of the developed method which might be recommended for wide using. Results reported in [21, 22, 23] were supported by Soros fund from the Russian side.

5. References

1. A.K.Cheetham, J.C.Taylor, *St.Chem.* **21** (1977) 253.
2. A.W.Hewat, *Nucl.Instr.and Meth.* **127** (1975) 361.
3. A.W.Hewat, *Nucl.Instr. and Meth.* **137** (1976) 463.
4. Proceedings of the Symposium on Accuracy in Powder Diffraction held at NBC, MD, June 11-15, 1979.
5. A.Tiitta, *Report of Technical Research Center of Finland,* publication 27, Espoo, 1980.
6. V.Trounov et al,. P.Hiismaki et al., *Preprint LNPI* **N1277** 1987; P.Hiismaki et al, V.Trounov et al, *Physica B* **156** (1987) 567.
7. H.Poyry,*Thesis*, Technical Research Center of Finland, 29th of June, 1978.
8. V.A.Trounov, V.A.Kudryashev, V.A. Ul`yanov et al, *Solid State Commun.* **59** (1986) 95.

9. R.L.Bolotovsky, A.P.Bulkin, V.A.Kudryashev et al. *Solid State Commun.* **76** (1990) 1045.
10. V.A. Trounov, E.V.Bessmertnaya, Neutron diffraction study of the crystal structure of Samarium Formate $Sm(DCOO)_3$ in temperature range (16-219)°C, *Preprint PNPI* **SS-71-1994**.
11. V.A.Trounov, A.L. Malyshev, D.Yu.Chernyshov, et al, *J.Appl. Cryst.* **24** (1991) 888.
12. V.A.Trounov, A.L. Malyshev, D.Yu.Chernyshov, et al, *J. Phis. Condens. Matter.* **5** (1993) 2479.
13. V.A.Trounov, A.L. Malyshev, D.Yu.Chernyshov, et al, *Phis. Solid. St.* **36** (1994) 2687 (Russian).
14. V.A.Trounov, A.L. Malyshev, D.Yu.Chernyshov, et al, *Phis. Solid. St.* **36** (1994) 585.
15. R.L.Bolotovsky, A.P.Bulkin, V.A.Kudryashev et al., *Solid St. Commun.* **65** (1988) 1167.
16. R.L.Bolotovsky, G.A.Krutov, V.A.Kudryashev et al. *Physica B* **156&157** (1989) 891.
17. V.A.Trounov, D.Yu.Chernychev, A.V.Matveev et al, *Preprint PNPI* **N1827** August 1992 (in Russian).
18. O.K.Antson, P.E.Hiismaki, H.D.Poury et al, *Solid St. Commun.* **64** (1987) 757.
19. V.A.Trounov, T.Yu.Kaganovich, A.I.Kurbakov et al, *Physica C* **194** (1992) 415.
20. V.A.Trounov, T.Yu.Kaganovich, A.I.Kurbakov et al, *Physica C* **197** (1992) 123.
21. M.Guillaume, P.Allenspach, W.Henggeler et al, *J.Phis.: Condens. Matter.* **6** (1994) 7963.
22. P.Fischer, E.Kaldis, J.Karpinscki et al, *Phisica C* **205** (1993) 259.
23. V.A.Trounov, T.Yu.Kaganovich, P.Fischer et al, *Physica C* **227** (1994) 285.

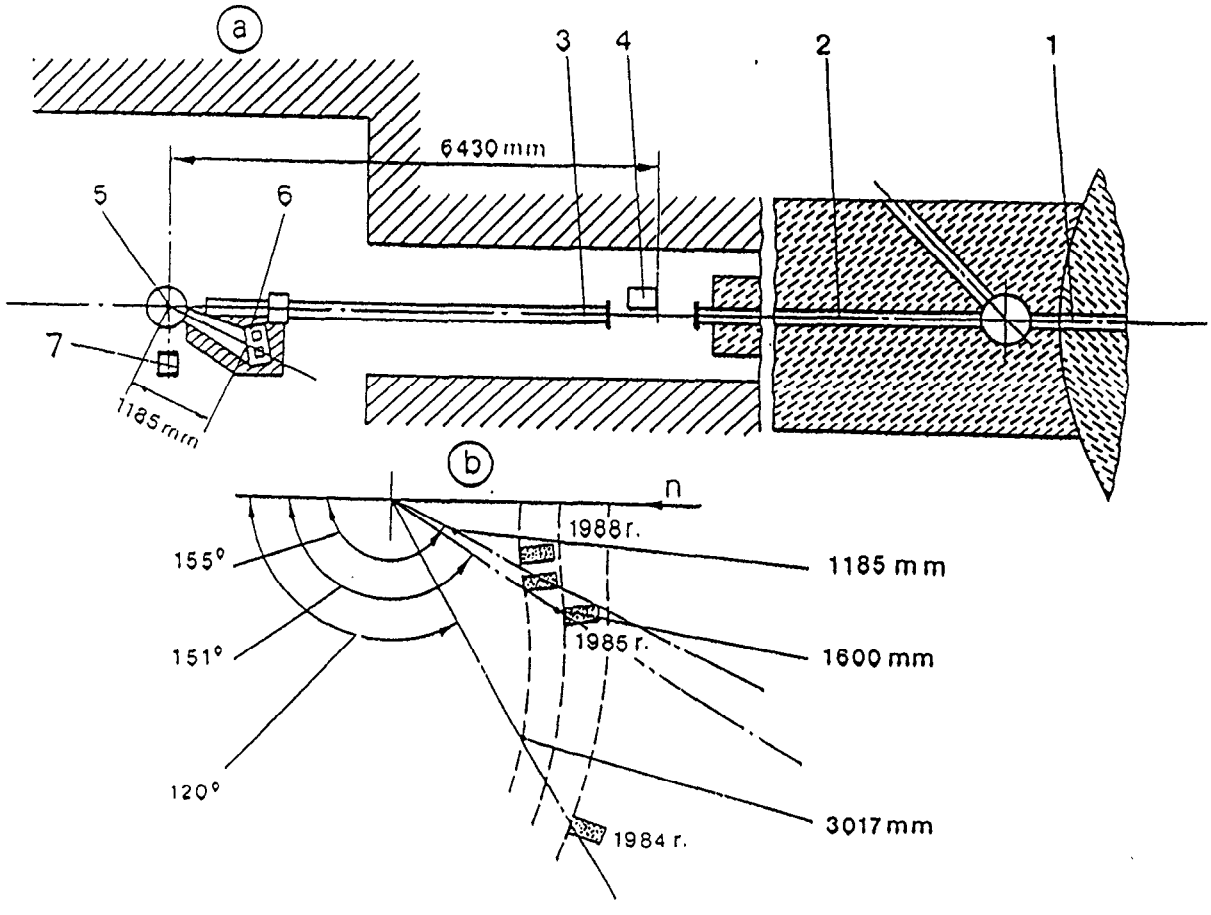

Fig.1 Layout of "M.SFINKS"-diffractometer and steps of its modernization.
1 - in-pile collimator, 2 - curved neutronguide, 3 - mirror collimator, 4 - Fourier chopper, 5 - sample position, 6 - back-scattering detector, 7 - 90^0-detector.

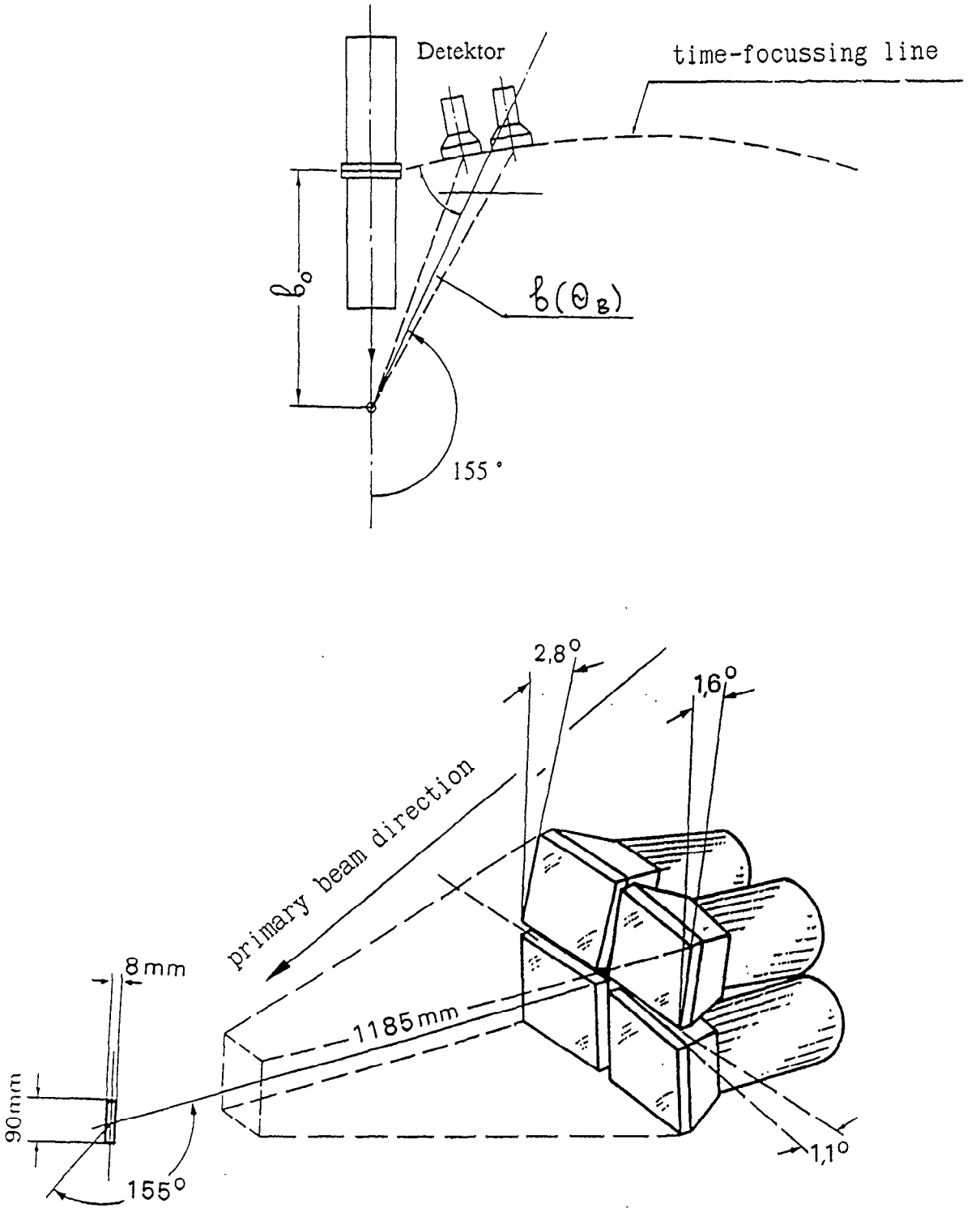

Fig.2 Scheme of the four-elements detector.

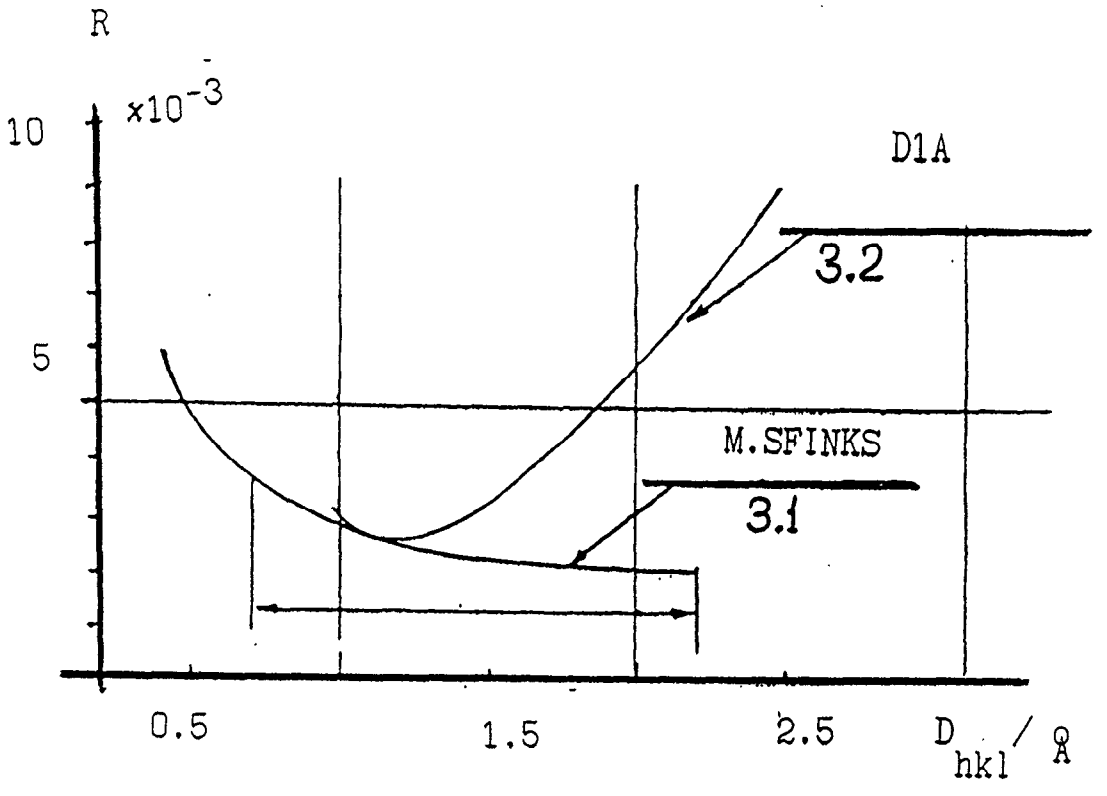

Fig.3 Resolution of "M.SFINKS"-diffractometer and D1A (old version, 1.909 Å).

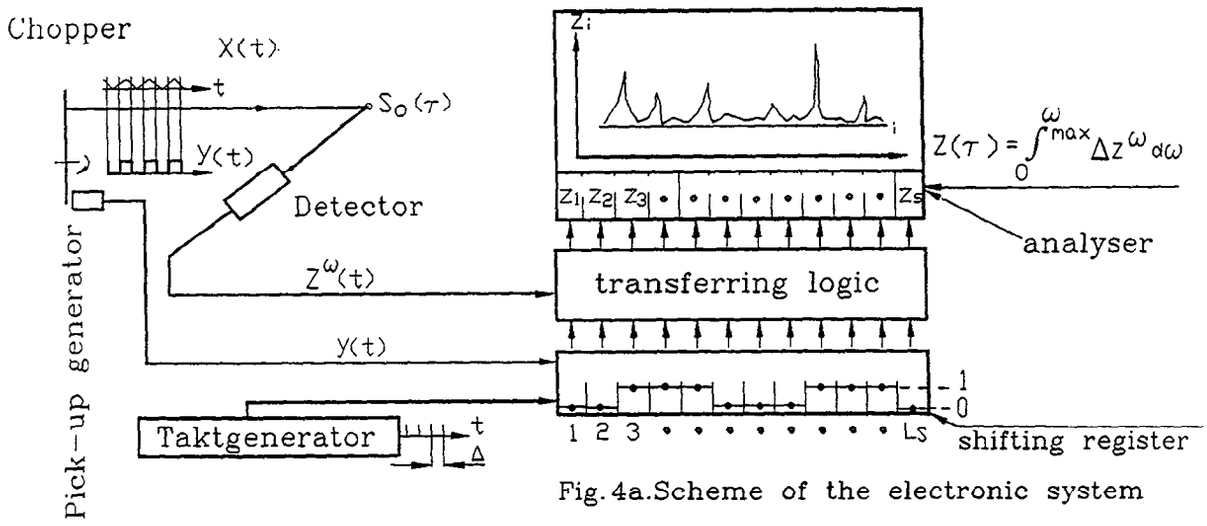

Fig. 4a. Scheme of the electronic system

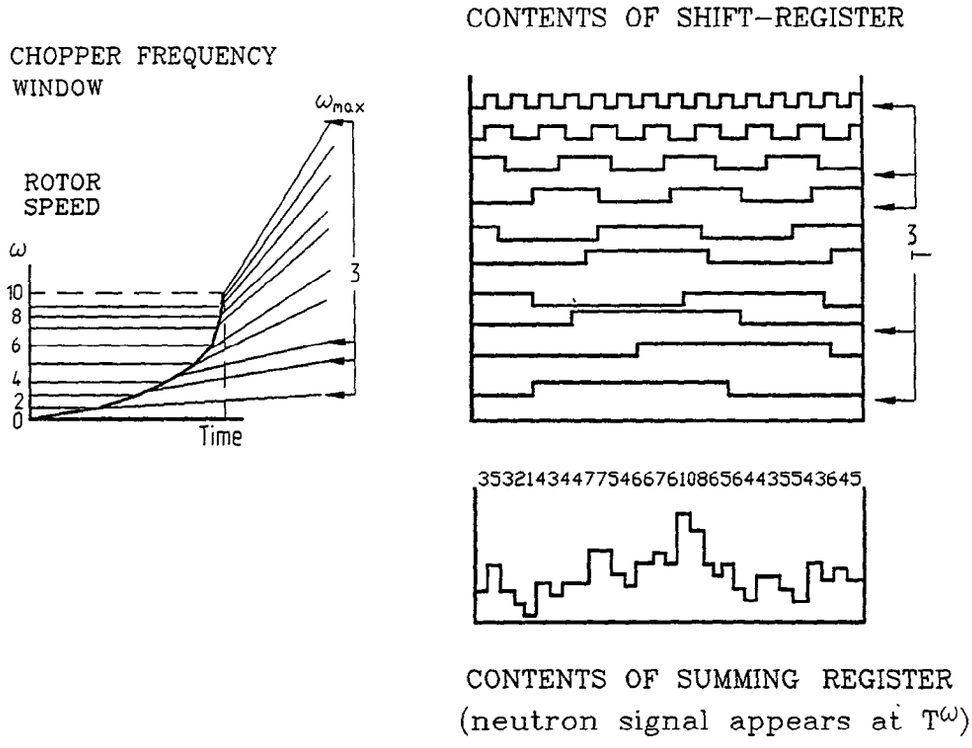

4b. Scheme of a synthesis of a diffraction spectrum by the reverse Fourier method.

Fig. 4. Principal scheme of the spectrum registration of the "M.SFINKS"-diffractometer.

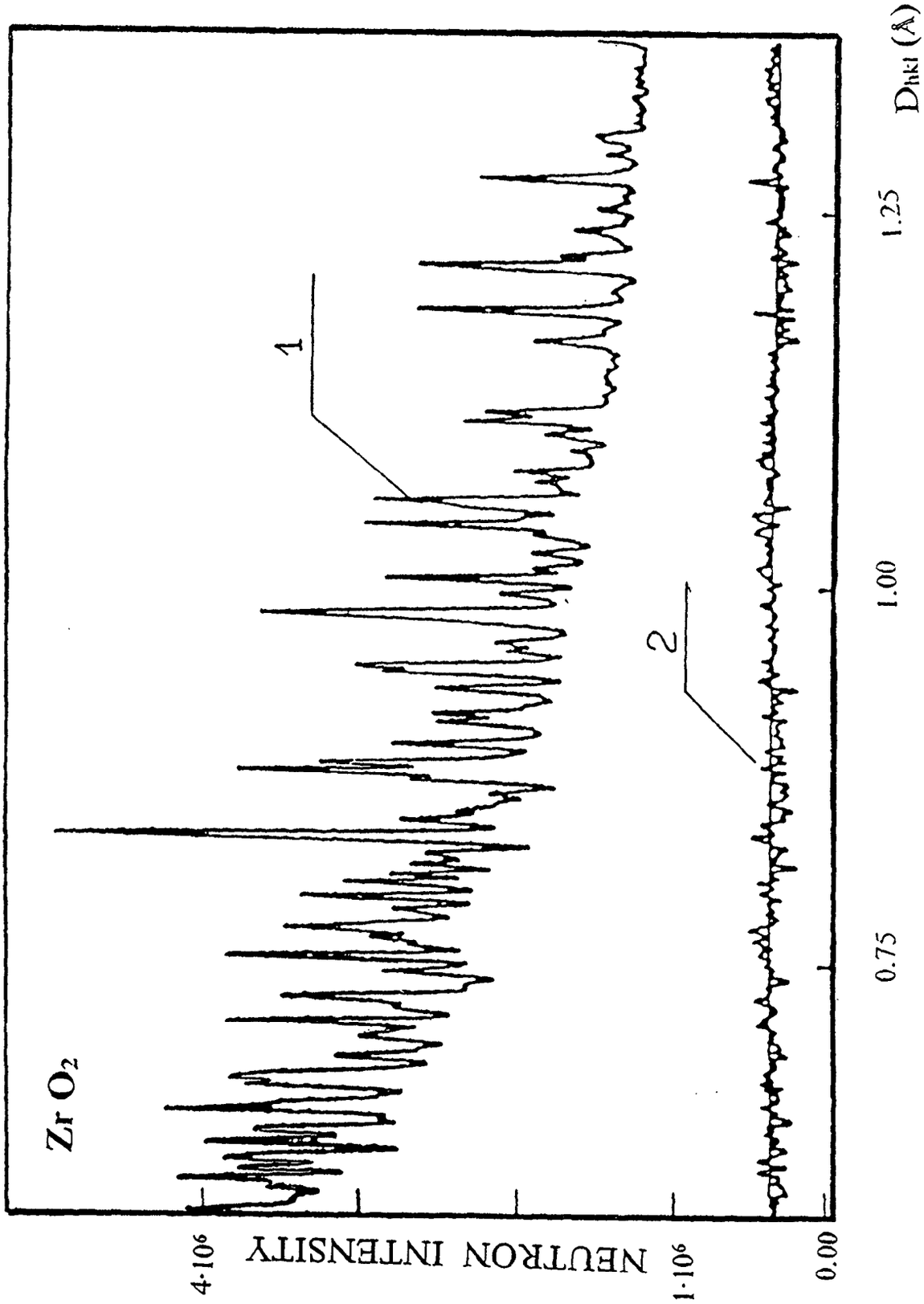

Fig.5 Diffraction pattern from $Zr_{0.98}$ $Hf_{0.02}$ O_2 sample (1) and difference experiment - computation (2).

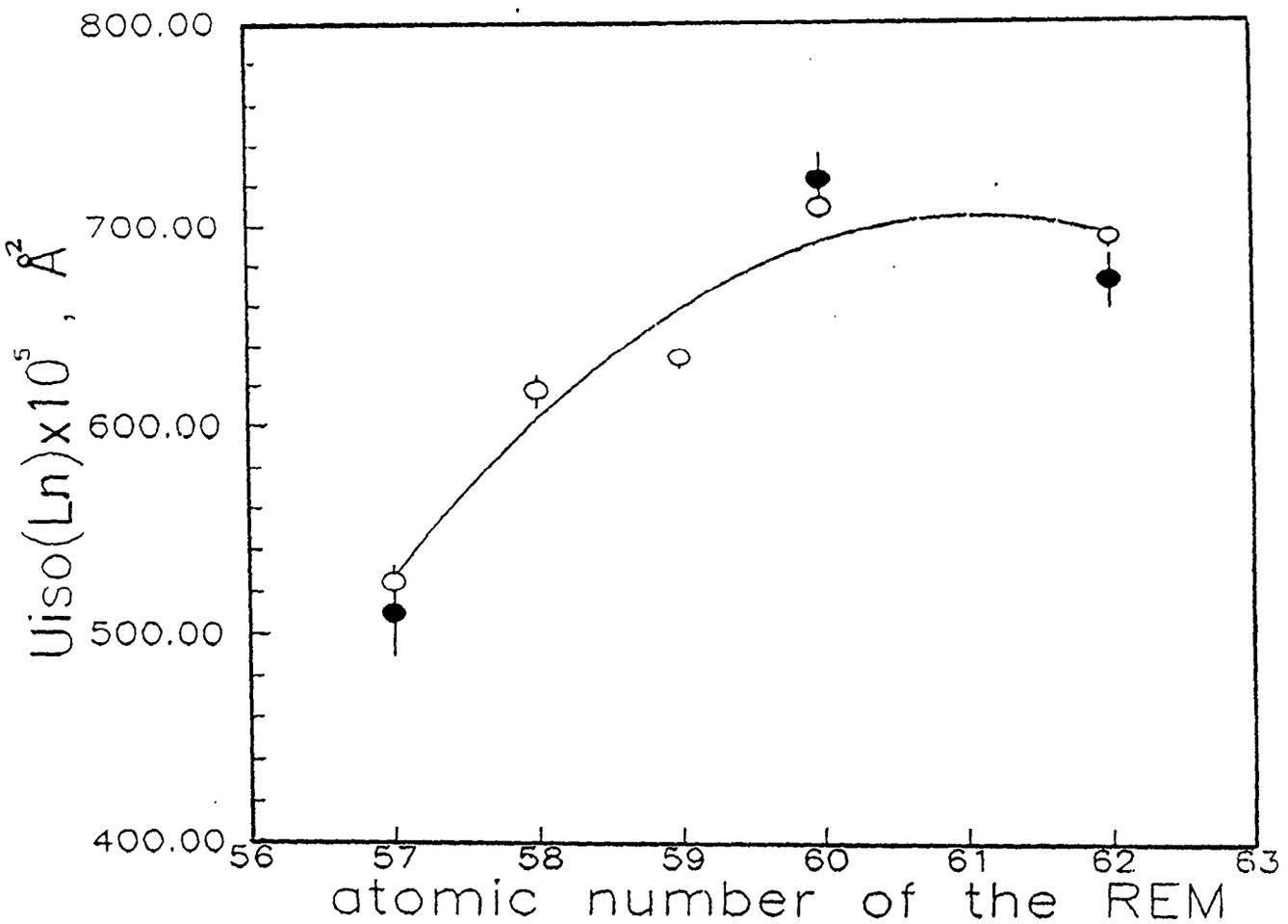

○- defined from single crystal X-ray data

●- defined from neutron powder data

Fig.6 Isotropical thermal parameters of Re atoms.
Neutron and *x*-ray diffraction data.

ICANS-XIII
13th Meeting of the International Collaboration on
Advanced Neutron Sources
October 11-14, 1995
Paul Scherrer Institut, 5232 Villigen PSI, Switzerland

Some Peculiarities of RTOF Method and Calibration of Diffractometer "Mini-Sfinks".

Chernyshov D.Yu., Kudryashev V.A., Trounov V.A.

St.-Petersburg Nuclear Physics Institute, Russia

ABSTRACT

The problems of correct definition of interplanar distances are discussed for RTOF diffractometer. The influence of absorption effect and phase error are described.

1. Introduction

Recently investigations of strain distribution using neutron diffraction attract much attention. Indeed, the neutron diffraction is a powerful tool for this purpose [1]. Such advantages of RTOF method [2] as a high level of utilization of neutron flux and observing a number of diffraction lines in one measurement make this method attractive for such investigation [1].

Some peculiarities of RTOF method introduce difficulties in correct extraction of interplanar distances from diffraction pattern. Main problem is so-cold "phase error" (the phase difference between modulation function and "Pick-up" signal) that can distort line shape and position [3]. Up to now all realizations of RTOF method work with phase unstability, because all of them use Pic-up signal obtained by analog method [4].

The phase problem is especially important for diffractometers with high (10^{-3}-10^{-4}) resolution.

The correct solution of this problem must include deconvolution of measured line shape to resolution function and scattering function of the sample. The resolution function can be obtained from measurement of sample with known scattering function (standard sample). This calibration measurement not so important for RTOF diffractometer with unstable phase because resolution function depends on phase error [3].

The other possibility to solve phase problem is introducing in fitting procedure varied parameters that describe influence of phase error. One possibility was described by Kudryashev et al. [3] for antisimmetric resolution function when asymmetry of line shape is proportional to phase error.

At present paper we shell show that using ordinary "looks like Gaussian" resolution function allows as to take in account the shift of line positions from phase error and other effects. It will be shown that with using some assumptions the problem can be practically reduced to the calibration of two diffractometer constants. This calibration must be done for every measurement when information about absolute values of line positions is extracted.

Keywords: RTOF, phase error, sample absorption

2. Structural studies. Results and problems.

"Mini- Sfinks" diffractometer has been used for investigation of structure of numerous compounds. There are a lot of results that are in agreement with results obtained by other techniques.

In case of $Zr_{0.98}Hf_{0.02}O_2$ (standard certificated sample) the excellent agreement of structure parameters obtained with tabulated data confirms the high resolution of diffractometer [5].

In case of hexaborides of rare-earth elements the mean-square displacements of atoms extracted by help of Rietveld method were confirmed by model calculations [6].

To get these results we used to allow variation of time shift (Delay) parameter, instead of traditional treatment of Delay as a diffractometer constant. The differences between initial and fitted values of Delay were higher than possible error of electronic equipment (0.1 μs) (See Table. 1).

Table. Fitted value of Delay for different experiment.
Rietveld analysis program "Mria" [7].

Compound	Fitted value of Delay channels, Δ, μs
[illegible]	[illegible]
[illegible]	[illegible]
[illegible]	[illegible]
[illegible]	[illegible]
[illegible]	[illegible]
[illegible]	[illegible]
[illegible]	[illegible]
[illegible]	[illegible]
$Tm(DCOO)_3$	1000.11

In addition, in case of hexaborides (samples with high absorption) we had to vary Lsin(Θ) parameter using fixed lattice constant obtained from X-ray single crystal measurement.

For structural investigation these deviations of diffractometer constants from initial values are not so important if the correlations between these constants and physical meaningful parameters are negligible.

For correct extraction of line positions we have to use the correct values of diffractometer constants and understand why the differences appear.

3. Lsin(Θ) and absorption

Lattice constant of lanthanum hexaboride calculated using the positions of separate diffraction lines shows unphysical dependence on neutron wavelength λ.

This dependence can be described by help of absorption correction. The main idea of this correction is following (Fig. 1): absorption attenuation is different for different λ, so every point (x,y) of sample cross-section produces intensity on the detector with weight:

$$P(x,y) = \exp\left[-\mu(\lambda)\cdot\left(a(x,y)+b(x,y)\right)\right], \qquad (1)$$

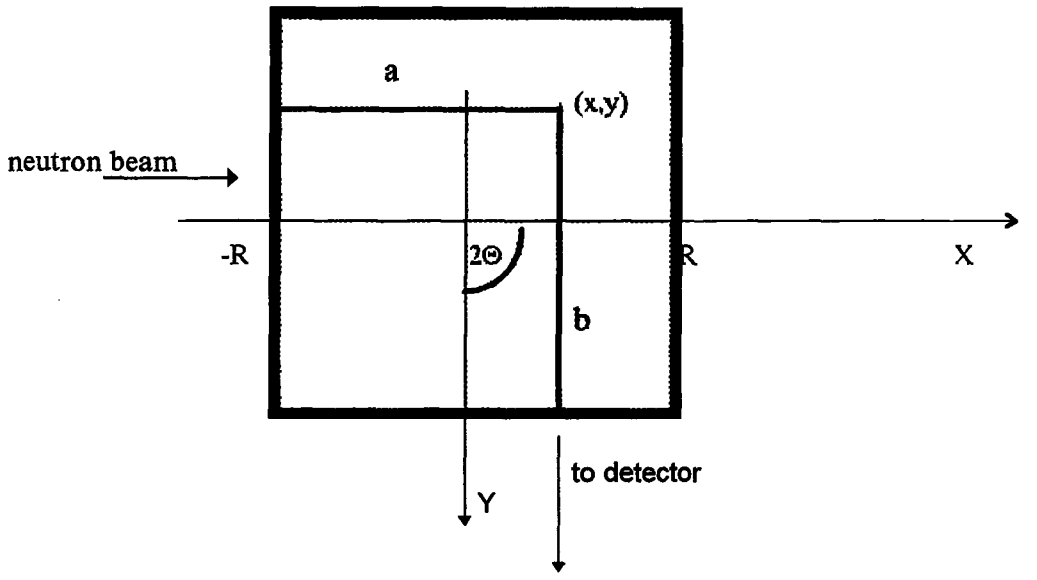

Fig. 1 Sample cross-section for $2\Theta=90^0$ geometry.

The coordinates of center of gravity of this weight distribution are coordinates of effective scattering center (x_c,y_c). The position of scattering center depends on linear absorption coefficient μ and so on λ. The actual L and Θ can be calculated using x_c and y_c.

$$\left.\begin{aligned} x_c &= \frac{1}{M}\cdot\iint_G \exp\left(-\mu\left(a(x,y)+b(x,y)\right)\right)x\,dx\,dy \\ y_c &= \frac{1}{M}\cdot\iint_G \exp\left(-\mu\left(a(x,y)+b(x,y)\right)\right)y\,dx\,dy \end{aligned}\right\} \qquad (2)$$

For cylindrical sample and backscattering geometry these integrals can be taken numerically.

Main assumptions we made are following:

- cinematic limit of diffraction,
- no divergence of primary beam,
- point detector assumption,
- uniform distribution of primary beam on width and height of sample.

Now corrected line positions can be calculated using formulas:

$$d_{hkl} = \frac{h\cdot\tau_{hkl}}{2m\cdot p_0\left(1-\frac{\delta p}{p_0}\right)}, \qquad (3)$$

$$\frac{\delta p}{p_0} = \frac{\delta L}{L_0} + \cot\Theta_0\cdot\delta\Theta, \qquad (4)$$

$$d_{hkl} = d^0_{hkl}\left(1+\frac{\delta p}{p_0}+\left(\frac{\delta p}{p_0}\right)^2+\cdots\right) \quad \text{where} \quad d^0_{hkl} = \frac{h\cdot\tau_{hkl}}{2m\cdot p_0} \quad \text{and } \delta p=\delta p(\lambda).$$

For LaB_6 data we can simplify this treatment using backscattering condition:

$\left(\cot\Theta \cdot \delta\Theta << \frac{\delta L}{L_0}\right)$ and the relation of lattice constant and hkl for cubic lattice:

$A = \sqrt{h^2 + k^2 + l^2} \cdot d_{hkl}$.

The result of calculation of this effect can be seen on Fig.2, where the experimental points and the results of modeling are in a good agreement.

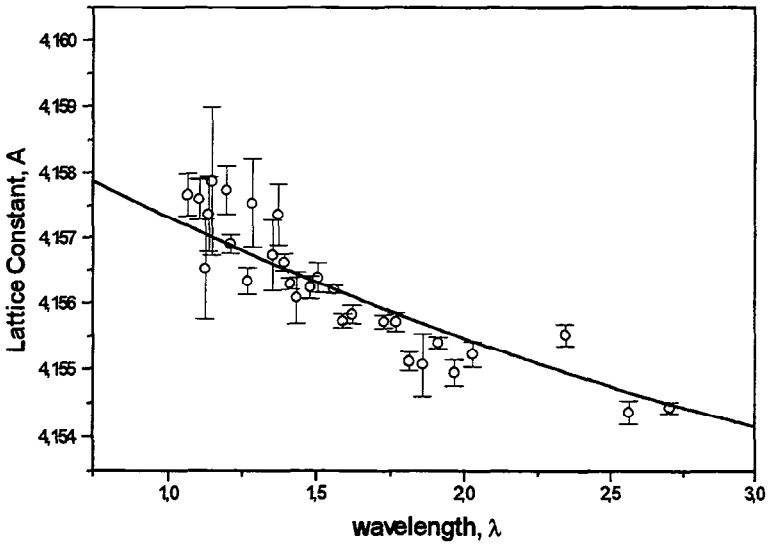

Fig. 2 Calculated from fitted line positions lattice constant of LaB_6.
Solid line is result of theoretical calculation.

It should be stressed that this effect can be visible for samples with high absorption in measurements made by using high resolution (10^{-3}-10^{-4}) machine.

4. Delay and phase error

The description of phase error influence on line positions is done by Kudryashev as well as the general method of fitting line positions when phase error is present [3]. For "Mini-Sfinks" fitting procedure this possibility in not realized, so phase error should influence on other parameters.

To describe the deviation of Delay from initial value we propose that the phase error can influence on line positions in the process of current fit.

We calculate the series of line shapes for different phase errors using as basic Gaussian line shape and method described in [3].

The results of fits of generated line shapes by Gaussian are shown at the Fig. 3.

It is clearly seen that for the small phase error there are not noticeable changes at line width and integral line intensity, but the line position shows strong linear dependence on phase error.

It means that all lines shift from these real positions with the same shift which depends on phase error. In process of fit we can see it in the deviation of fitted Delay value from initial Delay (see Table 1).

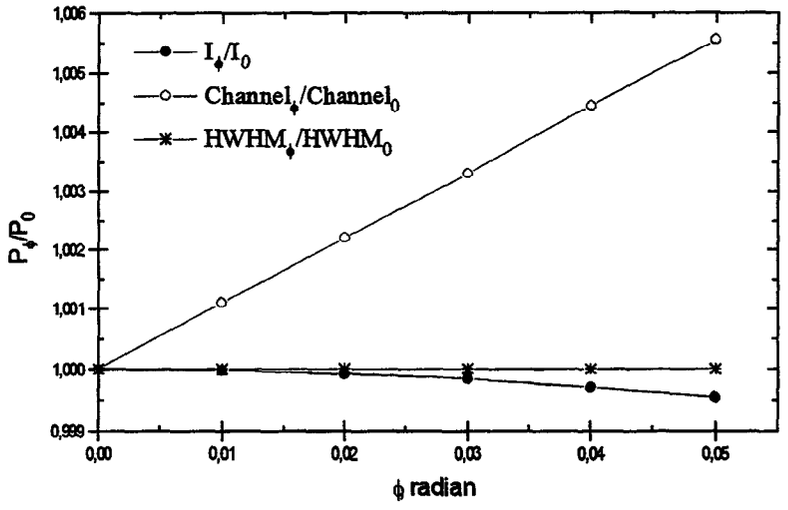

Fig. 3 Influence of phase error on integral intensity, HWHM and line position.

In case of measurement of investigated sample together with standard one the simple method should be proposed for calibration of Lsin(Θ) and Delay parameters. Using notation $\tau_{hkl} = \Delta \cdot \left(C_{hkl} + Delay\right)$ where Δ is channel width in μs, C_{hkl} is line position in channels, the formula (3) can be rewritten for cubic lattice in the following form:

$$C_{hkl} = \frac{h\Delta}{2m} \cdot A \cdot L \cdot \sin(\Theta) \cdot \frac{1}{\sqrt{h^2 + k^2 + l^2}} - Delay$$

Let us introduce following notations:

$$\alpha = \frac{h\Delta}{2m} \cdot A \cdot L \cdot \sin(\Theta)$$

$$P_{hkl} = \frac{1}{\sqrt{h^2 + k^2 + l^2}}$$

As one can see line positions C_{hkl} linearly depend on P_{hkl}. The slope α of straight line is proportional to the lattice constant and Lsin(Θ) parameter, the intercept is just (-Delay) value.

The results of such calibration measurements are shown at the Fig. 4 for simultaneous measurement of diamond powder and Mo-Cr alloy placed in one container. The fitted values of Delay are in a good agreement. The difference of slopes depends on the difference of lattice constants that allows to calculate the correct value of investigated alloy lattice constant instead of phase error.

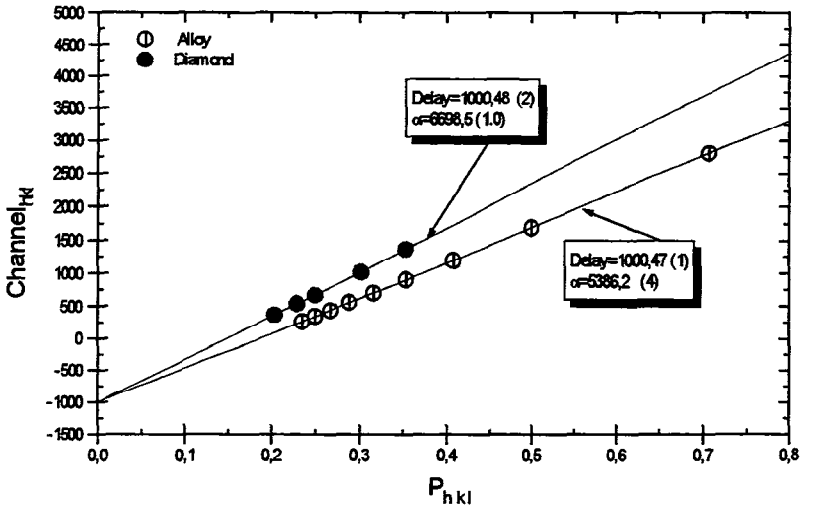

Fig.4 C_{hkl}-P_{hkl} plot for (diamond+Alloy) sample

5. Conclusion

For correct extraction of information from RTOF diffraction spectra it is needed to take in account the shifts of lines arising from Lsin(Θ)=f(λ) dependence and phase error.

There are few effects that could introduce the dependence of effective Lsin(Θ) parameter on neutron wavelength. Effective value of Lsin(Θ) can be calculated using coordinates of the center of weight distribution $P(x,y,z,\lambda)=\prod_i p_i(x,y,z,\lambda)$ where p_i describes influence of absorption, primary beam distribution on the exit of neutronguide, divergence effect et al.

Small phase errors mainly shift the line positions.

One can see these effects using "C_{hkl}-P_{hkl}" plots. The deviation of intercept from initial value of Delay must be proportional to phase error. Systematic deviations of experimental points from strait line will show on Lsin(Θ)=f(λ)dependence.

This work was supported by Russian fund "Neutron Research of Materials" and INTAS-94-3239 project.

[1] M.T. Hutching and A. Kravitz, "Measurement of Residual and Applied Stress Using Neutron Diffraction", NATO ASI series E: Vol 216, 1992

[2] P. E. Hiismaki, in IAEA Symp. on Neutron Inelastic Scattering, Grenoble, 1972, SM-155/F-10, p.803.

[3] V. A. Kudryashev et al. "Optimierung der RTOF-Methode", GKSS 94/E/29, GKSS-Forschungszentrum Geesthaht GmbH, Geesthaht, 1994

[4] A.Tiitta, Technical Research Centre of Finland, Helsinki, VTT Rep. 27, 1980.

[5] V.A. Trounov "M. Sfinks" Diffractometer at Gatchina Reactor", Proceedings of ICANS XIII, 1995

[6] D. Yu. Chernyshov et. al., Phys. Solid State **36** (4),1994, p.585

[7] V. B. Zlokazov and V.V. Chernyshov, J. Apll. Crystallogr. **25**, 1992, p.447

ICANS-XIII
13th Meeting of the International Collaboration on
Advanced Neutron Sources
October 11-14, 1995
Paul Scherrer Institut, 5232 Villigen PSI, Switzerland

WIDE BAND DEVICES

L.CSER
Research Institute for Solid State Physics, Budapest, H-1525, Budapest, POB. 49, Hungary

RESUME

Several methods helping to utilize the neutron spectra emitted by pulsed neutron sources with better efficiency are considered (e.g. supermirror neutron guides, multidetectors, wide band polarizers and the method of pseudostatistical modulation). The present status of proposed approaches are reviewed.

Keywords: polarization, pseudo statistical modulation

INTRODUCTION

No arguments, the future belongs to the pulsed neutron sources. Contemplating the experience collected at the operating pulsed sources (ISIS, IBR-2, LANCE, KENS,IPNS) all operating facilities were constructed according the principle of the most economical use of the emitted by the pulsed source neutrons. The explanation of such an effort is quite obvious. To increase of the luminosity of the source is limited both by technical and financial restrictions. Thus, the efficiency of any facility can be enhanced only by the use of better collection of scattered neutrons.
As any pulsed source emits a quasi-maxwellian neutron spectrum - which often is called as white one - during a very short time (typical pulse width is several microseconds) thus, those methods are effective which utilize the most wide part of this maxwellian spectrum.
After all, there are several parts of a neutron scattering device, efficiency of which can be drastically improved. All these improvements are using the principle of collecting maximum information.
In the following I should like shortly recall some of them without striving for completeness.

I. NEUTRON TRANSPORT AND DATA COLLECTION

At present time the simplest but not the cheapest way to conduct neutrons from the source to the sample seems to be supermirror neutron guides. Their aperture today achieves the value being comparable with the $3\theta_{critical}$ of natural nickel. Assuming a neutron guide of quasi-quadrangular cross section the gain factor may reach almost one order. The arguments in the favour of this type of neutron guide were all but a common place if their additional advantage, i.e. being able with considerably increased efficiency transport even short wavelength ($\lambda \geq 1\AA$) neutrons allowing to install at least two spectrometers at one channel. These guides indeed, have to be curved, so usual at the output port of the guide emits neutron beam without epithermal and gamma-ray con-

tamination. To my knowledge the first supermirror guide is under preparation in the Institute Laue-Langevin in Grenoble.
The increase of the demand for more effective the data collection seems to be even more trivial. Area detectors (position sensitive, or multiwire ones) operates in many laboratories. The tendency to cover more and more bigger section of the 4π solid angle surrounding the scatter can be observed in this area of activity. A new feature of this activity is manifested in search for new type of detecting principles, e.g. scintillators with high spatial resolution converters. The high spatial resolution makes easier and faster the study of the structure of crystals the unit cell of which comprises hundreds or even thousands atoms (see biological structures).

II. WIDE BAND POLARIZERS

At present time there are two main streams to construct wide band polarizers: the polarized ^{3}He target, and mechanical constructions using synchronously moving polarizing supermirrors.
a.) ^{3}He neutron polarization filter method.
The polarization mechanism in the case of a transmission polarizer comes from the spin dependent absorption process with the following cross section

$$\sigma_{\pm} = \sigma_0 \pm \sigma_p \tag{1}$$

where $\pm$ denotes the two possible states of the neutron spin. It was shown [1] that the ratio σ_p / σ_0 is just the polarization of ^{3}He. In the paper[2] four possible approaches for ^{3}He polarization have been mentioned.
1. *Brute force* That is the cooling the nuclear moments down to several mK in the solid phase (25 bar) with a high magnetic field (more than 10 T).
2. *Optical pumping.* The photons transfer angular momentum to atoms by resonant scattering and subsequently to ^{3}He nuclei by hyperfine coupling at room temperature.
3. *Pumping pure ^{3}He* The optical pumping acts on the pure gas in an exited metastable state. Metastability exchange collisions then transfer the polarization to the ground state.
4. *Pumping Rb/^{3}He mixture.* The ^{3}He polarization is produced by using spin transfer from optically pumped Rb vaporized at 200 ^{o}C.
Such type of filters would allow a beam of polarized neutrons with a broad wavelength band and can equally serve both for polarizers and analyzers. Unfortunately, at present time because of purely technical reasons the achieved level of polarization is far from the desired one (95%) and the opacity of the filter is too high. As the ^{3}He filter has many degree of freedom, the optimization of the quality factor Q = P$\sqrt{T}$ (P - is the polarization, T - is the transmission) can be considerably increased[3].

b.) Mechanical polarizers.

Mechanical polarizing devices are using movable polarizing supermirror system which would allow to tune glancing angles in time so that the total reflection condition is always fulfilled only for one of the neutron spin direction. (The principle of such a construction is shown in Figure 1[4]). In addition, this technical performance gives rise to use the angular region of the total reflection in which the contamination of neutrons with opposite polarization is absent. (See the insert of Figure 1). In order to satisfy this condition it is necessary to operate at large area moderator and to have a collimation angle less than the total reflection angular range. These conditions in practice, e.g. for small-angle scattering are usually satisfied.

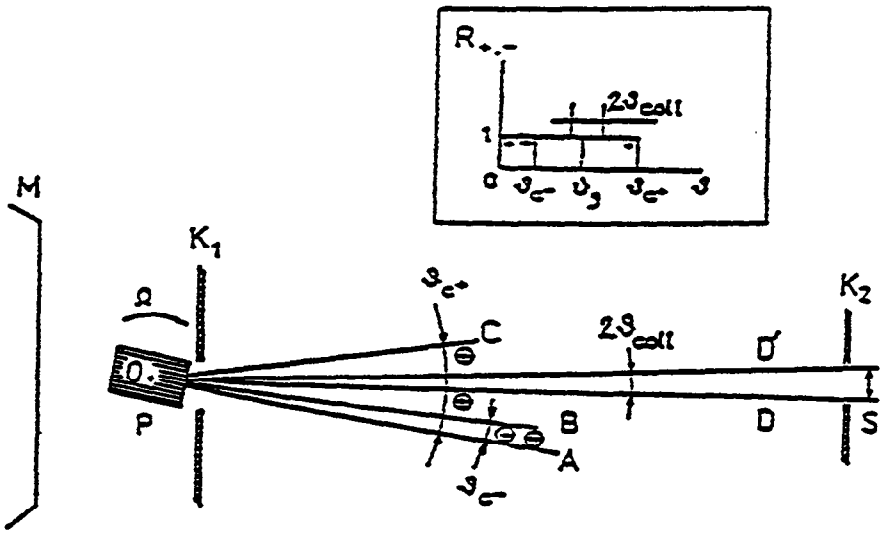

Figure 1. The schematical view of a broad-band polarizing setup for a TOF small-angle neutron scattering instrument. M - the moderator; P - the multimirror polarizing assembly, rotating around the center O with the angular velocity Ω. The neutrons with polarization (+) fill the angular range AOC, while neutrons of mixed polarization (+,-) fall in the angular range AOB. In the angular range DOD′ defined by the collimator K2 only neutrons with polarization (+) do appear. The rotation of P keeps the sample S in the middle of the angle BOC, while the neutron wavelength and the angle AOB and AOC increase in time. The insert shows the idealized reflectivity versus the glancing angle together with the collimation angle DOD′.

This approach can be improved by the use of multiple reflection of the neu-

trons on the neighboring mirrors plates provided, their both side are covered by polarizing supermirror multilayers (polarizing Soller collimator) and the length of the rotation system is long enough (e.g. several meters). If the neutron possesses with a velocity component being perpendicular to the plane of the moving mirrors the useful angular range can be considerably decreased (Figure 2a).

Evidently, the motion of the mirror does not affect the reflection process in this way if no movement normal to its plane occurs. This can be achieved when the mirror moves in its on plane. Different ways to arrange of mirrors satisfying to this conditions are shown in Figures 2b and 2c. An intermediate solution can be proposed using a set of coaxial truncated cones with generatrices inclined at an angle to the axis being equal to the "useful angle" θ_{us} (Figure 2d)[5]. It is worthy of note that the "density" of plates will be in an adequate way to follow the actual wavelength range.

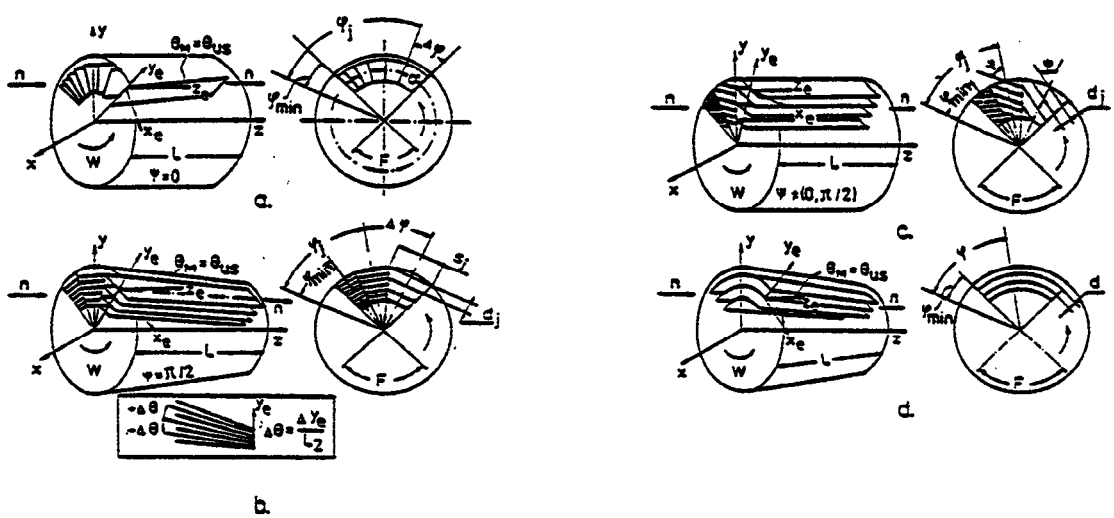

Figure 2. General outlook of various type of wide band neutron polarizing mirror setup.

a.) radialy arranged mirrors; b.) and c.) two different version of the arrangement mirrors moving in-plane. d.) coaxial truncated conical mirrors. L - the length of the mirror setup; W - is the angular velocity of the mirrors; ψ - the tilting angle of the mirrors relating to the axis of the rotation; x,y,z - the coordinates in the laboratory system of coordinates, x_e,y_e,z_e - the comoving coordinates of the comoving reference system; n- the neutron beam.

Unfortunately, the idea of mechanical wide band polarizer never was experimentally tested.
Nevertheless, it can be predicted a disadvantage of such construtions, i.e. they can serve only for polarizers and never can be used with acceptable efficiency for analyzers because they in principle can not be adapted geometrically to the divergent scattered neutron beam.

III. BEAM MODULATION

The time-of-flight (TOF) method of monochromatization is the greatest advantage of a pulsed source. Experiments aiming the investigation phenomena belonging to the elastic scattering type of measurements are profiting from this potentiality.
Inelastic scattering needs the analysis of the energy change of the scattered neutrons. A smart solution of this task was performed at the ISIS facility. The implementation of a large array of analayzer crystals and detectors provided an instrument of high efficiency and good resolution (the IRIS facility), but at sensitively high cost.
Some times the financial conditions do not allow to build up any similarly sophisticated devices and cheaper and one has to look for simpler solutions.
In the following I should like to discuss an old and almost forgotten approach to the task of the increase of the efficiency of inelastic scattering experiments, i.e. the beam modulation technique using the method of pseudostatistical modulation of the incoming neutron beam.
This method utilizes for the modulation of the beam in time a function a(t). Then the observed number of the scattered neutrons at moment t

$$Z(t) = \int_0^t S(t-t')a(t')dt' + b(t) \tag{2}$$

Here S(t) is the scattering function characterizing the physical properties of the sample. If the function a(t) satisfies the condition

$$C_{aa}(\tau) = n\int_{-\infty}^{\infty} a(t)a(t-\tau)dt = c_1\delta(\tau) + c_2 \tag{3}$$

where C_{aa} is the so called autocorrelation function, and the constants c_1 and c_2 depends on the duty cycle of the modulator, then the corresponding cross correlation function

$$K(\tau) = \int Z(t)a(t-\tau)dt = c_1 S(\tau) + c_2\int_0^T S(\tau)d\tau + c_3 \tag{4}$$

here

$$c_3 = \frac{1}{T}\int_0^T a(t)dt \tag{5}$$

It is well known that the modulation function possesses some characteristic feature of the white noise. In practice, white noise can not be prepare, so its more or less perfect discrete approximation has to be used.
Let us to have a series of elements a_i = either zero or to unit with relation

$$\sum_{i=0}^{N-1} a_i = m \tag{6}$$

and simultaneously

$$\sum_{i=0}^{N-1} a_{i+j} a_{i-k} = C_{aa}(j-k) \tag{7}$$

and

$$C_{aa}(j-k) = \begin{cases} m & \text{if } j-k = 0, \pm N, \pm 2N.. \\ K & \text{otherwise} \end{cases} \tag{8}$$

Or, in another way

$$C_{aa}(j-k) = m(1-c)\delta(j-k) + mc \tag{9}$$

where m - number of unit values in the series, N - is the length of the series and K = m(m-1)/(N-1), c = (m-1)/(N-1) is the duty cycle of the chosen series[6].
Then Eq.(2) can be transformed as

$$Z_n = \sum_{i=0}^{N-1} S_i a_{n-i} + b \tag{10}$$

After some algebraic transformation one gets

$$S_l = \frac{1}{(1-c)m} \sum_{k=1}^{n} (a_{k-l} - c) Z_k - \frac{b}{m} \tag{11}$$

This last expression shows how to obtain from the measured raw data the scattering function. Because of the large value of the duty cycle (almost 50%) the efficiency of the data collection can be characterized by a great gain value in comparison with the use e.g. a Fermi-chopper.
The pseudostatistical method can be applied to a pulsed source too. If the experimental setup is established as it is shown in the Figure 3. the scattered neutrons can be labeled by two indices: i - being proportional to the time elapsed between the neutron pulse and the moment of the registration of the given event, and k - which is the position of the pseudostatistical modulator at the instant of the detection of the scattered neutron.

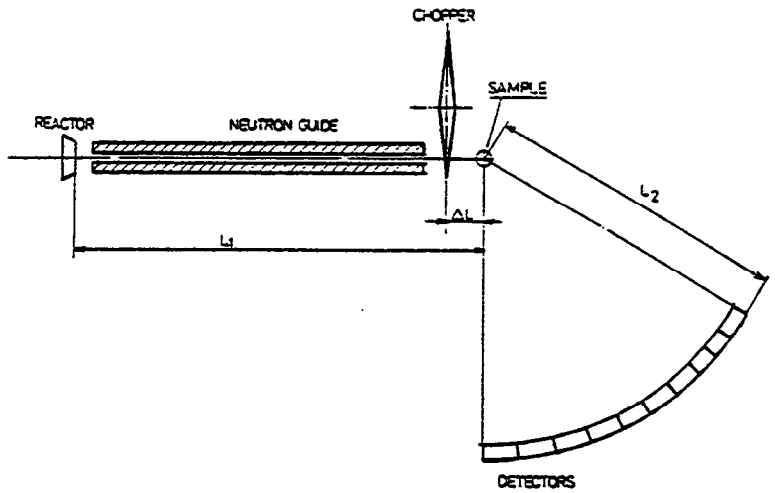

Figure 3. The schematical layout of a pseudostatistical modulation experiment at a pulsed source.

Then the registered spectrum has the form

$$Z_{ik} = \sum_{j=0}^{(N-1)} a_{(k-j)} S_{ij} + b \tag{12}$$

and for each i value the relation (10) is separately valid

$$S_{i\tau} = \frac{1}{m(1-c)} \sum_{k=0}^{(N-1)} (a_{(k-\tau)} Z_{ik} - \frac{b}{m} \tag{13}$$

By the help of the schemes given in Figures 4 and 5 it is easy to interpret the value τ as the time of flight over the flight path between the sample and the detector. Thus, from the simultaneous knowledge of the total time of flight and the value of τ the change of the kinetical energy of the scattered neutron can be evaluated.

The above described setup seems to be extremely effective for using it to carry out inelastic experiments at pulsed sources. However, a more detailed analysis of the error matrix makes it evident that the statistical accuracy of each S_l points are equal, and is proportional to the total number of the collected data. From this statement it follows that if S(t) contains several peaks the area of the dominant (as usual elastic) peak determines the error bars. In the most real cases this effect makes hopeless to observe small inelastic effects, like phonons, etc. on the presence of elastic scattering pattern.

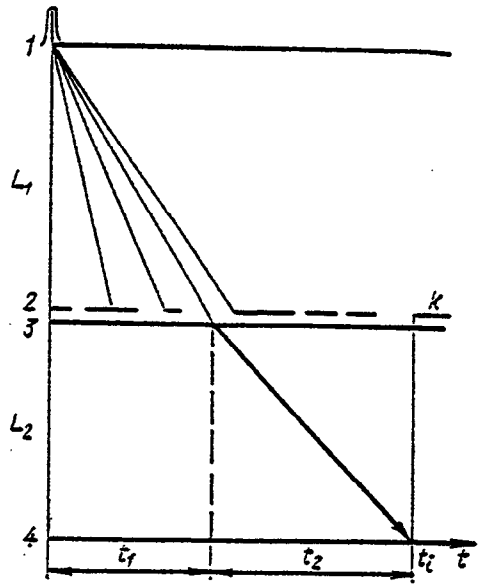

Figure 4. The time-of-flight versus flight path diagram of the pseudostatistical experiment at a pulsed source.

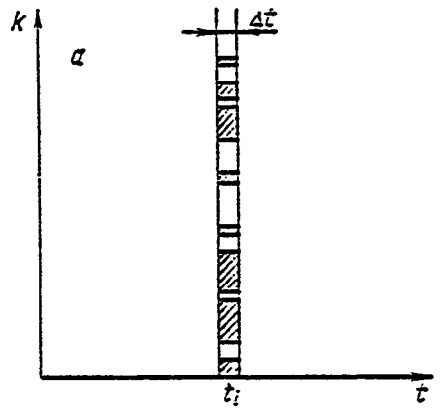

Figure 5a. The count distribution belonging to the position of the pseudostatistical modulator at instant t_i. t - is the total time-of-flight; k - is the pseudostatistical sequence. The segments marked with tilted lines correspond to channels filled with neutron count events, the white segments are the empty channels.

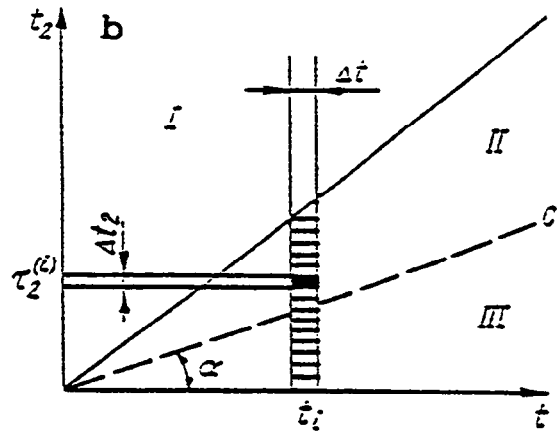

Figure 5b. Schematical view of a time-of-flight segment containing a sharp peak (the dark square) after the cross correlation procedure. c - the position of elastically scattered neutrons; I. - non-physical area; II. - area of the up-scattering; III. - area of the down-scattering;
The only exception would be the case when the physical information is connected with the most intensive peak. The quasi-elastic phenomena satisfy this condition.

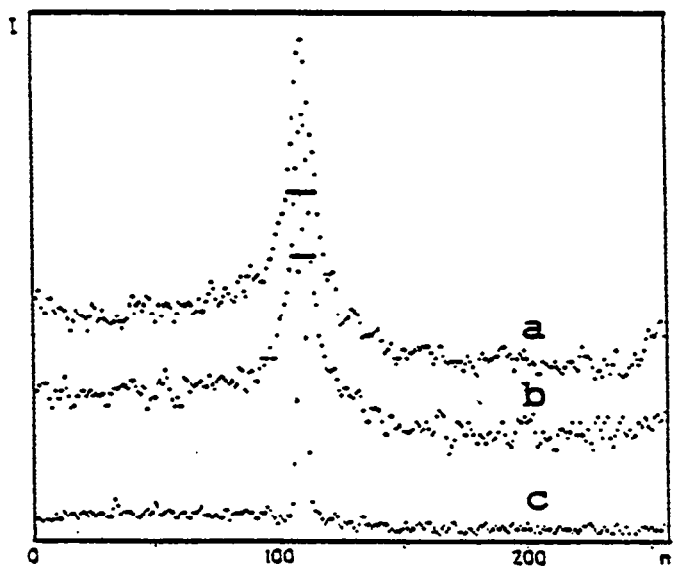

Figure 6. Three typical quasi-elastic spectra. a. - Pure water, b. - 2 mol TMU water solution, c. - sold EBBA liquid crystall. I - the scattered intensity in arbitrary units; n - the time-of-flight on the second flight path in channels (channel-width = 40 μs). The scattering angle 2θ=72°, the wavelength=4 Å.

In fact, in this case all information are concentrated to the most intense peak, which are set along the straight line on the (t,τ) plane and the quasi-elastic effects over a wide (Q,ω) range can be simultaneously studied.

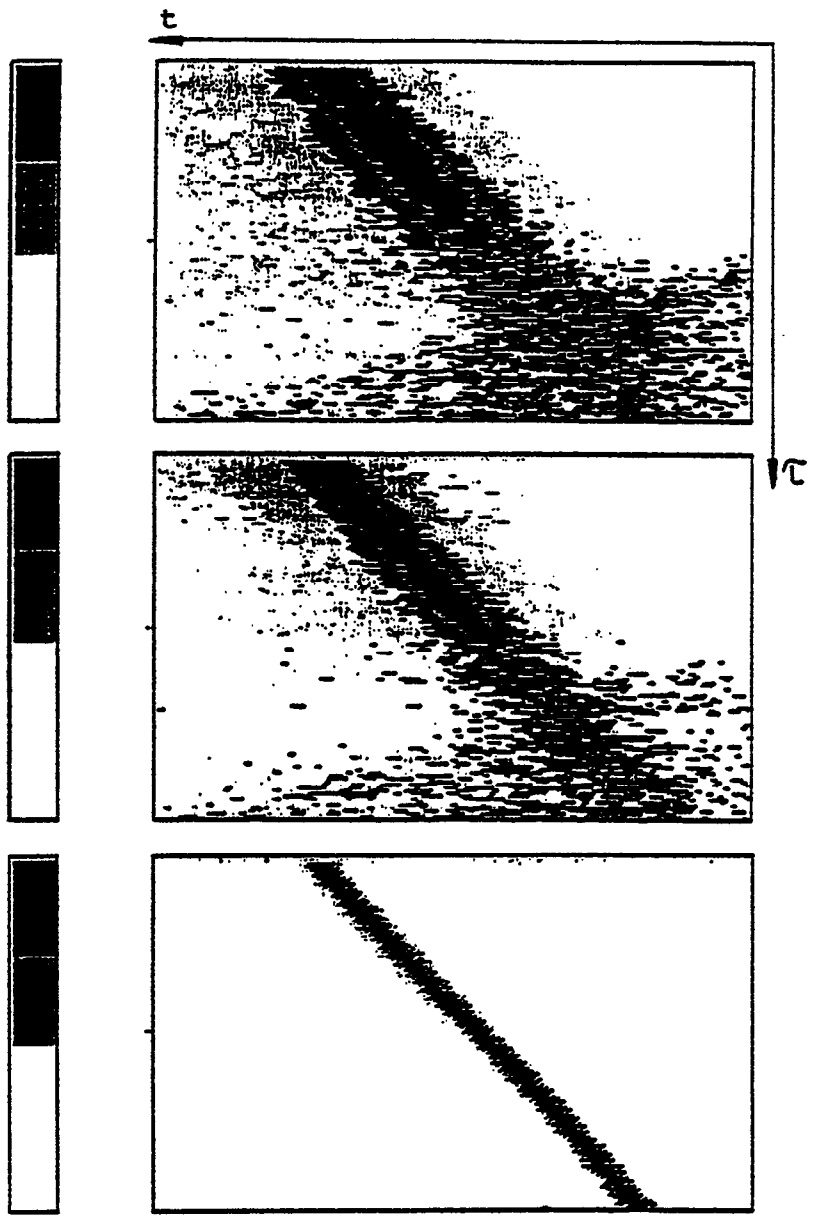

Figure 7. The (t,τ) intensity level diagrams: pure water (upper box); 2 mol TMU dissolved in water (middle box) and solid EBBA liquid crystal (lower box).

In order to demonstrate the power of the proposed method we carried out quasi-elastic investigation of tetramethylurea (TMU) water solution aiming to investigate the effect of dissolved TMU on the diffusion of the water molecules. The Figures 6 and 7 show the results of the experiment performed at the IBR-2 pulsed reactor.

The broadening of the quasi-elastic peaks takes it origin from the diffusion of the water. It was shown that the presence of TMU causes a considerable slowing down of the motion of the water molecules. The resolution function of the spectrometer was measured by using solid EBBA liquid crystal.

CONCLUSIONS

In the present paper we made an attempt to draw attention to the importance of the use of wide band instruments. The strong limitation of the increase of the luminosity of the neutron sources can be overcame only by methods of more economical use of the emitted neutrons.
The use of supermirror neutron guides together with two-dimensional multidetectors is obvious.
There are promising endeavours to improve the efficiency of the polarization techniques. The ^{3}He filters seems to be more promising than the mechanical polarizers provided their efficiency could be in the future acceptably improved. Otherwise, may be the combination of the two method seems to be realistic. That is, for the polarizer an ensemble of moving supermirror system will be used, whilst, for the analyzer the ^{3}He filter has to be utilized.
The old and almost forgotten pseudostatistical modulation method can be revived since this method was proven as a very effective approach to quasi-elastic experiments.

References

1. L.Passel and R.I.Schermer, Phys. Rev. 150 146, (1966)
2. F.Tasset, T.E.Chupp, J.P.Pique, A.Steinhof, A.Thompson, E.Wasserman and M.Ziade, Physica B 180 – 181, 896-898 (1992)
3. F.Tasset, E.Ressouche, Nucl. Instr. Meth. A 359, 537-541, (1995)
4. Yu.V.Nikitenko, Yu.M.Ostanevich, JINR Report Dubna E13-92-316, (1992)
5. Yu.V. Nikitenko, Nucl. Instr. Meth. A 337, 441-444, (1994)
6. F. Hossfeld, R. Amadori, Report KFA, JÜL-684-FF,(1970)

ACKNOWLEDGMENT

The present work was done by the help of OTKA T-017016 grant.

ICANS-XIII
13th Meeting of the International Collaboration on
Advanced Neutron Sources
October 11-14, 1995
Paul Scherrer Institut, 5232 Villigen PSI, Switzerland

MORPHOLOGY OF GLASS SURFACES: INFLUENCE ON THE PERFORMANCE OF SUPERMIRRORS

P. Böni, D. Clemens, H. Grimmer, and H. Van Swygenhoven

Labor für Neutronenstreuung ETH & PSI, CH-5232 Villigen PSI, Switzerland

ABSTRACT

Multilayer structures are often used for guiding, filtering, shaping, and monochromatizing electromagnetic radiation or particle beams. In order to assess the importance of the properties of the substrate on the performance of multilayers we have investigated glass substrates by means of atomic force microscopy, profilometry, and neutron- and x-ray reflectometry. Whereas the waviness of polished glass is excellent, when compared to float glass, the surface roughness of polished glass is significantly larger than for float glass. We find that the performance of supermirror coatings depends as essentially on the surface morphology as on the loss mechanisms that occur in the multilayer itself.

1. Introduction

Artificial multilayers are widely used for optical applications in neutron and x-ray scattering. In order to obtain a high performance of the devices it is necessary to reduce interface roughness and interdiffusion to the lowest possible values. During the production of supermirror coatings for the neutron guide system of the spallation source SINQ [1] we realized that the surface morphology of the glass substrates has also a strong influence on the reflectivity of supermirror coatings.

In visible light optics, the individual layers of the coatings have a thickness d of the order of the wavelength of light, i.e. $\lambda \simeq 5000$ Å. Hence a roughness [2] of the substrate $r_s \simeq 10$ Å does not impede the performance significantly. In contrast, for neutrons and x-rays, d is typically of the order of 10 to 700 Å, hence r_s must be very small in order to obtain useful coatings. For most applications the waviness of the substrates must also be small.

Before going into more detail, we should like to explain the term supermirror. Neutrons can be guided to the neutron spectrometers in hollow glass tubes by total internal reflection, similarly as light in a wave guide. The most suitable material is Ni, because it has the largest angle of total reflection, θ_c, of all naturally occuring materials. It is given by $\theta_c^{\mathrm{Ni}} = c\lambda$. Here $c = 0.099°/\text{Å} = 1.73$ mrad/Å. The glass plates must have a small waviness w and their alignment must be excellent because θ_c is so small. Typical neutron guides are more than 50 m long and have cross sections of the order of 120 mm by 50 mm.

Keywords: Supermirror, Glass, Roughness, Neutron Guide

In order to increase the neutron flux at the instruments, it has been suggested [3] to extend θ_c to $m\theta_c^{\mathrm{Ni}}$ ($m > 1$) by using interference coatings consisting of thin layers of Ni and Ti that reflect neutrons according to Bragg's law for $\theta_c > \theta_c^{\mathrm{Ni}}$. Such coatings are called supermirrors and have been developed at various places [4]. For $m = 2$ mirrors we shall achieve at SINQ flux gains of more than a factor of three for neutrons with $\lambda \simeq 4$Å [5].

As an example, we show in Fig. 1 the reflectivity R (squares) and the critical angle in units of θ_c^{Ni}, m (triangles), for a sequence of 8 successive production runs of supermirror coatings for the spallation source SINQ. They consist of 82 layers $\mathrm{NiN}_x\mathrm{O}_y/\mathrm{TiV}_z$ [1, 6]. The two pairs of polished (boron containing) glasses 50×500 mm^2 (open symbols) and the pair of float glass 50×500 mm^2 (filled symbols) were coated at the same time. The measurements have been done by determining the transmission of neutrons ($\lambda = 4.08$ Å) through a microguide that was assembled from a pair of plates [1, 6]. It can be seen that the sputtering process is very reproducible and that the reflectivity of supermirrors on polished glass is significantly ($\simeq 5\%$) lower than of supermirrors on float glass. Obviously, the performance of supermirrors is strongly affected by the substrate.

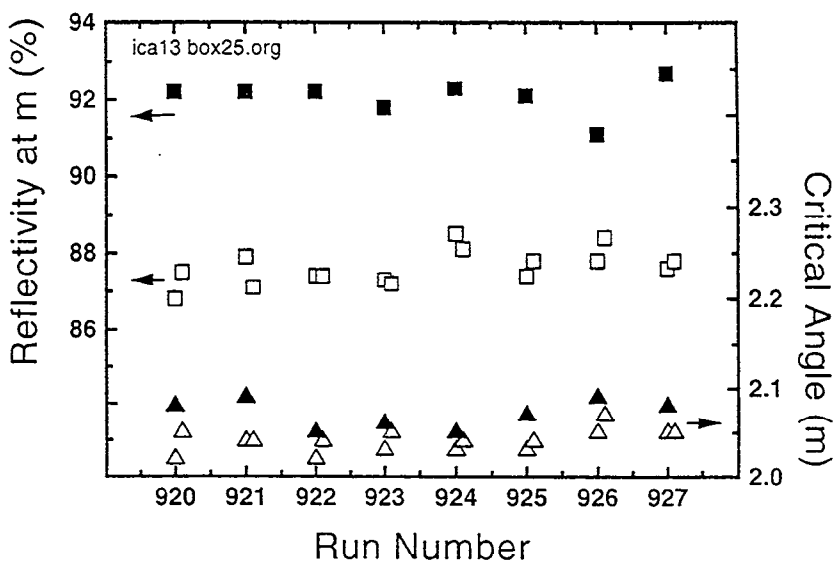

Figure 1: *Reflectivity (squares) of supermirrors $m \simeq 2$ at the angle of total reflection (triangles). θ_c is given in units of θ_c^{Ni}. The substrates are regular float glass ($d = 2$ mm, filled symbols) and polished glass (open symbols).*

In order to assess the influence of the substrate on the reflection properties of $\mathrm{NiN}_x\mathrm{O}_y/\mathrm{TiV}_z$ supermirrors we have investigated the surface of different glasses and coatings by means of x-ray diffraction, atomic force microscopy, and profilometry. In addition, we have measured the reflectivity of supermirror coatings by means of neutron reflection. Reflectivity losses due to imperfections of the multilayer structure itself have already been discussed in the literature [4]. Our results indicate clearly that the reflection losses due to non-perfect substrates can be as large as the losses caused by the imperfections of the coating.

2. Experimental

Atomic force microscopy (AFM) measurements on glass plates (500×150 mm^2) for the neutron guides of the spallation source SINQ have been performed on a Digital Instruments NanoScope III Large Sample Scanning Probe Microscope. Small samples have been investigated on a Park Scientific Instruments Autoprobe CP microscope. The microfabricated Si_3N_4 stylus tips have a diameter of $\simeq$ 100 Å, yielding a lateral resolution l_r < 100 Å. The AFM's were used in the tapping mode in order to overcome the electrostatic forces.

The grazing angle x-ray diffraction measurements were performed on a Philips X'Pert MPD diffractometer at PSI and on a reflectometer at HMI. From a comparison of the Q-dependence of the reflected intensity, $R(Q)$, with the reflectivity R_0 of an ideal surface we extracted the root mean square roughness r_s under the assumption of a Debye-Waller type behavior

$$W(r_s) = \frac{R(Q)}{R_0} = \exp\left(\frac{-(Qr_s)^2}{2}\right). \tag{1}$$

Such measurements yield an average of the surface roughness over the illuminated area of the sample.

The waviness w of the substrates was determined by means of a Wenzel 3-d coordinate measuring machine. In a first step the surface profile $z(x, y)$ was measured along four different rows with an accuracy of ± 1 μm yielding 188 data points per glass side. In a second step the surface normal in every point was determined by calculating the derivative of z with respect to x and y. We defined w to be the standard deviation of the surface normals from their mean value.

The surface properties of the float glass [7] and the extruded and fire-polished glass [8] were not specified by the supplier, whereas the roughness of the polished glass [9] was specified on the basis of interferometric measurements performed by means of a WYKO profilometer. We designate this number by r_w. Clearly r_w is expected to be smaller than r_s as determined by x-ray reflection or AFM, because of the coarse lateral resolution of the optical method.

3. Results

3.1 Roughness

The AFM patterns in Fig. 2 show that the surface profiles of float glass (thickness d = 10 mm) and polished glass are very different. Float glass consists of large smooth areas with r_s < 3.7 Å [10] and spots with crater-like damages having an amplitude of $\simeq$ 150 Å. They are caused by outgassing during solidification of the glass. The roughness over the measured area 25×25 μm^2 is r_s = 16.4 Å and is mostly determined by the localized damages (Table 1). Therefore the Debye-Waller approach for $R(Q)$ (Eq. 1) cannot be applied. We find that the reflectivity R of supermirror coatings decreases with an increasing number of damages, leading us to qualify float glass as being "good", if $R > 90\%$ and "bad", if $R < 88\%$.

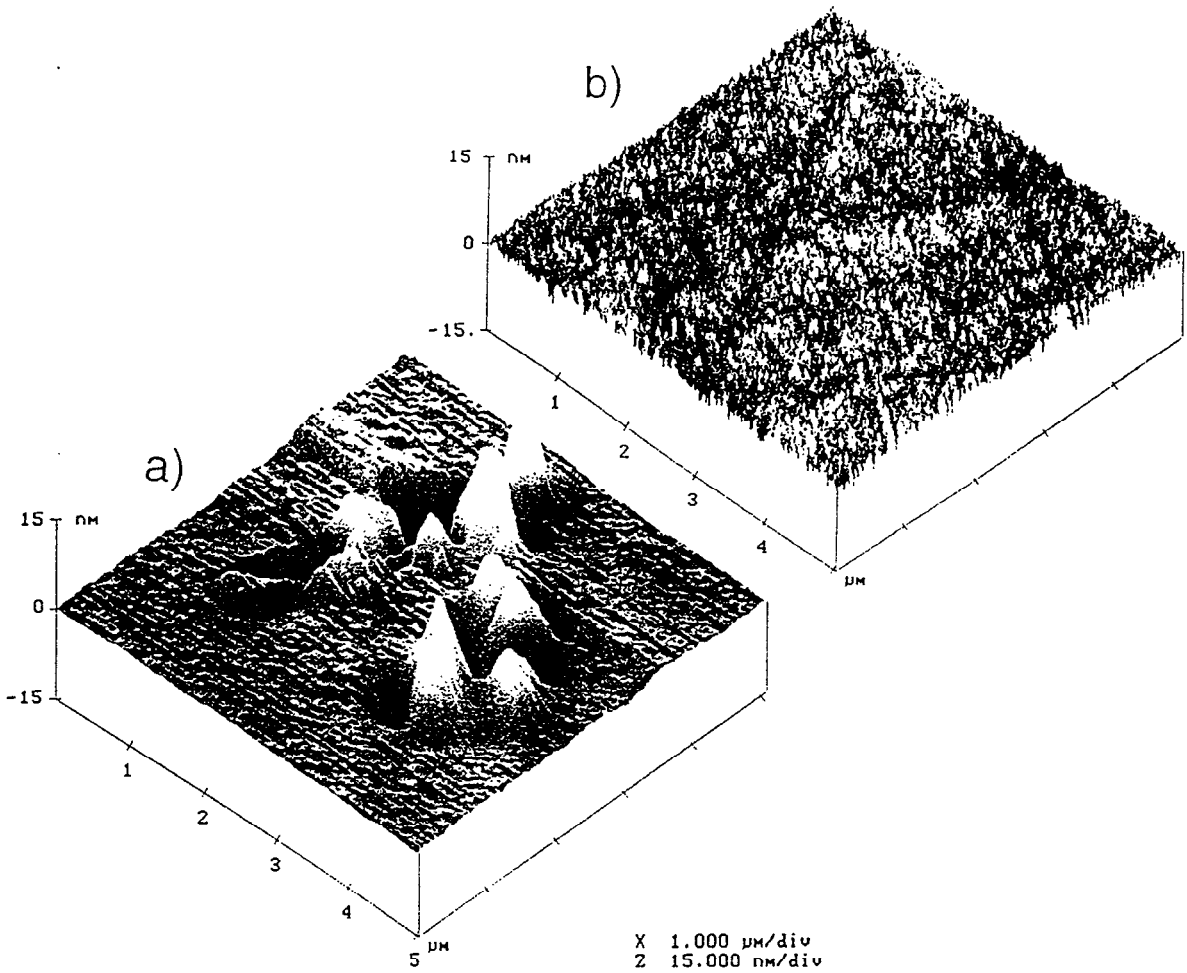

Figure 2: *a) AFM profile of a "damaged" part of float glass (d = 10 mm). The average distance between the damages is typically $\simeq$ 10 μm. b) AFM profile of polished, boron containing glass (d = 15 mm).*

In contrast, the polishing technique gives rise to a homogenous, rough surface. It contains scratches with an amplitude of about 25 Å from the polishing procedure. The roughness $r_s \simeq 8.4$ Å is about twice as large as the interferometric values, $2.5 \leq r_w \leq 5.0$ Å. Often, but not always, we find a clear correlation between r_w, as quoted by the supplier, and the reflectivity of supermirror coatings at $m = 2$ [1] (Fig. 3).

The roughness of various glass surfaces has been characterized also by means of x-ray reflection. "Good" float glass yielded $r_s \simeq 4$ Å for the side that floated on the tin bath during production and $r_s \simeq 9$ Å for the non-floated side [11]. Similar measurements performed at PSI on polished glass yield $r_s \simeq 9$ Å. These values compare well with the AFM results, i.e. $r_s < 3.7$ Å for the smooth areas of float glass and $r_s \simeq 8.4$ Å for polished glass. Therefore, x-ray reflection is mostly sensitive to the smooth areas of float glass, whereas the damaged areas may be considered as non-reflecting spots.

We have also found that the surface morphology of float glass depends on the thickness of the glass. All the investigated samples with $d \geq 8$ mm had crater-like

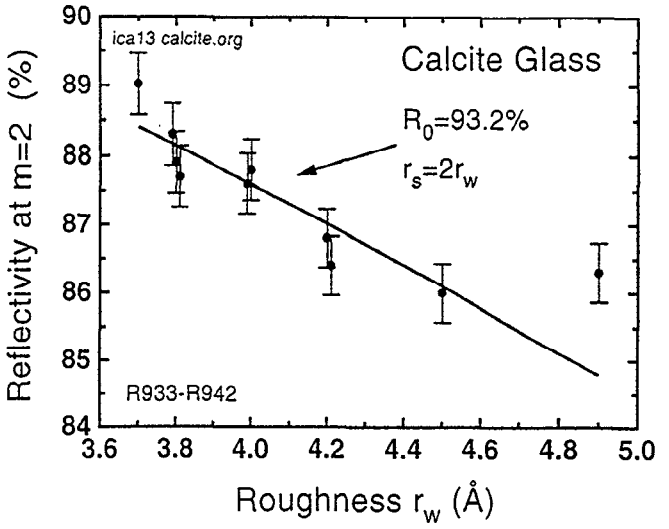

Figure 3: *Dependence of the neutron reflectivity on the surface roughness of polished calcite glass coated with supermirror $m = 2$. The solid line is a calculation as explained in the text.*

damages, whereas float glass and extruded fire-polished glass with $d \leq 2$ mm was essentially smooth (Fig. 4). The highest reflectivities have always been obtained with coatings on thin float glass.

The above results indicate that the different type of roughness between float glass and polished glass is responsible for the different reflectivity of the supermirror coatings. If we assume that our coatings have a reflectivity $R_0 \simeq 93\%$ on an ideal substrate, then we can estimate the influence of the roughness of the substrate on R on the basis of Eq. 1. If we set $r_s = 2r_w$, as discussed above, then we obtain the solid line in Fig. 3 that roughly follows the trend of the reflectivity data for supermirrors on polished glass.

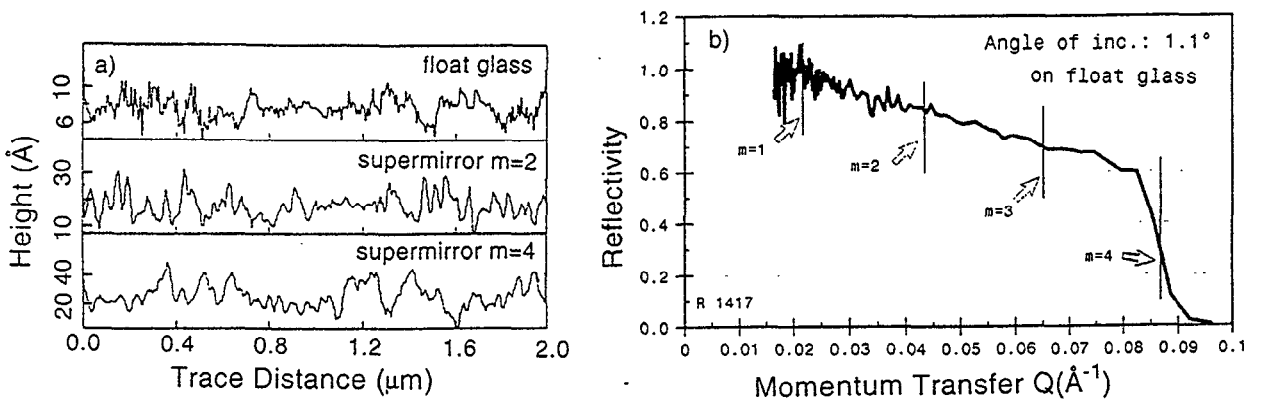

Figure 4: *a) AFM profile of float glass ($d = 2$ mm), without and with supermirror coatings $m = 2$ (82 layers) and $m = 4$ (900 layers). b) Reflectivity of the $m = 4$ supermirror.*

Finally, we measured the surface profile of supermirrors deposited on float glass (Fig. 4a). r_s increases slowly with an increasing number of layers, reaching $r_s = 7.8$ Å for $N = 900$ layers and a thickness of the coating $d_c = 4.5$ μm (Table 1). The reflectivity of the $m = 4$ mirror is shown in Fig. 4b. Above the critical angle of reflection of

Table 1: *Roughness and reflectivity measurements. $W(r_s)$ is given for Q at m times the critical angle of Ni* [12]. *R_c is the calculated reflectivity, including roughness, absorption and incoherent scattering, R_{exp} is the measured reflectivity.*

sample	d(mm)	N	$d_c(\mu m)$	r_s(Å) (from AFM)	$W(r_s)$	R_c	R_{exp}
extruded glass	0.21	0	0	1.5 ± 0.5			
float glass	2	0	0	1.6 ± 0.5			
with $m = 2$	2	82	0.9	4.4 ± 1	0.98	0.96	0.92
with $m = 3$	2	450	2.8	not measured			0.79
with $m = 4$	2	900	4.5	7.8 ± 1.5	0.80	0.72	0.60
float glass	10	0		$3.7 \pm 1^{\spadesuit}/16.4 \pm 3^{\heartsuit}$			
with $m = 2$	10	82	0.9	$5.2 \pm 1^{\spadesuit}$	0.97	0.95	0.90
polished glass	15	0		$8.4 \pm 2^{\diamondsuit}$			
with $m = 2$	15	82	0.8	8.6 ± 2	0.93	0.91	0.87
with $m = 3.3$	15	450	2.8	not measured			0.64

$^{\spadesuit}$ smooth area, $7.5 \times 7.0\ \mu m^2$ (R957) $^{\heartsuit}$ whole surface, $25 \times 25\ \mu m^2$
$^{\diamondsuit}$ area $5 \times 5\ \mu m^2$

bulk Ni ($m = 1$) R decreases to $\simeq 85\%$ at $m = 2$, finally reaching $R \simeq 60\%$ at $m \simeq 4$. At $m = 2$, R is only 2% lower than R of an $m = 2$ supermirror on polished glass (Fig. 1), indicating again that it is also the roughness of the substrate and not only the coating itself, that limits the reflectivity of mirrors. However, the low value $R_{exp} = 0.60 < R_c$ can only be understood if interdiffusion and roughness between the layers is taken into account. Interdiffusion is particularly important for the thinnest layers that have a thickness of only $\simeq 35$ Å.

3.2 Waviness

In real neutron guides losses occur not only due to imperfections of the coatings and the substrates. Losses occur also due to a possible misalignment of the guide sections and due to the waviness of the coated glass plates. Polished glass is usually specified to have $w < 0.1$ mrad. To put this number into perspective, a neutron guide with a supermirror coating $m = 2$ has $\theta_c = 6.9$ mrad $= 0.4°$ for neutrons with $\lambda = 2$ Å. Therefore the maximum loss per reflection due to waviness is 1.5%. For a Ni-coating it is 3%.

In order to assess the usefulness of float glass for the fabrication of neutron guides we have used profilometric measurements to determine the waviness of an arbitrary batch of 60 glass plates having a thickness $d = 10$ mm and a surface area 150 mm by 520 mm. Typical surface profiles are shown in Fig. 5a. The undulations on the front and the back side are correlated and their periode is $\simeq 250$ mm. Fig. 5b shows that the distribution of w for the same glass plate can be well described by a Gaussian distribution having a standard deviation $\sigma = 0.13$ mrad, i.e. a Gaussian with a HWHM of 0.16 ± 0.02 mrad.

A summary of the results from all 60 plates is given in Fig. 5c, and it shows that one half of the glass plates have a waviness $w < 0.2$ mrad. This corresponds to $\simeq 3\%$ of θ_c for $m = 2$ and $\lambda = 2$ Å, i.e. to a loss of less than 3% per neutron

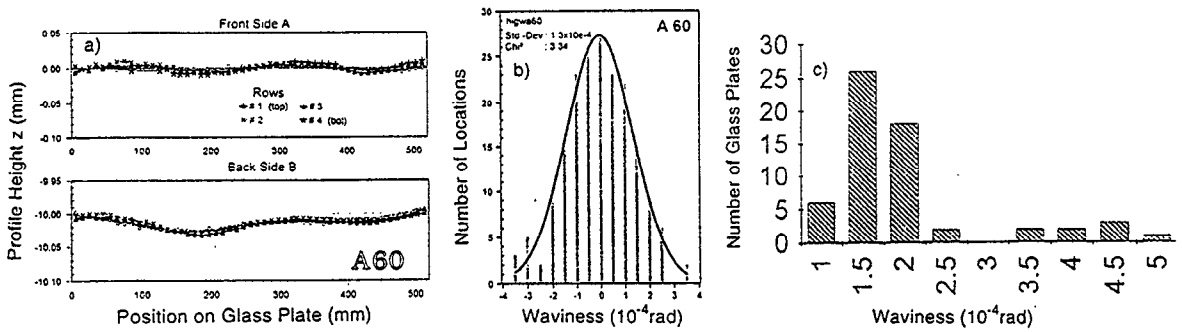

Figure 5: *a) Profile of glass surface. b) Distribution of waviness. c) Number of occurencies of glass plates with a certain waviness.*

reflection. These losses are partly compensated by those parts of the surface that have an opposite slope. The losses can be reduced simply by increasing θ_c by $2w$, i.e. by 6% to $m = 2.12$.

4. Conclusions

The very different surface morphology of polished glass and float glass has important implications for their use as substrates for neutron optical devices. Polished glass may be useful for applications that require high geometrical precision and moderate m, for example thermal neutron guides. For applications with large m one should avoid polished glass because of the exponential decrease of $R(Q)$ (Eq. 1) with increasing m. Hence, for focussing devices, float glass seems more favorable due to the small roughness and because the waviness is of minor concern for large reflection angles. At present the maximum angles of reflection for the coatings from our laboratoy are $m \simeq 4$. The reason being that the mechanical stress in the supermirror coatings is rather large, i.e. $\sigma \simeq 3 \cdot 10^9$ dyn/cm^2. For $d_c \simeq 4.5$ μm the force of the coating exceeds the mechanical strength of the glass and it fractures. This effect is more pronounced in boron containing glass [13].

Finally we should like to compare the reflectivity losses caused by substrate imperfections with the losses caused by imperfections of the coating. The maximum reflectivity, $R_{\text{exp}}^{\text{max}}$, for an $m = 2$ supermirror we have ever achieved until now on float glass, is $94 \pm 0.5\%$ at $\theta_c = 2\theta_c^{\text{Ni}}$ [6]. The design reflectivity R_d was 99.3% [14]. Losses occur (see Table 2) due to absorption, $\Delta_a = 0.7\%$, incoherent scattering, $\Delta_i = 0.7\%$, and due to roughness of the substrate, $\Delta_s^f \simeq 1.3\%$ ($r_s \simeq 3.7$ Å). The losses due to waviness can be neglected because the mirrors were mechanically constrained to be flat. Hence we obtain a theoretical reflectivity $R_c = 96.6\%$. We have neglected the losses due to Bragg scattering. Therefore, the losses due to interdiffusion and roughness at the interfaces of the coating account for $\Delta_{\text{sm}} = R_c - R_{\text{exp}}^{\text{max}} \simeq 2.6 \pm 0.5\%$. Obviously, Δ_{sm} is comparable or even smaller than the losses Δ_s and Δ_w caused by the substrate itself.

In conclusion, we point out that with today's sputtering techniques it is possible to grow multilayers that are so excellent, that the properties of the substrate become

Table 2: *Loss mechanisms of an $m = 2$ supermirror with a design reflectivity $R_d = 99.3\%$. The losses due to waviness decrease with increasing λ and m.*

mechanism		R / loss	comments
absorption	Δ_a	0.7%	Ni and Ti
incoherent scattering	Δ_i	0.7%	Ni and Ti
geometrically perfect superm.	R_c	96.6%	$R_c = R_d - \Delta_a - \Delta_i - \Delta_s^f$
maximum measured R	$R_{\rm exp}^{\rm max}$	$94.0 \pm 0.5\%$	Ref. [6]
interdiff., interface roughness	$\Delta_{\rm sm}$	$2.6 \pm 0.5\%$	$\Delta_{\rm sm} = R_c - R_{\rm exp}^{\rm max}$
roughness of polished glass	Δ_s^p	$\simeq 6.4\%$	$r_s = 8.4$ Å
waviness of polished glass	Δ_w^p	$\simeq 1.5\%$	$\lambda = 2$ Å, $w = 0.1$ mrad
roughness of float glass (10 mm)	Δ_s^f	$\simeq 1.3\%$	$r_s = 3.7$ Å
waviness of float glass (10 mm)	Δ_w^f	$\simeq 3\%$	$\lambda = 2$ Å, $w = 0.2$ mrad

a major concern. The ideal substrate should i) have a low roughness, ii) be flat, iii) be mechanically strong, and iv) be affordable. For very large m the layer thicknesses become rather small and interdiffusion and stress must be minimized. Here, new sputtering techniques combined with smoothing and stress-releasing layers may improve the performance of multilayers by another few percent.

5. Acknowledgements

We should like to thank M. Dänzer and H. P. Friedli for performing the measurements and the analysis of the profilometric data, O. Elsenhans and J. Söchtig for providing some AFM measurements, and A. Fleischmann for pointing out the problem of outgassing in float glass.

References

[1] P. Böni, I. S. Anderson, P. Buffat, O. Elsenhans, H. P. Friedli, H. Grimmer, R. Hauert, K. Leifer, J. Penfold, and J. Söchtig, Proceedings of the Twelfth Meeting of the International Collaboration on Advanced Neutron Sources ICANS-XII, Rutherford Appleton Laboratory Report Number 94-025 Volume 1, I-347 (1994).

[2] Roughness designates surface undulations with a length scale of the order of a few thousand Å or less. Waviness is a measure for surface undulations with a length scale of a few micrometers up to meters or more. Usually it is characterized by reflecting a laser beam from the surface.

[3] V. F. Turchin, Deposited Paper, At. Energy 22 (1967); F. Mezei, Communications on Physics 1, 81 (1976).

[4] C. F. Majkrzak and J. F. Ankner, SPIE Vol. 1738, 150 (1992); F. Samuel, B. Farnoux, B. Ballot, and B. Vidal, SPIE Vol. 1738, 54 (1992); O. Elsenhans, P. Böni, H. P. Friedli, H. Grimmer, P. Buffat, K. Leifer, and I. S. Anderson, SPIE Vol. 1738, 130 (1992).

[5] P. Böni, O. Elsenhans, H. P. Friedli, H. K. Grimmer, and I. S. Anderson, PSI Condensed Matter Research and Material Sciences, Progress Report 1993, Annex IIIA, 9 (1994).

[6] O. Elsenhans, P. Böni, H.P. Friedli, H. Grimmer, P. Buffat, K. Leifer, J. Söchtig, and I.S. Anderson, Thin Solid Films **246**, 110 (1994).

[7] Glasmanufaktur Baden AG, CH-5422 Oberehrendingen, Switzerland.

[8] Deutsche Spezialglas AG, Postfach 2032, D-31074 Grünenplan, Germany.

[9] CILAS, Compagnie Industrielle des Lasers, F-91460 Marcoussis, France.

[10] 3.7 Å is an upper limit because the large glass plate was very susceptible to the vibrations of the building. The measurements were performed on the tin bath side.

[11] D. Clemens, Thesis, Techn. University Berlin (1993), p. 95.

[12] One may argue that the roughness r_s of the glass substrate should be used for calculating the Debye-Waller factor at $m\theta_c^{\mathrm{Ni}}$. However, we believe, that it is more appropriate to use r_s of the coating: The upper layers become progressively more rough, thus scattering neutrons in non-specular directions. Therefore, some neutrons that are supposed to be reflected by the layers close to the substrate do not arrive there.

[13] On float glass ($d = 2$ mm), $m = 4$ coatings are stable between 2 days and several months and $m = 3.6$ coatings last for half a year or more; $m = 4$ coatings on boron containing glass started to peal off immediately after coating.

[14] J. B. Hayter and H. A. Mook, J. Appl. Cryst. **22**, 35 (1989).

ICANS-XIII
13th Meeting of the International Collaboration on
Advanced Neutron Sources
October 11-14, 1995
Paul Scherrer Institut, 5232 Villigen PSI, Switzerland

NEUTRON COMPOSITE GERMANIUM MONOCHROMATORS FOR DIFFRACTION INSTRUMENTS AT SINQ

J.Schefer, S.Fischer, M.Medarde, R.Thut, M.Koch, P.Fischer, U.Staub, A.Dönni, G.Böttger and M.Horisberger

Laboratory for Neutron Scattering ETHZ&PSI, Paul Scherrer Institute
CH-5232 Villigen PSI, Switzerland

ABSTRACT

Composite germanium monochromators are in the beginning of their application in neutron diffraction. In order to optimize their properties for high resolution neutron powder diffraction we significantly improved the alignment procedure of the individual wafers used for building the monochromator plates, as we added the tin necessary for soldering with a sputtering technique instead of tin foil spacers. Sputtering could also be replaced by evaporation giving similar results. A layout of the new vertical focusing monochromator is shown.

1. Introduction

Germanium is a widely used material for neutron monochromators, as it has both high scattering length density and moderate absorption when used in the thermal range. A particular advantage is the absence of second order contamination for certain reflections. However, it is also known that the introduction of a defect structure appropriate for an efficient neutron monochromator by plastic deformation has turned out in the past to be a severe problem, especially as an anisotropic mosaic is necessary in order to use this crystal for a focusing monochromator. This problem can be avoided by stacked composite wafers monochromators. Recent work at Brookhaven National Laboratory has demonstrated that a largely improved quality can be obtained when the crystals are assembled from plastically deformed thin wafers of 0.3 mm thickness [1]. First such ideas have been presented in [2]. Based on this achievement several groups are actively engaged in the production of Germanium monochromators along the procedure traced by BNL. We intend to use this monochromators at the new spallation source SINQ presently under completion at PSI Villigen.

Keywords: Diffraction, Monochromators, Germanium, Composite, Instrumentation
PACS: 61.12.Dw 62.20.Hg

As *hkk* (k≥0) reflections will be used on the new high-resolution powder diffractometer by simple turning the monochromator around the ω axis, we need a high precision re-assembling of the wafers after the bending and flattening processes necessary in order to introduce the anisotropic mosaic. Such a monochromator was in operation at the reactor SAPHIR [3], however, at this time there was a one block germanium monochromator with anisotropic mosaic available, where re-alignment is not necessary.

2. Materials, Methods and Production

Germanium wafers have been purchased from Eagle-Picher Industries with a thickness of 0.4 mm and a diameter of 76 mm. Before cutting the wafers from the single crystal block, two reference planes with different lengths perpendicular e.g. to [*0,1,-1*] and [*2,-5,-5*] for the Ge_{511} primary orientation have been cutted off from the entire boule in order to allow re-alignment and identification in a unique way. The surface was only etched, but not polished. Each wafer was marked with a diamond and cleaned with alcohol.

Figure 1:
Schematic drawing of the insert to the top-loading vacuum furnace used at PSI

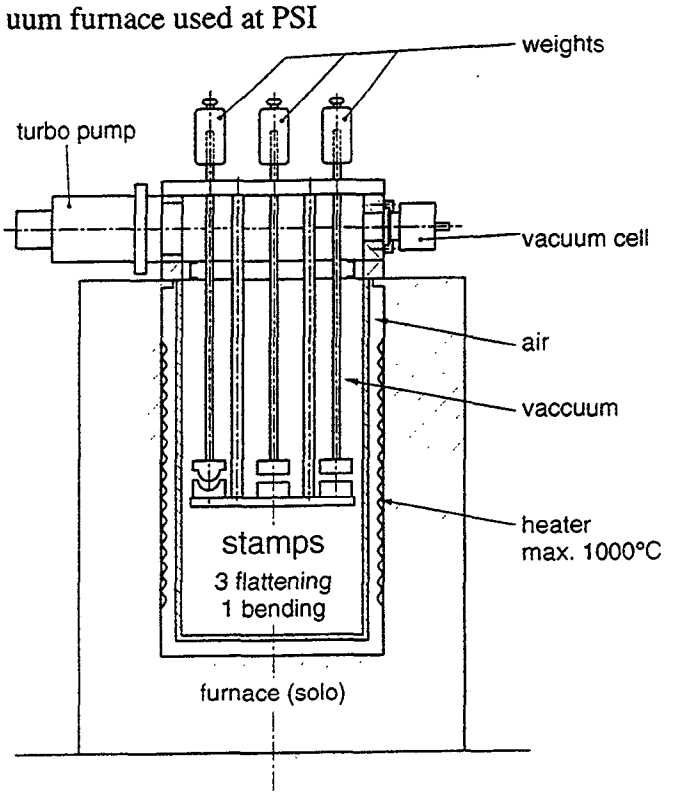

In the first bending and flattening process, we followed the method introduced by BNL [1]. We used stamps made of steel (Steel 304). The bending radius of the stamp and the corresponding matrix was 44.2 mm and 47.6 mm, respectively. The difference compensates for the 6 wafers and the 7 grafoils processed between. All stamps were protected with tantalum in order to avoid reactions between steel and germanium. A pressure of 3 N/cm^2 was loaded manually at 870 °C for 20 minutes on all stamps. We had simultaneously four stamps in the furnace: One for bending 6 wafers separated by 0.2 mm thick grafoils, and three stamps loaded with two wafers each separated by a grafoil. Ge_{511} wafers were bent twice (once to one side), Ge_{311} had to go another cycle. A Schematic cut through the furnace is shown in Fig. 1. This allows to proceed parallel with 12 wafers in one load, which is essential, as we can only operate one cycle per day due to the long cooling time (~20 hours) of our vacuum furnace.

Figure. 2:
Halfwidths of rocking curves (fwhm) of two Germanium 311 wafers (0.4 mm thick) at different ψ-orientations, showing an accepted (top) and a refused (bottom) wafer. The bottom wafer has to be re-flattened.

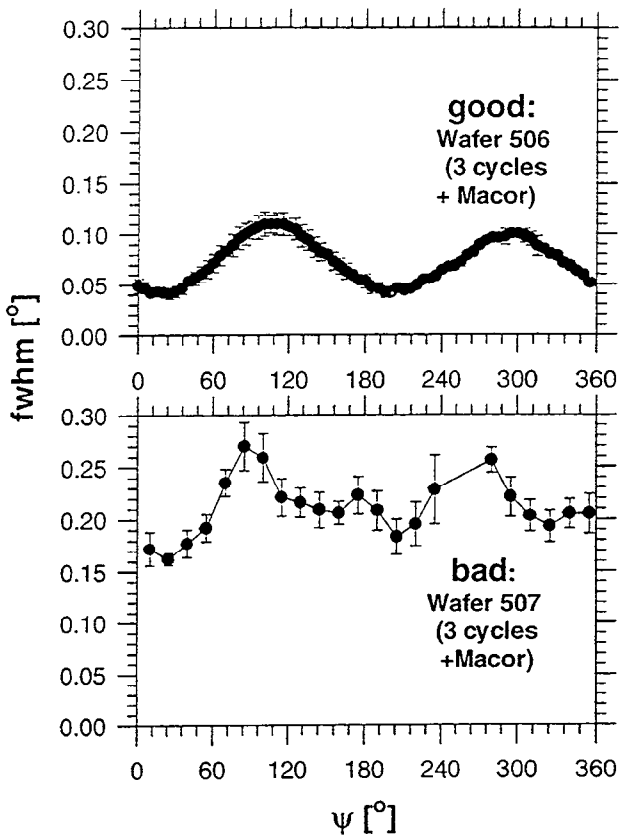

Flattening has proved to be the most difficult and essential step in the whole bending procedure. Using standard steel stamps protected by grafoil or tantalum has not given acceptable results for final use with neutrons. This step was only used during the bending process described above in order to re-flatten the wafers approximately. Unevenness could be observed by extended mosaics in neutron test measurements as shown in Figure 2 (bottom). We therefore have chosen a 8 mm thick ceramic (MICAR™), which was flattened to reach a parallelity of 20 μm. Such plates should be regularly tested for flatness and eventually remachined. The germanium was in direct contact with the ceramic up to 870 °C. The flattening step with the ceramic has been done twice, allowing an acceptance of the wafers close to 100%. About 5% got lost due to breakage during all the processes involved. A majority of the wafers was tested with rock scans at different ψ angles using neutrons (Saclay and T13C at ILL).

3. Sputtering Step

In order to reach a uniform coating of the flattened wafers, magnetron sputtering technique (Leybold) was chosen using a in-house built tin target. The goal of this step was to fix a uniform layer of tin directly to the wafers, allowing a precise alignment of the individual wafers against each other, as the package is not disturbed by the soft tin foils. Additionally the amount of tin can be reduced. We have chosen a thickness of 2.6 μm on both sides instead the 25 μm thick tin foils chosen by others [1]. There is still additional tin pressed out of the composite stack during the soldering process. The thickness of the tin layer was measured on a reference glass substrate. The coated wafers were afterwards aligned in a stamp made of graphite and pressed with their long reference cut of 25 mm length to the graphite block machined to 0.02 mm precision, using a excentric mounted bolt. Afterwards, the whole package was heated in our vacuum furnace (10^{-5} bar), loaded with 6 N/cm^2 at 350°C, stabilized at 450°C for approximately 10 minutes and afterwards cooled within 3 hours with the weight on the composite wafer package down to room temperature. First test cuts with a diamond saw show, that we can reach a stable monochromator package this way, which can be machined with standard tools.

Our monochromators will be cutted into pieces of 55 mm width and 25 mm height for the high resolution powder diffractometer HRPT and 55 mm width and 12.5 mm height for the four circle diffractometer SC3. A focusing monochromator which allows individual alignment of each piece is presently under construction. Focusing will be done by one motor only, using a method described elsewhere [4].

4. Results

The typical rocking curves at the extremes and the anistropic mosaic distribution as a function ψ of a single wafer of 0.4mm thickness are shown in Figs. 3 and 4, respectively. A first assembly with tin sputtered wafers has been tested with neutrons. Results are shown in Figs. 5 and 6, showing the almost sinusoidal mosaic spread. In addition, we also could measure a Ge_{004} -reflection in an off-centric beam geometry and therefore reached the goal of changing the wavelength by turning around the ω-axis only. The measured reflectivity of 35% and 30% at the minimal and maximal mosaic of 3.9' and 7.6', respectively, close to the calculated ones of 49% and 34% for λ=1.3 Å, respectively [4,5]. The incoming flux was $3.44 \cdot 10^3$ n/cm^2/s. The permanent quality control is essential, as shown in Figure 2 by two examples.

Figure 3:
Neutron rocking curves of a single wafer (Ge $_{511}$ orientation) at ψ=0° and ψ=90°, using a perfect Ge_{331} monochromator with λ=1.49 Å at Saclay.

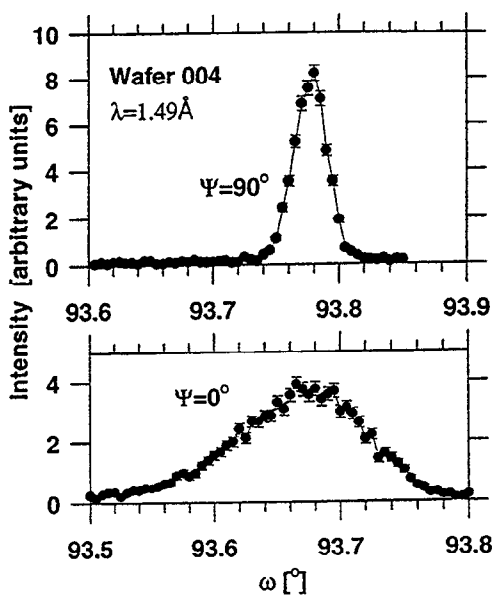

Figure 4:
Halfwidths of rocking curves (fwhm) of a single wafer (0.4 mm thick) at different ψ-orientations.

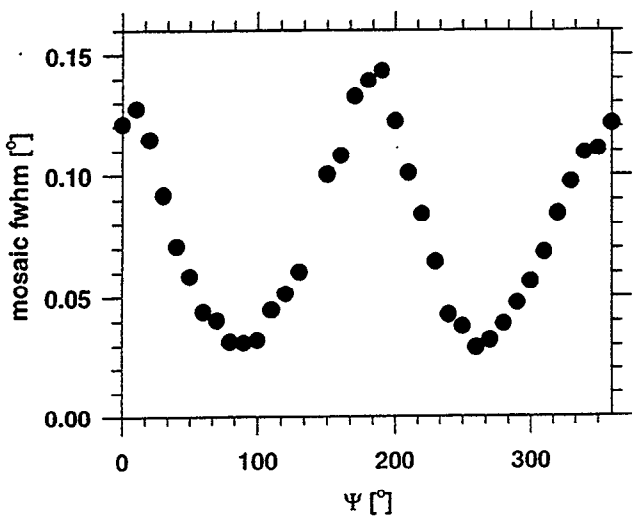

Figure 5:
Neutron rocking curves of a composite Germanium monochromator of 24 wafers (9.6 mm thick, Ge $_{511}$ orientation) at ψ=30° and ψ=120°, using a perfect Ge_{331} monochromator with λ=1.3 Å at T13C/ILL.

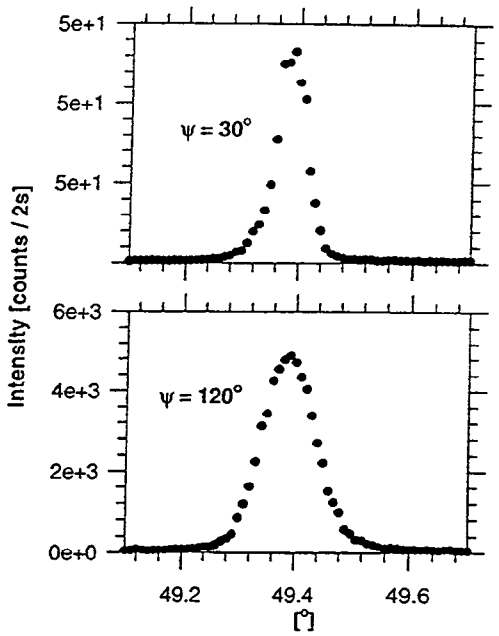

Figure 6:
Halfwidths of rocking curves (fwhm) of a composite Germanium monochromator of 24 wafers (9.6 mm thick) at different ψ-orientations.

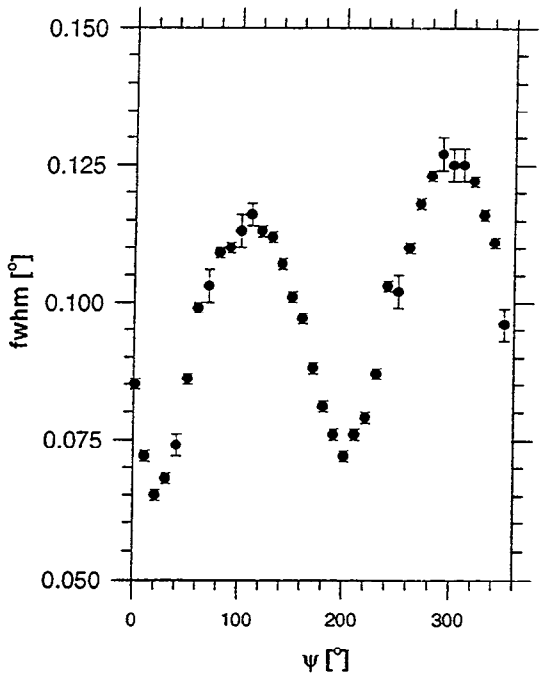

5. Mechanical Layout

The new high resolution powder diffractometer HRPT and single crystal diffractometer SC3 at SINQ will be equipped with a vertical focusing composite germanium monochromator of 280 mm height (Figure 7). Together with a lift system available, this allows a very flexible setting of the wavelengths without changing the instrument position. However, if additional wavelengths are asked for, the instrument may be manually moved from the 120° to the 90° take-off position. The single crystal diffractometer will mostly use the 311 reflection. The lift system allows the use of a high intensity/low resolution C002-monochromator for setting up the orientation matrix or for special applications with a high wavelength of λ= 2.34Å.

6. Summary

The method introduced by BNL [1] yields good Germanium composite wafer monochromators. Improvements by sputtering the tin to the wafers instead of using tin foils increases the accuracy of re-assembling the 'original' crystal. No additional mosaic increase due to misalignment is observed. A small decrease may be due to the better flatness of the composite monochromator compared to the single wafer, which is relatively thin and may be bent marginally due to the mounting pressure from the sample holder necessary for the neutron tests. We expect comparable results if using tin evaporation instead of sputtering. The sputtering technique was used by us due to the availability of such a machine at PSI. A 3 µm thick tin

layer is recommended instead of 2.6 μm in order to increase the amount of the tin, as the wafers are soldered on a large numbers of spots but not on the full surface as shown by the cuts with a diamond saw. Additionally, the primary reference planes should be elongated from 25 mm to 30-35 mm in order to lower errors in the alignment further. For the monochromator of the high resolution powder diffractometer, we will add one or two additional cycles to the present two in order increase the mosaic shown in Figs. 5 and 6 to approximately 12' or 16' respectively. Monochromators built in such a way will be especially interesting for instruments using a high take-off angle, as neighboring reflections are accessible by a limited angular motion in ω, therefore still covering the whole beam. Further improvement of the technique may be reached by using an improved bending technique as described by [8].

Figure 7:
Mechanical Layout of the new vertical focusing HRPT monochromator.

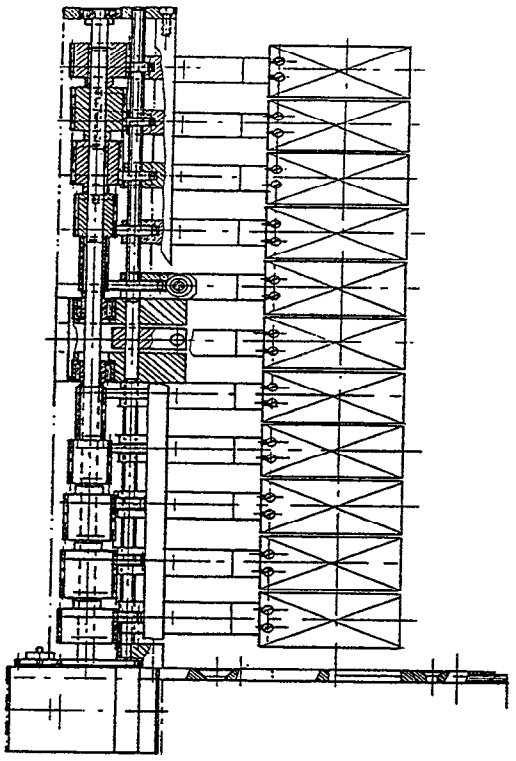

Acknowledgment

We would like to thank Dr. T. Vogt from Brookhaven National Laboratory for the generous support with technical information. We are indebted to Dr. A. Magerl from ILL and Dr. W. Paulus from LLB for beam time on their neutron test spectrometers, essential for the permanent quality control of our production. We thank Drs. P. Böni and W. Bührer for stimulating discussions, and last but not least the technique department from PSI for support in their workshops and using their vacuum furnace and J. Allibon at ILL for all the help with the 'specialties' of T13C.

References

[1] J.D. Axe, S.Cheung, D.E. Cos, L.Passell and T. Vogt, J. Neutr. Res. **2** (1994) 85
[2] H. Maier-Leibnitz, Annales Academic Scientarium Fennicae **A 267** (1967)
[3] J.Schefer et al, Nucl. Instr. Methods **A 288** (1990) 477
[4] W. Bührer, NIM **A 338** (1994) 44
[5] P.Fischer, AF-SSP-**10** (1967), Labor für Neutronenstreuung ETHZ&PSI, CH-5232 Villigen PSI
[6] W.H. Zachariasen, Theory of X-Ray Diffraction, Dover Publications (1944)
[7] H. Stehr, Z. Kristallographie **118** (1963) 263
[8] C.May, P. Klimanek and A.Magerl, Nucl. Instr. Methods **A 357** (1995) 511

ICANS-XIII
13th Meeting of the International Collaboration on
Advanced Neutron Sources
October 11-14, 1995
Paul Scherrer Institut, 5232 Villigen PSI, Switzerland

JULIOS DETECTORS COMBINED TO A PC-BASED DATA ACQUISITION SYSTEM

E. Jansen, W. Schäfer and G. Will

Mineralogisches Institut, Universität Bonn, D-53115 Bonn, Germany

R. Engels, R. Reinartz and K.D. Müller

Zentrallabor für Elektronik, Forschungszentrum (KFA), D-52425 Jülich, Germany

ABSTRACT

The linear JULIOS scintillation detector system, which is constructed for simultaneous position and time encoding of registered events, is extended and combined to a flexible and high capacity PC-based data acquisition system. A new timing interface module in the JULIOS electronics and a new memory module in the EISA-PC are based on user programmable logic cell arrays in the form of Xilinx XC4010 chips. The available address space can be flexibly allocated to a maximum of 12 bit position and 16 bit time channels. The standalone detector and data acquisition system is aimed at pulsed source instruments performing high resolution angle-dispersive time-of-flight experiments. Specific operational aspects of the system, which is installed at the redesigned ROTAX instrument at ISIS, are discussed.

1. Introduction

Linear and area solid state scintillations detectors are of special interest at pulsed spallation source instruments due to their comparatively wide spectral efficiency also at short wavelengths and due to their potential in high resolution time-of-flight applications. The physical characteristics and goodness of a pulsed white beam spallation source instrument is decisively determined by the potential of the detector system in collecting as many of the scattered neutrons as possible and in resolving the events sufficiently with respect to time-of-flight and scattering angle. For instance, angle-dispersive time-of-flight diffraction using pulsed white neutrons, is experienced as a highly efficient technology to exploit the thermal neutron spectrum and to gain simultaneous structural information in reciprocal space, which is obtained only in succession with monochromatic neutrons at steady state sources [1].

Keywords: linear detectors, TOF-diffraction, data acquisition, PC-system

A large neutron detector system performing high resolution time and position analysis, however, produces a huge amount of data to be stored in a huge memory during the measurement to be observed, handled and analysed possibly in the course of the experiment. For flexibility reasons and with respect to individual demands of data processing, we considered it desirable to have a standalone data acquisition system, which is permanently available and which operates independently from central data acquisition systems.

The combination of detector control and data acquisition into a standalone PC-based entity has been realized with the JULIOS scintillation detector system [2].

2. Linear JULIOS detectors

The linear JULIOS scintillation detectors are built in a modified Anger-technology using a 1 mm ^{6}Li-glass scintillator and a linear row of 24 photomultipliers (PM) for light spot position encoding [3]. Fast digital signal processing in a dedicated hardwired computer [4] results in a time resolution of subsequent events of better than 1 μs. Three types of linear JULIOS detectors are manufactured differing by spatial resolution and the dimensions of the effective detector windows; details are summarized in Table 1.

Table 1: Dimensions and physical properties of the linear JULIOS detectors: type H (high resolution), type S (standard) and type L (large window)

Type	JULIOS-H	JULIOS-S	JULIOS-L
Form	plane	plane	plane
Outer dimensions (mm)	320x390x115	900x450x125	1100x475x180
Sensitive window (mm)	200x20	680x25	940x75
Form of PM-photocathodes	rectangular	circular	rectangular
Size of PM-photocath. (mm)	6.8x24	28.6 Ø	40x80
Spatial resolution (mm)	1.2	2.3	3.3
Time resolution (s)	$< 10^{-6}$	$< 10^{-6}$	$< 10^{-6}$
Neutron efficiency, 1 Å (%)	65	65	65
Neutron efficiency, 2 Å (%)	85	85	85
Gamma sensitivity ($E_\gamma > 1$ MeV)	$< 10^{-4}$	$< 10^{-4}$	$< 10^{-4}$
Count rate capability (KHz)	100	100	100

The different JULIOS types are equipped with identical detector electronics made up of an analog and digital signal processing section, which is described in detail elsewhere, see e.g. [1]. Position computation is performed within 70 ns. The electronics provides for a 12 bit position resolution, at the most, exceeding the real linear physical resolution of the detectors by about one order of magnitude. The hardware of the JULIOS detectors and read out electronics comprising also modules for automatic gain stabilisation of the PMs and for correcting positional nonlinearities and inhomogenities of the scintillator material is shown in Fig. 1. The read out electronics is designed for on-line connection to a personal computer to control and process all detector activities and to store the data.

Alternatively to the PC data storage, the detector can be connected to an external timing and data acquisition system. For this purpose, the electronics interface provides a 12 bit position address with the necessary event flag to synchronize the detector events with an external timing reference.

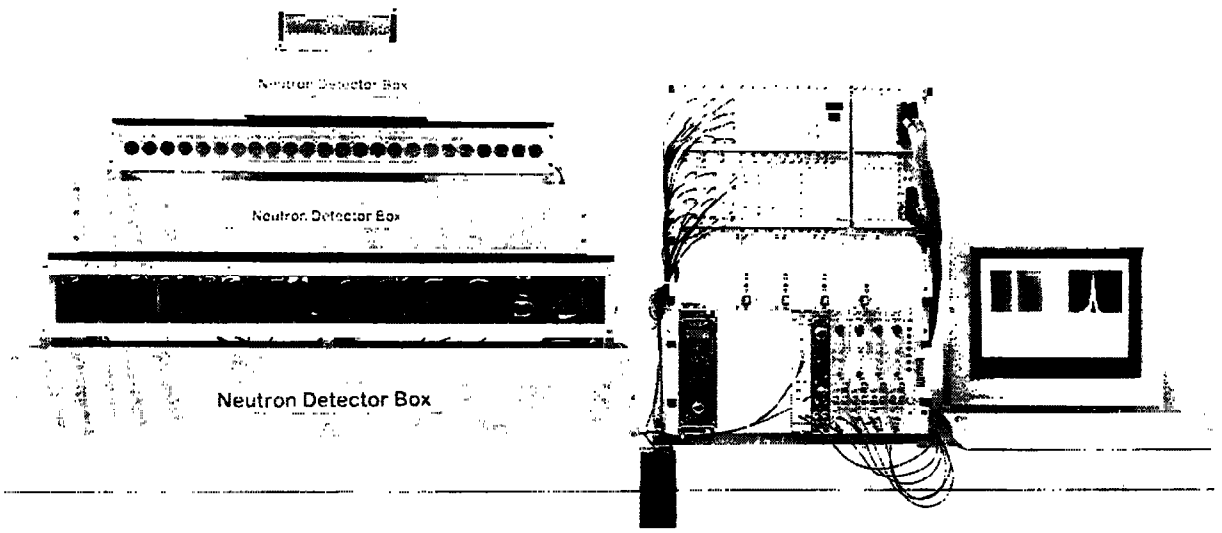

Fig. 1: Assembly of the JULIOS detector system: detector heads (on the left) 'type H' (top), 'type S' (middle), 'type L' (bottom); the units are taken out of the light-tight boxes (below in each case); associated detector electronics (on the right) connected to a PC

3. JULIOS timing interface

The interface module managing the signal transfer from the detector to the PC (Fig. 2) has been designed for high resolution time-of-flight applications. It is constructed as an integral part of the detector electronics which allows for setting a variable time window during which events are collected.

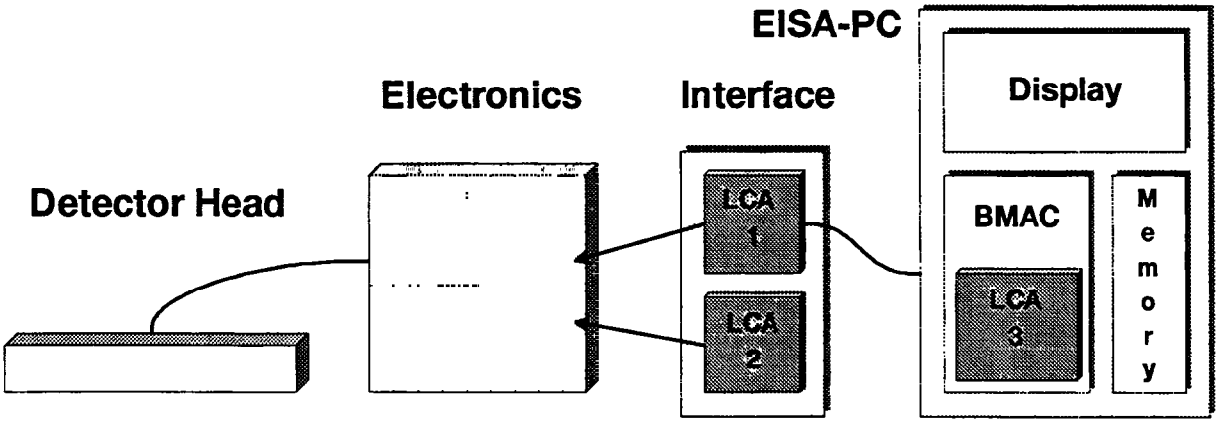

Fig. 2: Hardware structure of the JULIOS detector and data acquisition system (see text)

The core of the timing module are two user programmable logic cell arrays (LCA) in form of Xilinx XC4010 chips (see Fig. 2). The LCA-design offers high flexibility to realize variable configurations and several modes of operation. LCA-1 is used for initialization, configuration and control of the JULIOS detector; LCA-2 takes

care of the actual timing functions. With respect to detector configuration and signal control, there are options to vary the number of position and time bits and to set levels of all signals separately according to actual experimental requirements. These timer options and specifications have been realized by registers containing:

1. the number of position bits to be included in the time/position address,
2. the polarities of the I/O-signals,
3. the time delay between the external reference (e.g. master pulse) and the active time window in μs,
4. the number of time slices within the time window,
5. the length of the individual time slices in μs.

The control of the JULIOS activities is performed by the PC through a dedicated I/O-card but is also possible by a RS232 serial interface, instead.

4. PC data acquisition

Position encoded and time stamped JULIOS events are transferred via a 28 bit connection to the PC with EISA-bus architecture. The data acquisition is realized by the so-called BMAC PC-module, which acts as Bus Master ADC Controller [5]. The BMAC module, again, is based on a LCA-array Xilinx-chip (see Fig. 2) allowing flexible and programmable configurations with respect to variable time-of-flight applications (compare [6]).

The data received by the BMAC-card serve as pointers to locations in a reserved memory area of the PC, the contents of which is to be incremented, much like a multi channel analyzer. This action takes about 480 ns per event and is about one order of magnitude faster than the preceding ADC-conversion of the events in the JULIOS electronics (compare Table 1).

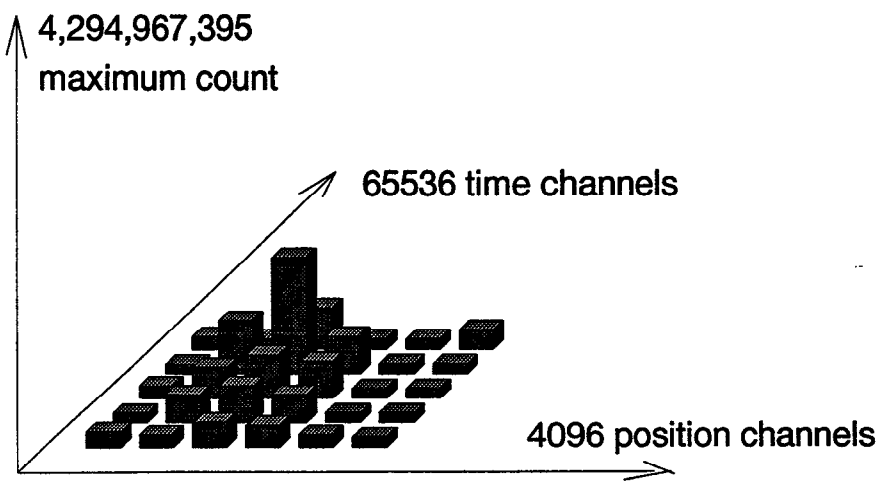

Fig. 3: Two-dimensional data array of the PC-memory for JULIOS time-of-flight data acquisition

For the total exploitation of the maximum position and time resolution, which can be provided by the detector electronics, an address space of 2^{28} locations of 4

Byte depth each would be required, which amounts to 1 GByte memory (Fig. 3). In practice, however, the address space can be reduced to about 2^{22} (= 4 M) taking into account the physical resolution of the detector. 16 MByte PC-memory are necessary to store double word data within the 4 M memory locations.

5. Software structure

The JULIOS detector and its PC-based processing electronics and data acquisition system is operated under the multitasking or quasimultitasking PC-shell of MS-WINDOWS (Fig. 4). Different functions can be performed simultaneously by opening several DOS-windows in the PC-shell. So it is possible to display spectra on-line on the PC-monitor and to evaluate them while collecting data.

The initialization of the detector is performed under DOS using the remote control program JULIOS-RM written in Turbo Pascal; specific parts like interrupt services are writen as assembler routines [7]. Different detector facilities and electronic configurations can be activated by special commands: e.g. performing PM calibration measurements, generation and loading of lookup-tables for fast position computation [4], control and stabilization of PM-gains [2], start and stop of the experimental data collection. The configuration of the BMAC-module, as well as the reservation of the PC-memory is performed under DOS.

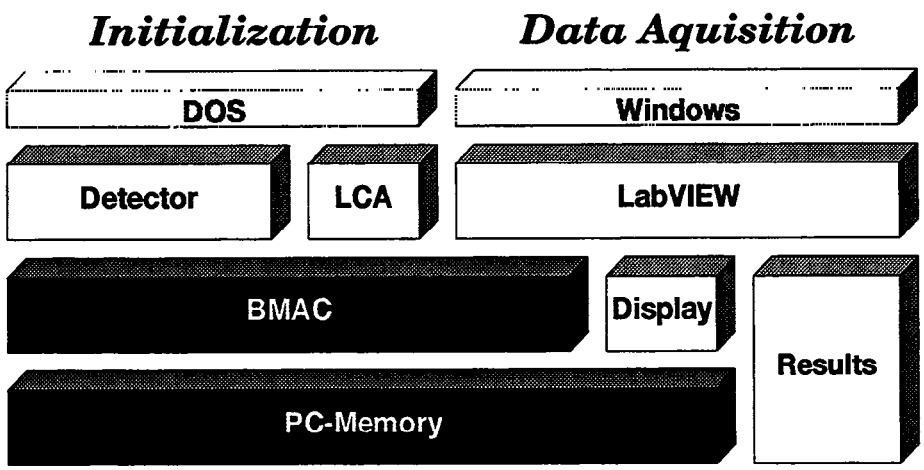

Fig. 4 Software structure of the combined JULIOS detector and data acquisition system

The data collected in the PC-memory are handled within another PC-window using the graphic facilities and service functions of the program package LabVIEW. Software has been developed, so far, to display the total data content of a 64 Mbyte memory on the PC-monitor. Special modes can be selected to display linear, two-dimensional or pseudo-three-dimensional spectra.

6. Discussion

The PC-based JULIOS detector and data acqusition system is in operation at the ROTAX-instrument at ISIS, which has been redesigned as angle-dispersive time-of-flight powder and texture diffractometer [8] The recent installation of the new JULIOS timing interface and the high capacity data acquisition system replaces the

previous ISA-PC system limited by the 16 bit address space of the ISA-slots; this has been experienced to be insufficient [9]. Test measurements with the new system are in progress to establish the most favourable ratio of electronic position and time channels for the instrumental setup at ROTAX. This configuration has to guarantee, on the one hand, the best $\Delta d/d$-resolution of the instrument, but it should not lead, on the other hand, to an unreasonable waste of data and PC-memory. Probably, the balance will be obtained with 512 channels (9 bit) for position and 4096 channels (12 bit) for time, requiring a total of 8 Mbyte PC-memory. 9 bit position resolution is roughly equivalent to a data point density of $\Delta 2\Theta = 0.1°$. 12 bit time resolution, which is equivalent to a wavelength resolution of 10^{-3} Å corresponds to time-slices of 4 μs with respect to the ROTAX-specific time-window from 0.5 to 16.5 ms out of the 20 ms ISIS pulse.

The PC-based data acquisition system can be characterized by its capability of easy configurational changes, its flexibility with respect to different applications, and its independence from local mainframe installations. Independent of these technological aspects, the whole data acquisition system is rather inexpensive. It seemed natural to combine the JULIOS detector with such a PC-based system, as the whole detector system is PC-processed, anyway.

Acknowledgement This work has been funded by the German Federal Government (BMBF) under contract-nos. 03-WI4BO2 and 03-WI4BO3.

7. References

[1] W. Schäfer, E. Jansen and G. Will, J. Appl. Cryst. **26** (1993) 660

[2] W. Schäfer, E. Jansen, A. Szpesvary, R. Skowronek, G. Will, R. Reinartz and K.D. Müller, Proc. ICANS-XII (ed. U. Steigenberger, T. Broome, G. Rees, A. Soper), RAL-Report 94-025 Vol. I, 1994, pp. I200

[3] J. Schelten, R. Kurz, I. Naday and W. Schäfer, Nucl. Instrum. Meth. **205** (1983) 319

[4] R. Kurz, K.D. Müller, J. Schelten, A. Szepesvary, W. Schäfer and G. Will, IEEE Trans. Nucl. Science **35** (1988) 78

[5] P. Reinhart, M.A. Ashour, K.D. Müller, S. Rongen, W. Tenten, Th. Oyevaar and H.F. Tammen, IEEE Trans. Nucl. Science **41** (1994) 89

[6] K.D. Müller, B. Alefeld, J. Lerch, R. Reinartz, P. Reinhart, F. Rongen, J. Schelten and W. Tenten, IEEE Trans. Nucl. Science (1995) in print

[7] A. Szepesvary, Internal Report, Zentrallabor für Elektronik, Forschungszentrum Jülich (KFA), 1989

[8] W. Schäfer, E. Jansen, R. Skowronek, G. Will, W. Kockelmann, W. Schmidt and H. Tietze-Jaensch, Nucl. Instrum. Meth. in Phys. Res. **A 364** (1995) 179.

[9] W. Schäfer, E. Jansen, R. Skowronek, G. Will, K.S. Knight and J.L. Finney, Nucl. Instrum. Meth. in Phys. Res. **A 317** (1992) 202

Proposal for a 30-T Pulsed Magnet Suitable for Neutron Scattering Experiments

R. A. Robinson[(a)], Y. M. Eyssa[(b)], H. J. Schneider-Muntau[(b)] and H. J. Boenig[(a)]
(a) *Los Alamos National Laboratory, Los Alamos, NM 87545, USA*
(b) *National High Magnetic Field Laboratory, Florida State University, Tallahassee, FL 32306, USA*

We describe a conceptual design for a 30-T vertical-field split-pair magnet suitable for neutron scattering studies. While the magnet is primarily intended for diffraction and spectroscopic studies using a pulsed neutron source, it might also have application for relaxational studies at steady-state sources. The magnet will have a 5-cm bore for sample environment equipment, a 1-cm gap for the neutrons to illuminate the sample and through which to observe the scattering. It will run with a repetition frequency of 2 Hz, and a pulse length of 3 ms. We discuss scientific and engineering considerations that led to this specification and describe the designs of both magnet and power supply.

1. Scientific Background

In this paper, we describe a conceptual design for a 30-T pulsed magnet that could be used in conjunction with neutron-scattering apparatus, along with the scientific opportunities that such a magnet might open up. *Neutron diffraction* has long been the technique of choice for determining the arrangements (magnetic structures) of magnetic moments in solids, the spatial extent of the magnetic electrons around their parent ions (form factors) and the full moment-density distribution function in real space. The proposed 30-T magnet would enable one to study such spatial aspects of many field-induced phase transitions for the first time, whether they are driven by competing exchange interactions, single-ion anisotropy, or a more radical change, say from an itinerant to a localised state. *Inelastic Neutron Scattering*, on the other hand, is the best general-purpose tool for the study of magnetic excitations like spin waves, crystal-field levels and spin fluctuations. These excitations manifest themselves in the imaginary part of the generalised magnetic susceptibility $\chi''(\mathbf{Q},\omega)$, which is measured directly in a neutron scattering experiment. A field of 30T acting on a moment of $1\mu_B$ corresponds to an energy of 1.7 meV, and we should be able to generate splittings or close gaps of this order. The present generation of spectrometers at spallation neutron sources have both sufficient resolution (as good as 10 μeV) and sufficient dynamic range (up to 2 eV) to cover the effects that might be induced by such a field.

To first order, one would imagine that almost all zero-field neutron scattering experiments on magnetic systems should be repeated in applied magnetic fields. Likewise, any measurement of bulk phenomena which show interesting properties in fields up to 30 T is likely to benefit from a complementary neutron study in the same field range. Some specific examples of fields of interest for such a combined high-field/neutron scattering capability are:

(a) Field-induced transitions in heavy-fermion materials. Metamagnetic transitions, in which small-moment antiferromagnetism is transformed into a state with moments of the order of $1\mu_B$, have been observed in a number of heavy-fermion

metals: at 8T for $CeRu_2Si_2$, 24T for UPt_3 and 38T in URu_2Si_2. In URu_2Si_2, 2 intermediate structures[1] both with magnetic unit cells larger than the chemical unit cell have been proposed to explain the magnetisation data. Neutron diffraction experiments would be able to test this hypothesis. In UPt_3, there is a single broadened transition above which "localised" moments appear and one might expect destruction of the heavy-fermion state. However, de Haas-van Alphen measurements[2] indicate that the masses remain very large even above 24T. It would be of interest both to study the magnetic order in the high-field state and to use inelastic neutron scattering to study the spin-fluctuation spectrum. Perhaps the best idea of what might be achieved comes from the study of Rossat-Mignod et al.[3] on $CeRu_2Si_2$, which has a transition in a field range that is accessible with a d.c. superconducting magnet. The observed magnetic scattering was separated into an "on-site" contribution and "inter-site" correlations. The latter were suppressed above the 8T transition.

(b) Non-Fermi Liquid scaling. One exciting topic at present is that in which paramagnetic correlated-electron systems exhibit power-law or logarithmic dependences in thermodynamic and transport properties. Such non-Fermi liquid behaviour is observed both in f-electron systems and in layered cuprates. One can think of this is as the quantum critical behaviour close to a zero-temperature phase transition. Some zero-field neutron experiments[4] have already been done, but the free energy is expected[5] to have a particular dependence on H and T. It would be of great interest to map out the excitation spectrum as a function of field, in the same way as has been done for temperature.

(c) Anisotropy in f-electron systems: Both rare-earth and actinide based intermetallic compounds exhibit huge magnetic anisotropies. In the case of rare-earth compounds containing Fe or Co, this anisotropy is exploited to make practical permanent magnet materials. Crystal-field effects are thought to drive the anisotropy. In contrast, the f-electrons in uranium compounds are hybridised strongly with ligand d- and p-electrons, and the magnetic anisotropy results from anisotropic exchange induced by the hybridisation. For antiferromagnets of either case, multiple field-induced transitions have been observed, at fields beyond 20T. Neutron diffraction experiments are needed to understand the structural changes at these transitions, while inelastic scattering experiments in field are likely to reveal the exact role of crystal-fields (via their Zeeman splittings), spin waves (which should exhibit anisotropy gaps) and spin fluctuations.

(d) Gap spectroscopy. Gaps in magnetic excitation spectra can occur for many physical reasons: due to magnetic anisotropy, due to fundamental topological considerations in quantum 1-D Heisenberg materials[6], due to transitions from insulating to metallic behaviour[7], and so on. In most cases, it is thought that an applied magnetic field will close such gaps. Very little work has been done along these lines so far.

2. Experience Elsewhere

To date, experience using high fields and pulsed neutron sources[8] has been concentrated at the Japanese pulsed spallation neutron source KENS[9], and the Russian pulsed reactor at Dubna[10]. In the western literature, considerably more information is available on the two Japanese magnets, which are capacitatively driven water-cooled copper Bitter magnets. One magnet is an 18-T single solenoid suitable for scattering experiments with $2\theta < 10^0$. The other is a 16-T split-pair magnet suitable for scattering at $2\theta = 30^0$. Its characteristics are listed in Table I. In both cases, the magnet repetition frequency is 0.5 Hz, with a semi-sinusoidal pulse length of 1ms. This results in a strong Fourier component at a frequency of 1kHz, and at this frequency the skin depth of pure copper is ~3 mm.

3. Our Conceptual Design for a Multi-Pancake Coil

In trying to go beyond the Japanese experience, we chose the maximum magnetic field of 30T, and it soon became clear that we need a geometry that allows the current density to spread over a radius greater than the skin depth. We came up with a winding design that uses a small conductor to minimise the eddy-current heating to an acceptable value. Figure 1 shows a simple pancake design whose physical parameters are listed in Table I. It is a radially water-cooled split-pair magnet, whose primary use would be with the field vertical (perpendicular to the neutron scattering plane) as shown in Fig. 2(a). It could also be laid on its side to do experiments with the field in the horizontal scattering plane, but parallel to the incident neutron wave-vector $\mathbf{k}_i$ as shown in Fig. 2(b) or with the field in the horizontal scattering plane but perpendicular to $\mathbf{k}_i$ as shown in Fig. 2(c). The coils would be wound from a single 4 x 15 mm^2 or double 2 x 15 mm^2 rectangular Glidcop conductor. The conductor is cooled at its edges with room-temperature water flowing between the individual pancakes. The winding is supported by a 10-cm wide stainless-steel laminate. The magnet would be constructed as two solenoids, with an interchangeable spacer in between. Some structural support would be needed in the gap, but we believe this could be reduced so that 80% of the available angular range could still be used (as shown in Figure 1(a)). In order to increase the neutron count rate, we would flare the support structure out as shown in Figure 1(b).

Capactitatively driven pulsed magnets are essentially resonant LC circuits, and develop a field that is semi-sinusoidal in shape, as shown in Figure 3 (b), with pulse length $\Delta T_{magnet} = \pi\sqrt{LC}$. Typical neutron pulse lengths at spallation sources are $\Delta T_{neutron}$ = 20 - 100 μs, depending on the moderator and the wavelength of interest. The field should be fairly steady over this time-scale, and therefore ΔT_{magnet} should at least an order of magnitude longer than $\Delta t_{neutron}$. For our magnet design, we find the minimum heat dissipation for a pulse-length close to 3ms, which meets this criterion.

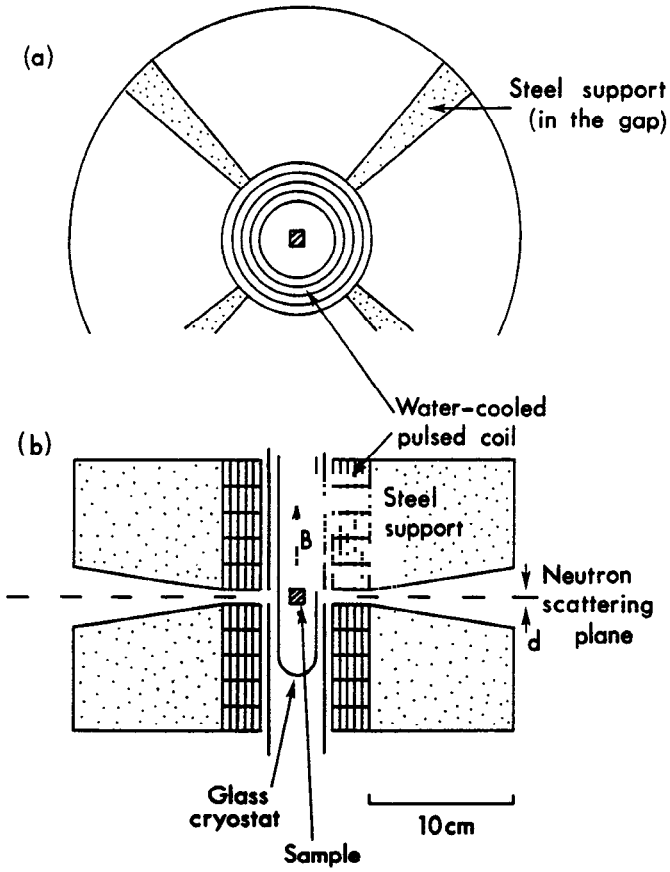

Figure 1. Schematic diagram of the proposed 30T split-pair pulsed magnet for neutron diffraction: (a) plan of an individual "pancake", (b) a vertical section through the whole magnet.

Table I Comparison of characteristics of proposed magnet with those elsewhere

	NHMFL/LANSCE (this work)	Kobe/KENS (Ref. 9)	Dubna (Ref. 10,11)
Maximum field (T)	30	16	15
Field Pulse length, ΔT_{magnet} (ms)	3	1	0.5 - 2
Neutron Pulse length, $\Delta T_{neutron}$ (ms)	0.025-0.1	0.025-0.1	0.215
Magnet Repetition frequency (Hz)	2	0.5	2.5
Neutron repetition frequency (Hz)	20	20	5 or 25
Gap in split pair (cm)	1(to 5)	1	1
Angular coverage within gap	4 x 80°	~2° at $2\theta = 30^o$	
Bore (cm)	5	4	
Capacitance (mF)	17.7	1.2	
Voltage (kV)	6.2	10	
Current (kA)	98	20	
Capacitor energy (kJ)	314	50	
Average heat dissipation (kW)	202		

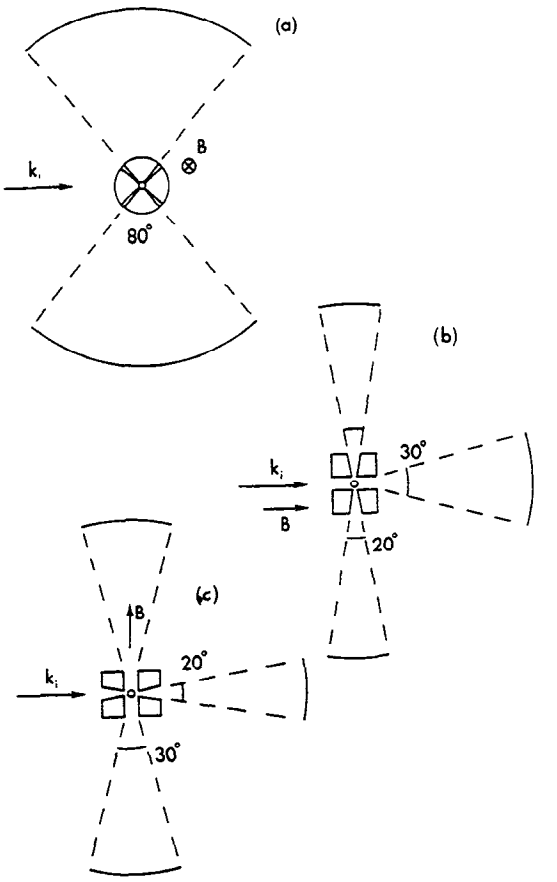

Figure 2. Possible configurations and ranges of angular coverage for the split-pair magnet (a) in the "standard geometry" with **B** perpendicular to the neutron scattering plane, (b) with **B** in the scattering plane and parallel to $\mathbf{k_i}$, and (c) with **B** in the scattering plane but perpendicular to $\mathbf{k_i}$..

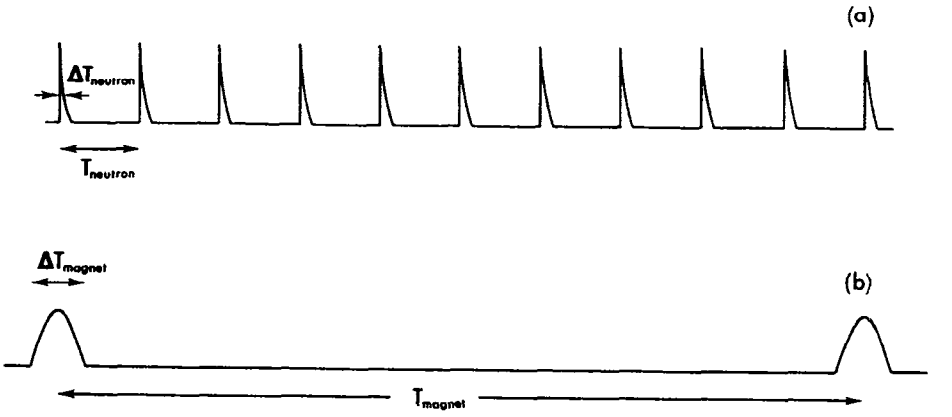

Figure 3. Schematic figure showing the pulse-lengths ΔT and periods T of (a) the pulsed spallation neutron source and (b) the pulsed magnet. In our proposal, $\Delta T_{neutron}$ = 25 - 100 μs, ΔT_{magnet} = 3 ms, $T_{neutron}$ = 50 ms, and T_{magnet} = 0.5 s.

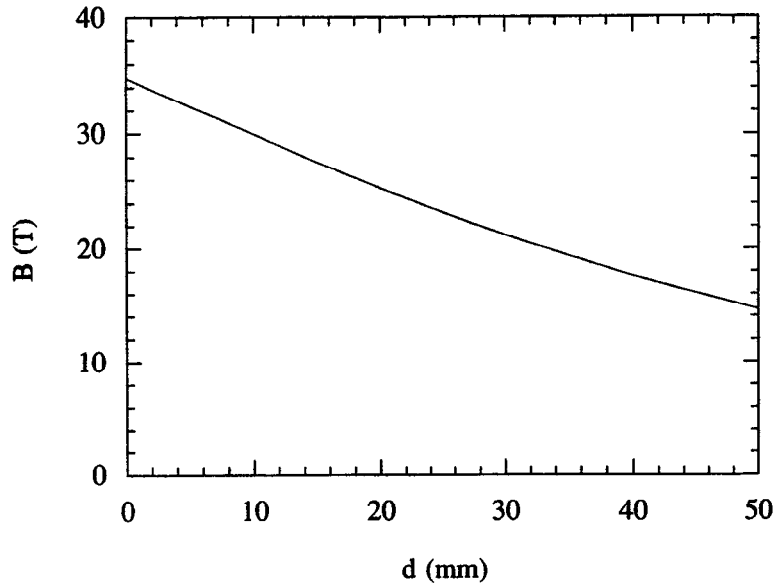

Figure 4. The variation of magnetic field at the sample as a function of gap spacing d.

The next consideration is the repetition frequency of the magnet. Pulsed spallation neutron sources operate at repetition frequencies of 20Hz (LANSCE and KENS) or more (IPNS and ISIS). Neutron scattering experiments are invariably limited by the available neutron flux, so it would be best to use every pulse from the source. However, "normal" pulsed magnets rely on their thermal capacity for cooling: they are bathed in a cryogenic fluid which is boiled off as a result of the field pulse. Cooling such a magnet down again can take several hours. For our application, the magnet must be cooled continuously (by water or liquid nitrogen), in much the same way as d.c. high-field magnets. The saving grace is that the pulse length can be reduced and, to first order, the required power (and cooling) can be reduced by the ratio of the pulse length to the period between pulses. While the KENS/Kobe system operates at 0.5 Hz, we chose a frequency of 2 Hz. In other words, we will use only one neutron pulse out of ten at LANSCE.

The main unresolved technical question with our proposal regards the fatigue lifetime of the components (conductors and insulation) in the magnet. Even in a single day, it will receive more pulses (172,800 @ 2Hz in 24 hours) than most pulsed high-field facilities experience in their whole lifetime. We are about to undertake a mechanical materials-testing program in Tallahassee to examine these issues.

4. Increasing the Gap for Inelastic Studies

For neutron-diffraction experiments (without energy analysis), a sample volume of 1 cm^3 is normally sufficient. However for inelastic scattering experiments, larger sample volumes are required. For instance, on the new chopper spectrometer PHAROS[12] at LANSCE, a beam area of up to 5 x 7.5 cm^2 can be used. If the gap d is increased to exploit the larger sample height, the penalty in terms of magnetic field is shown in Fig. 4. We also chose the magnet bore of 5 cm in part for similar reasons, so that large samples could be accommodated, and in part so that the full range of cryogenic apparatus might be installed when necessary.

Acknowledgements

We are glad to acknowledge a number of very helpful discussions with M. Motokawa, M. Arai, J. Sims, J. A. Mydosh, H. Nakotte and J. D. Thompson, as well as encouragement from R. Pynn and L. Campbell. This work was supported in part by the division of Basic Energy Sciences of the U.S. Department of Energy. An abbreviated version of this paper has been published previously[13].

References

[1] K. Sugiyama, H. Fuke, K. Kindo, K. Shimohata, A. A. Menovsky, J. A. Mydosh and M. Date, *J. Phys. Soc. Japan* **59**, (1990) 3331; J. A. Mydosh in *Proceedings of Conference on Physical Phenomena at High Magnetic Fields*, Tallahassee, Florida, 1991, ed. E. Manousakis et al., (Addison-Wesley, Redwood City, CA, 1991)., p.184.

[2] S. R. Julian, P. A. A. Teunissen and S. A. J. Wiegers, *Phys. Rev. B* **46**, (1992) 9821; S. R. Julian, P. A. A. Teunissen and S. A. J. Wiegers, *Physica B* **177**, (1992) 135.

[3] J. Rossat-Mignod, L. P. Regnault, J. L. Jacoud, C. Vettier, P. Lejay, J. Flouquet, E. Walker, D. Jaccard and A. Amato, *J. Magn. Magn. Mater.* **76 & 77** (1988) 376.

[4] M. C. Aronson, R. Osborn, R. A. Robinson, J. W. Lynn, R. Chau, C. L. Seaman and M. B. Maple, submitted to *Phys. Rev. Letts.* (1994).

[5] A. M. Tsvelik and M. Reixer, *Phys. Rev. B* **48**, (1993) 9887.

[6] F. D. M. Haldane, *Phys. Lett. A* **93**, (1993) 464; *Phys. Rev. Lett.* **50**, (1983) 1153 .

[7] G. S. Boebinger, *Physica B* **201**, (1994) 20.

[8] We also note that fields up to 25T have been employed in conjunction with a pulsed TRIGA reactor in Vienna (see R. Grössinger, G. Badurek, C. Gigler and C. Schotzko, *Physica B* **155**, (1989) 392 .), but this is essentially a single-shot method, rather than the repetitive method described here.

[9] M. Motokawa, H. Nojiri, J. Ishihara and K. Ohnishi, *Physica B* **155**, (1989) 39; H. Nojiri, M. Uchi, S. Watamura, M. Motokawa, H. Kawai, Y. Endoh and T. Shigeoka, *J. Phys. Soc. Japan* **60**, (1991) 2380.

[10] User Guide, *Neutron Experimental Facilities at JINR*, ed. Y. V. Taran, 1992

[11] D. Georgiev and V. Nietz, private communication

[12] R. A. Robinson, M. Nutter, R. L. Ricketts, E. Larson, J. P. Sandoval, P. Lysaght and B. J. Olivier, in *Proceedings of ICANS-XII*, Abingdon, U.K., 24-28 May 1993, Rutherford Appleton Laboratory Report 94-025, Vol. I, p.44-51.

[13] R. A. Robinson, Y. M. Eyssa, H. J. Schneider-Muntau, H. J. Boenig, in *Proceedings of Conference on Physical Phenomena at High Magnetic Fields II*, Tallahassee, Florida, May 6-9 1995.

ICANS-XIII
13th Meeting of the International Collaboration on Advanced Neutron Sources
October 11-14, 1995
Paul Scherrer Institut, 5232 Villigen PSI, Switzerland

A USER-FRIENDLY, GRAPHICAL INTERFACE FOR THE MONTE CARLO NEUTRON OPTICS CODE MCLIB

Thierry Thelliez *, Luc Daemen†, Phil A. Seeger ‡ and Rex P. Hjelm †

* Applications Programming Group, Computing, Information and Communications Division, Los Alamos National Laboratory, Los Alamos, NM 87545 USA
† Neutron Scattering Center, Los Alamos Neutron Science Center, Los Alamos National Laboratory, Los Alamos, NM, 87575 USA
‡ 239 Loma del Escolar, Los Alamos, NM 87544 USA

ABSTRACT

We describe a prototype of a new user interface for the Monte Carlo neutron optics simulation program MCLIB. At this point in its development the interface allows the user to define an instrument as a set of predefined instrument elements. The user can specify the intrinsic parameters of each element, its position and orientation. The interface then writes output to the MCLIB package and starts the simulation. The present prototype is an early development stage of a comprehensive Monte Carlo simulations package that will serve as a tool for the design, optimization and assessment of performance of new neutron scattering instruments. It will be an important tool for understanding the efficacy of new source designs in meeting the needs of these instruments.

1. Motivation

The process of designing new, advanced neutron sources, or even upgrading present sources, must start with the identification of an instrument suite to address the scientific and technical issues likely to be important in the future. The job of designing the instrument suite and neutron source involves extensive collaboration between instrument designers and target-moderator-reflector-shield system designers. The collaboration must start at an early stage of the facility design if the facility is to be properly optimized and its potentials fully realized.

As with any optimization the instrument suite and source design is an iterative process at several interacting levels, and there are important compromises at each level that must be assessed. For example, each instrument must be optimized to its resolution, intensity and measurement domain requirements, and the source must be optimized and matched to these needs. At a higher level conflicts need to be resolved between instruments that share moderators and even between instruments that are on different moderators on the same target.

New instrument and source designs should advance the state of the art, beyond the limits where we have operational experience. Thus, in order carry through the task of facility design

Keywords: Instruments, Simulations, Monte Carlo, MCLIB, User Interface

a means must be provided to predict instrument performance at each stage of the process. This is all the more important, as once the facility is built cost, inaccessibility and shear size make modification to correct mistakes difficult, if not impossible.

Computational assessment of instrument performance requires the calculation of complex integrals, which are currently best handled using Monte Carlo integration. The implementation of this technique requires detailed modeling of the neutron optics of the instrument elements, of the scattering laws of the sample and of detectors. The production of code for any one instrument is quite a considerable undertaking. The development of modular code libraries to simulate the different instrument elements makes the task considerably easier, as the instrument designer can string elements together to produce the needed code. This is the approach used in the modular instrument element Monte Carlo library, MCLIB, described in another contribution in this volume [1]. MCLIB is based on the MCLIB Monte Carlo library developed at the Rutherford Laboratory [2]. This library has been used extensively at Los Alamos to design, optimize and simulate instrument performance of SANS [3-6], neutron reflectometers [7] and chopper spectrometers [8].

The use of this package still requires considerable hand coding to simulate an instrument. Clearly, if research on instrument performance is to be done quickly and effectively, tools must be provided to the instrument designer that will allow him or her to understand the performance of an instrument design, and optimize the design quickly and accurately. This is essential in the development of effective procedures to optimize the instrument with the source and deal with issues that occur in designing the instrument suite. Thus we need to go one level further to provide a simulations package that will remove altogether the need for the end user to do coding. This implies that a user interface be written that will allow a user to build an instrument from predefined instrument elements, and specify the size, shape and position of these elements using simple dialog boxes. The user interface should allow the end user to control the operation of the simulation, then display data. The interface should also provide data assessment capabilities as well. Such an interface would not only be useable as a tool for instrument design, but also would be valuable in modeling for data analysis once the instrument is built, as instrument effects would be accurately included in the scattering simulations.

Our interest at Los Alamos in developing a simulations tool is driven by the need to understand instrument performance with different neutron source designs, to guide us in the design of new SPSS and LPSS facilities, and to understand the relative merits of instruments built for each kind of source. We see such a tool as being invaluable in coming to a consensus as what neutron scattering facilities should be built.

2. Approach

2.1. Basic Requirements

The basic features that must be present in the simulations package is that the user interface be easy to use and that it be interactive. The simulations must be fast to assure reasonable turn around times so that the instrument parameter space can be completely probed. Finally the system needs to be open. This final criterion implies the specification of standards to which others can write and thus make contributions to the program. In this report we address only certain aspects of the user interface, but the design strategy takes into account the other essential aspects that must be present in the entire system.

2.2 Package Design Philosophy:

In order to meet the needs of an easy to maintain, easy to use interactive user interface we use the object oriented paradigm. However, there are considerable drawbacks in run time overhead that would strongly impact performance if the entire Monte Carlo package were developed using this approach. Modern FORTRAN compilers produce highly optimized code for highly efficient and fast numerical calculations. Thus we choose a hybrid approach where the user interface is written in a language designed to support object oriented programming, Smalltalk, and the high performance part of the code is written in FORTRAN. The user interface defines the overall architecture of the package, provides for library management and supports the graphical interface. The interface thus functions to manage the difference modules of the FORTRAN code. This approach also allows us to use the considerable development in instrument simulations that has already been done in MCLIB [1].

2.3 The Architecture of the User Interface:

An instrument is an ordered set of elements, such as a source, a collimator, choppers, a sample and detectors. The elements operate on a neutron, in turn, in the Monte Carlo simulation. It is the function of the interface to allow the end user to define an instrument by specifying the instrument elements the element intrinsic properties positions and orientations and transfer this information to the simulation code. How this information is used and the internal architecture of the Monte Carlo simulation package can be found in reference [1]. These functions of the user interface are carried out by four managers as shown in Fig. 1.

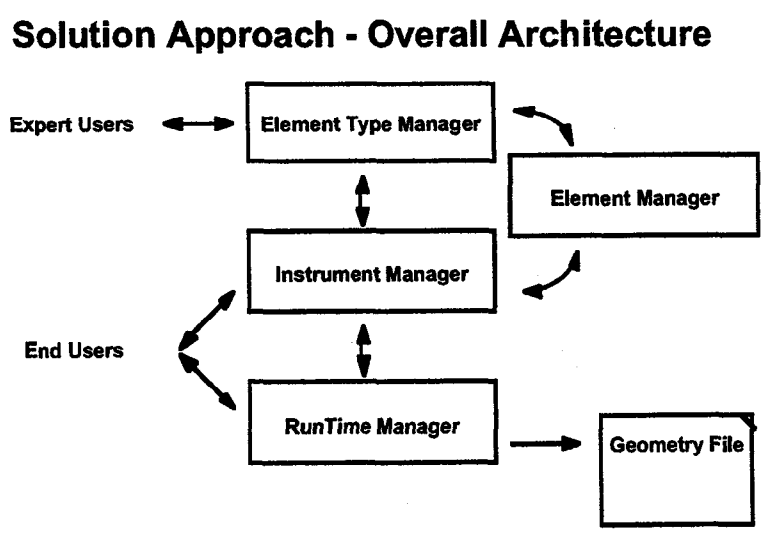

Figure 1: Overall architecture of the user interface and relationships of the managers with one another, the users and the simulation code.

The end user creates and manages the instruments using the Instrument Manager (Fig. 1). The instrument manager allows the user to define an instrument as a set of elements, chosen from a predefined element list. The instrument elements themselves are created and managed thorough the Element Manager (Fig. 1). The Element Manager allows the end user to select from a set of predefined instrument elements, specify the intrinsic parameters of the element (for example the radius of an aperture), and the extrinsic parameters (position and orientation).

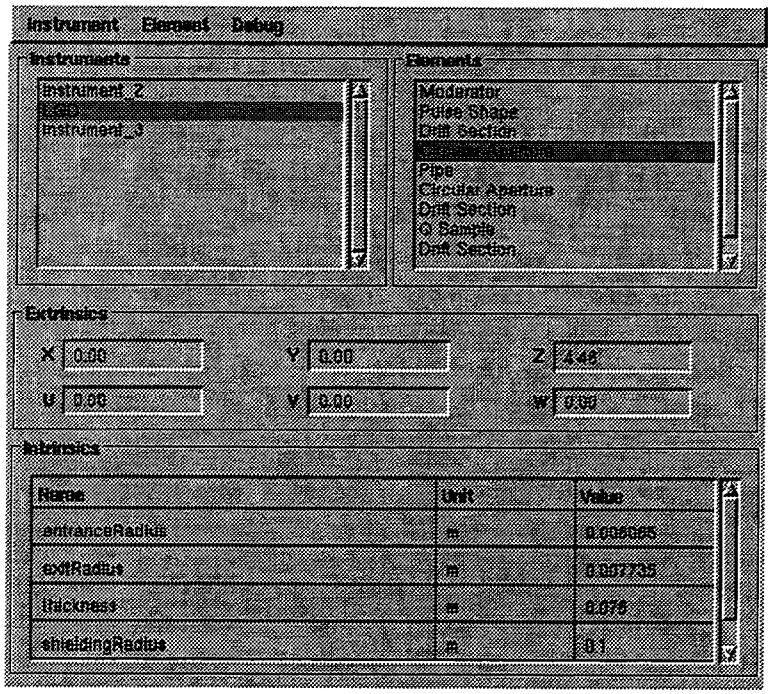

Figure 2: The Instrument Browser.

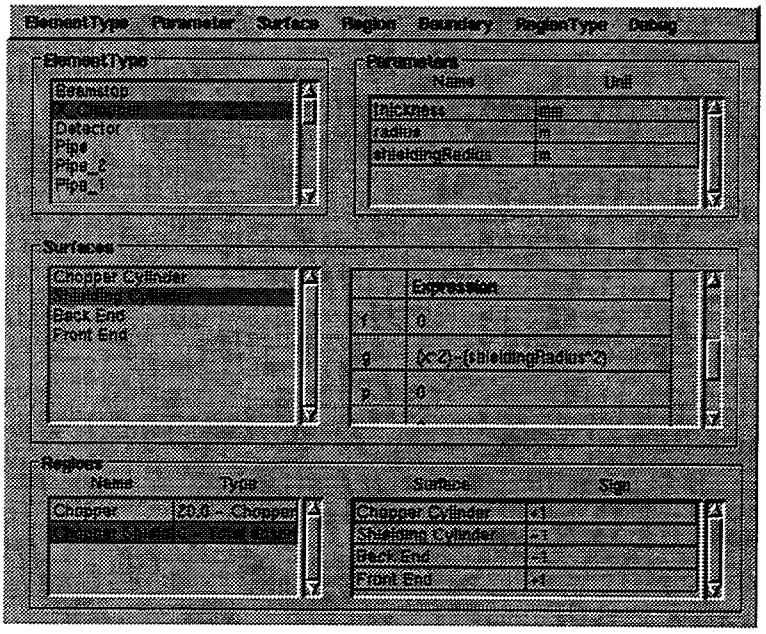

Figure 3: The Element Type Browser.

The interaction between the two managers and the end user is through the Instrument Browser (Fig. 2).

The instrument elements themselves are defined through the Element Types Manager (Fig. 1). This manager allows the expert user to create, define and manage element types through the Element Type Browser (Fig. 3). The physics model for an element is encoded in an MCLIB module [1], and this manager defines the element for the user interface and provides a means for specifying the surfaces and regions that define the element, as well as the intrinsic parameters that are needed to completely specify the surfaces [1]. This manager is maintained by expert users, those who also are also responsible for writing and maintaining the MCLIB codes. This part of the interface is not available to the end user.

Finally, once an instrument is set up through the Instrument Browser, the Runtime Manager, which functions to provide for the selection of an instrument and the simulation parameters, writes a geometry file as an output and starts the simulation. The geometry file completely specifies the elements and their arrangement in the instrument [1].

3. Future Work

The present geometry interface is an early prototype in the development of a comprehensive package for instrument design. Future work will expand on the capabilities of the user interface to control execution of the Monte Carlo simulation and provide facility for the display and assessment of results. The next prototype of the package will also provide for a graphical

representation of the instruments. We plan to investigate the generation of highly optimized FORTRAN code by the Run Manager as a strategy toward improving the runtime speed and efficiency of the simulation.

4. References

[1] P. A. Seeger, "The MCLIB Library: Monte Carlo Simulation of Neutron Scattering Instruments," Proceedings of ICANS-XIII, Paul Scherrer Institut, Villigen, Switzerland, Oct. 11-14, 1995.

[2] M. W. Johnson and C. Stephanou, "MCLIB: A Library of Monte Carlo Subroutines for Neutron Scattering Problems," Rutherford Laboratory report RL-78-090.

[3] P. A. Seeger and R. Pynn, "Resolution of Pulsed-Source Small-Angle Neutron Scattering," Nuclear Instruments and Methods in Physics Research A245 , 115-124 (1986).

[4] P. A. Seeger and R. P. Hjelm, "A Very-Low-Q-Diffractometer for an Advanced Spallation Source," Proceedings of ICANS-XII, Abingdon, U.K., May 24-28, 1993.

[5] P. A. Seeger and R. P. Hjelm, "Design and Implementation of Low-Q Diffractometers at Spallation Sources," American Crystallographic Association Symposia Proceedings, Albuquerque, NM, May 24-28, 1993.

[6] G.A. Olah, R.P. Hjelm and P.A. Seeger, "Small-angle Scattering Instrumentation on a 1 MW Long Pulse Spallation Source", Proceedings of ICANS-XIII, Paul Scherrer Institut, Villigen, Switzerland, Oct. 11-14, 1995.

[7] M.R. Fitzsimmons and R. Pynn, "the Performance of Reflectometers at Continuous Wave and Pulsed Neutron Sources", Proceedings of ICANS-XIII, Paul Scherrer Institut, Villigen, Switzerland, Oct. 11-14, 1995.

[8] L.L. Daemen, J. Eckert., R. Pynn and P.A. Seeger, "Monte Carlo Study of the Performance of a Time-of-Flight Multichopper Spectrometer", Proceedings of ICANS-XIII, Paul Scherrer Institut, Villigen, Switzerland, Oct. 11-14, 1995.

ICANS-XIII
13th Meeting of the International Collaboration on
Advanced Neutron Sources
October 11-14,1995
Paul Scherrer Institut, 5232 Villigen PSI, Switzerland

Remanent Multilayers for Polarized Neutron Instrumentation

D.Clemens*, W.Hahn†, A.Vananti*, P. Schubert-Bischoff‡, P.Böni*, M.Horisberger*

* Laboratorium für Neutronenstreuung ETH Zürich & Paul Scherrer Institut,
Paul Scherrer Institut, CH-5232 Villigen PSI, Switzerland
† Institut für Festkörperforschung,
Forschungszentrum Jülich (KFA), D-52425 Jülich, Germany
‡ Hahn-Meitner-Institut Berlin, Glienicker Str. 100, D-14109 Berlin, Germany

ABSTRACT

Polarizing multilayers and supermirrors for applications in neutron instrumentation have been produced using DC-magnetron sputtering. The chosen material combination $Ti_{1-u}N_u$-$Fe_{0.50}Co_{0.48}V_{0.02}$ offers the possibility to adjust the scattering length density of the 'contrast' material Ti to the value being effective on neutrons in the $|-\rangle$-state in the FeCoV alloy magnetized to saturation, by loading Ti with the suited amount of nitrogen. Neutron reflectometry data for supermirrors give flipping ratios of 40 and more and reflectivities better than 85% at twice the critical angle of Ni. The production process induces a magnetic anisotropy for directions lying within the layer plane. $Ti_{1-v}Gd_v$ absorbing subcoatings have been used to suppress the remaining reflectivity of the unwanted spin component from the substrate-mirror interface. SQUID and MOKE magnetometry accompanied the experiments performed with polarized neutrons.

1. Introduction

Besides polarizing filters and field gradient devices neutron beam polarization can be accomplished by reflection at a monochromator or a mirror which has different scattering cross sections for the two spin states of the neutron. The term neutron mirror includes thin film multilayers, single layer coatings and polished surfaces. Mirror coatings have the advantage of easy availability and relatively low costs, and to a certain measure they can be designed to the needs of the instrument they are aimed for. Their application is in particular advantageous for the polarization of cold neutrons. Thus, mirrors serve for this purpose since 1951 [1]. In particular the properties of FeCo alloys have been exploited for effective

Keywords: Polarizer, Supermirror

polarizers. This alloy can be easily saturated and the composition can be varied over a wide range to give the desired optimum scattering parameters either for a single layer [2,3] or a multilayer when combined with an adequate spacer material [4]. A giant step forward to make thin film polarizers useful for the large beam cross sections that are often required in neutron experiments has been made by the emergence of two ideas, one to extend the regime of total reflection by using multilayers and the other to cover the whole cross section with an array of bent mirrors on thin substrates, and thereby forcing the neutrons to be reflected at least once.

The first improvement originates from the work of Turchin [5] and Mezei [6] and consists of a stack of alternating layers of two materials made in such a way that constructive interference of the partial waves reflected at each interface takes place in a q-band ($q = 4\pi\frac{\sin\vartheta}{\lambda}$) adjacent to the edge of total reflection at q_c as one finds it for a bulk material. To achieve this, the layer thicknesses have to increase in a way that for the nth layer

$$d(n) = \frac{d_c}{4\sqrt[4]{n/2}} .$$

Herein, the scattering parameters for the material combination A-B are included through

$$d_c = \left(\sqrt{\left(\rho_{at}^{(A)} b^{(A)}/\pi\right)^2 - \left(\rho_{at}^{(B)} b^{(B)}/\pi\right)^2}\right)^{-1} .$$

$\rho_{at}^{(X)}$ denotes the atomic density and $b^{(X)}$ the scattering length of each material, respectively. Often, it is useful to calculate the layer sequence with a slightly increased d_c. Due to refraction the layer thickness for each material has to be corrected to give an optical thickness [6,7]:

$$d_{opt}^{(X)}(n) = \frac{d(n)}{\sqrt{1 - \frac{d(n)^2}{\pi/\rho_{at}^{(X)} b^{(X)}}}} .$$

The reflectivity in this band can be increased by selecting a material combination with a high contrast in scattering length density $\Delta\rho_{sc} = \rho_{at}^{(A)} b^{(A)} - \rho_{at}^{(B)} b^{(B)}$. Mezei and coworkers succeeded in producing a first Fe-Ag supermirror.

The second invention is the curved Soller guide [8] that has been equipped with thin films of a $Fe_{40}Co_{60}$ alloy to polarize the neutrons which pass through the narrow channels by reflection from the magnetized mirrors [9]. Consequently, a short time later supermirrors have been introduced into Soller guides. By thermal evaporation of a Gd-Ti multilayer that serves as antireflection coating and subsequent deposition of a sequence of Co-Ti bilayers O. Schärpf and co-workers produced thousands of polarizing supermirrors [10]. A large part of them have been mounted into 'superbender' Soller guides.

We aimed for a polarizer coating with a high $|+\rangle$-('spin up')-reflectivity $R^{|+\rangle}$ on the basis of a commercially available $Fe_{0.50}Co_{0.48}V_{0.02}$ alloy. The scattering length densities for this material are $\rho_{sc}^{|+\rangle} = 1066\ \mu m^{-2}$ and $\rho_{sc}^{|-\rangle} = -64\ \mu m^{-2}$. To minimize the $|-\rangle$-reflectivity $R^{|-\rangle}$ of the

multilayers, we combined the ferromagnetic alloy with titanium as the spacer material, loaded with nitrogen to give $\rho_{sc}(Ti) \cong \rho_{sc}^{|\rangle}(Fe_{0.50}Co_{0.48}V_{0.02})$.

2. Experimental

A Leybold Z600 DC-magnetron sputtering plant has been used to produce multilayers [11] for neutron reflection experiments and magnetometry. Supermirror layer sequence consisting of 150 single layers were calculated according to the formalism of Hayter and Mook [12]. Single layer $Fe_{0.50}Co_{0.48}V_{0.02}$ samples were produced under different sputtering conditions to perform stress and magnetometric measurements. As substrates we selected 2 mm float glass and 0.5 mm polished silicon wafers because of their very good surface microroughness [13]. The Ti:N layers were realized by reactive sputtering. The variation of the partial pressure of nitrogen p_{N_2} allows to regulate the amount of nitrogen embodied in the titanium layer. Neutron reflectometry experiments have been done mainly on V6 at BENSC/HMI and on the T3 mirror testing facility at the ILL. Both instruments work in the constant wavelength mode. An electromagnet on V6 makes it possible to reflect polarized neutrons from mirrors in a variable magnetization field.

Magnetometric measurements were conducted on a SQUID and a MOKE magnetometer at the KFA Jülich. Whereas the SQUID signal comes from the entire sample (5×10 mm^2 surface area), MOKE (magnetooptic Kerr effect) is only sensitive to the magnetization in a volume penetrable to light. The rotation of the polarization axis of the light is a measure for the component of the magnetization vector in the surface plane. The results from magnetometry are extracted from the diploma work of one of the authors [14]. It represents only a small fraction of his extensive characterization of magnetostriction in $Fe_{0.50}Co_{0.48}V_{0.02}$ layers. Additionally, TEM micrographs were taken at HMI to visualize the grown multilayer.

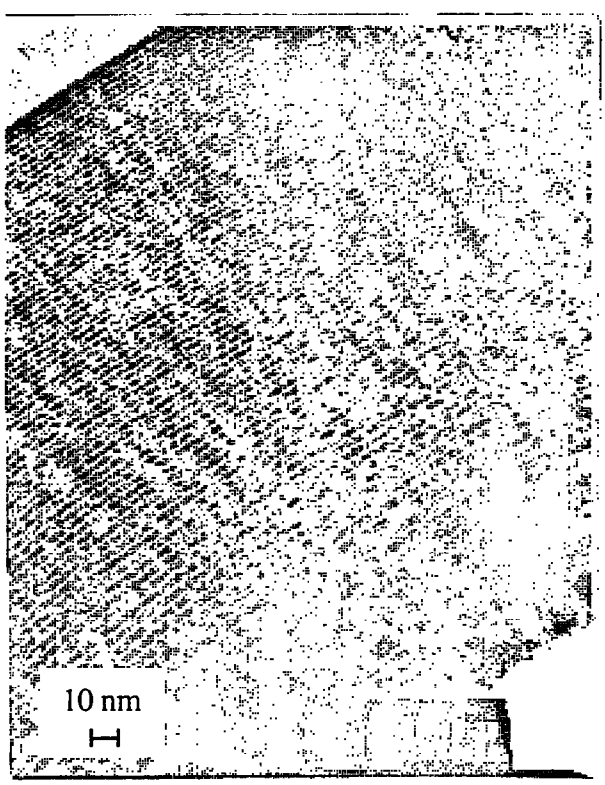

Fig. 1. Transmission electron microscopy (TEM) micrograph taken from an ultramicrotomy cut of a 150 layer $Ti_{1-u}N_u$-$Fe_{0.50}Co_{0.48}V_{0.02}$ supermirror (sample R1285). The substrate side is in the top left corner. The picture was taken with a Philips 120 keV microscope.

3. Results

Reflectivity measurements on a series of 'monochromator'-type $Ti_{1-u}N_u$-$Fe_{0.50}Co_{0.48}V_{0.02}$ multilayers showed that an increased p_{N_2} during the sputtering of Ti brings with it an increased $\rho_{sc}(Ti)$. The results led us to the deposition conditions under which we achieve the matching of the scattering length densities [15], i.e. $\rho_{sc}(Ti) \cong \rho_{sc}^{|-\rangle}(Fe_{0.50}Co_{0.48}V_{0.02})$. For this p_{N_2} the detected $R^{|-\rangle}$ was not discriminable from the remaining 1.5% $R^{|+\rangle}$–signal that originates from the imperfect efficiency of polarizer and flipper. We could not find any evidence for 'magnetically dead' layers at the interfaces although $R^{|-\rangle}$ is very sensitive to their appearance in the case of $\Delta\rho_{sc} = 0$ [16].

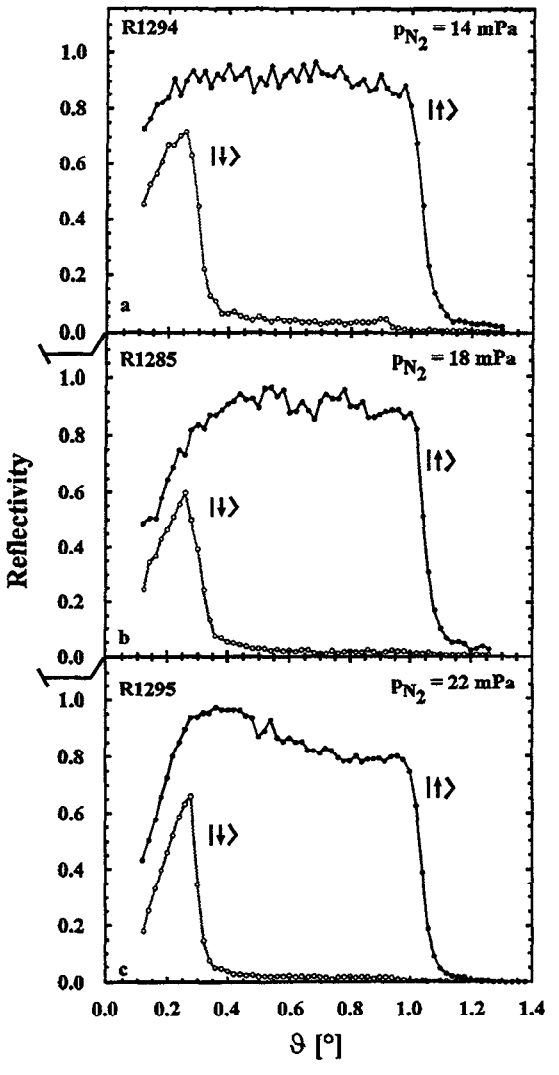

Fig. 2. Polarized neutron reflection from 150 layer $Ti_{1-u}N_u$-$Fe_{0.50}Co_{0.48}V_{0.02}$ supermirrors produced with nitrogen partial pressures of 14 mPa (a), 18 mPa (b) and 22 mPa (c). The data was taken at the V6 reflectometer at BENSC/HMI (λ = 0.47 nm, B_{ext} = 79 mT).

Consecutively, we produced supermirrors under the same conditions as for the monochromators. A copy of a TEM micrograph of such a supermirror is displayed in Fig. 1. Fig. 2 compiles the reflection data for the mirrors magnetized to saturation in an external field $B_{ext} = 79$ mT. It is obvious that for $p_{N_2} = 18$ mT a good matching has been achieved also giving a high $R^{|+\rangle} \cong 87$ %. The data was taken at $\lambda = 0.47$ nm, so that the measured cut-off of $R^{|+\rangle}$ at 1.04° corresponds to $m = 2.23$. Here, given by $\vartheta_c = m \cdot \vartheta_c(Ni)$, m characterizes the supermirror cut-off in terms of multiples of the critical angle of bulk nickel

$\vartheta_c(\mathrm{Ni}) = 0.99 \cdot \lambda[\mathrm{nm}]$. The $R^{|-\rangle}$–curves in Fig. 2 exhibit a cut-off that comes from the reflection of neutron transmitted through the supermirrors coating but reflected from the interface of the glass substrate. To avoid this effect which decreases the q-regime that is of use for beam polarization we followed the path of other groups and coated the substrate with an antireflecting layer of $Ti_{1-v}Gd_v$ before depositing the supermirror sequence. The adequate Gd concentration and thickness of the layer could to be found experimentally in an easy way. Because the sputtering in DC-magnetron mode is preferentially from a ditch defined by the arrangement of the magnets on the back of the target we only needed to insert 3 mm Gd pellets into this ditch. In three series for which we implemented an increasing number of pellets into the Ti target we coated antireflecting layers of 30 nm, 50 nm and 70 nm underneath the $Ti{:}N\text{-}Fe_{0.50}Co_{0.48}V_{0.02}$ supermirror. 50 nm Ti:Gd with the highest Gd concentration reduced the remaining $R^{|-\rangle}$–signal to 10%. Although a better damping of unwanted neutron reflection from the substrate can be achieved by depositing a Ti-Gd multilayer with decreasing Gd layers thicknesses [7] we assessed the single layer solution to be sufficient for multireflection devices as bent Sollers. Fig. 3 shows the performance of such a polarizing mirror.

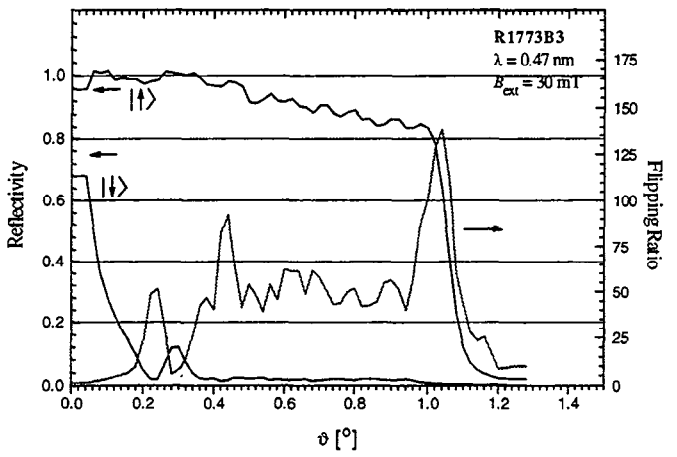

Fig. 3. Polarized neutron reflection from a 150 layer $Ti_{1-u}N_u\text{-}Fe_{0.50}Co_{0.48}V_{0.02}$ supermirror coated onto a 50 nm Ti:Gd antireflection layer. The magnetic layers are saturated in B_{ext} = 30 mT.

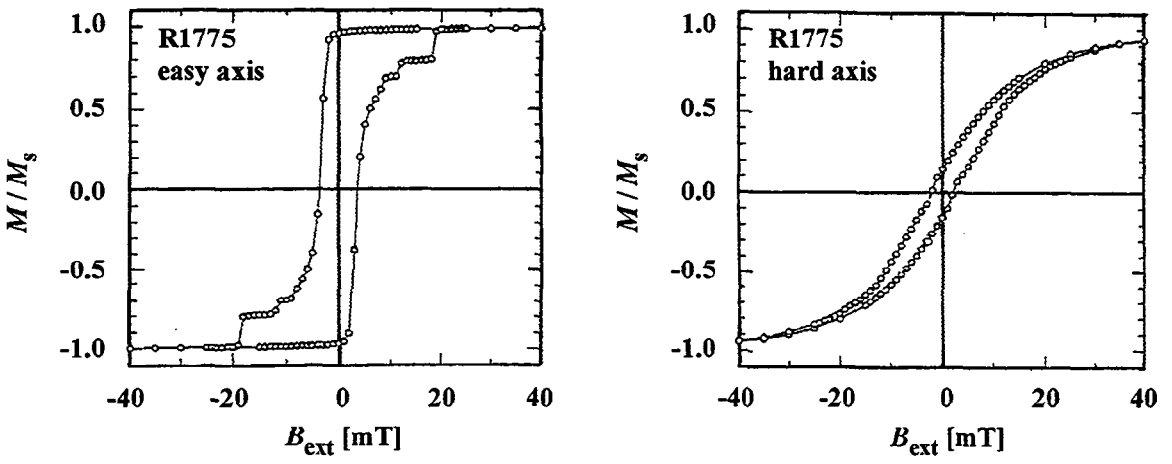

Fig. 4. Hysteresis loops for in-plane magnetization of a $Ti_{1-u}N_u\text{-}Fe_{0.50}Co_{0.48}V_{0.02}$ supermirror along the easy axis (left) and the hard axis (right) as measured with a SQUID magnetometer.

Additionally we can take advantage of the deposition procedure in the Z600. It gives rise to special characteristics of the $Fe_{0.50}Co_{0.48}V_{0.02}$ layers when they are produced under $p_{Ar} = 0.6$ mPa. The substrate table moves through underneath a rectangular target of approximately 88×500 mm^2 with a speed determined by the desired layer thickness. A diaphragm is used to get a homogeneous thickness in the direction perpendicular to the movement. These anisotropic deposition conditions give rise to a stress anisotropy in our films. The stress is high enough that in the extreme case of very thick multilayer (600 layers and more) the coatings rip off themselves in small strips from the substrates. As sputtered films especially those of Ti stick extremely good to our substrates, a part of the glass is torn away from the rest and stays connected to the dismantled films. Nevertheless this mechanical problem is not encountered for the coatings under investigation in this work. Moreover, the stress anisotropy implies a magnetic anisotropy caused by magnetostriction. This is revealed by the magnetometry data taken from the supermirrors (Fig. 4). An easy axis for saturation can be found in the direction perpendicular to the movement of the table. Along this axis the material can be saturated in fields as low as 25 mT. The remanent magnetization of more than 90% of the saturation level is sufficient to find a useful polarization in $B_{ext} = 0$. We measured coercitive fields in the range of $B_{coerc} \cong 4$ mT with a SQUID. Polarized neutron reflection still showed the remanent behavior when this field has been applied in opposite direction to a saturated supermirror (Fig. 5a). Then at $B_{ext} = -10$ mT the magnetization flipped within 20 min. and almost saturated again (Fig. 5b).

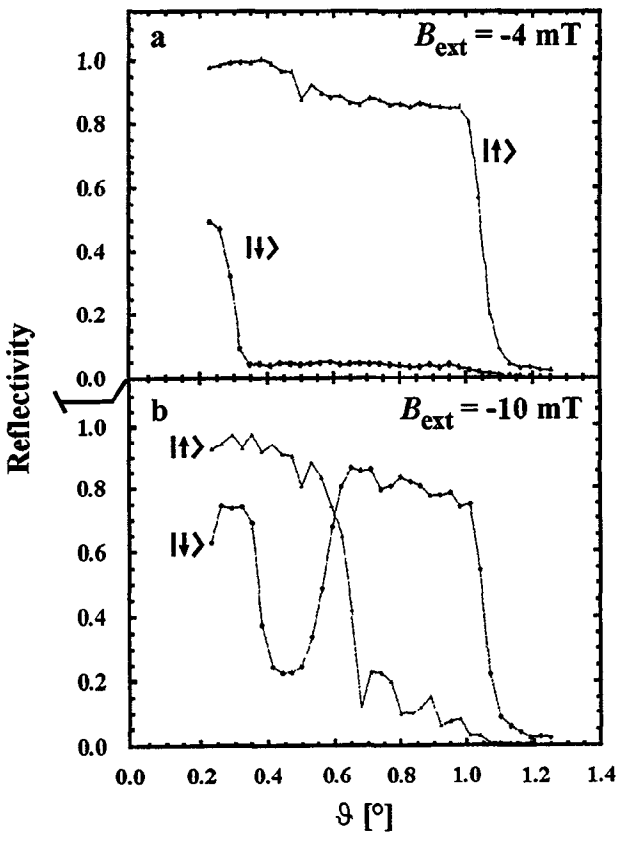

Fig. 5. Polarized neutron reflection from 150 layer $Ti_{1-u}N_u$-$Fe_{0.50}Co_{0.48}V_{0.02}$ supermirrors produced with a nitrogen partial pressure of 18 mPa in two external fields oppositely directed to the previously saturated magnetization ($\lambda = 0.47$ nm).

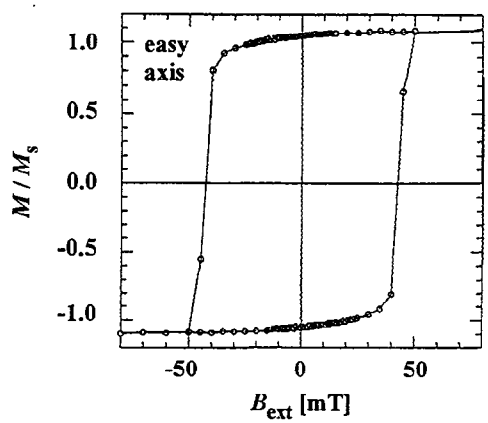

Fig. 6. SQUID hysteresis loop for in-plane magnetization along the easy axis of a 28 nm $Fe_{0.50}Co_{0.48}V_{0.02}$ film produced by stationary sputtering.

In Fig. 6 the hysteresis loop of a 28 nm single layer of $Fe_{0.50}Co_{0.48}V_{0.02}$ is displayed. This sample has been produced under conditions that are different to the previous examples. It is made in the static mode, i.e. the table did not move relative to the target. The substrate position was located 80 mm away from the center of a circular 75 mm target. Thus, only sputtered particles under oblique incidence arrive on the substrate. As can be deduced from Fig. 6 a substantially higher coercitive field can be achieved in the easy axis direction than for the 'dynamically' sputtered multilayers or single films.

The performance of the Ti:N-$Fe_{0.50}Co_{0.48}V_{0.02}$ multilayer supermirrors does not change after $2^1/_2$ hours heat treatment at 230°C. The flipping ratios $\tilde{R}$ for a saturated mirror calculated from the ratio of the neutron reflection spectra for the two spin states is $\tilde{R} \geq 40$ over a q-range exceeding from $m = 0.77$ to the cut-off (Fig. 3). In the remanent state we find $\tilde{R} \geq 25$, which gives a polarization $P \geq 0.92$. We also succeeded in producing a polarizing multilayer monochromator consisting of 251 layers on an antireflecting sublayer that reflects a wavelength band $\frac{\Delta\lambda}{\lambda} = 10\%$ (Fig. 7).

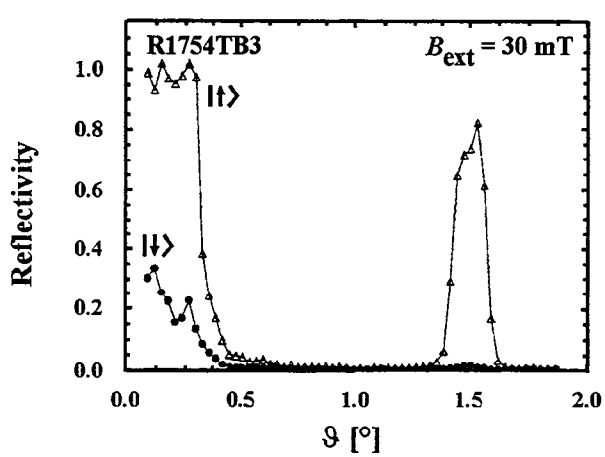

Fig. 7. Polarized neutron reflection from a 251 layer $Ti_{1-u}N_u$-$Fe_{0.50}Co_{0.48}V_{0.02}$ multilayer magnetized to saturation ($\lambda = 0.47$ nm).

4. Conclusions and Outlook

By matching the scattering length density of $Ti_{1-u}N_u$ with the one for $|-\rangle$-neutrons in magnetized $Fe_{0.50}Co_{0.48}V_{0.02}$ we succeeded to manufacture reproducibly a supermirror coating with the following useful properties:

(i) a high $|+\rangle$-reflectivity (87% at 2.1 times the critical angle of bulk Ni),

(ii) flipping ratio $\tilde{R} \geq 40$,

(iii) operational in zero field (important for neutron spin echo),

(iv) no clear evidence for 'magnetically dead' layers and

(v) stable with regard to temperature ($T \leq 230C$), therefore we expect that the layers hardly interdiffuse.

Presently, we are in the course of producing polarizing mirrors for focusing Soller 'superbenders' that will be operated in the DNS spectrometer and the neutron spin echo spectrometer at the Jülich neutron scattering facility, and for a triple axis spectrometer for polarized neutrons at the SINQ neutron source at PSI. The reflection spectrum for one of the representative mirror of the many that will be inserted is shown in Fig. 8.

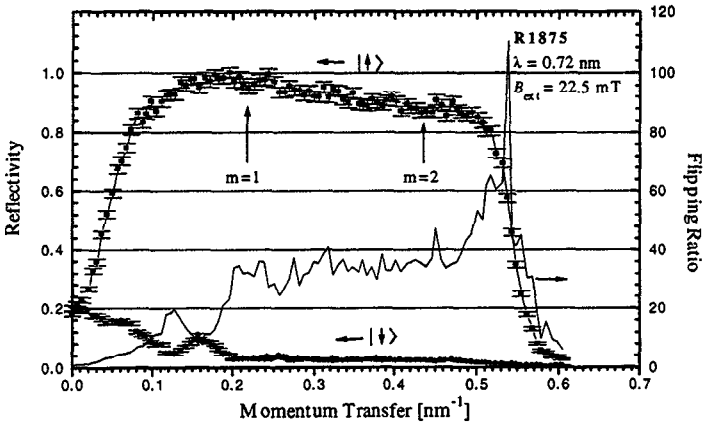

Fig. 8. Polarized neutron reflection from a 150 layer $Ti_{1-u}N_u$-$Fe_{0.50}Co_{0.48}V_{0.02}$ supermirror on a 50 nm antireflecting Ti:Gd sublayer supported by a 0.2 mm glass substrate.

Other applications are in a project state. An especially interesting application is considered for the reflectometer at SINQ/PSI [17]. This instrument can operate in the white beam time-of-flight mode. As the remanent mirrors can withstand an oppositely oriented magnetic field of the order of magnitude of a typical guide field, i.e. $B_{ext} = -5$ mT, they could be used as spin selecting device [18]. An external field pulse sufficient to saturate the layers can be applied by several small electromagnetic coils, and then set to zero in order to avoid any change in the direction of the guide field. By flipping the direction of the applied external magnetic field in a short pulse one can select the desired beam polarization.

References

[1] D.J. Hughes and M.T. Burgy, *Phys. Rev.* **81** (1951) 498
[2] J. Penfold et al., *Rutherford Laboratory Report* RL-75-112 (1975)
[3] G.M. Drabkin et al., *Leningrad Institute of Nuclear Physics Report* FTI-183 (1975)
[4] F. Mezei, *SPIE-Proc.* **1738** (1992) 107
[5] V.F. Turchin, *Soviet Atomic Energy* **22** (1967) 124
[6] F. Mezei, *Comm. Phys.* **1** (1976) 81; F. Mezei and P.A. Dagleish, *ibid* **2** (1977) 41
[7] O. Schärpf, *Physica B* **156 & 157** (1989) 631
[8] B. Jacrot, Instrumentation for Neutron Inelastic Scattering Research (I.A.E.A., Vienna, 1970), p.225
[9] J.B. Hayter and J. Penfold, *Z. Phys. B*, **35** (1979) 199
[10] O. Schärpf, *Physica B* **156 & 157** (1989) 639
[11] O. Elsenhans et al., *Thin Solid Films* **246** (1994) 110
[12] J.B. Hayter and H.A. Mook, *J. Appl. Crystallogr.* **22** (1989) 35
[13] P. Böni et al., this conference
[14] A. Vananti, *diploma thesis ETH Zürich*, Laboratorium für Neutronenstreuung report LNS-180
[15] D. Clemens et al., *Physica B* **213 & 214** (1995) 942
[16] D. Clemens et al., *Phys. Scripta* **50** (1994) 195
[17] D. Clemens, *Physica B*, accepted for publication
[18] P. Böni, *Journal of Neutron Research*, accepted for publication

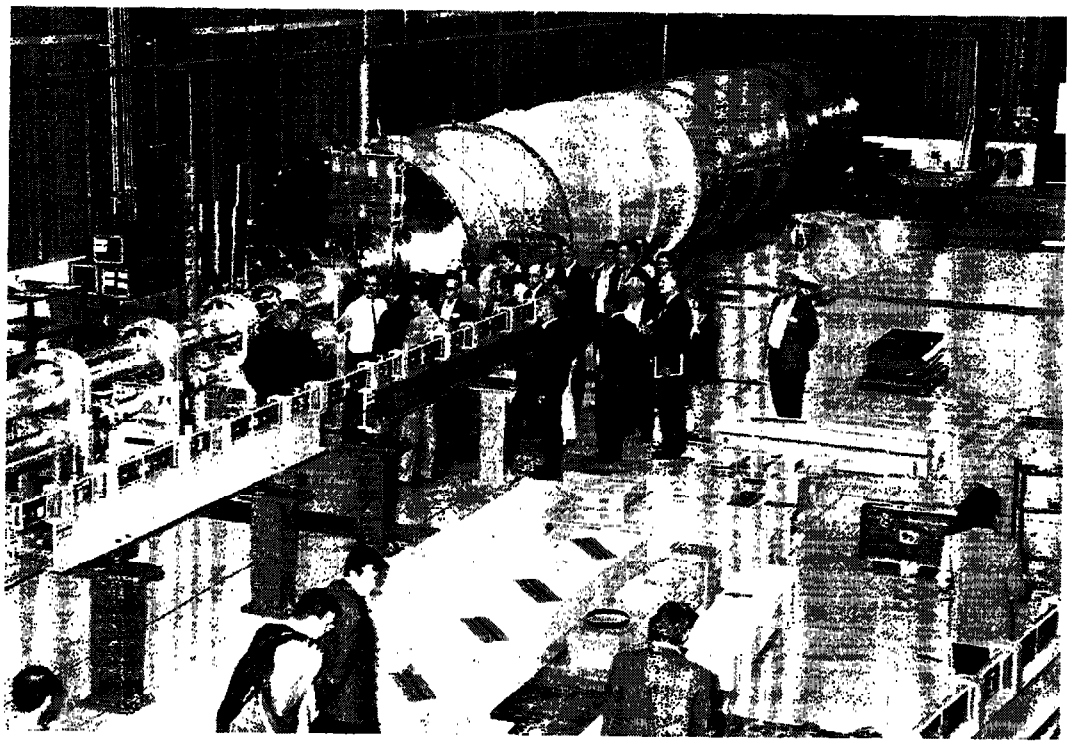

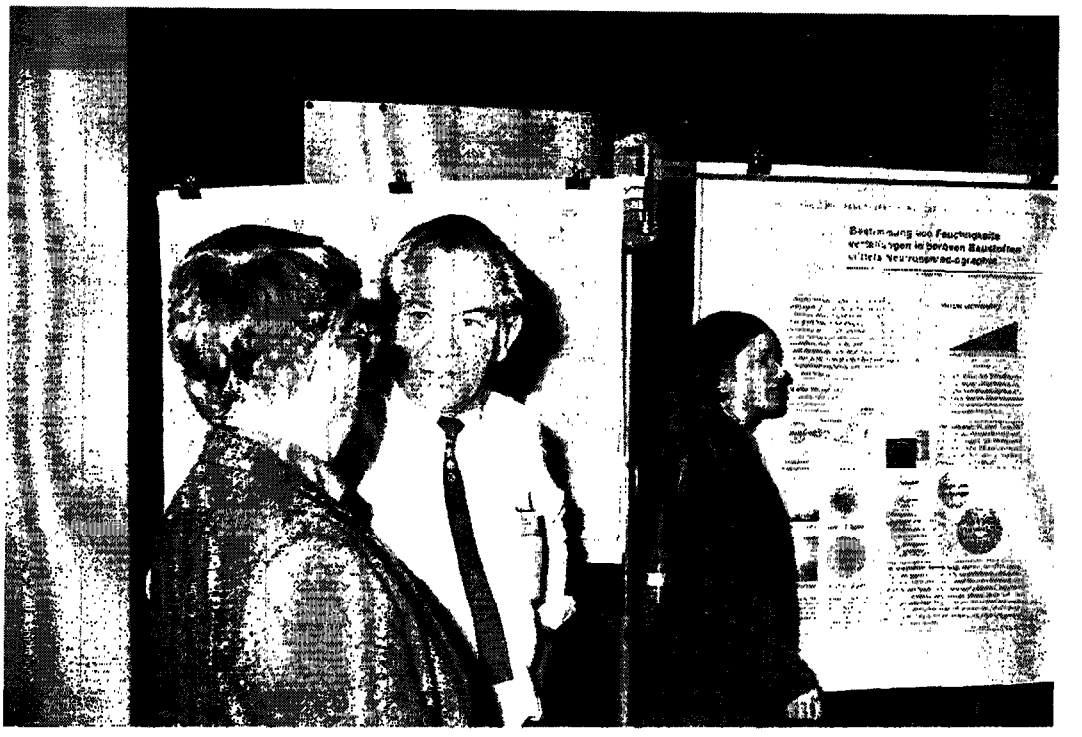

The Long Pulse Option

ICANS-XIII
13th Meeting of the International Collaboration on
Advanced Neutron Sources
October 11-14, 1995
Paul Scherrer Institut, 5232 Villigen PSI, Switzerland

PERFORMANCE OF LONG-PULSE SOURCE REFERENCE TARGET-MODERATOR-REFLECTOR CONFIGURATIONS

Eric J. Pitcher, Gary J. Russell, Philip A. Seeger, and Phillip D. Ferguson

Manuel Lujan, Jr. Neutron Scattering Center, Los Alamos National Laboratory, USA

ABSTRACT

We have calculated the performance of five similar target-moderator-reflector geometries that are reasonably well optimized for long-pulse source applications. For all cases, the moderators are fully coupled; that is, no poisons, decouplers, or liners are used. For each case, the energy- and time-dependent characteristics of the moderator source brightness have been parameterized using empirical functions. These parameterizations have been made available to users of the Monte Carlo neutron scattering instrument design code MCLIB for use in evaluating the performance of neutron scattering instruments on a long-pulse source.

1. Introduction

There is currently considerable debate within the neutron scattering community regarding the performance of certain classes of neutron scattering instruments on a "long-pulse" spallation source, that is, a neutron source fed by a proton beam whose pulse width is considerably longer than a few tens of microseconds. For proton beams with such pulse widths, the moderator pulse widths (or, more precisely, their full-widths at half-maximum) are governed by the proton pulse width rather than the storage time in the moderating media. As such, decoupling of the moderator does not lead to a reduction in the moderator pulse width and serves only to reduce the decay constant of the moderator pulse and, more significantly, reduce both the instantaneous and time-integrated source brightness [1].

Recently, the Monte Carlo-based neutron scattering instrument simulation code using the MCLIB library has been developed to such a state that it can now be used as a design tool [2]. The neutron source for this code is the leakage of neutrons from the moderator. Hence, one must provide the MCLIB source subroutine with a characterization of this leakage, both in time and in energy. We have performed this characterization for a reference coupled target system with five different reflector configurations.

Keywords: Coupled Moderator, Composite Reflector, Long-Pulse Source, MCLIB

2. Reference Target System Geometry

The reference geometry is a singly-split tungsten target with a square cross section. Horizontal and vertical cross sections along the proton beam axis are shown in Figure 1. The upper section of the target is $10 \times 10 \times 8.9$ cm^3, with a homogenized material composition equivalent to that of a clad rod target design capable of handling 1 MW of beam power (70.24 v% W, 18.66 v% Inconel-718, and 11.10 v% D_2O). The lower section has dimensions $12 \times 12 \times 23.1$ cm^3, and a homogenized material composition of 83.3 v% W and 16.7 v% D_2O. Both sections are completely enclosed in 0.2-cm-thick Inconel-718 target canisters. The flux trap gap between the two target sections is 14.6 cm high.

Surrounding the flux trap are four fully-coupled liquid-H_2 moderators, each 5 cm thick with a viewed surface area of 13×13 cm^2. The ortho/para-hydrogen fraction used in the calculation is 50/50 and the temperature is 20 K. Each moderator has wrapped about its perimeter a 1-cm-thick layer of H_2O, with a temperature of 293 K. The two surfaces of each moderator perpendicular to the neutron flight paths are covered by cryogenic moderator canisters, which, on each side of a moderator, are modeled as two 0.35-cm-thick plates of Aluminum-6061 separated by a 0.5-cm-thick vacuum gap. For each moderator, the distance from the proton beam centerline to the inner surface of liquid H_2 is 7.35 cm.

Before striking the target, the 800-MeV proton beam passes through a proton beam window, represented by two 0.108-cm-thick Inconel-718 plates separated by a 0.2-cm gap filled with H_2O. The proton beam profile is parabolic with a 7-cm circular diameter. The proton beam channel upstream of the target is 9 cm in diameter.

The total reflector size is fixed at 150 cm diameter by 150 cm high. The reflector composition and geometry were varied for the five reference cases reported here. In one case, the reflector has a single composition of 90 v% Be and 10 v% D_2O. For the other four cases, the reflector is

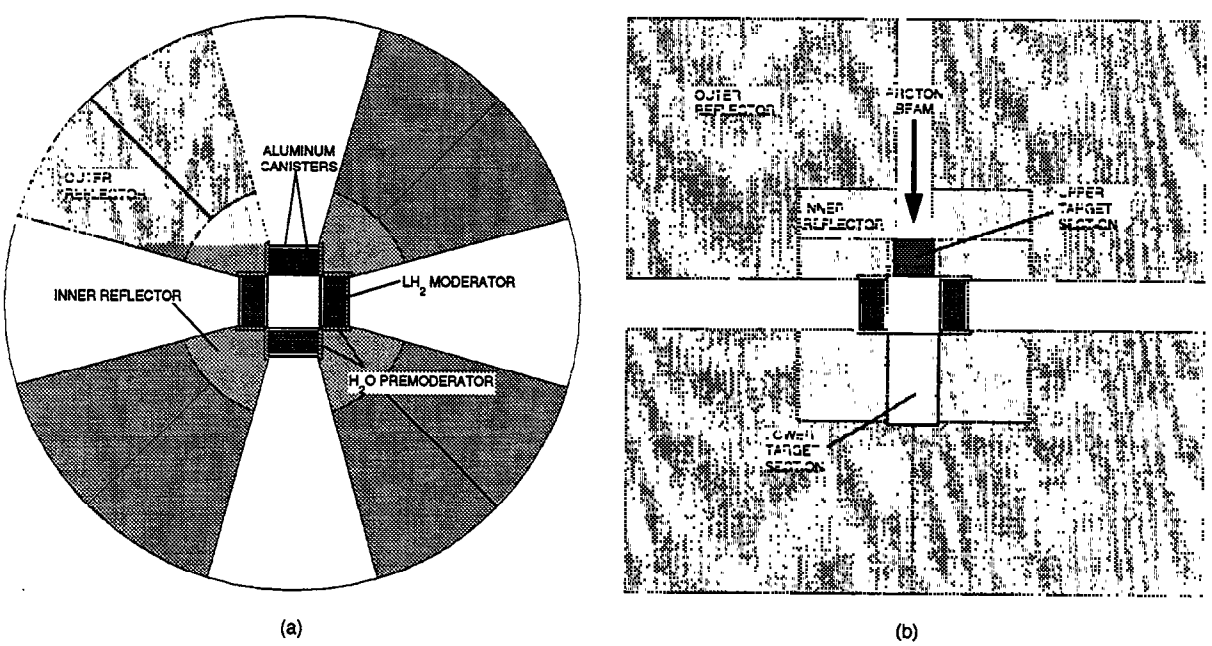

Figure 1. Cross-sectional views of the target station model. (a) Plan view, where the proton beam direction is perpendicular to the plane of the page; (b) Elevation view.

composite. The inner reflector is consistently 90 v% Be and 10 v% D_2O; for two cases the outer reflector is 90 v% Pb and 10 v% D_2O, while for the other two cases it is 90 v% Ni and 10 v% D_2O. For each outer reflector composition the inner reflector diameter and height were set to both 40 cm and 60 cm. These five reference reflector geometries are summarized in Table 1.

Table 1. Reflector characteristics for the five reference cases.

CASE	INNER REFLECTOR DIAMETER & HEIGHT (cm)	INNER REFLECTOR MATERIAL COMPOSITION	OUTER REFLECTOR MATERIAL COMPOSITION
40-cm Be/Ni	40	90 v% Be & 10 v% D_2O	90 v% Ni & 10 v% D_2O
60-cm Be/Ni	60	90 v% Be & 10 v% D_2O	90 v% Ni & 10 v% D_2O
40-cm Be/Pb	40	90 v% Be & 10 v% D_2O	90 v% Pb & 10 v% D_2O
60-cm Be/Pb	60	90 v% Be & 10 v% D_2O	90 v% Pb & 10 v% D_2O
150-cm Be	150	90 v% Be & 10 v% D_2O	n/a

3. Results

We used the LAHET Code System (LCS) to calculate the performance of each target-system geometry. The LCS is composed primarily of two Monte Carlo transport codes, LAHET and MCNP. LAHET is a model-based code that simulates the transport and interaction of high-energy nucleons, pions, and muons with stationary nuclei. The user may select from a variety of physics models [3] for simulating nuclear processes. For these calculations, we used the Bertini intranuclear cascade model, the GCCI level density model, the preequilibrium exciton model, the Dresner evaporation model, the Fermi breakup model, the RAL fission model, and neutron elastic scattering below 100 MeV. This combination of models shows good agreement with a broad range of experimentally-measured quantities [4]. MCNP is a data-based code that simulates the transport and nuclear interaction of neutrons with energies less than 20 MeV.

3.1 Energy Spectrum

The magnitude of the energy-dependent brightness is derived from point detector tallies placed 10 m from the moderator leakage surfaces. As all four moderators in the model are identical, the point detector tallies for all four moderators are averaged together in order to reduce the statistical error. Results for the five cases are shown in Figure 2. Also shown, for comparison, are the calculated results of Ageron [5] for the Cold Source 2 at the Institut Laue Langevin (ILL) in Grenoble, France, which is currently the world's most intense cold source. From Figure 2, it is evident that an all-beryllium reflector yields the highest time-integrated

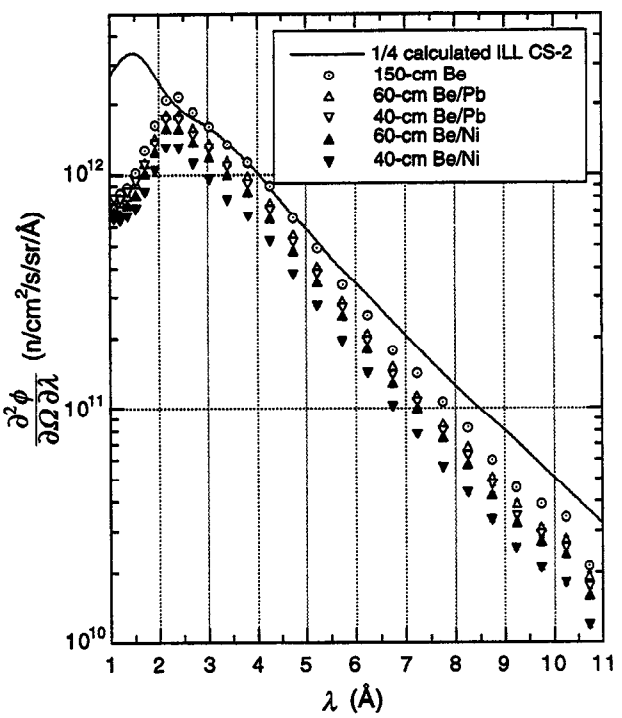

Figure 2. Brightness as a function of neutron wavelength λ for the five reference cases. For reference, the ILL CS2 spectrum at 1/4 power is also shown.

brightness at long wavelengths. Further, the Be-Pb composite provides a higher time-integrated brightness than does the Be-Ni composite. This is expected since Ni is a moderate neutron absorber and its presence should degrade the source brightness.

3.2 Time Spectrum

In addition, we calculated the time dependence of the source brightness by tallying neutrons crossing the moderator leakage surfaces. For the purpose of evaluating the temporal characteristics, we integrate the brightness from 0 to 5 meV (>4.04 Å), where the spectrum generally follows a linear dependence with energy. By setting the upper limit sufficiently low, we concentrate on the region of the spectrum that is typically most critical to optimize. Higher upper limits (e.g., 80 meV) could potentially lead to different conclusions about source performance. For example, the presence of an ambient premoderator and a sufficiently thin hydrogen moderator can significantly enhance the 20- to 80-meV region of the spectrum while it may have a detrimental effect on the 0 to 5-meV region.

Time-dependent pulse shapes for the five reference cases are shown in Figure 3 for an instantaneous proton pulse. From Figure 3(a), we see that the time-dependent peak brightness is the same to within 15% for all five reflector geometries. Note that the peak brightness for the 40-cm Be/Pb case is about 10% higher than for all other cases, which is a result of additional neutron production via spallation in the innermost portion of the outer Pb reflector. Figure 3(b) illustrates the decay constant. For reflector geometries with fast decays, a single decay constant fits the data well for times greater than about 300 μs. However, for geometries with appreciable tails, the decay is not a simple exponential and the value of the decay constant depends strongly on the time interval over which the fit is made.

Figure 4 shows the temporal response when the instantaneous pulses of Figure 3 are convolved with a 1-ms flat-top proton pulse. Here, three cases (150-cm Be, 60-cm Be/Pb, and 40-cm Be/Pb) exhibit nearly the same time-dependent peak brightness, while the 60-cm Be/Ni and 40-

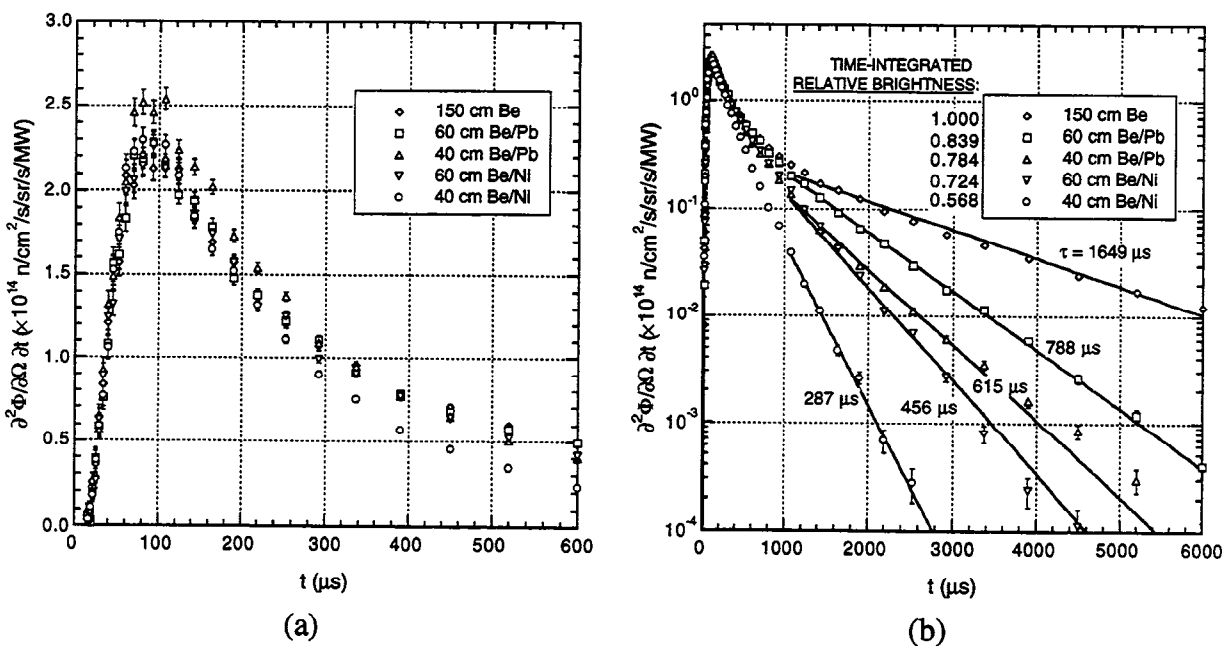

Figure 3. Instantaneous pulse shapes for neutrons with energy $E < 5$ meV for the five reference cases where the brightness is plotted on (a) a linear scale, and (b) a logarithmic scale.

cm Be/Ni are lower by about 7% and 23%, respectively. Note the effect of the decay constant on the brightness at 2 ms. For example, even though the 150-cm Be and 40-cm Be/Pb have nearly the same peak brightness, the 40-cm Be/Pb case is a factor of three lower in brightness at 2 ms. Depending on the application, this faster decay may prove to be a distinct advantage.

In Figure 5 we compare the temporal response of the source brightness for the 60-cm Be/Pb geometry for three cases: an instantaneous proton pulse, a 0.5-ms pulse, and a 1-ms pulse. The ratios of the time-dependent peak brightness is 3:1.6:1 for the instantaneous, 0.5-ms, and 1-ms pulses, respectively.

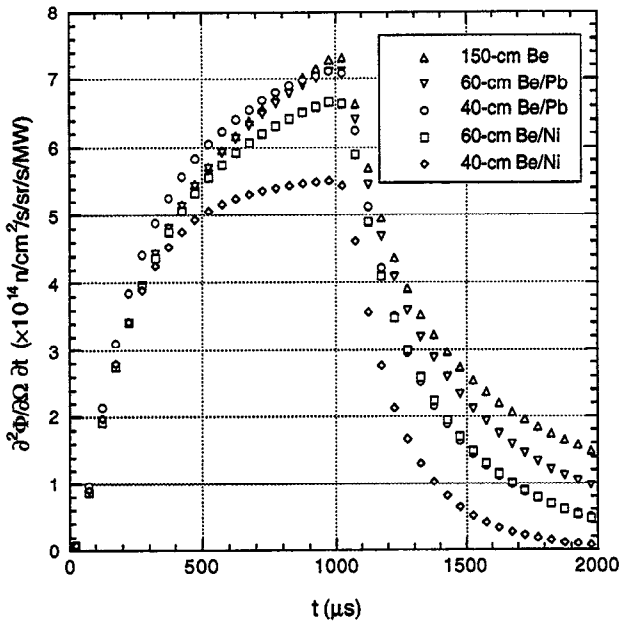

Figure 4. Pulse shapes (E < 5 meV) for a 1-ms proton pulse for the five reference cases.

3.3 Time-Energy Spectrum

A full characterization of the source brightness requires the calculation of the double differential of the source brightness in both time and energy. Tallying neutrons crossing the moderator leakage surfaces, we bin into 4 energy bins per decade from 178 μeV to 10 eV, and into 16 time bins per decade from 100 ns to 86.6 ms. An example of this detail is shown in Figure 6, which is a contour plot of source brightness as a function of time and energy for the 60-cm Be/Pb case. This detail is then used to evaluate the accuracy of source parameterization described in the next section.

3.4 Reduced Time Spectrum

In the slowing-down region, it is well known that the pulse shape is nearly invariant when the neutron leakage time t is normalized by the neutron wavelength λ. We take advantage of this fact when characterizing this region by tallying the neutrons crossing the moderator leakage surfaces as a function of the "reduced time" t/λ from 0.63 μs/Å to 100 μs/Å with a resolution of 20 bins per decade, and in coarse energy bins of one bin per decade from 1 meV to 1 keV. Results of this analysis are shown in Figure 7 for the 60-cm Be/Pb case. We see that the pulse shape when plotted as a function of reduced time is nearly the same for energies in the range 1 to 1000 eV.

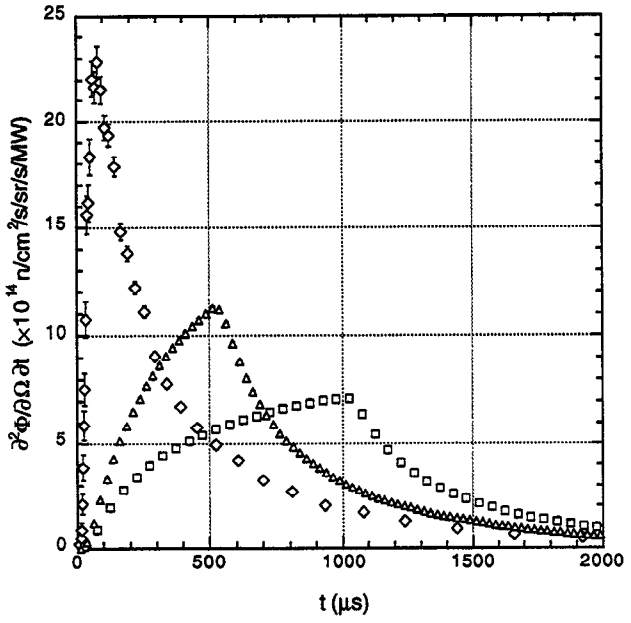

Figure 5. Pulse shapes (E < 5 meV) for the 60-cm Be/Pb case for three proton pulse widths: (◆) instantaneous; (▲) 0.5 ms; (■) 1 ms.

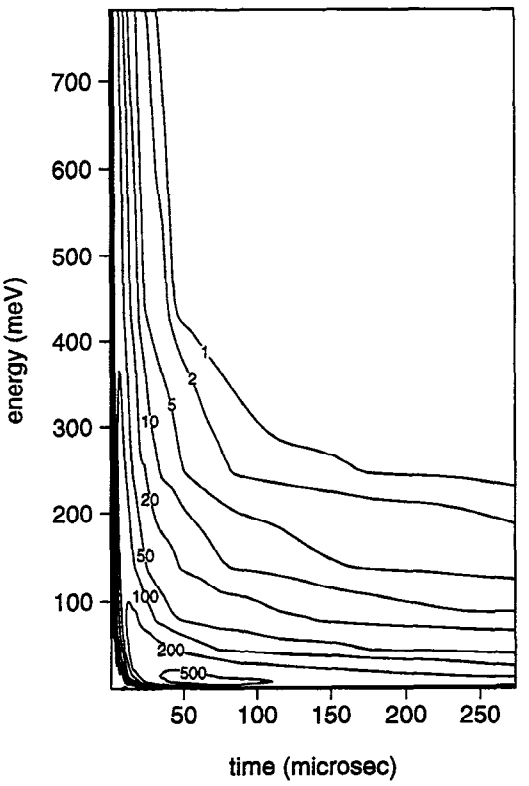

Figure 6. Contour plot of brightness as a function of time and energy for the 60-cm Be/Pb case. The units on the contour values are 10^{15} n/cm^2/s/sr/eV/s/MW.

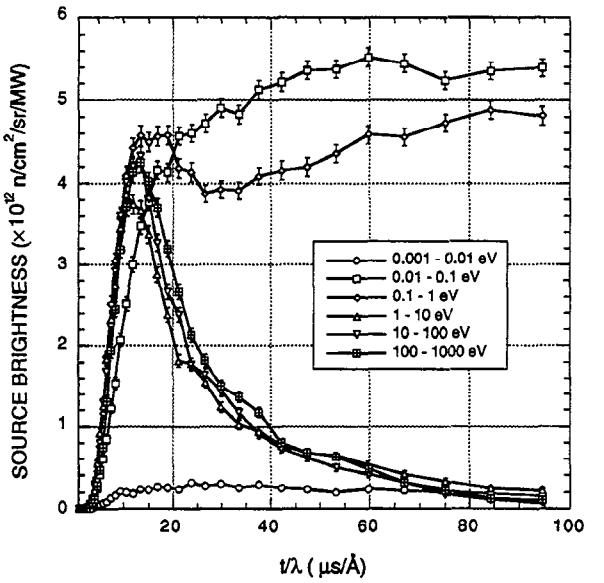

Figure 7. Reduced time spectrum for the 60-cm Be/Pb case.

3. Parameterization of the Source Brightness

The calculated brightness is used as a source term by the Monte Carlo instrument design code using the MCLIB library. Parameterization of time and energy dependence of the source brightness allows us to efficiently sample from a function describing the source distribution using simple random sampling.

The semi-empirical function used to characterize the source term is a Gaussian $G(t/\lambda)$ convolved with the sum of epithermal and thermal decay terms whose relative magnitudes are controlled by a switch function $S(\lambda)$:

$$I(t,\lambda) = G\left(\frac{t}{\lambda}\right) \otimes \left\{[1-S(\lambda)]\exp\left(-\frac{t/\lambda}{\eta}\right) + S(\lambda)\left[(1-R)\exp\left(-\frac{t}{\tau_1}\right) + R\exp\left(-\frac{t}{\tau_2}\right)\right]\right\}, \tag{1}$$

where

$$G\left(\frac{t}{\lambda}\right) \equiv \frac{1}{\sigma\sqrt{2\pi}} \exp\left\{-\frac{1}{2}\left[\frac{(t/\lambda)-\Delta}{\sigma}\right]^2\right\} \tag{2}$$

and

$$S(\lambda) = \exp\left(-\frac{\lambda_0}{\lambda}\right)^P. \tag{3}$$

There are eight fitting parameters in this function. The Gaussian $G(t/\lambda)$ is characterized by two parameters, the width σ and the delay Δ. The first term of the function with which the Gaussian is convolved describes the decay of the epithermal portion of the spectrum, where the "epithermal exponential" η defines the decay constant of epithermal neutrons. These three parameters, σ, Δ, and η, are determined by a least-squares fit to the reduced time spectrum over the range 1 μs/Å to 30 μs/Å. The parameters τ_1 and τ_2 are the long- and short-time decay

constants, respectively, on the tail of the thermal portion of the spectrum, while the ratio R defines the fraction of the tail populated by neutrons following the short-time decay. The switch function $S(\lambda)$ provides a smooth transition from an epithermal decay constant to a thermal decay constant. The switch function parameters λ_0 and P are determined by finding an appropriate value of the thermal/epithermal ratio at each of 18 wavelengths between 0.1 Å and 15 Å, and then least-squares fitting to these values (see also Figure 4 of ref. [2]).

Table 2 gives the values of the fitting parameters for the five reference cases. Note that, for all cases (except, perhaps, for the 60-cm Be/Pb case), only the thermal decay constants τ_1 and τ_2 vary appreciably, implying that the outer reflector size and material has a large effect on the tail of the thermal portion of the spectrum but only weakly impacts all other temporal characteristics.

Table 2. Fitting parameters for the five reference cases.

Case	τ_1 (μs)	τ_2 (μs)	R	η (μs/Å)	Δ (μs/Å)	σ (μs/Å)	λ_0 (Å)	P
40-cm Be/Ni	276	—	0	9.21	6.41	2.45	1.03	1.58
60-cm Be/Ni	414	—	0	9.24	6.40	2.34	0.90	1.81
40-cm Be/Pb	610	170	0.667	8.67	5.68	2.08	0.86	2.63
60-cm Be/Pb	734	170	0.4	7.37	3.32	3.32	1.2	0.6
150-cm Be	1710	380	0.6	8.96	6.45	2.54	0.77	2.3

5. Conclusion

We have characterized the temporal and energy dependence of the moderator brightness for five different reflector configurations for a flux-trap target system with four coupled liquid hydrogen moderators. An all-Be reflector yields the highest time-integrated low-energy brightness at the expense of very long tails. An outer reflector of Ni, which is a moderate thermal neutron absorber, exhibits very short tails. An outer reflector of Pb produces a higher peak brightness due to the additional neutron production derived from the Pb, while its low absorption cross section generates a high time-integrated brightness with only moderate tails.

6. Acknowledgements

This work was supported by the US. Department of Energy, BES-DMS, under Contract No. W-7405-Eng-36.

7. References

1 . G. Russell, et al., "Coupled Moderator Neutronics," these proceedings.

2 . P. Seeger, "The MCLIB Library: Monte Carlo Simulation of Neutron Scattering Instruments," these proceedings.

3 . R. E. Prael, "A Review of Physics Models in the LAHET™ Code," Los Alamos National Laboratory report LA-UR-94-1817, and references cited therein.

4. T. O. Brun, et al., "LAHET Code System/CINDER'90 Validation Calculations and Comparison with Experimental Data," Proceedings of the Twelfth Meeting of the International Collaboration on Advanced Neutron Sources, ICANS-XII, Abingdon, U. K., 24-28 May, 1993, Rutherford Appleton Laboratory Report 94-025.

5 . P. Ageron, Nucl. Instr. and Meth. **A284** (1989) 197.

ICANS-XIII
13th Meeting of the International Collaboration on
Advanced Neutron Sources
October 11-14, 1995
Paul Scherrer Institut, 5232 Villigen PSI, Switzerland

THE PERFORMANCE OF NEUTRON SPECTROMETERS AT A LONG-PULSE SPALLATION SOURCE

Roger Pynn and Luc Daemen
Los Alamos National Laboratory, Los Alamos, New Mexico 87545, USA

ABSTRACT

At a recent workshop at Lawrence Berkeley National Laboratory [1], members of the international neutron scattering community discussed the performance to be anticipated from neutron scattering instruments installed at a 1 MW long-pulse spallation source (LPSS). Although the report of this workshop is long, its principal conclusions can be easily summarised and almost as easily understood. This article presents such a synthesis for a 60 Hz LPSS with 1 msec proton pulses. We discuss some of the limitations of the workshop conclusions and suggest a simple analysis of the performance differences that might be expected between short- and long-pulse sources both of which exploit coupled moderators.

1. Results from the Berkeley Workshop[1]

The essential results are contained in Table 1. The rows of the table pertain to various types of instruments while the columns describe factors which affect the relative performance of spectrometers and diffractometers at the LPSS and the ILL, which is the benchmark for this comparison.

Total length, L (m) — except for SANS, the total length of each instrument is chosen to provide a wavelength resolution, $\delta\lambda$, that matches that traditionally used at a reactor. For pinhole SANS, the instrument length is dictated by the need for angular resolution that matches that at the reactor. In the case of NSE, the shortest spectrometer one can imagine building at the LPSS still does not have as poor wavelength resolution as is traditionally used at a reactor.

Chopper pulse length, Δt (msec) — in some cases, the 1 msec LPSS pulse is too long to allow the required wavelength resolution to be achieved with a flight path of reasonable length so a pulse-defining chopper must be used.

Incident wavelength bandwidth, $\Delta\lambda$ (Å) — this is the range of wavelengths that is used simultaneously at the LPSS. The maximum possible value of $\Delta\lambda$ is given approximately by 4.T/L where T is the inter-pulse spacing in milliseconds. For all instruments, the counting frame has to be reduced from its nominal value of 16.7 msec (for a 60 Hz source) to account for penum-

Keywords: Long Pulse Spallation Source, Figure of Merit, Pulse Shape

Table 1

Spectrometer Type	Equiv ILL Instr.	Total Length (m)	Chopper Δt (msec)	§ Δλ (Å)	§§ δλ (Å)	TOF Gain	¶ Relative Incident Δα	¶¶ Relative Detected Δα	* Relative Flux	** Relative Dyn. Rnge.	1 MW LPSS Performance
Small Angle Scattering											
– 21 m flight path; 10 Å wavelength	D22	21	-	3	1.2	2.5	1	1	0.25		0.6 x ILL
– 21 m flight path; 6 Å wavelength	D22	21	-	3	0.7	4.3	1	1	0.25		1 x ILL
Reflectometer	D17	60	-	1	0.07	15	1	1	0.25		3.5 x ILL
Powder Diffraction											
Low Resolution	D7	40	0.375	1.6	0.04	40	0.2	1	0.075		0.6 x ILL
Medium Resolution	D16	40	0.019	1.6	0.002	800	0.2	10	0.004		6 x ILL
High Resolution	D2B	160	0.02	0.4	0.0005	800	0.2	10	0.003		5 x ILL
Amorphous Material Diffraction	D4	40	0.019	1.6	0.002	800	0.2	1	0.004		0.6 x ILL
Single Crystal Diffraction											
Laue Diffraction		20	-	3.2	0.2	16	1	0.5	0.2		1.5 x ILL
Diffuse Scattering	D7	20	-	3.2	0.2	16	1	1	0.2		3 x ILL
High Resolution Inelastic Scattering											
– multi-chopper spectrometer	IN5						1	1	4	0.5 - 1.0	2 - 4 x ILL
– time focussed TOF spectrometer	IN6						1	1	3.2	0.5	1.6 x ILL
– backscattering (1 μeV resolution)	IN10	92	0.025	0.7	0.001	700	1	1	0.006	0.07 - 1.0	0.25 - 4 x ILL
– backscattering with MUSICAL mono.		92	0.025	0.7	0.001	700	1	1	0.006	1	4 x ILL
Neutron Spin Echo	IN15	16	-	4	1	4	1	1	0.25		1 x ILL
S(Q,E) Spectroscopy (2% resol)	IN4C	15	0.01	4.2	0.003	1400	1	1	0.002	0.2 - 0.8	0.7 - 2.5 x ILL
S(Q,E) Spectroscopy (20% resol)	IN4C	15	0.5	4.2	0.13	32	1	1	0.1	0.25 - 1.0	0.8 - 3.2 x ILL
Conventional Three Axis Machines											
Cold Neutron TAS	IN14		-			1	1	1	0.4		0.4 x ILL
Thermal/Hot Neutron TAS	IN8/IN1		-			1	1	1	0.2		0.2 x ILL
Augmented Three Axis Machines											
Multi-Analyser TAS (RITA)		30	0.2	1.85	0.13	14	0.3 - 1	1	0.25		1 - 3.5 x ILL

§ incident-wavelength bandwidth, including chopper penumbra effects (or usable bandwidth if this is smaller)
§§ incident-wavelength resolution (or required resolution if this is larger)
¶ maximum usable incident angular divergence compared to same quantity for reactor experiment
¶¶ maximum usable detected angular divergence compared to same quantity for reactor experiment
* time-average flux on sample for LPSS divided by same quantity for a 60 MW reactor. Flux is averaged over appropriate part of time pulse and harmonically averaged over wavelength bandwidth. This number also includes monochromator, chopper, guide, and filter transmissions.
** relative dynamic range of LPSS and reactor spectrometers if restricted by repetition frequency

bra effects. In one case (the augmented three-axis spectrometer) the counting frame has been reduced even further to avoid contamination from fast neutrons, although this might not be necessary if this spectrometer were to be located on a curved guide. If the useful wavelength bandwidth does not correspond to the entire measurement frame — as, for example, in the case of three axis spectrometers where only one (Q,E) point is measured — it is the useful bandwidth that appears in this column of the table.

Incident wavelength resolution, $\delta\lambda$ (Å) — whether the pulse width used at the LPSS is set by the neutron source or a chopper, the wavelength resolution is given by $\delta\lambda \approx 4.\Delta T/L$. In two cases — SANS and NSE — the wavelength resolution provided by the untailored pulse from the LPSS is too good. In this case, the resolution that would be used in a corresponding experiment at a reactor is entered in the table.

TOF Gain — this is simply the ratio of wavelength bandwidth, $\Delta\lambda$, to wavelength resolution, $\delta\lambda$, and reflects the number of different wavelengths which are used simultaneous at the LPSS. When a pulse-defining chopper is used at the LPSS, the TOF gain is increased from the inverse of the source duty factor (i.e. $1/0.06 \approx 17$) by a factor of $1/\Delta t$. The average flux on the sample is *reduced* by the same factor.

Relative incident angular bandwidth — this column contains the ratio of the incident angular bandwidth at LPSS to that at a reactor. With the exception of specular neutron reflection, incident angular bandwidth and incident angular collimation are the same, reflecting the fact that, for conventional neutron instruments, one has no method of coding the angle of incidence of neutrons within a divergent beam. Various focusing techniques are used to increase the incident angular bandwidth. At reactors, vertically (and in rare cases, horizontally) curved monochromators provide divergences of up to 5° (FWHM). At pulsed sources, optical elements such as converging guides are used to increase angular bandwidth. Such guides are limited to providing an angular divergence (FWHM) that is about 6 times the nickel critical angle, or $\approx 0.6\ \lambda°$. Even for cold neutrons, this divergence is generally less than that which can be obtained with focusing monochromators. However, for some applications — such as specular neutron reflection — increased horizontal and vertical angular bandwidth can be used at a pulsed source, while only increased vertical divergence is available at a reactor without affecting monochromatisation.

Relative detected angular bandwidth — this column contains the ratio of the detected angular bandwidth at the LPSS to that at a reactor. In most cases this ratio is unity, reflecting the fact that the same secondary spectrometer is used at both types of source. However, for wavelength-dispersive powder diffraction at the LPSS, it is sometimes possible to use very high angle detectors which can accept neutrons scattered into a large solid angle without affecting resolution. In the case of Laue diffraction, participants at the Berkeley workshop thought it likely that image plate technology would allow neutrons to be detected within a solid angle that is about twice as large as could be detected with conventional detectors at a pulsed source.

Relative flux on sample — this column contains the ratio of the time-averaged neutron flux incident on a sample at the LPSS to that at the ILL. There are a number of effects that have to be considered to derive this number:

- the time averaged cold flux of a 1 MW LPSS is 25% of that of the ILL and the time-averaged thermal and hot fluxes are both about 12% of the ILL.
- for those instrument — like IN5 or IN6 — that see the peak flux at the LPSS, the relative cold flux is about 4 times higher at the LPSS than at ILL.

- for those instruments which use a pulse-defining chopper at the LPSS but do not use a chopper at the ILL, the flux on the sample is reduced by the ratio of Δt and the natural pulse length of the source (1 msec). If the pulse-defining chopper cuts off the pulse tails there may be an additional reduction in intensity.
- transmission through monochromators and filters at the reactor and through choppers at the LPSS are considered here, as is guide transmission in appropriate cases.
- the intensity of the incident neutron beam is averaged over the incident wavelength band (the harmonic average turns out to be appropriate [2]).

Relative dynamic range — in some cases, notably for chopper spectrometers such as IN5, IN6, IN10, and IN4C, the 60 Hz repetition rate of the LPSS may yield a dynamic range in energy transfer which is larger than that used at the reactor. Depending on the experiment, this may be a disadvantage for the LPSS.

Overall Performance — the overall performance for neutron scattering relative to ILL is obtained by taking the product: (relative dynamical range) x (relative flux) x (relative detected angular bandwidth) x (relative incident angular bandwidth) x (time-of-flight gain). This number is given in the final column of the Table. The values given are in substantial agreement with those derived at the LBNL workshop.

The relative performances contained in the Table are those that apply to LPSS and ILL instruments with similar resolution in the important dimensions of Q and E space. It is worth emphasizing that the comparisons are for unoptimised instruments — we have simply tried to mimic a reactor experiment at an LPSS without trying to make any qualitative changes that would improve performance.

2. Resolution of LPSS and CW Instruments

The results of the Table assume that it is reasonable to compare instruments which have the same FWHM wavelength resolution, $\delta\lambda$, and that one does not need to account for the different shapes of the wavelength-resolution functions at reactors and the LPSS. To address the effects of pulse shape on wavelength resolution we make use of work by Sivia, Silver, and Pynn [3], who postulated that

$$FOM(\Delta t) = \frac{\phi_p \left|\hat{f}(\omega)\right|^2}{\hat{f}(0)[1 + N_B / N_S]}$$

could be used as a figure of merit when a neutron scattering instrument is used to obtain information on scale $\Delta t = 2\pi/\omega$ from a measurement made with a resolution function f(t) whose Fourier transform is $\hat{f}(\omega)$. In this expression, N_B is the background, N_S is the signal, and ϕ_p is the source flux.

In any neutron scattering instrument, the complete resolution function is obtained by convoluting the various contributions that arise from wavelength uncertainties, collimations etc. Since the FOM is proportional to the squared modulus of the Fourier transform of the resolution function, it will involve a product of terms arising from the various sources of resolution. We may thus compare the performance of instruments whose wavelength resolution functions have different shapes by considering the contribution to the FOM from wavelength resolution alone, provided the other sources of resolution are the same for the instruments we are comparing.

Figure 1 shows two resolution functions which have the same integral intensity and the same FWHM — a Gaussian which is supposed to represent wavelength resolution at a reactor instrument and an Ikeda-Carpenter [4] form for a liquid hydrogen moderator with a decay time constant of 700 μsec, folded with a 1 msec proton pulse to represent the LPSS wavelength resolution. We have evaluated the FOM given above with the background term N_B set to zero for both of these resolution functions and display the results in Fig 2. The horizontal axis in Fig. 2, called ω, is the Fourier inverse of λ. The units are chosen so that one wavelength unit in Fig 1 maps to $\omega = 2\pi$ in Fig. 2. Except for the sharp dip in the LPSS FOM, the two curves are fairly similar for values of $\omega < 2\pi$, indicating that it is reasonable to use the FWHM as a measure of resolution when comparing instruments at a reactor and an LPSS. Thus, the performance Table is expected to be reasonably accurate, in spite of the different shape of the wavelength resolution function at the two types of source.

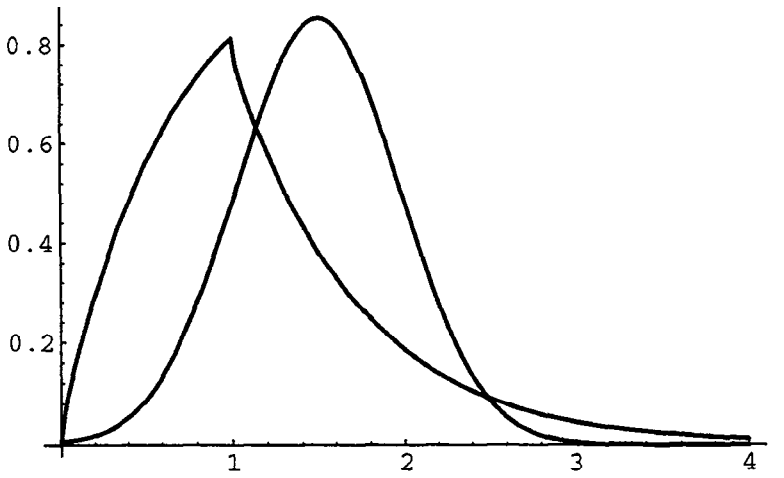

Figure 1. Normalised wavelength resolution functions for a reactor source (Gaussian) and an LPSS.

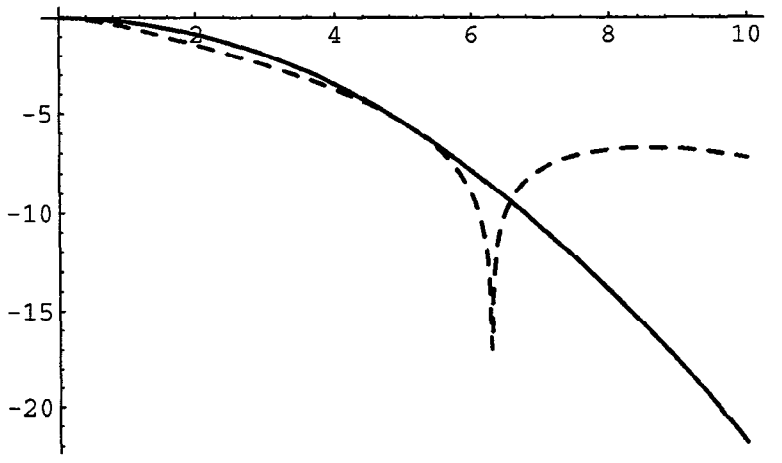

Figure 2. The natural logarithm of the FOM for Gaussian (solid curve) and LPSS (dashed curve) resolution functions is plotted against the Fourier variable ω.

The sharp dip in the FOM for the LPSS deserves comment. It arises from the fact that the proton pulse is assumed to be rectangular in shape. Since this pulse is convolved with the Ikeda-Carpenter form to obtain the overall LPSS pulse shape, the Fourier transform of the LPSS pulse will always have zeroes at multiples of 2π times the width of the proton pulse (taken as unity in plotting Figure 2). This means, of course, that one cannot measure this

Fourier component of a signal. One way to understand this a little better is to imagine a signal composed of equally spaced delta functions — a comb. If the spikes are separated by a distance x and they are measured using a "top hat" resolution function of width x, the measured signal will always be constant, wherever one centers the resolution function.

Before one condemns such a resolution function as useless one should realise that the same effect occurs for a triangular resolution function and that such a shape is highly prized on the spectrometer IN5 at ILL. The point is that although one cannot measure a few localised Fourier components using triangular or rectangular resolution functions, these functions have the advantage of facilitating measurement of high-ω Fourier components. This fact is also clear from Figure 2, where the Gaussian resolution function dies at large values of ω while the envelope of the LPSS resolution function preserves a fairly high value. In a Maximum Entropy type of data analysis [5], one would expect it to be easier to obtain reliable estimates of a few missing Fourier components than to divine the entire high frequency part of the map. In sum, the LPSS resolution function is probably preferable to a standard Gaussian because its leading edge is sharper.

3. Comparing Neutron Scattering Instruments at SPSS and LPSS

It is tempting to ask whether the results shown in the Table can be applied to instruments at an SPSS with coupled moderators. To answer this question, we first examine the pulse shapes that one might expect from SPSS and LPSS. These are shown in Figure 3. The upper part of the Figure shows Ikeda-Carpenter pulses for a liquid hydrogen moderator with a storage time constant of 300 μsec. The lower part displays pulses with a decay constant of 700 μsec. As Russell et al demonstrate elsewhere in these proceedings, the longer time constant is more typical of a coupled, strongly reflected target/moderator system (CSR), while the shorter one might refer to a coupled weakly-reflected system (CWR). Simulations show that the CSR provides about twice the integrated intensity of the CWR and this fact has been accounted for in plotting Figure 3.

The first conclusion one can draw from Figure 3 is that there is little point in strongly coupling the moderators at an SPSS if one is only interested in peak intensity — the peak value changes very little with increasing decay constant. Thus, for an instrument such as IN5, one could equally well use either CSR or CWR target systems at an SPSS. This is not true for the LPSS, which gains with a CSR target system. The reason for this is clear — because the LPSS pulse is derived by convolving a rectangular proton pulse with an SPSS pulse, the long tail of the latter contributes to the peak intensity of the LPSS pulse.

The bottom line from Figure 3 is that an SPSS of a given power and repetition rate is less than a factor of two better than an LPSS of the same power and repetition rate for instruments, like IN5 and IN6, which depend on the peak neutron flux.

Other instruments listed in the Table attain their performance gains over a CW source because they benefit from the full TOF gain given by the inverse duty cycle of the source. While one has to be careful extrapolating this argument to sources with lower and lower duty cycles (cf the article on reflectometry by Fitzsimmons in these proceedings), Figure 3 tells us what happens if the full TOF gain is relevant.

The relative TOF gains for the various pulses are given by the inverse ratios of their FWHMs, at least to the level of approximation in the Table. Measuring the peaks in Figure 3, one finds TOF gains in the ratio SPSS(300):SPSS(700):LPSS(300):LPSS(700) of

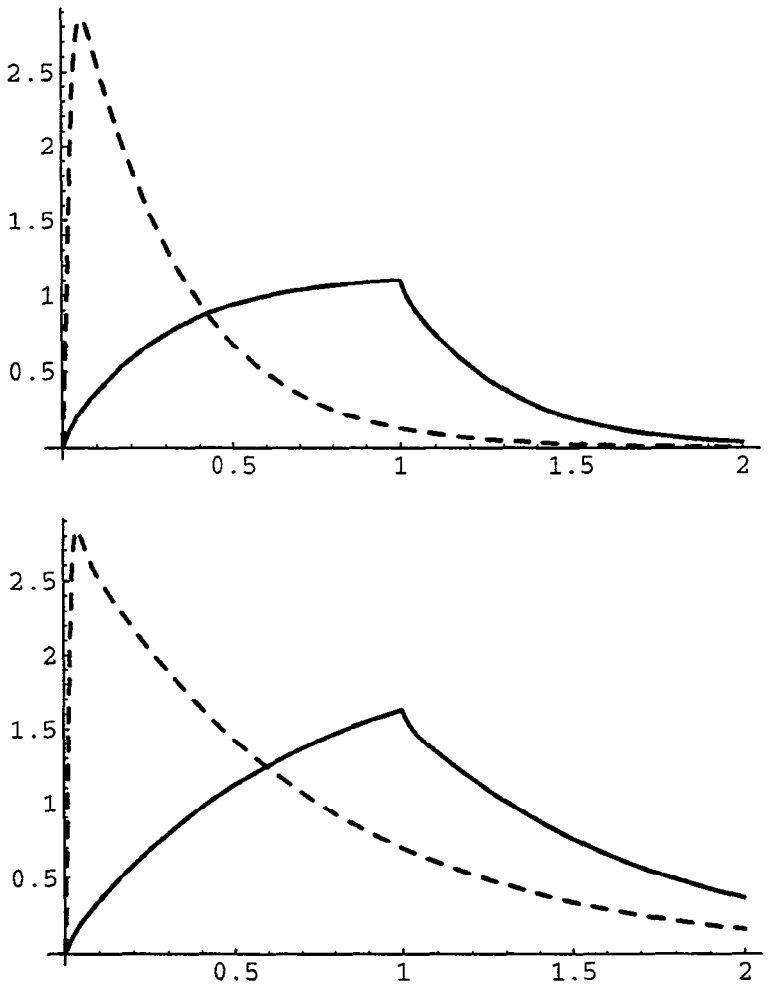

Figure 3. Pulse shapes for SPSS (dotted curve) and LPSS (solid curve) with different time constants. In the upper panel the decay constant is 300 μsec corresponding to a coupled, weakly-reflected target/moderator system (CWR) while in the lower panel the decay constant is 700 μsec, a value more typical of a strongly reflected system (CSR). The integrated intensity of the pulses in the lower panel is twice that of those in the upper panel.

4.2:2.2:1.1:1. The obvious conclusion is that, once more, there is little point in strongly coupling the target/moderator system at an SPSS. By doing so, one loses a factor of almost two in TOF gain and picks up the same factor in integrated intensity. For the LPSS on the other hand, the loss of TOF gain from strong coupling is about 10%, while the gain in overall intensity is a factor of 2.

The bottom line is that for instruments which can benefit from the full TOF gain, the SPSS with either a CWR or CSR target system performs about twice as well as a LPSS of the same power and repetition rate. An important caveat on this statement is that, for equal resolution, the SPSS will have about 4 times the dynamic range per measurement as the LPSS. The whole of this range must contain equally useful information for the performance comparison stated above to be true.

4. Pulse Shapes at SPSS and LPSS

Another instructive exercise is to compare FOM's for SPSS and LPSS pulse shapes. This is done in Figure 4 for a 300 μsec decay constant. Results for a 700 μsec decay constant are very similar. One sees that for measuring structure on a scale of a few times the FWHM of the resolution function (which is what a neutron scattering instrument is generally designed to do), the LPSS pulse shape in to be preferred. This is actually not very surprising when one

looks at the relative contributions of the pulse tails to the two peak shapes. Since the integrated intensity produced by both LPSS and SPSS is the same by construction, the FOMs for measuring integrated intensity (i.e. the values of the FOMs at $\omega = 0$) are identical for the two sources. For structure on a scale significantly finer than the FWHM (i.e. for large values of ω), the SPSS line shape is somewhat better because its sharp leading edge preserves high Fourier components of the signal.

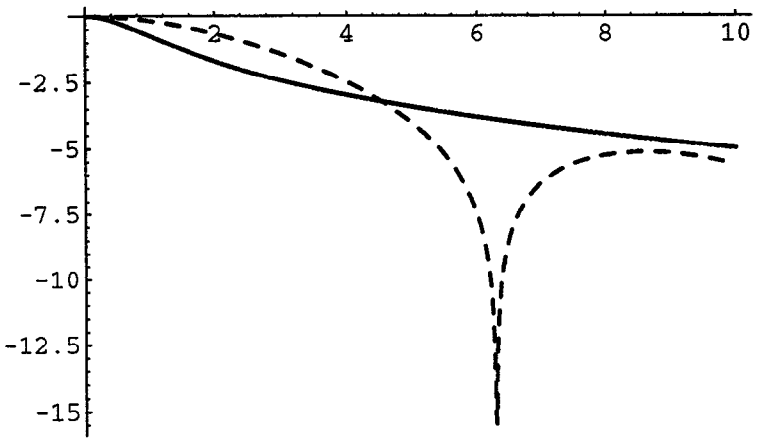

Figure 4. Natural logarithm of the FOM for the SPSS (solid line) and LPSS (dashed line).

Figure 5 shows the FOMs for SPSS and LPSS pulse shapes with 700 μsec decay constant on a linear (as opposed to logarithmic) scale. Recalling that the FOM is inversely proportional to the measurement time required to achieve a given accuracy, one sees that for measuring structure on a scale of two or three times the FWHM of the resolution function (i.e. for values of 2 to 3 on the abscissa of Figure 5), the LPSS out-performs the SPSS by a factor of two or more, effectively canceling the TOF gain noted above for the SPSS.

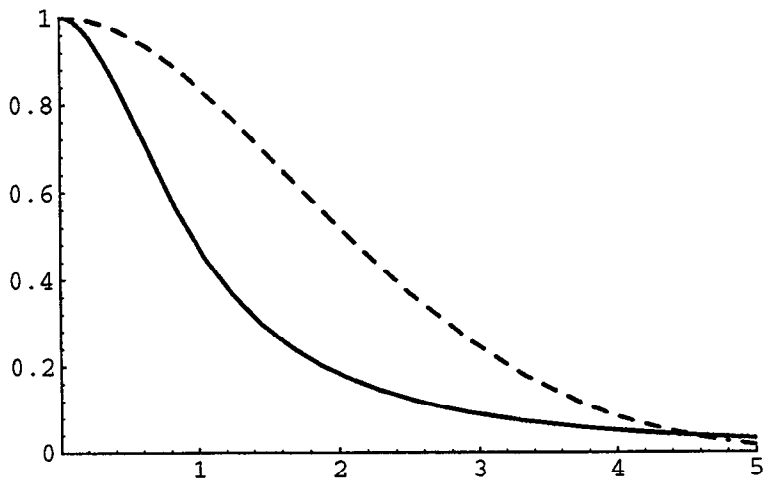

Figure 5. FOMs for SPSS (solid line) and LPSS (dashed line) on a linear scale. A 700 μsec decay constant was used for both pulses.

It is worth noting that the LPSS offers in principle, the possibility of tuning the FOM by tailoring the shape of the proton pulse, a problem we will treat in more detail in a forthcoming paper.

We have chosen to use the Ikeda-Carpenter form for the pulse shape at a spallation source because it provides a simple analytic expression that is easily Fourier transformed and integrated. However, we do not expect our quantitative results to depend very strongly on this

choice because it mimics rather well the exponential tail of the pulse — at least out to a time of order the proton pulse width at an LPSS. A minor change in pulse shape will not affect our qualitative conclusion that the effects of pulse tails on resolution need to be carefully considered in the design of both LPSS and SPSS and that these effect may substantially modify simple minded comparisons based only on peak flux arguments.

5. Conclusion

We have shown that simple scaling arguments involving few variables can be used to provide a first approximation to the comparison of instrument performance at LPSS and CW sources. In addition, we have demonstrated that a comparison of performance at SPSS and LPSS sources is more complex. It appears that the best target/moderator system for an SPSS designed for low-resolution studies will be a coupled, weakly reflected system. At an LPSS, a coupled, strongly reflected system is preferred. For SPSS and LPSS sources of equal power and repetition rate, the calculations presented here do not predict large performance differences for instruments at the two sources. Nevertheless, detailed Monte Carlo simulations will be required to reach firm, quantitative conclusions.

6. Acknowledgments

We are grateful to Devinder Sivia for a discussion of the properties of rectangular resolution functions. This work was approved by the U.S. Department of Energy under contract W-7405-ENG-36 with the University of California.

7. References

[1] Proceedings of a workshop on the performance of research instrumentation at a 1 MW LPSS held at Lawrence Berkeley National Laboratory in April 1995. [Available from Lee Schroeder at LBNL.]
[2] M. R. Fitzsimmons, Nucl. Instrum. Methods. {To be published.]
[3] D. S. Sivia, R. N. Silver, and R. Pynn, Nucl. Instrum. Methods, A287, 538 (1990)
[4] S. Ikeda and J. M. Carpenter, Nucl. Instrum. Methods, A239, 536 (1985)
[5] E. T. Jaynes, in: Maximum Entropy and Bayesian Methods in Applied Statistics, ed. J.H. Justice (CUP, 1986)

ICANS-XIII
13th Meeting of the International Collaboration on
Advanced Neutron Sources
October 11-14, 1995
Paul Scherrer Institut, 5232 Villigen PSI, Switzerland

OPTIONS FOR NEUTRON SCATTERING INSTRUMENTS ON LONG PULSE NEUTRON SOURCES

Günter S. Bauer

Paul Scherrer Institut, CH-5232 Villigen PSI, Switzerland

ABSTRACT

Instrumentation on long pulse sources can be approached either by instruments from short pulse sources and hence using mainly inverted time of flight techniques or by adopting reactor type instruments and making use of the time dependence of the source flux to enhance their performance substantially. While the first approach requires more or less single use of a beam line by one instrument, the second one allows multiple use of neutron guides, as customary on reactors and hence can make much better use of the source with gains up to 100 for time of flight spectrometers. To a certain extent, the design parameters of the source depend on which of the two approaches is chosen.

1. Introduction

While the scientific opportunities offered by neutron sources of different designs are - and should continue to be - the main line of arguments, cost effectiveness of their exploitation is another important issue. In this context long pulse neutron sources certainly have a certain leadway over short pulse sources, especially in the medium-to-high beam power regime (above a few Megawatts) [1], where a short pulse neutron source requires a linac capable to accelerate a sophisticatedly chopped beam of H^--ions and one or several rings to compress the linac macropulses into the desired short pulses. The design of the target and its surroundings is much more difficult for a short pulse source than for a source whose pulses are 200 μs long or more. The linac (no rings are required) for such a source can run on protons (suitable ion sources are available) and does not require chopping its macropulses, which is not only a significant technical simplification but also results in higher operating efficiency and probably in better reliability. Also, on the target side the mechanical load from long pulses is much smaller than from short pulses [2] which, if perhaps not a feasibility issue, will certainly affect the life time of the target and hence cost and availability of the source.

It is important, however, to keep in mind that short pulse neutron sources can offer certain possibilities in the use of epithermal neutrons and in very high resolution measurements which are unique and hence cannot be the subject of a debate on cost-effectiveness. Recent arguments on this subject therefore have concentrated more on the comparison in cold

Keywords: Instruments, time of flight, multiplexing, long pulse

neutron scattering and have been made on an instrument-to-instrument basis, using reactor instruments as the standard [3].

One problem of such a comparison is that, on the long pulse source, extensive use of inverse (or indirect) time of flight techniques has been assumed, whilst many of the reactor instruments are based on crystal monochromators. This not only leaves some ambiguity in the comparison (as manifest from the range in gain factors given for several of the instruments) but also does not account at all for the degree of source utilization, namely the number of instruments that can be accommodated at a source. The fact that the high flux reactor at ILL offers about 50 instrument locations whereas there are less than 20 on ISIS, has to do with the kind of technique used. It is the purpose of this paper to intensify the discussion on the options offered by adoption of essentially reactor-like instruments, which are well understood, to the opportunities of a time structure of the source. Clearly, most of these arguments are not really new. They have been extensively discussed in the context of the German SNQ-project a decade ago [4], [5], [6], but the present renaissance of the long pulse source enthusiasm seems to largely ignore them.

2. Energy selection in neutron scattering instruments

All neutron scattering instruments require some kind of energy selection in the beam incident on and/or scattered from the sample in order to obtain the desired information on momentum and energy transfer in the scattering process. The two traditional methods to accomplish this energy selection are Bragg-reflection from a crystal and selection by time of flight after a common starting time. Depending on which method is used, we can class the instruments according to Table 1, which also summarizes some of the consequences associated with the different selections.

Table 1: Beam utilization for different classes of neutron scattering experiments

Class of instrument	Technique	Primary energy selection	Secondary energy selection	Comments	
Crystal spectrometer (-diffractometer)	mono-chromatic incident beam	Crystal	Crystal none (difr.)	Multiple use use of beam or guide	Sample in monochro-mated beam
Direct time of flight spectrometer		Crystal Choppers	TOF	End position	
Inverted time of flight spectrometer (-diffractometer)	"white" incident beam	TOF	Crystals none (difr.)	Single use of beam or guide	Sample in direct beam

Since we can safely assume that, on a long pulse source, intensive use will be made of neutron guides, which can be quite effective also for thermal neutrons when coated with supermirrors, we will discuss very briefly the situation for this cases only.

The characteristic feature of a neutron guide is that the transverse momentum in both directions, Δk_x and Δk_y is constant for all neutron energies. This leads to a momentum distribution of constant width Δk_x and Δk_y and a variable length k_z, as shown in Fig. 1.

When momentum selection is done by time of flight with constant time intervals, the momentum interval selected, dk_z, is proportional to k^2. The intensity contained in each interval depends on the phase space density in the neutron guide, which is shown

(Maxwellian part of the spectrum only!) for two different moderator temperatures, namely 35 K and 350 K (note, that the curve for 350 K has been multiplied by a factor of 10!)

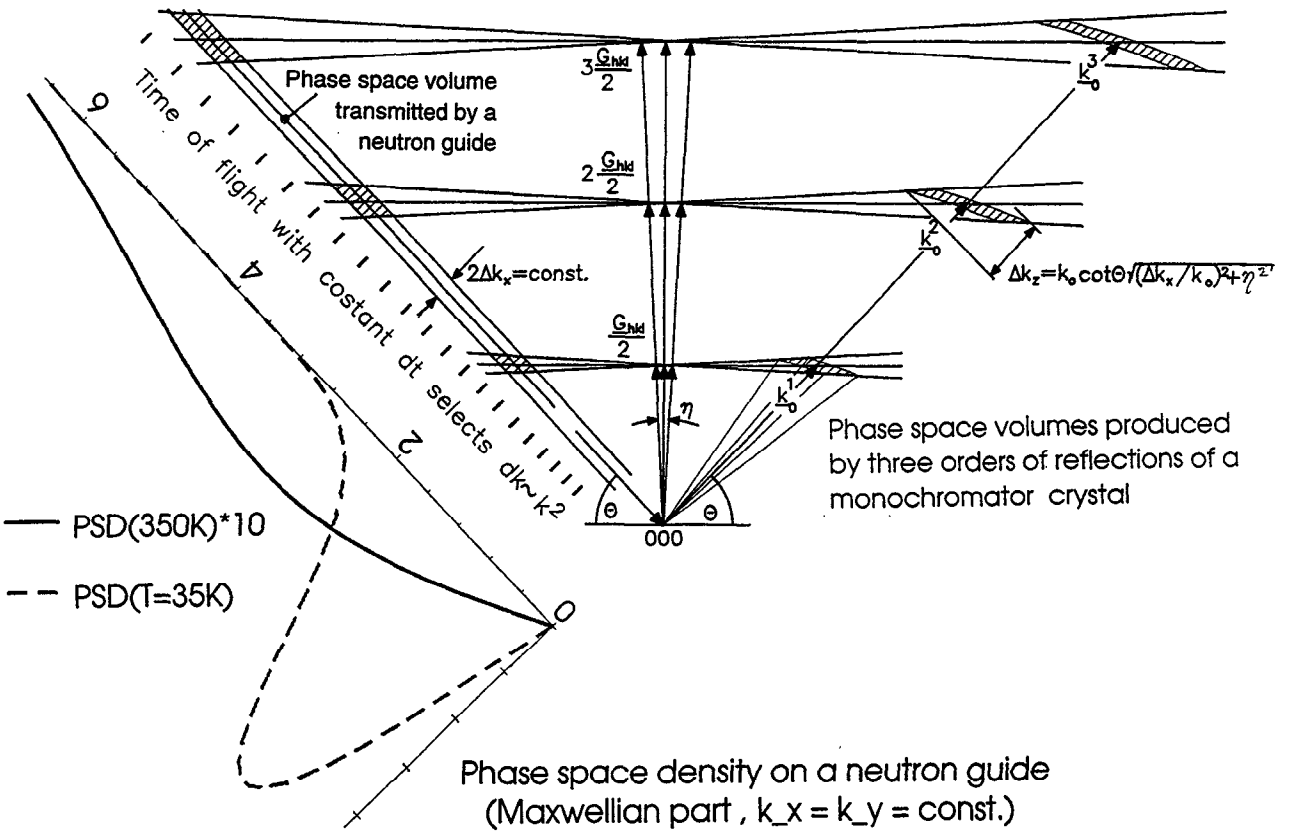

Figure 1: Neutron momentum selection at a neutron guide

Also shown is the situation for a monochromator crystal (or a multilayer, for small k_z), which deflects the beam by an angle of 2θ, with three orders. The angular mosaic spread causes the reflected beam to be fanned out in the transverse direction (vastly exaggerated in the figure for clearity) and also affects the width in Δk_z, which is otherwise proportional to k_0 and cot θ.

These differences must be borne in mind when comparing instruments using the two techniques but, as usual, the different characteristics can also be exploited beneficially in different ways.

For example, if Bragg reflection is used for energy selection, the time structure offers the opportunity to discriminate between the different orders of reflection and to either suppress their effects or use them in a convenient way. Collimators can be used to affect the instrument resolution in a flexible way. On the other hand, if energy selection by time of flight is used, the resolution can be affected by the pulse width and the distance L between the source and the detector.

At reasonable distances L of up to 40 m the pulse width offered by a long pulse source usually does not give good enough resolution. As a consequence a chopper system must be used to tailor the pulse. This poses several problems:

1. It is in general difficult to chop a wide beam (neutron guide) cross section with sufficiently short pulses and at high transmission. The solution to narrow the beam down at the chopper position by a tapered supermirror neutron guide and bring it back to more or less parallel rays by the opposite procedure may seem a way out at the first glance, but apart

form the technical difficulties, this requires that the neutron guide itself must have a significantly smaller angle of total reflection than the tapered sections, which counteracts their use for thermal neutrons where only supermirror guides will transmit a sufficiently large beam divergency.

2. As can be seen from Fig. 2, a chopper placed at a certain distance form the moderator (say at 4 m, which is well inside the target shield of a spallation neutron source) will have a pinhole effect, imposing an intensity modulation on the wavelength band transmitted, that reflects the pulse shape at the moderator.

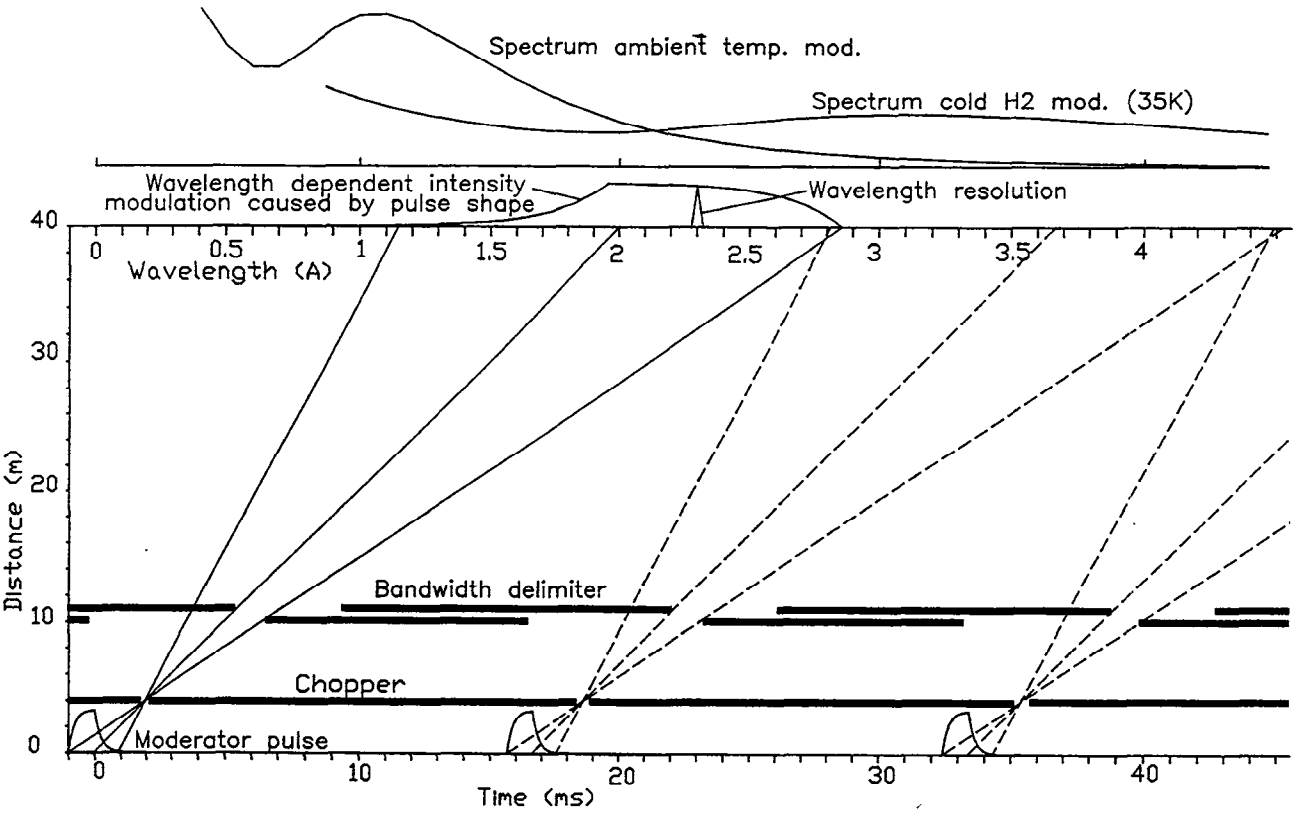

Figure 2: Space-time diagram for a pulsed neutron source with 1 ms pulse length and a chopper at 4 m from the moderator. In the example the chopper phase is shown set for 2.3 Å neutrons. The spectral distributions shown correspond to the first source pulse and do not account for wavelength-dependent transmission of the guide.

A band width delimiter (2nd chopper system) can be used to suppress those parts of the wavelength band which correspond to the trailing edge of the pulse (and to avoid frame overlap). The question whether the time between two pulses can actually be filled depends on the distance L chosen (as required by the desired resolution) and on the length of the proton pulse. Increasing the latter on the expense of the pulse current results in a lower peak-to-average intensity and hence has no benefit on the overall data taking rate. It simply increases the kinematic range of the scan which could otherwise be covered by selecting a different chopper phase (if needed; if not, this is a gain in measuring time!). On the other hand, increasing the pulse length and simultaneously reducing the repetion rate makes thermal cycling problems more severe and may well become a feasibiltiy issue at higher power levels (a few MW).

3. Even in those cases, where the full moderator pulse length gives sufficient resolution, such as small angle scattering [7], [8] and reflectometry [9], it is necessary to install more than

one chopper system in the guide to suppress frame overlap and penumbra effects, as can be seen from Fig. 3.

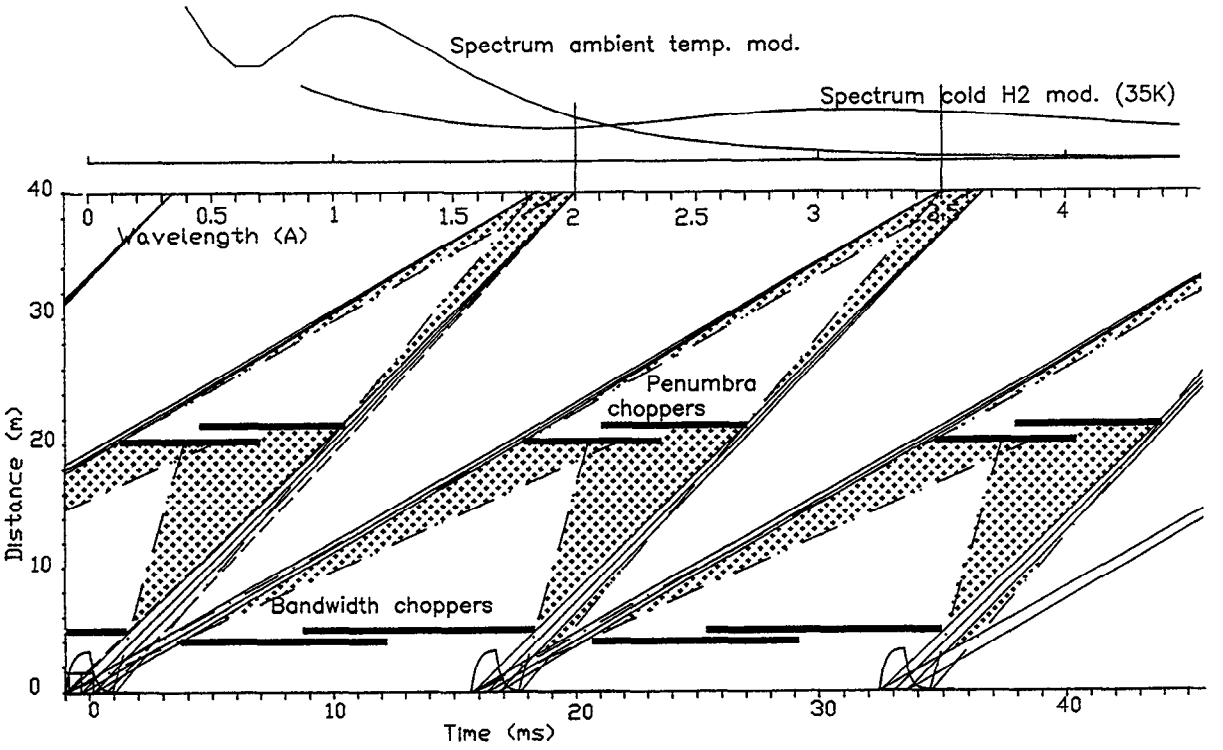

Figure 3: Space-time diagram for „long pulse" experiments with about 5% resolution for neutrons between 2 and 3.5 Å at 40 m from the moderator. At least two chopper systems are required to suppress frame overlap and penumbra effects.

In summary, using long source pulses to perform a time dependent energy selection on the incident beam requires a large technical effort, is limited in its usefulness and makes each guide unique for the instrument it is designed for. It also requires to locate the samples in the direct beam which further impedes multiple use of a guide and thus places a high share of the total facility cost on each instrument. The gains in measuring time often quoted for indirect ToF methods frequently result form the use of a large solid angle at the analyser side which, in addition to the proprietary use of a guide and the chopper system, adds significantly to the cost of such instruments. The question, whether this also produces useful information certainly depends very much on the problem under investigation (see below).

Another option is to use direct time of flight also on a long pulse source, similar to how it is done on a reactor, i.e. with a monochromator crystal and a chopper in the „monochromatic" beam and a detector system covering a large solid angle.

The first and most obvious advantage of this method is that the monochromator is placed in the intense beam of the neutron guide, rather than the sample. This makes multiple use of the guide easy. It may also have an effect on sample-generated backgrounds: If the sample is in the „white" beam much more parasitic scattering will occur in the sample than if it is hit only by the much smaller intensity of the monochromatic beam. For highly radiation sensitive samples this may even be an important issue relating to the effects under investigation ("in vivo") experiments.

In direct ToF-experiments the gain over a cw-source is easy to quantify. In the first approximation it is given by the peak-to-average flux ratio, multiplied by the source

utilization ratio, i.e. the ratio of actual pulse repetition rate to the optimum one chosen on a pulsed source. It will be higher, if the source pulses are shorter and the repetition rate of the source is higher. This issue was discussed extensively in a previous paper [1].

It may not always be possible to come sufficiently close to the optimum repetition rate with a long pulse source. There exists, however, the option to use more than one incident wavelengths, if the frames are long. This is shown for the case of a monochromator crystal in Fig. 4. A chopper has been introduced, which, rather than suppressing the second order of the monochromator reflection, allows it to pass on to the sample - well separated in time due to the distance from the moderator chosen. In this case, two different kinematic regions are covered simultaneously in one experiment (cf. Fig. 6).

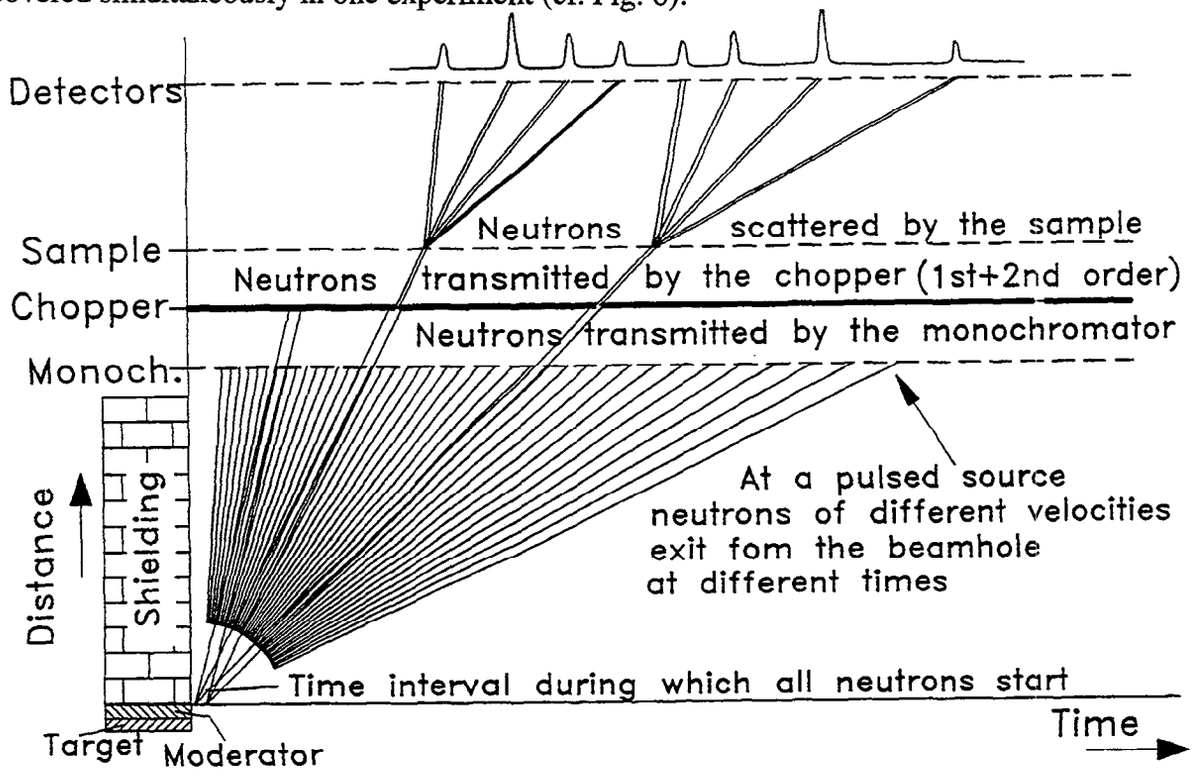

Figure 4: Space-time diagram for a direct ToF-spectrometer on a long pulse source using two orders of the monochromator reflection.

It is, of course, not necessary to use a monochromator in order to exploit more than one incident energy on a direct ToF-spectrometer. If an end position on a guide is available, a chopper system can in principle be used to select the incident energies. In this case no „higher order" restriction applies to the second energy chosen. It will simply be determined by the opening times of the chopper system.

At constant time average flux (same beam power and moderator-reflector configuration) the peak flux $\hat{\phi}$ is

$$\hat{\phi} = \bar{\phi} \cdot \frac{1}{f \cdot t_p}\left(1 - \exp\left\{-t_p / \tau(\mathrm{v})\right\}\right) \tag{1}$$

where t_p is the proton pulse duration and $\tau(\mathrm{v})$ is the life-time of neutrons of velocity v in the moderator. f is the source repetition rate and $f \cdot t_p$ is the duty cycle, which is assumed to be constant. If a chopper system rather than a monochromator is used to select more than one wavelength this requires, as a consequence of the pinhole effect shown in Fig. 2, a long t_p in

order to have sufficient intensity at all incident wavelengths and hence results in a much smaller $f \cdot \hat{\phi}$. Furthermore, fast choppers which control a large beam cross section near the moderator are a formidable task!

Clearly, for very low incident energies the choice of monochromators is restricted and the question whether to use direct or indirect time of flight involves more than only the issue of multiple use of guides and time utilization. While we are not going to deal in detail with questions of resolution, it seems appropriate to look at the kinematic range covered in the two techniques.

3. Scattering kinematics in direct and indirect time of flight techniques

It is customary to show the kinematic range covered by a scattering experiment as a function of Q and $\hbar\omega$. This is a helpful representation to give a quick overview, in particular if dealing with isotropic or polycrystalline samples, where no dependence of the scattering law on the direction of $\underline{Q}$ can be measured.

In fact, the conditions of conservation of energy

$$\Delta E = \hbar\omega = \frac{\hbar^2 k_i^2}{2m} - \frac{\hbar^2 k_f^2}{2m} \tag{2}$$

and of momentum

$$\underline{Q} = \underline{k}_i - \underline{k}_f \tag{3}$$

define a set of parabolae in the $\underline{Q}$-ω-space (on the surface of a paraboloid), whose apex is given by the energy of the incident neutron $\left((\hbar\omega)_{max} = E_i = \frac{\hbar^2 k_i^2}{2m} \right)$ and whose orientations in the Q_x-Q_y-plane are determined by the scattering angle ϕ_s at the sample (Fig. 5).

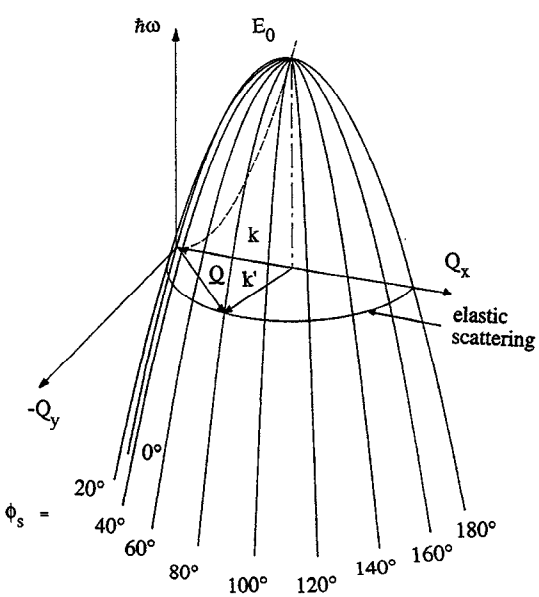

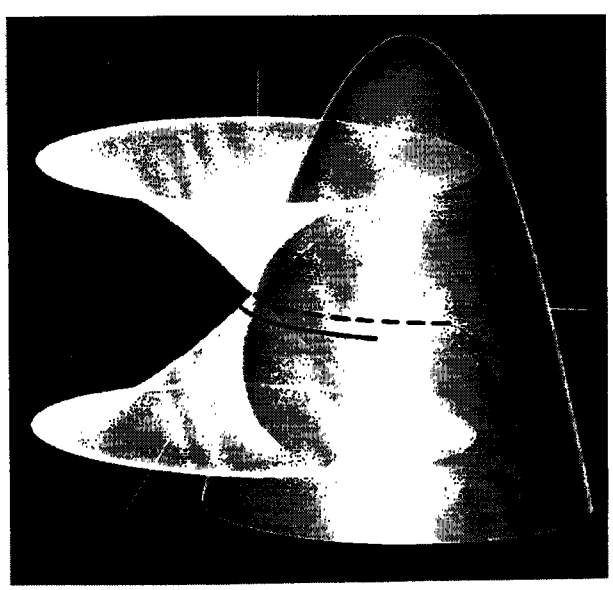

Figure 5: The kinematic range of a scattering experiment in the $\underline{Q}$-ω-space. Scattered intensity can be measured, when the scattering law intersects with the kinematic surface, as shown schematically in (b).

In a direct time of flight experiment the scan is along those parabolae which correspond to the individual detector settings at different scattering angles ϕ_s. The variation of $\underline{Q}$ as a function of time is along a line in the Q_x-Q_y-plane starting at the end point of the $\underline{k}_i$-vector and including an angle ϕ_s with this vector (bottom part of Fig. 6a). The $\underline{Q}$-range covered is determined by the area between two circles centered around the end of k_i and having radii equal to the highest and lowest neutron momenta that can be analysed with sufficient resolution. For each point in $\underline{Q}$ a unique value of $\hbar\omega$ can be measured, depending on k_i. The Q-$\hbar\omega$ representation mentioned above is obtained by a rotation of all $\underline{Q}$-vectors around the origin of the reciprocal space into the plane defined by $\underline{k}_i$ and $\hbar\omega$ (top part of Fig. 6). The curves are then described by:

$$Q^2 = \frac{2m}{\hbar^2}\left(2E_i - \hbar\omega - 2\cos\phi_s\sqrt{E_i(E_i - \hbar\omega)}\right) \tag{4}$$

Fig. 6a shows these curves for $k_i = 2$ Å^{-1} and 4 Å^{-1}, corresponding to two orders of reflection from the same monochromator crystal.

Although these facts are of course well known, it is important to keep them in mind when discussing the comparison between direct and indirect ToF techniques.

In an indirect ToF-experiment with crystal analysers set at a fixed value k_f the incident energy and hence the position of the kinematic scattering surface varies with time, the apex moving on a curve given by $(\hbar\omega)_{max} = E_0 = \frac{\hbar^2 k_i^2}{2m}$, the dispersion relation of the incident neutrons.

The loci for measurable combinations of energy- and momentum transfer are then obtained by introducing $E_f = E_i - \hbar\omega$ into eqn. (3) and are shown in Fig. 6b for the case of $k_f = 3$ and 4.5 Å^{-1}, and 1 Å^{-1} < k_i < 5 Å^{-1} (a reasonable range for a room temperature moderator according to Fig. 1).

Also shown in the bottom part of Fig. 6b are the scattering triangles for different times (values of k_i) corresponding to different scattering angles ϕ_s (10, 40, 80, 120 and 160°). It is obvious that the Q-vectors corresponding to a given scattering angle now lie on a line parallel to $\underline{k}_i$. If the k_f-values are the same for all ϕ_s, there is still a unique correspondence between $\underline{Q}$ and $\hbar\omega$ that can be measured. From Figs. 6a and 6b it is clear that the coverage of the $\underline{Q}$-space is different in the two techniques.

It is also obvious that, for indirect ToF-experiments the $\hbar\omega$-range is limited on the energy loss side of the neutron (positive values of $\hbar\omega$) by the maximum useful k_i and on the energy gain side by k_f. In direct ToF, the energy loss side is limited by k_i (and the time one is prepared to wait for down-scattered neutrons to arrive at the detector), while the limit on the energy gain side will be set by the resolution of the experiment.

Certain advantages for inverted time-of-flight techniques arise from the fact that the detectors will not see neutrons that have lost almost all of their energy and hence take a long time to arrive, eventually leading to frame overlap problems in direct ToF. They also cover a large Q-range for energy loss scattering of the neutron and hence depend less on the state under investigation to be occupied in the sample. On the other hand, while in direct ToF-experiments a k_i-value can be chosen that represents a high phase space density and the full peak height of the source pulse, the intensity associated with the different k_i in indirect ToF

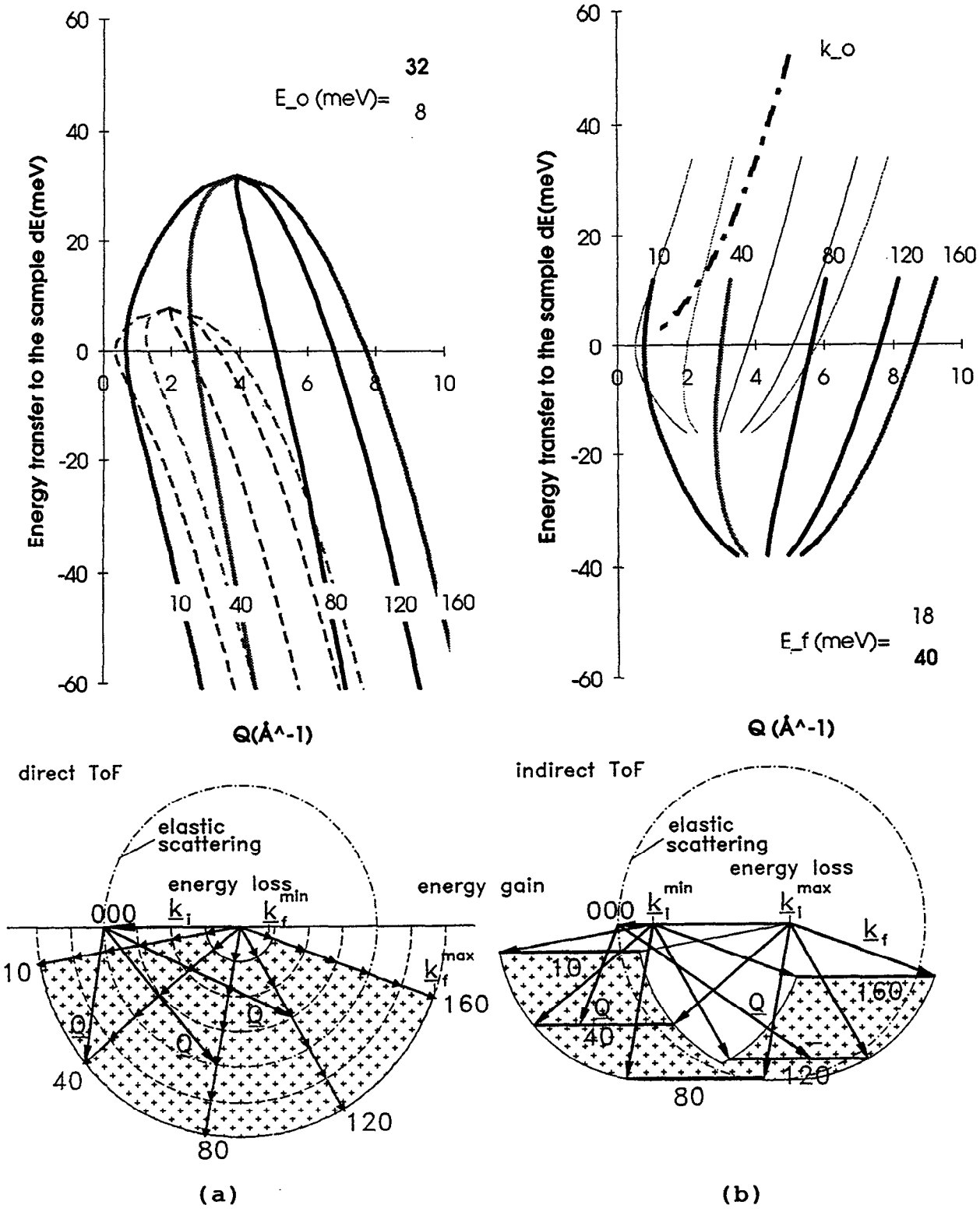

Figure 6: Kinematic range for time-of-flight experiments. Top: Q-$\hbar\omega$ representation; bottom: $\underline{Q}$-range covered.

a) direct ToF: for a given value ϕ_s (10°, 40°, 80°, 120° and 160° shown) $\underline{k}_f$ varies along a straight line beginning at the end point of $\underline{k}_f$ and including an angle ϕ_s with $\underline{k}_i$. Enegery gain scattering is limited by resolution, not by scattering kinematics. Q-$\hbar\omega$-curves are shown for two incident energies, 32 and 8 meV. The vector diagram at the bottom corresponds to the E_0 = 32 meV case.

b) indirect or inverted ToF: The magnitude and direction of $\underline{k}_f$ relative to $\underline{k}_i$ are fixed, hence the loci for $\underline{Q}$ lie on lines parallel to $\underline{k}_i$, as k_i varies. Examples shown pertain to ϕ_s = 10, 40, 80, 120 and 160°. Energy gain scattering is limited by the intensity distribution in the incident beam.

For both cases the $\underline{Q}$-range is shown by the shaded areas in the bottom part of the Figure. The condition for elastic scattering ($k_f = k_i$) gives the dash-dotted circles. $\underline{Q}$-values inside these circles are possible for energy loss of the neutrons, outside the circles for energy gain.

values not only represents the variation of the phase space density in the moderator, but also is subject to the pinhole effect by the chopper as shown in fig. 4, unless the source pulse is very long.

It is well known that by a suitable choice of k_f as a function of the scattering angle ϕ_s the loci for the $\underline{Q}$-vectors coverd for different ϕ_s can be shifted to the same distance from k_i („PRISMA"-condition: $\sin(\phi_s)_n/\sin(\vartheta_A)_n$ = const, with $(\vartheta_A)_n$ being the Bragg-angle for the n-th analyser). This option has been extensively discussed recently [12], [13] and can, in certain cases, be used to produce energy transfer scans for a fixed value of $\underline{Q}$ (or $\underline{q}$), i.e. to simulate constant $\underline{q}$-scans on a triple axis spectrometer. In practice, however, several difficulties may arise:

If one tries to set the spectrometer up such that the scanning line in $\underline{Q}$ coincides with a high symmetry direction in the crystal lattice, the choices are very restricted, because (a) every particular distance from the k_i-vector requires a unique set of analyser energies (k_f-values), (b) small k_f's are not easily accessible in practice due to the large Bragg-angles required, which cannot be realized in a multi-arm arrangement with closely spaced analysers, (c) large k_f's lead to poor resolution because of the small deflection angles at the analysers, and (d) the spacing between the $\hbar\omega$-values measured is determined by the angular spacing of the analyser arms and cannot easily be matched to the width of the peaks to be measured.

In summary, while it is clear that inverted ToF inelastic scattering has certain merits, the question, whether such an instrument should occupy a beam line of its own on a long pulse source must be considered very carefully because the alternative of a direct ToF-machine or triple axis spectrometer using a shared beamline may often offer even better opportunities.

4. Polarization effects - ToF versus TAS

One problem which makes time of flight techniques difficult to use in single crystal investigations is the question of the polarization of the elementary excitations or magnetic scattering relative to $\underline{Q}$. It is obvious from the dynamic structure factor

$$F_{dyn}^2 = \sum_{l=0}^{n} \left(b_l / \sqrt{M_l} \cdot \underline{Q} \cdot \underline{e}_l(q,i) \exp\left(i\underline{Q} \cdot \underline{\rho}_l\right) \exp(-W_l) \right) \tag{5}$$

and the magnetic scattering cross section

$$\left(\frac{d\sigma}{d\Omega}\right)_{mag} = \left(\frac{p}{\mu_p}\right) \left| < \underline{Q} x \left(\underline{\hat{M}} x \underline{Q}\right) > \right|^2 \tag{6}$$

that, in order to obtain clear quantitative results, $\underline{Q}$ should be oriented parallel to $\underline{e}_l$ in inelastic nuclear scattering and perpendicular to the Fourier transform of the magnetisation vector, $\underline{\hat{M}}$, in magnetic scattering. In ToF-measuremtns the direction of $\underline{Q}$ varies in a scan for each detector and the above condition can only be fulfilled for a range of $\underline{Q}$ by regrouping data from different detectors measured at different times. While this may be possible in direct ToF, with the detectors spaced closely enough, few directions exist in indirect ToF, where this is possible, as can be seen from the bottom part of Fig. 6a and b.

The best instrument to fulfill his condition is a triple axis spectrometer (TAS) which, as soon as the large kinematic range covered in time of flight cannot be fully exploited, becomes highly competitive. A TAS, too, uses a crystal monochromator and hence can share a neutron

guide with other instruments. On a long pulse source, the time structure can be exploited to enhance its performance significantly relative to a continuous source by suppression of spurious effects and background through a time gate at the detector [1].

This option poses no particular restrictions to the time structure of the source, but it will be the more effective, the shorter the pulses and the higher the intensity per pulse. It is, however perfectly compatible with a 100 Hz repetition rate and a pulse width of 200 μs, which would be a desirable set of parameters also for direct ToF-instruments. (A high pulse repetition rate also reduces thermal cycling loads on the system components of the source, which, as noted before, is a decisive advantage).

There will be many instances where the much higher gain factor that can be obtained for direct time of flight methods on such a source (of the order of 40) compared to triple axis machines (of the order of three), make it easier to perform certain research tasks by ToF rather than by TAS. This will certainly lead to a different "population structure" on a long pulse source than on a continuous source, but the principal character of the inelastic scattering instruments can remain the same.

5. Correlation ToF-Techniques

High intensity (long) pulsed neutron sources have been recognized early on [14] to offer unique options for correlation techniques in time of flight. In addition to correlating a measured event to the chopper sequence(s), the on-off condition of the beam at the moderator can be used to screen against the high background which otherwise plagues the technique on a cw-source. In the mean time the concept of inverse Fourier time of flight instruments has been developed to a high degree of perfection [10], [11].

For inelastic scattering the crucial advantage is that there is no need to fix k_f by crystal analysers. With two Fourier choppers of different grating and running independent of each other, the k_i and k_f values that shall be related to one another can be chosen virtually at random and independent of each other. This does not only allow to simulate the "PRISMA"-condition ($k_f \cdot \sin \phi_s$ = const) on a long pulse source with a resolution indepent of the pulse length and with every desired line in reciprocal space easily achievable, it also makes the very interesting mode possible, where k_i/k_f is constant for every detector. This results in a scan where the locus for $\underline{Q}$ is a straight line through the origin of the reciprocal space. Adjusting k_f for the different detectors properly will make all these lines coincide and enable a complete longitudinal phonon scan along a high symmetry direction to be performed in a single run. By the same token, the condition $\underline{Q} \perp \underline{\hat{M}}$ (eqn. 6) can be fulfilled for the whole set of detectors and incident scattering vectors.

With regard to transversely polarized phonons, a constant q scan should also be possible, but only one pair of k_i-k_f values will contribute for each scattering angle ϕ_s.

The criterion that needs to be fulfilled is

$$Q^2 = k_{i,n}^2 + k_{f,n}^2 - 2k_{i,n}k_{f,n}\cos\phi_{s,n} \tag{7}$$

with n designating the detecor number. This will require the use of variable time channels and predelay times but should be feasible with a predetermined measuring program for each value of $\underline{Q}$. If the opportunity exists to carry out more than one correlation program for each detector, several constant Q-values can be selected simultaneously.

The opportunities offered by this method have so far not been fully exploited in practice because of the lack of suitable sources; on cw-sources the need to introduce a "long pulse" chopper costs too much intensity and on short pulse sources the average intensity has been low to begin with. It should be noted that the introduction of two Fourier choppers means that only about 1/16th of the pulse intensity (average flux) is actually used, albeit at very good resolution. While this is about what one would expect for a standard direct ToF-instrument on a long pulse source, it is less than what inverted ToF uses on a pulsed source.

With respect to constant q-scans, the technique uses 1/16th of the full average flux at each detector and q-value selected. In a very crude approximation it would then become competitive to a TAS, if more than 16/m detectors can contribute to the scan with m being the number of meaningful q-values examined simultaneously.

It is probably worth emphazising that a Fourier chopper is the only device which can generate very short pulses on a large beam cross section.

The power of this technique certainly justifies an end position on a guide or even single use of a beam hole.

6. Diffraction

For single crystal diffractometers more or less the same is true, as for triple axis spectrometers:

Using the (position sensitive) detector(s) in a time resolving mode will not only make filters unnecessary and reduce the background contribution, it will also allow to distinguish higher order reflections and thus improve the information content of the measurement. Again, a monochromator (or a set of monochromators, see below) is used and multiple utilization of a (supermirror) guide is possible.

In the case of powder diffraction it is beyond doubt that short pulse spallation sources have a decisive advantage because (a) in the slowing down regime the pulse width is inversely proportional to the neutron velocity and hence $\Delta v/v = \Delta d/d$ is constant and very good. Similarly high quality data can also be obtained in the Maxwellian part of the neutron spectrum if the moderator pulse is kept suitably short by poisoning and decoupling the moderator. The large scanning range in inverted time of flight diffraction easily compensates for the factor of roughly 20 in the pulse integral lost in comparison to an optimized coupled moderator, as would be used on a long pulse source.

On a long pulse source it is, however, possible to improve the situation for diffraction by taking advantage of the time structure and using not only several orders of one monochromator crystal but stacking two or more crystals to deflect more wavelength packets [1]. The corresponding distance-time diagram is shown in Fig. 7. Here, a C-002 and Si-220 monochromator were assumed, set at an angle of $2\ \theta_m = 130°$. As can be seen, good separation of the reflected wavelengths is obtained at a distance of 25 m even for 1 ms long proton pulses. A background rotor placed at the edge of the target shielding will reduce the overall background from fast neutrons while the pulse is on and will, at the same time, suppress the C-002-reflex, which would otherwise interfere with the Si-220 reflex of the following pulse. Clearly, if the (position sensitive) detector of the spectrometer is operated in a time resolving mode, the contributions from the different wavelengths can be easily distinguished and used to improve the measurement. Without any attempt to optimize the resolution or intensity, the resolution curves obtained for this situation were calculated [15]

with the following assumptions given on the figure, where α_1, α_2, α_3, and β are the collimation angles in front of the monochromator, the sample and the detector respectively and β is the mosaic spread of the monochromator.

The result is shown in Fig. 8. It is obvious that in the d-range between 0.5 and 8 Å measurements with a resolution better than 2% can be performed. Between 0.4 and 2.5 Å a resolution better than 0.4 % is achieved. At the same time, most of the d-values are measured several times with different resolution, which should be valuable in sorting out wavelength dependent effects and carrying out a quantitative analysis of the intensities.

Again, while a standard powder diffractometer on a long pulse source will not be used to routinely solve complicated structures if a short pulse source (or an X-ray diffractometer) is available, there are many problems which do not require the large range in d-values. Those problems can be treated on the diffractometer described here with orders of magnitude better intensity.

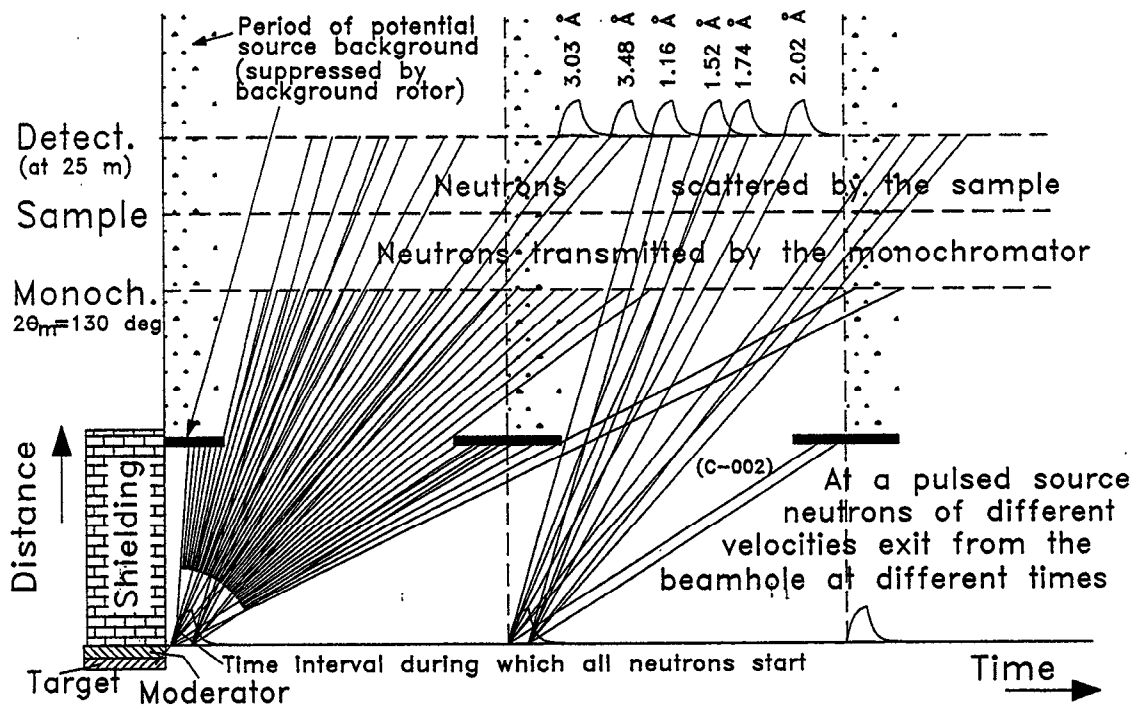

Figure 7: Distance-time diagram for a powder diffractometer with multiple monochromator on a pulsed source.

Although a collimator was assumed to be used in front of the monochromator, also this instrument can share a neutron guide.

Finally, it should be noted that the Fourier correlation technique mentioned in chapter 5 is, of course, also suitable for diffraction measurement. If used as total scattering instrument (as customary in diffraction), only one Fourier chopper is required and data taking is relatively straight forward, allowing very high resolution. The inelastic spectrometer with two Fourier choppers as outlined in chapter 5, however, allows to chose the condition $k_i = k_f$ for all detectors (with each scan running along a different line in Q-space) and to measure truely elastic or qusielastic scattering in a whole sector in reciprocal space simultaneously, using 1/16th of the time average flux of the source. Again, this instrument must occupy an end position of a guide or beam.

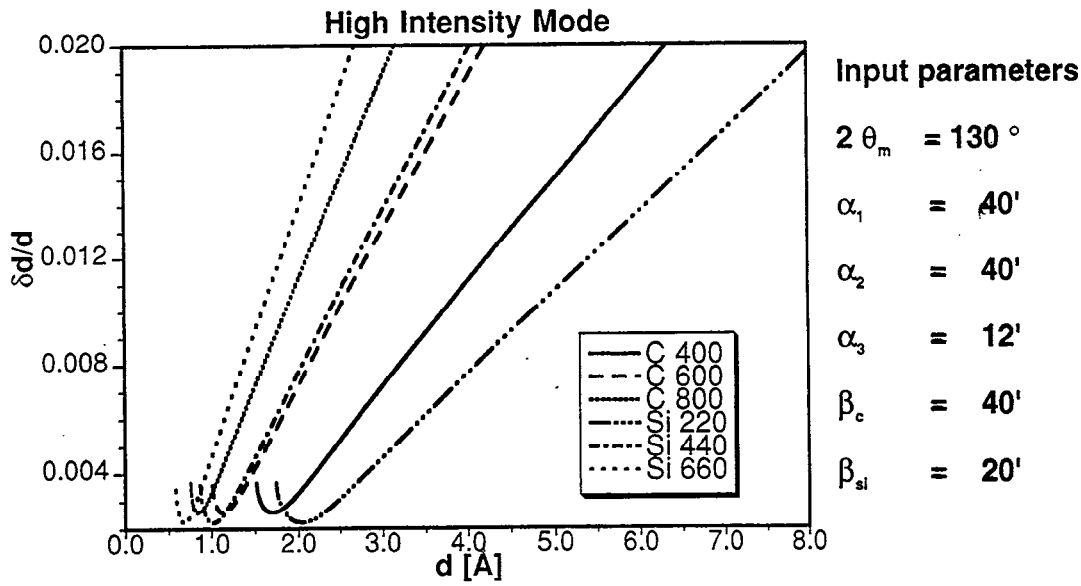

Figure 8: Multi-monochromator resolution functions in a high intensity mode of a powder diffractometer on a pulsed source.

7. Further options for multiplexing

The term "multiplexing" has been used to describe multiple use of the same pulse other than in inverted time of flight. Apart from the case of the powder diffractometer described above, also the simultaneous use of more than one pulses per frame in a direct ToF-spectrometer or a single crystal diffractometer would fall in this category. Other, more elaborate methods for multiplexing techniques have been proposed, such as the multicrystal-monochromator back scattering spectrometer "Musical" [5] where separation of closely neighbouring wavelengths is achieved by a "detour" through a stack of crystals in back scattering with appropriate mutual separation.

Other methods, using more high tech approaches have been developed by the group in Vienna hand have been described e.g. by Rauch [16]. We will not treat them in detail here. An overview over other options can be found also in [6]. The common features of these methods are that

- they provide useful neutrons practically throughout the frame between two pulses
- they are not very sensitive to pulse length but are most effectively applied for pulses of the order of 200 μs
- they can utilize the full intensity of coupled moderators with grooved surfaces
- they are applicable also at relatively high repetition rates, e.g. 100 Hz, which is favoured for direct ToF-techniques and from the point of view of thermal cycling.

8. Conclusions

Inverted time of flight techniques are the natural choice for short pulse spallation neutron sources, where they offer unique possibilities in powder diffraction, epithermal neutron spectroscopy and very high resolution spectroscopy on nearly dispersion-free modes. Trying to use the same techniques on long pulse sources either requires excessively long flight paths and low pulse repetition rates or difficult chopper systems and long pulses. One of the most important features of short pulse sources, the constant resolution due to the 1/v-dependence of the pulse width cannot be simulated in this way. They also imply more or less single use of a beamport by one instrument only and hence are not very cost effective. Their use should therefore be restricted to cases where no other alternatives exist. Long pulse spallation neutron sources can today be conceived with time average fluxes approaching those of the best existing high flux reactors and the most cost-effective way of using such sources is by multiple use of guides, as it has become standard practice on reactors. Also performance-enhancing techniques now in use of reactor sources, such as curved monochromators can be retained.

Practically all instrument types now in use at reactors can benefit from the time structure of a long pulse source by making more efficient use of the neutron beams and reducing backgrounds. While the gains will average around an order of magnitude if straight-forward improvements to the instruments are made, they will vary from one type of instrument to another approaching 100 for time of flight spectrometers. This will eventually lead to a different population of instrument types on a long pulse source compared to what we find at present reactors, driven by the best options to meet future scientific needs. As usual, new opportunities will trigger new developments. Some of them can already be seen on the horizon.

One important example are Fourier correlations techniques for which the pulsed nature of the source allows to overcome the background problems they suffer from on continuous sources, but which have no stringent requirements to pulse length. The important issue is that the decision on the future instrumentation affects the choice of parameters for the long pulse source: while inverted time of flight techniques prefer long pulses and low repetition rates, reactor-like methods can profit from shorter pulses and higher repetition rates. At the same time average beam power the second case makes the design of the linac and in particular of the target significantly easier because it reduces thermal cycling problems. If the source is fed from a ring accelerator which produces inherently short pulses, this will constitute a more difficult situation for the target, but will not affect the performance of the instruments adversely. On the contrary, for direct ToF-instruments the situation will be further improved and even neutrons in the slowing-down regime would become useable (albeit by inverted ToF-techniques!).

9. References

[1] G.S. Bauer "Some general reflexions on long pulse neutron sources" in *Proc. Int. Workshop on Long Pulse Spallation Sources Lawrence Berkeley Laboratory*, 18-21 April 1995 to be published. Submitted to J.N.R.(1995)

[2] K. Skala and G.S. Bauer "On the Pressure Wave Problem in Liquid Metal Targets" *Proc. ICANS-XIII, Paul Scherrer Insitut*, PSI-Proceedings 95-02 (1995)

[3] R. Pynn and L. Daemen "The Performance of Neutron Spectrometers at a Long-Pulse Spallation Source" *Proc. ICANS-XIII, Paul Scherrer Insitut*, PSI-Proceedings 95-02 (1995)

[4] G.S. Bauer, "The general concept for a spallation neutron source in the Federal Republic of Germany"; *Atomkernenergie-Kerntechnik* 41 (1982) p.234-242

[5] R. Scherm, B. Alefeld "Instruments for High Flux Sources with Time Structure of Neutron Flux" paper *IAEA-CN-46/80* in "Neutron Scattering in the 'Nineties", *IAEA conference procceedings, Vienna*, (1985) p. 247-259

[6] G. S. Bauer, R. Scherm, "Forthcoming Instrument Developments for Improved Utilization of Neutron Beams"; in "Neutron Scattering", *Proc. Int. Conf. Santa Fe*, physica 136B (1986), p 80-86 North Holland, Amsterdam

[7] H. Conrad "On Proton Pulse Lengths and Rep. Rates with Emphasis on SANS" *Proc. ICANS-XIII, Paul Scherrer Insitut*, PSI-Proceedings 95-02 (1995)

[8] Glenn A. Olah, Rex P. Hjelm and Phil A. Seeger "Small-Angle Scattering Instruments on a 1 MW Long Pulse Spallation Source" *Proc. ICANS-XIII, Paul Scherrer Insitut*, PSI-Proceedings 95-02 (1995)

[9] M.R. Fitzsimmons and Roger Pynn "The Performance of Reflectometers at Continuous Wave and Pulsed Neutron Sources" *Proc. ICANS-XIII, Paul Scherrer Insitut*, PSI-Proc. 95-02 (1995)

[10] P. Hiismäki "Principles of Reverse Time-of Flight Method an Fourier Technique" *Proc. ICANS-XIII, Paul Scherrer Insitut*, PSI-Proceedings 95-02 (1995)

[11] V.L. Aksenov, A.M. Balagurov, V.A. Trounov and P. Hiismäki "Performance of the High Resolution Fourier Diffractometer at the IBR-2 Pulsed Reactor; Latest Results" *Proc. ICANS-XIII, Paul Scherrer Insitut*, PSI-Proc. 95-02 (1995)

[12] B. Dorner "A Comparison of Time-of-Flight (TOF) and Three Axis Spectrometer (TAS) Techniques for the Study of Excitations in Single Crystals" *Journal of Neutron Research* 2 (1994) 115-127

[13] M. Hagen, U. Steigenberger, C. Petrillo and F. Sacchetti "Future opportunities and present possibilities for coherent inelastic single crystal measurements on pulsed neutron sources" to be published in *Nucl. Inst. Meth.*

[14] G.S. Bauer, H. Sebening, J.-E. Vetter, and H. Willax (eds.) "Realisierungsstudie zur Spallations-Neutronenquelle" report Jül-Spez-113 and KfK 3175 *Kernforschungsanlage Jülich und Kernforschungszentrum Karlsruhe* (1981), p. 129

[15] P. Fischer, private communication

[16] H. Rauch: 'Novel beam bunching methods by perfect crystals and electromagnetic means' paper IAEA-CN-46/40 in "*Neutron Scattering in the 'Nineties*", *IAEA conference procceedings*, Vienna, (1985) p. 35-52

ICANS–XIII
13th Meeting of the International Collaboration on
Advanced Neutron Sources
October 11–14, 1995
Paul–Scherrer–Institut, 5232 Villigen PSI, Switzerland

ON PROTON PULSE LENGTHS AND REP RATES WITH EMPHASIS ON SANS

Harald Conrad

Institut für Festkörperforschung
Forschungszentrum Jülich
Postfach 1913, D–52425 Jülich, Germany

ABSTRACT

The consequences of different proton pulse characteristics on the performance of neutron scattering instruments are discussed in general for a cryogenic moderator. The possible gain of pulsed operation for both time–of–flight and continuous source applications is outlined. Small angle neutron scattering (SANS), a classical technique at a continuous source is taken as an example to show pros and cons of different source concepts. It is shown that a single number (gain factor) is not sufficient to qualify SANS at a pulsed source. In addition to this integral quantity, a differential gain is defined. The latter can be used to better assess the most adequate source parameter specification.

1. Introduction

All existing spallation neutron sources are pulsed (the SINQ under construction at PSI becoming an exceptional case). This is equivalent to saying that the proton pulse duration t_p is negligibly short compared to both the slowing down times to thermal equilibrium in any moderator, t_e, and the storage times of thermalized neutrons in the moderators, τ. Although both times determine the detailed shape of the neutron pulse for neutrons in thermal equilibrium, the storage time usually dominates. Therefore the latter is responsible for the more or less slowly decaying pulse tails. It is this storage time, which can be changed drastically by moderator "tailoring" (poisoning, decoupling). Shortening the neutron pulse duration this way is essential for improving spectrometer or diffractometer resolution. On the other hand, the average neutron flux of pulsed

Keywords: Long pulse source, high intensity moderator, SANS, differential gain

sources strongly depend on this tailoring. It should be mentioned in this context that tailoring with long pulse sources (several hundred μs to a few ms) does not make sense, as will be discussed below. Although it is not the topic of this paper, we should not forget to mention the well–known fact that only pulsed sources gain two to three orders of magnitude in utilizing epithermal (slowing down) neutrons.

Until recently the only project, which abandoned the concept of a pulsed source in the sense defined at the beginning, was the German 5.5 MW SNQ. There were very good reasons for considering what was called an intensity modulated neutron source (IMNS), i.e. a linac only design with a proton pulse duration (in the final proposal) of 250 μs. Although a pulse compressor was considered as an add–on option, it was not included in the project proper because of the very ambitious source parameters, especially the 2.7×10^{14} protons per pulse at 1.1 GeV to be stored in a single ring. Even more than 10 years later the 5 MW ESS project resorts to two compressor rings, each to carry 2.3×10^{14} ppp at 1.33 GeV. (ESS is planned to operate at 50 Hz instead of 100 Hz with SNQ.)

Probably the most important reason for advocating an IMNS was that except for not utilizing epithermal neutrons most effectively, the performance of virtually all neutron scattering instruments was expected to be superior to equivalent ones at the ILL reactor [R.Scherm and H.Stiller].

As may be already inferred from the discussion above, moderator tailoring does not make sense at an IMNS, because it would only reduce the average neutron flux. The neutron pulse width would still be dominated by the proton pulse duration, as is shown in the next chapter. In the discussion of the pros and cons of source concepts with different proton pulse durations and repetition rates we will not consider moderator tailoring even for pulsed sources, for it would adulterate a fair comparison. In such a comparison we have at least to keep the moderator parameters fixed when varying the proton pulse data.

2. Pulse shapes, peak fluxes and rep rates

In the following we will consider only a cryogenic moderator in its so–called high intensity configuration, i.e. there are neither neutron poisons within nor decouplers around the moderator. To be quantitative we will rely on experimental data obtained with a liquid hydrogen moderator embedded in various reflector materials [G.Bauer et al. 1985]. The results are reproduced in Table 1.

Table 1 Storage times τ, average neutron fluxes $<\phi>$ and cold neutron pulse widths for a liquid H_2 moderator. ^{238}U target. The neutron pulse widths are calculated assuming a proton pulse duration $t_p = 250\ \mu s$. After G.S.Bauer et al. 1985.

reflector	neutron storage time $\tau/\mu s$	average flux $<\phi>/10^{14} cm^{-2}s^{-1}$	cold neutron pulse width FWHM/μs
Pb	230	4.3	320
C	350	5.4	390
D_2O	710	6.6	620

In order to be specific, we have selected the carbon reflected case from Table 1. Using the storage time $\tau = 350\ \mu s$, the neutron pulse shapes depicted in Figure 1 are calculated according to the relations

$$\begin{aligned} \phi(t) &= \phi_\infty \cdot (1 - e^{-t/\tau}) && t < t_p \\ \hat{\phi} &= \phi(t = t_p) = \phi_\infty \cdot (1 - e^{-t_p/\tau}) && \text{peak flux} \\ \phi(t) &= \hat{\phi} \cdot e^{-(t - t_p)/\tau} && t > t_p \end{aligned} \qquad (1)$$

where $\phi_\infty = <\phi> \cdot \frac{t_{rep}}{t_p}$ is the asymptotic flux, which would be obtained with d.c. proton peak current. Obviously, this asymptotic flux is related to the time average flux $<\phi>$ of a pulsed or modulated source by the last relation above, where t_{rep} is the time between two source pulses. These relations do not contain the slowing down time t_e, but are nevertheless good approximations, because $\tau >> t_e$ in all cases (see also section 3.1).
Figure 1 depicts the cold moderator response, i.e. the neutron pulse shapes, to several widely differing primary proton pulse shapes. Shown are a comparison of a pulsed source (the ESS concept) to three different long pulse source concepts:

- ESS (5 MW, 1.334 GeV, 50 Hz),
- the former German SNQ (5.5 MW, 1.1 GeV, 100 Hz),
- a linac only variant of the ESS based on the unchopped linac current and the proton pulse length matched in order to roughly equal the SNQ power, and
- a very long pulse source concept with alternating pulse lengths [Mezei, 1993].

Mezei's concept of very long pulses is an attempt to optimize the source utilization. The alternating pulse lengths with half the beam power in 4–ms–pulses at 12.5 Hz are meant to offer low resolution applications like SANS the possibility to exploit a wide

wavelength band (by suppressing the three intermittent pulses), while others use all pulses at 50 Hz. The gain for SANS with this concept will be discussed in more detail in chapter 4.

The neutron pulses plotted in Fig. 1, denoted as time–dependent fluxes, are normalized to the corresponding average neutron fluxes. As the proton beam power in all four cases is about the same, we may directly take the relative heights and shapes of the pulses as a

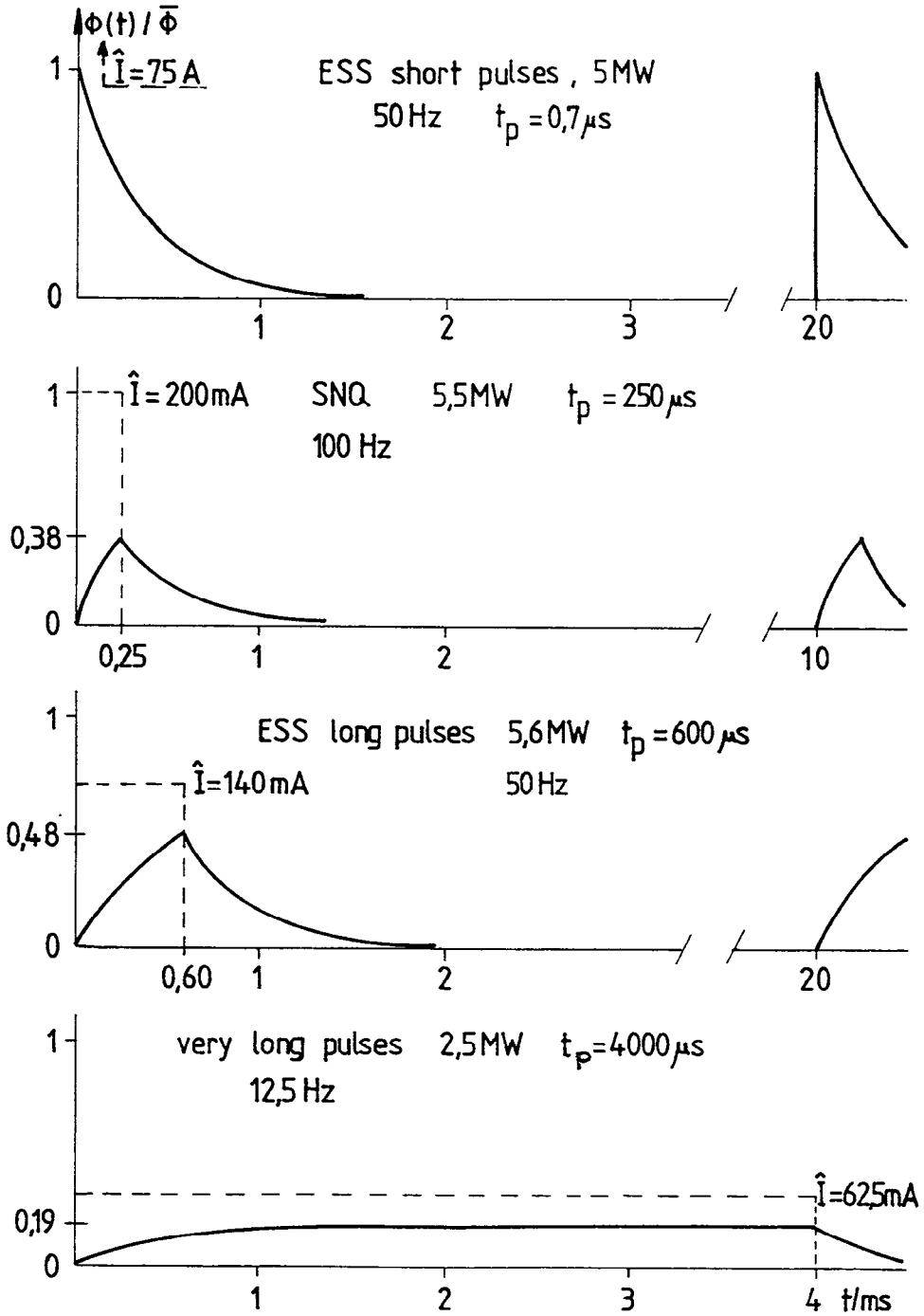

Figure 1 Cold neutron pulse shapes from a coupled, unpoisoned liquid hydrogen moderator surrounded by a graphite reflector for four source concepts: one short pulse and three different long pulse sources. The neutron storage time in this case is $\tau = 350\ \mu s$.

measure of the target–moderator performance. The most striking feature in comparing the four frames in Figure 1 is the (well–known) fact that we only gain about a factor of two in neutron peak flux in compressing e.g. the unchopped ESS limac current by nearly three orders of magnitude. This can easily be verified by calculating the peak flux of equation (1) for infinitely short proton pulse duration t_p

$$\lim \hat{\phi} = \frac{t_{rep.}}{\tau} \cdot <\phi>$$

and comparing this to the peak flux for e.g. $t_p = 2\tau$

$$\hat{\phi}(t_p = 2\tau) \simeq 0.43 \cdot \frac{t_{rep.}}{\tau} \cdot <\phi>.$$

It is evident now from Figure 1 that the neutron pulse widths do not essentially depend on the proton pulse width as stated in the Introduction.

3. General gain considerations

There are mainly two reasons why we expect a gain in counting rate of useful neutrons at an instrument's detector with a pulsed or intensity modulated source. Firstly, the peak flux of even a low power source may exceed the average flux of a high flux reactor and, secondly, we can attempt to utilize a polychromatic neutron band during times between the pulses. It is not an easy task to quantify a gain for a particular instrument. This is due to the fact that the instrument suites at reactors and the existing pulsed sources have been devised under strongly differing prerequisites. We do not have many examples if any at all, where a reliable comparison was made of the performance of a particular instrument at both a reactor and a pulsed source. A case, which is certainly close to this requirement, is the work of Schäfer et al. They tested a diffractometer set–up including identical primary collimation, an identical sample and an identical position sensitive detector both at ISIS and the FRJ–2 reactor [Schäfer et al. 1992]. Unfortunately, this comparison cannot simply be quantified by a single gain factor, because the number of measured Bragg reflections differ in the two cases. This situation we will often encounter.

3.1 Gain for time–of–flight applications

In contrast to the just mentioned case we may well be able to find in a straightforward manner gain factors for direct geometry time–of–flight instruments. Consider a chopper spectrometer with chopper frequency f_{ch} and imagine the same instrument operating at a pulsed source whose rep rate is f_{rep}. Then the obvious gain factor G is defined by

$$G = \frac{f_{rep} \cdot \hat{\phi}}{f_{ch} \cdot \phi_r} = \frac{1 - e^{-t_p/\tau}}{f_{ch} \cdot t_p} \cdot \frac{<\phi>}{\phi_r} \qquad (3)$$

where we have used equ. 1. ϕ_r denotes the (constant) reactor neutron flux. The gain appears to be independent of the rep rate of the pulsed (or intensity modulated) source. In order to understand this it is instructive to distinguisch two cases.

– Comparison short pulse source/reactor

Letting t_p tend to zero we get

$$G = \frac{1}{\tau \cdot f_{ch}} \cdot \frac{<\phi>}{\phi_r} \tag{4}$$

In this case, the gain is essentially independent of the source rep rate when keeping the average flux fixed. In other words, halving the rep rate requires doubling the number of protons per pulse for fixed pulse duration! It may be worthwhile to point out in this context that reducing the proton pulse duration below the slowing down time t_e does not raise the peak flux anymore. As an approximation we may replace equ. 4 by equ. 3 with inserting t_e for t_p. Taking $t_e = 20\mu s$ we get a result, which is lower by less than 3% than that using equ. 4.
The crucial factor $1/(\tau f_{ch})$ in equ. 4, which gives the gain with a pulsed source compared to a reactor of equal flux, is for cold neutrons of the order of

$$\frac{1}{\tau \cdot f_{ch}} = \frac{1}{3.5 \times 10^{-4} \times 200} \simeq 14$$

– Comparison long pulse source/reactor

Here the situation is a bit more involved, if we accept that the duty cycle $d = t_p/t_{rep}$ of a linac is not an entirely free parameter [G.Bauer, 1995]. If we assume a fixed duty cycle (the linac peak current cannot easily be increased), the gain actually increases with increasing rep rate $f_{rep} = 1/t_{rep}$. This is evident from rewriting equ. 3 in the form

$$G = G(f_{rep}) = \frac{f_{rep} \cdot [1 - e^{-c/(\tau f_{rep})}]}{c \cdot f_{ch}} \cdot \frac{<\phi>}{\phi_r}.$$

The graph of this function is shown in Figure 2. It should be mentioned that the gain plotted in Figure 2 approaches the short pulse case for very high rep rates. Clearly, this limiting case will not be reached, because it would not make sense to operate the pulsed source at rep rates higher than any reasonable chopper frequency of a reactor instrument.
Physically, the rep rate dependent gain can be understood by the non–linearity of the rising part of the neutron pulse as depicted in Figure 3. Doubling the peak current during t_p would double the peak flux, but doubling t_p at fixed peak current would not!

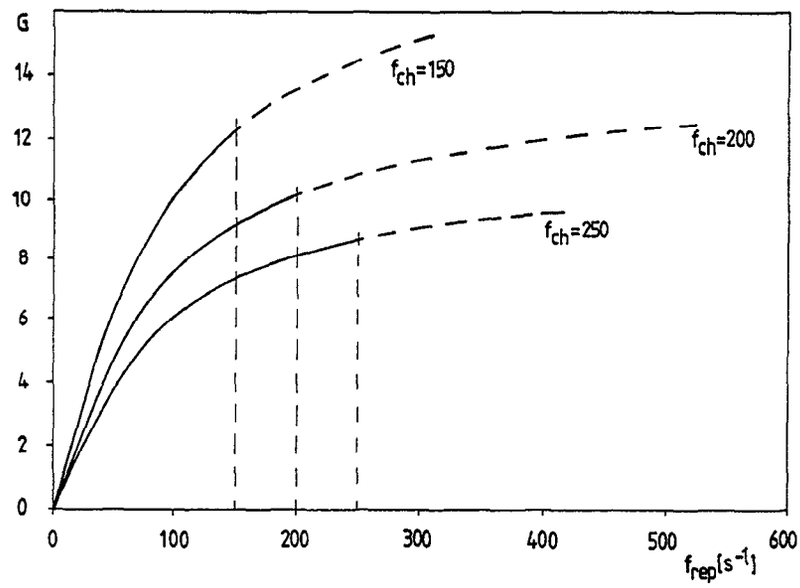

Figure 2 Rep rate dependent gain factor for a long pulse source with fixed duty cycle c = 0.05.

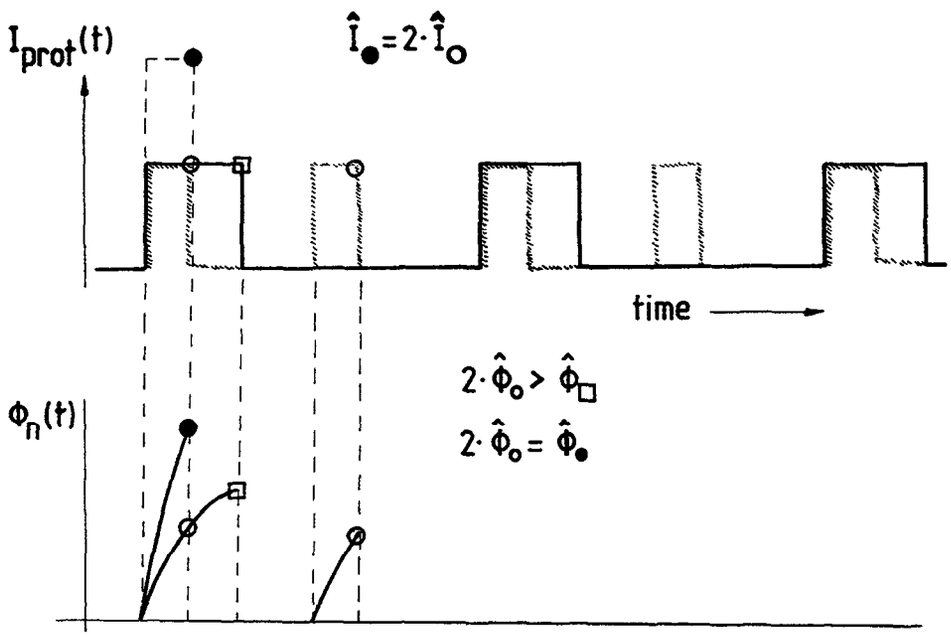

Figure 3 Increasing the rep rate at fixed duty cycle enhances the gain for a long pulse source as long as $f_{rep} \lesssim f_{ch}$

3.2 Gain for wide wavelength band applications

We are now turning to discuss the possibility of exploiting the time interval between pulses, i.e. the utilization of different wavelengths sequentially in time. In order to obtain as wide a wavelength band $\Delta\lambda$ as possible we demand short source–detector distances L and/or low rep rates. This can readily be seen from the familiar distance–time diagram shown in Figure 4, or from the well–known relation

$$\Delta\lambda = \frac{\text{const}}{L\cdot f_{rep}}, \qquad (\text{const} = 3956\ \text{Åms}^{-1}). \qquad (5)$$

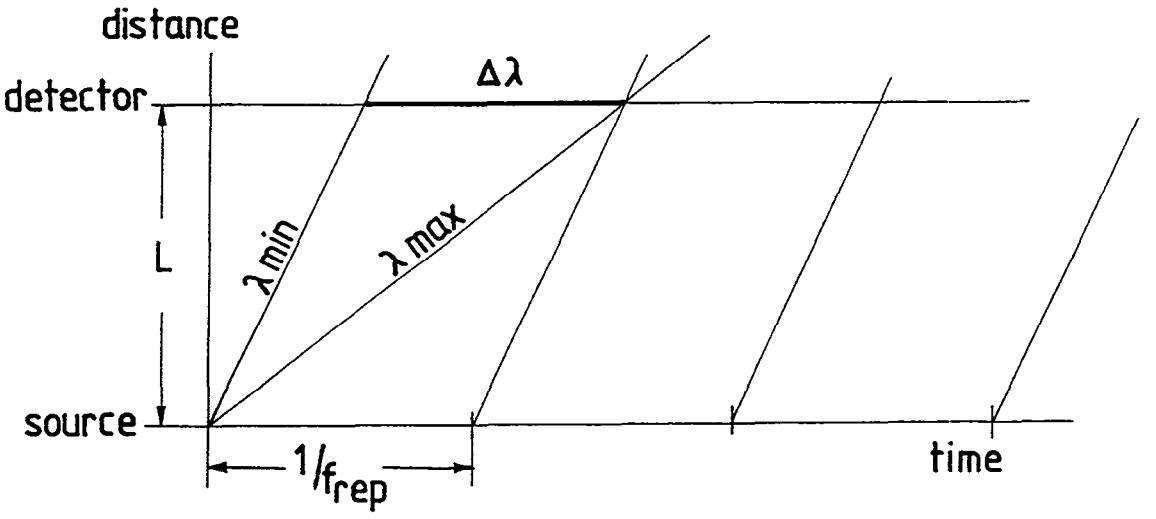

Figure 4 Distance—time—diagram for determining the maximum wavelength band

If L is determined by constraints like source shielding, minimum sample–detector distances or others, we might request the source with the lowest possible rep rate. This is now a conflicting situation, for we just showed that long pulse source (direct geometry) t–o–f applications demand high rep rates. In the case of short pulse sources the number of protons per pulse sets a technical lower limit to the rep rate at a given average beam power. In the remaining part of this paper we will discuss the consequences of different pulse lengths and rep rates on the possible gain for small angle neutron scattering.

4. Gain considerations for small angle neutron scattering

4.1 The influence of resolution requirements

We just stated that we want to use the highest feasible wavelength band. But we have to look somewhat closer to that demand, when we talk about applying this rule to SANS. We have to take into account the required resolution R, which can be written in different ways and is typically of the order of 0.1 to 0.15

$$R = \frac{\delta\lambda}{\lambda} = \frac{\delta t}{t} = \frac{\delta t}{L/v} \stackrel{!}{=} 0.1$$

where δt cannot be lower than the source neutron pulse width, which is roughly given by the moderator storage time τ (compare Fig. 1). This lower limit sets in turn a lower limit on the useful wavelength

$$\lambda_{min} = \frac{const}{L \cdot R} \cdot \delta t.$$

Setting $\delta t \simeq \tau \simeq 5\times 10^{-4}$s, we can calculate the cut–off wavelength λ_{min} for the three main source types presented in Figure 1.

– short pulse source: $\lambda_{min} \simeq 20/L$

Inserting L in meters we see that there is virtually no restriction, because even a very short instrument with L = 10 m (note: 6 m shielding thickness) would not pose a serious limit on λ (see Figure 5 below).

– long pulse source: $\lambda_{min} \simeq 20/L$,

which is the same as with the short pulse source, as long as we stick to the rule that the proton pulse length should be matched to the storage time, $t_p \simeq \tau$ (SNQ: $t_p = 250\ \mu s$).

– "very" long pulse source: $\lambda_{min} = 160/L$,

if we choose e.g. $t_p = 4000\ \mu s$. Even a 40–m–machine already has a cut–off at 4 Å.

Let us now turn to quantify the gain we can expect from exploiting a wide band of wavelengths. There will be mainly two points of view. An obvious definition of a gain is the ratio of the total detector counts from both the pulsed and the continuous operation. This is a common procedure and we will call this the integral gain. It certainly gives an idea of the advantage of the method, but the information content of a measurement is not only contained in the integral detector counts. The momentum transfer dependence of the scattered intensity I(Q) is the crucial point, so we will define a Q–dependent gain, which we call the differential gain. With the latter we have furthermore to distinguish between cases with and without restrictions on the useful band. In this context it may be useful to remark that the resolution imposed cut–off is equvalent to one, which we had to impose, if we had to avoid double Bragg scattering, i.e. $\lambda > \lambda_{bragg}$.

4.2 Integral gain

In calculating the ratio just mentioned we have to bear in mind that the total intensity scattered into forward direction is proportional to λ^2 [Guinier]. Therefore we will use the modified flux (better: current) $\lambda^2 \cdot j(\lambda)$ in computing the gain. Furthermore we will always assume that the experiment at the continuous source will be performed using the optimum wavelength λ_0, i.e. at the maximum in the $\lambda^2 \cdot j(\lambda)$–curve. So we define the integral gain as

$$G = \frac{\int_{\Delta\lambda} \lambda^2 j(\lambda) d\lambda}{\lambda_0^2 \cdot j(\lambda_0)\delta\lambda} \tag{6}$$

$\delta\lambda$ is taken as the FWHM of a typical triangular resolution element with $\delta\lambda/\lambda = 0.1$. In order to get the most from this integral, $\Delta\lambda$ has to be positioned such over the spectrum that $\lambda^2_{lo} j(\lambda_{lo}) = (\lambda_{lo} + \Delta\lambda)^2 j(\lambda_{lo}+\Delta\lambda)$, as indicated in Figure 5. Also shown in Figure 5 is the shift of $\Delta\lambda$ to longer wavelengths, if we cannot utilize neutrons below λ_{min}. Data collection at the pulsed source would be performed by non–equidistantly time slicing the interval $\Delta\lambda$ (resp. Δt) in order to keep the resolution fixed for every $\delta\lambda$–(δt)–bin (compare Fig. 5).

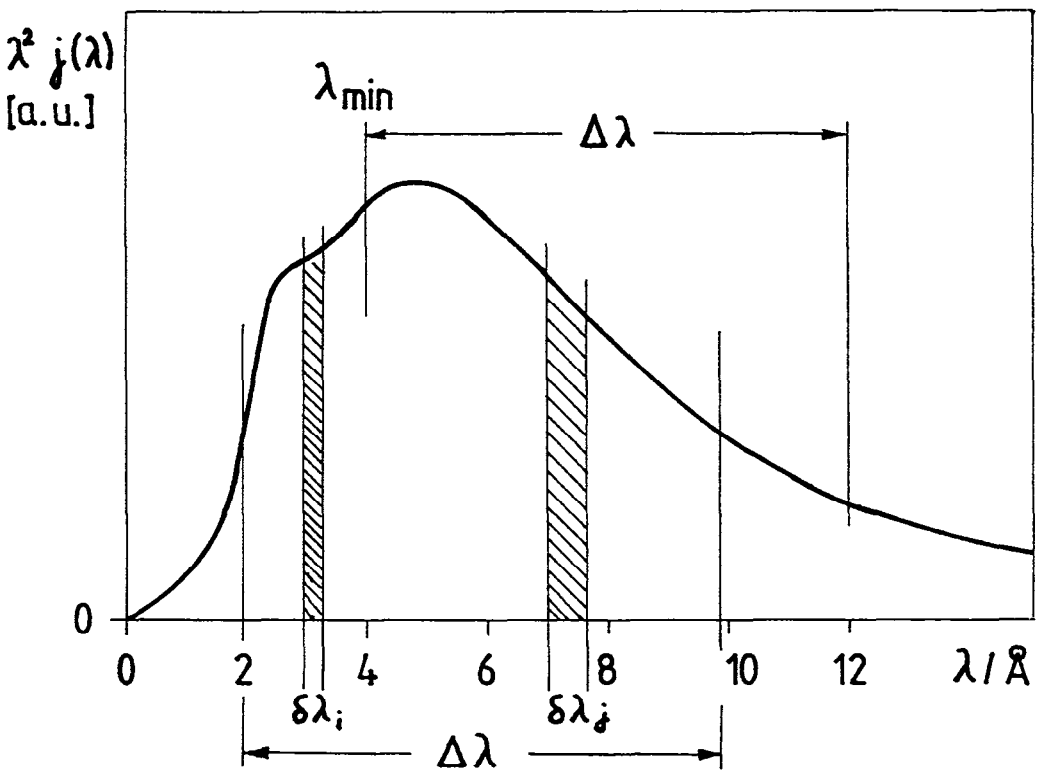

Figure 5 Positioning $\Delta\lambda(L,f_{rep})$ over the modified cold spectrum $\lambda^2 j(\lambda)$, where $j(\lambda)$ is the experimental ISIS 25 K moderator data.

In Figure 6 are compiled graphically all the gain factors calculated according to equ. 6 together with equ. 5. The scale is normalized to the average cold neutron flux of a 5 MW spallation source with a liquid hydrogen moderator (G = 1).

Two features of these integral gain factor functions should be pointed out. Firstly as expected, the wider $\Delta\lambda$ by suppressing 4 in 5 pulses (the 1 MW ESS target station L) cannot compensate the 80% loss in average neutron flux. The corresponding differential gain will be discussed in the following section. Secondly, the very long pulse source

variant at half the proton beam power of ESS would be superior to the latter for instruments longer than 30 m. Although the shock–like load of the target is absent with these long pulses, the 2.5 times larger temperature jump per pulse may pose a serious fatigue problem. This has to be investigated thoroughly.

We should not forget to mention the strong decrease of the long pulse gain factors for short distances, which is due to the resolution requirements and the corressponding shift of the $\Delta\lambda$–band to longer wavelengths (see section 4.1).

Finally we would like to point out that we cannot simply scale the short pulse 1 MW ESS case in order to outperform the 2.5 MW long pulse versions, because the enhanced shock load could not be taken by the target. Furthermore, the number of compressor rings had to altered from 2 to 6, a very unrealistic scenario.

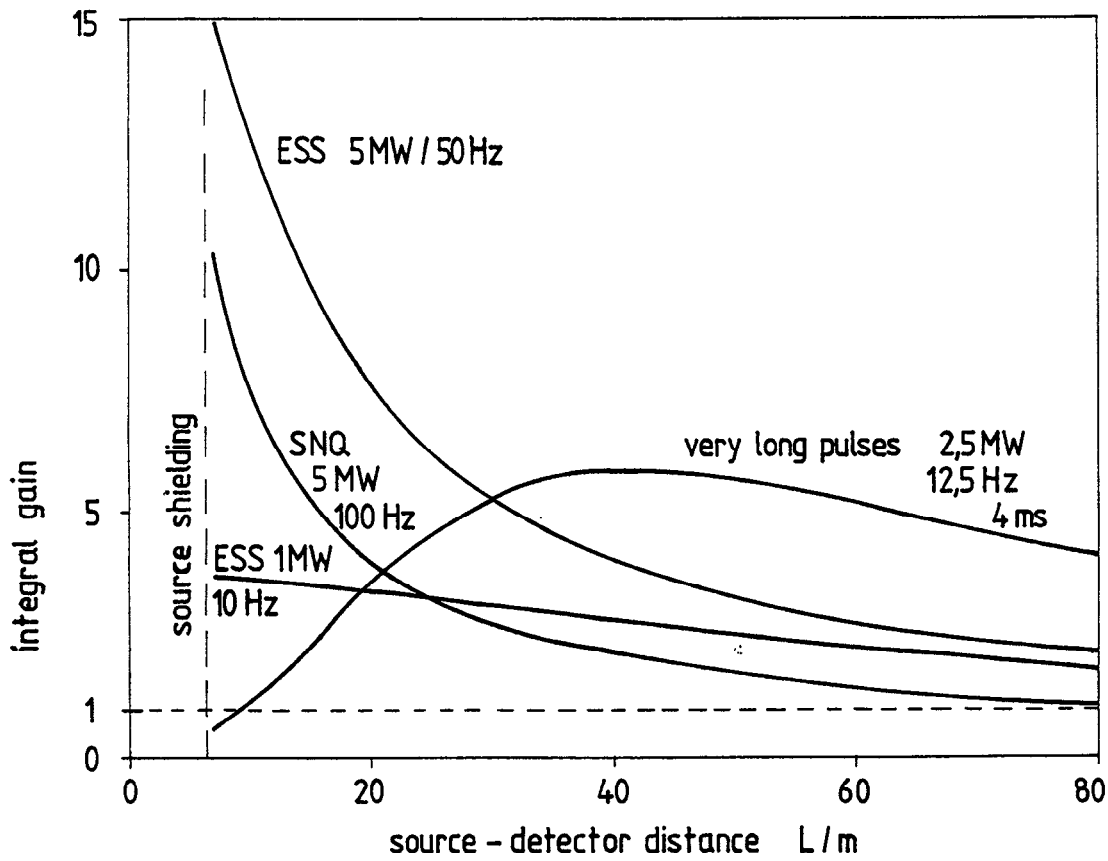

Figure 6 Integral gains for SANS as a function of source to detector distance for various source concepts. (G = 1 represents the continuous operation of a 5 MW source or the corresponding reactor equivalent.)

4.3 Differential gain G(Q)

Let us consider the standard SANS instrument equipped with a 2–dimensional position sensitive detector. At a continuous source we would select the optimum wavelength λ_0 from the moderator spectrum and accumulate the scattered intensity I(Q) from the

sample as a function of the momentum transfer Q. The latter is a single–valued function of the detector element coordinates x and y, say. At a pulsed source the Q–value corresponding to a certain (x,y) changes when scanning the $\Delta\lambda$–band. In other words, many detector elements represent as a function of time (wavelength) a certain Q–value. The differential gain, which we may also call a Q–dependent gain G(Q), therefore is obtained by summing up all the scattered intensities from different detector elements corresponding to a fixed Q–value. Clearly, the detector response depends on the actual sample, but for a quantification of G(Q) we may as well imagine a perfectly incoherent scatterer. On this basis we can easily depict G(Q), which has been calculated in the following according to the expression

$$G(Q) = \frac{\sum_{t\text{-bins}} I_t(Q)}{I_{mono}(Q)}.$$

The t–bins (λ–bins) are time (wavelength) slices of the spectrum of Fig. 5 with constant $\delta\lambda_n/\lambda_n$. The intensity in each slice t_n being scattered incoherently gives rise to a constant detector response $I_t(Q)$ between $Q_{min}(t_n)$ and $Q_{max}(t_n)$, with $Q_{max}(t_n)/Q_{min}(t_n)$ set equal to 8 (corresponding to detector pixel ratios x_{max}/x_{min} or $y_{max}/y_{min} = 8$), independent of t_n.

Examples

In the following we will show the results of these calculations for two instrument configurations and three different rep rate/pulse length combinations. We denote the moderator detector distance by L, moderator sample distance by D and sample detector distance by d, i.e. L = D + d.

- L = 15 m: D = 10 m, d = 5 m. ($1\ \mu s \leq t_p \leq 500\ \mu s$)

In Fig. 7a is shown the differential gain G(Q) for a short pulse or long ($t_p \leq \tau$) pulse source operated at 50 Hz. In the adjacent Fig. 7b is shown the gain when operating the source at reduced rep rate and power (10 Hz, one pulse in five). The horizontal rectangles on the abszissa depict the corresponding detector response with a continuous source of equal average flux as the 50 Hz pulsed source. Clearly, the accessible Q–range in one detector setting has doubled in the 10 Hz case, but only at very low intensity level. The discontinuous contour of the gain functions reflect the time slicing of the primary spectrum.

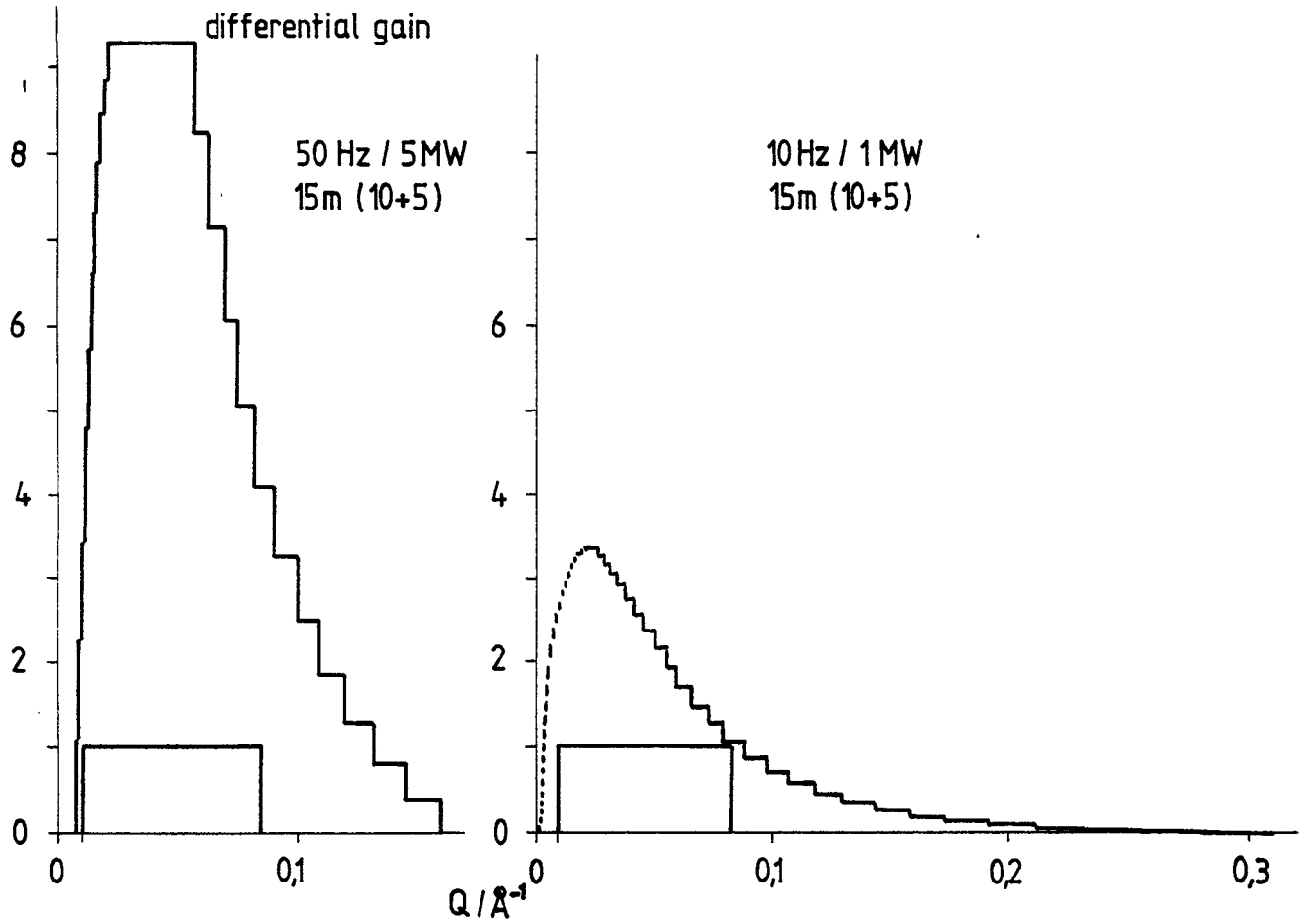

Figure 7 a: Differential gain G(Q) for pulsed or intensity modulated operation at 50 Hz (e.g. 5 MW) and detector setting L = D + d = 10 + 5 m. b: G(Q) at 10 Hz (i.e. 1 MW).

- L = 40 m: D = 20 m, d = 20 m. ($1\ \mu s \leq t_p \leq 500\ \mu s$)

In Fig. 8a is shown the differential gain G(Q) for a short pulse or long ($t_p \leq \tau$) pulse source again operated at 50 Hz. In Fig. 8b is shown the gain when operating the source at reduced rep rate and power (10 Hz, one pulse in five). The horizontal rectangles on the abszissa indicate as in Fig. 7 the detector response with a continuous source of equal average flux. The absolute scale of these graphs is of course different from those in Fig. 7. The differential gain is calculated within a chosen detector setting only. No attempt has been made to include an additional gain due to the fact that different detector settings in the continuous case may be comprised in one setting in the pulsed case because of the wider Q–range (compare Fig. 7).

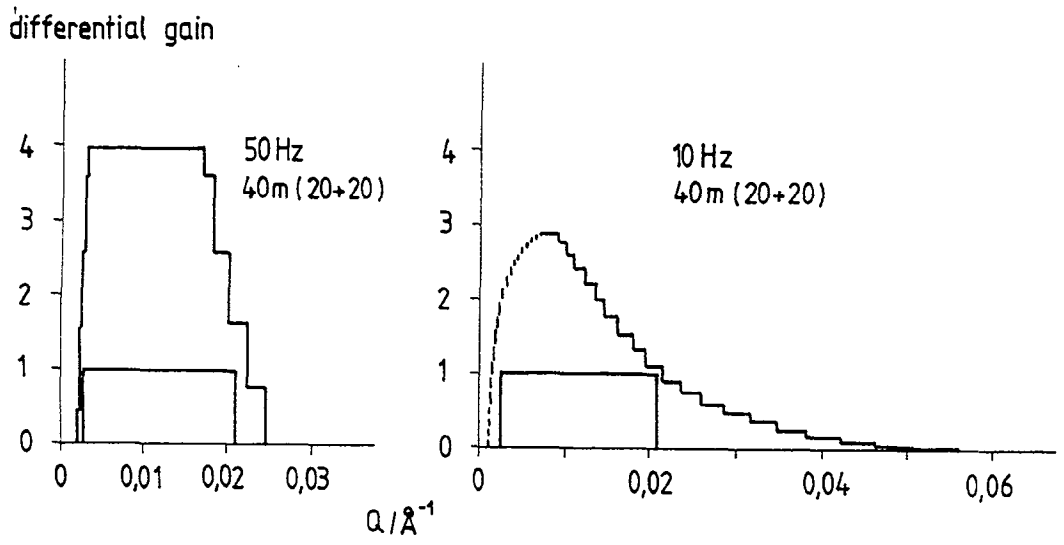

Figure 8 a: Differential gain G(Q) for pulsed or intensity modulated operation at 50 Hz (e.g. 5 MW) and detector setting L = D + d = 20 + 20 m. b: G(Q) at 10 Hz (i.e. 1 MW).

- L = 40 m: D = 20 m, d = 20 m. (t_p = 4000 μs)

For the 40–m–setting we have as well calculated the differential gain for a source with very long pulses, i.e. 4 milliseconds. The source is imagined to operate at 12.5 Hz at an average power of 2.5 MW. The result shown in Fig. 9 is correctly scaled and can be directly compared to Fig. 8. Because of the limitation of the $\Delta\lambda$–band to wavelengths larger than 4 Å (due to the long pulses) the accessible Q–range is strongly reduced as compared to the 1 MW/10 Hz case.

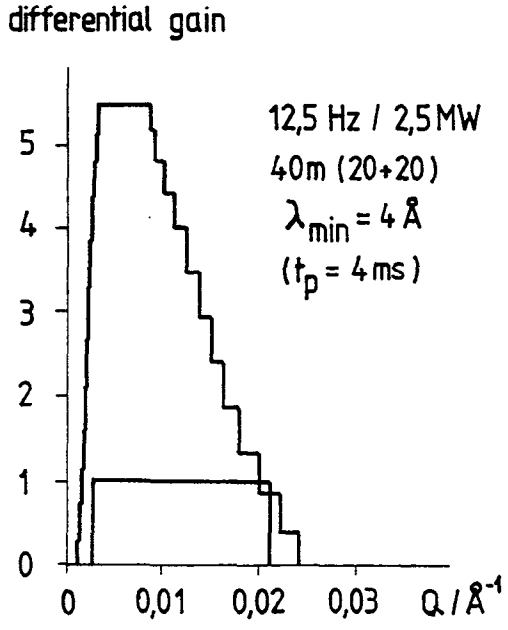

Figure 9 Differential gain G(Q) for a very long pulse source.

5. Conclusions

1. Short proton pulses are not necessary for applications, where a coarse primary wavelength resolution is needed only, such as small angle neutron scattering, neutron spin echo spectroscopy, diffuse scattering or others. On the other hand, they do not harm the performance of these instruments, if

- one can produce them at all (i.e. $\simeq 5\times 10^{14}$ protons per pulse with $t_p \leq 1\ \mu s$, ESS)
- one can afford the investment (compressors or synchrotrons)
- the target can stand the stress loads.

2. If one or several of the following reasons are true,

- a linac of sufficient power exists,
- one is aiming at an improved reactor performance "only", (intensity modulated source)
- one is planning for a spallation source with more than one target station,
- a high power ($\geq$ 5 MW) short pulse project should be realized in stages (e.g. in bypassing the ring(s) in a linac/compressor version),

then long proton pulses matched to the neutron storage time τ are recommended at a rep rate not too far below typical cold neutron chopper frequencies, i.e.

$t_p \simeq 0.3 \ldots 0.6$ ms

$f_{rep} \simeq 50$ Hz.

3. There is no "right" solution: t_p and f_{rep} have to be a compromise.

4. The usefulness of very long proton pulses ($t_p >> \tau$) is not convincing, particularly in view of target problems with thermal cycling.

6. References

G.S.Bauer, H.Conrad, W.Fischer, K.Grünhagen and H.Spitzer; Proc. ICANS–VIII (1985), RAL–85–110

G.S.Bauer, Workshop on Neutron Instrumentation for a Long Pulse Spallation Source, Berkeley (1995)

A.Guinier and G.Fournet, Small Angle Scattering of X–Rays (1955)

F.Mezei, ICANS–XII, Vol.I, 377 (1993)

W.Schäfer, E.Jansen, R.Skowronek, G.Will. K.S.Knight and J.L.Finney; Nucl. Instr. and Meth. A317 (1992) 202

R.Scherm and H.Stiller (eds.), Proceedings of the Workshop on Neutron Scattering Instrumentation for SNQ. Jül–Conf–1954 (1994)

ICANS-XIII
13th Meeting of the International Collaboration on
Advanced Neutron Sources
October 11-14, 1995
Paul Scherrer Institut, 5232 Villigen PSI, Switzerland

SMALL-ANGLE SCATTERING INSTRUMENTS ON A 1 MW LONG PULSE SPALLATION SOURCE

Glenn A. Olah *, Rex P. Hjelm † and Phil A. Seeger ‡

* Biosciences and Biotechnology Group, Chemical Science and Technology Division, Los Alamos National Laboratory, Los Alamos, NM 87545 USA
† Neutron Scattering Center, Los Alamos Neutron Science Center, Los Alamos National Laboratory, Los Alamos, NM, 87575 USA
‡ 239 Loma del Escolar, Los Alamos, NM 87544 USA

ABSTRACT

We have designed and optimized two small-angle neutron scattering instruments for installation at a 1 MW long pulse spallation source. The first of these instruments measures a Q-domain from 0.002 to 0.44 $Å^{-1}$, and the second instrument from 0.00069 - 0.17 $Å^{-1}$. Design characteristics were determined and optimization was done using a Monte Carlo instrument simulation package under development at Los Alamos. A performance comparison was made between these instruments with D11 at the ILL by evaluating the scattered intensity and rms resolution for the instrument response function at different Q values for various instrument configurations needed to span a Q-range of 0.0007 - 0.44 $Å^{-1}$. We concluded that the first of these instruments outperforms D11 in both intensity and resolution over most of the Q-domain and that the second is comparable to D11. Comparisons were also made of the performance of the optimized long pulse instruments with different reflectors and with a short pulse source, from which we concluded that there is an optimal moderator-reflector combination, and that a short pulse does not substantially improve the instrument performance.

1. Introduction

Small-angle neutron scattering (SANS) allows structural studies on length scales from about 10 to 1000 Å. The unique characteristics of neutron radiation give certain advantages over other types of radiation. For example, differences in scattering length between elements of similar atomic number and between different isotopes of the same element provide unique experimental capabilities. Varying the scattering contrast in polymeric and biological materials by selective deuteration in solvents and molecular subunits has led to information on the conformation of macromolecules unobtainable by any other technique. Neutron penetrability enables the application of SANS to nondestructive evaluation of nanoscale structure and in *in situ* measurements of samples in extreme environments requiring containment. All of these factors make SANS an indispensable tool in biological, chemical, physical and engineering research. It is therefore desirable to build SANS instruments on any high flux neutron source.

Keywords: SANS, Simulations, Monte Carlo, MCLIB, Long Pulse

We have begun evaluation of a new 1 MW long pulse spallation source (LPSS). At a recent workshop at Lawrence Berkeley National Laboratory [1], the panel on SANS instrumentation specified four characteristics of modern SANS instrumentation to meet the needs of emerging science. 1) A momentum transfer, Q, domain covering 0.5 to 0.001 $Å^{-1}$. ($Q = 4\pi\sin\theta/\lambda$, were θ is half the scattering angle from the incident beam and λ is the neutron wavelength.) 2) The ability to vary resolution, $\sigma(Q)/Q$ (rms), from no greater than 2% to 15%. 3) The ability to use different sample sizes and geometries. 4) The instruments should have low backgrounds.

In this report, we show the design and optimization of two LPSS-SANS instruments, which span the Q-domain from 0.0007 - 0.44 $Å^{-1}$. These include the Basic Low-Q Diffractometer (BLQD), which spans the Q-domain 0.002 to 0.44 $Å^{-1}$, and the Very Low-Q Diffractometer (VLQD), which spans the Q-domain 0.00069 - 0.17 $Å^{-1}$. These two proposed instruments meet the majority of requests made by participants from the Berkeley workshop [1]. We also characterize the performance of these instruments including a comparison with one of the world standards for SANS instruments, the 'as-built' D11 at the ILL in Grenoble, France.

2. Methods

Requirements for increased neutron flux, improved resolution, and a wider Q-range drive the designs of new SANS instrumentation and their sources of neutrons. A 1 MW long pulse source will provide long wavelength neutron fluxes considerably higher than that obtained at present day spallation sources, with average fluxes comparable to some present day reactors. In this paper we optimize the instruments for a case where the source is a 1 ms proton pulse operating at a frequency of 60 Hz. The total power dissipated on the tungsten target is 1 MW. We use the calculated brilliance ($n/cm^2/sterad/eV$) for a liquid H_2 moderator fully coupled with a reflector composed of 60 cm of Be surrounded by another 90 cm of Pb. The

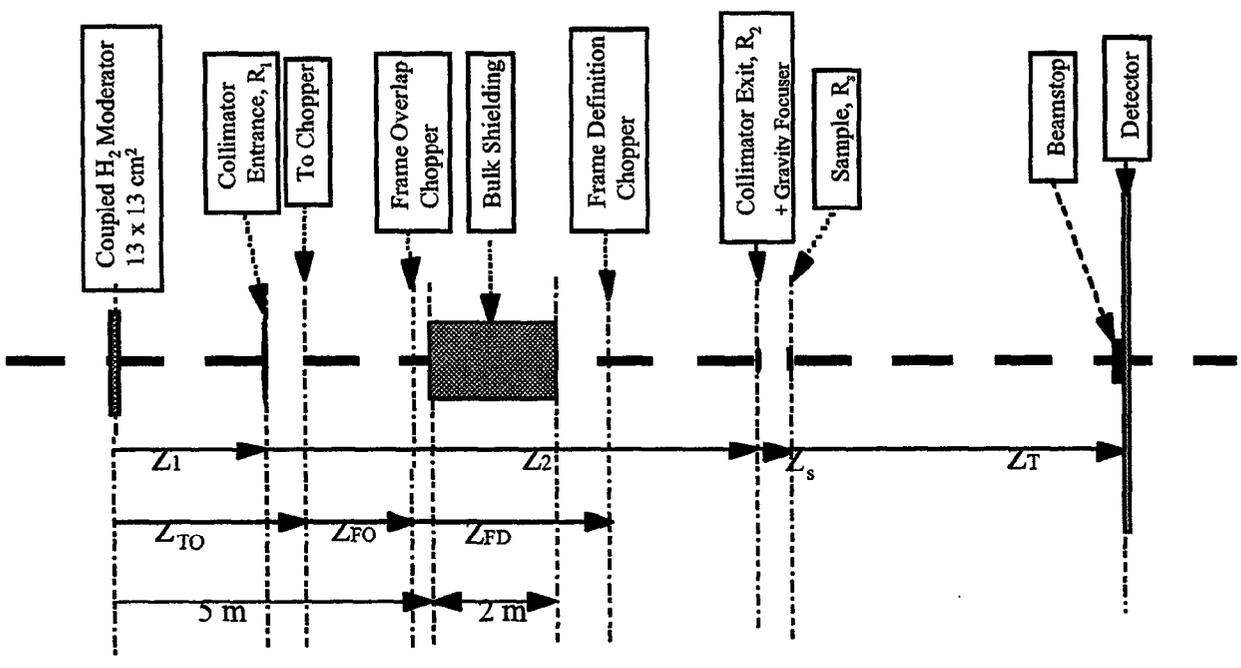

Figure 1. Schematic of simulated components for LPSS small-angle instrument. Bulk shielding was assumed fixed between 5 and 7 m from the moderator. A box will be located between 2.5 and 5 m which can house the T_0 and frame overlap choppers (and an additional chopper if necessary).

spectrum and pulse shape characteristics of the coupled moderator and reflector system were those calculated by Pitcher *et al.* using the Monte Carlo Nuclear Particle Transport code, MCNP [2]. Design characteristics were determined and optimization was done using the Monte Carlo instrument simulation package [3] under development at Los Alamos, which is based on the MCLIB Monte Carlo library originally developed at the Rutherford Laboratory [4]. The strongly coupled liquid hydrogen moderator 60 cm Be-90 cm Pb reflector source has a long tail in the low energy pulse structure characterized by a exponential decay with a time constant of 0.734 ms. Although these strongly coupled systems provide greater peak and integrated fluxes than more weakly coupled systems with shorter pulse tails, we must carefully consider the effects of the pulse tails on the instrument response function.

SANS instrument design used on the LPSS, like all SANS instruments, is inherently simple, consisting of a neutron source, a collimation system, choppers, shielding, and position sensitive detectors, see Figure 1. Instrument design and optimization for pulsed sources depends on obtaining as large a wavelength band width as possible (to maximum gains due to the use of time-of-flight (TOF) techniques) consistent with avoiding frame overlap. The first step taken in the instrument design involves the determination of the number and location of choppers, an initial assessment of which was done using a time-distance graphical utility developed by Luc Daemen at Los Alamos. The main objective of the chopper system is to define the wavelength bandwidth and to eliminate out of frame neutrons. System performance was evaluated by simulating a δ scatterer at fixed Q, and optimal configurations were determined by maximizing a figure of merit, FOM, which measures how long an experiment takes to get the same quality data

$$FOM = \frac{I(Q)}{V[Q]} \ln\left(\frac{Q_{\max}}{Q_{\min}}\right)$$

Parameters are chosen to give nearly the same value of the variance, V[Q], then the scattered intensity mapped into Q-space, I(Q), is compared. The logarithm of the Q-range represents the number of channels mapped into logarithmic Q-bins in a single instrument configuration. Resolution, $\sqrt{V(Q)}$, was calculated from the instrument response function determined from the scattering profile from the hypothetical δ scatterer. Thus the optimization is to maximize the count rate at fixed resolution. The maximum intensity of the instrument response function is dependent on the sample transmission which was assumed to vary as $\exp(-\alpha\lambda)$ and which was arbitrarily set at 68% for 10 Å neutrons. Here, the SANS instruments were designed and optimized by fixing the minimum desired Q at 0.0025 $Å^{-1}$ for the BLQD and at 0.0008 $Å^{-1}$ for the VLQD. For the fixed Q of the δ scatterer $\sigma(Q)/Q$ is fixed at 10%. Instrument optimization and performance simulations [2,5,6] included source energy and time structure, shielding location, wavelength-dependent effects from aluminum in the beam, chopper location, chopper opening and closing times and phase jitter, sample transmission and multiple scattering, and gravity.

3. Results

3.1. Basic Design Considerations and Optimization

Instrument designs used in this study take into account the current design of the target monolith shield. This includes a chopper box located between 2.5 and 5 m from the moderator can

house the T_0 and frame overlap choppers. Bulk shielding is placed between 5 and 7 m. We used single pinhole collimation with the entrance aperture located at 2.5 m from the moderator for both BLQD and VLQD. The exit aperture is 20 mm in front of the sample.

We have assumed in this report that large-area (1 m x 1 m) detectors with fast encoding will be available with 5 mm square pixels (and 3.4 mm resolution). For simulations of the BLQD and VLQD, two 1m x 1m detectors were used with one detector placed 0.25 m off-axis, and a second detector placed 0.75 m off-axis to extend the dynamic range.

We found that three choppers are needed to eliminate out of frame neutrons. A massive T_0 chopper eliminates the initial burst of high-energy neutrons and must block these fast neutrons over the total 13 cm x 13 cm moderator size. The location, opening time and phase of the T_0 chopper is important for defining the total usable wavelength range. Placing the T_0 at 2.8 m from the moderator maximizes the range from 2.5 to 12.8 Å. This is particularly important since we have made the instrument short to maximize the TOF gain. Should it be that cost, engineering and maintenance require that the T_0 chopper be moved farther out from the source, then we would have to optimize to a longer total flight path, similar to the low-Q instrument discussed previously [1]. The frame overlap chopper, located at 4.8 m for BLQD and 4.2 m for VLQD , assures that fast neutrons in the tail of the following pulse cannot reach the detector. The location of this chopper limits the maximum usable wavelength; the closer it is to the T_0 chopper the longer the wavelength that can be used. With these positions, the maximum wavelength is 12.8 Å for BLQD and 14.8 Å for VLQD. A third chopper, the frame definition chopper defines the time frame (T_{min} and T_{max}) to be measured within the 60 Hz cycle. Its phase is adjusted to be half closed for the maximum wavelength to be recorded for neutrons emitted at t = 0; thus, defining T_{max}. The chopper does not open again until the tail

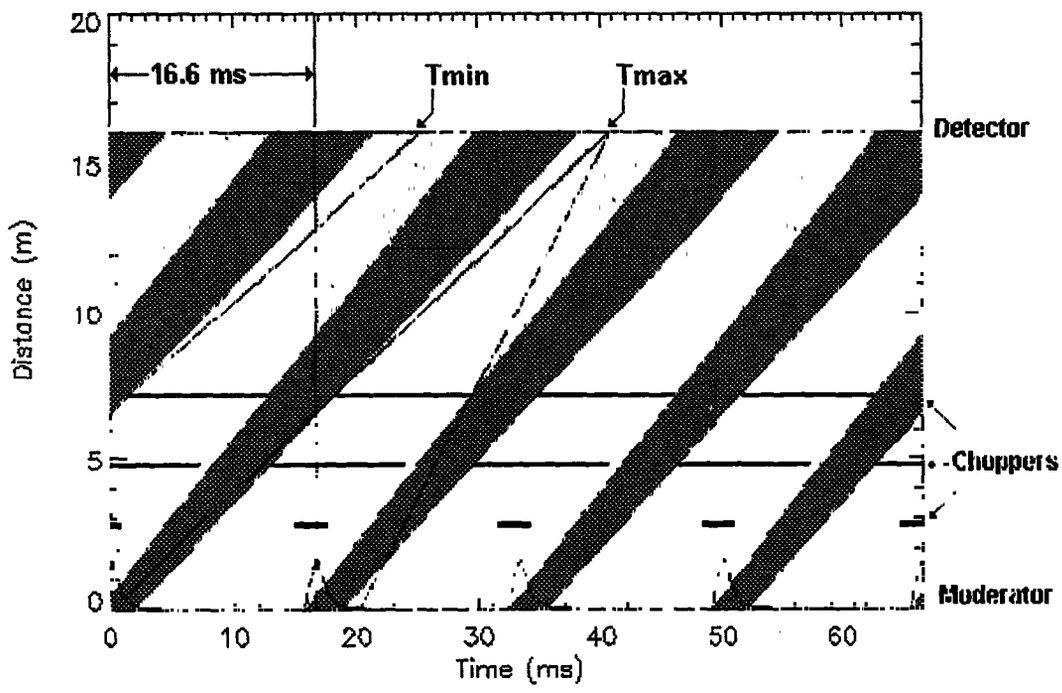

Figure 2. Distance-time diagram for BLQD showing the chopper phasing. The function of each of the choppers is defined in the text. Three lines represent choppers in the closed positions. The phasing shown gives neutrons from 6.4 Å to 10.2 Å.

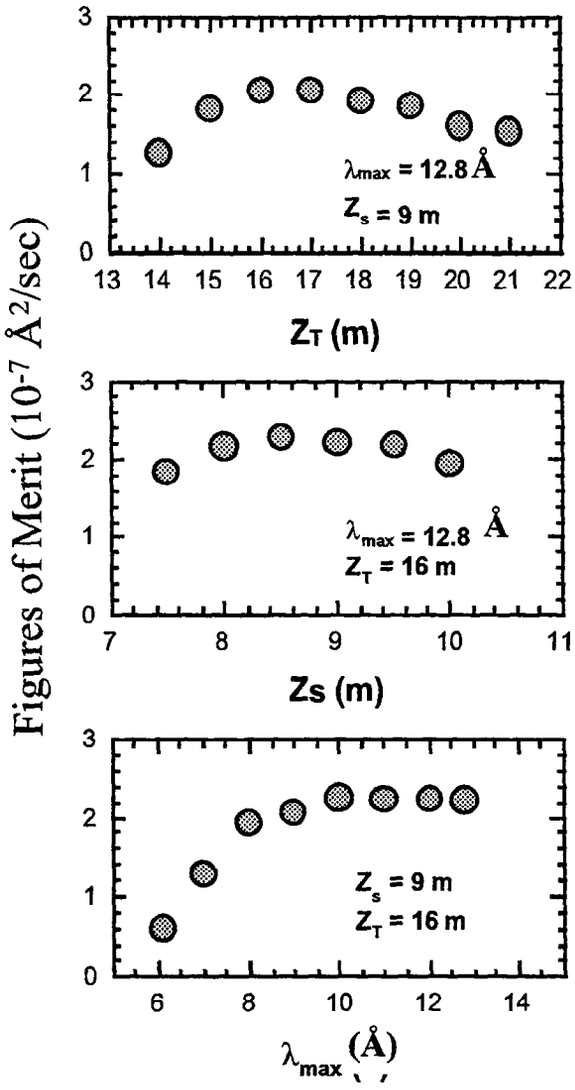

Figure 3. Parameter optimization for BLQD at Q = 0.01 Å^{-1}. The parameters Z_T, Z_s and λ_{max} were independently varied and the FOM calculated.

of the following pulse has decayed to 4.6 times the decay time constant to prevent frame overlap from neutrons originating in the tail of the following pulse. The T_{min} of the following pulse is defined by the delay after T_{max} after which we can guarantee that the frame definition chopper is fully closed (including three times the rms chopper jitter of 20 μs). The location of the frame definition chopper is important for blocking long wavelength (> 20 Å) out-of-frame neutrons from preceding pulses. Its optimal location depends on the location of the frame overlap chopper; therefore, positioning of the frame overlap and definition choppers requires an iterative process which depends on the T_{max} (or λ_{max}) desired. Figure 2 shows a distance-time diagram of the chopper configurations for the BLQD and a λ_{max} = 10.2 Å. In the unlikely event that long wavelength out of frame neutrons create background problems then these can be removed by placing a fourth chopper between the T_O and frame overlap chopper or by including a transmission Si mirror after the frame definition chopper.

The primary variables (see Figure 1) giving Q_{min} are the total instrument length, Z_T, the sample position, Z_s, and the maximum wavelength, λ_{max}. These values and the cone rule [7,8] give the sample radius, R_S, collimator entrance radius, R_1, collimator exit radius, R_2 , and the moderator penumbra radius, R_M. Z_T, Z_S and λ_{max} were independently varied and the figure of merit calculated. The results for BLQD are shown in Figure 3. The λ_{max} was fixed at 12.8 Å for both BLQD and VLQD when varying Z_T or Z_S. As Z_T is increased and with Z_S and λ_{max} fixed, a maximum in the figure of merit is reached. The figure of merit starts decreasing at larger Z_T due to the decrease in the usable wavelength band width and due to the decrease in the dynamic range. With Z_S and Z_T fixed and increasing λ_{max} , a plateau is reached at about 10 Å. For even larger wavelengths the resolution continues to improve but at the expense of dynamic range and incident flux. The Monte Carlo optimized parameters for the two instruments are given in Table 1. Possible layouts for BLQD and VLQD are given in Figure 4.

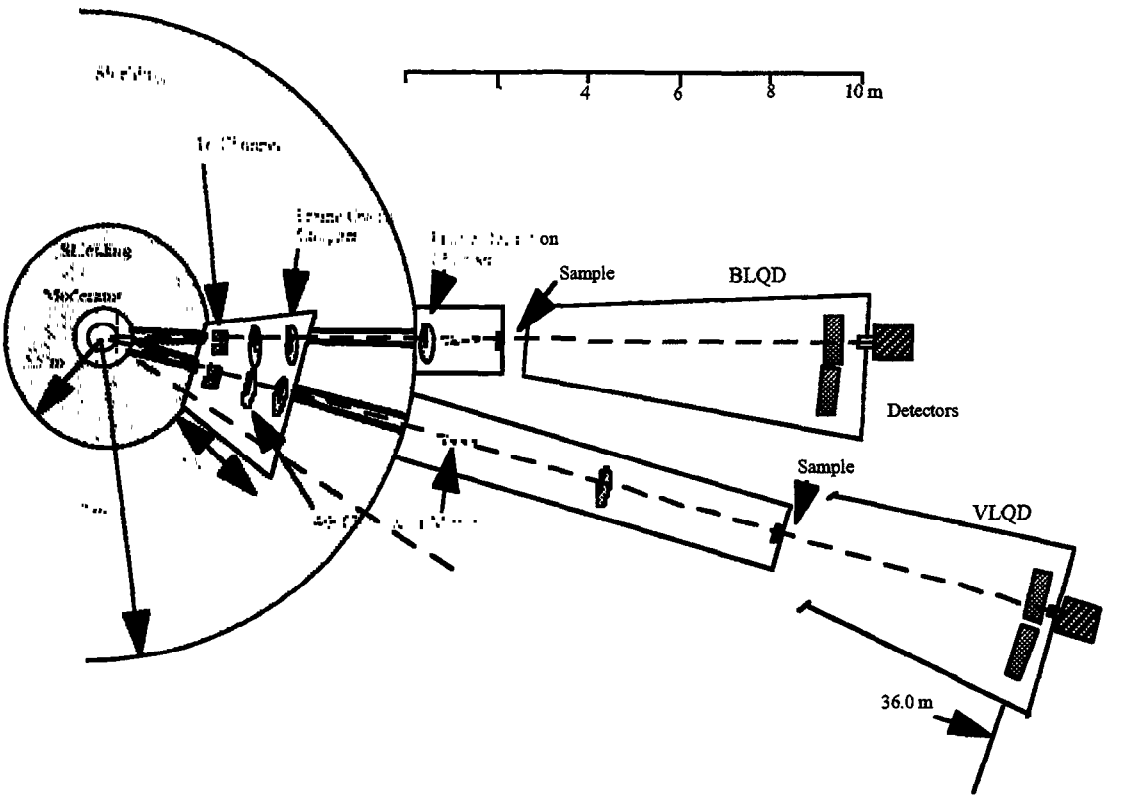

Figure 4. Possible layout for BLQD and VLQD.

Table 1
Optimized SANS Instruments

Instrument Parameter	Instrument BLQD	Instrument VLQD
Moderator-reflector Time Constant (μs)	734	734
Moderator-to-Collimator Entrance, Z_1 (m)	2.5	2.5
Entrance Aperture Radius, R_1 (mm)	9.8 - 32.0	8.6
Moderator-to-To Chopper, Z_{To} (m)	2.8	2.8
Moderator-to-Overlap Chopper, Z_{FO} (m)	4.8	4.2
Moderator-to-Frame Chopper, Z_{FD} (m)	7.2	10.5
Moderator-to-Collimator Exit, Z_2 (m)	9	16
Exit Aperture Radius, R_2 (mm)	5.07	5.11
Moderator Phase Space (mster-mm^2)	570 - 6150	120
Gravity Focus Stroke (mm)	1.2	25
Sample Radius, Rs (mm)	5.07	5.11
Moderator-to-Sample, Z_s (m)	9.02	16.02
Sample-to-Detector (m)	6.98	19.98
Beamstop Radius (mm)	21	26
λ_{max} (Å)	12.8	14.8
Q_{min} (Å^{-1})	0.002	0.00069
λ_{min} (Å)	2.5	2.5
Q_{max} with One Detector (Å^{-1})	0.21	0.089
Q_{max} with Two Detectors (Å^{-1})	0.44	0.17

3.2. Comparison with 'as-built' D11

In this report, we decided to make an initial comparison between the two LPSS instruments and the 'as-built' D11. This was done since many SANS users are already familiar with the 'as-built' D11; and we have successfully made benchmarked simulation of D11 [5,6]. However, we plan eventually to make comparisons with simulated instruments 'optimized' on a reactor with a state of the art cold moderator, such as D22. 'As-built' means using the specifications given for D11 in reference [9] including an increase by a factor of two in flux due to the installation of the COSTANZE velocity selector. When comparing instruments, the two most important parameters to compare are the resolution and intensity, or preferably intensity at the same resolution.

In Figure 5, resolution in Q is shown for D11 at various sample-to-detector settings and for BLQD and VLQD. A minimum scattering angle θ_{min} can be estimated from a penumbra radius projected on the detector using the cone rule [7,8]. The minimum measurable Q for different settings was determined from the estimated θ_{min} and λ_{max}. We assumed a beamstop 2 mm larger in radius than the prenumbra size in determinining θ_{min}. Each box representing a

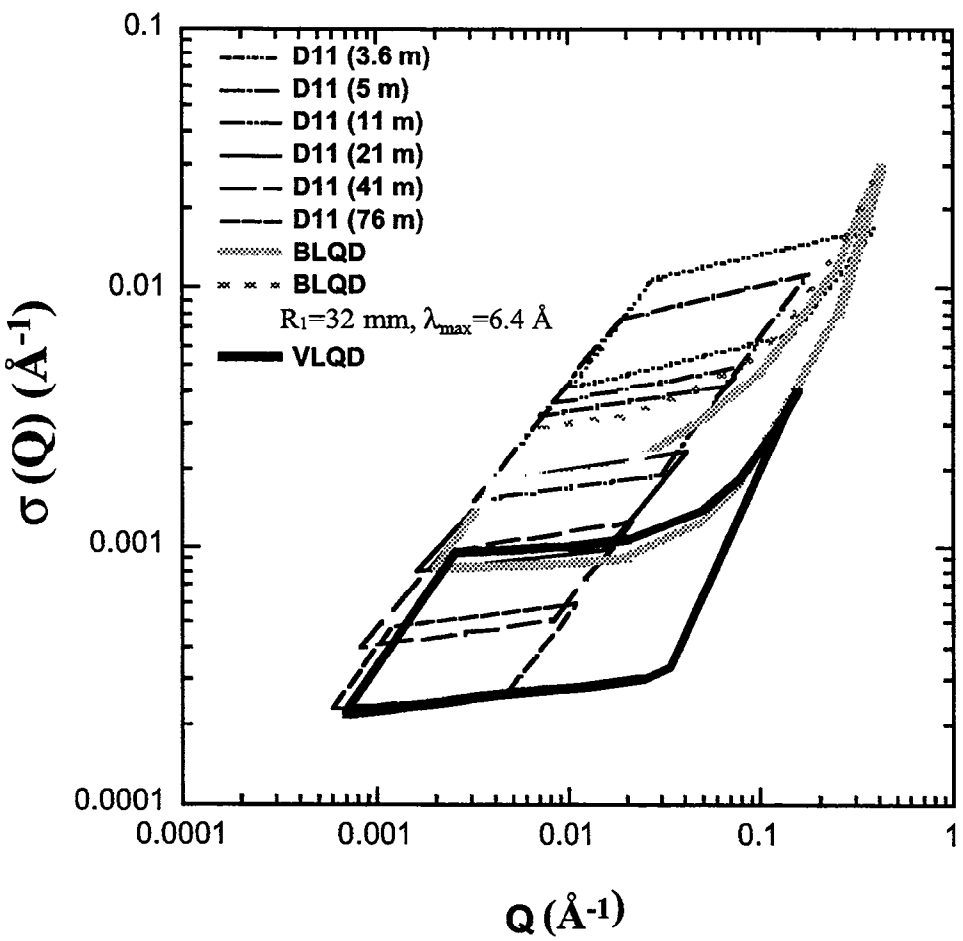

Figure 5. Comparison of resolution in Q for D11, BLQD and VLQD. The total collimation plus sample to detector distance is given in parentheses for D11. The sample to detector distance is half the total length except for the 3.6 and 76 m configurations in which case it is 1.1 m and 35.5 m, respectively.

D11 configuration corresponds to changing the velocity selector speed and thus selecting neutrons with different peak wavelengths between 4.5 and 12 Å. The 'as-built' D11 has a 64 cm x 64 cm area detector. Q_{max} of each box in Figure 5 was determined from the edge of this detector. Note that since the detector is flat, the resolution increases slightly as Q is increased for fixed wavelength. The boxes shown for BLQD and VLQD represent continuous choices of λ_{max}. BLQD can use wavelengths in the range from 2.5 to 12.8 Å and VLQD from 2.5 to 14.8 Å. Because TOF methods are used and the instruments are relatively short, slightly longer wavelengths can be used on the LPSS instruments.

Fair comparisons among different instruments consider scattering intensity mapped into Q-space using the same Q-precision and sample size in each case. The difference in detector size is dealt with below. Phase settings of choppers can be found for BLQD or VLQD that give the same resolution as D11 over roughly the same Q-range spanned by any one configuration of D11. We can begin making a comparison between D11 and the LPSS instruments by first asking the question: how would one measure the Q-range from 0.002 to 0.4 $Å^{-1}$ on D11? We then ask how would measurements on the LPSS instruments at the same resolution compare with the measurements on D11? As seen in Figure 6, three different sample-to-detector distances are required for D11 to measure this Q-range; namely, settings D11(21 m, 10 Å), D11(11 m, 5.5 Å) and D11(3.6 m, 4.5 Å), where the first number in parenthesis is Z_T and the second number is λ_0. BLQD at a phase setting of λ_{max} = 10 Å would have the same resolution as D11(21 m, 10 Å). This phase setting results in a factor of 2.8 more scattered intensity at any particular Q value between Q = 0.0025 - 0.018 $Å^{-1}$ relative to D11(21 m, 10 Å); how-

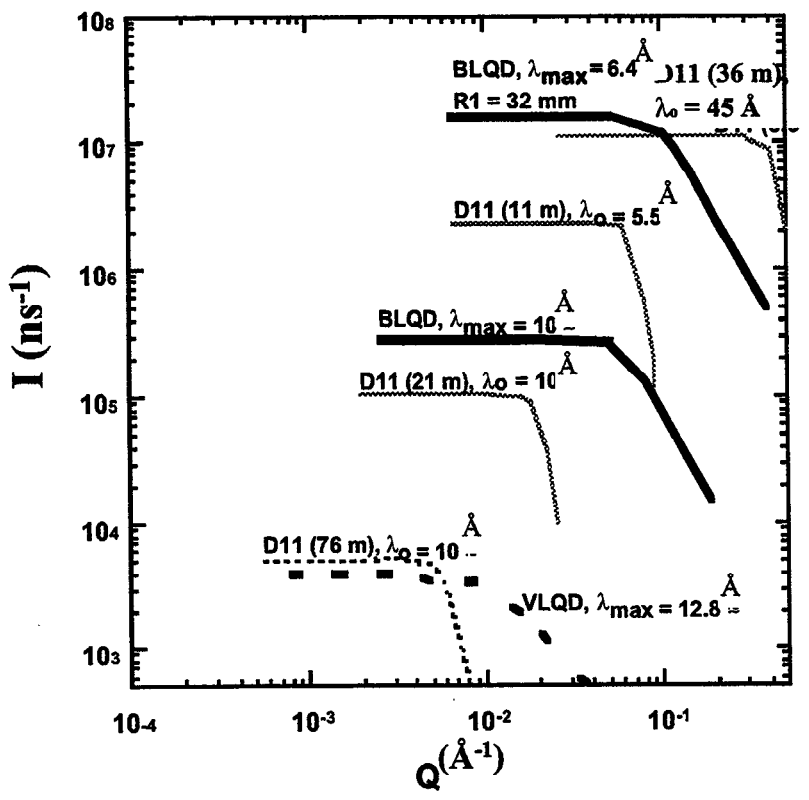

Figure 6. Comparison of scattered intensity for δ-scatterers for D11, BLQD and VLQD.

ever, LPSS does not reach a Q_{min} of 0.002 $Å^{-1}$. If a phase setting of λ_{max} = 12.8 Å is used then we obtain Q_{min} = 0.002 $Å^{-1}$, 30% better resolution and approximately the same scattered intensity. BLQD at the lowest wavelength phase setting of λ_{max} = 6.4 Å has approximately 23% better resolution than D11(11 m, 5.5 Å) but 30% less intensity. We can gain intensity at the expense of resolution by opening up the collimation entrance aperture R_1. The same resolution is obtained as D11 (11 m, 5.5 Å) over the Q-range 0.007-0.06 $Å^{-1}$ for R_1 = 32 mm. This BLQD setting gives a tremendous gain in scattered intensity of 7 relative to D11(11 m, 5.5 Å). The penumbra diameter projected on the moderator is 92 mm when R_1= 32 mm. Compared to D11(3.6 m, 4.5 Å), BLQD has approximately 15 % higher scattered intensity in the Q-range 0.007 - 0.12 $Å^{-1}$ and approximately 4 times better resolution over much of this range. Scattered intensity at the high Q-range (> 0.12 $Å^{-1}$) decreases by approximately a factor of 5 at 0.2 $Å^{-1}$ and 10 at 0.3 $Å^{-1}$ compared to D11(3.6, 4.5 Å); however, the resolution for BLQD still remains better than D11 by as much as a factor of 2. Only above a Q of 0.3 $Å^{-1}$ does the resolution become comparable then slightly worse than D11(3.6, 4.5 Å).The VLQD has approximately 35 % lower scattered intensity than D11(76 m, 12 Å) at the same resolution. It is not surprising that the gain from using time-of-flight is small considering that the wavelength band width is only 1.6 Å ; compare this to 3.64 Å for the BLQD. The VLQD bandwidth is comparable with the $\Delta\lambda/\lambda$ = 12 % FWHM obtained for D11. An intensity gain of 1.45 comes from the larger phase space sampled by the VLQD relative to D11.

We could place the same detector configuration on D11 as used in the design of BLQD and VLQD. In this case the Q_{max} for the three D11 settings shown in Figure 5 and 6 would approximately triple. When comparing BLQD and D11, the same three settings for D11 would still be needed to span the Q-range 0.002 - 0.4 $Å^{-1}$, except now the range would extent even further to around 0.9 $Å^{-1}$. Scattered intensity and resolution at any previous Q value would remain the same; however, intensity would taper off in a similar way as seen for BLQD and VLQD at the new higher Q values due to using an off-center detector arrangement.

We are currently investigating the design of a seven multiple-aperture configuration (with intermediate baffles to prevent crosstalk). This system would require larger samples (3 cm diameter), but would increase the intensity by five to seven-fold while retaining resolution.

3.3. Effects of source pulse width and pulse tail on performance

Simulations of various source configurations show that increased peak and integrated neutron flux in the pulse is achieved at the expense of longer pulse tails [2]. It is of interest to know what the effect of the source pulse width and pulse tail have on a δ scatterer at a particular Q value. We, therefore, used three different neutron sources with the BLQD geometry to see what the effect would be on a δ scatterer centered at a Q value of 0.1 $Å^{-1}$. The first source is the liquid H_2 moderator coupled with a 60 cm Be-90 cm Pb reflector, a 1000 μs pulse width, and 0.734 ms pulse tail used in the optimization calculations. This source is called the long pulse, strong reflector. The second source was a liquid H_2 moderator coupled with a 40 cm Be-110 cm Ni reflector, using a short proton pulse of width of 1 μs, and a decay time constant of 0.274 ms. This source is called the short pulse, weak reflector. The third source was a liquid H_2 moderator coupled with a 150 cm (∞) Be reflector, a proton pulse width of 1000 μs, and a decay time constant of 1.710 ms. This source is called the long pulse, infinite reflector. The results from using these three sources is tabulated in Table 2. One effect of using a long pulse and strong or infinite reflector is a wider spread in the instrument response function

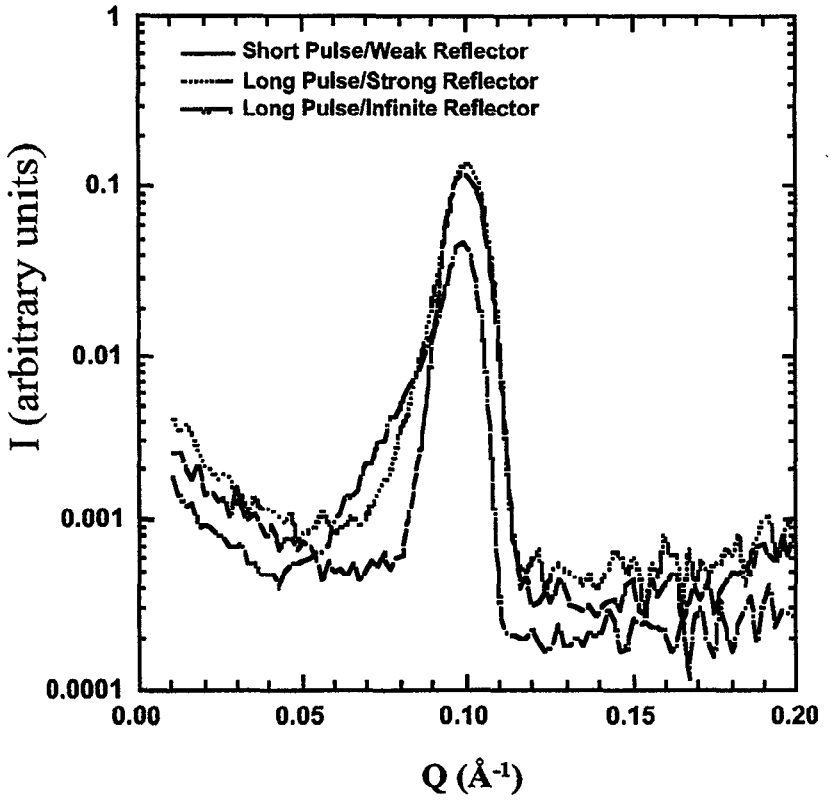

Figure 7. Effect on the resolution and scattering intensity from a d-scatterer using coupled moderator-reflector systems with different time constant in the exponential tail. BLQD is used in these simulations.

relative to the weak reflector, short pulse case (Fig. 7). This effect increases with Q and is quite apparent for $Q > 0.1$ Å^{-1} but is negligible for Q values < 0.05 Å^{-1}. The scattered intensity is highest for the long pulse, strong reflector suggesting that there is an optimal Be reflector thickness for the LPSS. The results indicate, further, that there is little to be gained by using a short pulse and weak reflector with this instrument.

Table 2.
Effects of Tails in Moderator-Reflector Configurations for a δ-scatterer on BLQD

	Reflector		
Parameter	40 cm Be, 110 cm Ni	60 cm Pb, 90 cm Be	Be (∞)
Proton Pulse Width (μs)	1	1000	1000
Moderator-reflector Time Constant (μs)	276	734	1710
Scattered Intensity ($MW^{-1}s^{-1}$)	8.95×10^6	1.15×10^7	4.31×10^6
Δλ (umbra) (Å)	3.56	2.92	1.56
Δλ (total) (Å)	3.96	3.64	3.64
σ rms @ Q=0.1 (Å^{-1})	0.0046	0.0056	0.0082

4. Conclusions

We optimized two instruments for a 1 MW LPSS operating at 60 Hz and a 1 ms proton pulse. In order to quantify the performance of these instruments, they were compared to D11 at the ILL. Scattered intensity gains between 3 - 7 for the BLQD over D11 were determined for the Q-range 0.0025 to 0.12 $Å^{-1}$. For Q > 0.12 $Å^{-1}$, scattered intensity for BLQD is lower than D11(3.6 m, 4.5 Å). However, the resolution is considerably better. We conclude that the two BLQD phase settings of λ_{max} = 10.2 and 6.4 Å can adequately cover the Q-range between 0.0025 - 0.44 $Å^{-1}$ and BLQD can perform better than D11 with regards to resolution and scattered intensity over most of this Q-range. The VLQD (λ_{max} = 12.8 Å) at the same resolution as D11(76 m, 12 Å) is approximately 35 % lower in scattered intensity. Because VLQD is only 36 m long, utilization of multiple aperture collimation on this instrument may be possible with an increase in scattered intensity by approximately a factor of 4 over D11(76 m, 12 Å). Similar gains can be expected if multiple aperture collimation is used on BLQD. Comparisons of the optimized instruments using long and short pulses and different reflectors suggest that there is an optimal moderator-reflector configuration, and that using a short pulse does not largely improve the performance of these instruments.

5. References

[1] Long Pulse Spallation Source Workshop, Berkeley National Laboratory, Berkeley, California, April 18 - 21, 1995.

[2] E.J. Pitcher, G. J. Russell, P.A. Seeger, and P.D. Fergusson,, "Performance of Long-pulse Source Reference Target-Moderator-Reflector Configurations" Proceedings of ICANS-XIII, Paul Scherrer Institut, Villigen, Switzerland, Oct. 11-14, 1995.

[3] P. A. Seeger, "The MCLIB Library: Monte Carlo Simulation of Neutron Scattering Instruments," Proceedings of ICANS-XIII, Paul Scherrer Institut, Villigen, Switzerland, Oct. 11-14, 1995.

[4] M. W. Johnson and C. Stephanou, "MCLIB: A Library of Monte Carlo Subroutines for Neutron Scattering Problems," Rutherford Laboratory report RL-78-090.

[5] P. A. Seeger and R. P. Hjelm, "A Very-Low-Q-Diffractometer for an Advanced Spallation Source," Proceedings of ICANS-XII, Abingdon, U.K., May 24-28, 1993.

[6] P. A. Seeger and R. P. Hjelm, "Design and Implementation of Low-Q Diffractometers at Spallation Sources," American Crystallographic Association Symposia Proceedings, Albuquerque, NM, May 24-28, 1993.

[7] P. A. Seeger, "Optimization of Geometric Resolution in Small-Angle Scattering," Nuclear Instruments and Methods 178, 157-161 (1980).

[8] P. A. Seeger and R. Pynn, "Resolution of Pulsed-Source Small-Angle Neutron Scattering," Nuclear Instruments and Methods in Physics Research A245 , 115-124 (1986).

[9] P. Lindner, R. P. May and P. A. Timmins, "Upgrading of the SANS instrument D11 ant ILL," Physica B 180 & 181, 967-972 (1992).

ICANS-XIII
13th Meeting of the International Collaboration on
Advanced Neutron Sources
October 11-14, 1995
Paul Scherrer Institut, 5232 Villigen PSI, Switzerland

THE PERFORMANCE OF REFLECTOMETERS AT CONTINUOUS WAVE AND PULSED-NEUTRON SOURCES

M. R. Fitzsimmons and Roger Pynn
Los Alamos National Laboratory, Los Alamos, New Mexico 87545, USA

ABSTRACT

To quantify gains from time-of-flight (TOF) methods, identical reflectometers viewing a continuous wave (CW) neutron source and a variety of pulsed-neutron sources were simulated using a Monte Carlo technique. Reflectivity profiles obtained for a simple thin-film, reflecting sample were nearly identical in all simulations, and models fitted to the simulated data yielded parameters (film thickness, surface roughness, and scattering length density) that were equally accurate and precise in all cases. The simulations confirm the power of the TOF method and demonstrate that the performance of pulsed sources for reflectometry does not scale simply as the inverse duty factor of the source. In the case of long-pulse sources, the simulations suggest that pulse tails have little effect on results obtained from specular reflectometry and that maximum brightness of the neutron source should be the primary design criterion.

1. The Reflectometers Simulated

This paper presents the results of Monte Carlo simulations of a traditional reflectometer at different neutron sources — CW sources, short pulse spallation sources (SPSS) and long pulse spallation sources (LPSS). The same reflectometer was used in all simulations. Only the characteristics of the neutron source, and the technique used to measure neutron wavelength were changed. In the case of the CW simulation, a monochromating crystal was used to select a nearly monochromatic beam (MB) from the neutron spectrum. In the simulations using the pulsed-sources, time of flight (TOF) was used to determine neutron wavelength.

A "reflectometer of traditional geometry" (cf Figure 1) is an instrument which uses a pair of slits of height h and width w separated by a distance L_S to define an incident beam that is highly collimated in the reflection plane [1]. Since studies of liquid surfaces are not to be excluded, the reflection plane is taken to lie in the vertical plane, so h is small and w is large.

In the simulations, each reflectivity profile was accumulated by following the same procedure that one would use in an actual experiment. The sample was lowered as the angle of incidence of neutrons on the sample, α_i, was increased so the footprint of the beam remained constant and centered on the sample. The widths of the slits defining the incident beam were equal (w = 40mm) and were not changed during the simulation. The vertical dimensions of the slits were also equal, but were adjusted to be proportional to the magnitude of the scattering vector, $Q=4\pi\sin(\alpha_i)/\lambda$, and equaled 1mm when $Q=0.1\text{Å}^{-1}$. By changing the vertical opening of the slits in this manner, the geometrical contribution, $\delta\alpha/\alpha_i$, to the resolution, $\delta Q/Q$ was kept constant as the wave-vector transfer perpendicular to the reflecting sample, Q, was varied.

Keywords: Neutron Sources, Reflectometry, Performance, MCLIB

Since the acceptance of the neutron beam by the slits varies as $\phi=(hw)^2/L_S^2$, the intensity of the neutron beam reaching the sample increases with Q^2. This increase partly negates the loss of signal owing to the decrease of the sample reflectivity which varies as approximately Q^{-4}.

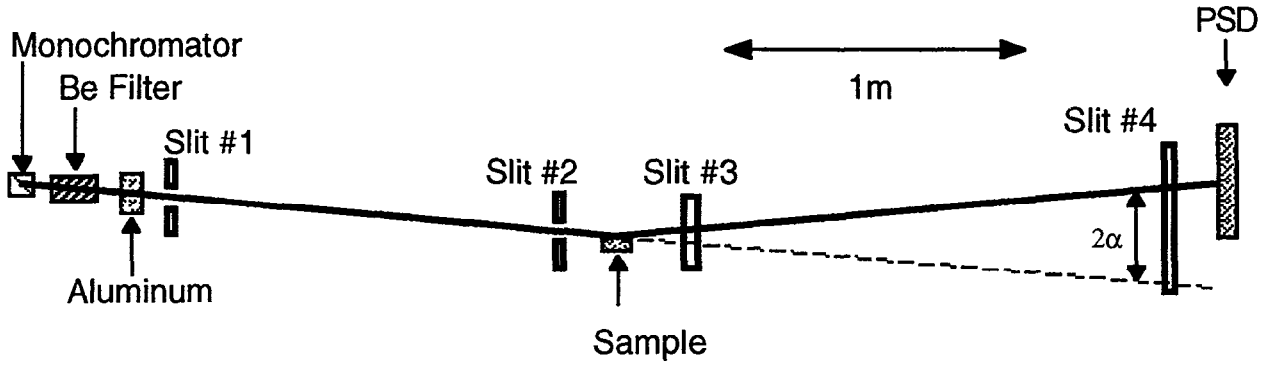

Figure 1: A reflectometer of traditional geometry is depicted. The reflectometer is configured with a monochromator and Be filter, which together produce a monochromatic neutron beam that is used in the MB simulation. The monochromator and Be filter are removed for the TOF simulations.

In the simulations of the MB technique, a graphite crystal was used to select a nearly monochromatic beam with a mean wavelength of 4 Å from a neutron spectrum that is typical of that produced by liquid H_2 moderators. The angular divergence of the neutron beam emanating from the moderator was chosen to be the same as that at the end of a Ni-coated neutron guide for λ_0=4.1Å neutrons, or 0.8° (FWHM). The mosaic spread of the monochromator in the diffraction plane of the crystal was 1.4° (FWHM). The crystal mosaic, the divergence of neutrons from the moderator, and the acceptance of the horizontal slits (in the diffraction plane of the monochromator) fixed the wavelength spread of the incident beam to be $\delta\lambda/\lambda_0$=2% (FWHM). The reflectivity of the monochromator was 80%.

The TOF studies involved simulations of the performance of the reflectometer at ten spallation sources with different proton pulse lengths and different target/moderator configurations. The neutron pulse shapes and spectra have been calculated by Pitcher et al [2] for various target/moderator configurations. The neutron spectra are tabulated and the shapes are fitted to simple functional forms for input into the present simulation of reflectometer performance [3]. The most significant operating parameters of each source are the pulse repetition frequency, the proton pulse width, δt, and the thermal time constant, τ, of the moderator [4]. These parameters are given in Table 1 for the different pulsed sources. In all cases, the proton power incident on the spallation target was held constant at 1 MW. The time-averaged brightness of the sources with τ = 370ms (PSS-1, -3, -5, -6, and -7) are the same as that of the CW source. Sources with longer time constants have larger time-averaged brightness. These are given in the Table.

In the TOF simulations, the length of the incident beam path was chosen so that FWHM wavelength resolution at the minimum wavelength used matched that used in the MB simulations. The operating parameters of the instruments investigated in the simulations are also given in Table 1.

In order to achieve good resolution in the TOF simulations either the time of flight must be large, or the neutron pulse duration must be small. The former can be accomplished by using very slow neutrons that travel a short distance (PSS-1), or by using shorter wavelength neutrons that travel a long distance (PSS-2 through -6). Alternatively, good temporal resolution can be achieved by using a combination of short proton pulses and moderator time constants (PSS-8 through -10), or by using a chopper (PSS-7). The chopper pulse width, δt_c, can be made as small or as large as needed for the measurement.

The TOF instruments vary in length from 16 to 60 m. Only the last 4 m of each instrument is the same for all simulations.

Table 1: Operating Parameters of the Instruments and Sources

Source	f [Hz]	δt [ms]	τ [us]	δt_n [ms]	$B \cdot 10^{16}$ n/st/m^2/s	L [m]	λ_{min} [Å]	$\Delta\lambda$ [Å]	F	t_{min} [ms]	M	Technique
CW	steady	-	-	-	5.5	4	4.1	$=\delta\lambda$	-	n/a	100	monochromator
PSS-1	60	1	375	1	5.5	18	7.85	3.25	3	35	8	short flight path, long λ, (cold neutrons)
PSS-2	60	1	230	1	3.9	60	3.38	0.94	4	51	13	long flight path, moderate λ, small τ
PSS-3	60	1	375	1	5.5	60	3.38	0.94	4	51	13	long flight path, moderate λ, moderate τ
PSS-4	60	1	490	1	6.7	60	3.38	0.94	4	51	13	long flight path, moderate λ, large τ
PSS-5	120	0.5	370	0.56	5.5	30	3.41	0.95	3	26	13	twice the freq. and half the width of PSS-3
PSS-6	120	0.735	370	0.76	3.9	36	3.76	0.62	4	34	21	somewhat longer pulse than PSS-5
PSS-7	60	1	370	0.33	5.5	23	2.86	2.76	2	16.7	4	short flight path, pulse-imaging chopper
PSS-8	10	0.3	230	0.33	3.9	30	1.96	11.3	1	15	1	moderate flight path, PSS-2 at 10Hz and 0.3ms pulse
PSS-9	10	0.1	230	0.20	3.9	16	1.64	23.2	1	6.6	1	SNQ facility
PSS-10	10	0.001	230	0.19	3.9	16	1.64	23.1	1	6.6	1	1MW low frequency target

f	source frequency = $1/\Delta T$
δt	proton pulse width
τ	composite moderator time constant
δt_n	neutron pulse width
B	source brightness
L	flight path length
λ_{min}	minimum neutron wavelength available
$\Delta\lambda$	wavelength bandwidth available
F	end of detection frame in units of 1/f (detection frame is 1/f long)
t_{min}	time-of-flight of a neutron with wavelength λ_{min} traveling a distance L
M	number of macro-measurements needed to measure the reflectivity profile from Q_c to 0.106Å^{-1}

The TOF instruments also use up to three choppers to condition the neutron beam. The first is called the t_0 chopper and is placed at 5 m from the moderator in our simulations. The purpose of the t_0 chopper is to stop most high energy neutrons and γ-radiation from reaching the experimental area. The second chopper is the frame overlap chopper and intercepts most of the very slow neutrons generated during earlier pulses [5]. The frame overlap chopper was located 6 m from the moderator. The third chopper is called the frame definition chopper and, as its name implies, serves to define the frame, F, in which neutrons are detected relative to their creation at t_0. The position of the frame definition chopper (between the frame overlap chopper and the reflectometer) was chosen to select neutrons with wavelengths between λ_{min} and λ_{max}. The frame definition chopper was not needed for the simulations PSS-8, -9, and -10, since these instruments use neutrons produced in the first frame.

2. The Reflecting Sample

The reflecting sample used in the simulations was a 600Å thick film of d-polystyrene (d-PS) on a Si substrate. The roughnesses of the air-PS and PS-Si interfaces were 5Å (FWHM). The selection of such a relatively simple sample tends to favor the simulation of the MB technique

over the TOF technique, since information over a very broad region of Q is not needed to fit a simple model. By favoring the MB technique, the intensity gains realized when employing the TOF technique over the MB technique are believed to be conservative estimates.

3. The Simulations

The reflectivity profile for the MB technique was simulated from Q=0.009 to 0.106Å^{-1} by taking equal steps in α_i of 0.02°. For Q>0.02Å^{-1}, the counting time was increased with Q^2. This increase combined with the increase of the acceptance of the slits yielded an exposure that varied as Q^4 and largely negated the Q^{-4} decay of the reflectivity profile. The result was a reflectivity curve whose fringe maxima had equal statistical precision.

The Monte Carlo simulations of the TOF instruments proceeded in the same manner as the MB simulation, except that neutrons traveled along a neutron guide and through choppers before entering the reflectometer. One important difference between the simulations involves the manner in which the data were simulated for different ranges of Q. In the MB simulation, λ_0 was fixed, so Q was sampled by changing α_i. For a TOF instrument, which utilizes a relatively small bandwidth, such as those for the simulations of an LPSS, the simulation can be conducted in one of two ways. The first, like the MB simulation, involves changing Q by changing α_i a few times. The second fixes α_i and increments the mean wavelength used. The best choice is not immediately clear, since the MB method always utilizes the most intense part of the spectrum at the expense of slit and/or sample acceptance.

The ability to select either constant-angle or constant-wavelength methods is an added degree of flexibility that is not found for reflectometers at CW or SPSS (e.g. PSS-8, -9 and -10). This extra degree of freedom is an advantage of the narrower bandwidth. For example, the ability to measure the reflectivity profile by scanning wavelength permits studies of samples in fixed geometry and is a virtue of the TOF technique. On the other hand, the ability to examine small portions of reciprocal space, e.g. a Bragg reflection from a multilayer sample, without suffering a loss of performance, is an advantage of the reflectometers at the longer pulsed-sources and CW sources.

Whereas the MB simulation required 100 separate measurements to sample the Q-range from 0.009 to 0.106Å^{-1}, a dozen or fewer separate measurements (called macro-measurements) were needed for the TOF simulations (within one macro-measurement are many more micro-measurements made as a function of neutron wavelength). For the SPSSs, a single macro-measurement sufficed for each of our simulations, whereas more such measurements are required to accumulate the full range of required data at an LPSS.

4. The Stopping Criterion

There are several criteria that one can imagine using to terminate each simulation. For example, one might assert that the total number of neutrons used in each simulation should be the same or one might demand equal statistical precision of the reflectivity profile at the largest value of Q interrogated. However, since experimenters are usually interested in fitting reflectivity data to a model, we have chosen to terminate each simulation when models fitted to the simulated data give equal statistical precision in the fitted parameters. These parameters were chosen to be the thickness, scattering length density and interfacial roughness of a film on a substrate whose scattering power was set equal to the known value for silicon. We found that, with this criterion, each simulation gave results of similar accuracy (i.e., there were no obvious systematic errors).

The measurement times deduced from the simulations depend, of course, on the stopping criteria used. However, the only really significant (i.e. > 10%) effects we have observed in this regard occur when the second stopping criterion (equal statistical precision at high Q) is used. In this case, the SPSS instruments need 4 to 6 times longer to collect data than they do when the third criterion (equal precision of fitted parameters) is used. In order not to introduce this sort of bias, we have chosen to present data only for the third criterion.

5. Gains Obtained at Pulsed Sources

In Table 2, we give the measurement times deduced from each simulation. The inverse of these numbers, normalized to the data collection time at the CW source, gives the overall gain, G_{Π}, for the pulsed sources. While the major part of this gain derives from the use of the TOF method, there are other factors that also need to be considered. All of these additional factors — monochromator reflectivity, transmission through slits of a given area, guide and filter transmissions, intensity variations across the neutron spectrum, and source brightness — can be quantified with a high degree of confidence. Noting that the total gain is the product of all gain factors, the TOF gain can be deduced by dividing the total calculated gain by the product of the additional gain factors noted above. The TOF gain calculated in this way is also given in Table 2, where it is compared with the naive values that would be deduced either from the inverse of the source duty cycle or a comparison of useful wavelength bandwidth and wavelength resolution at the minimum wavelength used.

Table 2: Collection Times, T, Performance, G_{Π}, and TOF Gain, G_{TOF} Factors

Source	T [s]	G_{Π}	G_{TOF}	$\frac{\Delta T}{\delta t_n}$	$\frac{\Delta\lambda}{\delta\lambda}$
CW	994	1	-	1	1
PSS-1	106	9.4	8	17	21
PSS-2	115	8.6	14	17	14
PSS-3	90	11	13	17	14
PSS-4	63	15.8	15	17	14
PSS-5	95	10.5	11	15	14
PSS-6	126	7.9	7	11	8
PSS-7	66	15	21	51	48
PSS-8	17	58	176	303	288
PSS-9	17	58	225	500	707
PSS-10	17	58	225	526	707

Several results are clear from Table 2:

- All of the pulsed sources give shorter collection times than the CW source, even though all but one of the pulsed sources (PSS-4) have equal or lower average source brightness than the CW source.

- The performance of pulsed source reflectometers does not scale simply as the inverse source duty cycle, because not all information obtained during a single TOF measurement is equally useful. For the simulations reported here, a logarithmic dependence of performance on inverse duty cycle appears to describe the results, but further simulations will be needed to establish whether this behavior is in any way universal.

- Comparing PSS-4 and PSS-10 shows that a reflectometer at a 1 MW, 10 Hz SPSS is likely to outperform that at a 1 MW, 60 Hz LPSS by about a factor of 4.

- Comparing PSS-8 and PSS-10 shows that there is no performance improvement obtained by shortening the proton pulse at an SPSS to a value below 300 μsec. Much of the effort and technical complexity that such sources invest in accumulator rings or rapid cycling synchrotrons is thus wasted for reflectometry.

- For reflectometers at an LPSS, the best performance is obtained by using the largest integrated intensity, even though this also implies that the neutron pulses have long tails.

- Comparing PSS-3 and PSS-5 shows that similar performance is obtained at 120 Hz and 60 Hz LPSS with equal duty cycles.

- Simulations PSS-3 and PSS-7 show that a pulse shortening chopper is advantageous at an LPSS, at least in the case considered. The added performance and flexibility provided by this chopper makes it attractive.

6. Final Remarks

The results presented here apply strictly to the performance that would be obtained for reflection experiments with a simple, single-layer sample and an experimental protocol that measures reflectivity out to Q = 0.1 $Å^{-1}$. One might argue that this is not a typical case. For example, studies of a Bragg reflection from a multilayer would normally not require such a large Q range, thus the performance of the SPSS compared to the LPSS would be more greatly

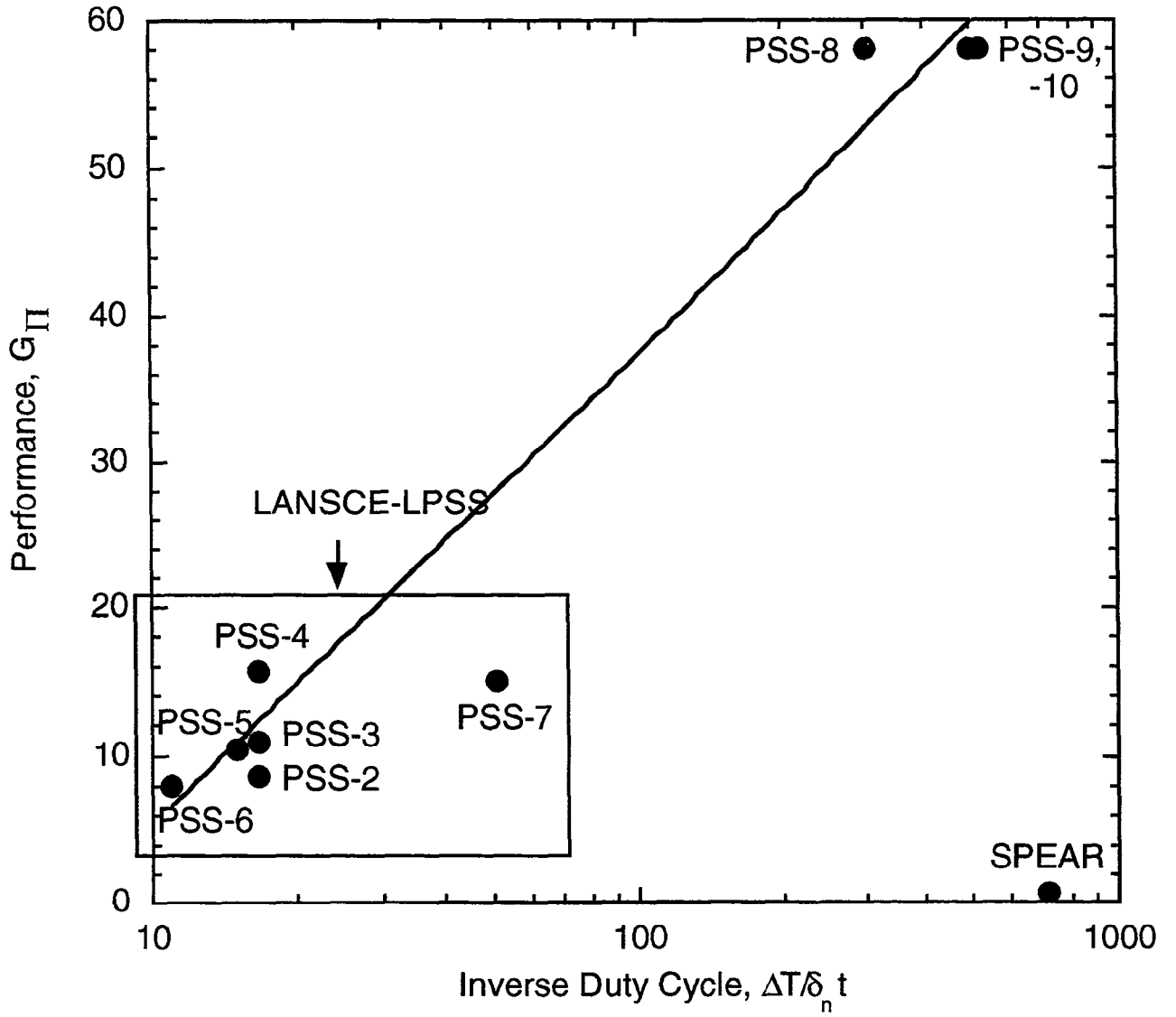

Figure 2: The performance of reflectometers at various spallation sources is plotted versus inverse duty cycle. For comparison purposes the performance of the reflectometer, SPEAR, at the existing LANSCE source (0.06MW) is also shown. The performance of a reflectometer at the ILL on this scale is taken as unity.

reduced than our results would indicate, since the CW and LPSS measurements would be quicker, ie. fewer macro-measurements would be required. On the other hand, there are many experiments that require an even wider range of Q than that studied here as well as high statistical accuracy of the data at large Q. The advantage of using a shorter pulse in this case is that most of the reflectivity profile, albeit the easiest and least time-consuming part of the profile to measure is measured during the time spent measuring the low reflectivity region.

7. Acknowledgments

We wish to thank P.A. Seeger for providing and maintaining the Monte Carlo simulation code with which this study was possible. We also acknowledge valuable discussions with L. Daemon, R. P. Hjelm, C. F. Majkrzak, E. Pitcher, S. Satija and G. S. Smith. This work was supported by the U.S. Department of Energy, BES-DMS, under Contract No. W-7405-Eng-36.

8. References

[1] For measurements of specular reflectivity, the use of a collimated beam is highly non-optimal. In fact, for specular scattering, the optimal condition for obtaining data is to use a highly divergent beam that converges at the sample position, and to measure the angle of incidence from the scattered radiation with a position sensitive detector. This procedure is employed with the reflectometer at the Los Alamos Neutron Scattering Center called SPEAR and decreases collection times dramatically (a factor of 2 is conservative).

[2] E.J. Pitcher, G.J. Russell, P.A. Seeger and P.D. Ferguson, "Performance of Long-Pulse Source Reference Target-Moderator-Reflector Configurations," these proceedings.

[3] P.A. Seeger, "The MCLIB Library: Monte Carlo Simulation of Neutron Scattering Instruments," these proceedings.

[4] The additional parameters used for the pulse shape were the same for all cases. The epithermal time constant (proportional to wavelength) was 8μs/Å and the switch function between the epithermal and thermal was exp[-(0.9Å/λ)2.5]. Both terms were convoluted with Gaussians proportional to wavelength. The rms width for the Gaussian representing the epithermal component was 1.9μs/Å and for thermal was 2.9μs/Å. These spectra were earlier versions of these tabulated in ref. [2], with composite Be/Ni reflectors.

[5] Alternatively, the frame overlap chopper can be replaced by a mirror whose angle of incidence relative to the neutron beam is set to reflect very long wavelength neutrons out of the beam. This approach has the advantage of removing one of the choppers; thus, reducing the cost of the instrument.

ICANS-XIII
13th Meeting of the International Collaboration on
Advanced Neutron Sources
October 11-14, 1995
Paul Scherrer Institut, 5232 Villigen PSI, Switzerland

MONTE CARLO STUDY OF THE PERFORMANCE OF A TIME-OF-FLIGHT MULTICHOPPER SPECTROMETER

L.L. Daemen, J. Eckert, R. Pynn, P.A. Seeger,
Manuel Lujan Jr. Neutron Scattering Center (LANSCE),
Los Alamos National Laboratory,
Los Alamos, New Mexico 87545, USA

ABSTRACT

The Monte Carlo method is a powerful technique for neutron transport studies. While it has been applied for many years to the study of nuclear systems, there are few codes available for neutron transport in the optical regime. The recent surge of interest in so-called next generation spallation neutron sources and the desire to design new and optimized instruments for these facilities has led us to develop a Monte Carlo code geared toward the simulation of neutron scattering instruments. The time-of-flight multichopper spectrometer, of which IN5 at the ILL is the prototypical example, is the first spectrometer studied with the code. Some of the results of a comparison between the IN5 performance at a reactor and at a Long Pulse Spallation Source (LPSS) are summarized here.

1. Introduction

Next-generation (> 1 MW) spallation neutron sources are currently being studied worldwide. The motivation behind the present flurry of activity stems partly from the desire to overcome the intensity "barrier" that presently limits many neutron scattering experiments, and partly from the rapidly increasing demand for neutrons as a tool for basic studies in many disciplines ranging from condensed matter physics to structural biology. In fact, the development of an accelerator-driven, 1 MW long-pulse spallation neutron source (LPSS), short-pulse spallation source (SPPS) for neutron scattering, and the upgrade of the existing short-pulse spallation source (LANSCE upgrade project) have been identified as main thrust areas at Los Alamos National Laboratory in the coming years.

Undoubtedly, the design, optimization, and analysis of new instruments for neutron sources is a major issue in the design of next-generation neutron sources. The complexity of these instruments coupled to the desire to optimize their performance as much as possible calls for design tools that go beyond traditional ray-tracing techniques. Simultaneously, the development of moderator simulation methods and recent advances in high-performance computing

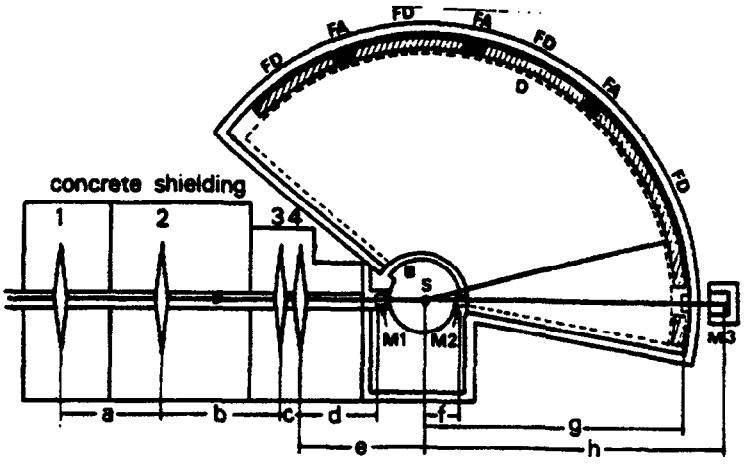

a = 260.0 cm, c = 40.4 cm,
b = 325.2 cm, d = 92.4 cm,
e = 128.8 cm, g = 397.7 cm,
f = 51.1 cm, h = 409.0 cm,

S : sample D : detectors M1, M2, M3 : monitors
B : sample-box with collimator
FD : fixed detectors : -10° to 130°
FA : forbidden angles: 47.5°-51°, 77°-81°, and 107°-111°

Figure 1: The IN5 spectrometer at the Institut Laue-Langevin.

make detailed moderator information (time and energy neutron pulse structure) available to the instrument designer. Quite often, the only way to make use of this information is in a computer simulation.

The MCLIB package and its various appendages are described elsewhere in these proceedings [1,2]. The code is a Monte Carlo neutron transport code specifically designed to do neutron optics. The code originated at the Rutherford-Appleton Laboratory in the late 70's [3]. It was subsequently revised by Seeger in 1984 and extensively rewritten and expanded in 1994.

The work described below is one example of the application of the MCLIB tools to the study of a neutron scattering instrument at various sources: We compared the operation of IN5 at a reactor (continuous) source and at the proposed LPSS source. We chose to model IN5 first because of its simplicity and its importance for quasi-elastic neutron scattering, and because it is reasonably easy to convince oneself that it is an instrument that would perform very well at a LPSS [4]. While our simulations of IN5 at a reactor source confirmed, by and large, the performance predictions from simple analytical calculations, the simulations at an LPSS source revealed some new, interesting features that add to the flexibility and performance of IN5 at this type of source.

2. The IN5 spectrometer

The strucure of the IN5 spectrometer is well-known. The instrument has been described in detail elswhere [5,6]. The instrument consists essentially of four disk choppers (Fig.1). The first and last choppers are used to determine the incident wavelength on the sample by adjusting their relative phase. The second chopper eliminates higher-order contamination from the beam. The third chopper is essentially a frame overlap chopper; it controls the repetition rate of the neutron bursts, and hence the data collection rate and achievable bandwidth. Chopper

1, 2, and 4 rotate at the same speed, typically 20000 rpm (667 Hz), whereas chopper 3 rotates more slowly, typically by a factor of two or three. The choppers are 24.2 cm in radius with 2 cm wide slits. The burst width produced by the wavelength selection choppers at 20000 rpm is approximately 40 μs. The choppers can be rotated as slowly as 6000 rpm (100 Hz) to increase the intensity on sample, but this occurs, of course, at the expense of energy resolution. Nickel-coated glass neutron guides from the ILL liquid hydrogen moderator to the first chopper and between consecutive choppers help increase the flux on sample. A set of 1200 helium-3 tube counters located on a segment of a sphere 4 m in radius and centered on the sample completes the instrument. The detector covers approximately 110° in the horizontal plane and has a total height of 2 m.

3. Simple Scaling Arguments

The IN5 instrument is simple enough that analytical calculations giving the instrument bandwidth, resolution, and intensity on sample can be performed easily without making drastic simplifying assumptions. This is useful for comparison with the Monte Carlo results, and so we will summarize the results of calculations by Lechner [5] for future reference. Notice however that while the analytical results provide a good description of IN5, the Monte Carlo simulations have uncovered a number of interesting features that would have been difficult to calculate, or even predict, from simple analytical considerations.

3.1 Bandwidth:

The bandwidth of the instrument is determined by chopper 4 and is given by:

$$\Delta E = \frac{h^3}{m^2} \frac{\tau_4}{L_{14}\lambda_0^3} \tag{1}$$

where τ_4 is the chopper open time, λ_0 is the incident wavelength, and L_{14} is the distance between chopper 1 and chopper 4.

3.2 Resolution:

For elastic scattering, Lechner obtained:

$$\delta E = C \frac{\tau_1^2 L_{4D}^2 + \tau_4^2 L_{1D}^2}{\lambda_0^3 L_{14} L_{SD}} \tag{2}$$

where L_{4D} is the chopper 4-detector distance, L_{1D} is the chopper 1-detector distance, L_{SD} is the sample-detector distance. A more general expression for the resolution at finite energy transfer is also given in Ref.[5] but will not be used here. It is interesting to remark that both ΔE and δE depend only on the relative phase and distance between chopper 1 and chopper 4, but not on their absolute distance from the source. Eqs.(1) and (2) are applicable to continuous and pulsed sources.

3.3 Intensity:

In Ref.[5] Lechner shows that:

$$I \propto \frac{\tau_1}{T_3} \times \frac{d\phi}{dE_0} \times \Delta E = \frac{1}{\lambda_0^3} \frac{d\phi}{dE_0} \frac{\tau_1 \tau_4}{L_{14} L_{SD}} \tag{3}$$

where T_3 is the period of the frame overlap chopper, $d\phi/dE_0$ is the flux at the incident energy, $E_0 = h^2/(2m\lambda_0^2)$, and ΔE is the instrument bandwidth given by Eq.(1) above.

At a reactor source, the factor $d\phi/dE_0$ is *fixed* and constant for a given selected wavelength. At a pulsed source, however, the neutron energy spectrum incident on the first chopper depends on the *phase difference* between the neutron pulse and the first chopper. One might think that because of the fairly complex time-energy structure of the neutron pulse produced by, say, a coupled, reflected moderator at an LPSS, this additional complication is undesirable, but we will show below that it leads in fact to new, interesting results regarding the operation of IN5.

4. Monte Carlo simulations of IN5 on a reactor source

It is useful, as well as instructive, to compare the instrument characteristics mentioned in the preceding section with similar quantities calculated with MCLIB. To this effect, we mocked up IN5 reasonably accurately. For the sake of expediency, we did not include the neutron guides in our simulations. (Notice that Lechner also ignored the guides in his calculations.) We performed the simulations for the best achievable resolution, i.e., with the wavelength selection choppers rotating at 20000 rpm (667 Hz). The distances between source, choppers, sample, and detector, and their dimensions were chosen identical to those at IN5. The neutron source used in our simulations was a simple Maxwell-Boltzmann energy spectrum. Deviations from a strict Maxwell-Boltzmann spectrum are observable in practice, but they need not concern us here where our main purposes are to validate Lechner's scaling arguments (or, vice-versa, to validate the Monte Carlo simulations), and to explore more subtle effects particularly at pulsed sources rather than to design accurately a fully optimized instrument. The sample scatters with a fixed value of $\hbar\omega$. Energy resolution was measured by determining the broadening of the delta function scatterer in the time-of-flight spectrum. The counts of all the helium-3 tubes were summed to obtain the time-of-flight spectrum. We restricted the bandwidth to about 12 meV in our simulations, -2 meV $< \hbar\omega <$ 10 meV.

We repeated the simulation at several incident wavelengths for elastic scattering. The results are shown in Fig.2. While the Monte Carlo result is not identical to Lechner's result, it is fairly close. The agreement with Lechner's result gets better as the wavelength increases. The trend is clearly toward a decrease of δE as $1/\lambda_0^3$, but there appears to be additional, wavelength-dependent corrections to Lechner's result. Also indicated on the figure is one result for a vanadium sample at $6\mathring{A}$ incident wavelength. The measured resolution is between the Monte Carlo result and Lechner's result.

Equally interesting is a study of the energy resolution at finite energy transfer, i.e., for a delta scatterer sample scattering inelastically. Since in practice, there is no known material that mimics perfectly this behavior (unlike vanadium for the elastic scattering case), one is reduced to estimate computationally the resolution of the instrument for inelastic scattering. Fig.3 shows the results of our Monte Carlo simulations for three incident wavelengths. The lines are Lechner's result, Ref.[5]. Again, the trend for the analytical results and the Monte Carlo results is the same. As observed for the elastic scattering case, the agreement between

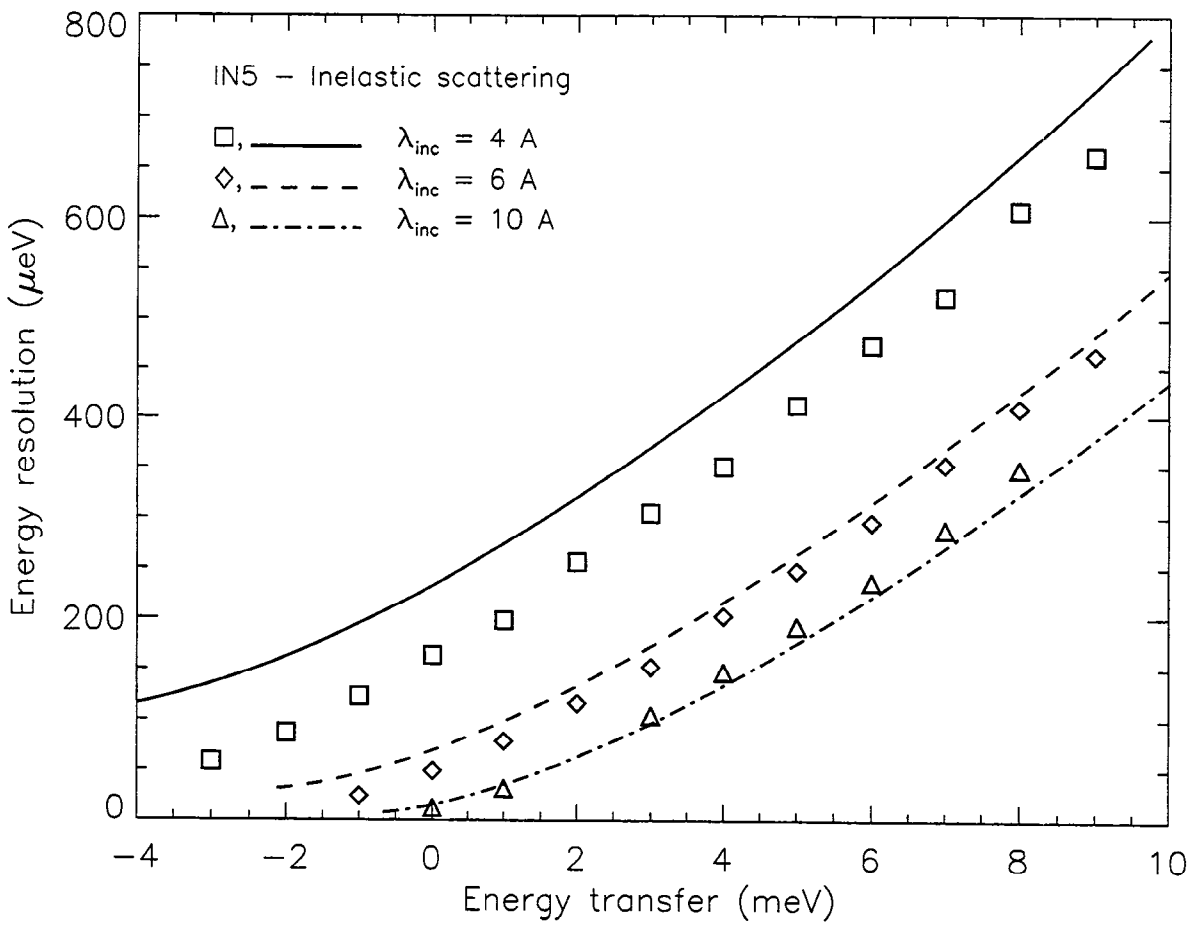

Figure 2: Monte Carlo calculation of the energy resolution for elastic scattering at IN5 with a continuous source. The solid line is a third degree polynomial fit to the data. The dashed line is Lechner's result, Eq.(3).

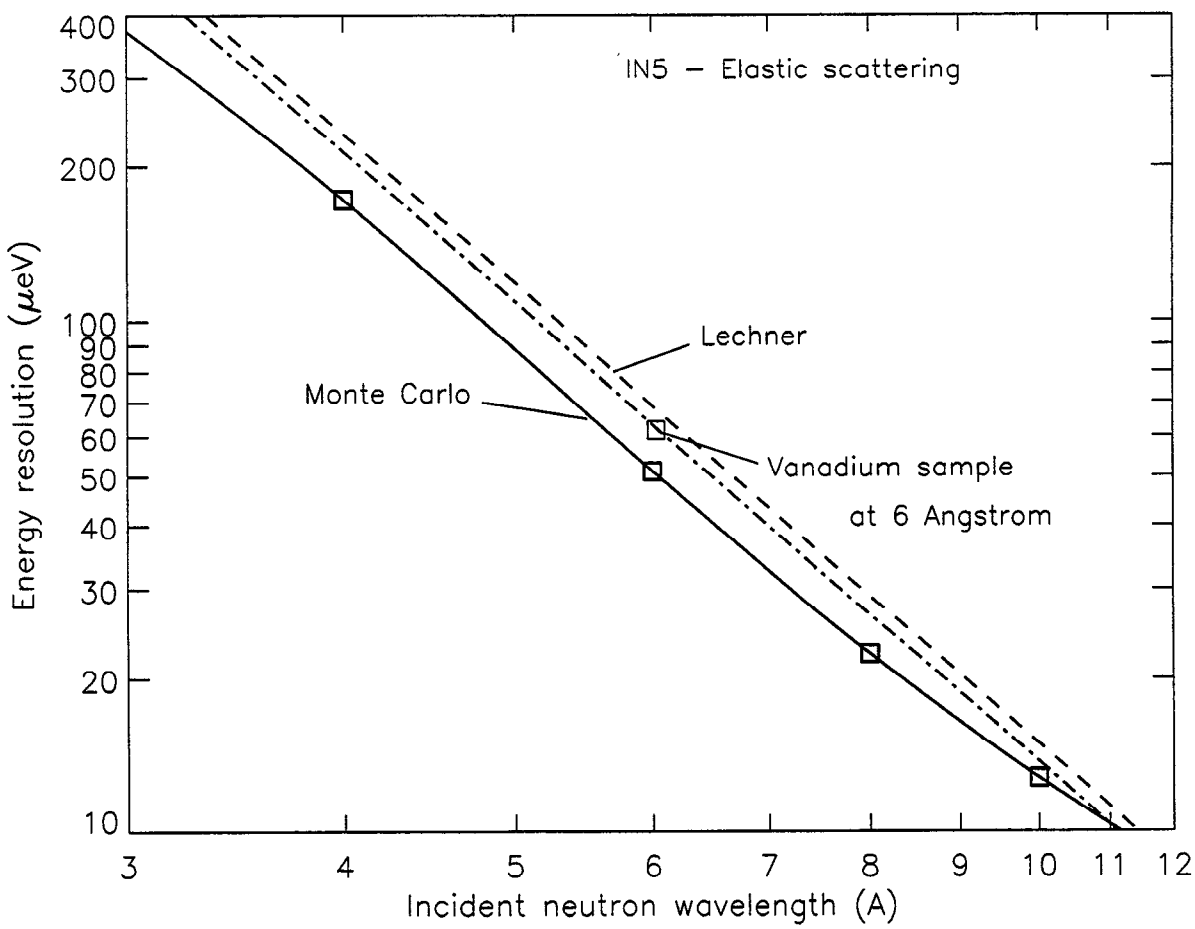

Figure 3: Monte Carlo calculation of the energy resolution for inelastic scattering at IN5 with a continuous source. The sample is a delta scatterer. The lines are Lechner's result, Ref.[5]; The symbols are the results of our Monte Carlo simulations.

Lechner's result and the Monte Carlo result seems to improve greatly with increasing wavelength. Altogether, the agreement between the two results is quite reasonable, even at shorter wavelengths, but it would be interesting to pursue this study and try to understand the exact origin of the discrepancy.

5. Monte Carlo simulations of IN5 on an LPSS source

As pointed out above, the IN5 would perform in a very similar way at a reactor and a pulsed source. However, we also remarked that the pulsed nature of the neutron source at an LPSS leads to the added complication of having to determine a *global* chopper phase with respect to the accelerator (or neutron) pulse, in addition to the *relative* phases between choppers. To study the impact of this global phase on the performance of IN5 at an LPSS, we varied this phase systematically by varying the t_{shift} parameter defined in Fig.4(a). The pulse shape in Fig.4(a) is typical of a coupled liquid hydrogen moderator at an LPSS. The cusp indicates the end of the 1 ms proton pulse on the neutron production target. The 370 μs decay constant of the exponentially decaying "tail" is also typical of a coupled, cold moderator at an LPSS. We used the Ikeda-Carpenter formula [7] to generate a source term for an LPSS in our simulation. Again, the emphasis is on understanding and exploring rather than on the production of a final, optimized design for an actual source. The Ikeda-Carpenter result is analytically expressible in a simple way, and lends itself to analytical treatment. In addition, its use allowed us to change moderator parameters rapidly and to explore systematically the effect of these changes on the instrument performance.

One disadvantage of using an accelerator to produce neutron pulses for IN5 is that the chopper rotaional frequency has to be equal to (or at least a multiple of) the accelerator frequency. We chose 120 Hz as a typical number in our simulations. It is trivial, however, to rescale the results for other frequencies. Similarly, at 120 Hz, the data collection rate is less than or equal to that achievable at ILL, so one must be careful in comparing intensities, resolution, and bandwidth between the two sources. The relative simplicity of the instrument, however, should allow the reader to perform comparisons that are meaningful for the particular situation at hand.

The effect of varying t_{shift} systematically between a negative value (-1 ms to 0 ms, i.e., when the proton pulse is "on") and a positive value ($>$ 0 ms, proton pulse "off") on the detected intensity and elastic resolution is shown in Figs.4(b) and (c), respectively. The simulations were performed for two different wavelengths, 4 and 10 $\AA$ corresponding to the typical range of wavelengths used in practice by most IN5 users. The sample was again a delta scatterer (zero energy transfer, i.e., elastic scattering). Clearly, the results are not as simple as one might have imagined. At a given incident wavelength, intensity and resolution "peak" at different values of t_{shift}. We intuitively expect the intensity to peak near $t_{shift} = 0$ since the longer we wait, the larger the population of thermalized neutrons in the moderator. Notice also that neutron thermalization times are wavelength-dependent, and the neutron flux in the moderator will "peak" at a time depending on the neutron wavelength. This is a degree of freedom offered by the (t,E) structure of the neutron pulse at an LPSS that can be taken advantage of: It should always be possible to adjust the global pulse-choppers phase to "ride" the peak intensity at the desired wavelength.

Similarly, it should be intuitively obvious that for $t_{shift} > 0$, we are making use of a heavily thermalized neutron population corresponding to a smaller energy range (ideally determined by the Maxwell-Boltzmann distribution) than during the transient period following the irradiation

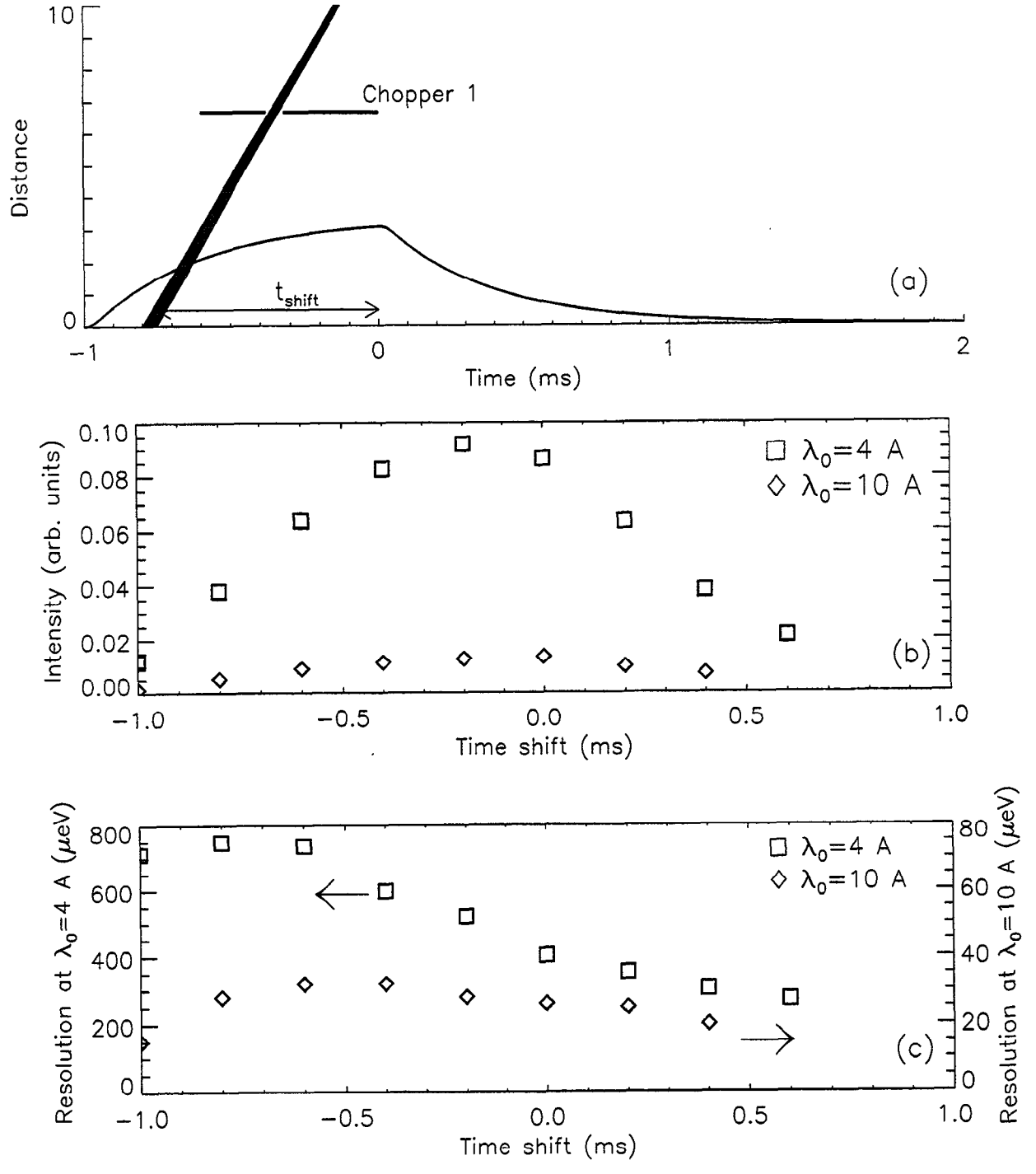

Figure 4: (a) Definition of t_{shift} and typical neutron pulse shape at an LPSS. The moderator decay time is 370 μs; the proton pulse duration is 1 ms; the accelerator frequency is 120 Hz; the choppers rotate at 120 Hz. (b) Detected intensity as a function of t_{shift} for two extreme wavelengths, 4 and 10 Å. (c) Corresponding elastic energy resolution as a function of t_{shift}.

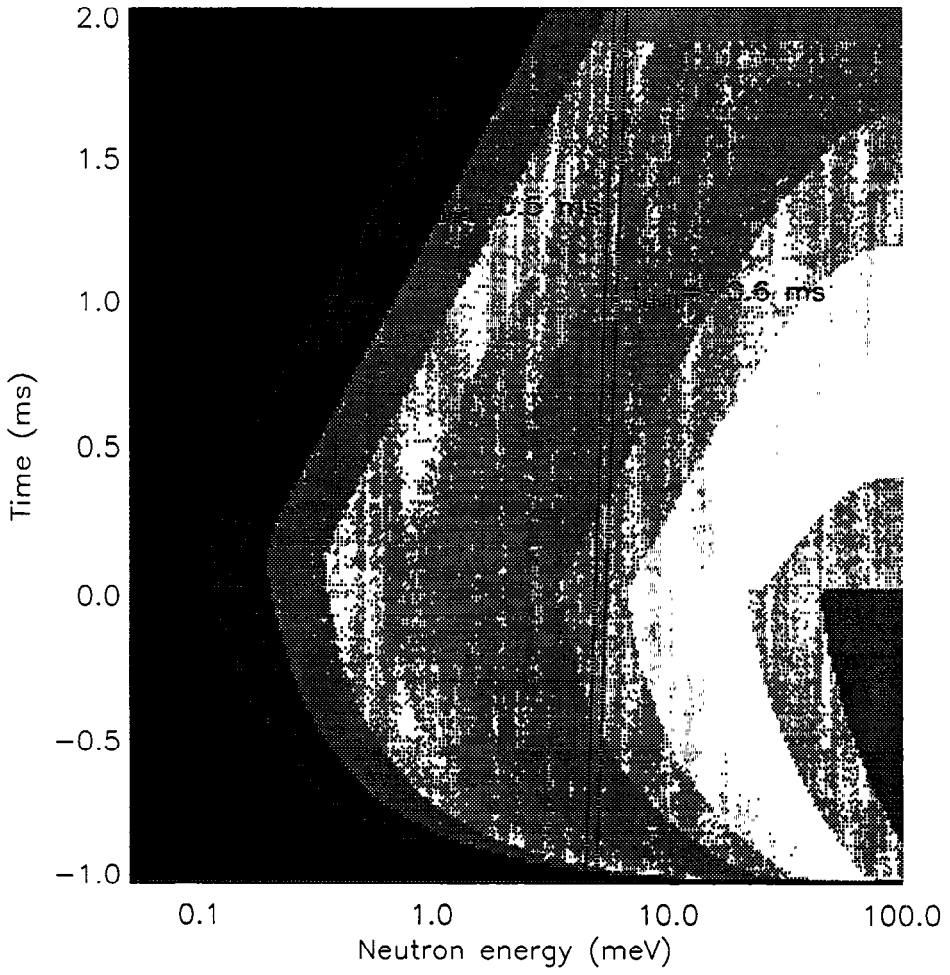

Figure 5: Ikeda-Carpenter time-energy distribution of the neutron pulse for the parameters given in the caption of Fig.4(a). The two curves are given by Eq.(4) for the values of t_{shift} indicated on the figure. The pulse is typical of a liquid hydrogen moderator at 20 K. The contour intervals are logartihmic.

of the neutron production target by the proton pulse since during this period, one has to deal with a more energetically diverse neutron population in the moderator as the neutron gas comes into thermal equilibrium with the moderating medium.

It is instructive to pursue this point a little further. It should be clear that neutrons emitted with energy E at time $t_{emission}$ such that

$$t_{emission} = t_{shift} + \frac{L_{M1}}{\frac{h}{m\lambda_0}} - L_{M1}(\frac{m}{2E})^{1/2}, \tag{4}$$

where L_{M1} is the moderator-to-chopper 1 distance (equal to 20.5 m in our simulations) and λ_0 is the selected incident wavelength all arrive at the first chopper at the same time. The second term in the above equation is the time-of-flight of a neutron with the nominal wavelength. (Neutrons with energy E slightly less than E_0 but leaving the moderator slightly before neutrons with energy E_0 can arrive at the chopper at the same time, as do slightly faster neutrons leaving the moderator somewhat later. Thus, neutrons whose time-of-emission and

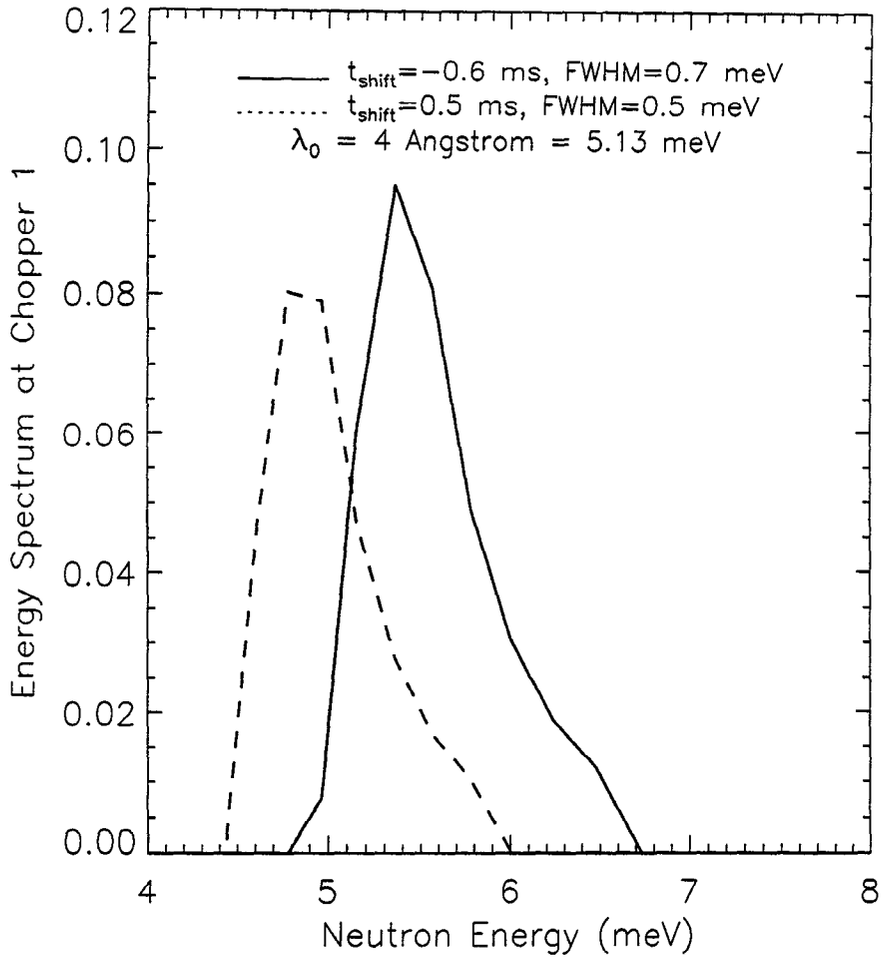

Figure 6: The neutron energy distributions corresponding to the two loci shown in Fig.5.

energy E are related via Eq.(4) arrive at the same time at the first chopper (and pass through the chopper). Eq.(4) determines a locus in the moderator (t,E)-space. Two of these curves are shown for two different values of t_{shift} in Fig.5. Changing t_{shift} amounts to shifting this curve vertically, along the energy axis, in the moderator (t,E)-plane; this does not change the shape of the curve. But the energy distribution of neutrons on two loci corresponding to two different values of t_{shift} are different: A larger t_{shift} corresponds to a greater degree of neutron thermalization and a narrower energy distribution (but also to less intensity when $t_{shift} > 0$, i.e., in the "tail"). The distribution of neutron energies for the two loci are show in Fig.6. Clearly the full-width at half-maximum of the two distributions is different, and it is not difficult to conclude the argument to explain the behavior of the elastic resolution as a function of t_{shift} shown in Fig.4(c).

It is also worth mentioning that by running IN5 at a reactor source with the choppers running at 120 Hz and all other things being equal, the resolution achievable at the reactor source is close to 1 ms, much worse than is possible at an LPSS by carefully "phasing" the pulse and the choppers.

6. Conclusions

We showed that the Monte Carlo results are in reasonable agreement with the simple scaling arguments advanced by Lechner. Clearly, there are some interesting deviations from the simple analytical arguments, and it would be interesting to explore this further.

The performance of an IN5-type instrument at an LPSS can be understood along the lines described in Ref.[5]. The global phasing of the proton (or neutron) pulse is an additional degree of freedom that is unique to the pulsed source and which can be taken advantage of to optimize the instrument performance or increase its flexibility.

An ideal moderator for IN5 at an LPSS would produce a neutron pulse with a long "tail" of highly thermalized neutrons (to improve the resolution), with as much intensity in the tail as possible (to increase the detected intensity). We have started to investigate the effect of varying the neutron pulse shape systematically (decay time, rise time, integrated and peak intensity, etc). The results will be reported elsewhere.

Many other aspects deserve to be investigated more closely, especially in view of the fact that they are not easily taken into account in simple analytical calculations. We have done some preliminary work on the effect of chopper jitter on the performance of IN5 at continuous and pulsed sources. The results show a modest improvement in energy resolution and a corresponding decrease in detected intensity. The relative loss of intensity at an LPSS seems to be somewhat less that the relative loss of intensity at a reactor. More work is needed to clarify the reason for this behavior.

Other, more complex chopper configurations can be considered. The fourth chopper, for instance, could be replaced by a pseudo-statistical chopper to measure several wavelengths simultaneously in one counting frame. Again, such ideas are best explored via the Monte Carlo technique.

7. Acknowledgements

We wish to thank Don Kearly at the ILL for many useful discussions about IN5, and for his continuing support and interest in this project.

8. References

[1] P.A. Seeger, "The MCLIB Library: Monte Carlo Simulation of Neutron Scattering Instruments," these proceedings.

[2] T.G. Thelliez, L.L. Daemen, P.A. Seeger, R.P. Hjelm, "A user-friendly geometry interface for the neutron optics MCLIB code," these proceedings.

[3] M.W. Johnson and C. Stephanou, "MCLIB: A Library of Monte Carlo Subroutines for Neutron Scattering Problems," Rutherford-Appleton Laboratory report RL-78-090, September 1978; M.W. Johnson, "MCGUIDE: A Thermal Neutron Guide Simulation Program,", Rutherford-Appleton Laboratory report RL-80-065, December 1980.

[4] R. Pynn and L.L. Daemen, "The performance of Neutron Spectrometers at a Long Pulse Spallation Source," these proceedings.

[5] R.E. Lechner, "TOF-TOF Spectrometers at Pulsed Neutron Sources and at Steady-State

Reactors", in Proceedings of the Workshop on Neutron Scattering Instrumentation for SNQ, Maria Laach, 3-5 September, 1984, R. Scherm and H. Stiller, Eds., Berichte der Kernforschungsanlage Jülich - Nr.1954, p.202.

[6] M. Bée, "Quasielastic Neutron Scattering," (Adam Hilger, Bristol, 1988), p.81.

[7] S. Ikeda and J.M. Carpenter, "Wide-Energy-Range, High-Resolution Measurements of Neutron Pulse Shapes of Polyethylene Moderators," Nucl.Instr.Meth. **A239**, 536 (1985).

ICANS–XIII
13th Meeting of the International Collaboration on
Advanced Neutron Sources
October 11–14, 1995
Paul Scherrer Institut, 5232 Villingen PSI, Switzerland

COMPLEMTARITY OF LONG PULSE AND SHORT PULSE SPALLATION SOURCES

F. Mezei

Hahn–Meitner–Institut, BENSC, Glienicker Str. 100, 14109 Berlin, Germany

ABSTRACT

The complementarity of short pulse spallation sources (SPSS) and steady state (CW) reactors is a widely accepted concept. SPSS and long pulse spallation sources (LPSS) are complementary in two ways: a) in their performance in neutron scattering experiments LPSS closely emulate CW reactors. In this respect two facets of the time–of–flight (TOF) monochromator method adequate for LPSS will be discussed: the superiority of the TOF approach to the crystal monochromator method in high resolution powder diffraction, and the novel technique of repetition rate multiplication in TOF spectroscopy. b) LPSS combined with adequate chopper systems can also emulate SPSS in a number of applications. It will be shown that the LPSS method of producing short neutron pulses is more efficient for cold and thermal neutrons (below an energy of about 100 meV), while SPSS is the more favourable approach for hot, epithermal neutrons, i.e. in the slowing down regime in contrast to the moderated regime. These two aspects of complementarity of LPSS and SPSS lead to the conclusions that for about 75% of the spectrum of neutron scattering experiments as known of today the LPSS approach is the most advantageous one with a feasible neutron intensity exceeding that available at ILL by a factor of about 30, while for the remaining 25% of applications the SPSS technique is superior with a well–known potential of a similar gain over present day performances.

1. Introduction and Overview

The complementarity of SPSS and CW reactor sources can be illustrated by comparing two facilities of roughly the same costs. The FRM-II 20 MW reactor project (Munich) and the AUSTRON 200 kW spallation source project (see report given at this meeting) happen to represent such a pair. The projected time averaged flux in the epithermal (slowing down) neutron range is equal for both facilities, while FRM-II should provide

Keywords: long pulse source, complementary, powder diffraction TOF- spectroscopy

a moderated thermal and cold average flux which is an order of magnitude higher than that of longest pulse length moderators (some 150 μs for thermal and 1 ms for cold neutrons) at AUSTRON. On the other hand, AUSTRON at a repetition rate of 25 Hz and with a pulse width of less than 10 μs in the slowing down regime should outperform FRM-II in respect of the peak flux by a factor of more than 4000, while for thermal and cold neutrons independently of the moderator type the gain "only" amounts to a factor of 30 and 4, respectively. These flux relations, as well known from several studies (cf. Abingdon workshop on ESS), make AUSTRON about an order of magnitude inferior for white beam irridiation and fixed wavelengths experiments (such as interferometry) and comparable or vastly superior to FRM–II in the rest of neutron scattering work (e.g. small angle scattering and short wavelength powder diffraction, respectively). This complementary performance in various utilizations is primarily due to the huge variation of the ratio of the peak fluxes of both facilities with the neutron energy.

In contrast, for a LPSS facility, due to the fact that the pulse length (which is in the ms range) is constant, the neutron wavelength dependence of the peak flux follows that of the average flux, i.e. it is rather similar to a reactor (with an enhanced slowing down range though). The difference between a CW and long pulse source resides in the potential for *more efficient utilization* of the average flux of the latter. The clue to this efficiency is to use a neutron monochromatization technique which only needs the source to be on for a limited time, i.e. some 10% of the total time. By the TOF wavelength band monochromatization technique a quasi–continuous monochromatic beam can be produced on the sample, which has about the same time averaged intensity as that on a CW source with a flux equal to the peak ("on") flux of the LPSS. However, there is one major difference: At the CW source we have a constant wavelength all the time, while on a LPSS we will have a well defined wavelength at any given time, which changes periodically within a more or less narrow band. The width of the wavelength band can be adapted to the various types of experiments, but it has to be at least $\delta\lambda/c$, where $\delta\lambda$ is the wavelength resolution aimed at, and c the duty factor of the source. The efficiency of the use of LPPS is thus determined by the relative merits of performing a given experiment with a series of adjacent wavelengths for the same total period of time instead of using a single wavelength all the time. If several different wavelengths, i.e. different intensities and resolutions, are used the experimental procedure requires an adequate combination of the information obtained at various wavelengths, and not only the simple summation of raw spectra. This kind of *information processing*, as opposed to *input data processing*, is usual in high energy physics experiments, and it is getting more and more common in the work at SPSS facilities, but it is still quite unusual at CW sources. The two examples of employing TOF monochromator techniques instead of the usual single wavelength approach at CW sources discussed below show, that the multiple wavelength approach can a) be largely superior in some, rather obvious cases or b) still be favourable or competitive in other cases, where this would not be expected on the basis of conventional wisdom.

The example for a) is high resolution powder diffraction, where the larger acceptable solid angle of the detector in the TOF approach is clearly advantageous. The case study for b) concerns TOF spectroscopy. The straightforward transfer of CW source TOF spectroscopy to pulsed sources is known to be disadvantaged by being tied to the repetition rate of the source, which is too low in most cases. If one accepts to use more than one wavelength (repetition rate multiplication), the same freedom of choice as on a CW source is regained in respect to the choice of the repetition rate. It will be shown below for a specific example that the multiple wavelength approach can offer a competitive (and actually better) information collection rate than the conventional single wavelength method. In most cases this new proposal of multiplying the repetition rate removes one last technical disadvantage that pulsed sources (short or long) were perceived to have in comparison to CW sources. Thus, with LPSS sources with an average power of 10 to 20 MW now appearing well within reach (cf. the 135 MW "on" linac power without proton beam chopping of the ESS reference design) the LPSS approach offers a capability to achieve average neutron intensities on the sample, which are 20 to 40 times higher than that of ILL for all neutron scattering applications.

Beyond the complementarity between LPSS and SPSS, which is due to the similarity of LPSS and CW reactors, there also is a technical complementarity in another respect: It turns out that it is more efficient to produce short pulses of cold and thermal neutrons by fast choppers on a LPSS than by a SPSS. The fundamental reason for this are the long moderation times for maximum time averaged flux moderator–reflector ensembles. Quite similarly to mechanical choppers the pulse length can only be shortened by taylored, short pulse moderators at the expense of the total neutron flux and to some extend also at the expense of the peak flux. If we thus consider a pair of a SPSS and a LPSS, which represent about the same investment, the technically less demanding LPSS will display some four times higher average power, mainly due to the higher "on" power of the linac operating without beam chopping and eventually with H^+. Beyond substantially higher peak fluxes for cold neutrons and comparable ones for thermal neutrons, the LPSS approach with choppers also offers more flexibility in the choice of pulse lengths, leading to improved resolution for cold neutrons in view of the shortest SPSS moderator pulse of 100 μs. Furthermore, present instrumentation concepts for SPSS favour short target to sample distances, and thus lead to the necessity to split the accelerator power between two target stations, which amounts to a flux reduction on all instruments. The TOF monochromator approach for LPSS instrumentation often calls for the use of neutron guides of substantial length (20–100 m), so that there is room for many instrument positions on a single target station. In sum, SPSS offer the most efficient way to produce short neutron pulses in the epithermal neutron energy range via the slowing down mechanism. (On a cold moderator the slowing down regime extends somewhat into the thermal energy range.) This mechanism provides pulse lengths $\lesssim$ 10 μs. LPSS complement SPSS performances by providing the most efficient way of producing variable length thermal and cold neutron pulses with pulse lengths ranging from 20 μs to several hundreds of μs using state of the art chopper technology.

In what follows various points mentioned in this chapter will be discussed in more detail.

2. Neutron monochromators and the principle of time-of-flight wavelength band monochromatization

In all neutron scattering experiments on a CW source a small, more or less precisely monochromatic fraction of the Maxwellian spectrum of the moderator is selected by eliminating the rest. Actually the precision of this monochromatization determines in nearly all cases the resolution of the experiment. The exceptions are Neutron Spin Echo (NSE) and TOF Fourier Diffraction. The clue of these Fourier methods is exactly the intensity gain achieved by the poor monochromatization required compared to the resolution offered. Unfortunately, such "simultaneous" methods, in which the signal from various wavelengths is detected at the same time and sorted out by signal processing methods standard in other modern experimental techniques (such as Fourier transformation e.g. in pulsed NMR) can only be used in a few special cases with neutrons, due to the inherent quantum noise of neutron signals. Namely neutron scattering spectra contain a very small number of quanta (neutrons) compared to microwave or light signals, for instance, so that the statistical Poisson noise is inevitably large. In simultaneous data processing this leads to masking the low intensity part of the spectra, which contain the hard-to-observe pieces of the information. (This was the reason of the practical abandoning of neutron correlation spectroscopy, a promising idea from the 1960's).

There are basically three types of successful monochromator devices used on CW sources, none of them without substantial drawbacks though. Crystals transmit not only the desired wavelength λ, but higher orders $\lambda/2$ and/or $\lambda/3$ etc. too, which has to be most often removed by a filter. Furthermore, the reflectivity of many crystal monochromators is considerably lower than 100% and the resolution curve shows up long tails. The optimal adjustment of the resolution, requiring a set of exchangeable crystals, is of limited flexibility. Last but not least, crystals also display other scattering processes than Bragg reflection. This often leads to "spurion" signals, which are time consuming and not always easy to be sorted out. Helical slot velocity selectors suffer from none of these drawbacks of crystal monochromators, but they cannot provide comparable resolution due to mechanical limitations of the speed of rotation. They are actually limited to some 5% best resolution and this holds for cold neutrons only. In contrast to these two continuous beam, (CW) monochromators, disc chopper systems of the type of IN5 at ILL provide a clean, tunable beam and to crystals comparable resolution, but only for a fraction of the time with duty factors around 1% or less.

In a neutron scattering experiment on a CW source one starts with choosing an optimal incoming neutron wavelength. This choice is never a unique, single value, it is rather one of many equivalent ones within a given more or less broad wavelength band. Conventionally a single wavelength within this "useful band" is selected for extended data collection periods. In many cases the best compromise between intensity,

resolution and dynamic range requirements is, however, achieved by dividing the beam time between runs with several incoming wavelengths within the useful range.

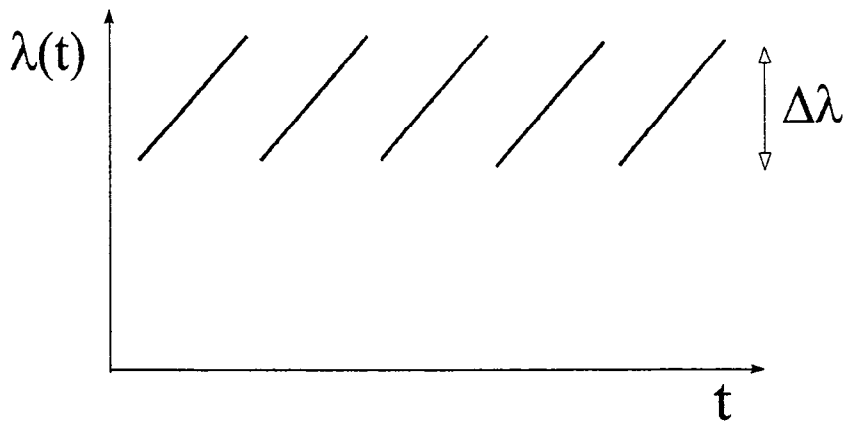

Fig. 1: Time dependence of the wavelength of the monchromatic beam in a TOF monochromator.

The basic idea of the approach of time-of-flight wavelength band monochromatization (TOF-monochromators) is to produce a set of monochromatic wavelengths (within a suitable range) one after the other with an appropriate periodic repetition. A TOF-monochromator provides a monochromatic beam at any instant of time t with a wavelength $\lambda(t)$ and a resolution $\delta\lambda(t)$, with $\lambda(t)$ and $\delta\lambda(t)$ periodically changing in time. Actually $\lambda(t)$ follows a sawtooth pattern within a band $\lambda_{max} - \lambda_{min} = \Delta\lambda$ (Fig. 1). Thus instead of using one single wavelength the measurement is performed with a set of wavelengths stretching over a range $\Delta\lambda$ which is chosen to be fully within the "useful range" so that each wavelength $\lambda(t)$ provides roughly equally useful information. Fig. 2 illustrates how this can be realized with a set of disc choppers [1].On this distance vs. time TOF-diagram the trajectory of an incoming neutron is a straight line with the slope corresponding to the velocity $v = h/m\lambda$.

The essential point is that the TOF monochromator delivers useful neutrons for nearly all the time onto the sample and maintains all the advantages of chopper systems compared to crystals (no higher orders, clean, well defined lineshape without tails, tunable resolution, 100% transmission at the center of the line). The price to be paid for is the more complex data collection (i.e. adding the additional parameter t which labels the various wavelengths $\lambda(t)$ used and combining the information content of data sets corresponding to a set of single wavelength bins $\lambda_1, \lambda_2, ...\lambda_n$). This complexity is, however, rather small compared to state-of-the-art methods in e.g. nuclear physics, and to a large extent well under control on existing spallation souces.

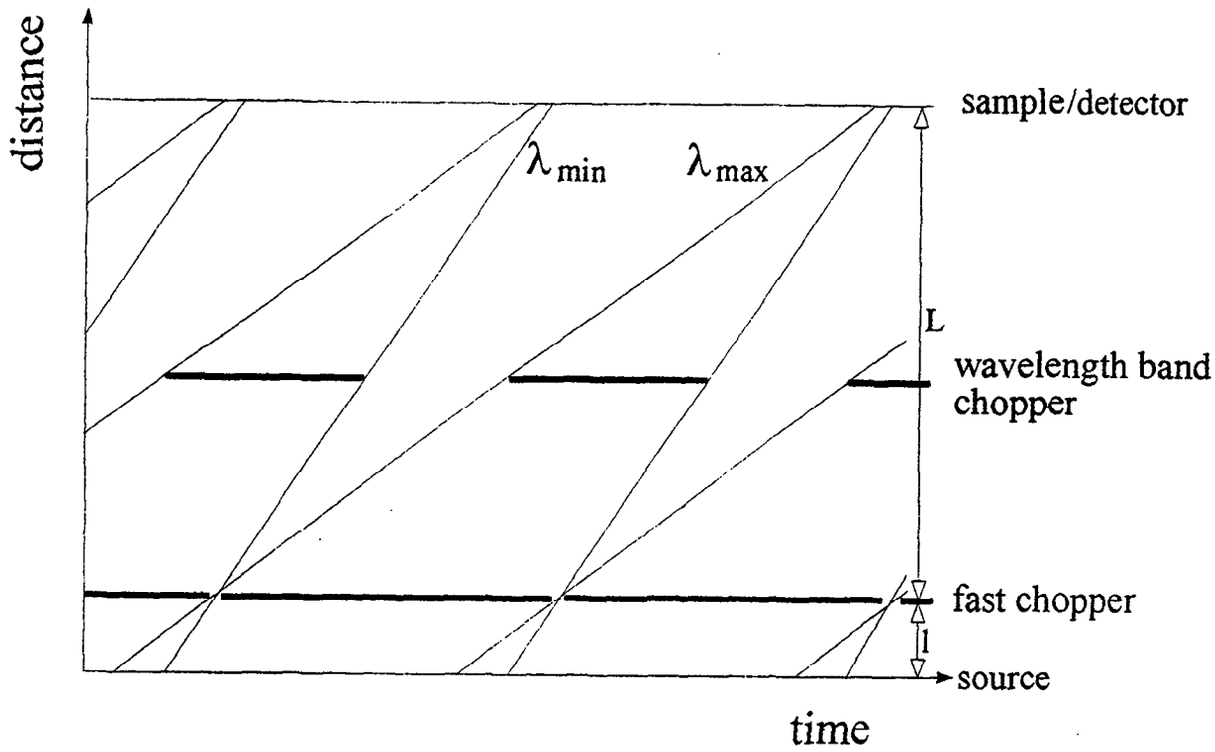

Fig. 2: The principle of TOF monchromators after Ref.[1].

The clue to making the whole wavelength band of a TOF-monochromator uniformly useful is to make it narrow enough. In some cases, e.g. TOF-diffraction as suggested long time ago by Buras [2], this restriction is rather mild since the relevant intensity parameter $\lambda^4\phi(\lambda)$ is flat over a large range of λ (where $\phi(\lambda)$ is the quasi-Maxwellian neutron flux distribution of the moderator). In other cases, such as triple-axis spectroscopy, where one wants to concentrate on a small range of momentum and energy transfer $\vec{q}$ and ω, $\Delta\lambda/\lambda$ might be chosen as small as 10–20%. We will show now, that under the condition of selecting an uniformly useful wavelength band $(\lambda_{min}, \lambda_{max})$ the time averaged flux produced by the TOF monochromator at the sample is equal to that of the CW-monochromator (assuming equal resolution and beam collimations, and neglecting losses such as finite crystal reflectivities, filter absorption etc.) [3]. Indeed:

$$\Phi_{CW} \simeq \phi(\lambda)\delta\lambda \tag{1}$$

and

$$\Phi_{TOF} \simeq c\phi(\lambda)\Delta\lambda \tag{2}$$

where c is the duty factor of the fast chopper in Fig. 2, and it is given as c = δt/t, i.e. the ratio of the chopper opening time δt to the pulse repetition time Δt. On the other hand

$$\delta\lambda = \frac{h}{m}\frac{\delta t}{L}, \qquad \Delta\lambda = \frac{h}{m}\frac{\Delta t}{L} \tag{3}$$

where L is the neutron flight path from the fast chopper to the detector or – in inverted geometry inelastic experiments – to the sample. Thus we find that

$$c = \frac{\delta t}{\Delta t} = \frac{\delta\lambda}{\Delta\lambda} \tag{4}$$

Substituting (4) into (2) and comparing to (1) we get the mean flux (MF) theorem:

$$\Phi_{TOF} = \Phi_{CW} \tag{5}$$

i.e., that the time averaged flux on the sample for the TOF monochromator is the same as that for the conventional CW monochromator of equal resolution (for equal beam collimatimations and neutron transmission efficiencies) if the wavelength band $\Delta\lambda$ is narrow enough.

The second half of the previous sentence is the crux of the matter. Without making the band $\Delta\lambda$ narrow enough, i.e. working with just one fast chopper and making the repetition rate small enough so that there is no frame overlap between the fastest and slowest neutrons from contiguous pulses (as originally proposed by Buras or actually done on short pulse spallation souces) $\delta\lambda$ is not uniformly useful. One reason for this is the strong wavelength dependence of the Maxwellian distribution $\phi(\lambda)$ with eventually the low intensity parts contributing little to the information gathered. Also the strongly λ dependent resolution might limit the usable range. Thus a narrow enough $\Delta\lambda$ is a guarantee to make all of it fully useful, which can be achieved by making L long enough and/or $\Delta\lambda$ short enough. (This latter choice applies to a CW source, where the chopper system can have any repetition rate mechanically feasible.)

The TOF wavelength band monochromator method can also be applied to generalize conventional TOF-inelastic spectroscopy. Here the difference between CW and pulsed operation is that in the first case the repetition rate is freely chosen as required by the secondary (sample to detector) flight-path. In the spirit of the present approach, however, we can run the monochromator system at a lower repetition rate than that of the analyser TOF system, so that we use instead of one a number of wavelengths in the $(\lambda_{min}, \lambda_{max})$ range, cf. Fig. 2. Thus eq. (5) also holds for this case, meaning that in this approach the flux of a chopper spectrometer is independent of the monochromator/source repetition rate. This solves a longstanding problem in spectroscopy on existing short pulse spallation sources, where the TOF spectrometers are running at the same repetition rate as the source, which is much lower than ideal for this kind of work, e.g. 50 Hz instead of 300 Hz. We will discuss this subject in more detail in chapter 4.

In connection with eq.(5) we used the expression "time averaged flux on the sample". Indeed, what matters for the experiments is the number of neutrons actually hitting the sample at a given angular and wavelength resolution within a given beam time, and not the number of neutrons in the core, target, or moderators. Thus this flux is the relevant number for comparing sources and instruments. In applying these arguments to actual SPSS instruments, we usually observe time averaged fluxes on the sample which are in contrast to LPSS much lower than those corresponding to the peak flux of the source as given by eq.(1), because $\Delta\lambda$ (i.e. L is too small cf. eq.(3)) is much too large. In addition with $\delta\lambda$ determined by the source and moderator ensemble, we sometimes have to work with better than necessary wavelength resolution (e.g. in small angle scattering), which can be avoided on CW and LPSS sources.

3. TOF–monochromator for high resolution powder diffraction on CW sources

High resolution powder diffractometry (HRPD) is one of the most successful ways of utilizing short pulse neutron sources. This is partially due to the excellent peak flux and short duration of the epithermal neutron pulses in the slowing down regime. Although the hot neutron flux on the hot source at ILL is proportionally higher with respect to the thermal flux than on a SPSS, no high resolution monochromatization method is known for hot neutrons on a CW source with a comparable efficiency to the shorter than 10 μs pulses of the SPSS. On the other hand, for thermal and cold neutrons both crystal monochromators and disc choppers give quite satisfactory resolutions on CW sources.

The other clue of the success of HRPD on SPSS has nothing to do with the source: It is due to the advantages of the TOF method itself, as early recognized by Buras [2]. In order to illustrate this point, we consider a detailed quantitative comparison of a crystal monochromator and a TOF monochromator instrument on the same thermal moderator of a CW reactor source. The scheme of the two instruments are shown in Fig. 3.

The crystal monochromator HRPD set–up is assumed to work at a fixed wavelength of 1.5 Å at the monchromator take–off angle of 90°, i.e. giving best resolution due to focussing for the lattice spacing d=1.06 Å. The in–pile collimation is 6' FWHM and the 62 detectors span 7.5°–150° scattering angle in steps of 2.5° with a 6' FWHM collimator infront of each detector. The width of each collimator was assumed to be sufficient to see the whole sample volume. The detectors are 20 cm high and installed at a distance of 1.5 m from the sample. The monochromator has a Gaussian mosaic distribution of 10' FWHM. A natural collimation of 40' FWHM was assumed between monochromator and sample as defined by the beam width and the distance. No losses have been assumed, i.e. the peak transmission of the collimator, the peak reflectivity of the monochromator, the transmission of the higher order filter and the efficiency of the detectors have been taken as 100%. The vertical collimation of the beam impinging on the sample was assumed to be the same as that of the neutron guide of the

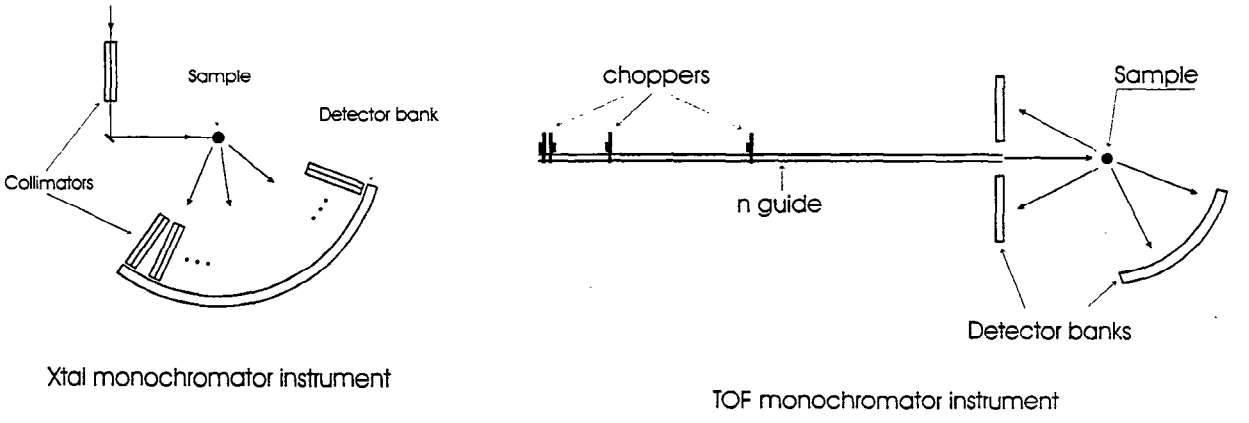

Fig. 3: Layout of a crystal (left) and a TOF monochromator high resolution powder diffractometer.

TOF instrument specified below, i.e. no vertically curved monochromator assembly has been assumed. We shall discuss this point later.

The TOF monochromator instrument has the following parameters: The pulse length of the counterrotating pair of choppers is 10 μsec, which is achievable for a beam width of 1 cm. The neutron guide follows the "eye–of–the–needle" principle [1] with a beam width of 1 cm at the the entrance and a width of 2 cm towards the sample and for most of its length. The length of the guide is 16 m and it stops 2 m before the sample position. The two single choppers determine the wavelength band which has been choosen to be 1.5–5 Å. At a repetition rate of 50 Hz this implies 12% dead time between successive frames. The detectors are 1.25 cm thick, with an efficiency of 70% at 1 Å. They form banks with a horizontal resolution of 1.25 cm and a hight of 20 cm. (Low resolution banana detectors could be an alternative.) Two banks on top of each other are placed on both sides of the incoming beam in order to cover the scattering angle range of 157°–175°. A third bank covers the low angle range from 15° to 60°. The sample is contained in a flat slab perpendicular to the incoming beam, 0.4 mm thick, 2 mm wide and 10 cm high. No collimators are used, the precision of the scattering angles is determined by the geometry of the set–up.

In Fig. 4 the resolutions for the determination of lattice spacings d and the relative intensities of the two instruments are compared as functions of d. The results were obtained by a complete Monte–Carlo simulation using the above instrumental parameters and the Maxwellian spectrum of thermal neutrons. The dashed lines for the TOF instrument indicate the behaviour for other wavelength bands obtained by shifting the phasing of the third and fourth chopper, e.g. 6.5–10 Å in order to explore

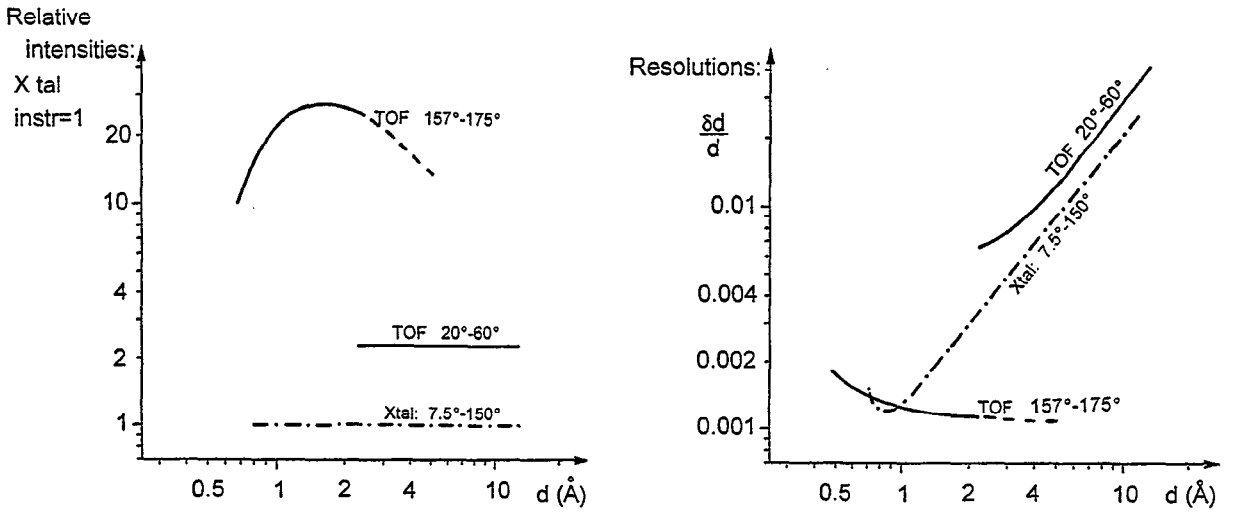

Fig. 4: Comparison of the intensity of the reflections (left) and the resolution as a function of the d–spacing for the crystal and TOF monochromator instruments described in the text.

d spacings in the range of 3.25–5 Å with high resolution. (On the Xtal instrument this would require a change of the monochromator in order to obtain an incoming wavelength of about 5 Å.)

The reason why the intensity offered by the TOF monochromator approach is about an order of magnitude superior can be understood by the following simplified reasoning: The same resolution requires a cruder beam collimation at both, higher scattering angles and longer neutron wavelengths. Therefore it is advantageous to use several wavelengths, since for all reflections data are collected under the best conditions, as opposed to the single wavelength monochromator method which would only allow for the use of the nearly backscattering geometry for an extremely narrow d range (some 2%), compared to 0.75–2.5 Å for TOF. For a given Bragg reflection we have a detector solid angle of 0.16 sterad with a duty factor of $10\mu s/20ms = 0.5 \times 10^{-3}$ with TOF, while the crystal instrument only offers a detector solid angle of 2×10^{-4} sterad with a duty factor of 4% (due to the necessity to scan the detector bank over the 2.5° gap between neighbouring detectors covering 0.1° each).

The intensity offered by the monochromator instrument can normally be improved by using a curved monochromator focussed to the sample. Compared to a flat monochromator without a guide the gain in incoming flux for a small sample (not higher than 2-3 cm) can optimally amount to a factor of 5. However, compared with a TOF monochromator, this gain is largely offset by the finite transmission of the collimators and the higher order filter and the finite reflectivity of the monochromator crystal. In addition by using guides coated with supermirrors on the top and on the bottom or with a vertically converging section in front of the sample some vertical focussing can also be achieved with TOF monochromators, which reach namely some 1° vertical divergence at 2 Å and more at higher wavelengths. Thus, the more

efficient vertical beam focussing capability of crystal monochromators on the whole compensates for the higher instrumental losses in this approach compared to the TOF method. This is why in the above comparison both vertical focussing and beam losses were ignored.

4. Repetition rate multiplication and constant $\vec{q}$ TOF spectroscopy

We will now consider in some detail how the main aspects of the TOF monochromator concept can also be applied to IN5 type multichopper TOF spectrometers [4]. The key idea of the TOF-monochromator approach is that the same information can be obtained by using not only a single incoming wavelength, but a set of eventually close wavelengths $\lambda_2 ... \lambda_n$ and combining the information obtained afterwards. Adding a fast chopper to the TOF monochromator set-up just infront of the sample with a repetition rate properly chosen for the TOF energy analysis in the secondary spectrometer and running synchronously with the TOF-monochromator, (i.e. with a frequency being an integer multiple of the that of the monochromator system) we get a set of short pulses with wavelengths $\lambda_1, \lambda_2, ... \lambda_n$, cf. Fig. 5. With each of these wavelengths we obtain a complete TOF spectrum of the sample, and the n spectra will carry essentially identical information if the total wavelength band $\lambda_n - \lambda_1$ is narrow, or eventually – and actually quite often – an improved data collection rate by extending the dynamic range of the data if $\lambda_n - \lambda_1$ is chosen to be substantial. Thus we can also formulate the mean-flux theorem eq. (5) for this case as follows: the mean flux on the sample in a TOF spectrometer of any repetion rate ν installed on a TOF monochromator with a repetition rate $\nu/$n (where n is an integer) is independent of n as long as the wavelength band $\lambda_n - \lambda_1$ is narrow enough

$$\Phi^{(\nu)} = \Phi_{TOF}^{(\nu/n)} \tag{6}$$

This TOF-monochromator – TOF secondary spectrometer combination also offers another new possibility: constant $\vec{q}$ scans on single crystal samples in a single run using TOF technique only, a problem which was deemed to be unsolvable. Instead of phasing the fast chopper in front of the sample to the TOF monochromator system we let it run asynchronously, so that we get TOF spectra with a quasi continuous set of incoming wavelengths (reasonably binned according to the resolution) within the $\Delta\lambda$ wavelength band. The thus obtained 2 dimensional data set $I(\lambda_{in}, \lambda_{out})$ contains many constant $\vec{q}$ energy spectra in an exended 2 dimensional (with detectors covering a large vertical angular range, as usual, 3 dimensional) $\vec{q}$ domain (cf. Fig. 6). The method is mechanically simpler than the TOF monochromator TAS approach described elsewhere [5], although in principle it provides inferior data rates if a single or a small number a constant $\vec{q}$ scans are required due to the additional duty factor loss by the sample-end chopper. This disadvantage could be partially compensated for by the larger solid angles attainable with TOF and by having no reflectivity losses and higher order reflections in the analyser system.

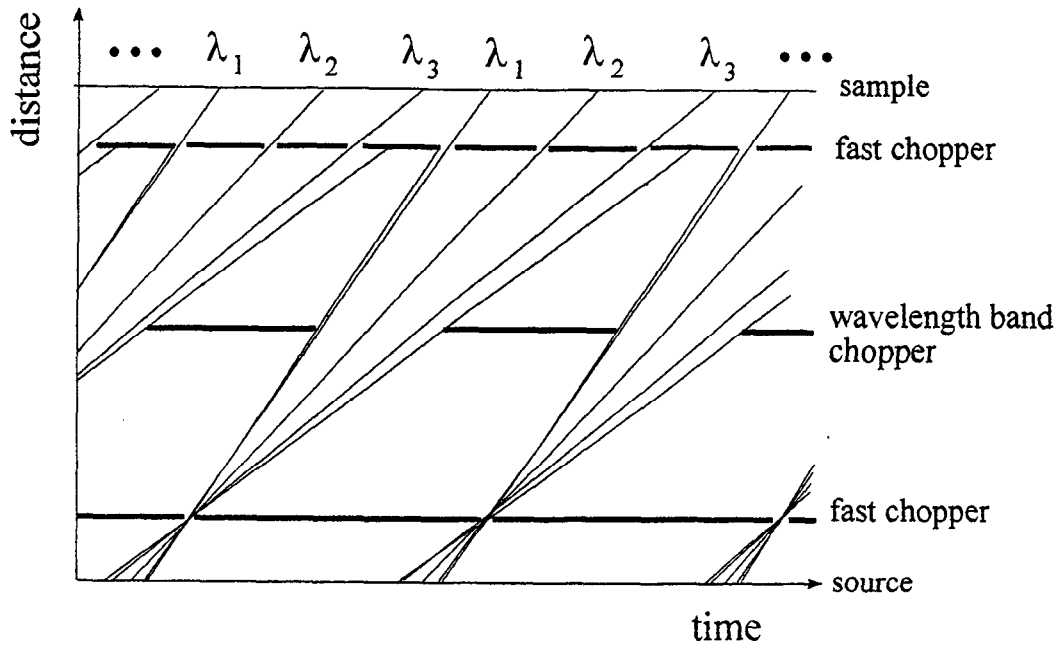

Fig. 5: Principle of TOF monochromator – TOF analyser inelastic spectroscopy with repetition rate multiplication [4].

In order to illustrate the main point of the present approach, i.e. the efficient combination of information obtained with different incoming wavelengths, a model example has been numerically evaluated and the results are shown in Fig. 7. A TOF spectrometer is considered here with a chopper system of the type shown in Fig. 5. The goal of the assumed experiment is to determine the linewidth Γ of quasielastic Lorentzian lines. The continuous line in the Fig. 7. shows the relative statistical error of the determination of Γ obtained in a given measuring time as a function of the ratio of Γ and the width Δ of the triangular resolution function of the chopper system at a chosen reference wavelength λ=2.5 Å, assuming that the two fast choppers in Fig. 5. run at the same repetition rate, i.e. single wavelength conventional operation. The best precision within a given measuring time is obtained at around $\Gamma \simeq 2.7\Delta$, an understandable conclusion. The two dashed curves shows the relative error of Γ obtained by combining (taking the error weighted average of) the Γ values obtained during the same measuring time with the fast chopper near to the source operating at 5 times lower repetition rate (but with the same pulse length), i.e. by taking 5 TOF spectra at 5 different wavelengths. Explicitely these 5 wavelengths were assumed to be 1.5, 2, 2.5, 3 and 3.5 Å. The intensity distribution across these wavelengths was assumed to correspond to a thermal moderator with the peak at 1 Å. The $\delta\Theta$ = const case corresponds to using equal collimations for all wavelengths, in which case the incoming beam intensity changes by a factor of 26 between 1.5 and 3.5 Å. Note, that the information obtained at 3.5 Å is still relevant at small Γ values. In contrast, if

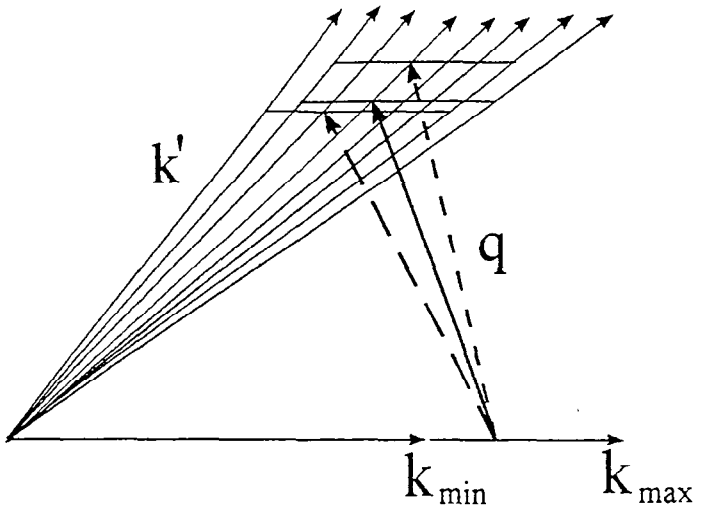

Fig. 6. Constant q scans on a TOF monochromator – TOF analyser inelastic spectrometer. The horizontal bars at the end of the q vectors and equal to the incoming k band represent the constant q cuts across the quasi–continuous set of TOF data at various fixed angle detectors.

constant q resolution is aimed at, a supermirror neutron guide can be envisaged for the incoming beam, and the a matching horizontal angular resolution can be achieved on the detector side by adding the spectra of more or less individual detectors. In this δq = const case (cf. Fig. 7) the incoming flux ratio between 1.5 and 3.5 Å is only 2. The spectrometer resolution in both cases, however, varies by a factor of 13 between the two extreme wavelengths, assuming constant chopper pulse lengths. The results in Fig. 7 clearly show, that the data collection rate on the whole is the same for all 3 cases and that, in contrast to the conventional wisdom, data taken for the same time with very different intensities and resolutions can in a very meaningful way be combined by using proper information processing. (Actually the δq = const curve shows the best characteristics in view of the smaller variation of the precision over a broad range of Γ values.) From the point of view of the time-of-flight wavelength band monochromator concept the fundamental conclusion from Fig. 7. is that quite different wavelengths can be included in a "useful" wavelengths band, which leaves us with a substantial flexibility.

This kind of repetition rate multiplying TOF-spectroscopy offers a new opportunity for the usual short pulse spallation sources too. It allows one to make optimal use of the source flux by being able to use a pulse repetition rate on the sample corresponding to the one optimal for the secondary spectromter, i.e. to the flight path

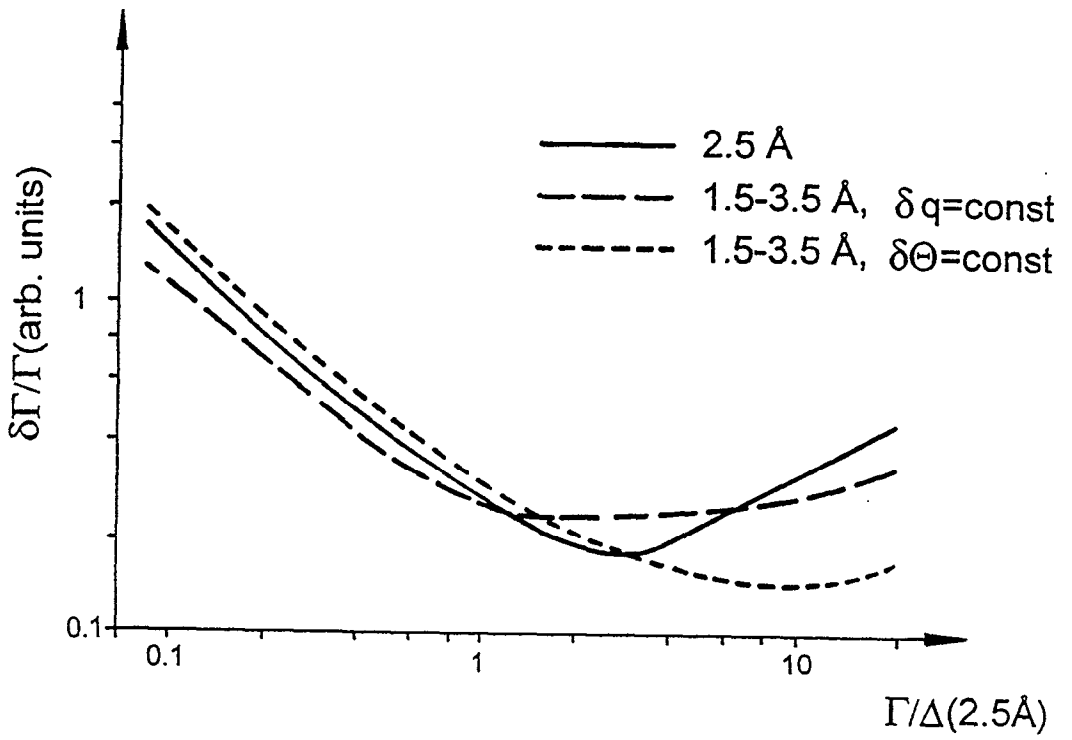

Fig. 7. Comparison of the data collection rates — as characterized by the error of the determination of quasielastic linewidts within a given measuring time — by the use of a single wavelength (continuous line) and five different wavelengths within the limits shown (see text).

of the scattered neutron, as usual on a CW source. The flux gain compared to the conventional use of TOF spectroscopy on SPSS will reach a factor of 5 - 10 in many cases, e.g. by running a spectrometer at 300 Hz on a 30 Hz source.

5. Producing short pulses: SPSS vs. choppers on LPSS

In the slowing down regime, i.e. for hot neutrons the time averaged luminosity of the moderators is to a large extent independent of the type of monochromator: coupled or decoupled, poisoned or not etc. [6]. In this regime the integrated intensity per pulse only depends on the energy per pulse. Thus typical neutron pulse lengths of 10 μs (or less) for sub μs proton pulses mean some 100 times higher peak flux than for an equal energy 1 ms proton pulse. We have to take into account however, that if one works with a linac and a proton storage ring for pulse compression from about 1 ms to 1 μsec, the linac beam chopping necessary for the injection and the injection losses themselves lead to an energy per pulse for the storage ring of about 1.5–1.8 smaller than the one the same linac would produce. Furthermore, if the additional costs for a

H^- source (also necessary for injection) instead of H^+, for the beam chopping device, for the beam preparation for injection, for the ring accelerators and for the two target stations instead of the one sufficient on an LPSS (due to the longer source to instrument distances) are used to build a linac and a long pulse target station of higher power, we will end up with a LPSS of about 4 times higher average power than the more powerful target station of a SPSS of equal costs. This would likely also apply for a 5 MW SPSS vs. a 20 MW LPSS. Thus we can conclude that for a pair of cost–equivalent SPSS and LPSS the peak flux of the epithermal neutron pulses of the SPSS exceeds by a factor of about 25 at low epithermal energies (and more at higher ones) the peak flux of the LPSS. In addition 10 μs FWHM is about the shortest pulse length choppers can produce, so for this neutron energy range the SPSS is clearly superior with respect to both flux and resolution.

The situation is drastically different for moderated (cold or thermal) neutrons. In this range the neutron pulse length on a SPSS becomes dramatically longer due to the moderation time, and the average brightness becomes strongly dependent on the type of moderator and reflector choosen [6]. The integrated neutron flux per pulse increases with the moderator pulse length in a way similar to variable pulse length choppers, and for slow (high intensity) moderators it is typically an order of magnitude higher than for fast (high resolution) ones. With moderation times for high intensity moderators being around 0.5 ms, or more, the peak flux gain achieved by compressing the proton pulse length fom 1 ms to a 1 μs is marginal, and more than off–set by the lower power available at the same costs. Thus the investment in making the proton pulses shorter is counterproductive for cold neutrons, it is more cost effective to produce short cold neutron pulses by choppers on LPSS than by SPSS. In addition, choppers can produce considerable shorter long wavelength pulses than the about 100 μs minimum achievable with tailored moderators. Thus for cold neutrons a LPSS source provides pulses with both superior peak intensity and superior resolution compared to a cost equivalent SPSS.

For thermal neutrons (10 to 100meV) the situation is basically similar to that of cold neutrons, but somewhat more favourable for the SPSS in view of the shorter moderation times. The difference might however be rather small, since time constants in efficient reflectors for thermal neutron production are not much shorter than those for cold neutrons [6]. Although this case has to be studied more in detail, one can expect the peak thermal fluxes to come out about equal for the above defined cost–equivalent LPSS and SPSS sources. The greater flexibility of disc chopper systems, their more favourable lineshape and the higher resolution (shorter pulse lengths) they offer are, however, a clear advantage for the LPSS approach in the production of short thermal neutron pulses, too. (Note that with the exception of TOF inelastic spectroscopy without repetition rate multiplication, chopper systems cannot efficiently be used on SPSS for reducing the neutron pulse lengths).

6. Conlcusion

In comparing the performance of a long pulse spallation source (LPSS) to a complementary pair a CW reactor and a usual short pulse spallation source (SPSS) one finds that: a) LPSS reproduce the utilization characteristics of CW reactors in neutron scattering applications with a LPSS providing time averaged fluxes on the sample which is about 4–8 times superior to that of a cost–equivalent reactor. This opens up the way to emulate by LPSS reactor sources with a flux 20–40 times superior to that of ILL. b) For the production of short neutron pulses a LPSS equipped with disc chopper systems (TOF monochromators) offers both superior peak flux and better resolution for cold neutrons, and equivalent peak flux and superior resolution for thermal neutrons compared to a cost–equivalent SPSS. In contrast in the slowing down regime (hot neutrons) the SPSS is clearly superior to the LPSS in both peak flux and resolution. Points a) and b) amount to conclude that for some 75 % of the neutron scattering work as practiced today the LPSS approach provides the most efficient source and the remaining 25 % is best served by SPSS.

7. References

[1] F. Mezei, Proc. ICANS XII (Rutherford Appleton Lab, 1994) p. I–377.

[2] B. Buras, AEC–ENEA Seminar, Santa Fe, New Mexico (1967); G.E. Bacon, Neutron Diffraction (Oxford, Clarendon Press, 1975), p. 144.

[3] F. Mezei, Neutron News, Vol. **5** issue 3 (1994) p. 2.

[4] F. Mezei, in press.

[5] Proceedings of a workshop on a 1 MW Long Pulse Spallation Source, April 1995 (Lawrence Berkeley National Laboratory).

[6] See G.J. Russell, E.J. Pitcher and P.D. Ferguson, in this proceedings.

Experiments

ICANS-XIII
13th Meeting of the International Collaboration on
Advanced Neutron Sources
October 11-14, 1995
Paul Scherrer Institut, 5232 Villigen PSI, Switzerland

List of Authors

Aksenov V.L.	S-4, I-2, I-11, I-17, N-5
Appleton, B.R.	P-6
Arai, M.	S-1
Arakawa, D.	A-6
Astakhov, Yu.A.	I-15
Balagurov, A.M.	I-2, I-17
Bauer, G.S.	L-3, T-12, T-13, T-17, T-19, A-8
Belushkin, A.V.	I-8
Beynon, T.D.	T-10
Boenig, H. J.	I-25
Bogdzel, A.A.	I-15
Böni, P.	I-22, I-27
Böttger, G.	I-23
Broome, T.A.	S-6, T-10, T-18
Brown, B.S.	N-2
Bryant, P.	P-8
Bucknall, D.G.	I-5
Bugg, W.	P-10
Camus, E.	T-26
Carpenter, J.M.	G-1, I-12, T-25, P-1
Catherall, R.	T-15
Chae, Y.-C.	A-9, P-2
Chernyshov, D.Yu.	I-20
Chiba, S.	T-2
Cho, Y.	A-9, P-2
Clemens, D.	I-22, I-27
Cohn, H.	P-10
Condo, G.	P-10
Conrad, H.	S-10, L-4
Crawford, R. K.	I-3
Crosbie, E.	A-9, P-2
Cser, L.	S-2, I-21
Daemen, L.	I-26, L-2, L-7
Dai, Y.	T-16
Dementyev, A.V.	T-1, T-4
Dickinson, E	I-5
Dölling, R.	A-4
Dönni, A.	I-23
Drumm, P.	T-15
Eckert, J.	L-7
Efremenko, Yu.	P-10
Ehrat, J.	T-24
Engels, R.	I-24
Epperson, J. E.	I-3
Evensen, A.	T-15
Eyssa, Y. M.	I-25
Faltens, A.	A-8
Ferguson, P.	L-1, T-7, T-8
Filges, D.	S-5, T-11
Firjahn-Andersch, A.	A-5
Fischer, P.	I-23
Fischer, S.	I-23
Fischer, W.E.	N-7
Fitzsimmons, M. R.	L-6
Fletcher, P	I-5
Friedsam, H.	A-9, P-2
Furusaka, M.	T-20, T-21, T-22, P-9
Geick, R.	I-6, I-13
Glazkov, V.P.	I-2
Grimm, H.	I-13
Grimmer, H.	I-22

Gross, P. A-4
Guttek, B. T-9
Hagen, M. I-9
Hahn, W. I-27
Harkay, K. A-9, P-2
Harnmonds, John P. G-1
Hempelmann, R. I-7
Higgins, JS I-5
Hiismäki, P. I-16, I-17
Hiraga, F. T-22
Hjelm, Rex P. S-8, I-26, L-5
Holitzner, L. I-7
Horan, D. A-9, P-2
Horisberger, M. I-23, I-27
Ignatiev, S.V. T-6
Ikeda, H. N-4, P-9
Ishibashi, K. T-2
Iwasa, H. T-20, T-22
Jansen, E. I-1, I-24
Janssen, S. I-7
Jason, A.J. A-1
Jones, R.A.L I-5
Jonsson, O. T-15
Kamyshkov, Yu. P-10
Kazimirov, V.Yu. I-8
Kim, S. P-2
Kishiro, J. A-6
Kiyanagi, Y. T-20, T-21, T-22
Kleb, R. I-3
Klein, H. A-3, A-4
Koch, M. I-23
Kockelmann, W. I-1
Kolesov, V.F. T-3
Konovalov, I.I. T-4
Kosugi, N. T-20, T-22
Kravchuk, L.V. A-2
Kugler, E. T-15
Kustom, R.L. A-7, A-8, A-9, P-2
Lakatos, A. A-3
Lamoreaux, S. P-10
Leach, D. I-3
Lebedev, S.G. T-1
Lee, Y.Y. P-4
Lengeler, H. P-7
Lessner, E. A-9
Lessner, E. P-2
Lettry, J. T-15
Levchanovsky, F.V. I-15
Likhachev, Y.N. T-3
Lillie, R. P-10
Lucas, A.T. T-19
Ludewig, H. P-5
Maaser, A. A-3
Macek, R. J. N-3
Madlung, J. A-5
Maehata, K. T-2
Martin, S. A-7, A-8
Maslov, A.A. T-4
Matsufuji, N. T-2
McDowell, W. A-9, P-2
McEwen, Keith I-10
McGhee, D. A-9, P-2
Meads, P.F. A-7, A-8
Medarde, M. I-23
Meigo, S. T-2
Mesot, J. I-7
Mezei, F. L-8
Michaelis, B. I-15
Mills, F. P-2
Miroshnichenko, V.G. T-3, T-4
Moe, H. A-9, P-2
Muhrer, G. T-5

Müller, K.D. I-24
Nakamoto, T. T-2
Naumov, I.V. I-2
Neef, R D. T-11
Nielsen, R. A-9, P-2
Nikitenko, Yu.V. I-11
Ninaus, W. T-5
Norek, G. A-9, P-2
North, Mark T. T-17
Novozhilov, V.E. I-15
Numajiri, M. T-2
Obert, J. T-15
Ogawa, Y. T-20, T-22
Olah, Glenn A. L-5
Ostrovnoy, A.I. I-15
Pankratov, D.V. T-6
Penfold, J I-5
Peterson, K.J. A-9, P-2
Petrillo, C. I-9
Picton, D.J. T-10
Pitcher, Eric L-1, T-7, T-8
Plasil, F. P-10
Platonov, S.L. I-2
Powell, J. P-5
Pozimski, J. A-4
Prager, M. I-7
Priesmeyer, H.G. I-18
Prikhodko, V.I. I-15
Primdahl, K. A-9, P-2
Putaux, J.C. T-15
Pynn, R. L-2, L-6, L-7, P-3
Qian, Y.L. A-9
Raman, S. P-10
Rauchas, A. P-2
Ravn, H. T-15
Reidelbach, K. A-4
Reinartz, R. I-24
Rennich, M. P-10
Rennie, A I-5
Rezaev, V.E. I-15
Richardson, RM I-5
Richter, D. I-7
Robinson, R. A. I-25
Rogov, A.D. T-4
Rosenfeld, J.H. T-17
Roser, S I-5
Ruggiero, A.G. A-8, P-4
Russell, G.J. S-9, L-1, T-7, T-8
Sacchetti, F. I-9
Sarraf, D. B. T-17
Sauvage, J. T-15
Savenko, B.N. I-2
Schaal, H. T-11
Schachinger, E. T-5
Schäfer, W. I-1, I-24
Schefer, J. I-23
Schempp, A. A-5
Schmidt, W. I-6, I-13
Schneider-Muntau, H. J. I-25
Schubert-Bischoff, P. I-27
Schuster, M. P-8
Seeger, P.A. S-7, I-14, I-26, L-1, L-5, L-7
Serdyuk, I. I-4
Shabalin, E.P. T-3
Sheptyakov, D.V. I-2
Shigyo, N. T-2
Shmakov, K. P-10
Sidorkin, S.F. T-3, T-4
Sirotin, A.P. I-15
Skala, K. T-13
Smirnova, O.N. T-1

Smith, B. L. T-14
Sobolevsky, N.M. T-1, T-4
Somenkov, V.A. I-2
Someya, H. A-6
Staub, U. I-23
Stavissky, Yu.Ya. T-1, T-3, T-4, N-6
Steigenberger, U. S-3, I-9, I-10
Stendal, K. T-23
Strain, R. V. T-25
Sukhomlinov, G.A. I-15
Sulfredge, C.D. T-19
Symon, K. P-2
Syrykh, G.F. I-2
Takada, H. T-2, T-17
Taylor, A. N-1
Thelliez, T. I-26
Thiyagarajan, P. I-3
Thomas, R.K. I-5
Thompson, K. A-9, P-2
Thut, R. I-23
Tietze-Jaensch, H. I-1, I-6, I-13
Todosow, M. P-5
Toulemonde, M. T-15
Tretyakov, I.T. T-4
Trounov, V. A. I-17, I-19
Trouw, F. I-3
Trushkin, V.I. T-4
Van Steenbergen, A. P-4
Van Swygenhoven, H. I-22
Vananti, A. I-27
Volk, K. A-3
Volkov, Yu.A. I-15
Wagner, W. T-24
Wakuta, Y. T-2
Wanderka, N. T-26
Watanabe, Y. T-2, T-20, T-21, T-22
Weber, M. A-3
Webster, J.R.P. I-5
Weinacht, D. P-3
Weng, W.T. P-4
White, M. A-9, P-2
Will, G. I-1, I-6, I-13, I-24
Wilson, R. P-10
Wollenberger, H. T-26
Wozniak, D I-3
Yamane, I. A-6
Yefimov, E.I. T-6
Young, G. P-10
Zaplatine, E. A-7, A-8
Zarbakhsh, A I-5
Ziegler, K. A-7, A-8

ICANS-XIII
13th Meeting of the International Collaboration on
Advanced Neutron Sources
October 11-14, 1995
Paul Scherrer Institut, 5232 Villigen PSI, Switzerland

List of Keywords

0.5 and 1.5 GeV	T-2
Accelerator	P-9, A-9, P-2
Accelerator design	I-12
Accelerator Ring	P-4
Activated inserts	T-24
Anvil	I-2
Argonne	P-1, T-25
AUSTRON Project	P-8, T-5
Beam port inserts	T-24
Beam transport	A-4
CERN-ISOLDE	T-15
Charge redistribution	A-4
Cold moderator	T-19
Cold moderator handling	T-24
Cold neutrons	T-20, T-22
Collimation	I-3
Complementarity	L-8
Composite	I-23
Composite Reflector	L-1
Conceptual design and R&D	P-6
Cooling	T-17
Corrosion	T-4
Coupled Moderator	L-1
Cryogenic moderator	T-21
Data acquisition	I-15, I-24
Data treatment	I-12
Deconvolution	I-12
Differential gain	L-4
Diffraction	I-16, I-19
Direct methods	I-4
Dual beam irradiation	T-26
Electron dumping system	A-3
Electronics	I-15
Emittance growth	A-4
Energy deposition	T-1

ESS T-9, T-10
ESS-Targets T-11
Experiment P-10
Extraction system A-3
Fermi Chopper I-7
FFAG Accelerator A-8
Figure of Merit L-2
Fissile target T-3
Fixed-Field A-7
Focusing I-7, P-10
Fourier I-16
Frequency Modulation A-7
Germanium I-23
Glass I-22
H^--linear accelerator P-7
Handling devices T-24
Heat pipe T-17
Helium cooling T-9
High current emittance measurements device A-3
High intensity moderator L-4
High pressure I-2
High-current low-energy beams A-5
High-Engery Protons T-6
History G-1
ICANS G-1
Inelastic scattering I-8
Instrument I-3, I-14, I-26, N-1, L-3
Instrumentation N-5
Intense Beams A-7
Intensity T-20
International cooperation P-6
Introduction Linacs A-8
Inverse geometry I-8
Ion source A-3
ISIS T-18, N-1
LANSCE A-1, T-8
LANSCE Upgrade Project N-3
Lead Fluoride Reflector P-5
Linac A-1
Linear detectors I-24

Liquid hydrogen	T-8, T-20, T-22
Liquid Metal	T-12, T-15, T-17
Liquid metal coolant	T-3
Liquid target	T-13
Long Pulse	L-3, L-5, A-1
Long pulse source	L-4, L-8
Long Pulse Spallation Source	L-1, L-2, P-3
Macromolecules	I-4
MCLIB	I-14, I-26, L-1, L-5, L-6
Meetings	G-1
Mercury	T-12, T-13
Metallurgy	T-25
Methane	T-19
Moderator	S-1, P-9, P-10, T-7, T-8, T-5, T-10, T-18
Monochromators	I-23
Monte Carlo	I-14, I-26, T-1, L-5
Multiplexing	L-3
Networks	I-15
Neutron	I-19
Neutron diffraction	I-23
Neutron guide	I-22
Neutron Pulse	T-5
Neutron Scattering	I-4
Neutron Source	P-8, L-6
Neutron spectrum	T-2
Neutron yield	T-1
NMTC/JAERI	T-2
Oscillation	P-10
Particle Bed Target	P-5
PC-system	I-24
Pellets	T-19
Performance	L-6
Phase error	I-20
Phonons	I-16
Polarization	I-21
Polarizer	I-27
Pole-figure scanning	I-1
Powder diffraction	L-8
Pressure waves	T-13
Proceedings	G-1

Proton A-9, P-2
Proton Accumulator ring P-7
Pseudo statistical modulation I-21
Pulse broadening I-12
Pulse length P-5
Pulse pauses A-5
Pulse Shape L-2
Pulsed Neutron T-20, T-21, T-22
Pulsed Neutron Source P-1
Pulsed reactor N-5
Pulsed Spallation Source N-1
Radiation effects T-19
Radioactive Halogens T-6
Reflectometry L-6
Reflector S-1, T-7
Resolution function I-13
Reverse TOF I-16
RFQ accelerators A-5
Ring-Accelerator A-7
ROTAX I-1
Roughness I-22
RTOF I-20
Sample absorption I-20
SANS L-4, L-5
Science N-1
Shock-waves T-15
Short pulses T-22
Simulation I-14, I-26, T-11, L-5
SINQ I-7, N-7
Small-angle I-3
Solenoid lenses A-4
Solubility T-12
Space charge compensation A-4
Spallation T-10, T-11
Spallation neutron P-9
Spallation neutron source P-6, P-7, P-8, T-5
Spallation Target T-17
Steels T-26
Stress T-13
Structure material T-26

Structure properties	I-19
Superconducting Linac	P-4
Supermirror	I-22, I-27
Supply system for Cold Neutron Sources	T-23
Synchrotron	A-9, P-2
Synchrotron Ring	P-4
Tantalum	T-9
Target	S-1, T-1, T-4, T-6, T-7, T-9, T-10, T-15, P-1, T-18, T-25
Target material	T-26
Target-System	S-1, T-7
Targets for Spallation Sources	P-7
Texture diffratometer	I-1
Thermal shock	T-3
Time of flight	L-3, I-2, I-13
Time of flight and unfolding technique	T-2
Time-of-flight Spectrometer	I-7
TOF spectroscopy	L-8
TOF-diffraction	I-1, I-24,
Triple-axis	I-13
Tungsten	T-4, T-6
Two beam RFQ	A-5
Upgrade	P-1
Uranium	T-4, T-25
User Interface	I-26
Vapour Pressure	T-12
Water	T-8
Water cooling	T-9
Workstations	I-15
Yields	T-6

PAUL SCHERRER INSTITUT

Paul Scherrer Institut
CH-5232 Villigen PSI

Phone 056 310 21 11
Fax 056 310 21 99